Synthesis and Characterization of Mixed-Metal Germanates

A thesis submitted for the degree of Doctor of Philosophy to the Division of Mathematical, Physical and Life Sciences at the University of Oxford

Diming Xu

Somerville College

Michaelmas Term 2017

Michaelmas Term 2017

Synthesis and Characterisation of Mixed-Metal Germanates

Diming Xu
Somerville College

A thesis submitted for the degree of Doctor of Philosophy to the Division of Mathematics, Physical and Life Sciences at the University of Oxford

Abstract

Mixed-metal germanates with the general formula $ABB'Ge_4O_{12}$ have been synthesised using the ceramic method and their properties characterised by X-ray diffraction, neutron diffraction, dc and ac magnetometry, specific heat and Mossbauer spectroscopy. DFT calculations were conducted on two compounds $ZrM_2Ge_4O_{12}$ (*M* = Mn, Co). All compositions adopt a tetragonal structure (space group *P*4/*nbm* with the unit-cell parameters $a = b \sim 2c$). The cation *A* occupies the 2*b* site and is coordinated by eight oxide ions at the corners of a square antiprism whereas *B* and *B*' are disordered over the 4*f* site which is at the centre of a distorted octahedron of oxide ions. They can be considered to lie in layers perpendicular to the [001] axis. These layers are separated from each other by layers containing $[Ge_4O_{12}]^{8-}$ rings, each ring being comprised of four vertex-sharing GeO_4 tetrahedra.

$CeMn_{2-x}Co_xGe_4O_{12}$ (x = 0.0, 0.5, 1.0, 1.5, and 2.0) become anti-ferromagnetic (x = 0.0, 1.5, 2.0) or weakly ferromagnetic (x = 0.5, 1.0) at $4.2 \leq T \leq 7.6$ K. The ordered moments lie along [001] when x = 0.0 and in the (001) plane otherwise. The unit cell doubles along [001] when x = 1.5 and 2.0, but the doubling is lost when a first-order metamagnetic transition occurs on the application of a 10 kOe magnetic field. The ordered moments at 1.6 K for x = 0.0 and 2.0 are 4.61(2) and 2.58(2) μ_B, respectively; the corresponding effective moments in the paramagnetic phase are 5.91 and 5.36 μ_B. $CeM_{1.5}M'_{0.5}Ge_4O_{12}$ (*M* = Mn, Co; *M'* = Zn, Ni, Cu) show similar magnetic properties as $CeM_2Ge_4O_{12}$ albeit with changes in the Néel temperature and Weiss constant due to the differences between the cations used.

$ZrMn_{2-x}Co_xGe_4O_{12}$ (x = 0.0, 0.5, 1.0, 1.5, and 2.0) show long-range magnetic order with transition temperatures, T_C, in the range $2 \leq T_C/K \leq 10$. The underlying magnetic structure is the same in each case but the ordered spins lie along [001] when x = 0.0 and in the (001) plane for all other compositions. In all cases the magnetically-ordered phase is a weak ferromagnet although the magnitude of the spontaneous magnetisation and the strength of the coercive field are composition-dependent. The magnetic structure can be rationalized by considering the strengths of the interactions along the distinct *M*–O–Ge–O–*M* superexchange pathways in the crystal and the observed magnetic structure is entirely consistent with the predictions of *ab* initio calculations.

$LnFeMGe_4O_{12}$ (*Ln* = Y, Eu, Gd, Lu; *M* = Mn, Zn) show long-range antiferromagnetic order with transition temperatures $15 \leq T_N/K \leq 30$. The magnetic structure is the same in each case and consists of an A-type ordering of (001) planes; the ordered spins lie in the (001) plane. Comparison with isostructural compounds leads to the conclusion that subtle structural changes play a greater role than the electronic configuration of the cation in determining the magnetic structure.

$Ln_2MGe_4O_{12}$ (*Ln* = Gd-Yb; *M* = Ca, Mn, Co) and $LnBCoGe_4O_{12}$ (*B* = Sc or Lu) show various magnetic behaviours. The calcium-, holmium- and erbium-containing compositions remain paramagnetic down to 2 K; the other cases show a transition at the temperatures ~ 4 K. $Dy_2CoGe_4O_{12}$ and $DyScCoGe_4O_{12}$ behave as spin glasses and the terbium- and gadolinium-cobalt-containing compounds show long-range magnetic order. $Tb_2MnGe_4O_{12}$ shows a weakly ferromagnetic phase and $Gd_2MnGe_4O_{12}$, $Dy_2MnGe_4O_{12}$ are antiferromagnets. The data can be rationalized qualitatively in terms of the interplay between magnetic anisotropy and crystal field effects.

Declaration

The work described in this thesis was carried out in the Inorganic Chemistry Laboratory at the University of Oxford between October 2014 and Octorber 2017 under the supervision of Prof. P. D. Battle. All the work is my own except where stated, and has not been submitted by the author for any degree at this, or any other, university.

Diming Xu

November 2017

Acknowledgements

Firstly, I would like to thank my parents and my family for supporting me over the past years financially and mentally.

I would also like to thank Prof. P. D. Battle for the help and advice he has provided during the course of my DPhil. I am also grateful to my colleagues from Battle's group for their generous assistance.

I would like to thank M. Avdeev for his help on the neutron diffraction; J. M. Cadogan on the Mossbauer spectrum; D. H. Ryan on the Mossbauer spectrum and the neutron diffraction on Gd-containing compound; C. Topping and E. C. Hunter on the specific heat measurements; M. Sale and C. D. Ling on the DFT calculation.

Finally I would like to thank me myself dedicating on the research over the past three years.

Contents

Chapter 1 - Introduction

1.1 Introduction

Oxide materials have been used in all kinds of areas [1] due to their physical properties which include superconductivity ($YBa_2Cu_3O_7$) [2], magnetism ($BaFe_{12}O_{19}$) [3], ferroelectricity ($BaTiO_3$) [4], photoelectricity (RMO_3) [5] and catalysis (V_2O_5) [6]. Scientists have focused on studying the structures of oxide materials to reveal the origins of these properties. Magnetism is one of the properties that has been studied in detail for years, originally in Fe_3O_4 and more recently in the spin ice material, $Dy_2Ge_2O_7$ [7]. The magnetisation of oxide materials comes from the magnetic moment of the constituent metal atoms and the interactions between them in a crystal. These interactions can be described in these basic ways: no interaction (paramagnetic), ferromagnetic interactions and antiferromagnetic interactions. Different types of interactions will result in various types of magnetic system. Furthermore, they can be used in applications.

1.2 Magnetisation of single atom

1.2.1 Origin of magnetisation

An atom or an ion which has unpaired electrons will possess a magnetic moment [8]. Normally, a magnetic moment is associated with a transition-metal or a rare-earth-metal atom or cation. The movement of an electron can generate a current and the current leads to magnetisation. Compared to an electron, the nucleus has a positive charge, a much smaller radius of movement and a much larger mass. Thus, the contribution of the magnetic moment from the nucleus can be neglected. To calculate the magnetic moment from an electron, the Bohr model [9] was used.

The orbital moment comes from an electron circulating around a nucleus. The periodic rotation of the electron generates a current and furthermore forms magnetization. The unit of electronic magnetism is defined as the Bohr magneton, μ_B, where

$$\mu_B = \frac{e\hbar}{2m_e} = 9.274 \times 10^{-24} \text{ A m}^2 \quad (1.1)$$

For multi-electron system, $\boldsymbol{S} = \sum \boldsymbol{s}$, $\boldsymbol{L} = \sum \boldsymbol{l}$, $\boldsymbol{J} = \boldsymbol{S} + \boldsymbol{L}$ and the total magnetic moment is

$$\boldsymbol{\mu} = -g\mu_B \boldsymbol{J} \quad (1.2)$$

The Lande factor, describing the degree of spin-orbital coupling, is

$$g_J = g_L \frac{J(J+1)-S(S+1)+L(L+1)}{2J(J+1)} + g_S \frac{J(J+1)+S(S+1)-L(L+1)}{2J(J+1)} \quad (1.3)$$

where $g_L = 1$ and $g_S \approx 2$, then

$$g_J = \frac{3}{2} + \frac{S(S+1)-L(L+1)}{2J(J+1)} \quad (1.4)$$

The magnetization of atoms are often characterized by the effective Bohr magneton number, μ_{eff}, where

$$\mu_{eff} = g_J\sqrt{J(J+1)} \quad (1.5)$$

1.2.2 Crystal-field effects

For a free ion or an atom, the effective magnetic moment can be calculated from Equation 1.5 providing that only one *J* state is occupied. However, in a real crystal, an atom is normally in a coordination environment and the crystal field effect is not negligible. The crystal field originates from the interaction between a metal atom and its ligands. The crystal field effect leads to the breaking of degeneracies of electron orbital states because the electron cloud of the metal atom is changed by the ligand field. A strong crystal field can alter a high-spin electron configuration to a low-spin one and this alteration is able to change the magnetisation dramatically [10], [11], [12], for example, a high-spin Fe^{2+} has an effective moment of 4.90 μ_B whereas it is 0 for a low-spin Fe^{2+}.

In NiO [13], the Ni^{2+} free ion (d^8) has S = 1, L = 3, J = 4, and g_J = 5/4. From Equation 1.5, Ni^{2+} should have an effective moment of 5.59 μ_B but it actually has an effective moment of 2.87 μ_B [14]. The real value is slightly higher than the spin-only value, μ_s = 2.83 μ_B, but much lower than the full-orbital contributed value, 5.59 μ_B. This is because Ni^{2+} is in an octahedral centre in NiO and the d-orbitals split into t_{2g}^6 (d_{xy}^2, d_{xz}^2, d_{yz}^2) and e_g^2 (d_{x2-y2}^1,

d_{z2}^{1}). Such splitting causes a significant change to the effective moment of Ni^{2+} because of the quenching of orbital angular momentum by the crystal field. Moreover, any non-cubic distortion of the cation environment will further reduce the degeneracy of orbitals and consequently influence the effective magnetic moment. Some first-row transition-metal cations will be affected by the Jahn-Teller effects or by a geometric distortion from the crystal structure that the degeneracy will be fully removed. For most first-row transition-metal cations, the effective moment is close to the spin-only value because of the quenching of orbital angular momentum, and thus $\mu_{\text{spin-only}} = 2\sqrt{S(S+1)}$. However, for some cases including Co^{2+}, if there still exists some orbital contribution, the Equation 1.5 is applied instead of the spin-only one.

1.2.3 Bond covalence effect

Griffiths *et al.* [15] and Stevens [16] did an in-depth study on the reduction of orbital angular momentum. They measured the electron spin resonance of two metal complexes, $IrCl_6^{2-}$ and $IrBr_6^{2-}$. They found that the experimental g value is much lower than the theoretical value. The ligand orbitals were taken into consideration to explain the low g value as chlorine superhyperfine-splittings were detected. This means the unpaired electrons from Ir^{4+} interact with the nuclei of the chloride ligands. In this case, the bonding effect between the metal cation and the ligand cannot be neglected.

Molecular orbital theory uses a linear combination of atomic orbitals to represent molecular orbitals. For a complex coordination system, group theory is introduced to simplify the question. Group theory can combine all ligand orbitals and use irreducible representations to generate total ligand orbitals. A linear combination of metal cation orbitals and ligand orbitals gives rise to covalent bonds. In the complex $MnCl_6^{4-}$ [17], Mn^{2+} (d^5) is in an octahedral centre; 6 σ-bonds and 6 π-bonds are formed. As shown in Figure 1.1, σ-bonds come from e_g (d_{x2-y2}, d_{z2}), a_{1g} (4s), t_{1u} (4p) of Mn^{2+} and t_{1u}, e_g, a_{1g} of ligand orbitals whereas π-bonds are from t_{2g} (d_{xy}, d_{xz}, d_{yz}) of Mn^{2+} and t_{1u}, t_{2g} of ligand orbitals. t_{2u}, t_{1g} ligand orbitals have no relevant metal cation orbital to combine with and they remain as non-bonding orbitals. Finally, all paired electrons are distributed in bonding molecular orbitals and only the unpaired electrons reside in the antibonding orbitals e_g^*, t_{2g}^*. Magnetic properties come from the unpaired electrons and the molecular orbital theory

makes the unpaired electron density spread over the molecular orbitals, which means the unpaired electrons have some density near to the ligands. When considering a nearest-neighbour or next-nearest neighbour atom $Mn^{2+}(2)$, connected by the same ligand ($Mn^{2+}(1) – Cl^- – Mn^{2+}(2)$), the unpaired electrons on the ligand would produce an equal but opposite contribution and lead to the bond covalence effect. Many neutron diffraction studies [18], [19], [20], [21], [22], [23] were carried out to detect the degree of the covalency.

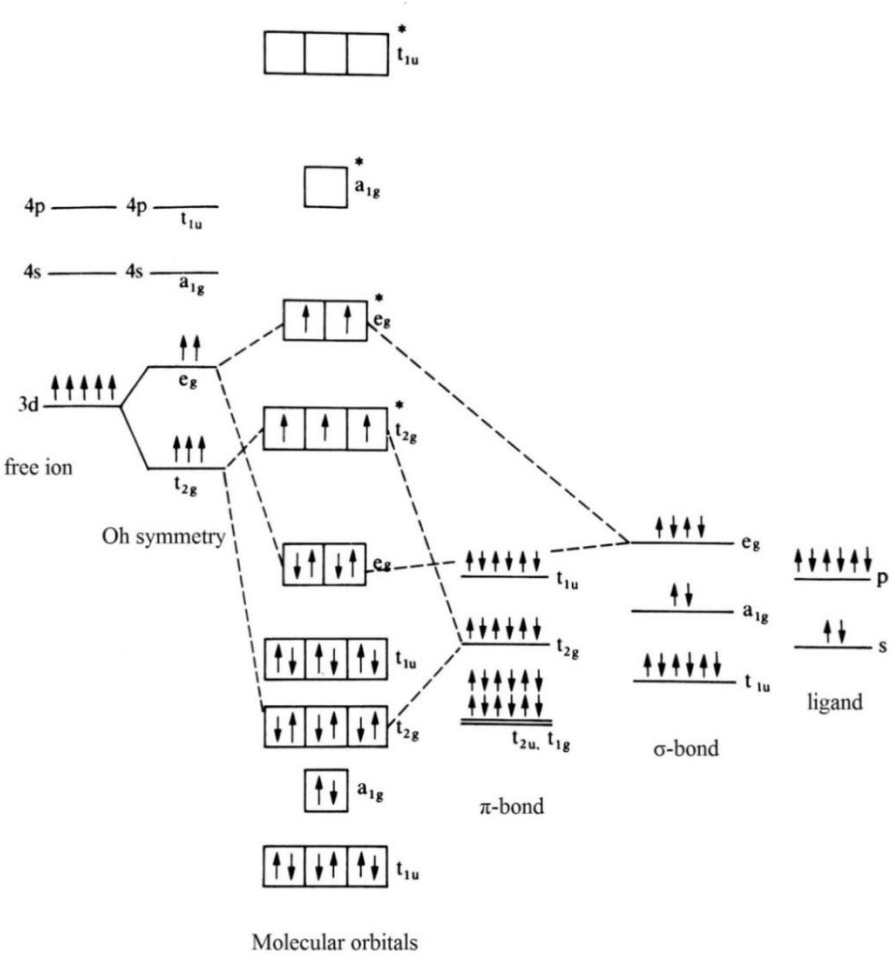

Figure 1.1 Molecular orbitals for $MnCl_6^{4-}$ complex. [17]

1.3 Magnetic Systems

The non-zero spin on some of the atoms in inorganic compounds gives rise to the phenomena of paramagnetism, ferromagnetism and antiferromagnetism which are discussed below. In contrast, the magnetism associated with the paired electrons in closed shells is known as diamagnetism. This makes a weak, negative contribution to the susceptibility at all temperatures in each compound. It will not be considered in this thesis.

1.3.1 Paramagnetism

Paramagnetism is a consequence of the interaction between the unpaired electrons and the applied magnetic field. The interactions between atoms can be neglected compared to the contribution of electrons from the atom itself.

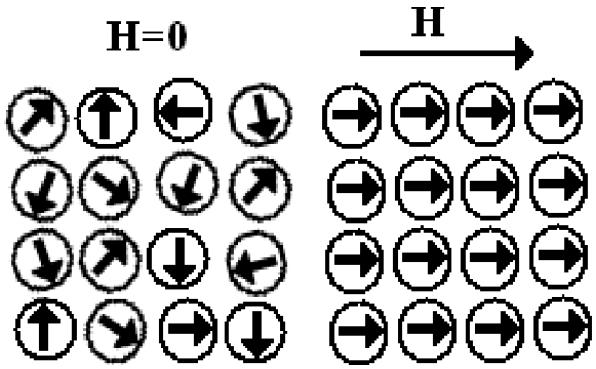

Figure 1.2 Atomic moment arrangements without (left) / within (right) an external magnetic field for a paramagnetic system.

For a paramagnetic system in the absence of an applied field, all the atomic moments are randomly distributed. When a magnetic field is applied, the moments will be driven to the direction of the field at low temperatures and/or strong fields. The total magnetization is the sum of all individual atomic moments. However, temperature can break such moment arrangement by thermal randomisation. The competition between these two interactions leads to the paramagnetic susceptibility independent of field but only governed by temperature at high temperatures.

$$\chi_m = \frac{M_m}{H} \tag{1.6}$$

The Curie-Weiss law reveals the relationship between the paramagnetic susceptibility and temperature

$$\chi_m = \frac{C_m}{T - \theta} \tag{1.7}$$

where θ is the Weiss constant and C_m is Curie constant.

For an ideal paramagnetic compound, the Weiss constant should be zero as in the case of $EuSiO_3$ [24]. However, most compounds have non-zero Weiss temperature value and the

Weiss constant reveals the overall interactions between atoms. A positive Weiss temperature suggests ferromagnetic interaction whereas a negative one leads to antiferromagnetic interaction.

The Curie constant is normally used to calculate the effective moments.

1.3.2 Ferromagnetism

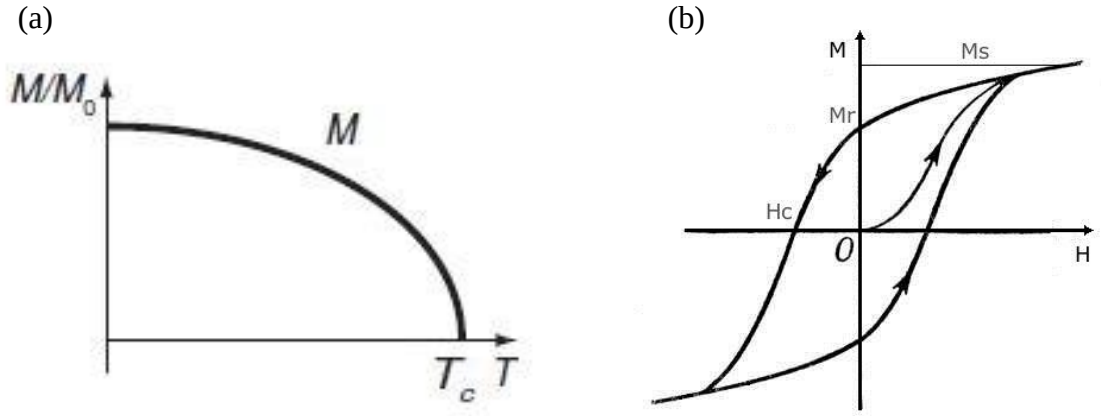

Figure 1.3 Magnetisation of a ferromagnet as a function of (a) temperature and (b) magnetic field. [8]

As explained before, there is always a competition between the energy that the atomic moment gains in field $\mu_B H$ and the energy of temperature $k_B T$. Ferromagnetism occurs below the transition temperature T_C, the Curie temperature. At this specific temperature, $\mu_B H = k_B T_C$. All the atomic moments would point to the same direction though there is no external field applied. Weiss put up an idea that an internal field, or molecular field, can induce the spontaneous magnetization. This internal field comes from the interaction between unpaired electrons and it is actually an electrostatic field. The electrons could have direct interaction by electron clouds overlapping [25] if the atoms are adjacent to each other or by exchange via an anion or an aromatic system.

Fe, Co, and Ni are well known as ferromagnets with the Curie temperatures 1043, 1388, and 627 K [26] respectively. The atomic moments of 2.22, 1.72, and 0.61 μ_B, respectively, are lower than the gS value due to the band theory. In a pure metal, each metal atom interacts directly with its neighbour and their electron clouds can conduct direct exchange.

Domain structures [27] can directly be observed in these metals as evidence of an internal field and spontaneous magnetization. Some metal oxides, $SrRuO_3$ [28] and the high-pressure phase of $BaRuO_3$ [29], are also ferromagnetic compounds. A ferromagnet should behave as a paramagnetic compound above the Curie temperature and have a positive Weiss constant. When the temperature is lower than the Curie temperature, spontaneous magnetization is formed and the susceptibility grows significantly.

1.3.3 Antiferromagnetism

In some compounds, antiferromagnetism is observed below the transition temperature T_N, the Néel temperature. Contrary to ferromagnetism, antiferromagnetism has a net magnetization of zero. A classic Néel antiferromagnet has two opposite magnetic sublatices and thus the total magnetisation is zero. Many metal oxides are antiferromagnets, for example, MnO, NiO, CoO [30], [31], [32]. For an antiferromagnetic system, it is also paramagnetic above the Néel temperature but has a negative Weiss constant and the susceptibility decreases below the Néel temperature because the magnetisations from two sublatices work against each other to give a zero net magnetisation.

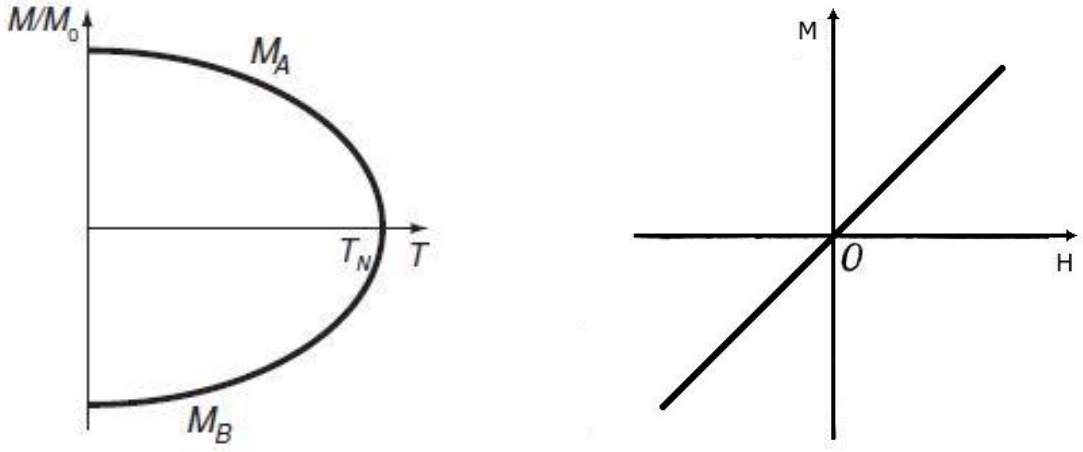

Figure 1.4 Magnetisation of an antiferromagnet as a function of (a) temperature and (b) magnetic field. [8]

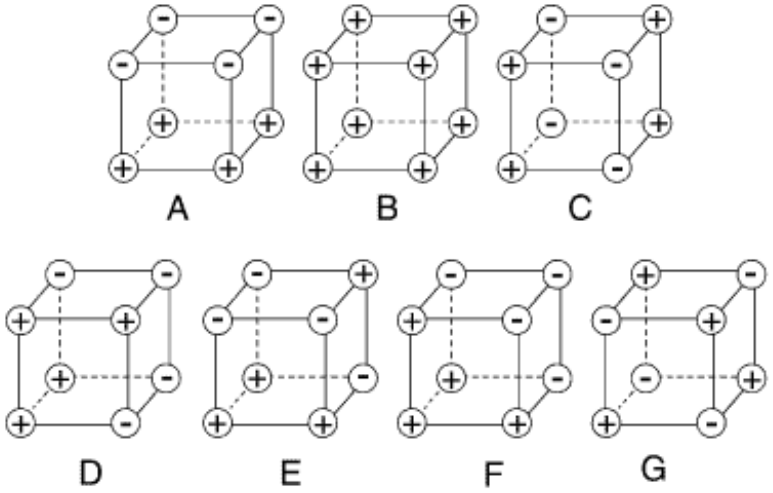

Figure 1.5 Different kinds of magnetic structures in a cubic lattice.

For a simple cubic unit cell, 7 different kinds of magnetic structures can be listed as shown in Figure 1.5. Type B is ferromagnetic while all the others are antiferromagnetic. Among the antiferromagnetic structures, type G, type A, and type C have been widely observed and carefully studied. Type G is a type with one moment being opposite to all adjacent ones, both in the *ab* plane and along the *c* axis; type A is ferromagnetic in the *ab* plane but antiferromagnetic along the *c* axis and type C is antiferromagnetic in the *ab* plane but ferromagnetic along the *c* axis. Different antiferromagnetic structures are adopted depending on the crystal structure and the arrangement of the cations. [33]

1.3.4 Other types of magnetism

1.3.4.1 Ferrimagnetism

Ferrimagnetism is related to antiferromagnetism. It can be considered in terms of two unequal sublattices aligned antiferromagnetically. Hence, the net magnetisation is not zero. The non-zero net magnetisation behaves similarly as ferromagnets. Fe_3O_4 is a classic ferrimagnet with T_c = 858 K. [34] It crystalizes in a cubic structure (space group O_h^7, *Fd*3*m*) with lattice parameter *a* = 8.3794 Å. The Fe^{3+} (d^5) and Fe^{2+} (d^6) have spin-only atomic moments of 5 and 4 μ_B, respectively. From the magnetic structure derived from the neutron diffraction data [33], [35], the net magnetic moment then is expected to be (5+4) − 5 = 4 μ_B and the experimental value, 4.1 μ_B, is close to the theoretical value.

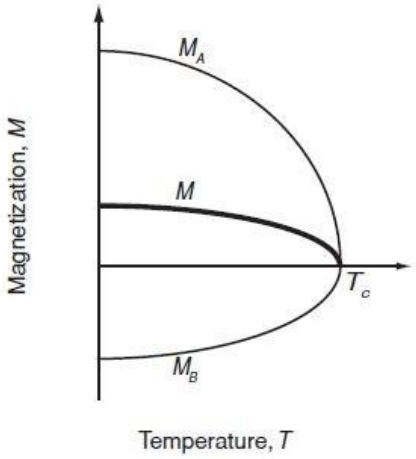

Figure 1.6 Sublattice magnetisation of a ferrimagnet. [8]

1.3.4.2 Weak Ferromagnetism

Spin canting leads to weak ferromagnetism. Classic antiferromagnets normally have parallel but opposite atomic moments. However, for a spin canting system, see Figure 1.7, atomic moments are antiferromagnetic in one direction but ferromagnetic in some other directions and they are not parallel anymore. The ferromagnetic component makes the compound behave as a ferromagnet in magnetisation measurements. $MnCO_3$ [36], [37] is a classical canted antiferromagnet proved by low temperature neutron diffraction measurements. The antisymmetric exchange (Dzyaloshinsky−Moriya interaction) [38], [39] is the reason for spin canting in many cases.

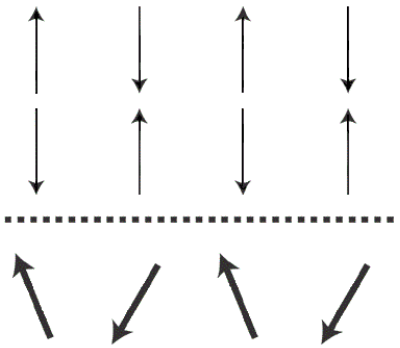

Figure 1.7 Antiferromagnetic magnetic structure (top) and spin canting magnetic structure (bottom).

1.3.4.3 Metamagnetism

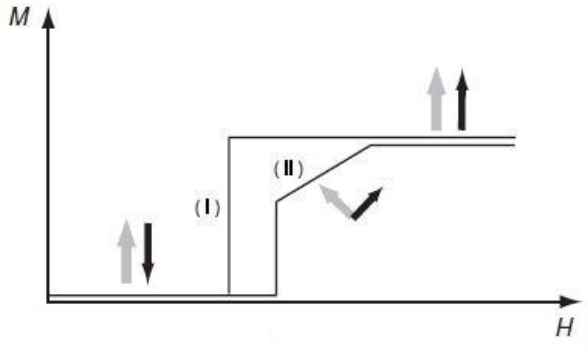

Figure 1.8 Magnetisation of a metamagnet. [8]

Metamagnetism [40] describes a process where an external field can change an antiferromagnet into a ferromagnet. Using the molecular field theory, at the Curie temperature, the thermal energy and the internal field energy should balance, so

$$\mathrm{H}_{in} g S \mu_B = k_B \mathrm{T}_c \tag{1.8}$$

where $\mathrm{H}_{in} = \frac{\theta}{C} \cdot M_0$,then $\mathrm{H}_{in} = \frac{k_B \mathrm{T}_c}{g S \mu_B}$.

Take Fe for instance, T_c = 1043 K, g = 2, S = 2, so $H_{in} = 7.73 \times 10^6$ Oe, which is a strong field that cannot be produced in the lab. However, if the transition temperature is low, assuming 5 K, the internal field is about 40 kOe, large but possible to reach. Therefore, for some special systems, when the internal field is not too strong, an external field is able to change the arrangement of atomic moments. Figure 1.8 has shown two procedures of spin reversal: immediate transition and slow transition. For real systems, a metamagnetic compound may show one or several transition steps. $FeCl_2$ [40] is one of the classical metamagnetic compounds with first-order one-step transition in a 10 kOe field. Other compounds were reported to have metamagnetic transitions, including CoV_2O_6 [41], [42] and $R_{1-x}Ca_xMnO_3$ (R = Pr, Nd) [43].

1.3.4.4 Frustrated Magnetic Systems

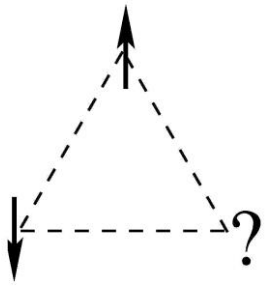

Figure 1.9 Frustrated triangular lattice.

For the ferromagnetic and antiferromagnetic systems described above, atomic moments can not only satisfy local interactions but also produce a long-range magnetic structure. However, for a frustrated system, local interactions cannot be satisfied as shown in Figure 1.9. Such frustration [44] normally leads to a low transition temperature, or the freezing temperature, T_f. Atomic moments would be frozen from their paramagnetic phase below the freezing temperature. Hence, long-range magnetic order is not formed. However, the arrangement of the moments leads to the lowest system entropy. AC measurements are applied for spin-frustrated systems as the frozen moments can follow the oscillating magnetic field. A frequency dependence of the transition temperature is the sign of a frustrated magnetic system.

Spin glasses, spin ices, and spin liquids are some frustrated systems that have been widely studied. Due to the nature of the 3D pyrochlore crystal structure, many $A_2B_2O_7$ compounds are frustrated materials. $A_2B_2O_7$ compounds containing rare earth cation in the A-site [7], [45], [46], [47], [48], [49] are known as spin ice. Below the freezing temperature (less than 2 K), there are $2^4 = 16$ different arrangements existing in a tetrahedral. Ideally, the two-in two-out way (see Figure 1.10 (a)) is the most stable state with a degeneracy of 6. [50] However, some other ways {three-in one-out/three-out one-in (see Figure 1.10 (b)) or all-in/all-out (see Figure 1.10 (c))} also exist in pairs. The system has some entropy not released, which is called the residual entropy, because of the geometrical frustration. Moreover, an $A_2B_2O_7$ composition with a magnetic cation at the B-site, $Y_2Mo_2O_7$ [51], is also a famous spin glass material.

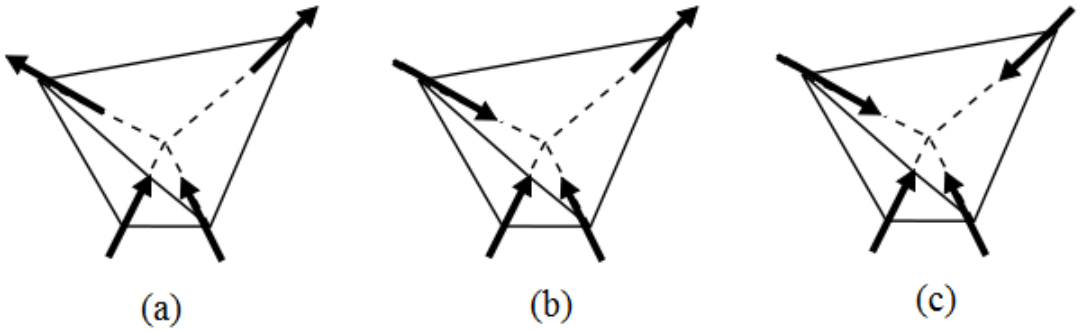

Figure 1.10 The arrangements of magnetic moments in spin ice.

The factor introduced by J. A. Mydosh [52] is normally used to determine the system as spin glass ($0.01 < \Phi < 0.08$) or superparamagnetic (involving Single-Molecule Magnet and Single-Chain Magnet) [53], [54]

$$\Phi = \frac{\Delta T_f}{T_f \Delta(\log \omega)} \tag{1.9}$$

where ΔT_f is the change in transition temperature that occurs when the frequency of the ac field, ω, changes.

For a spin frustrated system, the obtained imaginary data shows a maximum at $\omega\tau = 1$ where ω is the frequency of the ac field times 2π. The Arrhenius Equation can derive the effective barrier energy (U_{eff}) and the relaxation time (τ_0)

$$\ln(\tau) = \ln(\tau_0) + \frac{U_{eff}}{kT} \tag{1.10}$$

If the imaginary part does show a frequency-dependent behaviour but the maximum is lower beyond the experiment condition (< 2 K), Arrhenius Equation then is

$$\ln(\chi''/\chi') = \ln(\omega\tau_0) + \frac{U_{eff}}{kT} \tag{1.11}$$

1.4 Magnetic Exchange Interactions

Following years of study, scientists have derived some equations for magnetic behaviour. However, most of the equations are based on statistics and have not explained how the moments interact with each other. Heisenberg established a model to explain the spontaneous magnetisation for ferromagnets. Later, Kramers [55] and Anderson [56] used the

superexchange model to explain the interaction for antiferromagnets. Some basic exchange interactions are listed below.

1.4.1 Direct Exchange Interaction

For two-atom magnetic exchange, the hydrogen molecule, H_2, is the simplest example to illustrate the procedure. From Schrődinger's equation [57]

$$\hat{\mathcal{H}}\psi = E\psi \tag{1.12}$$

The energy difference between the singlet (S = 0) and the triplet states (S = 1), see Figure 1.11, is

$$\Delta E = E_1 - E_2 = -2\mathcal{J}_{12}\boldsymbol{s_1}\cdot\boldsymbol{s_2} \tag{1.13}$$

The exchange operator can thus be written as

$$\hat{\mathcal{H}}_{ex} = -2\mathcal{J}_{12}\boldsymbol{s_1}\cdot\boldsymbol{s_2} \tag{1.14}$$

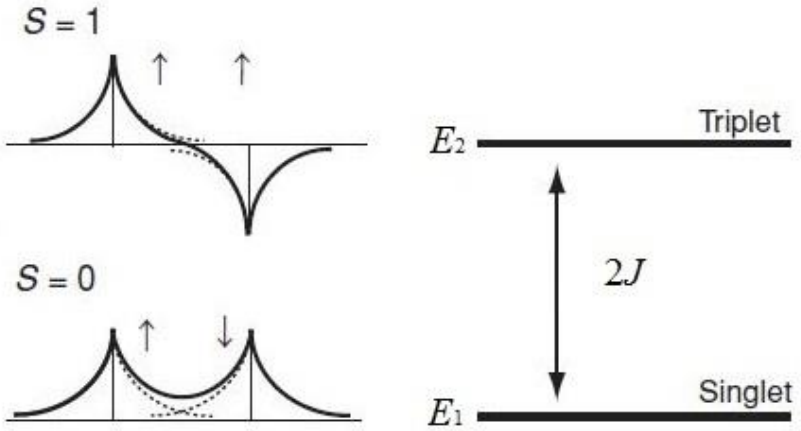

Figure 1.11 The wave function and energy states for H_2 molecule. [8]

The equation is also true for a multi-electron system

$$\hat{\mathcal{H}}_{ex} = -2\sum_{i<j}\mathcal{J}_{ij}\,\boldsymbol{S_i}\cdot\boldsymbol{S_j} \tag{1.15}$$

A positive $\mathcal{J}_{ij}$ value indicates ferromagnetic exchange whereas a negative one means antiferromagnetic exchange. The value of the integral $\mathcal{J}_{ij}$ also implies the strength of the exchange interaction.

To simplify the calculation, only the nearest-neighbour atoms would be considered. For a simple ferromagnet, the electron interaction leads to an internal field and every atomic moment align to the field. Then the site Hamiltonian is

$$\widehat{\mathcal{H}}_i = -\mathbf{H}^i g\mu_B \boldsymbol{S}_i \tag{1.16}$$

where $\mathbf{H}^i = \frac{\theta}{C} \cdot \mathbf{M} = \frac{\theta}{C} ng\mu_B \boldsymbol{S}$, θ is the Weiss constant and *n* is the number of the magnetic atoms.

Thus, the exchange integral $\mathcal{J}_{ij}$ has relationship with the Weiss constant θ as

$$\mathcal{J}_{ij} = 3k_B\theta/2ZS(S+1) \tag{1.17}$$

where *Z* is the number of the nearest neighbouring atoms.

However, such equations are derived under the approximation that only the nearest neighbouring direct exchange is considered. In addition, some other interactions also exist in certain circumstances. An external magnetic field will change the energy of the spin and this term can significantly change the total energy. The anisotropy of the atom can lead to an easy-axis or easy-plane of magnetization. The exchange of anisotropy between atoms can not only produce strong interaction between neighbouring magnetic atoms but also lead to further Dzyaloshinsky−Moriya exchange. For a general consideration for spins, the wave function [58], [59] can be written as

$$\widehat{\mathcal{H}}\psi = E\psi$$
$$\widehat{\mathcal{H}}_{spin} = \widehat{\mathcal{H}}_H + \widehat{\mathcal{H}}_{An} + \widehat{\mathcal{H}}_{ex} + \widehat{\mathcal{H}}_{DM} + \widehat{\mathcal{H}}_{an-ex} + \widehat{\mathcal{H}}_{di} \tag{1.18}$$

where $\widehat{\mathcal{H}}_H$ is magnetic field coupling, $\widehat{\mathcal{H}}_H = -\mathbf{H} \cdot \sum_i g_i\mu_B \boldsymbol{S}_i$;

$\widehat{\mathcal{H}}_{An}$ is single ion anisotropy term, $\widehat{\mathcal{H}}_{An} = \sum_i \varepsilon_{An}(\boldsymbol{S}_i)$, $\varepsilon_{An}(\boldsymbol{S}_i) = -\frac{1}{2} D {S_z}^2$;

$\widehat{\mathcal{H}}_{ex}$ is the exchange interaction, $\widehat{\mathcal{H}}_{ex} = -\sum_{i>j} \mathcal{J}_{ij} \boldsymbol{S}_i \cdot \boldsymbol{S}_j$;

$\widehat{\mathcal{H}}_{DM}$ is antisymmetric exchange (Dzyaloshinsky−Moriya interaction),

$\widehat{\mathcal{H}}_{DM} = -\sum_{i>j} \boldsymbol{D}_{ij} \cdot \boldsymbol{S}_i \times \boldsymbol{S}_j$;

$\widehat{\mathcal{H}}_{an-ex}$ is anisotropy exchange,

$\widehat{\mathcal{H}}_{an-ex} = -\sum_{i>j} [\, {\mathcal{J}_{ij}}^{xy} (\boldsymbol{S}_{ix} \cdot \boldsymbol{S}_{jx} + \boldsymbol{S}_{iy} \cdot \boldsymbol{S}_{jy}) + {\mathcal{J}_{ij}}^{z} \boldsymbol{S}_{iz} \cdot \boldsymbol{S}_{jz} \,]$;

$\widehat{\mathcal{H}}_{di}$ is dipolar interaction, $\widehat{\mathcal{H}}_{di} = \sum_{ij} \frac{(g\mu_B)^2}{{r_{ij}}^3} [\, 3(\hat{\boldsymbol{r}}_{ij} \cdot \boldsymbol{S}_i)(\hat{\boldsymbol{r}}_{ij} \cdot \boldsymbol{S}_j) - \boldsymbol{S}_i \cdot \boldsymbol{S}_j]$.

1.4.2 Superexchange Interaction

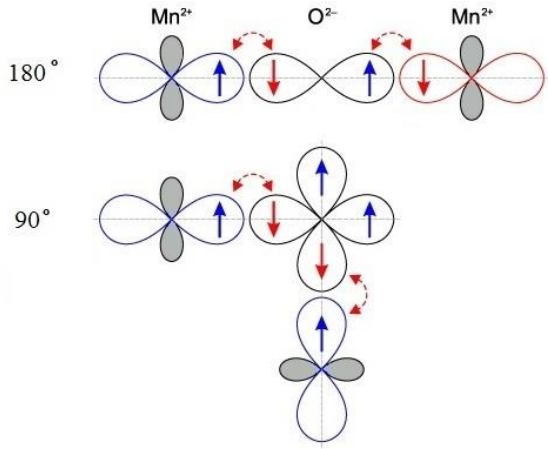

Figure 1.12 Two superexchange pathways of MnO.

As the direct exchange model can only explain a limited number of systems, superexchange [55], [56] has been proposed to account for more complex cases. MnO [60], [61], [62], [63] has a face-centered cubic rock-salt crystal structure and Mn^{2+} is in an octahedral center, $[MnO_6]^{10-}$. Hence, one manganese cation can interact with another manganese cation in two ways, the σ bond interaction and the π bond interaction. However, the π bond interaction is much weaker than the σ bond interaction because the distance between the electron clouds is much further and thus the overlapping of the electron clouds is less possible. We will concentrate on the σ bond interaction below. There are two kinds of σ bond interactions: 180° Mn^{2+} - O^{2-} - Mn^{2+} interaction along one axis and 90° Mn^{2+} - O^{2-} - Mn^{2+} interaction within the plane. For each Mn, six 180° Mn^{2+} - O^{2-} - Mn^{2+} interaction and twelve 90° Mn^{2+} - O^{2-} - Mn^{2+} interaction are formed. The exchange happens when an electron from the 2p orbital of O^{2-} migrates to the 3d orbital of Mn^{2+} and the system becomes Mn^{+} - O^{-} - Mn^{2+}, which can induce further exchange. In the case of MnO, the strength of the 180° Mn^{2+} - O^{2-} - Mn^{2+} interaction is larger than the 90° Mn^{2+} - O^{2-} - Mn^{2+}. Generally, the strength of the 180° superexchange interaction and the 90° superexchange interaction depends on the electron configuration. The Goodenough-Kanamori rules [60], [61], [64], [65] state that superexchange interactions are antiferromagnetic when the electron transfer is between overlapping orbitals that are each half-filled, but ferromagnetic when the electron transfer is from a half-filled to an empty orbital or from a filled to a half-filled orbital.

In the case of an antiferromagnet, two opposite antiferromagnetic sublattices R_l and R_m can be modelled [56], [58]. The exchange operator can be written as

$$\widehat{\mathcal{H}}_{ex} = -2\mathcal{J}\boldsymbol{S_1}\cdot\boldsymbol{S_2}$$

$$\widehat{\mathcal{H}}_{ex} = -2\mathcal{J}(R_l\,R_m)\widehat{\boldsymbol{S}}(R_l)\cdot\widehat{\boldsymbol{S}}(R_m) \tag{1.19}$$

$$\mathcal{J}(R_l\,R_m) = \frac{1}{4S^2}\left[\sum_{n,n'} J_{nn'}(R_l,R_m) - \frac{2b^2}{E(\uparrow\downarrow)}\right] \tag{1.20}$$

where b is the integral term describing excited state that one electron immigrate from the sublattice R_l to R_m and $E(\uparrow\downarrow)$ is the energy of the excited state.

Considering the energy between the exchanging electrons, atomic potential energy and anisotropic energy, first and second order perturbations are involved

$$\Delta E = -\sum_{l,m}\sum_{n,n'}\left[J_{nn'}(R_l,R_m) - \frac{2b_{nn'}^2}{E(\uparrow\downarrow)}\right]\widehat{\boldsymbol{S}}_n(R_l)\cdot\widehat{\boldsymbol{S}}_{n'}(R_m) + constant \tag{1.21}$$

If only considering the interaction between magnetic cations and assuming the interactions are isotropic, then

$$\mathcal{J}(R_l\,R_m) = \frac{1}{4S^2}\sum_{n,n'}\left[J_{nn'}(R_l,R_m) - \frac{2\left|b_{nn'}(R_l-R_m)\right|^2}{E(\uparrow\downarrow)}\right] \tag{1.22}$$

$$T_N = \frac{12J_{180}S(S+1)}{3k} \tag{1.23}$$

$$\theta = \frac{12(2J_{90}+J_{180})S(S+1)}{3k} \tag{1.24}$$

With the Néel temperature and the Weiss constant, the exchange integrals through the 180° superexchange interaction and the 90° superexchange interaction can be estimated.

For most crystals, there would be a distorted local environment for metal atoms and the superexchange pathways would also distort somehow. Hence, the angle of Mn^{2+} - O^{2-} - Mn^{2+} can be 120 - 180° for the 180° superexchange interaction and otherwise for the 90° superexchange interaction.

With the superexchange model, the magnetization of most metal oxides can be explained. However, the crystal field effects would also influence the exchange energies; the polarization and electronegativity of the anions would all result in differences.

1.4.3 Interactions Involving Rare-Earth Elements

The magnetization of rare-earth atoms comes from the electrons in their 4f orbitals. However, the 4f orbital electrons are in the inner shell where there are still $5p^6 5d^1 6s^2$ electron clouds at the outside. When a rare-earth cation R^{3+} is in a coordination environment, it is the outer electrons that are involved in the bonding and the 4f orbital electrons are less involved. To conduct magnetic exchange, the unpaired electrons in the 4f orbitals need to interact with the outer electrons which then become involved in the direct exchange or superexchange. In contrast, magnetic moment of the first-row transition-metal cations comes from the $3d^n$ electrons and these electrons also involve in the bonding. Moreover, the radii of rare-earth atoms are large, leading to a long exchange distance with the interaction strength decreasing rapidly as a function of distance; the interaction integral is normally negligible at a distance of 4 Å. Hence, it is much easier to conduct direct exchange or superexchange between a transition-metal cation and another transition-metal cation (T – T) than between a transition-metal cation and a rare-earth cation (R – T) or between a rare-earth atom and another rare-earth atom (R – R).

However, for rare-earth atoms, some other interactions listed in Equation 1.18 are significant. Due to the 4f orbital electrons are less influenced by the crystal field, the angular orbital momentum quenching of rare-earth atoms is less likely. The shape of the electron cloud is determined by the degree of spin-orbital coupling and the electron cloud shapes of lanthanides are drafted in Figure 1.13.

Heavy atoms usually have strong spin-orbital coupling and their ground states can therefore be described by the J value. Note that in rare-earth systems at room temperature, the crystal field splitting is less than the thermal energy and can often be ignored. However, the crystal field effects became more important at lower temperatures and can have a strong influence on the ground state.

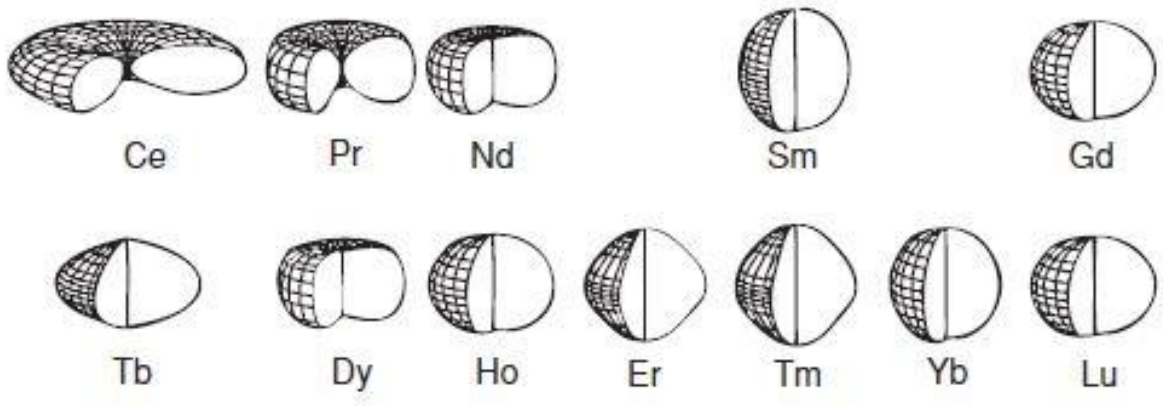

Figure 1.13 The shape of rare earth metal atom electron clouds. [8]

1.5 Magnetism in Inorganic Compounds

The discussion above has introduced some basic principles of magnetism and exchange interactions. As direct exchange can only be applied to the system in which metal atoms are less than 3 Å apart, superexchange model is widely used in most situations. Some examples are given below.

1.5.1 Simple Metal Oxides

MnO, FeO, CoO, and NiO [13], [20], [30], [31], [32], [62], [63], [66], [67], [68], [69], [70] are a series of antiferromagnetic metal monoxides that have been detailed studied. They adopt a rock-salt crystal structure. NiO has the highest Néel temperature T_N = 523 K and it is a type II antiferromagnet. Roth [31] showed by neutron diffraction that the magnetic structure of NiO can be described in a magnetic cell of $a_{mag} = 2\ a_{crystal}$. The atomic moments are ordered ferromagnetically in (111) planes and aligned along the $[11\bar{2}]$ axis. The 180° superexchange interaction and the 90° superexchange interaction Ni^{2+} - O^{2-} - Ni^{2+} superexchange pathways are clearly illustrated by Figure 1.14. By fitting the neutron diffraction data, magnetic susceptibility and Raman scattering data, the 180° superexchange interaction integral was determined to be $J_{180°}$ = -211 K and the 90° superexchange interaction superexchange integral is $J_{90°}$ = 16 K. [66], [71], [72]

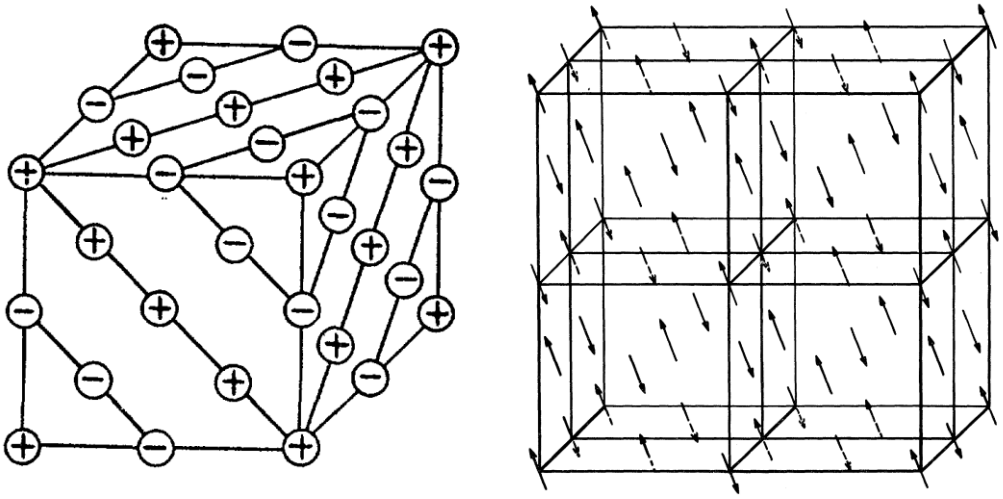

Figure 1.14 Magnetic structure of NiO. [31]

In NiO, the 180° superexchange interaction dominates the antiferromagnetic interaction whereas the the 90° superexchange interaction superexchange contributes a ferromagnetic component; the 180° superexchange interaction integral is 10 times stronger than the 90° superexchange interaction. The length of the 180° superexchange interaction pathway is a_{crystal} and the length of the 180° superexchange interaction pathway is $\sqrt{2}/2\ a_{\text{crystal}}$. Though having a shorter superexchange pathway, ~ 1.25 Å less, the 90° superexchange interaction still is weaker compared to the 180° superexchange interaction because only one 2p orbital of oxygen atom is involved in the 180° superexchange interaction but two in the 90° superexchange interaction. The possibility is much less for the 90° superexchange interaction. Hence, the nearest-neighbour (NN) the 90° superexchange interaction is weak but the next-nearest-neighbour (NNN) the 180° superexchange interaction is strong. MnO and CoO have the same magnetic structure as NiO from the neutron diffraction data. Their magnetic cells also double from their crystal units. The atomic moments are aligned parallel to (111) planes for MnO but along the $[\bar{1}\bar{1}7]$ axis for CoO. The Néel temperatures for MnO and CoO are 122 K and 291 K, respectively. Superexchange integrals[69], [70] are determined to be $J_{180°}$ = -32 K and $J_{90°}$ = -24 K for MnO; $J_{180°}$ = -135 K and $J_{90°}$ = 20 K for CoO. From Equation 1.23 and the superexchange integrals, the calculated Néel temperature is about 1120 K for MnO and 2025 K for CoO, much higher than their experimental value 118 and 289 K[69], [70], respectively. This is because the Equation 1.23 only concerns a simple model with only the 180° superexchange interaction.

For a more complex system, for example the ABO_3 perovskite system, superexchange is basically the same as the metal oxides but more complex since the bond angles are usually not typical 90° or 180°. Normally, 120° is the critical point to distinguish the two superexchange pathways. $LaMnO_3$ and $CaMnO_3$ [73], [74], [75] are two perovskites having the same crystal structure but Mn is +3 in $LaMnO_3$ but +4 in $CaMnO_3$. $LaMnO_3$ adopts space group *Pbnm* (No. 62) with a = 5.5367(1) Å, b = 5.7473(1) Å, c = 7.6929(2) Å and $CaMnO_3$ adopts space group *Pbnm* (No. 62) with a = 5.264(1) Å, b = 5.279(1) Å, c = 7.448(1) Å. A mixture of these two compounds has been made, $La_{1-x}Ca_xMnO_3$. $LaMnO_3$ is a type A antiferromagnet with the Néel temperature T_N ~ 140 K whereas $CaMnO_3$ is type G with the Néel temperature T_N ~ 130 K. One mixture, $La_{0.2}Ca_{0.8}MnO_3$, is type C and the other mixtures can be indexed with some more complicated magnetic structures.

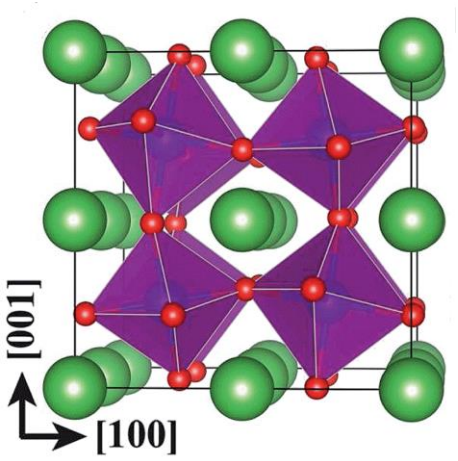

Figure 1.15 Crystal structure of $LaMnO_3$ or $CaMnO_3$, green ball is La or Ca, blue ball is Mn, red ball is O. [75]

Due to the Jahn-Teller effect, the $[MnO_6]$ octahedron is distorted in $LaMnO_3$ and such distortion leads to some changes in bond angles and bond lengths. In $LaMnO_3$, all the Mn – O – Mn bond angles are about 155°. The direct Mn – Mn length is 3.990 Å in the *ab* plane and 3.846 Å along the *c* axis. The Mn – O bond lengths are 2×2.180(1) Å, 2×1.968(1) Å, 2×1.906(1) Å. The Mn – O – Mn bond length is 4.086 Å in the *ab* plane and 3.937 Å along the *c* axis. Such differences make the superexchange along the *c* axis stronger than that in the *ab* plane and the moments are thus antiparallel along the *c* axis. The neutron diffraction data show that $LaMnO_3$ is a type A antiferromagnet. Thus, Mn moments in the *ab* plane interact ferromagnetically. The calculated superexchange integrals are $J_{\text{in-plane}}$ = 10 K, J_c = -70 K [63]. This means Mn in the *ab* plane can be considered as NNN atoms and the Mn

along the *c* axis are NN atoms. In $CaMnO_3$, all the Mn – O – Mn bond angles are about 158°. The direct Mn – Mn length is 3.728 Å in the *ab* plane and 3.724 Å along the *c* axis. The Mn – O bond lengths are 2×1.903(1) Å, 2×1.900(1) Å, 2×1.895(1) Å. The Mn – O – Mn bond length is 3.803 Å in the *ab* plane and 3.790 Å along the *c* axis. Due to the distances and angles are about the same in $CaMnO_3$, it adopts the type G magnetic structure. Every Mn moment has 6 NN Mn and they all interact antiferromagneticly with each other. The calculated superexchange integral J = -10 K [63].

These examples demonstrate that superexchange is influenced by many factors, for example, orbital occupancy, bond length, bong angle and spin-orbital coupling of the metal atom.

1.5.2 Oxo-acid Salts

M – O – X – O – M (X is a non-metal cation or a transition-metal cation with d^0 or d^{10} electron configuration) is another significant superexchange pathway in some oxo-acid salts, for example $[SO_4]^{2-}$, $[PO_4]^{3-}$, $[AsO_4]^{3-}$, $[MoO_4]^{2-}$ and $[GeO_4]^{4-}$. Compared to M – O – M superexchange, M – O – X – O – M superexchange is much longer and the bond angles are more complex. Thus, the Néel temperatures for oxo-acid salts are relatively low and their magnetic properties are more complex. Some examples are given below to illustrate the M – O – X – O – M superexchange where the cation M is in an octahedral site $[MO_6]$ and the cation X is in a tetrahedral site $[XO_4]$; the polyhedra are connected by vertex-sharing. Moreover, Fe^{3+} was chosen as the cation to discuss the influence of the non-magnetic atom X on the magnetic interaction.

1.5.2.1 Sulfate Salts

Iron (III) sulfate, $Fe_2(SO_4)_3$ [22], was found to be an simple antiferromagnet below 28.8 K. It adopts space group $P2_1/n$ with the unit cell parameters a = 11.573(3) Å, b = 8.25(3) Å, c = 8.262(3) Å, β = 90.81(1) °. The crystal structure of $Fe_2(SO_4)_3$ is shown in Figure 1.16. Every $[FeO_6]$ octahedron is linked to another 18 $[FeO_6]$ octahedral by six vertex-sharing $[SO_4]$ tetrahedra. The neutron diffraction data were collected at 4.2 K to obtain the magnetic information. The magnetic unit cell was found to be identical to its crystal unit.

The atomic moment of Fe(1) is opposite to Fe(2) lying in the *ac* plane and the value of each Fe^{3+} atomic moment was determined to be 4.52(8) μ_B with components M_x = 3.88(6) μ_B and M_z = 2.36(12) μ_B. There are 18 Fe – O – S – O – Fe superexchange pathways linking every Fe to its neighbouring iron atoms. Due to Fe(1) and Fe(2) has opposite moments, three types of superexchange pathways can be generated, namely Fe(1) – O – S – O – Fe(1), Fe(2) – O – S – O – Fe(2), and Fe(1) – O – S – O – Fe(2). Considering the multiplicity of each pathway, the values of average distances for exchange pathway and the average angles at the tetrahedral sulfate centre can be calculated: 6.94 Å and 110.7 ° for Fe(1) – O – S – O – Fe(1); 6.90 Å and 109.9 ° for Fe(2) – O – S – O – Fe(2); 6.92 Å and 109.3 ° for Fe(1) – O – S – O – Fe(2). The small differences of these two parameters cannot distinguish one pathway from another. For each Fe atom, 18 different superexchange pathways link it to another iron atom. The total effect of all Fe – O – S – O – Fe superexchange pathways produces the magnetic order of $Fe_2(SO_4)_3$.

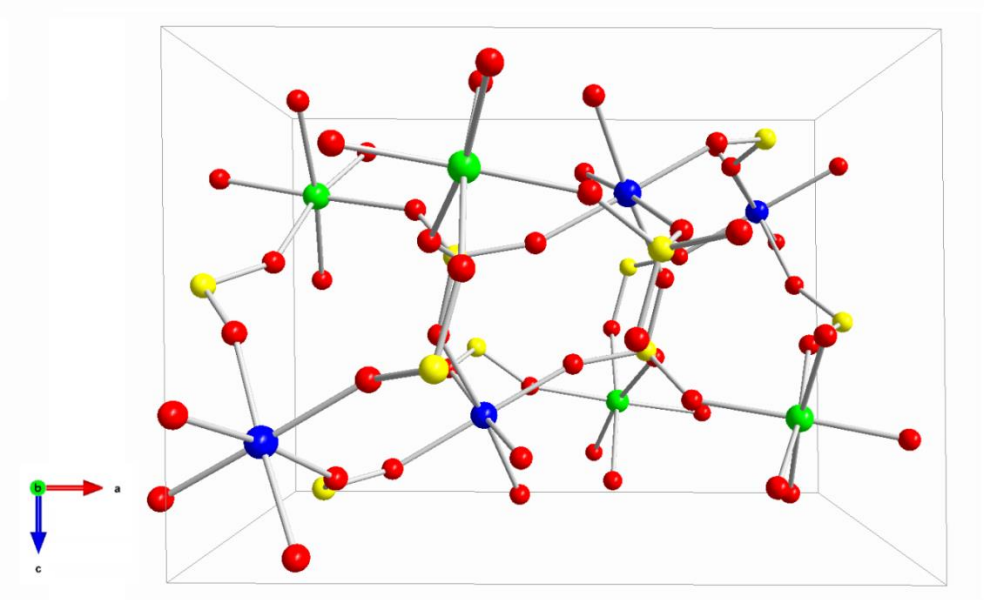

Figure 1.16 Crystal structure of $Fe_2(SO_4)_3$, green ball is Fe(1), blue ball is Fe(2), red ball is O, and yellow ball is S.

1.5.2.2 Phosphate Salts

Iron (III) phosphate, $FePO_4$, has two different forms. Trigonal $FePO_4$ [23], [76] has space group $P3_121$ with the unit cell parameters *a* = 5.036(2) Å, *b* = 5.036(2) Å, *c* = 11.255(4) Å, γ = 120 °. Orthorhombic $FePO_4$ [77], [78], [79] has space group *Pnma* with the unit cell

parameters a = 9.8142(2) Å, b = 5.7893(2) Å, c = 4.7820(2) Å. Crystal structure diagrams of the two forms are shown in Figure 1.17. In the trigonal phase, tetrahedral [FeO_4] and [PO_4] units generate the structure in a vertex-sharing way and it is octahedral [FeO_6] and tetrahedral [PO_4] units that form the orthorhombic phase. The different coordination environment of Fe (III) leads to different Néel temperatures, T_N = 25 K and 125 K for the trigonal and the orthorhombic phase, respectively. The magnetic structure of the trigonal $FePO_4$ has a double unit cell along the c axis, $c_{mag} = 2\ c_{crystal}$. The moments of Fe^{3+} order ferromagnetically within the (001) plane and the adjacent (001) planes are antiferromagnetic. The value of each moment was determined to be 4.53 μ_B at 5 K. Within the structure, the Fe – O distances are all about 1.850(7) Å and 1.524(7) Å of the P – O bond. Every Fe atom is linked to another 12 Fe atom via Fe – O – P – O – Fe pathway where four Fe atoms are in the same layer with the straight distance of 5.036(2) Å. The other eight Fe atoms are in adjacent (001) layers with the straight distances of 4×4.533(2) Å, 2×5.482(2) Å, 2×6.033(2) Å. The orthorhombic $FePO_4$ has a magnetic unit cell the same as its crystal structure. The moments of Fe^{3+} order antiferromagnetically between adjacent (001) planes whereas within the (001) plane, the moments are canted with the antiferromagnetic component M_x = 4.05(2) μ_B and the ferromagnetic component M_y = 0.90(6) μ_B at 2 K. Within the (001) plane, every Fe atom has four NN Fe atoms and four NNN Fe atoms. Different from the trigonal $FePO_4$, the Fe atoms in orthorhombic $FePO_4$ are linked to their NN Fe atoms by not only Fe – O – P – O – Fe but also Fe – O – Fe superexchange pathway. This makes the interaction much stronger and thus the Néel temperature is much higher.

(a)

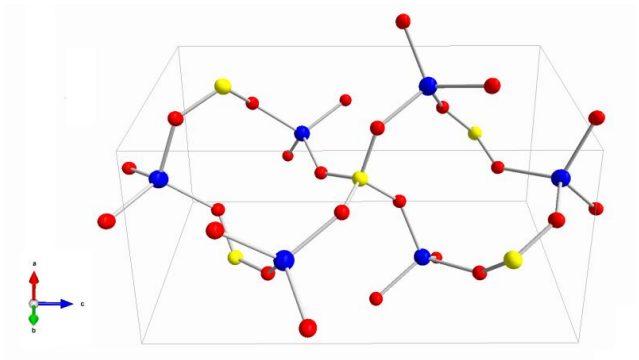

(b)

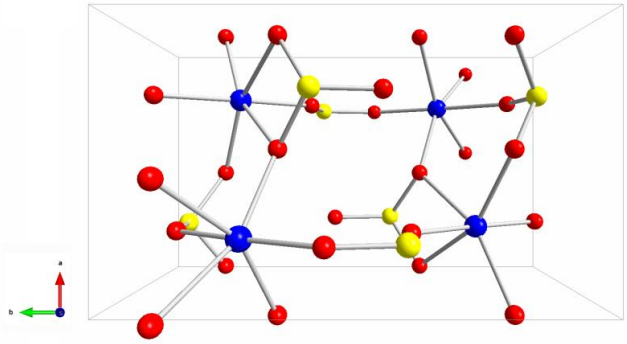

Figure 1.17 Crystal structures of (a) *P3₁21* $FePO_4$ and (b) *Pnma* $FePO_4$, blue ball is Fe, red ball is O, and yellow ball is P.

1.5.2.3 Molybdate Salts

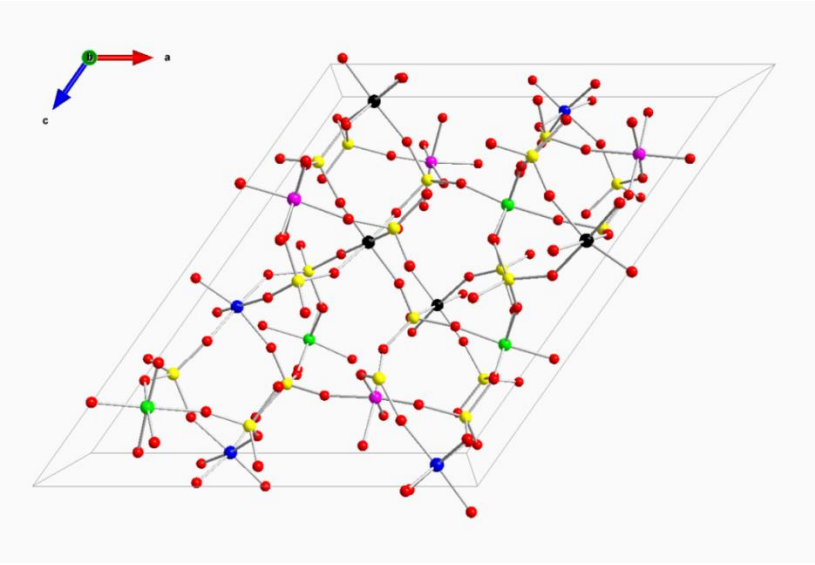

Figure 1.18 Crystal structure of $Fe_2(MoO_4)_3$, green ball is Fe(1), blue ball is Fe(2), pink ball is Fe(3), black ball is Fe(4), red ball is O, and yellow ball is Mo.

Iron (III) molybdate, $Fe_2(MoO_4)_3$ [80], has a similar crystal structure to iron (III) sulfate. Iron (III) molybdate crystalizes in the space group $P2_1/a$ with the unit cell parameters a = 15.637(3) Å, b = 9.224(3) Å, c = 18.173(3) Å, β = 125.26(1) °. The crystal structure of $Fe_2(MoO_4)_3$ is shown in Figure 1.18. $Fe_2(MoO_4)_3$ is an antiferromagnet with the Néel temperature T_N = 11.72 K. The neutron diffraction data was collected at 2 K to obtain more magnetic information and the magnetic unit was found to be identical to its crystal unit. The magnetic structure shows that Fe(1) and Fe(3) are parallel whereas Fe(2) and Fe(4) are opposite. Each moment was determined to be 4.34(3) μ_B along the b axis. The bond covalency of iron molybdate is stronger than that of iron sulfate determined by the neutron diffraction data; 9.15% in Fe – O bond in $Fe_2(MoO_4)_3$ and 6.1% in $Fe_2(SO_4)_3$. This explains the different moments for Fe in these two compounds. Superexchange pathways in $Fe_2(MoO_4)_3$ are almost the same as in $Fe_2(SO_4)_3$. The difference between Mo^{6+} and S^{6+} leads to different pathway length and furthermore the strength of each pathway.

1.5.2.4 Germanate Salts

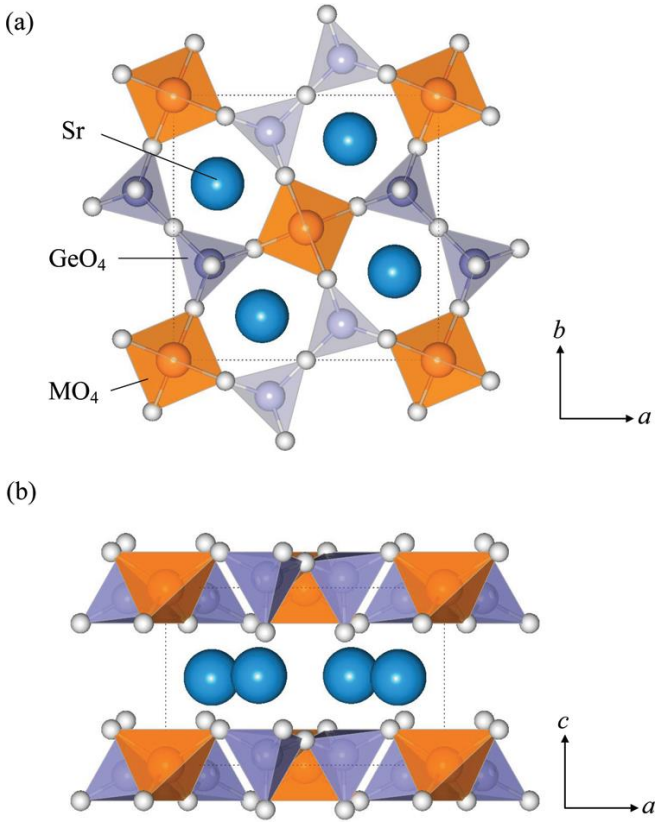

Figure 1.19 Crystal structure of $Sr_2MGe_2O_7$ (M = Mn, Co). [81]

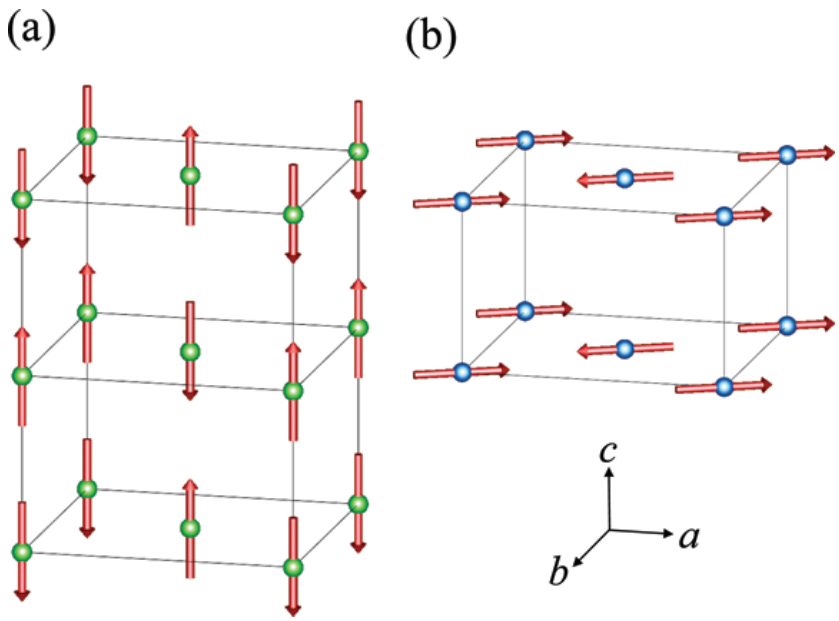

Figure 1.20 Magnetic structure of (a) $Sr_2MnGe_2O_7$ and (b) $Sr_2CoGe_2O_7$. [81]

$Sr_2MGe_2O_7$ (M = Mn, Co) [81], [82], [83], [84] has a tetragonal unit cell (a ~ 8 Å, c ~ 5 Å) with the space group $P\bar{4}2_1m$. Two vertex-sharing tetrahedral [GeO_4] units generate a [Ge_2O_7] unit. The [Ge_2O_7] units and the tetrahedral [MO_4] units build up the (001) layers by vertex-sharing and Sr^{2+} cations are located within these layers. The DC susceptibility of $Sr_2MnGe_2O_7$ reaches a maximum at 6.0 K with an anomaly at around 4 K, showing to be an antiferromagnet. Zero field cooling (ZFC) and field cooling (FC) susceptibilities of $Sr_2CoGe_2O_7$ diverge below 8.4 K and the increasing FC susceptibility indicates a ferromagnetic component. However, the field dependence of magnetization suggests the ferromagnetic component is relatively small and it may come from the Dzyaloshinsky−Moriya interaction. Further specific heat measurements suggest that they are antiferromagnets because the specific heat data show a λ-type anomaly at 4.4 K for $Sr_2MnGe_2O_7$ and at 6.5 K for $Sr_2CoGe_2O_7$. The neutron diffraction data also prove it. Their magnetic structures are shown in Figure 1.20. The magnetic structure of $Sr_2MnGe_2O_7$ doubles along the c axis from its crystal structure. The moment of each Mn^{2+} orders along the c axis and is antiferromagnetic to its six NN Mn^{2+}. The determined value for each Mn is 3.99(5) μ_B at 2.5 K. The magnetic structure of $Sr_2CoGe_2O_7$ is the same as its crystal structure. The spins of Co^{2+} lie in the (001) plane and each spin is antiferromagnetic to its four NN Co^{2+} within the (001) plane. The exact direction of the spin cannot be fixed due to the crystal symmetry. The determined moment of each Co is 2.81(5) μ_B at 2.5 K. The superexchange pathway of $Sr_2MGe_2O_7$ is M – O – Ge – O – M. Every metal cation M has

this interaction with its four NN metal cations M along the [110] and the [1$\bar{1}$0] axis. Such interaction produces the same pattern of magnetic structure within the (001) plane and the different anisotropy between a d^5 cation (Mn^{2+}) and a d^7 cation (Co^{2+}) leads the magnetic moment lying along the [001] axis or within the (001) plane. From the DC susceptibility data of $Sr_2MnGe_2O_7$, the overall exchange integral within the (001) planes was determined to be -0.34 K and -0.07 K along the [001] axis. Furthermore, $Sr_2MnGe_2S_6O$ [85] was synthesized. It has almost the same crystal structure and magnetic properties as $Sr_2MnGe_2O_7$ but the Néel temperature is 15.5 K, which indicates the superexchange interactions are stronger. The overall exchange integrals is now -1.03 K within the (001) planes and -0.35 K along the [001] axis.

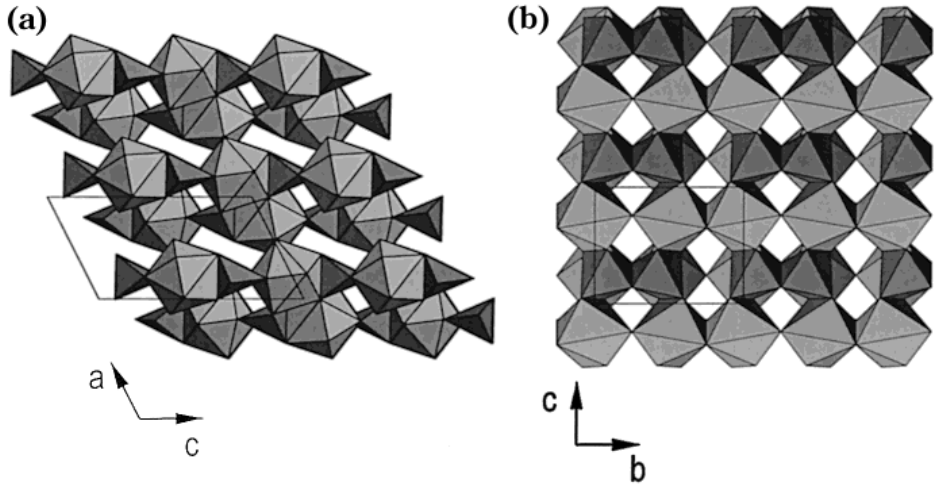

Figure 1.21 (a) Crystal structure of *R*$FeGe_2O_7$, space group *P2₁/c*; large (gray) and small (dark gray) polyhedra correspond to *R*O_9 tricapped trigonal prisms and FeO_5 trigonal bipyramids, respectively. (b) Crystal structure of *R*$FeGe_2O_7$, space group *P2₁/m*; large (gray) and small (dark gray) polyhedra correspond to *R*O_7 capped octahedron and FeO_6 octahedron, respectively. [86]

A series of *R*$FeGe_2O_7$ (*R* = rare earth lanthanides, Y) [86], [87], [88] compounds were synthesized by Cascales *et al*. All the compositions are monoclinic but the space group is *P2₁/c* for *R* = La – Gd and *P2₁/m* for *R* = Tb – Lu, Y due to the difference in the radii of rare earth cations. Basically in *R*$FeGe_2O_7$, metal cation polyhedra construct the (100) layers and such layers are separated by the layers containing the [Ge_2O_7] units. Different space groups have different local environments. It is [*R*O_9] and [FeO_5] making up the

metal containing (100) layers of the space group $P2_1/c$ and [RO_7] and [FeO_6] of the space group $P2_1/m$. In the *bc* plane, the rare-earth cations and Fe^{3+} are linked by – FeO_5 – RO_9 – FeO_5 – (or – FeO_6 – RO_7 – FeO_6 –) chains along the *c* axis by edge sharing. The rare-earth cations are connected by – RO_9 – RO_9 – RO_9 – (or – RO_7 – RO_7 – RO_7 –) chains along the *b* axis by edge and vertex sharing. Two neighbour Fe^{3+} polyhedra along the *b* axis are also linked to be a [Fe_2O_8] (or [Fe_2O_{10}]) unit by edge sharing, but such small units are separated in one (001) layer. Super-superexchange pathways link the (100) layers by Fe – O – Ge – O – Fe, Fe – O – Ge – O –*R* and *R* – O – Ge – O – *R*. As discussed in Chapter 1.4.3, only short range Fe – O – Fe superexchange in the [Fe_2O_8] (or [Fe_2O_{10}]) units, Fe – O – *R* superexchange in the – FeO_5 – PrO_9 – FeO_5 – (or – FeO_6 – TbO_7 – FeO_6 –) chains along the *c* axis and the Fe – O – Ge – O – Fe super-superexchange linking the (100) layers are considered to be significant. Further magnetometry and neutron diffraction measurements were conducted on these compounds. For $PrFeGe_2O_7$, space group $P2_1/c$, it only shows one transition with the Néel temperature 3 K. The compounds containing the nonmagnetic cation, $YFeGe_2O_7$, has the space group $P2_1/m$ and it also shows one transition but at a higher Néel temperature, 38 K. The other cases, *R*$FeGe_2O_7$ (*R* = Tb – Yb), space group $P2_1/m$, have two transitions, see Figure 1.22(a), T_1 = 40 K and T_2 = 20, 24, 12, 8, 6, 5 K for *R* = Tb – Yb, respectively. However, the second transition was found by the differential method $d\chi T/dT$. The neutron diffraction data illustrate that all the compounds have 3D magnetic structures below T_2. It suggests that the higher Néel temperature T_1 ~ 40 K corresponds to the Fe^{3+} ordering and the lower one T_2 corresponds to the R^{3+} ordering, see Figure 1.22(b). The ordered magnetic structure of $PrFeGe_2O_7$ can be described with the propagation vector $\boldsymbol{k}$ = [1/2, 1/2, 0] in a magnetic unit cell *a'* = 2*a*, *b'* = 2*b*, *c'* = *c*. Fe^{3+} and Pr^{3+} order ferromagnetic along the *c* axis via the – FeO_5 – PrO_9 – FeO_5 – chains whereas their moments are antiferromagnetic along the other two axes. In *R*$FeGe_2O_7$ (*R* = Tb – Yb), the propagation vector is $\boldsymbol{k}$ = [0, 0, 0] and the magnetic unit cell is the same as its crystal unit cell. The moments of Fe^{3+} and R^{3+} couple ferromagnetically within the *ac* plane and antiferromagnetically along the *b* axis. The mean ordered moment of Fe^{3+} are all about 4 μ_B at ~ 2 K whereas the ordered moments of R^{3+} are close to their $g_{Ln}J_{Ln}$ values. The complicated 3D antiferromagnetic-based magnetic structure is not surprising as the interactions are complex. That the cations order antiferromagnetically via Fe – O – Fe and *R* – O – *R* superexchange along the *b* axis in the two structures is consistent with the Goodenough-Kanamori rules. The long range superexchange *R* – O – Fe results in the R^{3+} and Fe^{3+} ordering ferromagnetically within each chain whereas the nearest-neighbour

chains are antiferromagnetic along the *b* axis. Different Néel temperatures T_2 may come from the dipolar interactions and the anisotropic terms of the lanthanide cations, which also have considerable influence on the magnetic exchange.

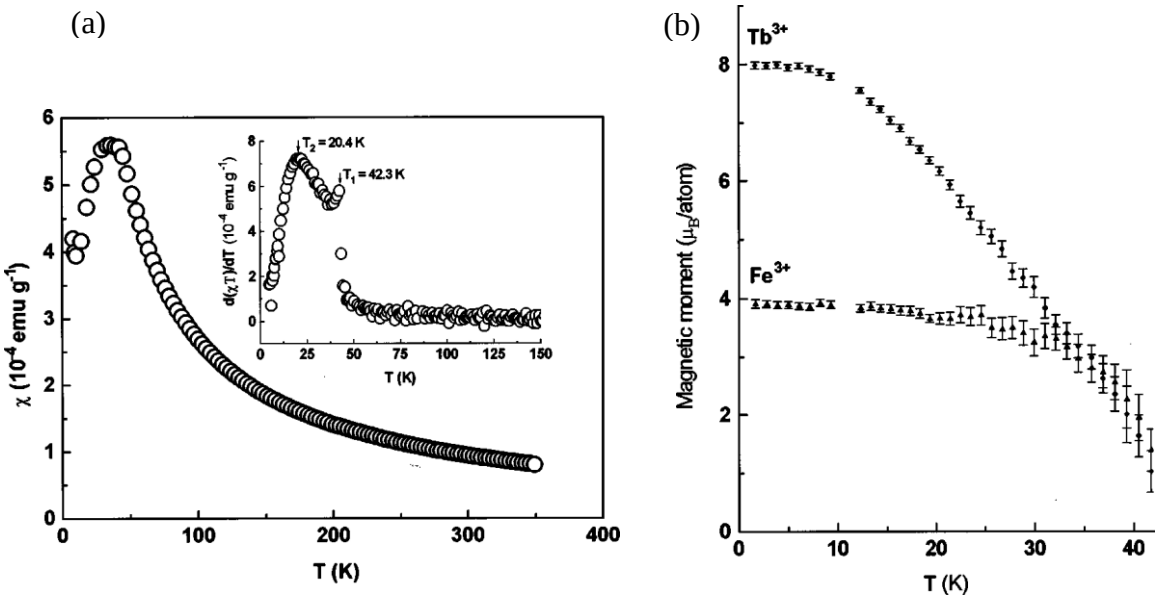

Figure 1.22 (a) Magnetic susceptibility χ(T) for $FeTbGe_2O_7$. (inset) A second anomaly appears in d(χT)dT. (b) Thermal evolution of the ordered magnetic moments of Fe^{3+} and Tb^{3+} in $FeTbGe_2O_7$. [87]

Cascales *et al*. had also studied $R_2CuGe_4O_{12}$ (*R* = Y, Eu – Lu) [89], [90], [91], [92]. With the presence of the strong Jahn-Teller effect cation Cu^{2+}, the compounds crystallize in a triclinic phase with the space group $P\bar{1}$. Similar to $RFeGe_2O_7$, $R_2CuGe_4O_{12}$ has the metal-containing layers and the diamagnetic $[Ge_4O_{12}]$ unit layers. Metal cation polyhedral, $[RO_7]$ and $[CuO_6]$, construct the (001) layers and such layers are separated by the $[Ge_4O_{12}]$ layers constructed by four vertex sharing $[GeO_4]$ tetrahedra. Within the metal (001) layers, $[RO_7]$ units line up along the [100] axis by edge sharing and the lines are connected by $[CuO_6]$ octehedra by edge sharing, see Figure 1.23. In these compounds, the *R* – O – *R* superexchange makes up long range chains along the *a* axis whereas the *R* – O – Cu superexchange only links two lanthanide cations to one Cu^{2+} over a short range. Moreover, Cu – O – Ge – O – Cu super-superexchange along the c axis is also significant. The magnetometry data show that the compounds only have one transition temperature below 10 K; ~ 6 K for *R* = Tb and Dy; 3.3 K for Ho and Er. The neutron diffraction data illustrate that the compounds are also 3D antiferromagnets. However, the propagation vector are different based on different lanthanide cations; $\boldsymbol{k}$ = [1/2, 1/2, 1/2] with the magnetic unit

cell *a'* = 2*a*, *b'* = 2*b*, *c'* = 2*c* for Tb and Dy; $\boldsymbol{k}$ = [0, 0, 1/2] with the magnetic unit cell *a'* = *a*, *b'* = *b*, *c'* = 2*c* for Ho; $\boldsymbol{k}$ = [0, 1/2, 1/2] with the magnetic unit cell *a'* = *a*, *b'* = 2*b*, *c'* = 2*c* for Er. The magnetic structures of the compounds are complex and different, see Figure 1.24 and Figure 1.24. In the case of *R* = Tb and Dy, the moments of R^{3+} mainly couple antiferromagnetically along the *b* axis (Tb) or the *a* axis (Dy) whereas for the coupling is ferromagnetic along the *a* axis (Ho) or the *b* axis (Er). The moments of Cu^{2+} respond differently to different lanthanide cations. The mean ordered moments of R^{3+} and Cu^{2+} at 1.6 K were determined to be 7.6(2) and 1.5(6) μ_B of Tb; 7.6(1) and 1.6(6) μ_B of Dy; 6.10(4) and 1.05(7) μ_B of Ho; 6.76(8) and 1.2(1) μ_B of Er whereas their theoretical values to be $g_{Ln}J_{Ln}$ = 9, 10, 10, 9 μ_B for Tb-Er, respectively, and 1 μ_B for Cu^{2+} in the spin-only case. That the moments of the lanthanides are lower than their theoretical value may be because the temperature of the neutron diffraction experiments were not low enough for the moments to be fully ordered. As mentioned above, the significant exchange pathways are *R* – O – *R* along the *a* axis, *R* – O – Cu along the *b* axis and Cu – O – Ge – O – Cu along the *c* axis. However, the anisotropic exchanges in this system and also the existence of the dipolar interaction lead the compounds behaving different from the $RFeGe_2O_7$ ones. The radii of the cations may also result in the difference.

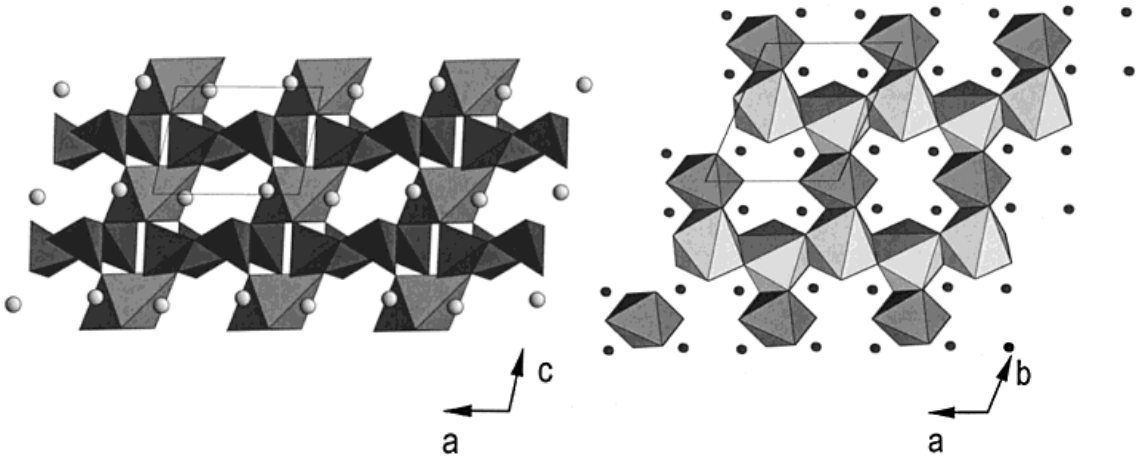

Figure 1.23 View of the lattice of $R_2CuGe_4O_{12}$ along the *b* direction (left), showing connections between [Ge_4O_{12}] (deep gray) tetrahedra layers through isolated CuO_6 octahedra (medium gray) in the *c* direction. Spheres represent R^{3+} cations; *c* direction (right), chains running along the a axis of RO_7 (light gray) polyhedra, linked in the b direction through CuO_6 octahedra. Small spheres represent Ge positions. [91]

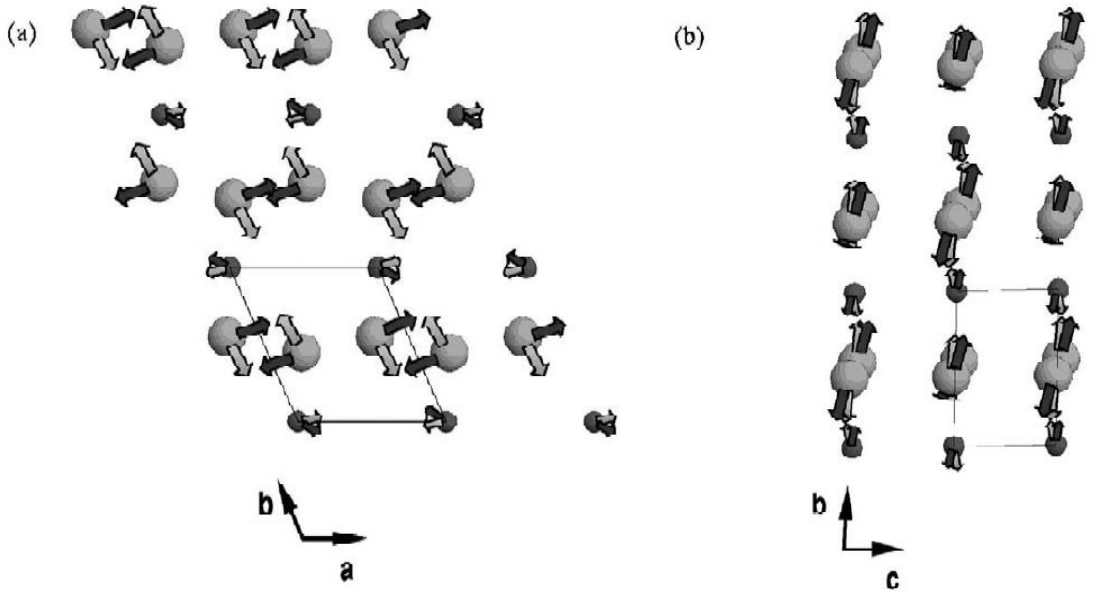

Figure 1.24 Projection of the arrangement of magnetic moments of *R* and Cu onto (a) *ab* planes and (b) *bc* planes, small and large spheres are representing Cu and *R* atoms, gray and black arrows correspond to Tb and Dy compounds, respectively. [92]

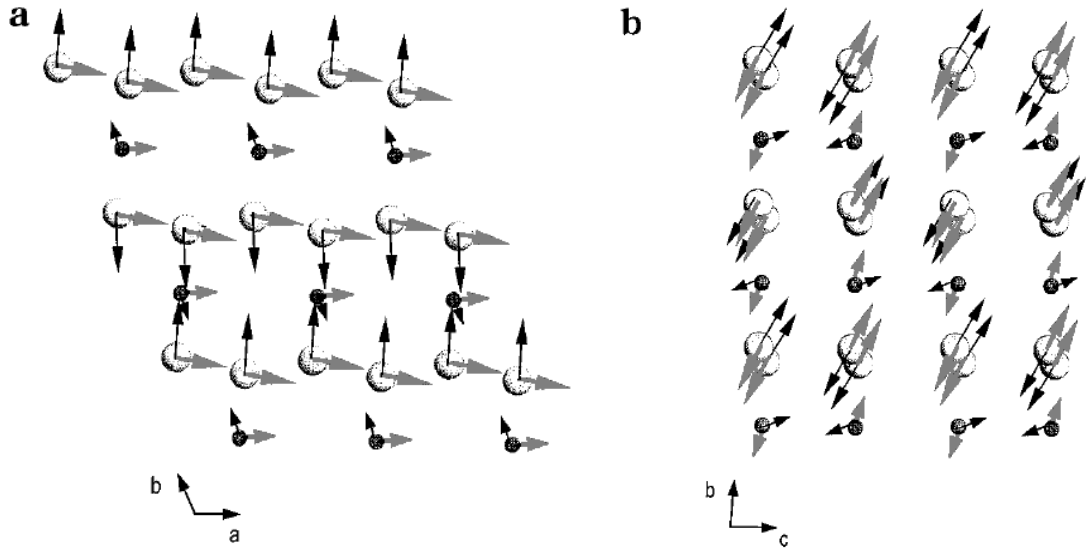

Figure 1.25 Projection of the arrangement of magnetic moments of *R* and Cu onto (a) *ab* planes and (b) *bc* planes, small and large spheres are representing Cu and *R* atoms, gray and black arrows correspond to Ho and Er compounds, respectively. [91]

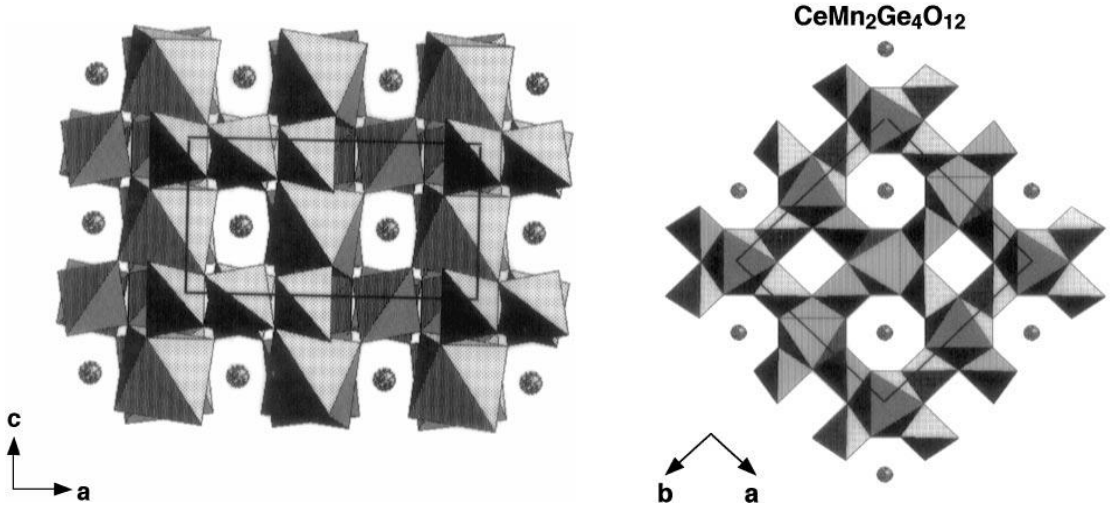

Figure 1.26 Structure of $CeMn_2Ge_4O_{12}$ in the ac-plane. Small filled circles represent cerium atoms. [93]

Taviot-Gueho [93] *et al*. have reported the synthesis but not the magnetic properties of $CeMn_2Ge_4O_{12}$ and $GdMnGe_2O_7$. $GdMnGe_2O_7$ has a similar crystal structure as $RFeGe_2O_7$ whereas $CeMn_2Ge_4O_{12}$ crystallises in the space group *P*4/*nbm* with the *2b* site being occupied by Ce^{4+} and the *4f* site by Mn^{2+}. The two distinct cation sites are coordinated by eight and six oxygen atoms, respectively, and have square-antiprismatic and octahedral geometries. They can be considered to lie in layers perpendicular to the [001] axis; separated by layers the containing $[Ge_4O_{12}]^{8-}$ rings, each ring being comprised of four vertex-sharing $[GeO_4]$ tetrahedra, see Figure 1.26. Many compounds with the formula $R_2MGe_4O_{12}$, where *R* is a lanthanide or Y and *M* is Ca, Mn or Zn were then studied by Zubkov [94], [95], [96], [97] *et al*. in depth. These compounds also crystallise in the space group *P*4/*nbm* and have the same structure as $CeMn_2Ge_4O_{12}$. However, the *4f* site is now occupied by a disordered 1:1 distribution of *R* and *M*. Attempts to incorporate large lanthanide cations (*R* = La - Sm) were not successful. The interest of Zubkov *et al*. centred on the luminescence properties of these compounds. The only magnetic study was a dc susceptibility measurement of $Eu_2MnGe_4O_{12}$, which was found to be paramagnetic till 1.5 K. Following the fitting to the Curie-Weiss Law, $Eu_2MnGe_4O_{12}$ was suggested to be $Eu_{1.3}{}^{2+}Eu_{0.7}{}^{3+}Mn_{0.65}{}^{4+}Mn_{0.35}{}^{2+}MnGe_4O_{12}$ to explain the abnormally high Curie constant.

This thesis focuses on the magnetic properties of germanates that are isostructural with those reported by Taviot-Gueho *et al*. and Zubkov *et al*. A series of tetragonal (space group *P*4/*nbm*) germanates with a general formula $ABB'Ge_4O_{12}$ have been studied. Different

cations were chosen for the *B* and *B'* sites, for example spherical Mn^{2+}, cations with different anisotropies (Co^{2+}, Ni^{2+} and Cu^{2+}) and the non-magnetic cation Zn^{2+}. Solid solutions have been made to study the influence of the cation electron configuration on the magnetic properties. Moreover, the *A* site cation was varied to reach a better understanding of the influence of the unit cell parameters on magnetic properties. More specifically, the systems $CeMn_{2-x}Co_xGe_4O_{12}$, $ZrMn_{2-x}Co_xGe_4O_{12}$ and $LnFeMGe_4O_{12}$ (*Ln* = Eu, Lu and Y) have been synthesized and characterized. Rare-earth cations were then allowed to occupy the square-antiprism site and half of the octahedral sites. This part of work can be exemplified by the compositions $Tb_2CoGe_4O_{12}$ and $TbScCoGe_4O_{12}$, amongst others. Different types of magnetic behaviour have been observed in different compounds. They are discussed in terms of the crystal field effects, magnetic anisotropy and the relative strengths of competing superexchange interactions.

1.6 References

[1] A. R. West, *Solid state Chemistry and its Applications*, John Wiley & Sons Ltd.: **1984**.

[2] G. Calestani, and C. Rizzoli, Crystal structure of the $YBa_2Cu_3O_7$ superconductor by single-crystal X-ray diffraction, *Nature*, **1987**, *328*, 606-607.

[3] B. T. Shirk, and W. R. Buessem, Temperature Dependence of M_s and K_1 of $BaFe_{12}O_{19}$ and $SrFe_{12}O_{19}$ Single Crystals, *Journal of Applied Physics*, **1969**, *40*, 1294-1296.

[4] G. H. Kwei, A. C. Lawson, S. J. L. Billinge, and S. W. Cheong, Structures of the ferroelectric phases of barium titanate, *The Journal of Physical Chemistry*, **1993**, *97*, 2368-2377.

[5] T. Arima, Y. Tokura, and J. B. Torrance, Variation of optical gaps in perovskite-type 3d transition-metal oxides, *Physical Review B*, **1993**, *48*, 17006.

[6] M. Gasior, and T. Machej, Morphological aspects in the oxidation of o-xylene on V_2O_5 catalysts, *Journal of Catalysis*, **1983**, *83*, 472-476.

[7] X. Ke, M. L. Dahlberg, E. Morosan, J. A. Fleitman, R. J. Cava, and P. Schiffer, Magnetothermodynamics of the Ising antiferromagnet $Dy_2Ge_2O_7$, *Physical Review B*, **2008**, *78*, 104411.

[8] J. M. D. Coey, *Magnetism and Magnetic Materials*, Cambridge University Press: **2010**.

[9] L. Wilets, and D. M. Chase, Angular Distribution of Fission Fragments at Threshold According to the Bohr Model, *Physical Review*, **1956**, *103*, 1296.

[10] R. A. Bari, and J. Sivardière, Low-Spin-High-Spin Transitions in Transition-Metal-Ion Compounds, *Physical Review B*, **1972**, *5*, 4466.

[11] H. Spiering, E. Meissner, H. Köppen, E. W. Müller, and P. Gütlich, The effect of the lattice expansion on high spin ⇌ low spin transitions, *Chemical Physics*, **1982**, *68*, 65-71.

[12] G. J. Halder, C. J. Kepert, B. Moubaraki, K. S. Murray, and J. D. Cashion, Guest-Dependent Spin Crossover in a Nanoporous Molecular Framework Material, *Science*, **2002**, *298*, 1762-1765.

[13] R. J. Radwanski, and Z. Ropka, Orbital moment in CoO and in NiO, *Physica B: Condensed Matter*, **2004**, *345*, 107-110.

[14] M. Tadic, D. Nikolic, M. Panjan, and G. R. Blake, Magnetic properties of NiO (nickel oxide) nanoparticles: Blocking temperature and Neel temperature, *Journal of Alloys and Compounds*, **2015**, *647*, 1061-1068.

[15] J. H. E. Griffiths, and J. Owen, Complex Hyperfine Structures in Microwave Spectra of Covalent Iridium Compounds, *Proceedings of the Royal Society of London A*, **1954**, *226*, 96-111.

[16] J. Owen, and K. W. H. Stevens, Paramagnetic Resonance and Covalent Bonding, *Nature*, **1953**, *171*, 836.

[17] K. W. H. Stevens, On the Magnetic Properties of Covalent XY_6 Complexes, *Proceedings of the Royal Society of London A*, **1953**, *219*, 542-555.

[18] R. Nathans, H. A. Alperin, S. J. Pickart, and P. J. Brown, Measurement of the Covalent Spin Distribution in Manganous Fluoride Using Polarized Neutrons, *Journal of Applied Physics*, **1963**, *34*, 1182-1186.

[19] J. Hubbard, and W. Marshall, Covalency effects in neutron diffraction from ferromagnetic and antiferromagnetic salts, *Proceedings of the Physical Society*, **1965**, *86*, 561-572.

[20] B. E. F. Fender, A. J. Jacobson, and F. A. Wedgwood, Covalency Parameters in MnO, α-MnS, and NiO, *The Journal of Chemical Physics*, **1968**, *48*, 990-994.

[21] M. T. Hutchings, and H. J. Guggenheim, Neutron Diffraction Measurement of the Effective Magnetic Moment of Ni^{2+} in $KNiF_3$, *Journal of Applied Physics*, **1970**, *41*, 945-945.

[22] G. J. Long, G. Longworth, P. Battle, A. K. Cheetham, R. V. Thundathil, and D. Beveridge, A Study of Anhydrous Iron(III) Sulfate by Magnetic Susceptibility, Mossbauer, and Neutron Diffraction Techniques, *Inorganic Chemistry*, **1979**, *18*, 624-632.

[23] P. D. Battle, A. K. Cheetham, C Gleitzertt, W. T. A. Harrison, G. J. Long, and G. Longworth, A novel magnetic phase transition in anhydrous iron (III) phosphate, $FePO_4$, *Journal of Physics C: Solid State Physics*, **1982**, *15*, L919-L924.

[24] T. R. McGuire, and M. W. Shafer, Ferromagnetic Europium Compounds, *Journal of Applied Physics*, **1964**, *35*, 984-988.

[25] H. S. Jarrett, W. H. Cloud, R. J. Bouchard, S. R. Butler, C. G. Frederick, and J. L. Gillson, Evidence for Itinerant d-Electron Ferromagnetism, *Physical Review Letters*, **1968**, *21*, 617.

[26] W. Gong, H. Li, Z. Zhao, and J. Chen, Ultrafine particles of Fe, Co, and Ni ferromagnetic metals, *Journal of Applied Physics*, **1991**, *69*, 5119.

[27] V. L. Moruzzi, and P. M. Marcus, Ferromagnetic phases of bcc and fcc Fe, Co, and Ni, *Physical Review B*, **1986**, *34*, 1784-1791.

[28] J. G. Cheng, J. S. Zhou, J. B. Goodenough, and C. Q. Jin, Critical behavior of ferromagnetic perovskite ruthenates, *Physical Review B*, **2012**, *85*, 184430.

[29] J. S. Zhou, K. Matsubayashi, Y. Uwatoko, C. Q. Jin, J. G. Cheng, J. B. Goodenough, Q. Q. Liu, T. Katsura, A. Shatskiy, and E. Ito, Critical Behavior of the Ferromagnetic Perovskite $BaRuO_3$, *Physical Review Letters*, **2008**, *101*, 077206.

[30] J. R. Singer, Magnetic Susceptibility of NiO and CoO Single Crystals, *Physical Review*, **1956**, *104*, 929-932.

[31] W. L. Roth, Magnetic Structures of MnO, FeO, CoO, and NiO, *Physical Review*, **1958**, *110*, 1333-1341.

[32] F. U. Hillebrecht, H. Ohldag, N. B. Weber, C. Bethke, U. Mick, M. Weiss, and J. Bahrdt, Magnetic moments at the surface of antiferromagnetic NiO(100), *Physical Review Letters*, **2001**, *86*, 3419-3422.

[33] C. G. Shull, E. O. Wollan, and W. C. Koehler, Neutron Scattering and Polarization by Ferromagnetic Materials, *Physical Review B*, **1951**, *84*, 912.

[34] F. Söffge, AC susceptability and static magnetic properties of AN Fe_3O_4 ferrofluid, *Journal of Magnetism and Magnetic Materials*, **1981**, *24*, 54-66.

[35] A. W. McReynolds, and T. Riste, Magnetic Neutron Diffraction from Fe_3O_4, *Physical Review B*, **1954**, *95*, 1161.

[36] D. Shaltiel, Nuclear Magnetic Resonance of $MnCO_3$ in the Canted Spin State, *Physical Review*, **1966**, *142*, 300-306.

[37] P. J. Brown, and J. B. Forsyth, The spatial distribution of ferromagnetic moment in $MnCO_3$, *Proceedings of the Physical Society*, **1967**, *92*, 125-135.

[38] I. Dzyaloshinsky, A thermodynamic theory of "weak" ferromagnetism of antiferromagnetics, *Journal of Physics and Chemistry of Solids*, **1958**, *4*, 241-255.

[39] T. Moriya, Anisotropic Superexchange Interaction and Weak Ferromagnetism, *Physical Review*, **1960**, *120*, 91-98.

[40] E. Stryjewski, and N. Giordano, Metamagnetism, *Advances in Physics*, **1977**, *26*, 487-650.

[41] M. Lenertz, J. Alaria, D. Stoeffler, S. Colis, and A. Dinia, Magnetic Properties of Low-Dimensional r and γ CoV_2O_6, *Journal of Physical Chemistry C*, **2011**, *115*, 17190-17196.

[42] S. A. J. Kimber, H. Mutka, T. Chatterji, T. Hofmann, P. F. Henry, H. N. Bordallo, D. N. Argyriou, and J. P. Attfield, Metamagnetism and soliton excitations in the modulated ferromagnetic Ising chain CoV_2O_6, *Physical Review B*, **2011**, *84*, 104425.

[43] M. Tokunaga, and N. Miura, High-magnetic-field study of the phase transitions of $R_{1-x}Ca_xMnO_3$ (R = Pr, Nd), *Physical Review B*, **1998**, *57*, 5259-5264.

[44] C. Lacroix, P. Mendels, and F. Mila, *Introduction to Frustrated Magnetism*, Springer: **2011**.

[45] E. Morosan, J. A. Fleitman, Q. Huang, J. W. Lynn, Y. Chen, X. Ke, M. L. Dahlberg, P. Schiffer, C. R. Craley, and R. J. Cava, Structure and magnetic properties of the $Ho_2Ge_2O_7$ pyrogermanate, *Physical Review B*, **2008**, *77*, 224423.

[46] H. D. Zhou, S. T. Bramwell, J. G. Cheng, C. R. Wiebe, G. Li, L. Balicas, J. A. Bloxsom, H. J. Silverstein, J. S. Zhou, J. B. Goodenough, and J. S. Gardner, High pressure route to generate magnetic monopole dimers in spin ice, *Nature Communication*, **2011**, *2*, 478.

[47] A. M. Hallas, J. A. M. Paddison, H. J. Silverstein, A. L. Goodwin, J. R. Stewart, A. R. Wildes, J. G. Cheng, J. S. Zhou, J. B. Goodenough, E. S. Choi, G. Ehlers, J. S. Gardner, J. S. Wiebe, and H. D. Zhou, Statics and dynamics of the highly correlated spin ice $Ho_2Ge_2O_7$, *Physical Review B*, **2012**, *86*, 134431.

[48] A. M. Hallas, J. G. Cheng, A. M. Arevalo-Lopez, H. J. Silverstein, Y. Su, P. M. Sarte, H. D. Zhou, E. S. Choi, J. P. Attfield, G. M. Luke, and C. R. Wiebe, Incipient ferromagnetism in $Tb_2Ge_2O_7$: application of chemical pressure to the enigmatic spin-liquid compound $Tb_2Ti_2O_7$, *Physical Review Letters*, **2014**, *113*, 267205.

[49] C. R. Wiebe, and A. M. Hallas, Frustration under pressure: Exotic magnetism in new pyrochlore oxides, *APL Materials*, **2015**, *3*, 041519.

[50] L. Pauling, The Structure and Entropy of Ice and of Other Crystals with Some Randomness of Atomic Arrangement, *Journal of the American Chemical Society*, **1935**, *57*, 2680-2684.

[51] H. J. Silverstein, K. Fritsch, F. Flicker, A. M. Hallas, J. S. Gardner, Y. Qiu, G. Ehlers, A. T. Savici, Z. Yamani, K. A. Ross, B. D. Gaulin, M. J. P. Gingras, J. A. M. Paddison, K. Foyevtsova, R. Valenti, F. Hawthorne, C. R. Wiebe, and H. D. Zhou, Liquidlike correlations in single-crystalline $Y_2Mo_2O_7$: An unconventional spin glass, *Physical Review B*, **2014**, *89*, 054433.

[52] J. A. Mydosh, *Spin Glasses: An Experimental Introduction*, Taylor & Francis, London: **1993**.

[53] N. Ishii, Y. Okamura, S. Chiba, T. Nogami and T. Ishida, Giant Coercivity in a One-Dimensional Cobalt-Radical Coordination Magnet, *Journal of the American Chemical Society*, **2008**, *130*, 24-25.

[54] Y. Ma, G. Xu, X. Yang, L. Li, J. Tang, S. Yan, P. Cheng, and D. Liao, Pyrazine-bridged Dy_2 single-molecule magnet with a large anisotropic barrier, *Chemical Communications*, **2010**, *46*, 8264-8266.

[55] H. A. Kramers, L'interaction Entre les Atomes Magnétogènes dans un Cristal Paramagnétique, *Physica*, **1934**, *1*, 182-192.

[56] P. W. Anderson, Antiferromagnetism. Theory of Superexchange Interaction, *Physical Review*, **1950**, *79*, 350.

[57] D. A. McQuarrie, and J. D. Simon, *Physical Chemistry: A Molecular Approach*, University Science Books: **1997**.

[58] W. Nolting, and A. Ramakanth, *Quantum Theory of Magnetism*, Springer: **2009**.

[59] J. Tang, and P. Zhang, *Lanthanide Single Molecule Magnets*, Springer: **2015**.

[60] J. B. Goodenough, Theory of the Role of Covalence in the Perovskite-Type Manganites [La, M(II)]MnO_3, *Physical Review B*, **1955**, *100*, 564.

[61] J. Kanamori, Superexchange interaction and symmetry properties of electron orbitals, *Journal of Physics and Chemistry of Solids*, **1959**, *10*, 87-98.

[62] J. Kondo, Superexchange Interaction of MnO, *Progress of Theoretical Physics*, **1959**, *22*, 41-61.

[63] A. J. Millis, Orbital ordering and superexchange in manganite oxides, *Physical Review B*, **1997**, *55*, 6405-6408.

[64] J. B. Goodenough, An interpretation of the magnetic properties of the perovskite-type mixed crystals $La_{1-x}Sr_xCoO_{3-\lambda}$, *Journal of Physics and Chemistry of Solids*, **1958**, *6*, 287-297.

[65] J. Kanamori, Theory of the Magnetic Properties of Ferrous and Cobaltous Oxides, *Progress of Theoretical Physics*, **1957**, *17*, 177–196; 197–222.

[66] M. T. Hutchings, and E. J. Samuelsen, Measurement of Spin-Wave Dispersion in NiO by Inelastic Neutron Scattering and Its Relation to Magnetic Properties, *Physical Review B*, **1972**, *6*, 3447-3461.

[67] D. A. O. Hope, and A. K. Cheetham, A low-temperature powder neutron diffraction study of the antiferromagnetic phase of $Mn_xCo_{1-x}O$, *Journal of Solid State Chemistry*, **1988**, *72*, 42-51.

[68] N. Mironova-Ulmane, V. Skvortsova, A. Kuzmin, U. Ulmanis, I. Sildos, E. Cazzanelli, and G. Mariotto, Magnetic ion exchange interactions in NiO-MgO solid solutions, *Physics of the Solid State*, **2005**, *47*, 1516-1522.

[69] G. Fischer, M. Dane, A. Ernst, P. Bruno, M. Luders, Z. Szotek, W. Temmerman, and W. Hergert, Exchange coupling in transition metal monoxides, *Physical Review B*, **2009**, *80*, 014408.

[70] W. A. Harrison, Heisenberg exchange in the magnetic monoxides, *Physical Review B*, **2007**, *76*, 054417.

[71] R. E. Dietz, W. F. Brinkman, A. E. Meixner, and H. J. Guggenheim, Raman Scattering by Four Magnons in NiO and $KNiF_3$, *Physical Review Letters*, **1971**, *27*, 814.

[72] M. J. Massey, N. H. Chen, J. W. Allen, and R. Merlin, Pressure dependence of two-magnon Raman scattering in NiO, *Physical Review B*, **1990**, *42*, 8776.

[73] E. O. Wollan, and W. C. Koehler, Neutron Diffraction Study of the Magnetic Properties of the Series of Perovskite-Type Compounds[(1−x)La, xCa]MnO_3, *Physical Review*, **1955**, *100*, 545-563.

[74] T. Hotta, S. Yunoki, M. Mayr, and E. Dagotto, A-type antiferromagnetic and C-type orbital-ordered states in $LaMnO_3$ using cooperative Jahn-Teller phonons, *Physical Review B*, **1999**, *60*, R15009-R15012.

[75] L. Y. Gan, S. O. Akande, and U. Schwingenschlögl, Anisotropic O vacancy formation and diffusion in $LaMnO_3$, *Journal of Materials Chemistry A*, **2014**, *2*, 19733-19737.

[76] A. Goñi, L. Lezama, A. Espina, C. Trobajo, J. R. García, and T. Rojo, Magnetic properties of two hydrothermally synthesized iron(iii) phosphates: $Fe(NH_3)_2PO_4$ and $Fe(NH_4)(HPO_4)_2$, *Journal of Materials Chemistry*, **2001**, *11*, 2315-2319.

[77] G. Rousse, J. Rodriguez-Carvajal, S. Patoux, and C. Masquelier, Magnetic Structures of the Triphylite $LiFePO_4$ and of Its Delithiated Form $FePO_4$, *Chemistry of Materials*, **2003**, *15*, 4082-4090.

[78] D. Dai, M. H. Whangbo, H. J. Koo, X. Rocquefelte, S. Jobic, and A. Villesuzanne, Analysis of the Spin Exchange Interactions and the Ordered Magnetic Structures of Lithium Transition Metal Phosphates $LiMPO_4$ (M= Mn, Fe, Co, Ni) with the Olivine Structure, *Inorganic Chemistry*, **2005**, *44*, 2407-2413.

[79] M. S. Whittingham, Y. Song, S. Lutta, P. Y. Zavalij, and N. A. Chernova, Some transition metal (oxy)phosphates and vanadium oxides for lithium batteries, *Journal of Materials Chemistry*, **2005**, *15*, 3362-3379.

[80] P. D. Battle, A. K. Cheetham, G. J. Long, and G. Longworth, Study of the Magnetic Properties of Iron(III) Molybdate, by Susceptibility, Mossbauer, and Neutron Diffraction Techniques, *Inorganic Chemistry*, **1982**, *21*, 4223-4228.

[81] T. Endo, Y. Doi, Y. Hinatsu, and K. Ohoyama, Magnetic and neutron diffraction study on melilite-type oxides $Sr_2MGe_2O_7$ (M = Mn, Co), *Inorganic Chemistry*, **2012**, *51*, 3572-3578.

[82] T. Endo, Y. Doi, M. Wakeshima, and Y. Hinatsu, Crystal structures and magnetic properties of new europium melilites $Eu_2MSi_2O_7$ (M = Mg, Mn) and their strontium analogues, *Inorganic Chemistry*, **2010**, *49*, 10809-10814.

[83] I. V. Solovyev, Magnetization-induced local electric dipoles and multiferroic properties of $Ba_2CoGe_2O_7$, *Physical Review B*, **2015**, *91*, 224423.

[84] T. Nakajima, Y. Tokunaga, V. Kocsis, Y. Taguchi, Y. Tokura, and T. H. Arima, Uniaxial-stress control of spin-driven ferroelectricity in multiferroic $Ba_2CoGe_2O_7$, *Physical Review Letters*, **2015**, *114*, 067201.

[85] T. Endo, Y. Doi, M. Wakeshima, K. Suzuki, Y. Matsuo, K. Tezuka, T. Ohtsuki, Y. J. Shan, and Y. Hinatsu, Magnetic Properties of the Melilite-Type Oxysulfide $Sr_2MnGe_2S_6O$: Magnetic Interactions Enhanced by Anion Substitution, *Inorganic Chemistry*, **2017**, *56*, 2459-2466.

[86] C. Cascales, M. T. Fernandez-Diaz, M. A. Monge, and L. Bucio, Crystal Structure and Low-Temperature Magnetic Ordering in Rare Earth Iron Germanates $RFeGe_2O_7$, R = Y, Pr, Dy, Tm, and Yb, *Chemistry of Materials*, **2002**, *14*, 1995-2003.

[87] C. Cascales, L. Bucio, E. G. Puebla, and I. Rasines, Magnetic ordering of Fe and Tb in the ab initio determined Fe*R*Ge_2O_7 structure (*R* = Y, Tb), *Physical Review B*, **1998**, *57*, 5240-5249.

[88] C. Cascales, E. G. Puebla, S. Klimin, B. Lebech, A. Monge, and M. N. Popova, Magnetic Ordering in the Rare Earth Iron Germanates $HoFeGe_2O_7$ and $ErFeGe_2O_7$, *Chemistry of Materials*, **1999**, *11*, 2520-2526.

[89] J. A. Campa, C. Cascales, E. Gutierrez-Puebla, M. A. Monge, I. Rasines, and C. R. Valero, $CuYb_2Ge_4O_{12}$, a New Bidimensionally Tunneled Structure, *Journal of Solid State Chemistry*, **1996**, *124*, 17-23.

[90] E. J. Baran, C. C. Wagner, A. E. Lavat, and C. Cascales, Vibrational Spectra of Tetrametagermanates of the Type $Ln_2CuGe_4O_{12}$ (Ln= Lanthanide or Y), *Journal of Raman Spectroscopy*, **1997**, *28*, 927-931.

[91] C. Cascales, M. T. Fernandez Diaz, and M. A. Monge, Low-Temperature Magnetic Ordering in Rare-Earth Copper Germanates $R_2CuGe_4O_{12}$, R = Ho, Er, *Chemistry of Materials*, **2000**, *12*, 3369-3375.

[92] C. Cascales, and M. A. Monge, Crystal structure and influence of the rare-earth on the magnetic structure of copper germanates $R_2CuGe_4O_{12}$, *Journal of Alloys and Compounds*, **2002**, *344*, 379-384.

[93] C. Taviot-Gueho, P. Leone, P. Palvadeau, and J. Rouxel, Synthesis and structural characterization of ywo new rare-earth maganese germanates: $CeMn_2Ge_4O_{12}$ and $GdMnGe_2O_7$, *Journal of Solid State Chemistry*, **1999**, *143*, 145-150.

[94] V. G. Zubkov, N. V. Tarakina, I. I. Leonidov, A. P. Tyutyunnik, L. L. Surat, M. A. Melkozerova, E. V. Zabolotskaya, and D. G. Kellerman, Synthesis and crystal structure of $Ln_2M^{2+}Ge_4O_{12}$, Ln=rare-earth element or Y; M=Ca, Mn, Zn, *Journal of Solid State Chemistry*, **2010**, *183*, 1186-1193.

[95] I. I. Leonidov, V. G. Zubkov, A. P. Tyutyunnik, N. V. Tarakina, L. L. Surat, O. V. Koryakova, and E. G. Vovkotrub, Upconversion luminescence in Er^{3+}/Yb^{3+} codoped $Y_2CaGe_4O_{12}$, *Journal of Alloys and Compounds*, **2011**, *509*, 1339-1346.

[96] M. A. Melkozerova, N. V. Tarakina, L. G. Maksimova, A. P. Tyutyunnik, L. L. Surat, I. I. Leonidov, V. G. Zubkov, E. V. Zabolotskaya, and R. F. Samigullina, Application of a modified Pechini method for the synthesis of $Ln_2MGe_4O_{12}$ (Ln = Y, Eu; M = Ca, Zn, Mn) optical hosts, *Journal of Sol-Gel Science and Technology*, **2011**, *59*, 338-344.

[97] I. I. Leonidov, V. P. Petrov, V. A. Chernyshev, A. E. Nikiforov, E. G. Vovkotrub, A. P. Tyutyunnik, and V. G. Zubkov, Structural and Vibrational Properties of the Ordered $Y_2CaGe_4O_{12}$ Germanate: A Periodic Ab Initio Study, *Journal of Physical Chemistry C*, **2014**, *118*, 8090-8101.

Chapter 2 - Experimental Techniques

2.1 Synthesis of Oxide Materials

Solid-state reaction [1] is a main route to synthesize inorganic solid-state materials. Generally, all reactions that involve solids can be called solid-state reactions, including gas-solid phase reactions, liquid-solid phase reactions, solid-solid phase reactions and solid-phase decomposition or polymerization. The synthesis of inorganic oxide materials can be achieved in several ways: using a flux method to get a crystal, using a ceramic method to get polycrystalline solid or using a gel method to get a nanoparticle powder. The ceramic method [2], [3] is the most common and useful method to synthesize solid-state materials due to its easy procedure and quick approach. In the ceramic synthesis, stoichiometric quantities of starting materials are weighed and finely ground. Then, the mixture is fired in a furnace until a single-phase product is formed. Several intermediate coolings and regrinds are used to help increase the rate of reaction. Pellet-making is also a way to accelerate the synthesis.

The mechanism of ceramic synthesis can be explained by three steps. The first stage happens at the contact surface of reagent particles to generate crystal centres. This involves a series of rearrangements including chemical bonds breaking and reforming. The second stage requires cations in the mixture to escape from their origin position, diffuse and get into a defect in order to impel further reaction. The final stage needs the reagent to diffuse and grow around the crystal centre until a single phase is formed. The key factors that influence the speed of reaction are: temperature, pressure, atmosphere, surface area, particle size and chemical composition. Increasing temperature would increase the reaction rate constant $k = A\exp(-\Delta G^{\neq}/RT)$ and the diffusion constant $D = D_0\exp(-\Delta G^{\neq}//RT)$. Pressure is applied by making a pellet in order to decrease the distance between particles and increase the contact surface area. Atmosphere would affect reactions that are sensitive to oxygen/nitrogen. With more surface area, the possibility of reaction is much higher and also the diffusion area. Particle size can dramatically influence the reaction rate because the reaction rate is in inverse proportion to the square of the particle diameter and the contact surface area is also influenced by particle size. Finally, chemical composition can

determine the reaction rate because the activities of different reagents are different. $MnCO_3$ is always used instead of MnO and Co_3O_4 is used instead of CoO become the MnO and CoO formed by decomposition have a higher reactivity.

In this thesis, the ceramic method is used for all the synthesis. All the lanthanide oxides as well as Y_2O_3 were dried at 800 °C in a furnace overnight with immediate cooling and weighing. Proper quantities of starting materials were weighed, ground and fired at 1050 °C, 1075 °C, 1100 °C or 1125 °C [4], [5], [6], [7], [8], [9], [10], [11] depending on the chemical composition. 5 – 10 % more germanium dioxide was added if the furnace temperature was above 1075 °C due to the melting temperature for GeO_2 is around 1086 °C. Some compositions require to be pressed into pellets to achieve a single-phase product. Intermediate cooling and regrinding was applied every two days. The reactions were monitored by X-ray diffraction until a single phase was obtained. Detailed synthesis procedures are described in each chapter.

2.2 Diffraction Techniques

Diffraction is the main method to analyse solid state materials for crystal structure information. [12] In this thesis, X-ray and neutron diffraction were used to characterize the reaction products.

2.2.1 Basic Crystallography

A crystal is a three-dimensional repetition of some unit of atoms or molecules. The periodic repetition can be considered as a diffraction grating. When the wavelength of the wave is chosen to be similar in size of the crystal unit, diffraction occurs.

Laue derived a series of conditions showing that periodic repetition of atoms can produce crystal diffraction. To start with, a one-dimension repetition unit is constructed, see Figure 2.1.

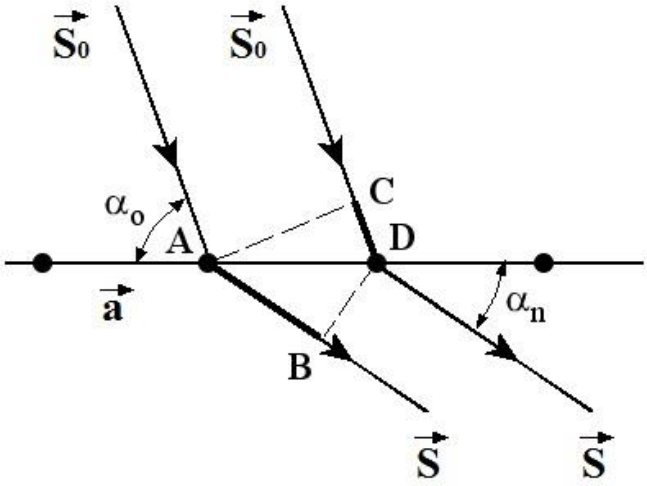

Figure 2.1 Diffraction for one-dimensional scatterers.

The one-dimensional row of periodic scatterers can be represented by the vector **a**. Radiation with the wavelength λ encounters the scatterers in the direction $\mathbf{S_0}$ with an angle α_0. The direction changes to **S** with an angle α_n after diffraction. The constructive interference happens when the wave path difference is a multiple of wavelength

$$n\lambda = AB - CD = |\boldsymbol{a}|cos\alpha_n - |\boldsymbol{a}|cos\alpha_0 \tag{2.1}$$

Using the normalized vectors $\mathbf{S_0}$ and **S** ($|\boldsymbol{S}| = |\boldsymbol{S_0}| = \frac{2\pi}{\lambda}$), the equation can be written as

$$n = \boldsymbol{a}\cdot\boldsymbol{S} - \boldsymbol{a}\cdot\boldsymbol{S_0} = \boldsymbol{a}\cdot(\boldsymbol{S} - \boldsymbol{S_0}) \tag{2.2}$$

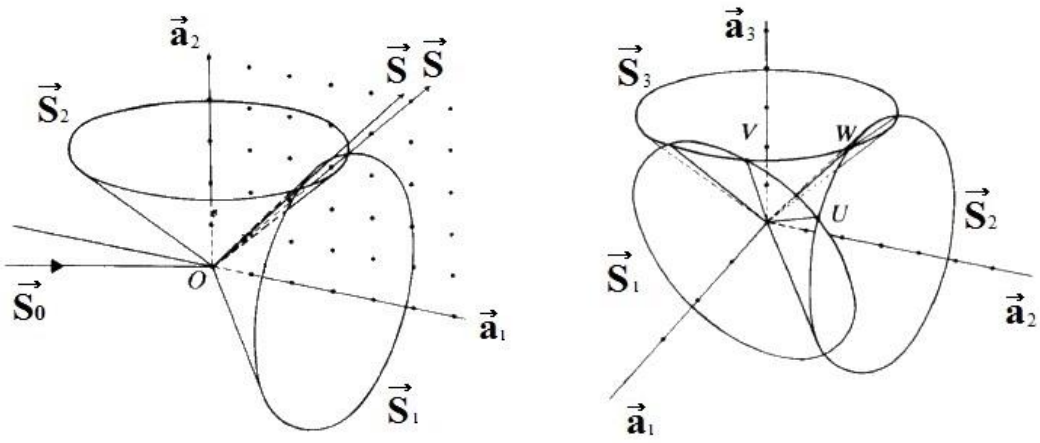

Figure 2.2 Diffraction for two-dimension (left) and three-dimensional (right) scatterers.

For two-dimensional and three-dimensional scatterers, the diffraction can be considered to conduct in different crystal vectors separately. Hence, a series of conic sections are generated along different crystal vectors, see Figure 2.2. The diffraction only happens at the direction where the conic sections meet. The three-dimension Laue equation is

$$\begin{aligned} \boldsymbol{a_1} \cdot (\boldsymbol{S_1} - \boldsymbol{S_0}) &= h \\ \boldsymbol{a_2} \cdot (\boldsymbol{S_2} - \boldsymbol{S_0}) &= k \\ \boldsymbol{a_3} \cdot (\boldsymbol{S_3} - \boldsymbol{S_0}) &= l \end{aligned} \tag{2.3}$$

where *h*, *k*, *l* are integers.

Bragg and his son derived the Bragg's law for crystal diffraction in another way, showing that the planes comprising of the periodically repeated atoms produce crystal diffraction when

$$n\lambda = 2dsin\theta \tag{2.4}$$

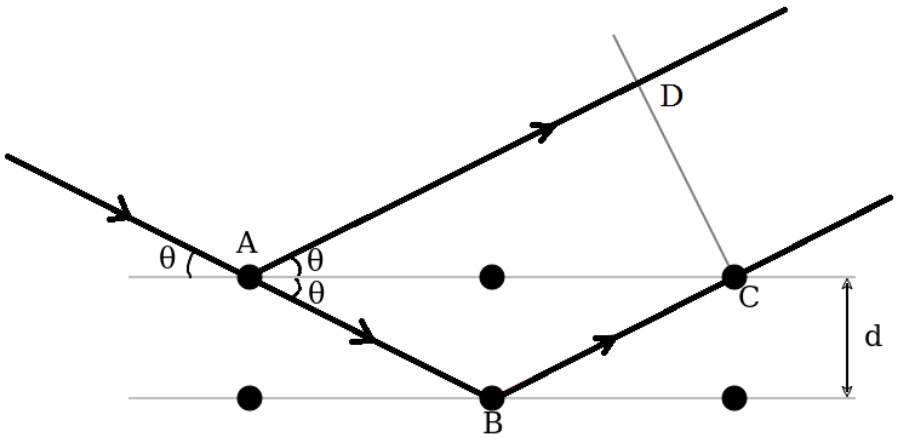

Figure 2.3 Diffraction by lattice planes.

When the wave path distance is the same as the wavelength or a multiple integer of the wavelength, the inference of waves would provide a maximum. From Figure 2.3, the Bragg's law can be written as

$$n\lambda = AB + BC - AD = 2AB - AD = \frac{2d}{sin\theta} - \frac{2d}{tan\theta} cos\theta = 2dsin\theta \tag{2.5}$$

The value *d* represents the distance between different reflection planes and it can also be written as d_{hkl}. For an orthorhombic crystal, the inter-plane spacing, d_{hkl}, is described as

$$\frac{1}{d_{hkl}^2} = \frac{h^2}{a^2} + \frac{k^2}{b^2} + \frac{l^2}{c^2} \tag{2.6}$$

Both Laue's and Bragg's equation explain how diffraction happens in different ways. In depth, they are the same. To represent a crystal, three lattice vectors $\mathbf{a_1}$,$\mathbf{a_2}$,$\mathbf{a_3}$ are used. Then the reciprocal vectors can be represented by the vectors $\mathbf{b_1}$,$\mathbf{b_2}$,$\mathbf{b_3}$, where

$$\boldsymbol{b_1} = \frac{\boldsymbol{a_2}\times\boldsymbol{a_3}}{\boldsymbol{a_1}\cdot\boldsymbol{a_2}\times\boldsymbol{a_3}},\ \boldsymbol{b_2} = \frac{\boldsymbol{a_1}\times\boldsymbol{a_3}}{\boldsymbol{a_2}\cdot\boldsymbol{a_1}\times\boldsymbol{a_3}},\ \boldsymbol{b_3} = \frac{\boldsymbol{a_1}\times\boldsymbol{a_2}}{\boldsymbol{a_3}\cdot\boldsymbol{a_1}\times\boldsymbol{a_2}} \tag{2.7}$$

The reciprocal lattice vector is defined as

$$\mathbf{H}_{hkl} = h\,\boldsymbol{b_1} + k\,\boldsymbol{b_2} + l\,\boldsymbol{b_3} \tag{2.8}$$

where *h*, *k*, *l* are integers.

The reciprocal lattice vector and crystal vectors have the relationship

$$\mathbf{H}_{hkl}\cdot(\boldsymbol{a_1} + \boldsymbol{a_2} + \boldsymbol{a_3}) = 2\pi(h + k + l) \tag{2.9}$$

and the Laue equation can be written as

$$(\boldsymbol{S} - \boldsymbol{S_0})\cdot(\boldsymbol{a_1} + \boldsymbol{a_2} + \boldsymbol{a_3}) = 2\pi(h + k + l) \tag{2.10}$$

Thus, diffraction happens under the condition

$$\boldsymbol{S} - \boldsymbol{S_0} = \mathbf{H}_{hkl} \tag{2.11}$$

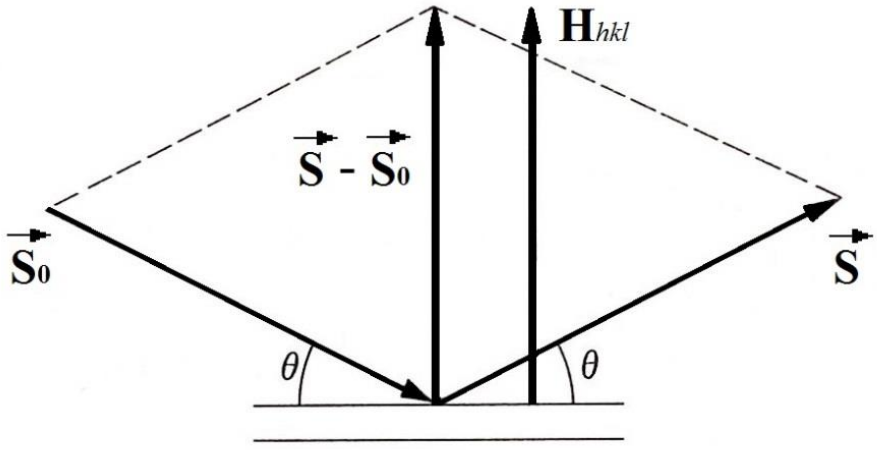

Figure 2.4 Diffraction condition represented by vectors.

Powder samples can be treated as randomly oriented polycrystals and the diffracted beam can be detected by a one or two-dimensional detector. At each specific position with the scattering angle, θ, a signal would be captured. A maximum appears under the condition described by Equation 2.11 and each maximum corresponds to a *hkl* value. In the X-ray

diffraction pattern, a series of maxima are captured and they indicate a series of *hkl* values. The reciprocal lattice vector and the crystal vectors have the relationship shown in Equation 2.9. Thus, with the series of *hkl* values, the crystal unit cell parameters *a*, *b*, *c*, α, β, γ can be calculated. Furthermore, the intensity of each maximum provides more information, for example atom coordination, atom displacement factor and atom occupancy.

The intensity of diffracted radiation is a function of several factors

$$I_{hkl} = s\, F_{hkl}^2\, L(\theta)\, P(\theta)\, A(\theta) \tag{2.12}$$

where s is the scale factor; F_{hkl} is the structure factor; L(θ) is the Lorentz geometric correction factor; P(θ) is the polarisation correction factor; T(θ) is the atomic displacement factor; A(θ) is the absorption correction factor.

The structure factor F_{hkl} is given by

$$F_{hkl} = \sum_j s_j(\theta) T_j(\theta) exp\{-2\pi i(hx_j + ky_j + lz_j)\} \tag{2.13}$$

The structure factor comes from the total contribution of each individual atom in the crystal unit at each specific diffraction plane (*hkl*). The extinction of some *hkl* peaks in some systems is the result of $F_{hkl} = 0$. $s_j(\theta)$ represents the form factor $f_j(\theta)$ for X-ray diffraction and the nuclear scattering length $b_j(\theta)$ for neutron diffraction. The displacement factor $T_j(\theta)$ represents the vibration of an atom in the crystal where

$$T_j(\theta) = exp\left\{-\frac{B_{iso} sin^2\theta}{\lambda^2}\right\} \tag{2.14}$$

where $B_{iso} = 8\pi^2 U_{iso}$, B_{iso} and U_{iso} are atomic displacement factor for each atom.

Both B_{iso} and U_{iso} can be represented in either an isotropic or an anisotropic way. An anisotropic atomic displacement factor allows atoms to have different degrees of displacement in different directions whereas an isotropic atomic displacement factor considers the atoms having the same degree of displacement in any direction. In this thesis, isotropic atomic displacement factor was used to simplify the analysis.

The Lorentz factor is introduced to correct the geometric distribution whereas the polarization factor is to allow for any polarization of the radiation. The total Lorentz–polarization factor can be written as

$$\mathrm{LP}(\theta) = \frac{1+A\cos^2 2\theta}{(1+A)\sin 2\theta} \quad (2.15)$$

where $A = \cos^2\theta_M$ and θ_M is Bragg angle of the monochromator crystal.

The absorption correction factor is also important. Atoms absorb radiations differently. For example, Gd is a strongly absorbing atom of neutrons and Fe can absorb 1.54 Å X-rays severely.

For most diffraction experiments, the process is considered as elastic scattering. Only the direction of the radiation would be changed rather than the energy (wavelength). Inelastic scattering is another method to learn about molecular vibrations, magnetic excitations, electronic transitions and other nuclear or electronic information. In this thesis, only elastic scattering is considered.

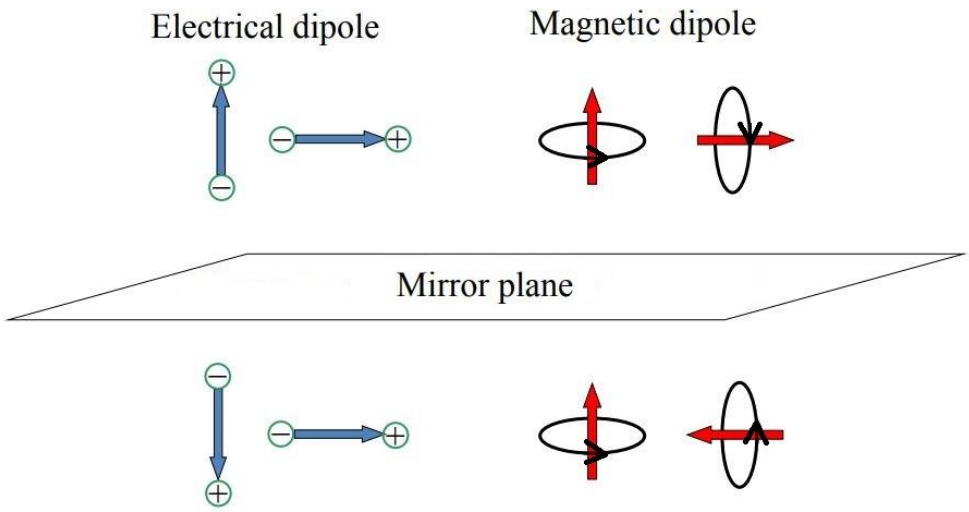

Figure 2.5 Effect of mirror plane operation on an electrical dipole and a magnetic dipole.

As described before, a crystal is a three-dimensional repetition of some unit of atoms or molecules. There are three basic symmetry operations in a crystal, namely the plane of symmetry *m*, axes of symmetry (2, 3, 4 or 6-fold) and the centre of symmetry $\bar{1}$. Using the symmetry of a crystal, the crystal structure can be described by one of the 230 space groups in the International Tables for Crystallography [13], the combination of the 14 Bravais lattices and 32 point groups. However, there are 122 magnetic point groups and 1651 magnetic space groups because a new antisymmetry operator **1'** is introduced. [14], [15] The new operator is a time reversal (spin reversal) operator and it can flip the magnetic

moment. The mirror plane operation on an electrical dipole reflects the dipole, see Figure 2.5 left. However, for a magnetic dipole, the mirror operation can only reflect the electron circulating direction but not the magnetic moment, see Figure 2.5 right, and thus the antisymmetry operator is introduced. Due to this fact, magnetic space group symmetry is more complex than the crystal space group symmetry but with the help of the symmetry the magnetic structure can determined more easily.

2.2.2 Powder X-ray Diffraction

X-radiation (X-ray) is a kind of electromagnetic radiation with wavelengths ranging from 0.001 to 10 nm. To reveal information in crystals, X-rays with wavelength around 0.1 nm are normally chosen for X-ray diffraction because the scale of chemical bond length is also about 0.1 nm. [16]

When the X-ray encounters the powder sample, several things happen including transmission, coherent diffraction, incoherent diffraction, photoelectric effect and fluorescence. Coherent diffraction occurs when the electrons in the sample are forced to vibrate by the electromagnetic field from the incident X-ray. The electrons are then generating same-wavelength electromagnetic radiation (elastic model) in all directions and thus diffraction can occur. Due to the fact that X-ray is scattered by the interaction between the incident beam and the electrons in the atoms, the X-ray diffraction is actually dominated by the electron clouds. Specifically, atoms and chemical bonds are built up by electron clouds. Hence, X-ray diffraction can precisely detect the position of the atoms and their packing pattern. However, on another hand, as the accuracy of X-ray diffraction depends on the density of electron clouds, heavy atoms have much more electrons than light atoms and thus hydrogen, nitrogen, oxygen and other light atoms are difficult to locate. The scattering factor, $f_j(\theta)$, is a function of scattering the angle, 2θ, and the atomic number. Moreover, X-ray diffraction cannot distinguish different elements when they have similar atomic numbers, for example neighbouring first-transition-series atoms or lanthanides. The scattering factor also has a strong dependence on the scattering angle, 2θ, and falls off as the scattering angle increases because the wavelength of the X-rays is close to the atom diameter and thus much less electrons will take part in the diffraction at higher angles.

The X-ray diffractometers in laboratories use metal anodes to generate X-rays with certain wavelength. Cu (1.54 Å) is the most frequently used anode material while Cr (2.29 Å), Co (1.79 Å), Mo (0.71 Å) and Ag (0.56 Å) are also applied sometimes. To produce X-rays, electrons would be generated and accelerated from the cathode towards the anode to bombard it. Then the kinetic energy of the cathode electrons can excite the electrons of the anode metal into higher energy levels. When the excited electrons fall back to their ground state, the energy is emitted in the form of electromagnetic radiation and X-rays are produced. Though radiations with different wavelengths would be produced, the one released from the first excited energy state to the ground state is the most populated and it is marked as Kα radiation where K represents the n=1 energy level and α is Δn=1 transitions. $K\alpha_1$ and $K\alpha_2$ illustrate different angular momentum quantum number of 1 and 0 respectively. For Cu, $K\alpha_1$ =1.5406 Å and $K\alpha_2$ = 1.5444 Å. A monochromator is introduced to purify the incident X-ray. Using the specific diffraction planes from some crystals, only the certain wavelength can be diffracted and thus to monochromate the incident radiation. Single crystal LiF, quartz, InSb, Si, Ge, PET are all used as Johansson monochromators. In this thesis, Ge is chosen for Cu beam using its (111) plane to generate the Cu $K\alpha_1$ radiation.

For normal powder samples, the scale of the particles is around several micrometres. For experiment, the powder would be mounted on an aluminium plate and pressed by a glass sheet to make the powder condense and have a smooth surface. Condensed powder can minimize the air gap to avoid absorption of X-rays. Smooth surfaces can avoid surface influence because rough surface can diffract X-ray in other directions leading to a decrease in the intensity. However, the powder may align with its preferred orientation by pressing. Alternatively, the powder can be spread on a silicon sheet with grease. In this way, random orientation can be guaranteed but not the intensity. Hence, fine step and long collection time X-ray diffraction experiments are used to collect high-resolution data.

Early X-ray diffraction experiments were conducted using the Debye-Scherrer method; X-rays irradiated the sample and the scattered cones were captured on a film; the angle of each pairs of arcs could be calculated for analysis. Obviously, this method is not accurate enough. The Bragg-Brentano geometry method is now applied to provide high intensity and better resolution data. In a Bragg-Brentano geometry system, see Figure 2.6, sample is place at the centre of a diffractometer circle while the X-ray source and the detector are on

the circle. The X-ray source is fixed at one position and the sample stage as well as the detector is rotating. The detector has double rotating speed to the sample stage in order to satisfy the Bragg's equation. Moreover, a set of slits are used to narrow the radiation beam to achieve high resolution.

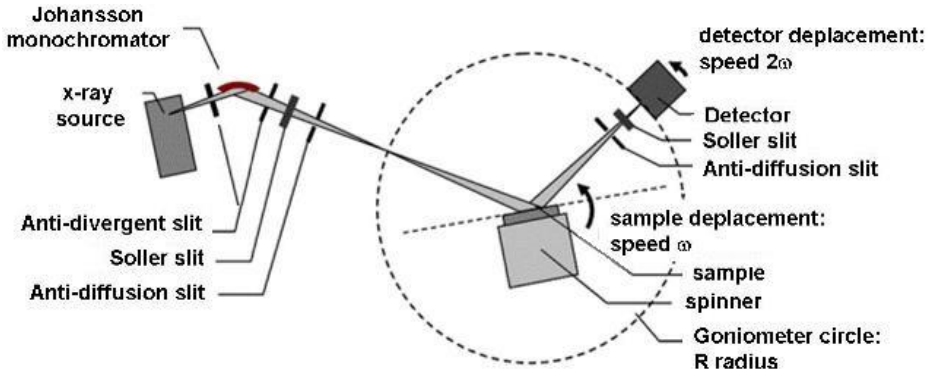

Figure 2.6 Bragg-Brentano geometry diffractometer.

2.2.2.1 Experimental X-ray Diffractometers

A monochromated Panalytical Empyrean diffractometer operating at 45 kV and 40 mA with copper $K\alpha_1$ radiation was used to monitor the progress of reactions during the synthesis. Data were collected in the angular range $10\,^\circ \leq 2\theta \leq 90\,^\circ$ with a step size of $\Delta 2\theta = 0.02\,^\circ$ and time per step $\tau = 50$ s at room temperature on an aluminium plate. The data collection took about 0.5 hour. 0.04 rad soller slit and 1 ° anti-diffusion slit were used at the X-ray source.

High resolution X-ray patterns were collected on a monochromated Panalytical X'Pert diffractometer operating at 45 kV and 40 mA with copper $K\alpha_1$ radiation. Data were collected in the angular range $10\,^\circ \leq 2\theta \leq 130\,^\circ$ with a step size of $\Delta 2\theta = 0.0084\,^\circ$ and time per step $\tau = 70$ s at room temperature. The sample was mounted on a silicon disc with Dow Corning high-vacuum grease. The data collection took about 2.5 hours. The sample disc was spun at 2 revolutions per second to counter orientation effects and the silicon disc was cut on (110) plane to minimize its contribution to the X-ray pattern. 0.04 rad soller slit and 1 ° anti-diffusion slit were used at X-ray source; 5 ° anti-diffusion slit and 2 ° anti-divergence slit were used at the detector.

Figure 2.7 Panalytical Empyrean diffractometer (left) and Panalytical X'Pert diffractometer (right).

2.2.3 Neutron Diffraction

The neutron [17] is a subatomic particle labelled as n^0, which has no electric charge but has a mass close to a proton. The neutron is also a spin ½ particle with angular momentum $\hbar/2$. Hence, neutrons can be used in determining the magnetic structures for materials. Due to the wave-particle duality, neutrons can also be considered as a radiation. The equation is described as

$$\lambda = h/mv \tag{2.16}$$

The energy of the neutrons could be described by the kinetic energy and/or the Boltzmann energy. To simplify, we only consider the peak value of the Boltzmann distribution.

$$E_k = \frac{1}{2}mv^2 = E = \frac{3}{2}k_BT \tag{2.17}$$

To combine the equations

$$\lambda^2 = h^2/3mkT \tag{2.18}$$

Equation 2.18 shows that the wavelength of the neutron is a function of temperature. For instance, the wavelength of the neutron is 1.55 Å at 0 °C whereas it is 1.33 Å at 100 °C.

However, for a real neutron source, the neutrons have a range of energies and thus a continuous band of wavelengths.

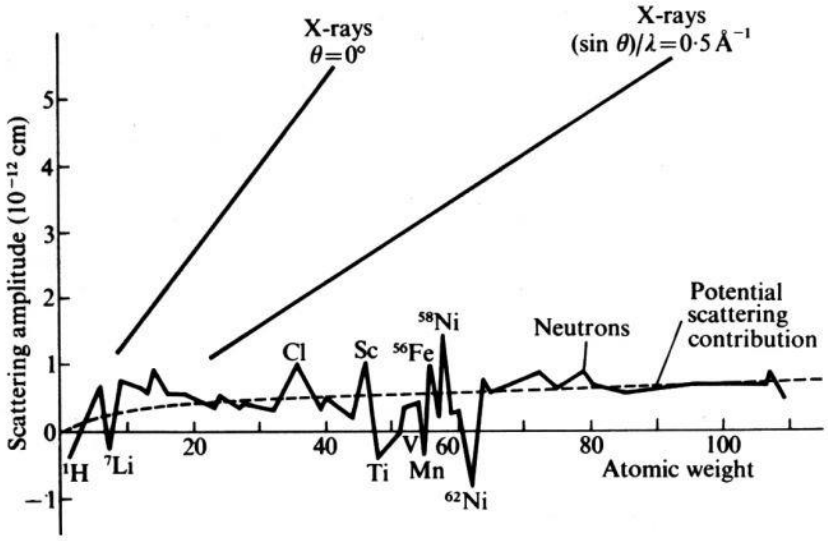

Figure 2.8 Variation of neutron scattering amplitude to atomic weight. [17]

As discussed above, X-rays interact with the electrons to diffract. On the contrary, neutrons interact with the nucleus. Hence, light atoms can also be accurately located in neutron diffraction measurements. The nuclear scattering length, b_j, is a function of the strength of the interaction between the neutrons and the nucleus of the atoms. Hence, the data collected at high angles do not show a loss of intensity because the nuclei are much smaller compared to the radiation wavelength and the nuclei therefore act as point scatterers.

Neutron used in diffraction experiments can be generated in two ways: at a thermal neutron reactor or at a spallation neutron source. The thermal neutrons come from the fission of ^{235}U while spallation neutrons come from bombarding a heavy metal by protons. By controlling the temperature of the reactor and using a neutron moderator, the neutrons can then be controlled to have appropriate velocity for experiments. A collimator is used to narrow the beam and a monochromator is also applied. The neutrons encounter the sample to conduct diffraction. Finally, the collimators and detectors array captures the neutrons to register a diffraction pattern. ^{3}He gas-filled proportional detectors or $^{10}BF_3$ gas-filled proportional detectors are normally used to detect the neutrons according to the reactions

$$^{3}_{2}He + ^{1}_{0}n = ^{1}_{1}H + ^{3}_{1}H + 0.76MeV$$

$$^{10}_{5}B + ^{1}_{0}n = ^{7}_{3}Li + ^{4}_{2}He + 2.8MeV$$

2.2.3.1 Magnetic Scattering

Due to the neutrons having angular momentum $\hbar/2$, they can also be diffracted by a periodic array of magnetic moments, *i.e*. the magnetic structure. For a short-range ordering or a paramagnetic system, the overall magnetic structure do not have the long-range periodicity and thus no magnetic Bragg peaks.

For the magnetic scattering, the neutrons are not interacting with the atomic nuclei because the magnetic moments come from the unpaired electrons. Hence, the magnetic neutron scattering is a result of interactions with electrons and thus it behaves similar to the X-ray diffraction. The intensity of the magnetic Bragg's peaks also falls off dramatically when the diffraction angle increases. The magnetic scattering can not only detect the magnetic structure but also the mean value of the magnetic moments.

2.2.3.2 The ECHIDNA neutron diffractometer, ANSTO

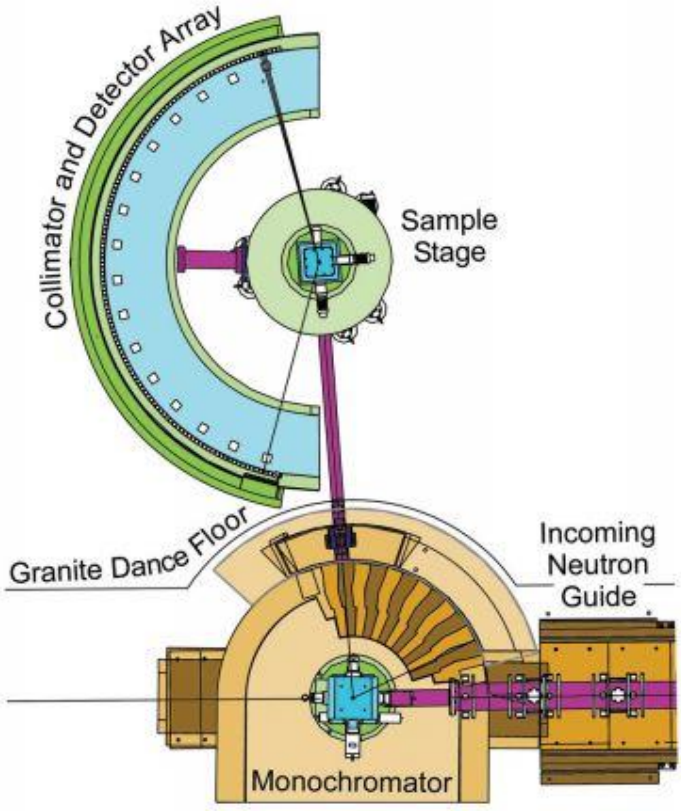

Figure 2.9 Instrument layout for Echidna at Ansto. [18]

For the majority of the samples in this thesis, the neutron diffraction data were collected by M. Avdeev on samples provided by the author on Echidna, a high resolution neutron diffractometer at ANSTO, Australia. All data analysis were performed by the author. Collimated thermal neutrons from the reactor core go through a single-crystal Ge monochromator to produce a single-wavelength neutron beam. Depending on the orientation of the Ge crystal, the wavelengths can vary from 1Å to 3Å. The monochromator take-off angle can be varied between 90° and 140°. In this thesis, two wavelengths were used: 1.622 Å from the Ge (115) planes and 2.4395 Å from the Ge (335) planes. 128 individual ^{3}He detectors of 25 mm diameter × 300 mm height filled to 10 bar pressure were used to capture the neutrons. Data were collected in the angular range $8\,^\circ \leq 2\theta \leq 160\,^\circ$ with a step size of $\Delta 2\theta = 0.05\,^\circ$ over a 3 hour period. The sample was mounted in a vanadium can. A vanadium container was used because vanadium has an almost zero coherent nuclear scattering length. Data were recorded in the temperature range $1.6\ \mathrm{K} \leq T \leq 300\ \mathrm{K}$. Magnetic fields of up to 3 T were applied for some experiments. In order to prevent movement in the magnetic field, the sample was pressed into a pellet which was subsequently broken into fragments; each just small enough to be loaded into a standard vanadium container. The measurements in zero field were repeated after the in-field neutron diffraction experiments to ensure the application of the field had not caused preferred orientation of the powder granules.

Moreover, the neutron diffraction data on the compound $GdFeZnGe_4O_{12}$ were collected by D. H. Ryan, McGill University, at CNBC.

2.3 Rietveld Refinement

Rietveld [19] invented a technique to characterize powder samples of crystalline materials. The Rietveld method is used to extract crystalline information by fitting the whole diffraction pattern [20]. Different from analysing each peak of the pattern individually, the Rietveld method concerns with the peak positions, peak widths and peak shapes of the whole pattern. During the refinement, both the structural and the instrumental parameters are taken into consideration using a least-squares approach to match the observed and the calculated diffraction patterns. All refinements of both X-ray and neutron diffraction

patterns in the thesis were conducted using the General Structural Analysis System (GSAS) program suite [21], [22].

To evaluate the quality of the refinement, three reliability parameters were introduced, R_{wp}, R_p and χ^2. The three parameters can be descried as

$$R_{wp} = \left\{\frac{\sum w_i[y_i(obs)-y_i(cal)]^2}{\sum w_i[y_i(obs)]^2}\right\}^{\frac{1}{2}} \times 100\% \quad (2.19)$$

where $w_i = \frac{1}{y_i(obs)}$; y_i(obs) is the observation intensity and y_i(cal) is the calculation intensity at each point.

$$R_p = \frac{\sum|y_i(obs)-y_i(cal)|}{y_i(obs)} \times 100\% \quad (2.20)$$

$$\chi^2 = \left\{\frac{\sum w_i[y_i(obs)-y_i(cal)]^2}{N-P}\right\}^{\frac{1}{2}} \quad (2.21)$$

where N is the number of observation points and P is the number of parameters involved in the refinement.

To calculate the intensity y_i(cal) at each point, the following equation is used

$$y_i(cal) = s\sum_{hkl} L_{hkl}|F_{hkl}|^2\varphi(2\theta_i - 2\theta_{hkl})P_{hkl}A + y_i(bkg) \quad (2.21)$$

where *hkl* is the Miller indices for the Bragg reflection; s is the scale factor; L_{hkl} is the Lorentz-polarization-multiplicity factor; F_{hkl} is the structural factor; φ is the profile function for the peaks; P_{hkl} is the preferred orientation function; A is the absorption factor and y_i(bkg) is the background intensity.

As explained before, the Lorentz–polarization factor is introduced to correct the geometric distribution and any polarization of the radiation. In the powder diffraction, the multiplicity factor is also used to allow for the degeneracy of the *hkl* values due to the crystal symmetry.

In the Equation 2.21, y_i(bkg) can be modelled by a function to describe incoherent scattering and background noise. The background is important because not only the reflection points but also the background points are involved in the whole pattern. In this work, one of two background functions was chosen depending on the radiation, X-ray or neutron. A 12-16 order polynomial Shifted Chebyshev function was applied for the neutron data and a 10-14 order Cosine Fourier series function for the X-ray data.

The peak shape and peak width vary as a function of the angle 2θ. A Pseudo-Voigt function, $\varphi(2\theta_i - 2\theta_{hkl})$, is a linear combination of the Gaussian function and the Lorentzian function and is applied to model the peaks.

$$\varphi(2\theta_i - 2\theta_{hkl}) = \eta\, G(\theta) + (1-\eta)L(\theta) \tag{2.22}$$

$$G(\theta) = \left\{Utan^2\theta + Vtan\theta + W + \frac{P}{cos^2\theta}\right\}^2$$

$$L(\theta) = \frac{X}{cos\theta} + Ytan\theta$$

The profile parameters, GU, GV, GW, GP, LX, LY, are refinable to obtain the best fitting. Normally, GU, GV, GW, LX, LY are used to refine the X-ray data and GU, GV, GW, LX for the neutron data. GP refers to the Gaussian crystallite size broadening. Besides these, the peak asymmetry parameter, instrumental zero point error and the POLA factor are also taken into consideration. The asymmetry parameters describe the asymmetry of the peaks seen at the low angles and the POLA factor is used to represent the quality of monochoramator.

2.4 Magnetometry Experiments

The magnetic behaviour of selected samples was investigated using a magnetometer based on a Superconducting Quantum Interference Device (SQUID) in the Inorganic Chemistry Laboratory, University of Oxford. The measurements involved temperature dependence of dc molar susceptibility, field dependence of the magnetization and temperature dependence of ac molar susceptibility.

2.4.1 SQUID Magnetometry

A SQUID device relies on the Josephson junctions to measure magnetisation. The Josephson junctions, see Figure 2.10, are the insulating barriers used to separate the loop of two superconducting sections. A current, I_0, is going through from one side to the other side. When the thickness of the Josephson junction is small enough, quantum tunnelling of Cooper pairs occurs. Hence, the current can flow through the insulating barriers and the current is $I_0/2$ through each Josephson junction. If a small change of magnetic flux, $\Delta\Phi$, is

crossing perpendicular to the loop, a screening current, I_s, forms. For one junction, the current becomes $I_0/2+I_s$ and the other becomes $I_0/2-I_s$. When either $I_0/2+I_s$ or $I_0/2-I_s$ exceeds critical current, I_c, a voltage, ΔV, appears across the loop. Then the change of magnetic flux, $\Delta\Phi$, can be estimated by the voltage, ΔV. The magnetic moment of the sample can then be deduced from the voltage if the instrument has been calibrated with a standard sample; Pt metal was used to calibrate the ICL SQUID. The change of magnetic flux can be achieved by moving the sample through the ring (dc) or by applying an oscillating magnetic field (ac). To make the result more accurate, a series of detection coils were used to minimise other effects. However, a residual field in the chamber exists influencing the result because the earth has a magnetic field of 0.5 Oe and there is a small field formed by the superconducting shield.

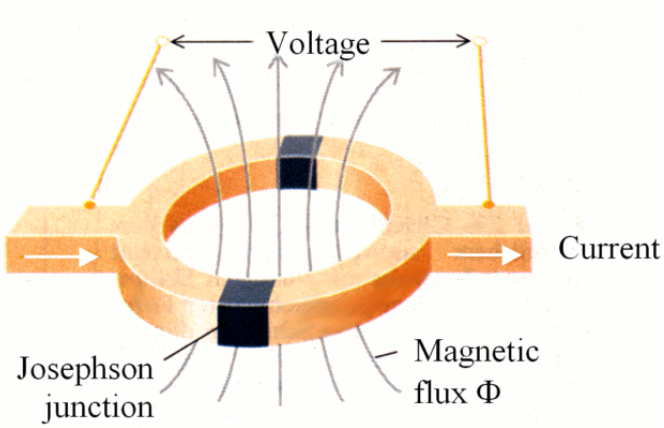

Figure 2.10 Josephson junctions in SQUID device.

The measurements in this thesis were conducted on two Quantum Design SQUID magnetometers, MPMS 5 and MPMS XL. A small quantity of sample (30 - 50 mg) was loaded into a gelatine capsule and fixed by another empty capsule to avoid sample movement in a high magnetic field. Then the capsule was loaded in a plastic straw with four empty capsules on each side to ensure accurate location of the sample inside the SQUID and to provide a constant background. During the measurement, the straw was mounted on the sample rod using a diamagnetic tape and then it was put into the air lock to remove the air as oxygen is paramagnetic. The chamber is constantly extracting air by a pump to minimise the effects from air. The sample is centred in the chamber with a weak field (100 Oe) to make sure the sample is at the right place. A 4 cm scan length was used for dc measurements and a 6 cm length for ac measurements. 4 repeated scans with scan length of 4 cm were conducted for dc measurements and the position of straw was fixed in

the chamber for ac measurements. A degaussing procedure was sometimes applied to counter any remaining field in the chamber to assure zero field. Liquid helium was used to cool the chamber down to 2 K. The data were recorded whilst warming.

Figure 2.11 Quantum Design SQUID magnetometer MPMS-5 (left) and MPMS XL (right)

2.4.2 DC Magnetisation Measurements

In measurements of the temperature dependence of dc molar susceptibility and the field dependence of the magnetization, a direct current is used to create a constant magnetic field. Samples were cooled in zero field (ZFC) or in a magnetic field (FC) initially. The temperature dependence of the dc molar susceptibility data was normally collected in a dc field of 100 Oe over the temperature range 2 K ≤ T ≤ 300 K. In some cases, data were also collected in additional dc fields. The field dependence of the magnetization was measured over the magnetic field range -50 kOe ≤ H ≤ 50 kOe at 2K with the samples initially cooled in a 50 kOe magnetic field. More data were collected at other temperatures in some cases.

The dc molar susceptibility can be calculated from Equation 1.6

$$\chi_m = \frac{M_m}{H} = \frac{MM_0}{Hm_0} \tag{2.23}$$

where M is the magnetization recorded by the SQUID; M_0 is the molar mass of the compound; H is the applied measuring dc field and m_0 is the mass of the compound.

The magnetic parameters, C_m and θ, resulting from fitting the Curie-Weiss law to the dc molar susceptibility data of T > 150 K are derived by

$$\frac{1}{\chi_m} = \frac{T}{C_m} - \frac{\theta}{C_m} \tag{2.24}$$

The effective moment of the magnetic atom thus can be calculated from the Curie constant

$$C_m = \sum \frac{N\mu_0\mu^2}{3k_B} \approx \frac{1}{8}\sum n_i \mu_{eff}^2 \tag{2.25}$$

where N is the Avogadro's number; k_B is the Boltzmann constant; μ_0 is the vacuum permeability (equal to 1 in c.g.s units); n_i is the molar number of each magnetic atom.

2.4.3 AC Magnetisation Measurements

Instead of using a dc current, the ac magnetic measurements use an ac current to produce an oscillating magnetic field. Hence, the ac measurement is a function not only of temperature but also the oscillating frequency of the ac magnetic field.

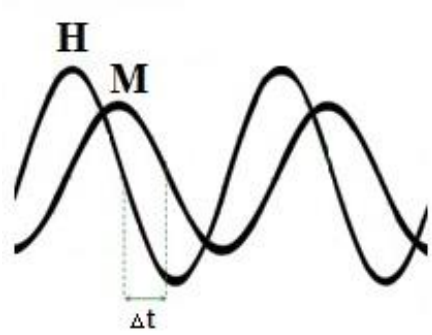

Figure 2.12 The phase shift between magnetic field and detected magnetization in ac magnetic measurements.

The ac current can be expressed in a sine wave function

$$i_{ac} = i_{max} \sin(\omega t) \tag{2.26}$$

The inducing magnetic field can be represented in a similar way

$$H_{ac}(t) = H_0 + h \sin(\omega t) \tag{2.27}$$

where H_0 is a zero- or non-zero- constant dc magnetic field parallel to oscillating field; h is the amplitude of the ac magnetic field and the value is normally set small (< 5 Oe) in the ac measurements.

The ac magnetization captured by the instrument is noted as

$$M = (dM/dH)\, H_{ac}(t) \quad \text{and} \quad \chi = dM/dH \tag{2.28}$$

At low frequencies, the magnetic field is not changing very fast and the result is similar to dc measurements. However, at high frequencies, the dynamic alternation of the magnetic field is fast and the detected magnetization may lag behind the field, see Figure 2.12. Thus, the measured susceptibility yields two values: the detected susceptibility χ and the phase shift φ (relevant to the frequency). The in-phase or real part susceptibility, χ', and out-of-phase or imaginary part susceptibility, χ", are used. The ac susceptibility can be represented by

$$\begin{aligned} \chi &= \sqrt{\chi'^2 + \chi''^2} \\ \varphi &= \arctan(\chi''/\chi') \\ \chi' &= \chi \cos\varphi \\ \chi'' &= \chi \sin\varphi \end{aligned} \tag{2.29}$$

The real part refers to magnetic dispersion while the imaginary part refers to magnetic absorption. Therefore, the ac measurements can reveal the dynamic properties of the magnetic moments. It is known that the sine and cosine function have a phase shift of 90 degrees. From equation 2.26, to measure the real part and the imaginary part susceptibility at the same time, two orthogonal coils are used to capture signal together, see Figure 2.13. Thus, one coil records the real part of the magnetization and another measures the imaginary part of the magnetization.

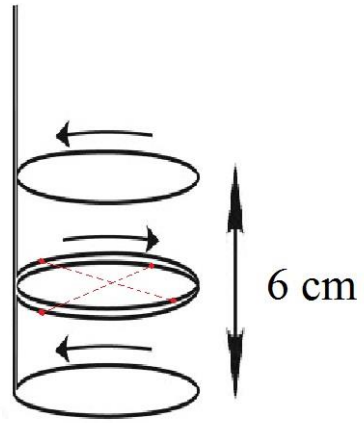

Figure 2.13 The orthogonal measuring coils for ac magnetic measurements.

AC measurements were conducted on a Quantum Design MPMS XL. Data were collected over the temperature range $2\ K \leq T \leq 20\ K$ with a 3.5 Oe driving ac field. Samples were ac-degaussed before cooling to counter the remaining dc field in the instrument. For ac measurements in an applied dc field, samples were cooled in the dc field. Four frequencies, 1/10/100/1000 Hz, were selected. For some sensitive measurements, a furnace-dried sample of gadolinium oxide, Gd_2O_3, was used to record the instrumental internal field at 300 K as Gd_2O_3 obeys Curie-Weiss law with $\theta = -17.2\ K$ [23], [24]. Thus the exact internal field could be calculated.

2.5 Heat Capacity

Heat capacity measurements can provide structural, electronic and magnetic information of materials. Data were collected on a Quantum Design PPMS (Physical Properties Measuring System) at Department of Physics, University of Oxford with help from C. V. Topping and E. C. Hunter. Data were collected over the temperature range $2\ K \leq T \leq 30\ K$ in zero field and in a 20 kOe magnetic field. The calibration was conducted with a blank sample platform in zero field or in a 20 kOe magnetic field. Powder samples were made into thin pellet (less than 1 mm thickness) and then broken into small pieces. A small fragment in square shape (2 mm × 2 mm) was selected to conduct the experiment. The fragment was stabilized on the sample platform with some Apiezon grease under a microscope. The sample platform was then put inside the measuring chamber. A vacuum pump was constantly working to remove residual gas in the chamber and the internal pressure was normally less than 1 mTorr.

Figure 2.14 Quantum Design PPMS.

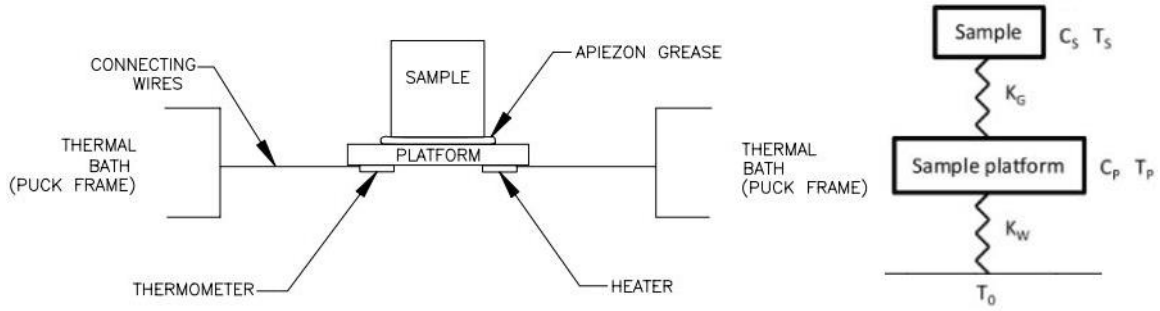

Figure 2.15 Graph of sample and sample platform in PPMS Heat Capacity Option.

As shown in Figure 2.15, the sample platform is placed in the chamber with a thermal bath. At one specific temperature, a small quantity of heat is produced from the heater and the heat is absorbed by the puck and the sample. After a period of time, τ, the temperature of the thermometer can reach the same temperature as the heater. With the addenda measurements, the background heat of the puck is recorded. Thus, the heat capacity of the sample can be obtained. The heat power, P(t), can be written as

$$P(t) = C_P \frac{dT_P(t)}{dt} + K_G[T_P(t) - T_s(t)] + K_W[T_P(t) - T_0] \quad (2.30)$$

$$\text{and } K_G[T_P(t) - T_s(t)] = C_S \frac{dT_S(t)}{dt}$$

where C_P and C_S are the heat capacity of the sample platform and the sample respectively; T_P and T_S are the temperatures of the sample platform and the sample respectively; T_0 is the temperature of the thermal bath; K_G is the thermal conductance of the grease and K_W is the combined thermal conductance of eight wires.

The heat capacity scales the amount of heat at each temperature with the unit J/K and the specific heat describes the heat capacity per unit amount of material with the unit J/(K·mol). The Debye temperature, θ_D, is used to describe the phonon contribution; electronic and magnetic properties are shown below the Debye temperature. For instance, an antiferromagnet would show a λ-shaped peak in a specific heat figure. The total equation to describe the heat capacity is

$$C_S = C_{lattice} + C_{electron} + C_{nuclear} + C_{magnetic} \quad (2.31)$$

In the equation, the Debye model describes the lattice contribution ($C \propto T^3$) and the Einstein model describes the electronic contribution ($C \propto T$). However, for some heavy-

element containing compounds, the nuclear contribution ($C \propto T^5$) also needs to be calculated. For a paramagnetic phase, the data can be modelled by the equation

$$C = \alpha T + \beta T^3 + \gamma T^5 \tag{2.32}$$

After fitting the paramagnetic data, the pure magnetic contribution can be estimated from the difference between the raw data and the fitted data. For a long-range magnetic transition, a peak would appear in a specific heat figure. Below the transition temperature, the magnetic specific heat has a complex relationship to temperature ($C \propto T^{d/n}$, where d is the magnetic dimension and n is 1 for AFM or 2 for FM). Given that the temperature cannot cool down to 0 K, the magnetic specific heat data at very low temperatures can be modelled by $C \propto T^{d/n}$. Then the magnetic entropy then can be calculated by

$$\Delta S = \int \frac{C_{mag}}{T} dT \tag{2.33}$$

For magnetic materials, normally the magnetic entropy is a function of the number of unpaired electrons in the system and the theoretical value of the system is

$$\mathrm{S} = \Sigma R ln(2S + 1) \tag{2.34}$$

2.6 Mössbauer Spectroscopy

Mössbauer Spectroscopy [25] uses recoilless nuclear resonant absorption to study the environment of the nucleus.

Like the electrons in an atom, a nucleus has its ground state and excited states. If a nucleus in the ground state absorbs a γ-ray, it goes to an excited state. The nucleus then decays to its ground state by the emission of a γ-ray. The emitted γ-ray can subsequently excite a second nucleus providing that the energy of the γ-ray is not degraded. For a free nucleus, the energy of the emitted γ-ray is smaller than the energy needed for reabsorption at the second nucleus because the nucleus needs to recoil in order to conserve energy and momentum. If E_{ex} represents the energy difference between the nuclear ground state and its first excited state and using E_γ to represent the energy of the γ-ray, then the energy conservation is

$$E_\gamma = E_{ex} + \frac{1}{2}Mv^2 \quad and \quad \frac{1}{2}Mv^2 = E_R = \frac{(Mv)^2}{2M} = \frac{p_\gamma^2}{2M} = \frac{E_\gamma^2}{2Mc^2} \tag{2.35}$$

where M is the mass of the nucleus and *v* is its recoil velocity.

The recoil energy is the energy loss during the γ-ray emitting procedure. Take Fe for instance, E_{ex} = 14.41 keV and the recoil energy E_R = 0.002 eV. The emitted γ-ray then cannot excite a second nucleus. If the nucleus is no longer independent and is bound in a crystal lattice, the entire crystal can now act as the recoiling body and the mass, M in Equation 2.35, is now the mass of the whole crystal. Thus, the recoil energy is small enough to neglect. Relaxation in order to conserve energy and momentum therefore occurs through either lattice vibrations or the recoil of the whole crystal. Phonons, which describe the degree of lattice vibration, are quantised and can be excited. Their energy is normally on the order of 10^{-2} eV. Commonly, the recoil energy is smaller than the energy of the smallest phonon and the nuclear relaxation occurs via the recoil of the whole crystal. When the mass of the recoiling body is large (the whole crystal), the velocity (in the representation of the recoil energy E_R) is small enough to be considered negligible. Hence, some fraction of the emission can be said to be recoil free and it can therefore excite a second nucleus.

Experimentally Mössbauer Spectroscopy relies on low-energy γ-rays (10-200 keV) to excite the nuclei. γ-rays with energy less than 10 keV are not suitable because the energy is not enough to transmit through the sample and γ-rays with energy larger than 200 keV are also not suitable because the recoil energy would be too large that cannot be neglected. Moreover, the excitation lifetime influences the result. A short lifetime leads to wide spectral lines and hides the hyperfine structure. A long excitation lifetime leads to sharp spectral lines and the spectrum is sensitive to small vibrations of the instrument or temperature fluctuations. 0.1 ns – 1 μs is a suitable excitation lifetime. Also, the radiation source should be a long-lived precursor with stable ground state and high yields.

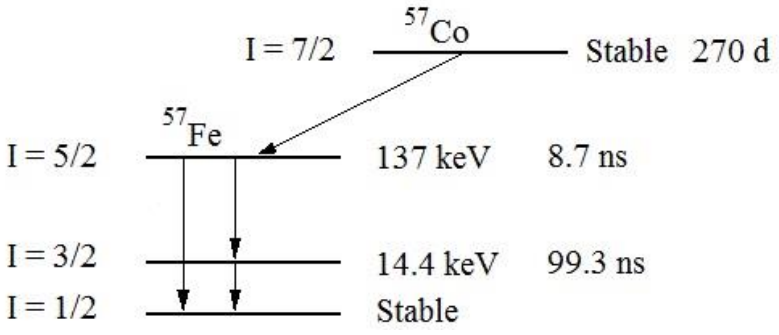

Figure 2.16 The decay of ^{57}Co.

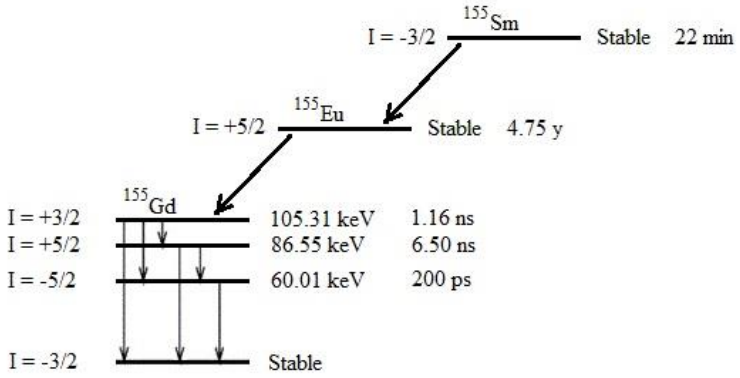

Figure 2.17 The decay of ^{155}Sm.

^{57}Fe Mössbauer spectroscopy and ^{155}Gd Mössbauer spectroscopy were used in the research described in this thesis. For ^{57}Fe Mössbauer spectroscopy, 20mCi ^{57}Co**Rh** is selected as the source, see Figure 2.16. The excited ^{57}Fe comes from the decay of ^{57}Co with a half-life of 270 days. A 14.4 keV γ-ray from an excited state with a half-life of 99.3 ns is chosen as the experimental γ-ray. ^{57}Fe Mössbauer spectroscopy was conducted in the temperature range 5-30 K and at room temperature. The system was calibrated using a laser interferometer with velocities crosschecked against ^{57}Co**Rh**/α-Fe at room temperature. For ^{155}Gd Mössbauer spectroscopy, 50mCi ^{155}Sm is selected as the source, see Figure 2.17. A 86.55 keV γ-ray with a half-life of 6.5 ns is chosen as the experimental γ-ray. The γ-ray originates from the β-decay of ^{155}Eu (4.75 years half-life) and ^{155}Eu results from the β-decay of ^{155}Sm (22 minutes half-life). The 86.55 keV γ-ray was isolated from the various radiations by a high-purity Ge detector. ^{155}Gd Mössbauer spectroscopy was conducted at low temperatures (< 5 K) in a helium flow cryostat to ensure a high recoilless fraction. The system was calibrated using a laser interferometer with velocities crosschecked against ^{57}Co**Rh**/α-Fe at room temperature and both $^{155}SmPd_3$/$GdFe_2$ and cubic Gd_2O_3 at 5 K.

The nuclei in the source and the nuclei in the absorber have different chemical environments and therefore the excitation energies are slightly different. With a relative velocity between the sample and the source in the measuring system, the small energy difference can be made up as a consequence of the Doppler Effect. As shown in Figure 2.18 and Figure 2.19, the isomer shift, δ, is a measure of the energy difference between the sample nuclei and the standard absorber nuclei. Fe, Fe^{2+} and Fe^{3+} nuclei have different electronic environments because of different oxidation states. Therefore, the nuclei have different Coulomb forces from their different electron clouds. The isomer shift, δ, with the

unit of mm/s, can distinguish the oxidation state and/or the electron spin state (high-spin or low-spin). Furthermore, the electron electric field gradient (EFG) can then cause quadrupole splitting and lead to the single-peak splitting into a doublet depending on the quadrupole moment, ΔE_Q, see Figure 2.18. A magnetic field can cause further splitting, see Figure 2.19, because of the nuclear Zeeman Effect. The magnetic field can arise in three ways: applying an external magnetic field, exciting an internal molecular magnetic field below the Curie/Néel temperature or exciting an internal magnetic field by dipole interaction. The ^{57}Fe Mössbauer spectra show a sextet in a field characterised by the hyperfine field, B_{hf}.

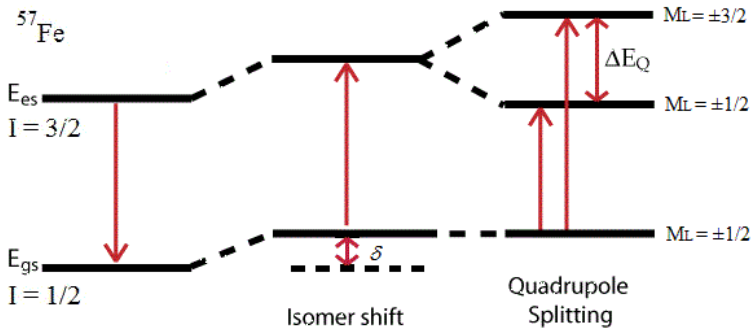

Figure 2.18 Energy level schemes for isomer shift and quadrupole splitting of ^{57}Fe.

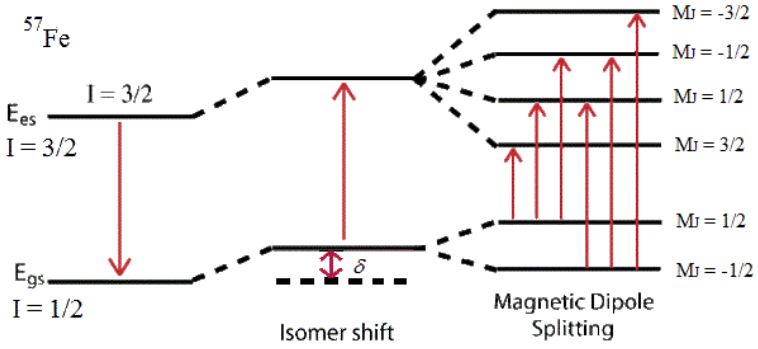

Figure 2.19 Energy level schemes for isomer shift and magnetic dipole splitting of ^{57}Fe.

The Mossbauer data reported in this thesis were collected by J. M. Cadogan at UNSW Canberra, Australian Defence Force Academy, Australia and by D. H. Ryan at McGill University, Canada. All data were fitted by them using a non-linear least-squares minimization routine with line positions and intensities derived from an exact solution to the full Hamiltonian.

2.7 References

[1] A. R. West, *Solid State Chemistry and its Applications*, John Wiley & Sons: **1987**.

[2] C. N. R. Rao, and K. Biswas, *Essentials of Inorganic Materials Synthesis*, John Wiley & Sons: **2015**.

[3] L. B. Kong, Y. Z. Huang, W. X. Que, T. S. Zhang, S. Li, J. Zhang, Z. L. Dong, and D. Y. Tang, *Transparent Ceramics*, Springer International Publishing: **2015**.

[4] J. A. Campa, C. Cascales, E. Gutierrez-Puebla, M. A. Monge, I. Rasines, and C. R. Valero, $CuYb_2Ge_4O_{12}$, a New Bidimensionally Tunneled Structure, *Journal of Solid State Chemistry*, **1996**, *124*, 17-23.

[5] C. Taviot-Gueho, P. Leone, P. Palvadeau, and J. Rouxel, Synthesis and structural characterization of two new rare-earth maganese germanates: $CeMn_2Ge_4O_{12}$ and $GdMnGe_2O_7$, *Journal of Solid State Chemistry*, **1999**, *143*, 145-150.

[6] C. Cascales, M. T. Fernandez Diaz, and M. A. Monge, Low-Temperature Magnetic Ordering in Rare-Earth Copper Germanates $R_2CuGe_4O_{12}$, R = Ho, Er, *Chemistry of Materials*, **2000**, *12*, 3369-3375.

[7] C. Cascales, and M. A. Monge, Crystal structure and influence of the rare-earth on the magnetic structure of copper germanates $R_2CuGe_4O_{12}$, *Journal of Alloys and Compounds*, **2002**, *344*, 379-384.

[8] V. G. Zubkov, N. V. Tarakina, I. I. Leonidov, A. P. Tyutyunnik, L. L. Surat, M. A. Melkozerova, E. V. Zabolotskaya, and D. G. Kellerman, Synthesis and crystal structure of $Ln_2M^{2+}Ge_4O_{12}$, Ln=rare-earth element or Y; M=Ca, Mn, Zn, *Journal of Solid State Chemistry*, **2010**, *183*, 1186-1193.

[9] M. A. Melkozerova, N. V. Tarakina, L. G. Maksimova, A. P. Tyutyunnik, L. L. Surat, I. I. Leonidov, V. G. Zubkov, E. V. Zabolotskaya, and R. F. Samigullina, Application of a modified Pechini method for the synthesis of $Ln_2MGe_4O_{12}$ (Ln = Y, Eu; M = Ca, Zn, Mn) optical hosts, *Journal of Sol-Gel Science and Technology*, **2011**, *59*, 338-344.

[10] I. I. Leonidov, V. P. Petrov, V. A. Chernyshev, A. E. Nikiforov, E. G. Vovkotrub, A. P. Tyutyunnik, and V. G. Zubkov, Structural and Vibrational Properties of the Ordered $Y_2CaGe_4O_{12}$ Germanate: A Periodic Ab Initio Study, *Journal of Physical Chemistry C*, **2014**, *118*, 8090-8101.

[11] H. Yamane, R. Tanimura, T. Yamada, J. Takahashi, T. Kajiwara, and M. Shimada, Synthesis and crystal structures of $CaY_2Ge_3O_{10}$ and $CaY_2Ge_4O_{12}$, *Journal of Solid State Chemistry*, **2016**, *179*, 289-295.

[12] R. E. Dinnebier, and S. J. L. Billinge, *Powder diffraction*, The Royal Society of Chemistry: **2008**.

[13] T. Hahn, *International Tables for Crystallography. Volume A, Space-Group Symmetry.*, Kluwer Academic Publishers: **2006**.

[14] A. V. Shubnikov, *Symmetry and Antisymmetry of Asymetrical Finite Figures*, Izd. Akad. Nauk SSSR: **1951**.

[15] R. Mirman, *Point Groups, Space Groups, Crystals, Molecules*, World Scientific: **1999**.

[16] B. E. Warren, *X-ray Diifraction*, Addison-Wesley Publishing Company: **1969**.

[17] G. E. Bacon, *Neutron Diffraction*, Oxford University Press: **1975**.

[18] http://www.ansto.gov.au/ResearchHub/OurInfrastructure/ACNS/Facilities/Instruments/Echidna/index.htm.

[19] H. M. Rietveld, A profile refinement method for nuclear and magnetic structures, *Journal of Applied Crystallography*, **1969**, *2*, 65-71.

[20] R. A. Young, *The Rietveld Method*, Oxford University Press **1993**.

[21] B. H. Toby, EXPGUI, a graphical user interface for GSAS, *Journal of Applied Crystallography*, **2001**, *34*, 210-213.

[22] A. C. Larson, and R. B. Von Dreele, *General Structure Analysis System (GSAS)*, Los Alamos National Laboratory Report LAUR 86-748: **2004**.

[23] S. Arajs, and R. V. Colvin, Magnetic Susceptibility of Gadolinium and Dysprosium Sesquioxides at Elevated Temperatures, *Journal of Applied Physics*, **1962**, *33*, 2517.

[24] R. M. Moon, and W. C. Koehler, Magnetic properties of Gd_2O_3, *Physical Review B*, **1975**, *11*, 1609-1622.

[25] T. C. Gibb, *Principles of Mossbauer Spectroscopy*, John Wiley & Sons: **1976**.

Chapter 3 - Synthesis and Characterisation of $CeMn_{2-x}Co_xGe_4O_{12}$ ($0 \leqslant x \leqslant 2$)

3.1 Introduction

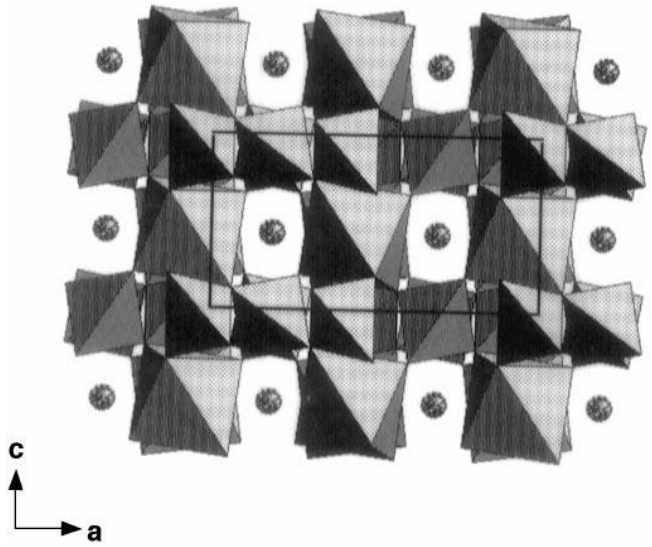

Figure 3.1 The crystal structure of $CeMn_2Ge_4O_{12}$ in *ac* plane [1]

As discussed in Chapter 1, Taviot-Guého *et al.* synthesized a tetragonal compound $CeMn_2Ge_4O_{12}$ [1]. It crystallises in the space group *P*4/*nbm* with the *2b* site occupied by a diamagnetic rare-earth cation Ce and the *4f* site by a magnetic first-row-transition metal cation Mn. The two distinct cation sites are coordinated by eight and six oxygen atoms and have square-antiprismatic and octahedral geometries, respectively. The [RO_8] and [MO_6] polyhedra make up the cation-containing layers at z = ½ perpendicular to the [001] axis. These layers are separated by diamagnetic layers comprising of $[Ge_4O_{12}]^{8-}$ rings; each ring formed by four vertex-sharing [GeO_4] tetrahedra. The crystal structure is shown in Figure 3.1. However, the magnetic properties of this compound were not reported, thus providing a starting point for the work to be described in this thesis.

We showed in Chapter 1 that compounds that are isostructural in the paramagnetic phase can adopt different low-temperature magnetic structures, for example MnO and CoO [2]. Although both of these compounds can be described as Type II antiferromagnets [3], [4], the atomic moments align along different crystallographic axes within the unit cell. The

transition from one structure to another can be followed by studying compounds in the intervening solid solution, for example $Mn_{1-x}Co_xO$. This composition-dependent variation in magnetic behaviour is not restricted to simple binary oxides and halides and in this chapter we report the progression in magnetic properties along the solid solution $CeMn_{2-x}Co_xGe_4O_{12}$.

3.2 Experimental

Polycrystalline samples of $CeMn_{2-x}Co_xGe_4O_{12}$ (x = 0.0, 0.5, 2.0) were synthesised by solid-state reaction. Stoichiometric quantities of CeO_2, Co_3O_4, $MnCO_3$, and GeO_2 were mixed thoroughly in an agate mortar, along with a 10% excess of GeO_2 to counteract its loss at high temperature. The mixtures were heated at 1075 °C for 4 days with intermediate cooling and regrinding every two days. They were then pressed into pellets and annealed at the same temperature for another 4 days with intermediate cooling and regrinding every two days. Further heating at 1100 °C for 1 day was carried out if GeO_2 was detected as an impurity phase. $CeMn_{2-x}Co_xGe_4O_{12}$ (x = 1.0 and 1.5) were synthesised by a former visiting fellow, X. Liu, in similar manner.

X-ray powder diffraction patterns were recorded at room temperature using Cu $K\alpha_1$ radiation. Neutron powder diffraction patterns were collected using a wavelength of either 1.622 Å or 2.4395 Å. The measurements were performed at room temperature and low temperatures. The measurements were also conducted in zero field and in an applied magnetic field (0 – 30 kOe). The data were analysed by the Rietveld method [5] using the program GSAS [6], [7] and the peak function developed by van Laar and Yelon [8]. The magnetic structures were drawn using VESTA [9].

Magnetic measurements were performed using both Quantum Design MPMS XL and Quantum Design MPMS 5 SQUID magnetometers. DC susceptibility measurements were made over the temperature range 2 K ≤ T ≤ 300 K in an applied field of 100 Oe with both zero-field cooling (ZFC) and field-cooling (FC) of the samples. The temperature and field dependence of the DC molar magnetic susceptibilities of $CeMn_{2-x}Co_xGe_4O_{12}$ (x = 1.5 and 2.0) were studied over the temperature range 2 K ≤ T ≤ 300 K in applied fields of 1, 3, 6, 10, 20, 50 kOe following field cooling of the samples. The field dependence of the

magnetization was measured over the field range -50 kOe ≤ H ≤ 50 kOe at 2K with the samples initially cooled in a 50 kOe magnetic field. AC susceptibilities were measured at frequencies 1 Hz/10 Hz/100 Hz/1000 Hz over the temperature range 2 K ≤ T ≤ 12 K in a 3.5 Oe AC driving field. Samples were ac-degaussed and then cooled in a small dc field of 3 Oe to counteract the remaining field in the SQUID. Further in-field AC measurements were made under the same condition in fields of 0.01, 0.5, 2, 20 kOe.

Specific heat data were collected on the compound $CeCo_2Ge_4O_{12}$ over the temperature range 2 K ≤ T ≤ 20 K in zero field and in an applied field of 20 kOe.

3.3 Results

3.3.1 Structural Chemistry

3.3.1.1 X-ray Diffraction

Single phase samples of $CeMn_{2-x}Co_xGe_4O_{12}$ (x = 0.0, 0.5 and 2.0) were obtained using the method described above. CeO_2 and $CoGeO_3$ were detected as impurities in the other two solid solutions. $CeCo_2Ge_4O_{12}$ was green in colour whereas the other four compositions were brown. The XRPD patterns collected from the five samples could all be indexed in the tetragonal space group *P*4/*nbm* (No. 125) as described by Taviot-Guého *et al* [1]. The atom coordination is also consistent with that listed by Taviot-Guého *et al*. The *2b* site is occupied by diamagnetic Ce^{4+} and the *4f* site is randomly occupied by the mixture of magnetic cations Co^{2+} and Mn^{2+}. The crystal structure of the solid solutions is shown in Figure 3.2. The coordination environments of the *2b* and *4f* sites are shown in Figure 3.3. The fitted room temperature X-ray diffraction pattern of $CeMn_2Ge_4O_{12}$ is shown in Figure 3.4 and the other patterns are shown in Appendix A Figure A.1 – Figure A.4. Structural parameters derived from the refinements are listed in Table 3.1.

As described before, $CoGeO_3$ exists in the solid solutions $CeMn_{2-x}Co_xGe_4O_{12}$ (x = 1.0 and 1.5) and has two phases, orthorhombic and monoclinic [10]. However, the phase type and the amount of the impurity $CoGeO_3$ are hard to determine from the X-ray data. Further neutron experiments (see Chapter 3.3.1.2) proved that the $CoGeO_3$ is in the orthorhombic phase. The refinement of XRPD data then give the impurity levels of 0.38(8) wt% and

0.47(8) wt% for $CeMnCoGe_4O_{12}$ and $CeMn_{0.5}Co_{1.5}Ge_4O_{12}$ respectively. CeO_2 impurity concentrations are 1.26(8) wt% and 1.26(6) wt% for the two compounds.

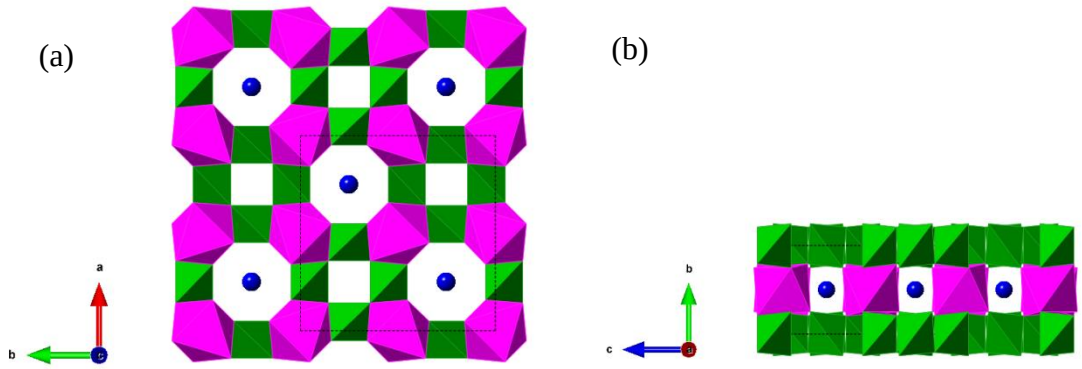

Figure 3.2 Polyhedral representation of the crystal structure of $CeMn_{2-x}Co_xGe_4O_{12}$ viewed along (a) [001] and (b) [100]: green tetrahedra and purple octahedra represent GeO_4 and $(Mn/Co)O_6$ groups, respectively; blue circles represent Ce^{4+} cations.

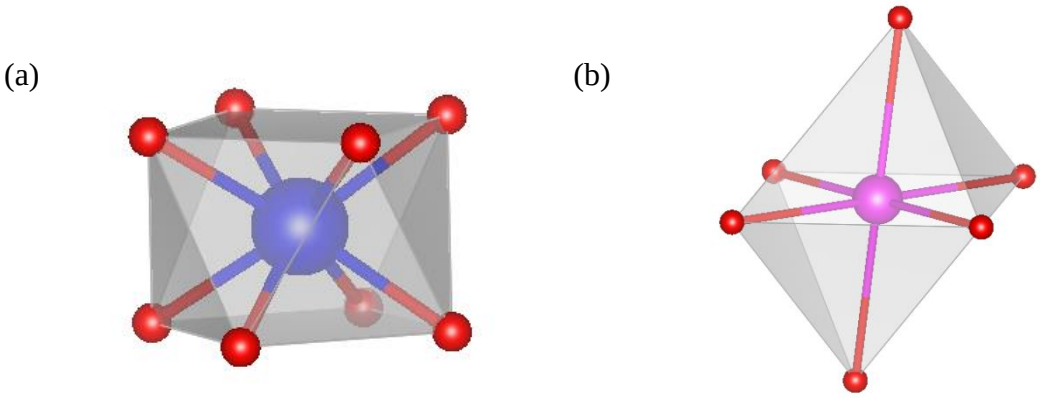

Figure 3.3 Polyhedral representations of the (a) *2b* site and the (b) *4f* site.

Table 3.1 Structural parameters of $CeMn_{2-x}Co_xGe_4O_{12}$ at room temperature derived from X-ray diffraction data (λ = 1.5406 Å)

		X				
		0.0	0.5	1.0†	1.5‡	2.0
Ge	*x*	0.5254(1)	0.5259(2)	0.5258(1)	0.5248(2)	0.5259(2)
O1	*x*	-0.3614(5)	-0.3579(7)	-0.3663(5)	-0.3642(7)	-0.3587(6)
	z	0.2003(13)	0.2153(17)	0.1780(12)	0.1867(15)	0.2105(15)
O2	*x*	0.1644(5)	0.1626(6)	0.1645(5)	0.1620(7)	0.1583(7)
	y	0.0494(4)	0.0506(5)	0.0591(5)	0.0596(6)	0.0498(5)
	z	0.2461(8)	0.2464(10)	0.2524(8)	0.2524(11)	0.2483(12)
a/Å		9.8427(1)	9.8164(1)	9.7914(1)	9.7714(1)	9.7470(1)
c/Å		4.9109(1)	4.8868(1)	4.8634(1)	4.8434(1)	4.8218(1)
V/Å^3		475.76(1)	470.90(1)	466.26(1)	462.44(1)	458.09(1)
R_{wpr}		7.76%	5.63%	6.68%	4.91%	5.34%
χ^2		1.500	1.791	2.016	0.872	1.235

Space group *P*4/*nbm* (No. 125), Z = 2

Ce on 2*b* (¼, ¼, ½); Mn/Co on 4*f* (0, 0, ½);

Ge on 8*k* (*x*, ¼, 0); O1 on 8*m* (*x*, -*x*, *z*); O2 on 16*n* (*x*, *y*, *z*)

† Contains 0.38(8) wt % $CoGeO_3$ and 1.26(8) wt % CeO_2

‡ Contains 0.47(8) wt % $CoGeO_3$ and 1.26(6) wt % CeO_2

The U_{iso} parameter of each atom was constrained to that reported by Taviot-Gueho. [1]

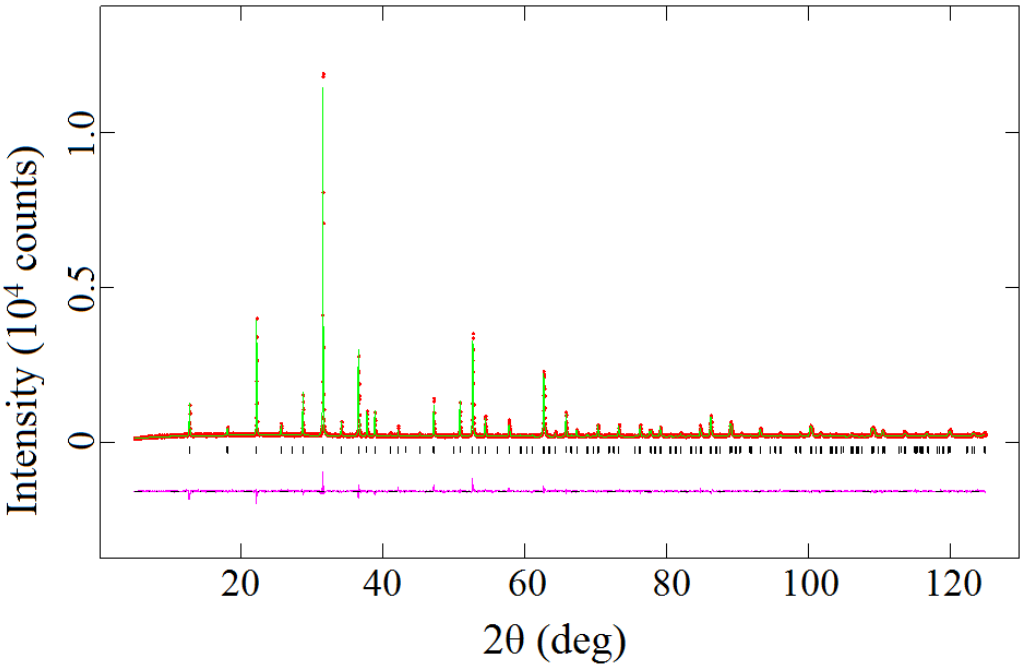

Figure 3.4 Observed (red dots) and calculated (green line) XRPD patterns of $CeMn_2Ge_4O_{12}$ at room temperature; Cu Kα1. A difference curve (purple line) is shown and reflection positions are marked.

3.3.1.2 Room Temperature Neutron Diffraction

Neutron-diffraction data were collected on all the samples at room temperature using a wavelength λ = 1.622 Å. The fitted room-temperature neutron diffraction pattern of $CeMn_2Ge_4O_{12}$ is shown in Figure 3.5 and the other patterns are shown in Appendix B Figure B.1 – Figure B.4. Structural parameters derived from the refinements are listed in Table 3.2. Some selected bond lengths and bond angles derived from the room-temperature neutron diffraction data are listed in Table 3.3.

As mentioned above, $CoGeO_3$ [10] has two phases, orthorhombic (*Pbca*) and monoclinic (*C*2/*c*). These two phases are formed at different temperatures, 1175 and 1000 °C respectively. The two phases are both antiferromagnets with the Néel temperatures 35.8(1) and 33.0(1) K, respectively. As we shall show below, the $CeMn_{2-x}Co_xGe_4O_{12}$ solutions all have transition temperature below 10 K. Hence, at around 10 K, $CoGeO_3$ has already ordered antiferromagnetically whereas the main phase is still paramagnetic. The orthorhombic $CoGeO_3$ has the magnetic propagation vector $\boldsymbol{k}$ = (0,0,0) and the monoclinic

$CoGeO_3$ has the magnetic propagation vector $\boldsymbol{k}$ = (1,0,0). As the two phases have different magnetic structures, the different magnetic peak positions can be used to identify the impurity phase type and analyse the amount. Therefore, neutron diffraction data were also collected on all the samples at low temperature but slightly above the magnetic transition temperature (approximately 10 K) using wavelength λ = 1.622 and/or 2.4365 Å. These NPD data were collected to identify the impurities. The magnetic peaks from $CoGeO_3$ in $CeMnCoGe_4O_{12}$ and $CeMn_{0.5}Co_{1.5}Ge_4O_{12}$ confirmed that the impurity is the orthorhombic phase. Moreover, $CeMnCoGe_4O_{12}$ has 1.3(2) wt% $CoGeO_3$ and 0.3(1) wt% CeO_2; $CeMn_{0.5}Co_{1.5}Ge_4O_{12}$ has 4.1(6) wt% $CoGeO_3$ and 0.9(1) wt% CeO_2. These impurity concentrations were included in all relevant data analysis.

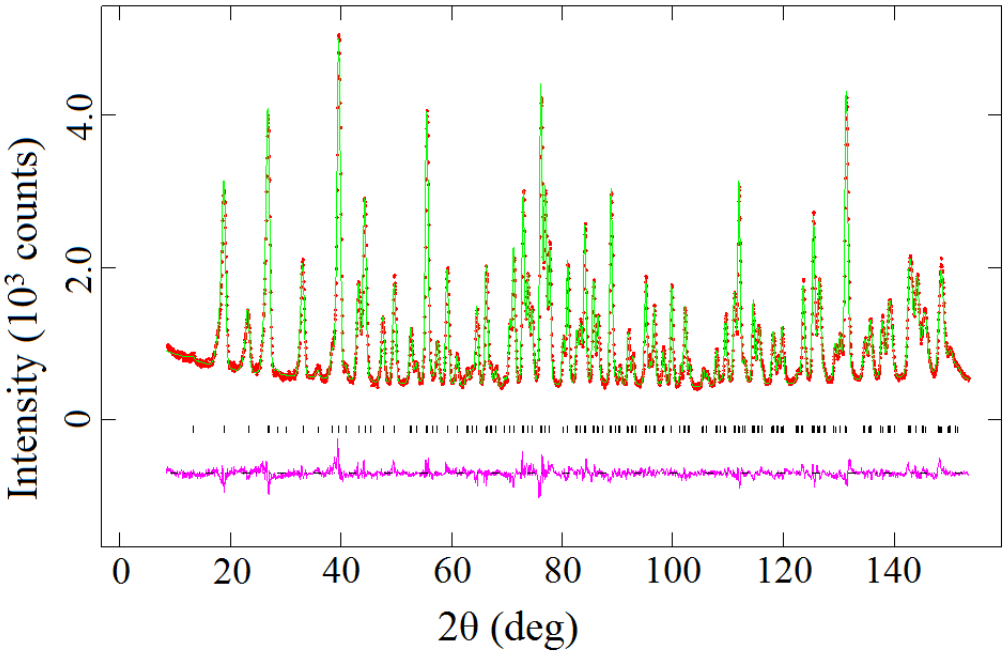

Figure 3.5 Observed (red dots) and calculated (green line) NPD patterns of $CeMn_2Ge_4O_{12}$ at room temperature; λ = 1.622 Å. A difference curve (purple line) is shown and reflection positions are marked.

Table 3.2 Structural parameters of $CeMn_{2-x}Co_xGe_4O_{12}$ at room temperature derived from neutron diffraction data ($\lambda = 1.622$ Å)

		x				
		0.0	0.5	1.0†	1.5‡	2.0
Ce	U_{iso}/Å^2	0.0037(8)	0.0040(7)	0.0084(7)	0.0085(8)	0.0031(8)
Mn/Co	U_{iso}/Å^2	0.0070(5)	0.0107(9)	0.0144(6)	0.0242(2)	0.0052(1)
Ge	*x*	0.5233(1)	0.5240(1)	0.5232(2)	0.5234(2)	0.5242(1)
	U_{iso}/Å^2	0.0025(2)	0.0040(2)	0.0078(4)	0.0081(6)	0.0031(2)
O1	*x*	-0.3694(1)	-0.3692(1)	-0.3692(2)	-0.3691(2)	-0.3689(1)
	z	0.1697(3)	0.1728(3)	0.1754(5)	0.1778(5)	0.1803(3)
	U_{iso}/Å^2	0.0040(3)	0.0062(3)	0.0109(8)	0.0110(7)	0.0053(4)
O2	*x*	0.1672(1)	0.1660(1)	0.1646(2)	0.1636(2)	0.1621(1)
	y	0.0646(1)	0.0645(1)	0.0644(2)	0.0640(2)	0.0640(1)
	z	0.2551(2)	0.2560(2)	0.2550(4)	0.2542(4)	0.2561(3)
	U_{iso}/Å^2	0.0044(2)	0.0065(2)	0.0094(5)	0.0091(5)	0.0058(3)
a/Å		9.8382(1)	9.8130(1)	9.7925(2)	9.7695(2)	9.7434(1)
c/Å		4.9096(1)	4.8861(1)	4.8640(1)	4.8423(2)	4.8207(1)
V/Å^3		475.20(1)	470.52(1)	466.42(3)	462.10(3)	457.65(2)
R_{wpr}		4.74%	4.48%	5.81%	6.06%	4.80%
χ^2		2.206	2.439	2.090	2.276	2.432

Space group *P*4/*nbm* (No. 125), Z = 2

Ce on 2*b* (¼, ¼, ½); Mn/Co on 4*f* (0, 0, ½);

Ge on 8*k* (*x*, ¼, 0); O1 on 8*m* (*x*, -*x*, *z*); O2 on 16*n* (*x*, *y*, *z*)

† Contains 1.3(2) wt % $CoGeO_3$ and 0.3(1) wt % CeO_2

‡ Contains 4.1(6) wt % $CoGeO_3$ and 0.9(1) wt % CeO_2

Table 3.3 Bond lengths (Å) and bond angles (degrees) in $CeMn_{2-x}Co_xGe_4O_{12}$ at room temperature derived from neutron diffraction data ($\lambda = 1.622$ Å)

	x				
	0.0	0.5	1.0	1.5	2.0
Ce-O2 × 8	2.331(1)	2.327(1)	2.329(2)	2.331(2)	2.324(1)
Mn/Co-O1 × 2	2.435(1)	2.419(1)	2.402(3)	2.388(3)	2.374(2)
Mn/Co-O2 × 4	2.134(1)	2.116(1)	2.102(2)	2.088(2)	2.066(1)
O2-O2' *	3.225(1)	3.199(1)	3.172(3)	3.143(3)	3.116(2)
O2-O2" *	2.796(1)	2.770(1)	2.758(3)	2.750(3)	2.712(2)
Ge-O1 × 2	1.786(1)	1.783(1)	1.789(1)	1.789(2)	1.784(1)
Ge-O2 × 2	1.727(1)	1.731(1)	1.725(2)	1.719(2)	1.731(1)
O2-Mn/Co-O2'	98.16(4)	98.22(4)	97.98(7)	97.65(7)	97.92(5)
O2-Mn/Co-O2"	81.84(4)	81.78(4)	82.02(7)	82.35(7)	82.01(5)
O1-Mn/Co-O2'	82.77(4)	82.96(4)	82.90(8)	82.94(8)	83.09(5)
O1-Mn/Co-O2"	97.23(4)	97.04(4)	97.10(8)	97.06(8)	96.92(5)
O1-Ge-O1	107.57(11)	108.04(10)	107.90(21)	108.05(22)	108.58(13)
O1-Ge-O2	105.56(5)	105.36(5)	105.43(9)	105.44(10)	105.27(6)
O1-Ge-O2	108.91(7)	108.94(6)	108.64(13)	108.46(13)	108.42(8)
O2-Ge-O2	119.84(8)	119.78(8)	120.31(15)	120.51(16)	120.48(10)

* distances within the equatorial plane of the $(Mn/Co)O_6$ octahedra

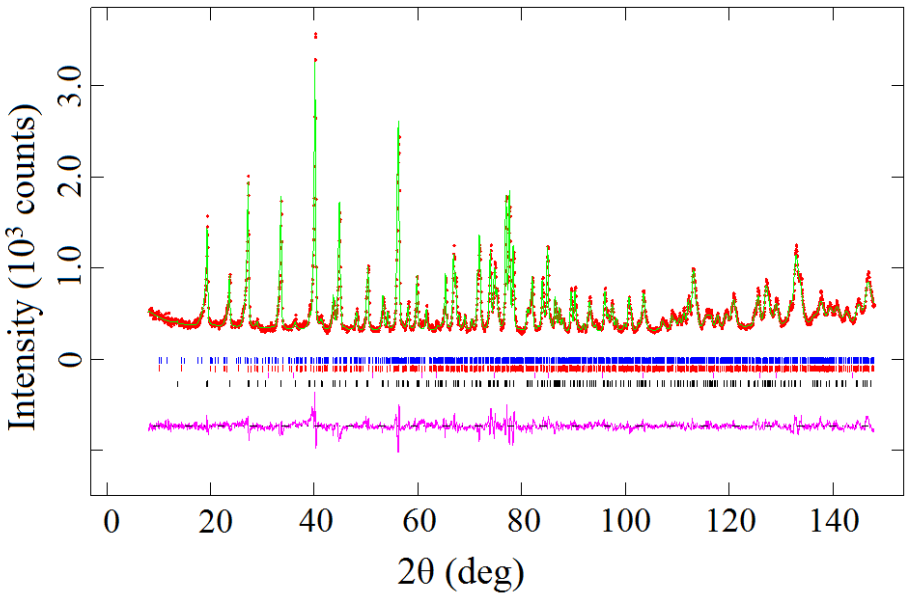

Figure 3.6 Observed (red dots) and calculated (green line) NPD patterns of $CeMnCoGe_4O_{12}$ at 10 K; λ = 1.622 Å. A difference curve (purple line) is shown and reflection positions are marked for $CeMnCoGe_4O_{12}$ (black), CeO_2 (pink), $CoGeO_3$ (red), and $CoGeO_3$ magnetic phase (blue).

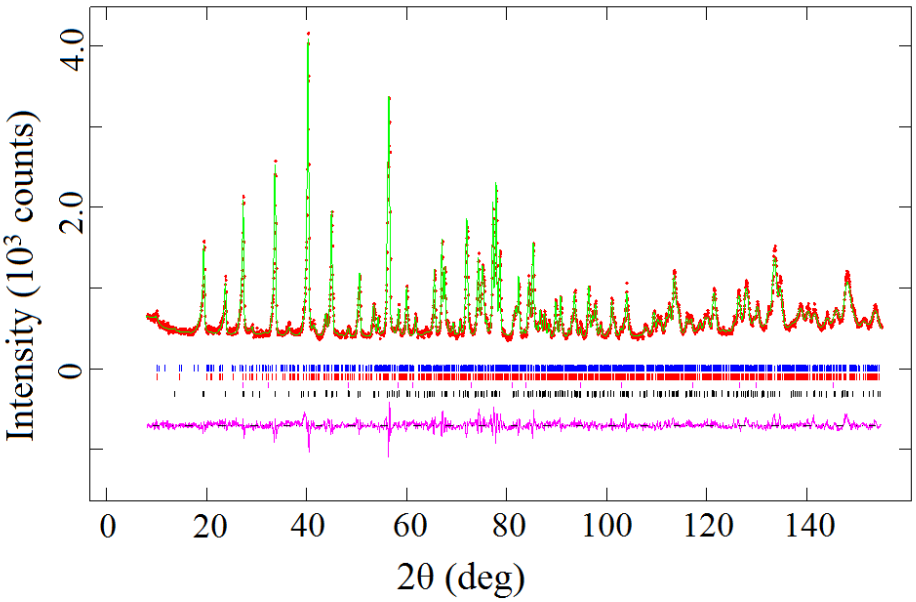

Figure 3.7 Observed (red dots) and calculated (green line) NPD patterns of $CeMn_{0.5}Co_{1.5}Ge_4O_{12}$ at 10 K; λ = 1.622 Å. A difference curve (purple line) is shown and reflection positions are marked for $CeMn_{0.5}Co_{1.5}Ge_4O_{12}$ (black), CeO_2 (pink), $CoGeO_3$ (red), and $CoGeO_3$ magnetic phase (blue).

3.3.1.3 Low Temperature Neutron Diffraction

Neutron diffraction data were collected on all the samples at 1.6 K using wavelength λ = 1.622 and 2.4395 Å. Structural parameters derived from λ = 1.622 Å NPD data are listed in Table 3.4. The fitted low temperature neutron diffraction pattern of $CeMn_2Ge_4O_{12}$ is shown in Figure 3.8 and the fitted patterns shown in Appendix B Figure B.5 – Figure B.8. Some selected bond lengths and bond angles derived from the neutron diffraction data collected at 1.6 K are listed in Table 3.5.

The magnetic structure derived from λ = 2.4395 Å NPD data will be discussed in section 3.3.2.3.

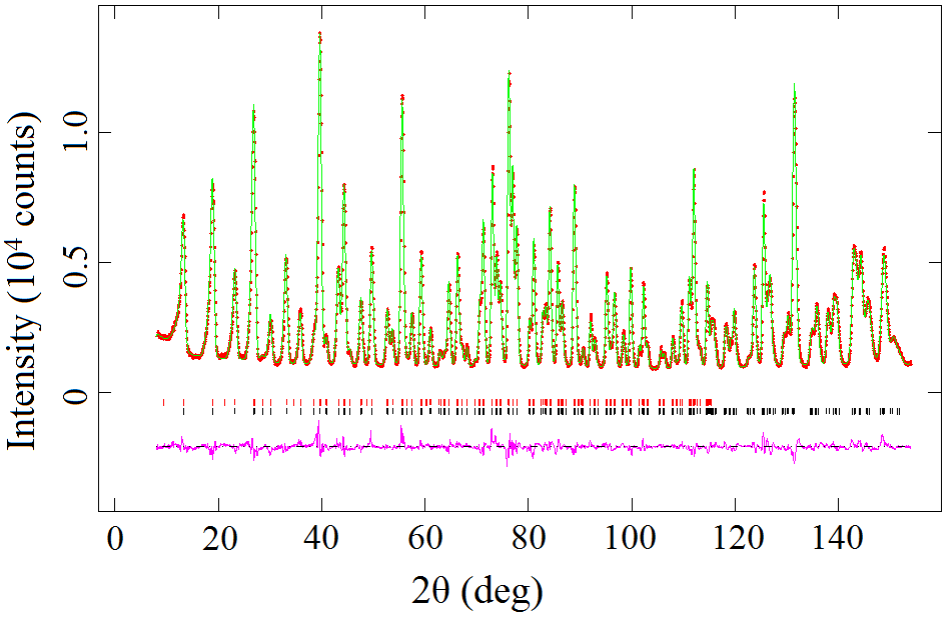

Figure 3.8 Observed (red dots) and calculated (green line) NPD patterns of $CeMn_2Ge_4O_{12}$ at 1.6 K; λ = 1.622 Å. A difference curve (purple line) is shown and reflection positions are marked for the crystal structure (bottom) and the magnetic structure (top).

Table 3.4 Structural parameters of $CeMn_{2-x}Co_xGe_4O_{12}$ at 1.6 K derived from neutron diffraction data (λ = 1.622 Å)

		x				
		0.0	0.5	1.0†	1.5‡	2.0
Ce	U_{iso}/Å^2	0.0016(5)	0.0010(2)	0.0051(5)	0.0063(3)	0.0048(3)
Mn/Co	U_{iso}/Å^2	0.0017(3)	0.0064(3)	0.0033(3)	0.0196(6)	0.0020(4)
Ge	*x*	0.5234(1)	0.5240(1)	0.5232(2)	0.5231(2)	0.5244(1)
	U_{iso}/Å^2	0.0008(2)	0.0006(1)	0.0044(4)	0.0046(4)	0.0016(2)
O1	*x*	-0.3698(1)	-0.3696(1)	-0.3686(2)	-0.3690(2)	-0.3690(1)
	z	0.1710(2)	0.1730(2)	0.1753(4)	0.1787(5)	0.1806(2)
	U_{iso}/Å^2	0.0014(2)	0.0020(2)	0.0048(5)	0.0061(6)	0.0040(3)
O2	*x*	0.1669(1)	0.1655(1)	0.1646(2)	0.1633(2)	0.1619(1)
	y	0.0647(1)	0.0645(1)	0.0643(2)	0.0644(2)	0.0642(1)
	z	0.2550(2)	0.2556(2)	0.2542(4)	0.2544(4)	0.2569(2)
	U_{iso}/Å^2	0.0025(2)	0.0029(2)	0.0046(2)	0.0050(3)	0.0039(4)
a/Å		9.8317(1)	9.8080(1)	9.7892(2)	9.7668(1)	9.7369(1)
c/Å		4.9024(1)	4.8794(1)	4.8570(1)	4.8356(1)	4.8126(1)
V/Å^3		473.88(1)	469.39(1)	465.44(1)	461.27(1)	456.27(1)
R_{wpr}		4.20%	4.49%	6.52%	6.38%	3.62%
χ^2		4.570	2.322	2.418	2.601	3.392

Space group *P*4/*nbm* (No. 125), Z = 2

Ce on 2*b* (¼, ¼, ½); Mn/Co on 4*f* (0, 0, ½);

Ge on 8*k* (*x*, ¼, 0); O1 on 8*m* (*x*, -*x*, *z*); O2 on 16*n* (*x*, *y*, *z*)

† Contains 1.3(2) wt % $CoGeO_3$ and 0.3(1) wt % CeO_2

‡ Contains 4.1(6) wt % $CoGeO_3$ and 0.9(1) wt % CeO_2

Table 3.5 Bond lengths (Å) and bond angles (degrees) in $CeMn_{2-x}Co_xGe_4O_{12}$ at 1.6 K derived from neutron diffraction data (λ = 1.622 Å)

	x				
	0.0	0.5	1.0	1.5	2.0
Ce-O2 × 8	2.330(1)	2.328(1)	2.330(2)	2.327(2)	2.320(1)
Mn/Co-O1 × 2	2.425(1)	2.411(1)	2.408(3)	2.385(3)	2.370(1)
Mn/Co-O2 × 4	2.131(1)	2.111(1)	2.102(2)	2.085(2)	2.060(1)
O2-O2' *	3.220(1)	3.190(1)	3.169(3)	3.143(3)	3.114(1)
O2-O2" *	2.790(1)	2.766(1)	2.762(3)	2.741(3)	2.699(2)
Ge-O1 × 2	1.786(1)	1.783(1)	1.787(2)	1.791(2)	1.782(1)
Ge-O2 × 2	1.727(1)	1.731(1)	1.719(2)	1.721(2)	1.734(1)
O2-Mn/Co-O2'	98.19(3)	98.13(3)	97.84(7)	97.82(7)	98.16(3)
O2-Mn/Co-O2"	81.81(3)	81.87(3)	82.16(7)	82.18(7)	81.84(3)
O1-Mn/Co-O2'	82.75(3)	82.82(3)	82.98(7)	82.93(7)	83.12(3)
O1-Mn/Co-O2"	97.25(3)	97.18(3)	97.02(7)	97.07(7)	96.88(3)
O1-Ge-O1	108.04(8)	108.37(9)	107.28(20)	107.95(20)	108.71(8)
O1-Ge-O2	105.50(4)	105.51(4)	105.60(9)	105.47(9)	105.29(4)
O1-Ge-O2	108.82(5)	108.63(6)	108.76(12)	108.50(12)	108.43(5)
O2-Ge-O2	119.73(6)	119.82(7)	120.26(15)	120.47(15)	120.33(6)

* distances within the equatorial plane of the $(Mn/Co)O_6$ octahedra

3.3.2 Magnetic Properties

3.3.2.1 DC Magnetisation Measurements

The temperature dependence of the dc molar susceptibility, measured in 100 Oe, of each sample is shown in Figure 3.9. The field dependence of the magnetisation measured at 2 K is also shown in Figure 3.9. The transition temperature, T_c, represents the Curie temperature for x = 0.5, 1.0 and the Néel temperature for x = 0.0, 1.5, 2.0. The magnetic parameters resulting from fitting the Curie-Weiss law to the FC data for T > 150 K are listed in Table 3.6. Values of the coercive field, H_c, and the remanent magnetisation, M_r, for x = 0.0, 1.5 are also included in Table 3.6.

Further susceptibility measurements were made in higher fields on the samples x = 1.5, 2.0, shown in Figure 3.10. Further M(H) data measured at 4 K is shown in Figure 3.11.

Table 3.6 Magnetic parameters of $CeMn_{2-x}Co_xGe_4O_{12}$

	x				
	0.0	0.5	1.0	1.5	2.0
C /cm^3 K mol^{-1}	8.745(1)	8.344(4)	7.943(1)	7.586(1)	7.186(2)
θ /K	-7.59(3)	-13.06(8)	-17.50(2)	-21.96(2)	-15.93(2)
μ^{Co}_{eff}*	5.91$	5.36	5.35	5.37	5.36
T_c /K	7.6	6.5	5.8	5.4	4.2
M_r /μ_B per formula unit		0.38	0.67		
H_c /Oe		688	626		

$ μ_{eff} (Mn)

*calculated for 0.5 ≤ x 1.5 using μ_{eff} (Mn) = 5.91.

x	**χ** / $cm^3\ mol^{-1}$	***M*** / μ_B per f.u.
0.0	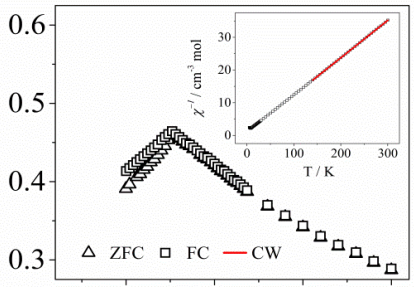	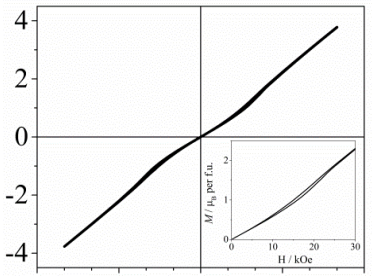
0.5	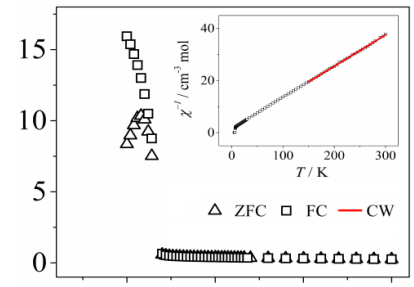	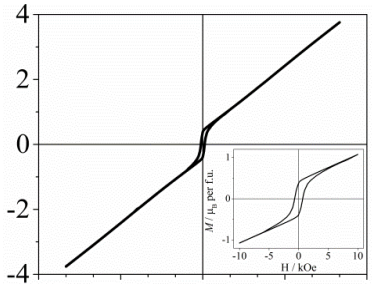
1.0	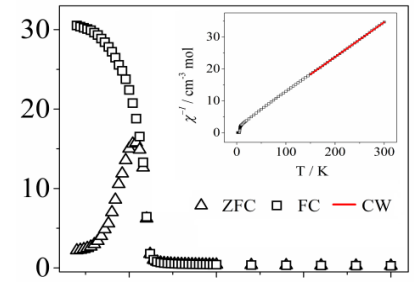	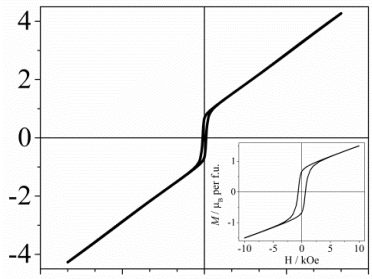
1.5	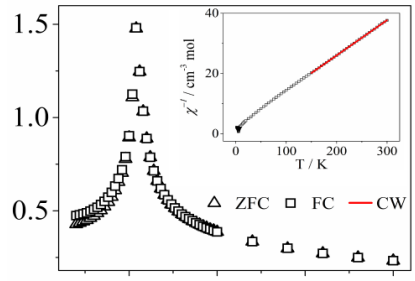	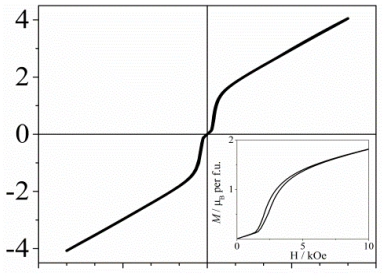
2.0	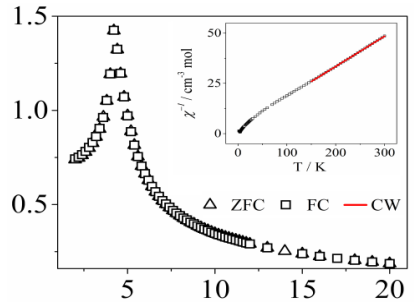	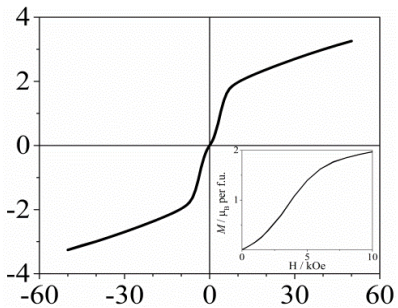
	T / K	**H** / kOe

Figure 3.9 Temperature dependence of the dc molar magnetic susceptibility, measured in 100 Oe, and the field dependence of the magnetization at 2 K of $CeMn_{2-x}Co_xGe_4O_{12}$. (inset) The inverse susceptibility; data points highlighted in red were fitted to the Curie−Weiss law.

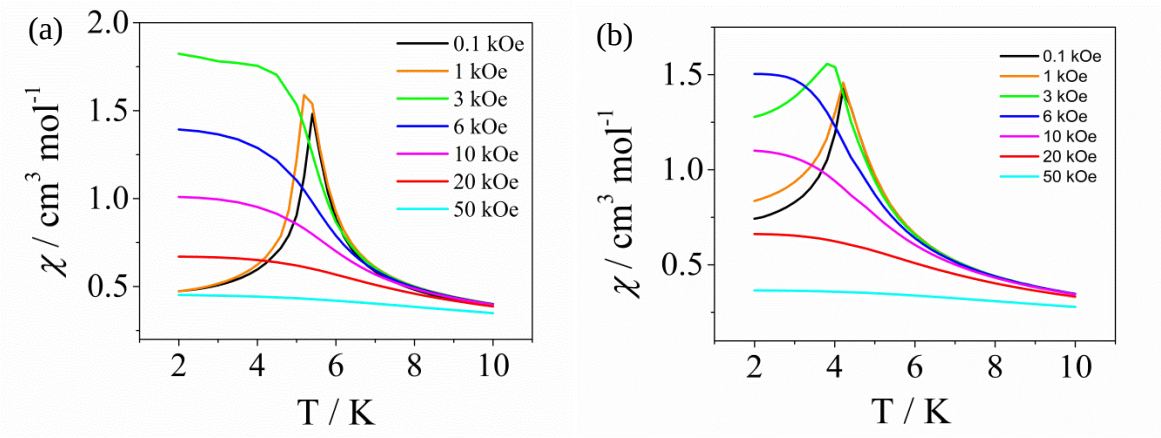

Figure 3.10 Temperature and field dependence of the dc molar magnetic susceptibility of (a) $CeMn_{0.5}Co_{1.5}Ge_4O_{12}$ and (b) $CeCo_2Ge_4O_{12}$.

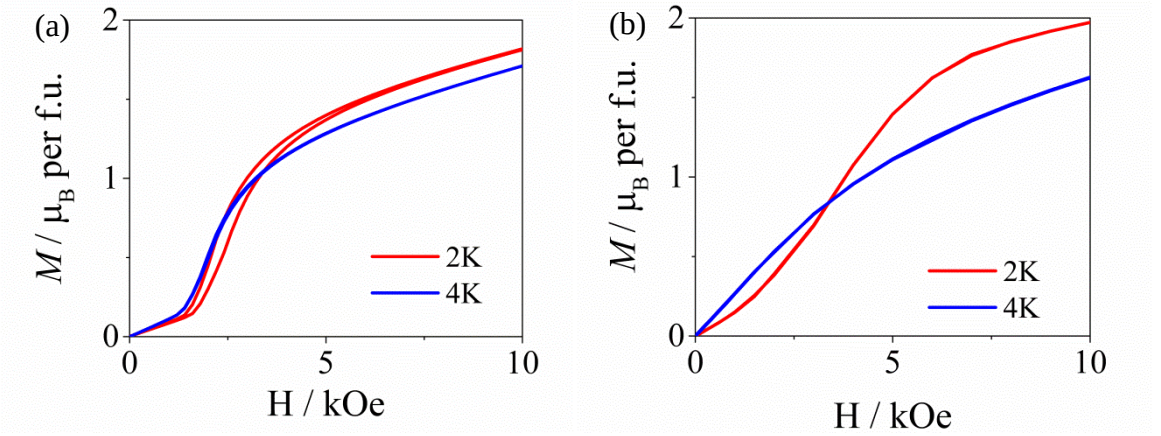

Figure 3.11 Field dependence of the magnetisation at 2 and 4 K of (a) $CeMn_{0.5}Co_{1.5}Ge_4O_{12}$ and (b) $CeCo_2Ge_4O_{12}$.

From the dc susceptibilities, the solid solutions having x = 0.5, 1.0 are ferro/ferrimagnets and those having x = 0.0, 1.5, 2.0 are antiferromagnets. The transition temperatures are all below 10 K. The transition temperature decreases as the cobalt content increases from x = 0.0 to x = 2.0 in a linear way. However, $CeMn_2Ge_4O_{12}$ is not a classic antiferromagnet as the ZFC/FC susceptibilities are unequal below the transition temperature and the M(H) curve is non-linear. A weak hysteresis between 10 < H/kOe < 25 is also shown in the M(H) curve. $CeMn_{0.5}Co_{1.5}Ge_4O_{12}$ and $CeCo_2Ge_4O_{12}$ show a metamagnetic transition starting from an approximate 1.5 kOe magnetic field. The transition is complete for both compositions in a 20 kOe magnetic field. Furthermore, the M(H) data of $CeMn_{0.5}Co_{1.5}Ge_4O_{12}$ shows a weak hysteresis when 1.5 < H/kOe < 5.

From the Curie-Weiss fitting of $CeMn_2Ge_4O_{12}$, the effective moment of Mn^{2+} is 5.91 μ_B, which is close to the spin-only value 5.92 μ_B. Assuming Mn^{2+} has the moment of 5.91 μ_B in all the other compounds, the effective moment of Co^{2+} in all the Co-containing solid solutions is approximately 5.36 μ_B. The spin-only value for Co^{2+} is 3.87 μ_B. Assuming full orbital contribution, Co^{2+} has L = 3, S = 3/2, J = 9/2, g = 4/3, which leads to an effective moment of 6.63 μ_B.

3.3.2.2 AC Magnetisation Measurements

AC susceptibility measurements were carried out in zero field on all the compositions and the result is shown in Figure 3.12. Moreover, in-field ac susceptibility measurements were conducted in dc fields on $CeMn_2Ge_4O_{12}$. Relevant graphs are shown in Figure 3.13. The ac susceptibilities prove that the solid solutions having x = 0.5, 1.0 are ferro/ferrimagnets whereas those having x = 1.5, 2.0 are antiferromagnets. However, $CeMn_2Ge_4O_{12}$ shows an anomaly below the Néel temperature, 7.6 K. A plateau in the real part and a small peak in the imaginary part at 6 K in zero field were found; the imaginary peak is slightly frequency dependent. When a dc field was applied, the plateau remains but appears at a lower temperature, 5 K, and the imaginary peak disappears. Interestingly, the real part of the ac susceptibility of $CeMn_2Ge_4O_{12}$ in a 20 kOe magnetic field increases below the Néel temperature when the temperature decreases.

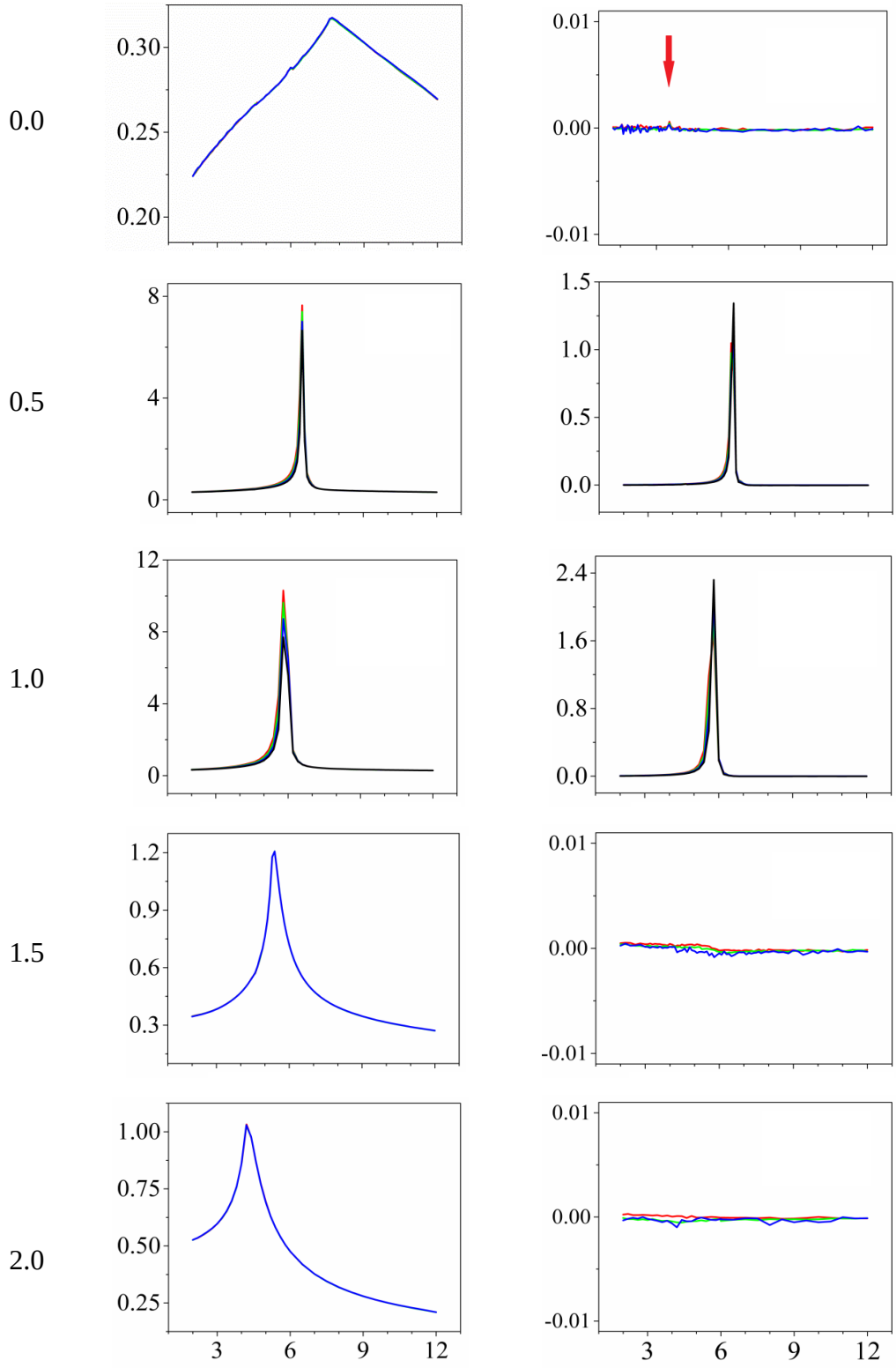

Figure 3.12 Temperature and frequency dependence of the ac molar magnetic susceptibility of $CeMn_{2-x}Co_xGe_4O_{12}$.

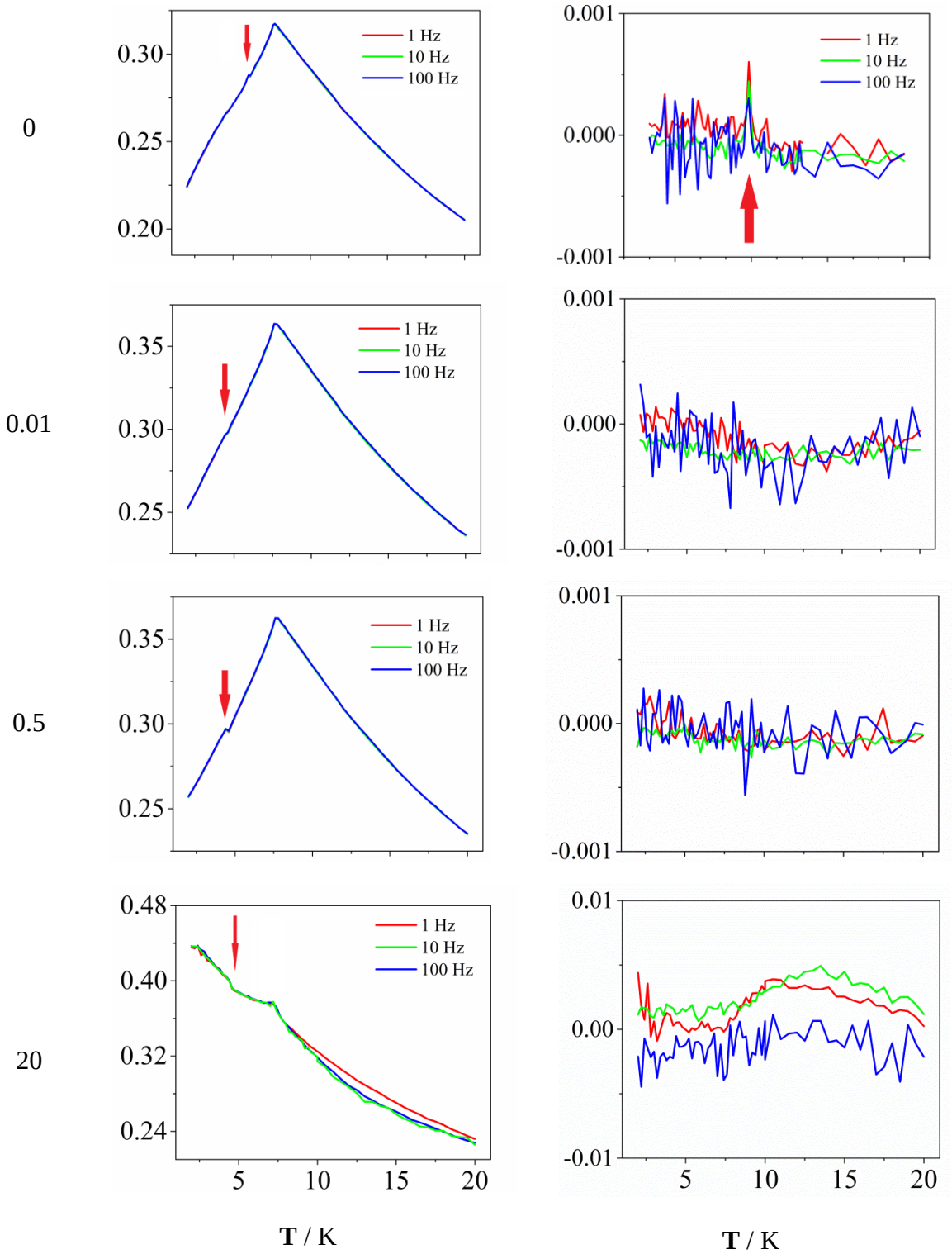

Figure 3.13 Temperature, frequency and field dependence of the ac molar magnetic susceptibility of $CeMn_2Ge_4O_{12}$. The red arrows point out the anomaly in the ac measurements.

3.3.2.3 Zero-Field Low Temperature Neutron Diffraction

Neutron diffraction data were collected on all the samples at 1.6 K using wavelengths λ = 1.622 and 2.4395 Å. The magnetic structures and the mean ordered atomic moment values at the *4f* site derived from λ = 2.4395 Å NPD data are shown in Figure 3.14 and Table 3.7. The structural parameters were constrained to that from the λ = 1.622 Å NPD data. The magnetic structures were determined by fitting the data with some possible magnetic structures and were attributed to their magnetic space group afterwards. The same method was applied in the following chapters.

Table 3.7 Mean ordered atomic moments (μ_B) at the 4*f* site in $CeMn_{2-x}Co_xGe_4O_{12}$ at 1.6 K derived from neutron diffraction data (λ = 2.4395 Å)

	x				
	0.0	0.5	1.0	1.5	2.0
M_x	0	3.92(2)	3.13(4)	2.68(3)	2.29(2)
M_y†	0	0	0	0.91(6)	1.19(3)
M_z	4.61(2)	0	0	0	0
M_T	4.61(2)	3.92(2)	3.13(4)	2.83(3)	2.58(2)

† the ferromagnetic component

The magnetic structure of $CeMn_2Ge_4O_{12}$ can be described in the magnetic space group *P4'/nbm'* (No. 125.5.1035). The structural and magnetic unit cells are the same size. Nearest-neighbour (NN) Mn^{2+} cations within the (001) sheet at z = ½ couple antiferromagnetically and align along the [001] axis. Next-nearest-neighbour (NNN) cations within this sheet align in a ferromagnetic manner and the NN cation-containing (001) layers are also in a ferromagnetic arrangement. The ordered moment for Mn^{2+} was determined to be 4.61 μ_B, close to the theoretical value gS = 5 μ_B.

The magnetic structure of $CeMn_{1.5}Co_{0.5}Ge_4O_{12}$ and $CeMnCoGe_4O_{12}$ can be described in the magnetic space group *Pb'an'* (No. 50.6.382). The structural and magnetic unit cells are the same size. The replacement of the Mn^{2+} cations by Co^{2+} causes the spins to rotate into the (001) plane. NN cations within the (001) sheet at z = ½ couple antiferromagnetically and NNN cations within this sheet align in a ferromagnetic manner. Due to the symmetry

of the crystal structure, the direction of the moments do not have a specific direction in the (001) plane. The ordered moments for the two compounds are listed in Table 3.7.

The magnetic structure of $CeMn_{0.5}Co_{1.5}Ge_4O_{12}$ and $CeCo_2Ge_4O_{12}$ can be described in the magnetic space group $P_{2c}b'an$ (No. 50.9.385). The unit cell doubles along the [001] axis with $c_{mag} = 2\ c$. The NN layer coupling along the [001] axis changes from ferromagnetic to antiferromagnetic. Within one (001) sheet, the moment coupling is antiferromagnetic along one axis ([100] axis is chosen in this thesis) and ferromagnetic along another axis ([010] axis is chosen in this thesis). Hence, the magnetic structure can thus be described as an antiferromagnetic stacking of weakly-ferromagnetic sheets. The ordered moment for Co^{2+} was determined to be 2.58 μ_B, close to the theoretical value gS = 3 μ_B.

(a)

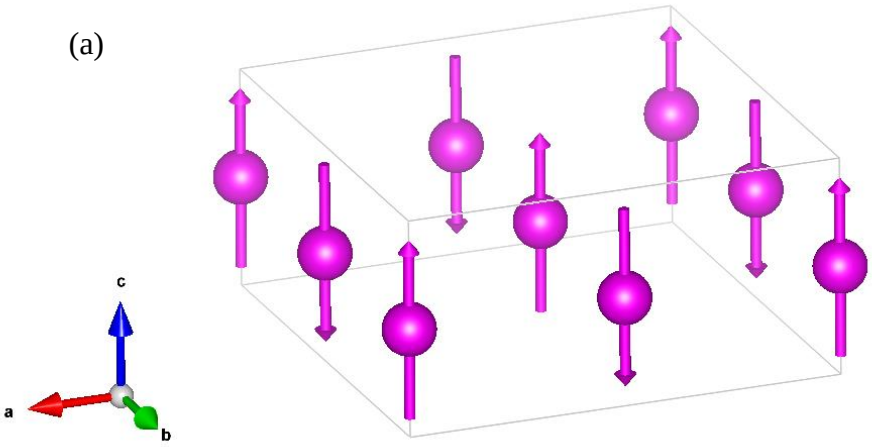

(b)

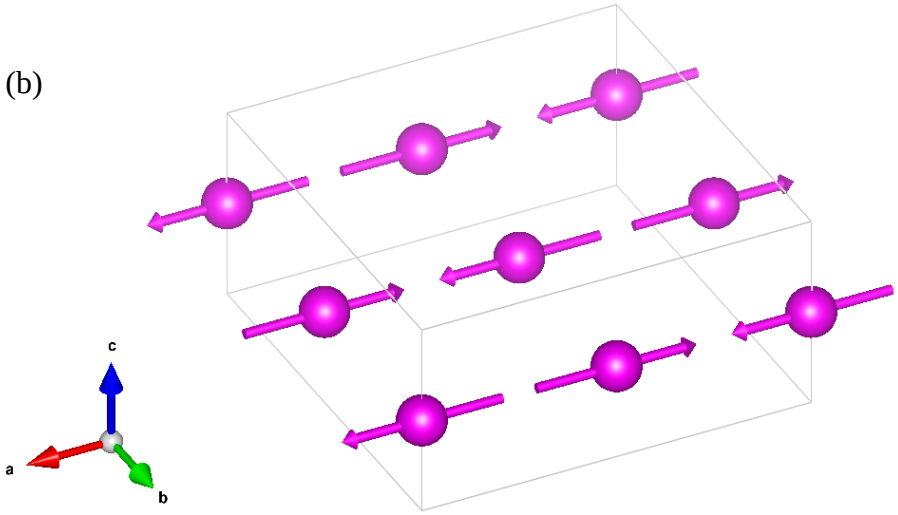

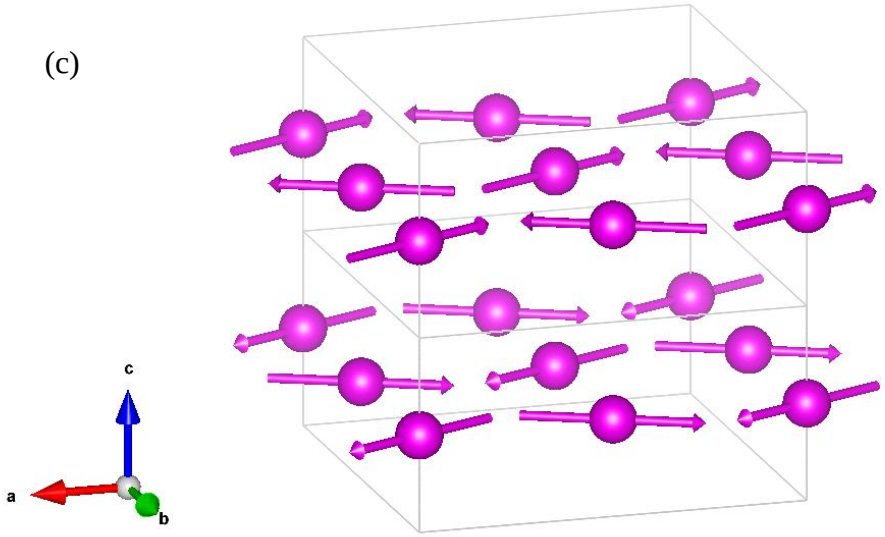

Figure 3.14 Magnetic structures in zero field of $CeMn_{2-x}Co_xGe_4O_{12}$ with x = (a) 0.0, (b) 0.5 and 1.0, (c) 1.5 and 2.0. Diamagnetic ions are omitted.

3.3.2.4 In-Field Low Temperature Neutron Diffraction

Due to the unusual ac susceptibility behaviour of $CeMn_2Ge_4O_{12}$ and the metamagnetic transition of $CeMn_{0.5}Co_{1.5}Ge_4O_{12}$ and $CeCo_2Ge_4O_{12}$ in an applied field, in-field low temperature neutron diffraction experiments were conducted on all compositions.

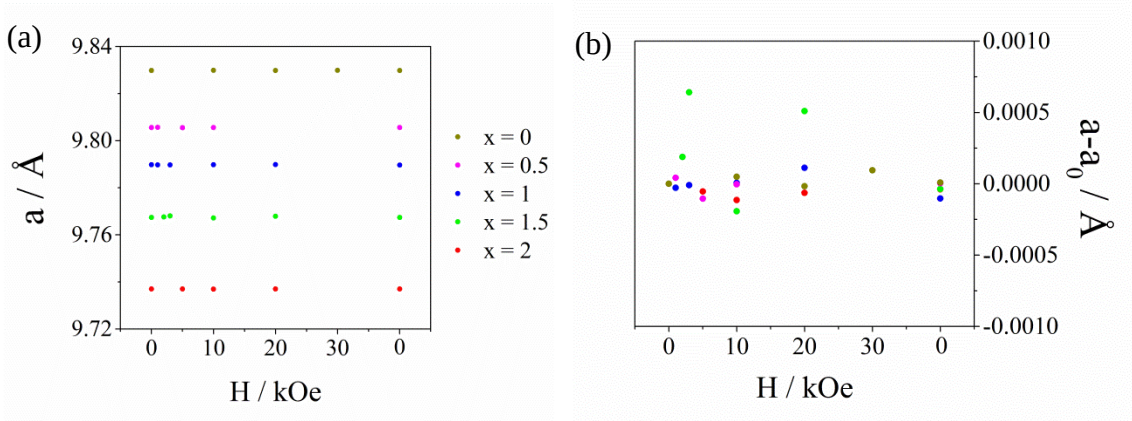

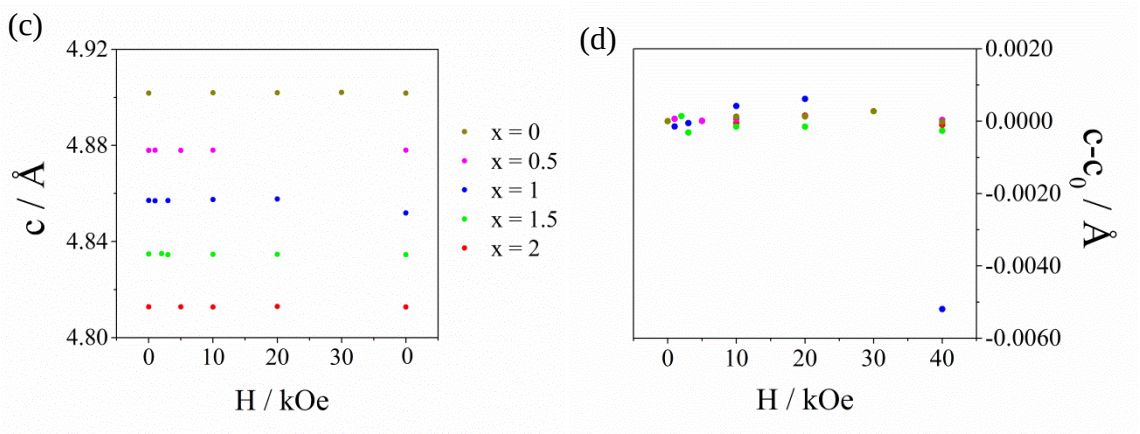

Figure 3.15 Dependence of the unit cell parameters (a) a, (b) a-a_0 (c) c and (d) c-c_0 (a_0 and c_0 are the unit cell parameters of each composition determined in zero-field) on compositions $CeMn_{2-x}Co_xGe_4O_{12}$ and applied magnetic field at 1.6 K. The field was increased to the maximum value and then returned to zero. The error bars are smaller than the size of the points.

During the analysis of the in-field, low-temperature neutron diffraction data, the unit cell parameters and the atomic coordinates were set free. The result shows that the influence of the magnetic field on these parameters is negligible, see Figure 3.15. The in-field low temperature neutron diffraction data gave almost the same results as those in zero-field. One exception, $CeMnCoGe_4O_{12}$, was seen when the magnetic field was turned back to zero again. We do not have a satisfactory explanation for this abnormal but it may come from the experimental error from the equipment. Relevant fitted patterns and refinements profiles are shown in Appendix C Figure C.1 - Figure C.27 and Table C.1 - Table C.5. Some selected bond lengths and bond angles are also listed.

The magnetic structure of $CeMn_2Ge_4O_{12}$ remains the same in a magnetic field. The difference comes in the intensity of each magnetic peak, see Figure 3.18, which leads to the change of the ordered moment value of Mn^{2+}. The ordered moments in different fields are listed in Table 3.8.

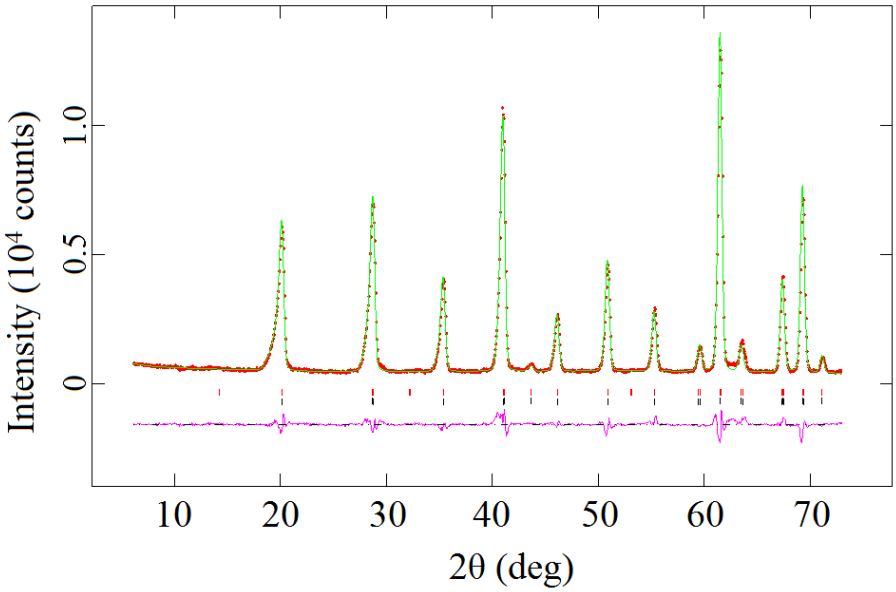

Figure 3.16 Low-angle region of observed (red dots) and calculated (green line) NPD patterns of $CeMn_2Ge_4O_{12}$ at 1.6 K, λ = 2.4395 Å, H = 0 Oe. A difference curve (purple line) is shown and reflection positions are marked.

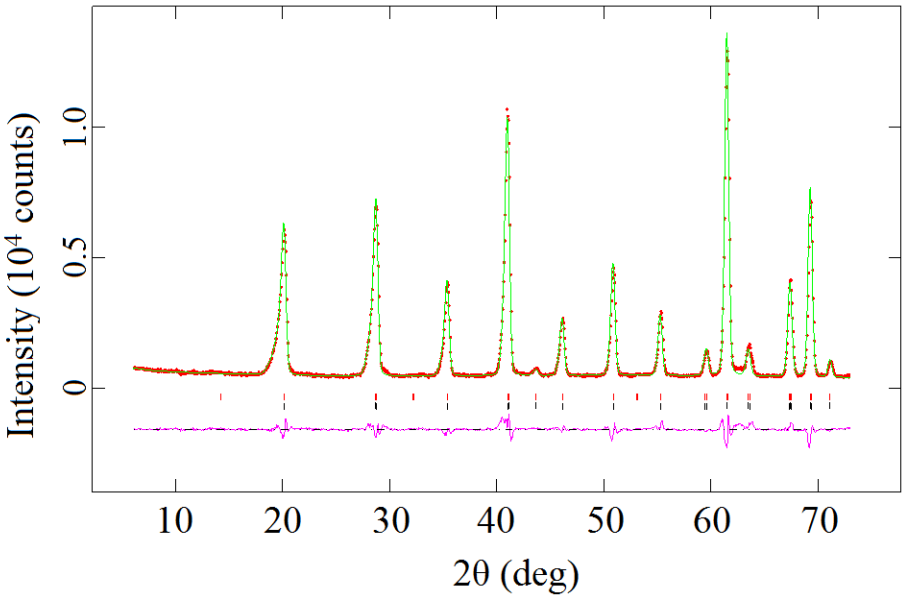

Figure 3.17 Low-angle region of observed (red dots) and calculated (green line) NPD patterns of $CeMn_2Ge_4O_{12}$ at 1.6 K, λ = 2.4395 Å, H =30 kOe. A difference curve (purple line) is shown and reflection positions are marked.

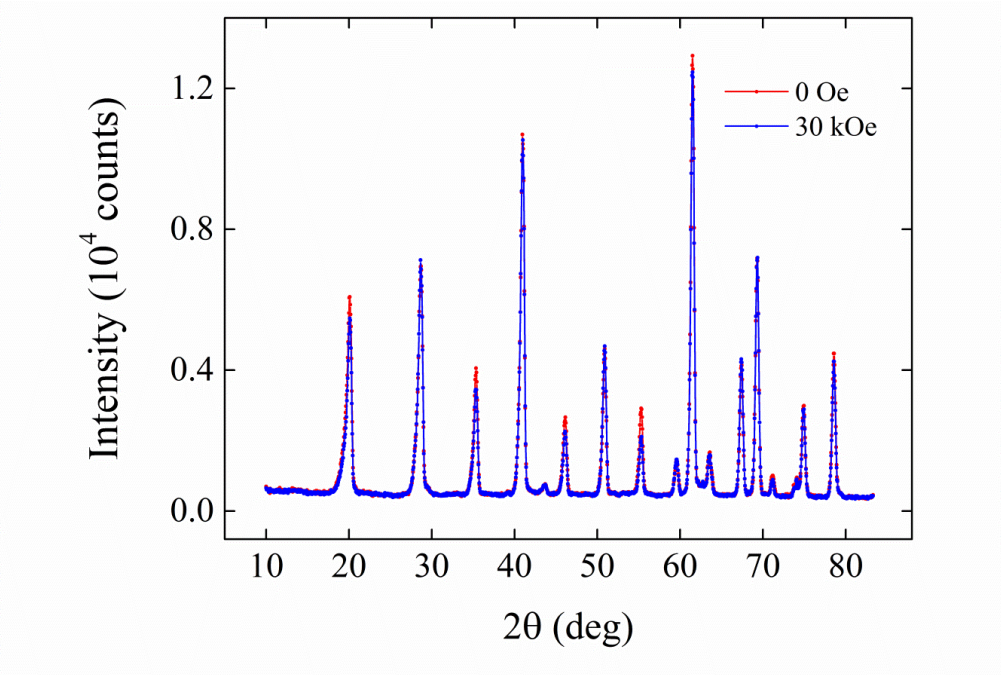

Figure 3.18 Low-angle region of the neutron diffraction pattern of $CeMn_2Ge_4O_{12}$ in applied fields of 0 (blue) and 30 (red) kOe at 1.6 K, λ = 2.4395 Å.

Table 3.8 Mean ordered atomic moments (μ_B) of Mn^{2+} site in $CeMn_2Ge_4O_{12}$ as a function of applied magnetic field at 1.6 K

H/ kOe	0	10	20	30	0
M_z	4.61(2)	4.56(2)	4.34(2)	4.18(2)	4.61(2)

The magnetic structure of $CeMn_{1.5}Co_{0.5}Ge_4O_{12}$ and $CeMnCoGe_4O_{12}$ also remain the same in a magnetic field. The difference again comes in the intensity of the magnetic peaks. The ordered moments in different fields are listed in Table 3.9 and Table 3.10. However, we saw a reduction of intensity on the 310 reflection in field. When the field was turned back to zero, the intensity of this peak did not come back. Only if the temperature was heated to 15 K, above the transition temperature, and cooled back to 1.6 K, the peak reversed. This phenomenon may come from the domain arrangements in the compound. However, no further analysis was conducted.

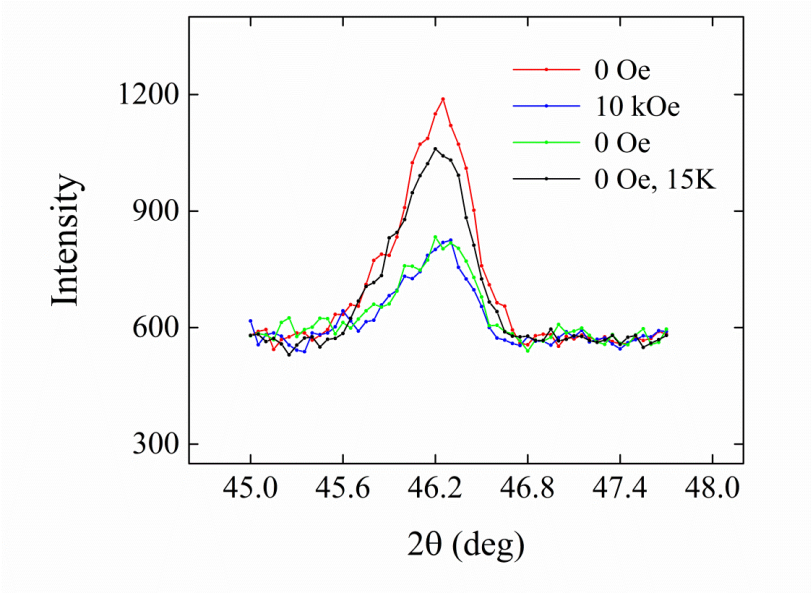

Figure 3.19 The 310 reflection before (red), during (blue) and after (green) the application of a 10 kOe field for $CeMn_{1.5}Co_{0.5}Ge_4O_{12}$ at 1.6 K, λ = 2.4395 Å. The black curve was recorded after heating the sample to 15 K and re-cooling to 1.6 K.

Table 3.9 Mean ordered atomic moments (μ_B) of Mn^{2+} site in $CeMn_{1.5}Co_{0.5}Ge_4O_{12}$ as a function of applied magnetic field at 1.6 K

H/ kOe	0	1	5	10	0
M_z	3.92(2)	3.90(2)	3.87(2)	3.84(2)	3.80(2)

Table 3.10 Mean ordered atomic moments (μ_B) of Mn^{2+} site in $CeMnCoGe_4O_{12}$ as a function of applied magnetic field at 1.6 K

H/ kOe	0	1	3	10	20	0
M_z	3.13(4)	3.15(4)	3.12(4)	3.30(4)	3.22(4)	3.18(3)

$CeMn_{0.5}Co_{1.5}Ge_4O_{12}$ behaves in a similar way to $CeCo_2Ge_4O_{12}$. As discussed before, in zero field, the magnetic unit cell doubles along [001]. The magnetic field can remove such doubling and leads to the magnetic unit cell the same size as the structural unit cell $c_{mag} = c$. The new magnetic structure is shown in Figure 3.20. However, the arrangement within the (001) sheets remains the same. Hence, the coupling between NN (001) layers is now ferromagnetic. The compound then behaves as a weak ferromagnet. The alternation of the magnetic structure in field is the origin of the metamagnetism. From intermediate magnetic field NPD data, the co-existence of the two magnetic structure phases proves it is a first-order metamagnetic transition. The refinement of intermediate magnetic field NPD data

was performed using the magnetic structure and the constrained moments from the zero-field data and the highest field data (20 kOe). The proportion of the two phases for intermediate magnetic field data is listed in Table 3.13.

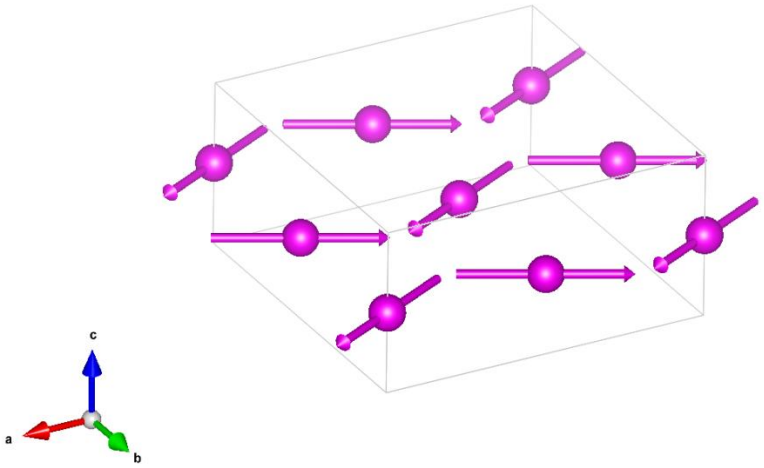

Figure 3.20 Magnetic structures in high magnetic field of $CeMn_{2-x}Co_xGe_4O_{12}$ with x = 1.5 and 2.0. Diamagnetic ions are omitted.

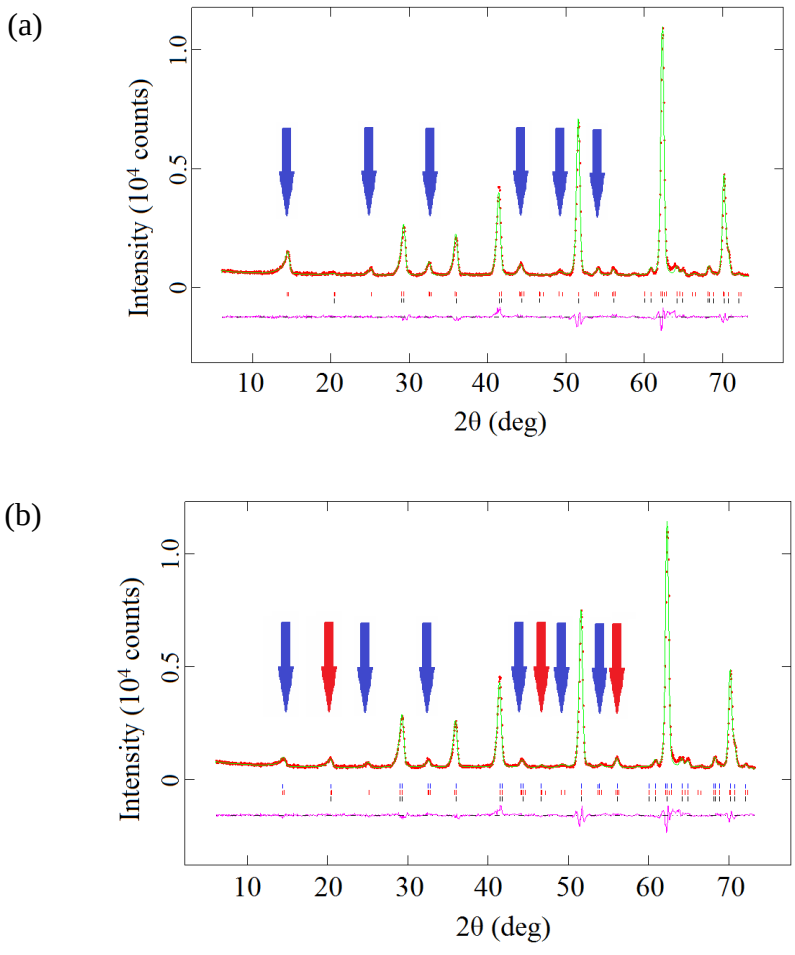

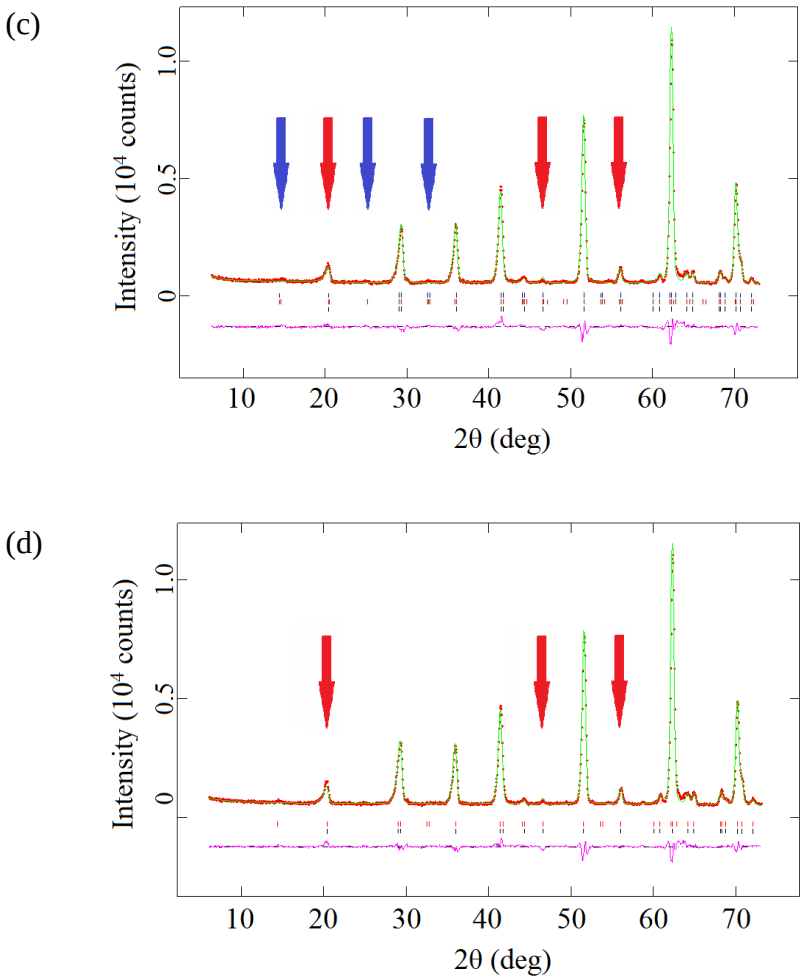

Figure 3.21 Low-angle region of observed (red dots) and calculated (green line) NPD patterns of $CeCo_2Ge_4O_{12}$ at 1.6 K, λ = 2.4395 Å with (a) H = 0 Oe, (b) H = 5 kOe, (c) H = 10 kOe and (d) H = 20 kOe. A difference curve (purple line) is shown and reflection positions are marked. The blue arrows point out the magnetic peaks of the magnetic structure that the magnetic unit cell doubles in size along [001], see Figure 3.14(c), and the red arrows point out the magnetic peaks of the magnetic structure that the magnetic unit cell does not have the doubling, see Figure 3.20.

Table 3.11 Mean ordered average atomic moments (μ_B) of the *4f* site in $CeMn_{0.5}Co_{1.5}Ge_4O_{12}$ as a function of applied magnetic field at 1.6 K

H/ kOe	0	10	20	0
M_x	2.68(3)	2.66(4)	2.69(4)	2.60(3)
M_y†	0.91(6)	1.41(11)	1.53(11)	0.61(9)
M_T	2.83(3)	3.01(7)	3.10(7)	2.67(3)

† the ferromagnetic component

Table 3.12 Mean ordered atomic moments (μ_B) of Co^{2+} site in $CeCo_2Ge_4O_{12}$ as a function of applied magnetic field at 1.6 K

H/ kOe	0	20	0
M_x	2.29(2)	2.41(3)	2.28(2)
M_y†	1.19(3)	1.85(5)	1.20(3)
M_T	2.58(2)	3.06(4)	2.58(2)

† the ferromagnetic component

Table 3.13 Relative phase fractions of high-field and low-field phases present in $CeMn_{2-x}Co_xGe_4O_{12}$ (x = 1.5, 2.0) at intermediate fields

x	H/kOe	% high-field phase	% low-field-phase
1.5	2	19 (1)	81(1)
	3	22(2)	78(2)
2.0	5	32.8(9)	67.2(9)
	10	90.2(6)	9.8(6)

3.3.2.5 Specific Heat

Specific heat measurements were conducted to confirm the long-range magnetic transition of $CeCo_2Ge_4O_{12}$. A λ-shape peak was shown at 4.6 K in zero field, which corresponds to the Néel temperature. That the peak is broadened in a 2 T magnetic field suggesting that the long-range order is replaced by short-range correlations [11]. The crystal, electron, and nuclear contributions were derived from the fitting of zero-field heat capacity data over the temperature range $10 \leqslant T/K \leqslant 20$ using Equation 2.32 with a = 0.38(2) $J/K^2 \cdot mol$, b = 5.27(11) $mJ/K^4 \cdot mol$, c = - 3.15(19) $\mu J/K^6 \cdot mol$. The magnetic specific heat below 2 K was extrapolated by the relation $C_{mag} \propto T^3$ from the spin-wave model for an antiferromagnet [12]. The magnetic entropy derived from Equation 2.33 was 8.34(4) J/K·mol in zero-field and 8.16(4) J/K·mol in a 2 T field. The theoretical value for one Co^{2+} is Rln(2S+1) = 11.52 J/K·mol according to Equation 2.34, where R is the gas constant. $CeCo_2Ge_4O_{12}$ contains two Co^{2+} and the entropy should be 2Rln(2S+1) = 23.05 J/K·mol, which is much higher than the experimental value. The error may come from the limited data as the lattice/electron contribution is normally fitted by data over the temperature range $30 \leqslant$

T/K $\leqslant$ 300. Hence, the limited data lead to abnormal specific heat fitting parameters a, b, c. This error can explain the difference between the experimental value 8.34(4) J/K·mol and the theoretical value 11.52 J/K·mol. The calculated magnetic entropy is only half the theoretical value and it is seen previously by others [13], [14], [15]. About half of the magnetic entropy is released below the T_N in zero-field measurement, which indicates the presence of short-range magnetic correlations above the long-range ordering temperature. About 1/3 of the magnetic entropy is released below T_N in 2 T field measurement, which suggests that the short-range magnetic interactions are much stronger than the long-range ordering. The phenomenon is also observed in low-dimension magnets [15], [16].

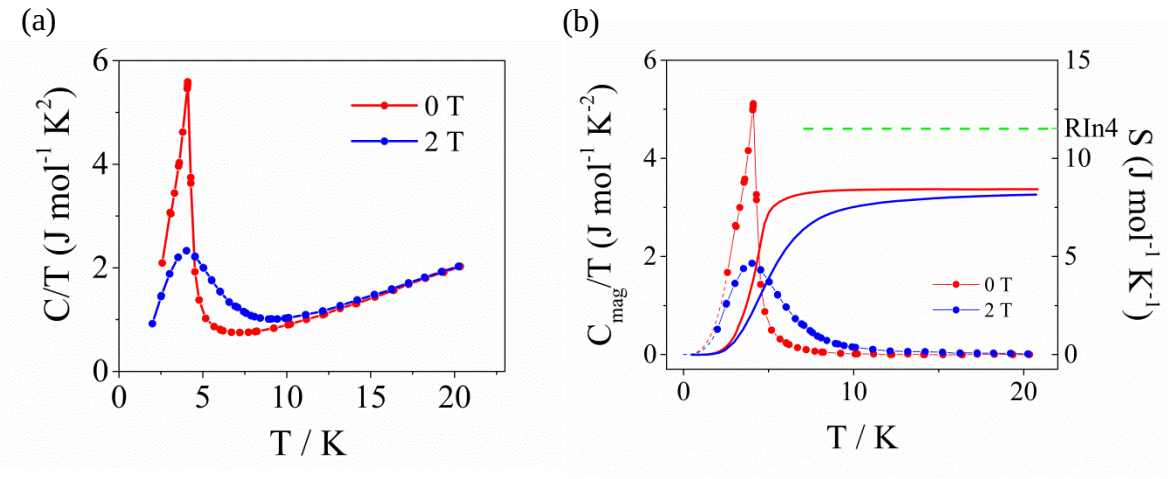

Figure 3.22 (a) Heat capacity and (b) magnetic specific heat and entropy calculation of $CeCo_2Ge_4O_{12}$ in zero field and 2 T magnetic field.

3.3.3 Discussion

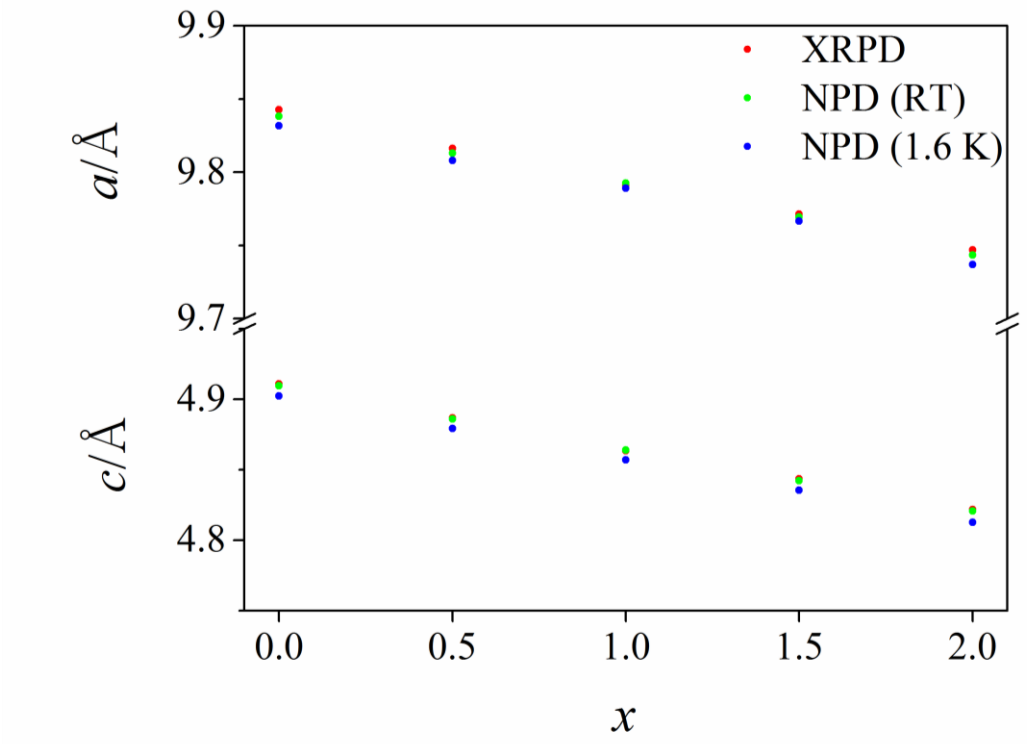

Figure 3.23 Structural unit cell parameters *a* and *c* derived from diffraction data. The error bars are smaller than the size of the points.

Due to the difference in cation size between Mn^{2+} (r = 0.83 Å) and Co^{2+} (r = 0.745 Å) [17], the unit cell parameter *a* and *c* in the Ce-based solid solutions decreases as the cobalt content increases from *x* = 0.0 to *x* = 2.0, *a* by 0.96 % and *c* by 1.81 % in a linear way; the ratio 2*c*/*a* consequently decreases from 0.9974 to 0.9886. The bond lengths of Ge – O1 and Ge – O2 are all about 1.786 and 1.727 Å in all the solid solutions and the bond angles do not change significantly. The longer Ge – O1 bonds provide the connectivity between the four [GeO_4] tetrahedra that make up a [Ge_4O_{12}] group whereas each O2 atom is bonded to only one germanium atom. As shown in Figure 3.2, the $[Ge_4O_{12}]^{8-}$ rings are linked by the [MO_6] octahedra and [CeO_8] antiprisms. The substitution of Mn^{2+} from Co^{2+} can change the size of these octahedra and thus change the ratio 2*c*/*a*. A ratio of cation radii at the two sites, $\langle r_{4f} \rangle / r_{2b}$, can be used to describe the relationship between the cation radius and the unit cell parameters, see Table 3.14. The unit cell parameters derived from XRPD and NPD collected at room temperature are in good agreement. No significant structural change was detected on cooling from room temperature to 1.6 K.

Table 3.14 Derived structural parameters for $CeMn_{2-x}Co_xGe_4O_{12}$ from low temperature NPD, $\lambda = 1.622$ Å

x	$\langle r_{4f}\rangle/r_{2b}$	$2c/a$	$d(M_{4f}-O2)/d(M_{4f}-O1)$	φ /°	ψ /°	q
0.0	0.856	0.9974	0.879(1)	78.36(12)	42.04(5)	0.856(1)
0.5	0.834	0.9950	0.876(1)	78.69(12)	41.60(6)	0.847(1)
1.0	0.812	0.9926	0.873(1)	78.32(22)	41.55(11)	0.838(2)
1.5	0.790	0.9902	0.874(1)	78.98(23)	41.04(12)	0.833(2)
2.0	0.768	0.9886	0.869(1)	79.18(13)	40.74(5)	0.831(1)

φ Angle between M_{4f} – O1 bond and M_{4f} – O2 plane

ψ Angle between the M_{4f} – O1 bond and the (001) plane

q Ratio of O2 – O2 distance in square face of antiprism to perpendicular distance between faces

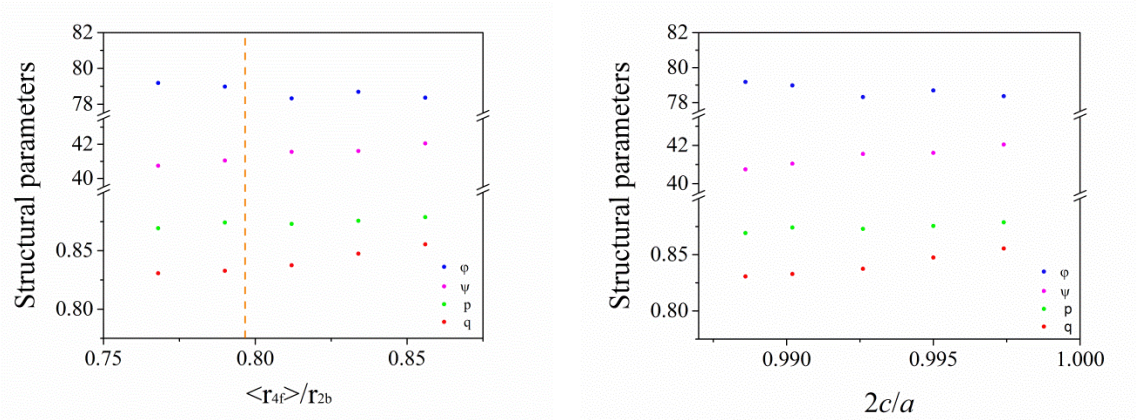

Figure 3.24 Structural parameters for $CeMn_{2-x}Co_xGe_4O_{12}$ derived from low temperature NPD. The error bars are smaller than the size of the points. φ is the angle between M_{4f} – O1 bond and M_{4f} – O2 plane; ψ is the angle between the M_{4f} – O1 bond and the (001) plane; p is the ratio of M_{4f} – O2 bond length to M_{4f} – O1 bond length; q is the ratio of O2 – O2 distance in square face of antiprism to perpendicular distance between faces.

As discussed above, the cation size leads to the change of the unit cell parameter. Hence, the [MO_6] octahedron is the key in changing the structure. The Mn^{2+} and Co^{2+} cations occupy the *4f* site with the point symmetry 2/*m* and therefore it is not a regular octahedron, see Figure 3.3. For each octahedron, there are two long *trans* bonds to O1 and four shorter coplanar bonds to O2. The plane made up by four O2 is not perpendicular to the axis formed by the long bonds. Moreover, the plane is not a square but a rectangle with O2 – O2 distances of 3.220 and 2.790 Å at 1.6 K in x = 0.0 and 3.114 and 2.699 Å at 1.6 K in x = 2.0. The mean bond lengths in the [MnO_6] and [CoO_6] octahedra of the compositions x = 0.0 and 2.0 are 2.234 and 2.168 Å at room temperature, respectively; the corresponding values in MnO and CoO [18] are 2.223 and 2.132 Å at room temperature. The ratio of the short bond length to the long bong length, defined as d(M_{4f} – O2)/d(M_{4f} – O1), is also listed in Table 3.14 and Figure 3.24. φ defines the angle between the M_{4f} – O1 bond and the M_{4f} – O2 plane; ψ defines the angle between the M_{4f} – O1 bond and the (001) plane. The d(M_{4f} – O2)/d(M_{4f} – O1) ratio shows a subtle decrease from x = 0.0 to x = 2.0 whereas the angle φ has an obvious increase and the angle ψ has an obvious decrease.

The Ce – O2 distances within the square antiprism of oxide ions that surround the 2*b* site in $CeMn_2Ge_4O_{12}$ and $CeCo_2Ge_4O_{12}$ are very similar to each other and also to the value of 2.343 Å determined for 8-coordinate Ce^{4+} in cubic CeO_2 [19]. We shall use the parameter q to describe the ratio of the O2 – O2 distance in the square face of the antiprism to the perpendicular distance between the faces, see Table 3.14. Due to the fact that the oxide ions in the [CeO_8] antiprisms are all O2, the [MO_6] octahedra share their coplanar short edges with neighbouring [CeO_8] antiprisms. Hence, the [MO_6] octahedral also influence the shape of [CeO_8] antiprisms. A decrease of q value is observed with increasing x, which leads to a compressed antiprism along the [001] axis.

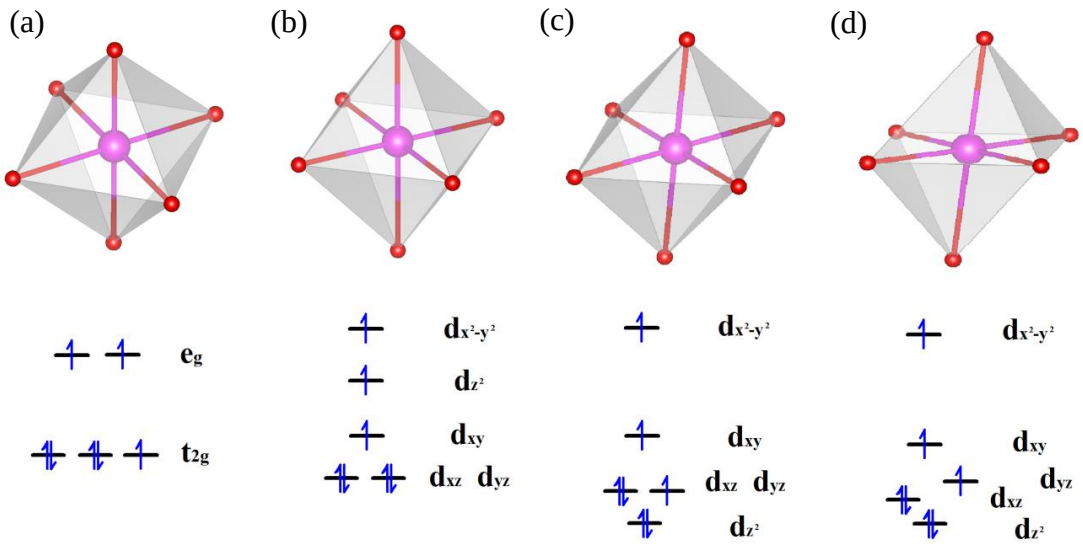

Figure 3.25 The crystal field splitting of the *d* orbitals for six-coordinate Co^{2+} in (a) a regular octahedron (b) an octahedron with a small tetragonal elongation (c) an octahedron with a large tetragonal elongation and (d) an octahedron with a monoclinic distortion in addition to a large tetragonal elongation.

The magnetic properties of $CeMn_{2-x}Co_xGe_4O_{12}$ clearly vary markedly with both composition and applied field. The negative Weiss temperatures listed in Table 3.6 indicate that antiferromagnetic interactions are dominant in every composition. The effective magnetic moment of Mn^{2+} is in good agreement with the spin-only value of 5.92 μ_B. The derived moment value of Co^{2+}, 5.36 μ_B, is larger than the spin-only value but lower than the full orbital contribution value. This indicates the orbital quenching exists but there is still a considerable orbital contribution to the moment due to the effective moment of Co^{2+} is normally in the range 4.3 – 5.2 μ_B [20]. The relatively low 2/*m* point symmetry of the *4f* site provides a large distortion of the [MO_6] octahedron. The large octahedral distortion can strongly affect the crystal field splitting of the d-orbitals, see Figure 3.25.

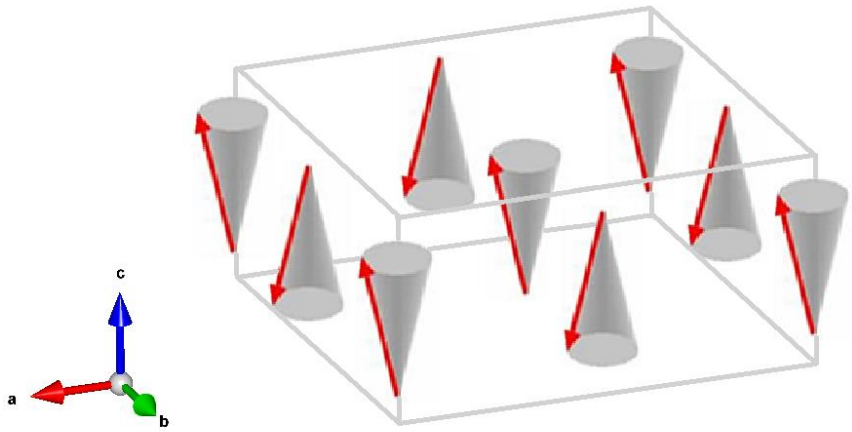

Figure 3.26 A possible magnetic structure of $CeMn_2Ge_4O_{12}$.

The dc susceptibility of $CeMn_2Ge_4O_{12}$ suggests that the compound is antiferromagnetic. However, the ZFC/FC hysteresis in the dc susceptibility and the non-linear M(H) curve showing a weak hysteresis when $10 < H/kOe < 25$ proves $CeMn_2Ge_4O_{12}$ is not a classic antiferromagnet, see Figure 3.9. The magnetic structure determined by neutron diffraction in zero field is antiferromagnetic with an ordered moment of 4.61(2) μ_B per Mn^{2+} cation. This value is the same as that in MnO [2], [21]; the reduction from the saturation value $gS = 5$ μ_B is attributable to the covalency in the Mn – O bonds. The magnitude of the ordered moment decreases when a field is applied. The ac susceptibility of $CeMn_2Ge_4O_{12}$ shows an anomaly below the Néel temperature: a plateau in real part and a small peak in imaginary part at 6 K in the absence of an applied field. Moreover, this imaginary part peak is slightly frequency dependent. When a dc field was applied, the real part plateau remains but appears at a lower temperature, 5 K, but the peak in the imaginary part disappears. When a strong dc field was applied, 20 kOe, the real part of the ac susceptibility shows an apparently paramagnetic component below the Néel temperature. All the facts suggest that this composition has a disordered component. To simplify, we constrain the disordered spin components lying in the *ab* plane, which is perpendicular to the [001] axis. A possible magnetic structure of $CeMn_2Ge_4O_{12}$ is shown in Figure 3.26. When a dc field is applied, the disordered components in (001) planes will align to the direction of the external field, creating a hysteresis in the ZFC/FC data. When the dc field is larger, the decrease of the ordered moment and the paramagnetic component in high dc field ac measurement perhaps indicates that part of the ordered moment goes into (001) planes and becomes disordered. Combining the M(H) curve, the disordered moments would still interact antiferromagnetically and such antiferromagnetic interaction perhaps changes in a 10 kOe

magnetic field into ferromagnetic interaction. Hence, a weak hysteresis appears and the gradient of the M(H) curve in the range H/kOe > 25 is larger than that in 0 < H/kOe < 10. We don't have a satisfactory explanation to the abnormal behaviour. A hypothesis to the second peak below T_N is that it may correspond to the freezing temperature of the disordered components in zero field. An antiferromagnetic compound, MnF_2 with the Néel temperature T_N = 67 K [22], [23], [24], [25], has its disordered moment described as a spin wave with a freezing point 4.2 K. A spin-flop was observed in a magnetic field, which is similar to our hypothesis that the disordered moments in $CeMn_2Ge_4O_{12}$ change from an antiferromagnetic order to a ferromagnetic order in a 10 kOe magnetic field. Further experiments would be needed to test the hypothesis.

The replacement of Mn^{2+} cations by Co^{2+} moves the ordered magnetic moments from the [001] axis into the (001) plane because Mn^{2+} is an isotropic cation whereas Co^{2+} is anisotropic. The rotation of the spin axis between the [001] axis and the *ab* plane as a function of composition is not surprising in view of different anisotropies between Co^{2+} and Mn^{2+}. A similar change was observed between $Sr_2MnGe_2O_7$ and $Sr_2CoGe_2O_7$ [26]. $CeMn_{1.5}Co_{0.5}Ge_4O_{12}$ and $CeMnCoGe_4O_{12}$ have the same magnetic structure as $CeMn_2Ge_4O_{12}$ with ordered magnetic moments lie in (001) plane. $\chi(T)_{dc,}$ $\chi(T)_{ac}$ and M(H) are all consistent with the formation of a weakly ferromagnetic phase. As the remanent magnetisations measured by magnetometry of the two compounds are too small to be detected from neutron diffraction, see Figure 3.6, we can only determine the net ordered moment. The ordered moments for the two compounds are 3.92 and 3.13 μ_B and the identified remanent magnetisations are 0.38 and 0.67 μ_B per formula unit respectively. The facts suggest that the weakly ferromagnetic phase may come from a canted antiferromagnet at low temperatures and the weak ferromagnetic component is too weak to be detected by neutron diffraction. Interestingly, a large hysteresis in ZFC/FC was detected in both compounds. The ZFC curve decreases at low temperatures, which indicates antiferromagnetic interaction exists. This phenomenon is similar to $CeMn_2Ge_4O_{12}$ but no second glassy phase was detected in the ac measurements. The decrease of the 310 peak for the two compounds in in-field neutron diffraction refinements may correspond to their preferred orientation by the weakly ferromagnetic phase domains. Also, due to the high crystal symmetry and the random distribution of the powder sample, we are not able to do any further analysis.

The behaviour of $CeMn_{0.5}Co_{1.5}Ge_4O_{12}$ and $CeCo_2Ge_4O_{12}$ are very different to that of the compositions described above. The ac susceptibilities of both compounds show they are antiferromagnetic in zero field, proved by the dc susceptibilities measured in a 100 Oe magnetic field. However, the M(H) curves indicate that the application of a high magnetic field can disrupt this state and $\chi(T)_{dc}$ measured in higher fields, see Figure 3.10, shows that fields greater than 3 kOe are able to change their ground state. The neutron data reveal the details of the change. The two compounds are indeed antiferromagnets in zero field at 1.6 K. The magnetic structure for the two compounds can be described as an antiferromagnetic packing of weakly ferromagnetic NN sheets perpendicular to [001], with $c_{mag} = 2c$, doubling the periodicity of the crystal unit cell and cancelling the weak ferromagnetism. When a magnetic field is applied, the doubling is lost and the structure transforms to that of the weak ferromagnet shown in Figure 3.20. $CeCo_2Ge_4O_{12}$ has an ordered magnetic moment of 2.58(2) μ_B for Co^{2+} in zero field. The theoretical value is $gS = 3$ for a d^7 configuration cation. In the case of CoO, which has an effective magnetic moment of 5.1 μ_B in the paramagnetic phase [27], ordered moments in the range 3.35 – 3.8 μ_B have been determined by neutron diffraction [2], [28], [29]. Hence, the data suggest that the Co^{2+} cations have a considerable orbital contribution to their angular momentum in the high-temperature, paramagnetic phase but that this component is absent from the low-temperature, magnetically-ordered phase, which has been seen previously in other compounds [26], [30], [31]. The existence of such a contribution at low temperatures will depend on the relative magnitudes of k_BT, the non-cubic component of the crystal-field splitting, the spin-orbit coupling constant and the Zeeman splitting caused by the internal molecular field [32], [33], [34]. We consider the crystal field effect from the strongly distorted octehedra to be significant. The distortion of the octahedra is not purely tetragonal, see Figure 3.25, as is demonstrated by the difference, 0.601 Å, between the O2 – O2' and O2 – O2" distances. This additional strain will remove the degeneracy of the d_{xz} and d_{yz} orbitals that is required to maintain the orbital contribution, see Figure 3.25(d). We must assume that in the paramagnetic phase the splitting of these two orbitals is relatively small compared to thermal energy and hence an orbital contribution is retained. However, below 4.2 K, the Néel temperature, the splitting is presumably large compared to the thermal energy and so the orbital angular momentum is diminished. A significant increase in the ordered moment is observed in an applied field, see Table 3.11 and Table 3.12. We cannot deduce the cause of this from the available experimental data, but we note that $\mu_BH/k_B \approx 2$ K for a field of 20 kOe, a temperature that is comparable to both T_N and the measuring

temperature. The large pseudo-tetragonal strain and the overall 2/*m* symmetry at the 4*f* site play a key role in determining the magnetic properties. The application of a magnetic field reverses the direction of all the atomic moments in alternate *ab* layers of $CeCo_2Ge_4O_{12}$ and converts an antiferromagnet into a weak ferromagnet. Similar metamagnetic transitions have been reported previously in compounds of both Co^{2+} [35] and Mn^{2+} [36].

In order to rationalise the magnetic structures adopted and the changes therein as a function of composition it is necessary to consider the superexchange pathways that operate within the crystal structure. The magnetic coupling between pairs of d^5 and d^7 cations is expected to be antiferromagnetic. Each cation within the layer at z = ½ has four nearest-neighbour (NN_i) cations in the layer at a distance $a/2$ and four next-nearest-neighbour (NNN_i) cations at a distance $\sqrt{2}a/2$; each cation has two NN_o cations along [001] axis at a distance c and eight NNN_o cations at a distance $\sqrt{a^4/4+c^2}$; the subscripts i and o will be used to distinguish neighbours within and out of a single layer, see Figure 3.27. Each cation is linked with another 18 cations with M – O – Ge – O – M super-superexchange pathway, which is similar to $Fe_2(SO_4)_3$, $Fe_2(PO_4)_3$ and $Fe_2(MoO_4)_3$ as discussed in Chapter 1. Each pair of NN_i cations are linked via two Mn/Co – O1 – Ge – O2 – Mn/Co superexchange pathways involving germanate groups lying both above and below the z = ½ layer. No Mn/Co – O – Ge – O – Mn/Co superexchange pathways couple NNN_i cations along <110>. They are linked instead via Mn/Co – O2 – Ce – O2 – Mn/Co pathways which are both longer and less covalent than those involving germanium. The NN_i superexchange is therefore expected to be stronger than that between NNN_i and so the resulting in-plane ordering preferentially leaves each Mn/Co cation coupled antiferromagnetically to four NN_i cations and consequently aligned ferromagnetically with four NNN_i cations. The interlayer coupling is less easy to predict because both NN_o and NNN_o cations are linked by Mn/Co – O – Ge – O – Mn/Co pathways. Each cation is coupled to both the NN_o cation above it and that below it along [001] by four Mn/Co – O1 – Ge – O2 – Mn/Co superexchange pathways. It is also linked along <101> to four NNN_o cations in the plane above and four in the plane below. Of these eight pathways, four are of the form Mn/Co – O1 – Ge – O1 – Mn/Co and the remainder are Mn/Co – O2 – Ge – O2 – Mn/Co pathways. The Mn/Co – O2 bonds are shorter than the Mn/Co – O1 bonds and the O2 – Ge – O2

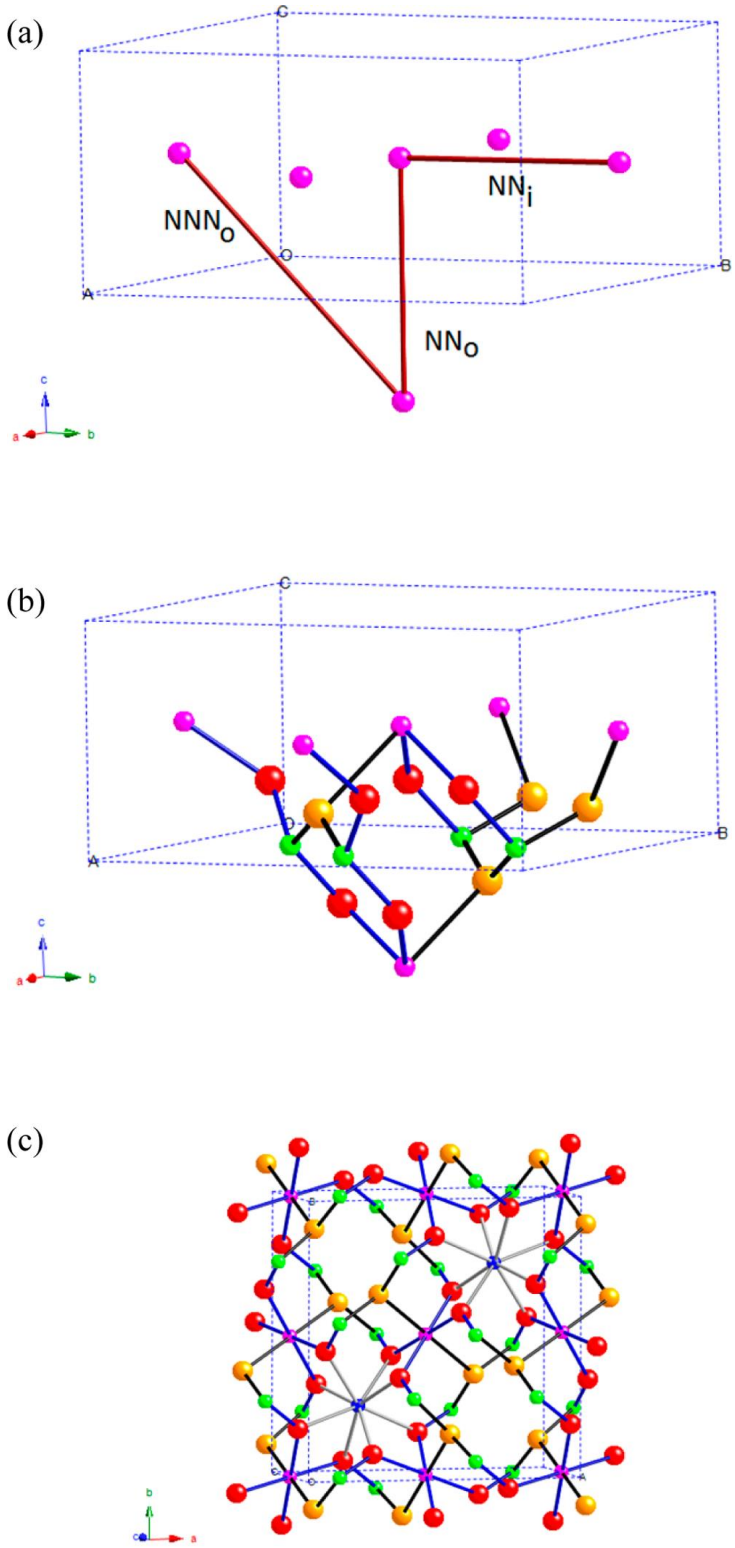

Figure 3.27 Structure of $CeMn_{2-x}Co_xGe_4O_{12}$ viewed to show (a) the principal superexchange interactions between magnetic cations and (b) an atomistic view of the principal superexchange pathways. Gold, red, green, and purple circles represent O1, O2, Ge, and Mn/Co, respectively. Bonds to O1 and O2 are black and blue, respectively. Two distinct NNN_o pathways can be seen. (c) The [001] view showing weak superexchange pathways involving Ce^{4+} cations (blue).

bond angle is more open than the O1 – Ge – O2 angle. It might therefore be expected that the Mn/Co – O2 – Ge – O2 – Mn/Co pathway between NNN_o provides the strongest antiferromagnetic superexchange interaction in the structure. The above discussion focuses on Mn/Co – O2 – Ge – O2 – Mn/Co pathways. Others have considered the interactions in comparable compounds in terms of simpler cation – O – O – cation pathways [37], [38], [39]. The O – O distances, *d*, in the GeO_4 tetrahedra of $CeMn_{2-x}Co_xGe_4O_{12}$ ($2.794 < d/Å < 3.012$ for $x = 2$) are too long for this interaction to dominate, and the involvement of the electron density in the bonds within the GeO_4 tetrahedra is likely to be crucial in establishing intercation coupling in this case.

The magnetic structure of $CeMn_2Ge_4O_{12}$ in the absence of an applied field is consistent with this account; each spin is aligned antiparallel to four NN_i spins in the same (001) sheet and antiparallel to eight <101> NNN_o spins in the sheets above and below. The alignment of the spins along [001] minimises dipolar repulsions within the structure. The magnetic structure of $CeMn_{2-x}Co_xGe_4O_{12}$; $x = 0.5$ and 1.0 retains the underlying pattern of spin ordering but the aligned spins now lie in the *ab* plane. The change in the preferred spin axis can be attributed to the asymmetric electronic ground state of Co^{2+} which introduces an in-plane anisotropy that is strong enough, even at a concentration of 25 %, to overcome the dipolar interactions. The spin-orbit coupling associated with the anisotropy is likely to be responsible for the weak ferromagnetism that could not be detected by neutron diffraction but which M(H) shows to be present. The antiferromagnetic spin structure adopted by $x = 1.5$ and 2.0 in zero applied field also has the spins confined to the *ab* planes but there is now antiferromagnetic alignment of NN_o along <001>, causing a doubling of the unit cell parameter *c*. The loss of purely antiferromagnetic NN_i coupling and the consequent development of weak ferromagnetism within the *ab* planes can be deduced from the neutron data collected on these compositions; each of these planes has a net magnetisation, the direction of which reverses between successive planes. The antiferromagnetic coupling between out-of-plane NNN_o cations, predicted on the basis of the bond lengths to be the strongest interaction, is also lost, although the alignment between third-nearest out-of- plane neighbours, separated by a vector $0.5\mathbf{a} + 0.5\mathbf{b} + \mathbf{c}$, changes from ferromagnetic to antiferromagnetic. We conclude that at high cobalt concentrations the energy of the system is minimised by the adoption of a structure different to that dictated by exchange energy alone. Moreover, <110> is the direction along which the long edges of the coplanar rectangle around the *4f* site octahedron align. The

angles between the moment of Co and the <110> direction are 28.07(1.03) ° and 19.50(50) ° for $CeMn_{0.5}Co_{1.5}Ge_4O_{12}$ and $CeCo_2Ge_4O_{12}$, respectively. This may come from the anisotropy of the Co^{2+} cation and thus not only superexchange but also Dzyaloshinsky-Moriya interaction need to be considered. The DM interaction can furthermore induce the weakly ferromagnetic interaction in the canted antiferromagnet.

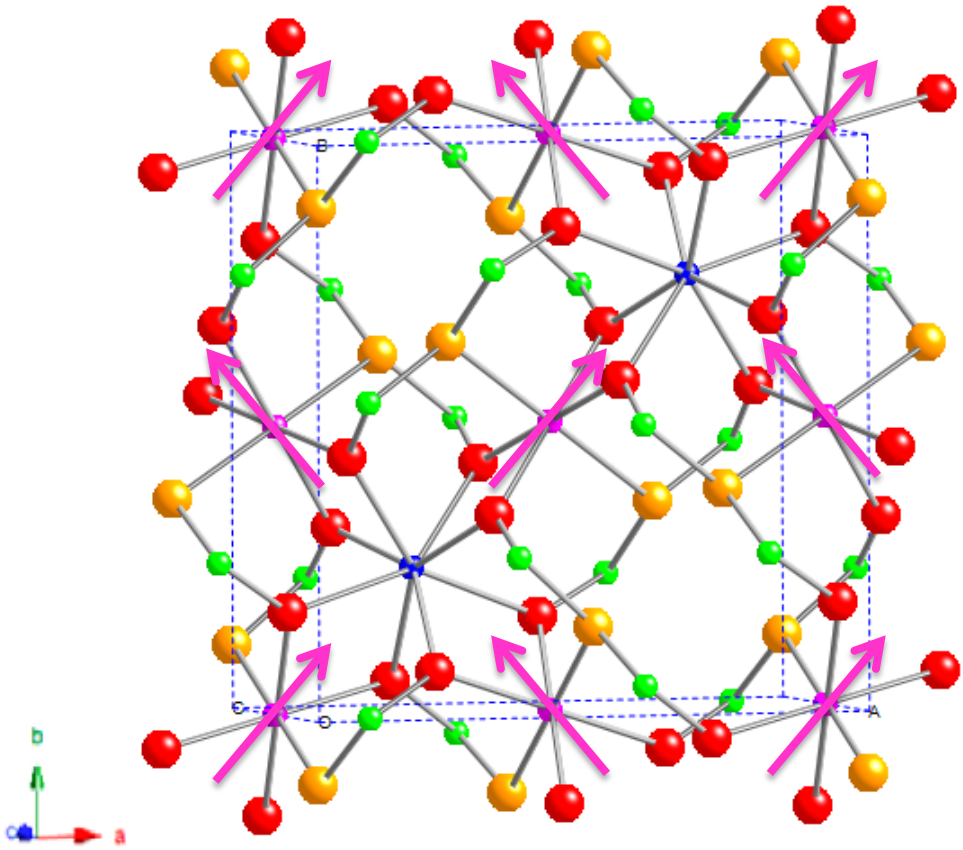

Figure 3.28 Crystal structure and magnetic moments of $CeCo_2Ge_4O_{12}$ in high field.

3.3.4 Conclusion

The solid solution $CeMn_{2-x}Co_xGe_4O_{12}$ can be prepared for $0 \leq x \leq 2$. All compositions in the solution order magnetically at low temperature, T < 8 K, but the properties of the low-temperature phase vary with the Mn^{2+}:Co^{2+} ratio. When x = 0.0, the ground state is antiferromagnetic with the atomic moments aligned along [001]. The replacement of 25 % Mn^{2+} by Co^{2+} is enough to rotate the spins into the (001) plane with the concomitant introduction of weak ferromagnetism. When the Co concentration is 75 % or greater the

magnetic unit cell doubles in size along [001] as weakly-ferromagnetic (001) sheets stack antiferromagnetically. The application of an external field induces a first-order phase change to a weakly-ferromagnetic structure with the smaller unit cell volume. The changes in magnetic behaviour are thought to stem from the different anisotropies associated with Mn^{2+} and Co^{2+}, although the low point symmetry of the magnetic site, 2/*m*, makes detailed interpretation difficult without spectroscopic data. Magnetometry data recorded in the paramagnetic region show that the Co^{2+} cations have a large orbital contribution to their effective magnetic moment but the atomic moment in the ordered phase is lower than the spin-only value.

The work described in this Chapter has been published as *Magnetic properties of $CeMn_{2-x}Co_xGe_4O_{12}$ as a function of composition, temperature and magnetic field*, D. Xu, M. Avdeev, P. D. Battle, and X. Liu, *Inorganic Chemistry*, 2017, **56**, 2750-2762.

3.4 References

[1] C. Taviot-Gueho, P. Leone, P. Palvadeau, and J. Rouxel, Synthesis and structural characterization of two new rare-earth maganese germanates: $CeMn_2Ge_4O_{12}$ and $GdMnGe_2O_7$, *Journal of Solid State Chemistry*, **1999**, *143*, 145-150.

[2] W. L. Roth, Magnetic Structures of MnO, FeO, CoO, and NiO, *Physical Review*, **1958**, *110*, 1333-1341.

[3] R. A. Tahir-Kheli, H. B. Callen, and H. Jarrett, Magnetic ordering in cubic crystals with first and second neighbor exchange, *Journal of Physics and Chemistry of Solids*, **1960**, *27*, 23-32.

[4] R. H. Swendsen, Antiferromagnetic order in cubic crystals, *Journal of Physics C: Solid State Physics*, **1973**, *6*, 3763-3773.

[5] H. M. Rietveld, A profile refinement method for nuclear and magnetic structures, *Journal of Applied Crystallography*, **1969**, *2*, 65-71.

[6] B. H. Toby, EXPGUI, a graphical user interface for GSAS, *Journal of Applied Crystallography*, **2001**, *34*, 210-213.

[7] A. C. Larson, and R. B. Von Dreele, *General Structure Analysis System (GSAS)*, Los Alamos National Laboratory Report LAUR 86-748: **2004**.

[8] B. van Laar, and W. B. Yelon, The peak in Neutron Powder Diffraction, *Journal of Applied Crystallography*, **1984**, *17*, 47-54.

[9] K. Momma, and F. Izumi, VESTA: a three-dimensional visualization system for electronic and structural analysis, *Journal of Applied Crystallography*, **2008**, *41*, 653-658.

[10] G. J. Redhammer, A. Senyshyn, G. Tippelt, C. Pietzonka, G. Roth, and G. Amthauer, Magnetic and nuclear structure and thermal expansion of orthorhombic and monoclinic polymorphs of $CoGeO_3$ pyroxene, *Physics and Chemistry of Minerals*, **2010**, *37*, 311-332.

[11] X. Ke, M. L. Dahlberg, E. Morosan, J. A. Fleitman, R. J. Cava, and P. Schiffer, Magnetothermodynamics of the Ising antiferromagnet $Dy_2Ge_2O_7$, *Physical Review B*, **2008**, *78*, 104411.

[12] S. J. Joshua, and A. P. Cracknell, The spin-wave contribution to the specific heat of NiF_2, *Physical Letters A*, **1969**, *28*, 562-563.

[13] D. C. Freitas, M. A. Continentino, R. B. Guimarães, J. C. Fernandes, J. Ellena, and L. Ghivelder, Structure and magnetism of homometallic ludwigites: $Co_3O_2BO_3$ versus $Fe_3O_2BO_3$, *Physical Review B*, **2008**, *77*, 184422.

[14] B. C. Melot, B. Paden, R. Seshadri, E. Suard, G. Nénert, A. Dixit, and G. Lawes, Magnetic structure and susceptibility of $CoSe_2O_5$: An antiferromagnetic chain compound, *Physical Review B*, **2010**, *82*, 014411.

[15] E. A. Zvereva, M. I. Stratan, A. V. Ushakov, V. B. Nalbandyan, I. L. Shukaev, A. V. Silhanek, M. Abdel-Hafiez, S. V. Streltsov, and A. N. Vasiliev, Orbitally induced hierarchy of exchange interactions in the zigzag antiferromagnetic state of honeycomb silver delafossite $Ag_3Co_2SbO_6$, *Dalton Trans*, **2016**, *45*, 7373-7384.

[16] M. Isobe, Y. Ueda, A. N. Vasiliev, T. N. Voloshok, and O. L. Ignatchik, Long-range and short-range magnetic order in $NaVGe_2O_6$, *Journal of Magnetism and Magnetic Materials*, **2003**, *258-259*, 125-127.

[17] R. D. Shannon, Revised effective ionic radii and systematic studies of interatomic distances in halides and chalcogenides, *Acta Crystallographica Section A: Crystal Physics, Diffraction Theoretical, and General Crystallography*, **1976**, *A32*, 751.

[18] S. Sasaki, K. Fujino, and Y. Takeuchi, X-ray determination of electron-density distributions in oxides, MgO, MnO, CoO, and NiO, *Proceedings of the Japan Academy, Ser. B, Physical and Biological Sciences*, **1979**, *55*, 43-48.

[19] E. A. Kummerle, and G. Heger, The Structures of C–$Ce_2O_{3+\delta}$, Ce_7O_{12}, and $Ce_{11}O_{20}$, *Journal of Solid State Chemistry*, **1999**, *147*, 485-500.

[20] D. I. Khomskii, *Transition Metal Compounds*, Cambridge University Press: **2014**.

[21] D. A. O. Hope, and A. K. Cheetham, A low-temperature powder neutron diffraction study of the antiferromagnetic phase of $Mn_xCo_{1-x}O$, *Journal of Solid State Chemistry*, **1988**, *72*, 42-51.

[22] I. S. Jacobs, Spin-Flopping in MnF_2 by High Magnetic Fields, *Journal of Applied Physics*, **1961**, *32*, S61.

[23] G. G. Low, A. Okazaki, R. W. H. Stevenson, and K. C. Turberfield, A Measurement of Spin-Wave Dispersion in MnF_2 at 4.2°K, *Journal of Applied Physics*, **1964**, *35*, 998.

[24] A. R. King, and H. Rohrer, Spin-flop bicritical point in MnF_2, *Physical Review B*, **1979**, *19*, 5864-5876.

[25] G. P. Felcher, and R. Kleb, Antiferromagnetic domains and the spin-flop transition of MnF_2, *Europhysics Letters*, **1996**, *36*, 455-460.

[26] T. Endo, Y. Doi, Y. Hinatsu, and K. Ohoyama, Magnetic and neutron diffraction study on melilite-type oxides $Sr_2MGe_2O_7$ (M = Mn, Co), *Inorganic Chemistry*, **2012**, *51*, 3572-3578.

[27] N. Elliott, Magnetic Behavior of the System CoO–MgO at Elevated Temperatures, *The Journal of Chemical Physics*, **1954**, *22*, 1924-1925.

[28] B. van Laar, Multi-Spin-Axis Structure for CoO, *Physical Review*, **1965**, *138*, A584-A587.

[29] D. C. Khan, and R. A. Erickson, Magnetic Form Factor of Co^{++} Ion in Cobaltous Oxide, *Physical Review B*, **1970**, *1*, 2243-2249.

[30] M. C. Viola, M. J. Martínez-Lope, J. A. Alonso, J. L. Martínez, J. M. De Paoli, S. Pagola, J. C. Pedregosa, M. T. Fernández-Díaz, and R. E. Carbonio, Structure and Magnetic Properties of Sr_2CoWO_6: An Ordered Double Perovskite Containing Co^{2+}(HS) with Unquenched Orbital Magnetic Moment, *Chemistry of Materials*, **2003**, *15*, 1655-1663.

[31] H. B. Yahia, M. Shikano, M. Tabuchi, H. Kobayashi, M. Avdeev, T. T. Tan, S. Liu, and C. D. Ling, Synthesis and Characterization of the Crystal and Magnetic Structures and Properties of the Hydroxyfluorides Fe(OH)F and Co(OH)F, *Inorganic Chemistry*, **2014**, *53*, 365-374.

[32] M. Lenertz, J. Alaria, D. Stoeffler, S. Colis, and A. Dinia, Magnetic Properties of Low-Dimensional r and γ CoV_2O_6, *Journal of Physical Chemistry C*, **2011**, *115*, 17190-17196.

[33] S. A. J. Kimber, H. Mutka, T. Chatterji, T. Hofmann, P. F. Henry, H. N. Bordallo, D. N. Argyriou, and J. P. Attfield, Metamagnetism and soliton excitations in the modulated ferromagnetic Ising chain CoV_2O_6, *Physical Review B*, **2011**, *84*, 104425.

[34] F. Wallington, A. M. Arevalo-Lopez, J. W. Taylor, J. R. Stewart, V. Garcia-Sakai, J. P. Attfield, and C. Stock, Spin-orbit transitions in α- and γ−CoV_2O_6, *Physical Review B*, **2015**, *92*, 125116.

[35] R. David, H. Kabbour, S. Colis, and O. Mentré, Slow Spin Dynamics between Ferromagnetic Chains in a Pure-Inorganic Framework, *Inorganic Chemistry*, **2013**, *52*, 13742-13750.

[36] D. Wang, Y. Guo, K. Liang, and K. Tao, Crystal structure of zirconia by Rietveld refinement, *Science China Section A*, **1999**, *42*, 80-86.

[37] M. H. Whangbo, H. J. Koo, J. Dumas, and M. A. Continentino, Theoretical Investigation of the Spin Exchange Interactions and Magnetic Properties of the Homometallic Ludwigite $Fe_3O_2BO_3$, *Inorganic Chemistry*, **2002**, *41*, 2193-2201.

[38] M. H. Whangbo, D. Dai, and H. J. Koo, Spin dimer and classical spin analyses of the ordered magnetic structures of alkali iron pyrophosphates $NaFeP_2O_7$ and $LiFeP_2O_7$, *Dalton Transactions*, **2004**, *2004*, 3019-3025.

[39] D. Dai, M. H. Whangbo, H. J. Koo, X. Rocquefelte, S. Jobic, and A. Villesuzanne, Analysis of the Spin Exchange Interactions and the Ordered Magnetic Structures of Lithium Transition Metal Phosphates $LiMPO_4$ (M= Mn, Fe, Co, Ni) with the Olivine Structure, *Inorganic Chemistry*, **2005**, *44*, 2407-2413.

Chapter 4 - Synthesis and Characterisation of $ZrMn_{2-x}Co_xGe_4O_{12}$ ($0 \leqslant x \leqslant 2$)

4.1 Introduction

The magnetic properties of any compound clearly depend on the nature of the magnetic cation present and we showed in Chapter 3 that $CeMn_2Ge_4O_{12}$ and $CeCo_2Ge_4O_{12}$ behave very differently at low temperatures. However, the properties of inorganic magnets are also sensitive to the nature of the non-magnetic cations present, for example ferromagnetic $SrFeO_3$ and antiferromagnetic $CaFeO_3$ [1]. The factors that are important appear to include the ionic radius and the electron configuration, which together influence the acidity and polarizability. In this chapter, by way of comparison with the cerium-containing compositions discussed in Chapter 3, we report a study of the solid solution $ZrMn_{2-x}Co_xGe_4O_{12}$.

4.2 Experimental

Polycrystalline samples of $ZrMn_{2-x}Co_xGe_4O_{12}$ (x = 0.0, 0.5, 1.0, 1.5, 2.0) were synthesised in solid-state reactions. Stoichiometric quantities of ZrO_2, Co_3O_4, $MnCO_3$, and GeO_2 were mixed thoroughly in an agate mortar, along with a 10% excess of GeO_2 to counteract its loss at high temperature. The mixtures were heated at 1100 °C for 2 days with intermediate cooling and regrinding every day. They were then pressed into a pellet and annealed at 1125 °C for another 14 days with intermediate cooling and regrinding every two days.

X-ray powder diffraction patterns were recorded at room temperature using Cu $K\alpha_1$ radiation. Neutron powder diffraction patterns were collected using a wavelength of either 1.622 Å or 2.4395 Å. The measurements were performed at room temperature and low temperatures. The measurements were also conducted in zero field and magnetic field (0 – 30 kOe). The data were analysed by the Rietveld method [2], [3] using the program GSAS [4], [5] and the peak function developed by van Laar and Yelon [6]. The magnetic structure was drawn using VESTA [7].

Magnetic measurements were performed using Quantum Design MPMS XL SQUID magnetometers. DC susceptibility measurements were made over the temperature range $2\ K \leq T \leq 300\ K$ in an applied field of 100 Oe with both zero-field cooling (ZFC) and field-cooling (FC) of the samples. The temperature and field dependence of the DC molar magnetic susceptibility of $ZrMn_2Ge_4O_{12}$ was determined over the temperature range $2\ K \leq T \leq 300\ K$ in applied fields of 0.01, 1 and 10 kOe following both ZFC and FC. The field dependence of the magnetization was measured at 2 K over the field range $-50\ kOe \leq H \leq 50\ kOe$ with the samples initially cooled in a magnetic field of 50 kOe. The AC susceptibility was measured at frequencies of 1, 10, 100 and 1000 Hz over the temperature range $2\ K \leq T \leq 10\ K$ in a 3.5 Oe AC driving field. Samples were ac-degaussed and then cooled in a small dc field of 3 Oe to counteract the remaining field in the SQUID. Further in-field AC measurements were made under the same conditions with applied dc fields of 0.01, 0.5, 20 kOe in the case of $ZrMn_2Ge_4O_{12}$ and 0.1, 1 kOe in the case of $ZrCo_2Ge_4O_{12}$ following cooling in the dc field.

Specific heat data were collected on the compound $ZrMn_2Ge_4O_{12}$ over the temperature range $2\ K \leq T \leq 30\ K$ in zero field.

Density Functional Theory (DFT) calculations were conducted by co-workers M. Sale and C. D. Ling on the compounds $ZrMn_2Ge_4O_{12}$ and $ZrCo_2Ge_4O_{12}$ using the Vienna *Ab-initio* Simulation Package (VASP, version 5.2.12) [8], [9], [10], [11], [12] in the generalized gradient approximation (GGA) of Perdew, Burke and Ernzerhof [13] with the projector augmented-wave (PAW) method [12], [14]. A Γ-centered 5x5x5 Monkhorst-Pack *k*-point mesh [15] with Gaussian smearing [16] was used in the calculations with a plane wave energy cut-off of 600 eV; tests were performed to verify that this combination of mesh size and cut-off energy resulted in a converged system. The GGA + onsite repulsion (GGA+*U*) method was used to correct the well-known over-binding of electrons in 3*d* metal atoms. [17] A 1x1x2 super-cell was initially used for the calculation of the spin exchange constants of these materials. This allowed us to consider magnetic structures other than that found by experiment. Ionic relaxation was performed starting with the experimental crystal and magnetic structures and *U*-values of 5.0 and 4.0 eV for $ZrMn_2Ge_4O_{12}$ and $ZrCo_2Ge_4O_{12}$, respectively. All unit cell parameters were allowed to vary and the relaxations were re-started several times to eliminate the effects of Pulay stress. [18] Even though no space-group symmetry was imposed on the degrees of freedom of the atomic positions, the final symmetry was the

same as the original space-group symmetry. The atomic positions of these relaxed structures were subsequently used to calculate magnetic energies using an isotropic Heisenberg model. The exchange constants and the Weiss temperature, θ, were subsequently derived from these energies, the latter using mean-field theory. Calculations performed to establish the sensitivity of the exchange constants to variations in U over the range $3 < U/\text{eV} < 6$ led to the conclusion that the chosen values, $U = 5$ and 4 eV, were appropriate values to use for $ZrMn_2Ge_4O_{12}$ and $ZrCo_2Ge_4O_{12}$. These values are similar to those used on other magnetic oxide materials with the same magnetic cations. [19], [20]

The superexchange interactions that need to be taken into account within this structure were described in our earlier account of $CeMn_{2-x}Co_xGe_4O_{12}$. For the purposes of our computational study, the corresponding exchange constants were labelled as follows: J_1; the interaction between nearest-neighbour (NN) cations along [001]; J_2, the interaction between NN cations within a (001) plane; J_3 and J_4, two similar but unequal interactions along <101> between cations in neighbouring planes; J_5 and J_6, two similar but unequal interactions between next-nearest-neighbour (NNN) cations in a (001) plane, see Figure 4.1. J_3 and J_4 differ in that the former pathway involves O1 and the latter involves O2; J_5 and J_6 in that the latter involves Zr whereas the former does not. Our initial calculations in a 1 x 1 x 2 supercell were unable to distinguish the individual interaction strengths within the pairs J_3, J_4. and J_5, J_6; only mean values could be calculated. However, it became apparent that the interactions along <101> represented by J_3 and J_4 were the strongest in the structure and further calculations in an enlarged supercell ($a_\mathbf{c} = 2a$, $b_\mathbf{c} = b$, $c_\mathbf{c} = a + 2c$) were therefore undertaken in order to separate their contributions. Given that our initial calculations showed that the NNN interactions represented by J_5 and J_6 were very weak, no further calculations were undertaken in order to resolve their individual contributions. The values of U derived using the 1 x 1 x 2 supercell were used in the calculations based on the enlarged supercell.

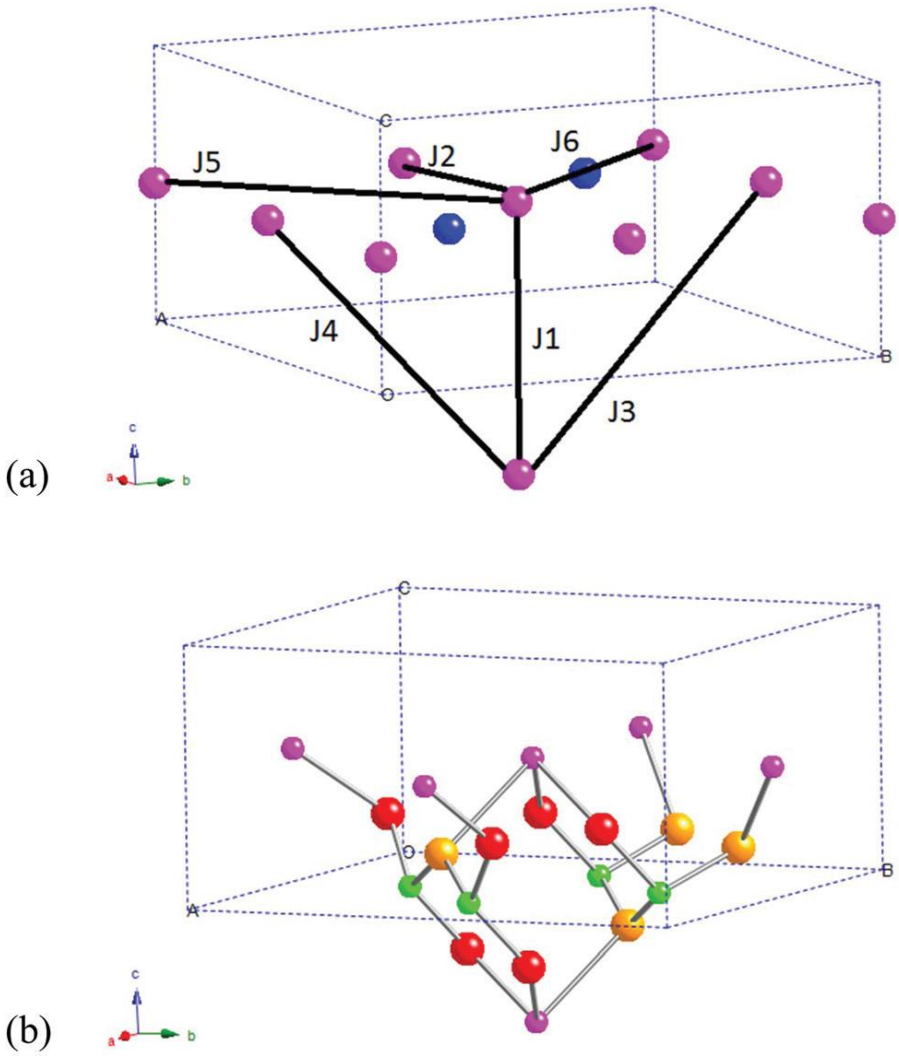

Figure 4.1 (a) Schematic representation of superexchange interactions in $ZrMn_{2-x}Co_xGe_4O_{12}$; (b) Atomistic view showing the difference between J3 and J4. Pink balls represent cobalt, purple balls represent zirconium, green balls represent germanium, gold and red circles represent O1 and O2, respectively

4.3 Results

4.3.1 Structural Chemistry

4.3.1.1 X-ray Diffraction

Single phases were obtained for x = 1.5, 2.0. $CoGeO_3$ was detected as an impurity in x = 0.0, 0.5, 1.0. $ZrMn_2Ge_4O_{12}$ was brown in colour whereas the other four compositions were pink. The crystal structure of the solid solutions is the same as that of $CeMn_{2-x}Co_xGe_4O_{12}$.

The fitted room temperature X-ray diffraction patterns of $ZrMn_{2-x}Co_xGe_4O_{12}$ are shown in Appendix A Figure A.5 – Figure A.9. Structural parameters derived from the refinements are listed in Table 4.1. The impurity levels of the orthorhombic phase $CoGeO_3$ [21] were determined to be 1.29(62) wt% and 5.21(89) wt% for $ZrMn_{0.5}Co_{1.5}Ge_4O_{12}$ and $ZrCo_2Ge_4O_{12}$ respectively from XRPD.

Table 4.1 Structural parameters of $ZrMn_{2-x}Co_xGe_4O_{12}$ at room temperature derived from X-ray diffraction data (λ = 1.5406 Å)

		x				
		0.0	0.5	1.0	1.5†	2.0‡
Ge	*x*	0.5169(1)	0.5172(1)	0.5172(1)	0.5174(1)	0.5172(3)
O1	*x*	-0.3709(2)	-0.3709(3)	-0.3705(4)	-0.3705(4)	-0.3670(10)
	z	0.1656(6)	0.1685(7)	0.1711(7)	0.1762(8)	0.1754(19)
O2	*x*	0.1674(3)	0.1651(3)	0.1651(3)	0.1634(4)	0.1612(10)
	y	0.0696(2)	0.0679(3)	0.0703(3)	0.0687(4)	0.0681(9)
	z	0.2622(4)	0.2622(4)	0.2613(5)	0.2615(6)	0.2614(14)
a/Å		9.6560(1)	9.6302(1)	9.6053(1)	9.5799(1)	9.5494(2)
c/Å		4.8636(1)	4.8436(1)	4.8244(1)	4.8047(1)	4.7838(2)
V/Å^3		453.47(1)	449.21(1)	445.10(1)	440.95(1)	436.24(2)
R_{wpr}		7.14%	5.41%	4.35%	3.36%	5.71%
χ^2		1.839	1.696	1.567	1.443	1.121

Space group *P*4/*nbm* (No. 125), Z = 2

Zr on 2*b* (¼, ¼, ½); Mn/Co on 4*f* (0, 0, ½);

Ge on 8*k* (*x*, ¼, 0); O1 on 8*m* (*x*, -*x*, *z*); O2 on 16*n* (*x*, *y*, *z*)

† Contains 1.29(62) wt % $CoGeO_3$

‡ Contains 5.21(89) wt % $CoGeO_3$

The U_{iso} parameter of each atom was constrained to that reported by Taviot-Gueho. [1]

4.3.1.2 Room Temperature and Low Temperature Neutron Diffraction

Neutron-diffraction data were collected on $ZrMn_{2-x}Co_xGe_4O_{12}$ (x = 0.0, 2.0) at room temperature using wavelength λ = 1.622 Å. The fitted room temperature neutron diffraction pattern of $ZrMn_{2-x}Co_xGe_4O_{12}$ (x = 0.0, 2.0) are shown in Figure 4.2 and Appendix B Figure B.14. Structural parameters derived from the refinements were listed in Table 4.2. Some selected bond lengths and bond angles derived from room temperature neutron diffraction are listed in Table 4.3.

Neutron diffraction data were also collected on the three samples at low temperature but slightly above the magnetic transition temperature (approximately 10 K) using wavelength λ = 1.622 and/or 2.4365 Å. These NPD data were collected to determine the impurities. The impurity levels of the orthorhombic phase $CoGeO_3$ were determined to be 0.7(1) wt % and 4.4(2) wt% for $ZrMnCoGe_4O_{12}$ and $ZrCo_2Ge_4O_{12}$ respectively. The impurity amounts were fixed in all relevant neutron data refinements.

Neutron-diffraction data were collected on $ZrMn_{2-x}Co_xGe_4O_{12}$ (x = 0.0, 1.0) at 3 K and on $ZrCo_2Ge_4O_{12}$ at 1.6 K using wavelength λ = 1.622 and 2.4395 Å. Structural parameters were derived from the λ = 1.622 Å NPD data. The fitted patterns of λ = 1.622 Å NPD data are shown in Figure 4.3 and Appendix B Figure B.15 – Figure B.16. Structural parameters derived from the refinements are listed in Table 4.2. Some selected bond lengths and bond angles derived from low temperature neutron diffraction are listed in Table 4.3.

The magnetic structures derived from λ = 2.4395 Å NPD will be discussed in section 4.3.2.3.

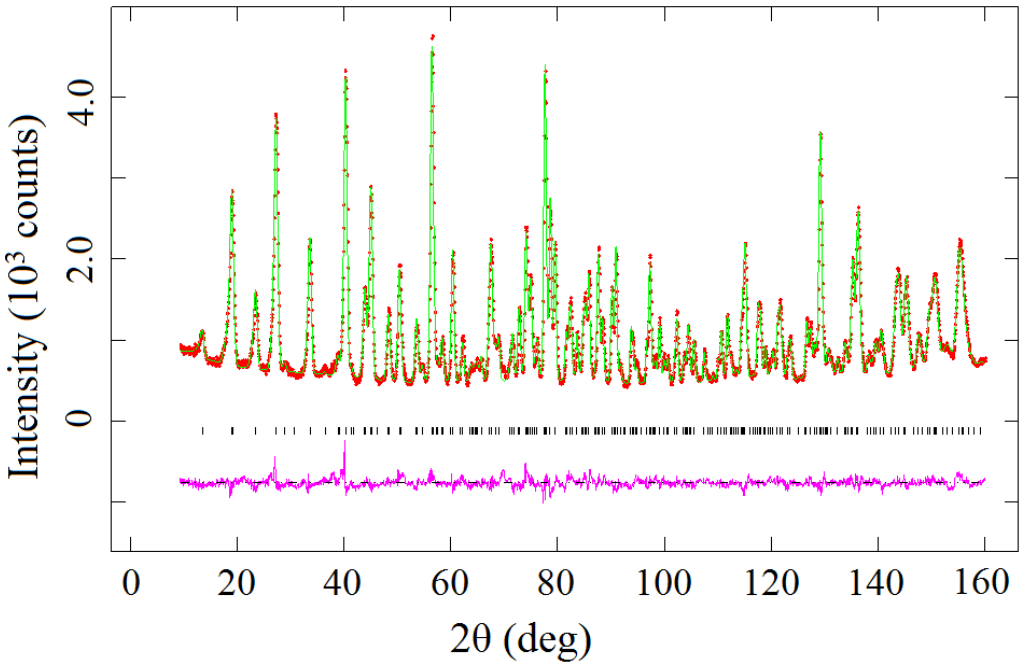

Figure 4.2 Observed (red dots) and calculated (green line) NPD patterns of $ZrMn_2Ge_4O_{12}$ at room temperature; λ = 1.622 Å. A difference curve (purple line) is shown and reflection positions are marked.

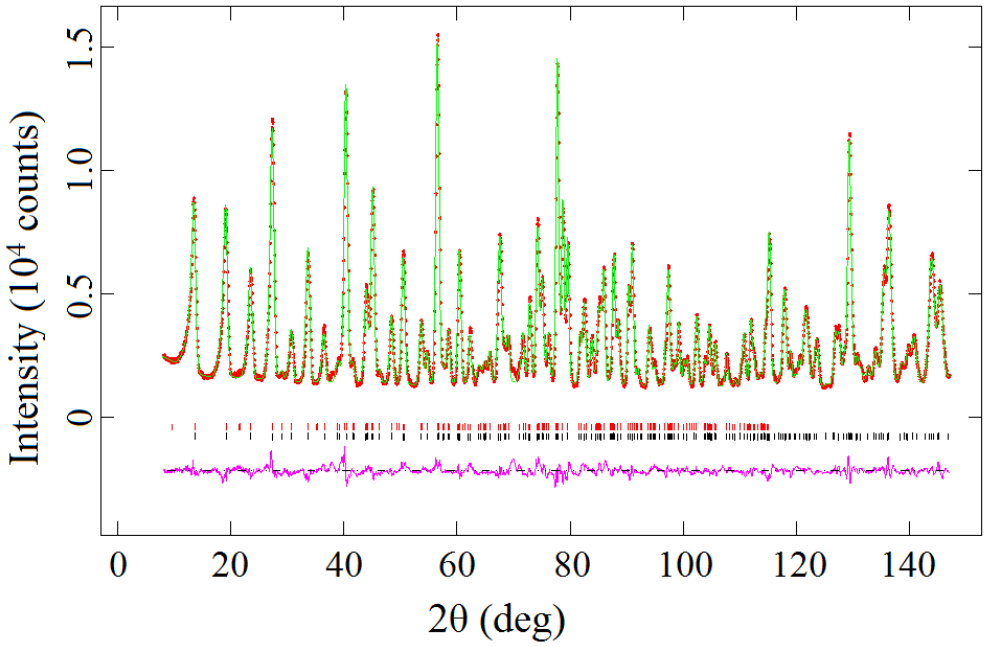

Figure 4.3 Observed (red dots) and calculated (green line) NPD patterns of $ZrMn_2Ge_4O_{12}$ at 3 K; λ = 1.622 Å. A difference curve (purple line) is shown and reflection positions are marked for the crystal structure (bottom) and the magnetic structure (top).

Table 4.2 Structural parameters of $ZrMn_{2-x}Co_xGe_4O_{12}$ derived from neutron diffraction data ($\lambda = 1.622$ Å) as a function of composition and temperature

		x, T				
		0.0, 3 K	0.0, 300 K	1.0†, 3 K	2.0‡, 1.6 K	2.0‡, 300 K
Zr	U_{iso}/Å^2	0.0020(2)	0.0037(4)	0.0020(2)	0.0028(3)	0.0037(4)
Mn/Co	U_{iso}/Å^2	0.0052(5)	0.0090(5)	0.0039(4)	0.0023(4)	0.0078(5)
Ge	*x*	0.5161(1)	0.5160(1)	0.5169(1)	0.5172(1)	0.5169(1)
	U_{iso}/Å^2	0.0014(1)	0.0031(2)	0.0012(2)	0.0012(2)	0.0026(2)
O1	*x*	-0.3733(1)	-0.3727(1)	-0.3726(1)	-0.3724(1)	-0.3719(1)
	z	0.1651(2)	0.1638(3)	0.1693(3)	0.1755(4)	0.1732(4)
	U_{iso}/Å^2	0.0013(3)	0.0041(3)	0.0032(3)	0.0030(3)	0.0045(3)
O2	*x*	0.1687(1)	0.1687(1)	0.1659(1)	0.1633(2)	0.1638(2)
	y	0.0732(1)	0.0732(1)	0.0733(1)	0.0730(2)	0.0733(2)
	z	0.2622(2)	0.2622(2)	0.2630(2)	0.2636(2)	0.2643(3)
	U_{iso}/Å^2	0.0028(3)	0.0038(2)	0.0022(4)	0.0022(4)	0.0039(2)
a/Å		9.6502(1)	9.6532(1)	9.5970(1)	9.5477(1)	9.5526(1)
c/Å		4.8567(1)	4.8623(1)	4.8165(1)	4.7791(1)	4.7850(1)
V/Å^3		452.28(1)	453.09(1)	443.61(1)	435.66(1)	435.66(2)
R_{wpr}		4.65%	4.94%	4.82%	4.09%	5.87%
χ^2		6.569	2.430	4.459	3.170	3.241

Space group *P*4/*nbm* (No. 125), Z = 2

Zr on 2*b* (¼, ¼, ½); Mn/Co on 4*f* (0, 0, ½);

Ge on 8*k* (*x*, ¼, 0); O1 on 8*m* (*x*, -*x*, *z*); O2 on 16*n* (*x*, *y*, *z*)

† Contains 0.7(1) wt % $CoGeO_3$
‡ Contains 4.4(2) wt % $CoGeO_3$

Table 4.3 Bond lengths (Å) and bond angles (degrees) in $ZrMn_{2-x}Co_xGe_4O_{12}$ derived from neutron diffraction data as a function of composition and temperature ($\lambda = 1.622$ Å)

	x				
	0.0, 3 K	0.0, 300 K	1.0, 3 K	2.0, 1.6 K	2.0, 300 K
Zr-O2 × 8	2.205(1)	2.206(1)	2.198(1)	2.194(1)	2.191(2)
Mn/Co-O1 × 2	2.374(1)	2.386(2)	2.351(2)	2.320(1)	2.332(2)
Mn/Co-O2 × 4	2.117(1)	2.119(1)	2.082(1)	2.050(1)	2.052(2)
O2-O2' *	3.301(1)	3.302(1)	3.247(2)	3.196(1)	3.203(2)
O2-O2" *	2.652(1)	2.655(1)	2.606(2)	2.569(1)	2.565(2)
Ge-O1 × 2	1.788(1)	1.787(1)	1.782(1)	1.782(1)	1.781(1)
Ge-O2 × 2	1.726(1)	1.727(1)	1.734(1)	1.735(1)	1.738(2)
O2-Mn/Co-O2'	102.45(5)	102.42(6)	102.50(6)	102.41(4)	102.61(9)
O2-Mn/Co-O2"	77.55(5)	77.58(6)	77.50(6)	77.59(4)	77.39(9)
O1-Mn/Co-O2'	81.40(4)	81.38(4)	81.41(4)	81.54(4)	81.51(6)
O1-Mn/Co-O2"	98.60(4)	98.62(4)	98.59(4)	98.46(4)	98.49(6)
O1-Ge-O1	106.73(10)	106.04(11)	106.89(11)	107.46(10)	106.77(16)
O1-Ge-O2	105.63(5)	105.78(5)	105.67(6)	105.34(5)	105.49(9)
O1-Ge-O2	109.04(7)	109.13(7)	108.93(8)	108.85(7)	108.93(11)
O2-Ge-O2	120.12(7)	120.20(8)	120.11(8)	120.43(7)	120.55(11)

* distances within the equatorial plane of the $(Mn/Co)O_6$ octahedra

4.3.2 Magnetic Properties

4.3.2.1 DC Magnetisation Measurements

The temperature dependence of the dc molar susceptibility of each sample measured in 100 Oe is shown in Figure 4.4, along with the field dependence of the magnetisation measured at 2 K. The transition temperature, T_c, represents the Curie temperature for x = 0.5, 1.0, 1.5, 2.0 and the Néel temperature for x = 0.0. The magnetic parameters resulting from fitting the Curie-Weiss law to the FC data for T > 150 K are listed in Table 4.4. Values of the coercive field, H_c, and remanent magnetisation, M_r, are also included in Table 4.4. Further susceptibility measurements were made in various fields on $ZrMn_2Ge_4O_{12}$, as shown in Figure 4.5.

Table 4.4 Magnetic parameters of $ZrMn_{2-x}Co_xGe_4O_{12}$

	x				
	0.0	0.5	1.0	1.5	2.0
C /cm^3 K mol^{-1}	8.696(1)	8.332(6)	7.743(1)	7.586(1)	7.186(2)
θ /K	-11.38(2)	-14.74(2)	-17.50(2)	-21.96(2)	-15.93(2)
μ^{Co}_{eff}*	5.90$	5.37	5.36	5.37	5.36
T_c /K	8.0	6.7	6.0	5.2	3.5
M_r /μ_B per formula unit		0.48	0.78	0.80	0.068
H_c /Oe		893	786	261	10.6

$ μ_{eff} (Mn)

*calculated for $0.5 \leq x \leq 1.5$ using μ_{eff} (Mn) = 5.90.

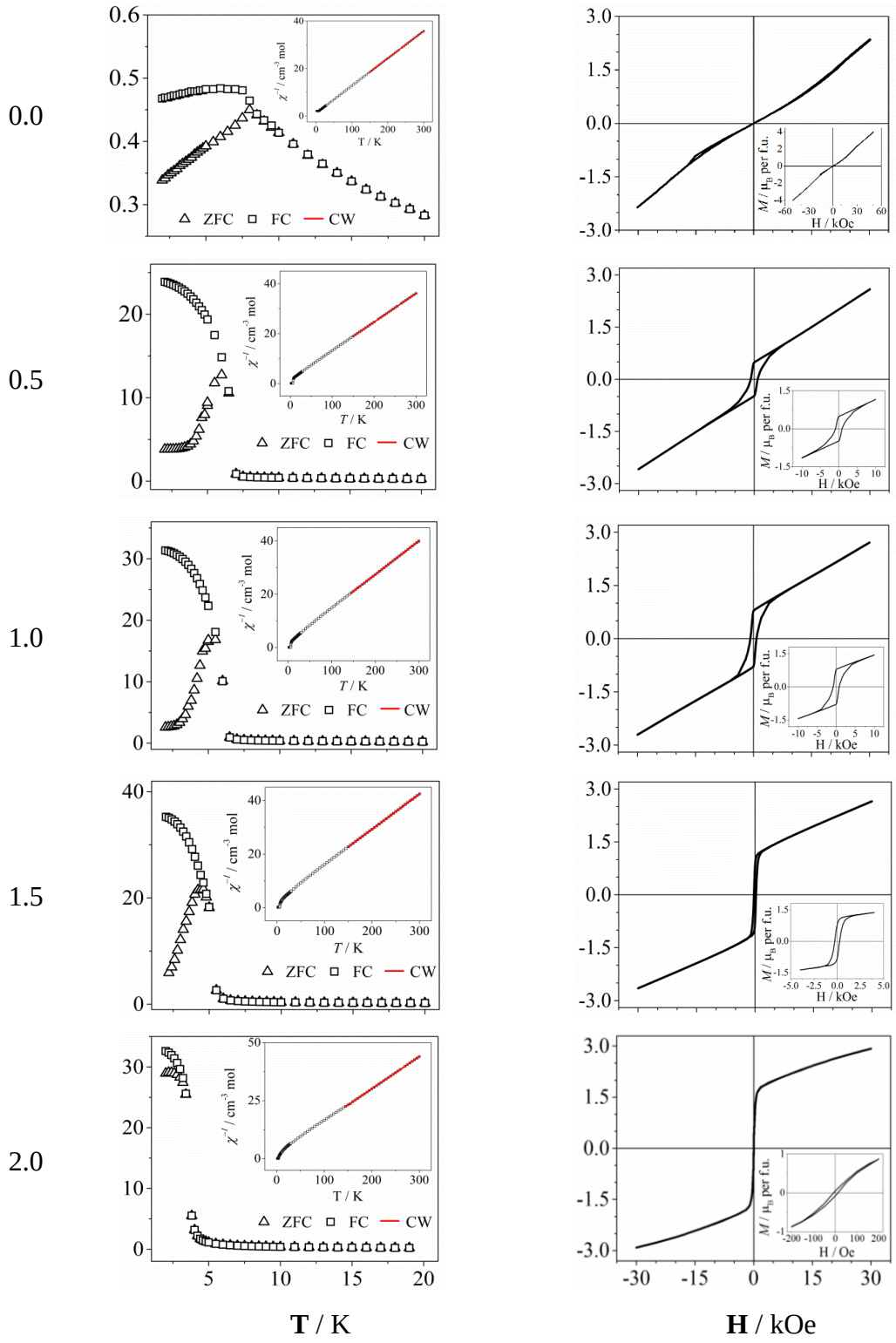

Figure 4.4 Temperature dependence of the dc molar magnetic susceptibility, measured in 100 Oe, and the field dependence of the magnetization at 2 K of $ZrMn_{2-x}Co_xGe_4O_{12}$. (inset) The inverse susceptibility; data points highlighted in red were fitted to the Curie−Weiss law.

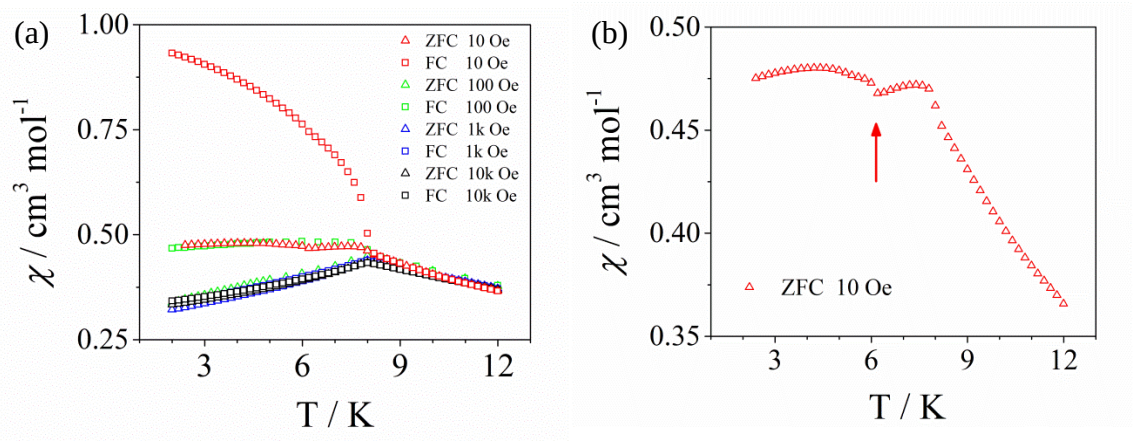

Figure 4.5 Temperature dependence of the dc molar magnetic susceptibility of $ZrMn_2Ge_4O_{12}$ (a) as a function of field and (b) in 10 Oe.

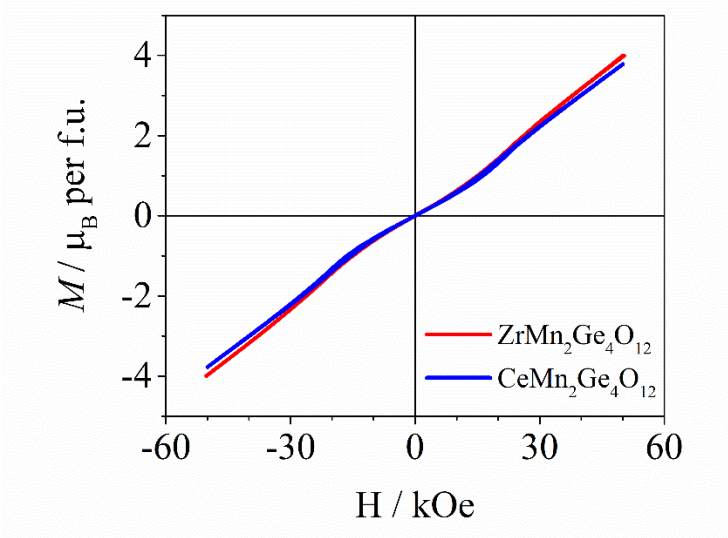

Figure 4.6 Field dependence of the magnetisation of $ZrMn_2Ge_4O_{12}$ (red) and $CeMn_2Ge_4O_{12}$ (blue) at 2 K.

From the dc susceptibilities, the solid solutions for x = 0.5, 1.0, 1.5, 2.0 are ferro/ferrimagnets and x = 0.0 is an antiferromaget. The transition temperatures are all below 10 K and they decrease as the cobalt content increases from x = 0.0 to x = 2.0 in a linear way. $ZrMn_2Ge_4O_{12}$ is also not a classic antiferromagnet as the ZFC/FC susceptibilities are unequal below the transition temperature. The deviation is much stronger in a low field as shown in Figure 4.5. A field of 1 kOe can remove the deviation. An anomaly at 6 K can be seen in the susceptibility data collected in 10 Oe after ZFC. Further measurements were conducted to study this feature. Moreover, the M(H) data is non-linear and shows a weak hysteresis when 10 < H/kOe < 25, which is similar to the behaviour of $CeMn_2Ge_4O_{12}$, see Figure 4.6.

From Curie-Weiss fitting, the effective moment of Mn^{2+} is 5.90 μ_B, which is close to the spin-only value of 5.92 μ_B. Assuming Mn^{2+} has a moment of 5.90 μ_B, the effective moments of Co^{2+} in the Co containing solid solutions are all about 5.36 μ_B, which is the same as in the $CeMn_{2-x}Co_xGe_4O_{12}$ series.

4.3.2.2 AC Magnetisation Measurements

AC susceptibility measurements were carried out in zero field on all the compositions and the results were shown in Figure 4.7. Moreover, in-field ac susceptibility measurements were conducted in dc fields 10 Oe, 500 Oe, 20 kOe for $ZrMn_2Ge_4O_{12}$ and 100 Oe, 1000 Oe for $ZrCo_2Ge_4O_{12}$. The results are shown in Figure 4.8 and Figure 4.9. $ZrMn_2Ge_4O_{12}$ shows an anomaly below the Néel temperature 8.0 K, which is similar to $CeMn_2Ge_4O_{12}$. A plateau in the real part and a small peak in the imaginary part at 6 K in zero field were found. However, the imaginary-part peak at 6 K is hardly frequency dependent but the peak at the Néel temperature, 8.0 K, is slightly frequency dependent. When a small field (10 Oe) was applied, see Figure 4.8, the real part becomes frequency dependent and the small abnormal peak still exists at 6 K whereas the peak at the Néel temperature disappears (pointed by red arrows in Figure 4.8). With a stronger dc field, the real part plateau remains but appears at a lower temperature, 5 K (pointed by red arrows in Figure 4.8), and the imaginary part peak disappears, which is consistent with $CeMn_2Ge_4O_{12}$. Moreover, the ac susceptibility in a 20 kOe magnetic field behaves the same as $CeMn_2Ge_4O_{12}$. The ac susceptibility proves that solid solutions for x = 0.5, 1.0, 1.5 are ferro/ferrimagnets. $ZrCo_2Ge_4O_{12}$ appears to be a weak ferromagnet from the dc susceptibility with T_C = 3.5 K. A peak at 3.5 K in zero-field ac susceptibility corresponds to the Curie temperature. However, the imaginary susceptibility goes up below this peak, which proves $ZrCo_2Ge_4O_{12}$ is not a classic ferromagnet. Further in-field ac measurements were conducted and when a small magnetic field (100 Oe) was applied, $ZrCo_2Ge_4O_{12}$ shows a frequency-dependent behaviour below the Curie temperature. The Φ value, 0.019, calculated from Equation 1.9 suggests that it behaves as a spin glass ($0.01 < \Phi < 0.08$). Furthermore, when the external dc field is increased, the peak is broadened and shifted to higher temperature.

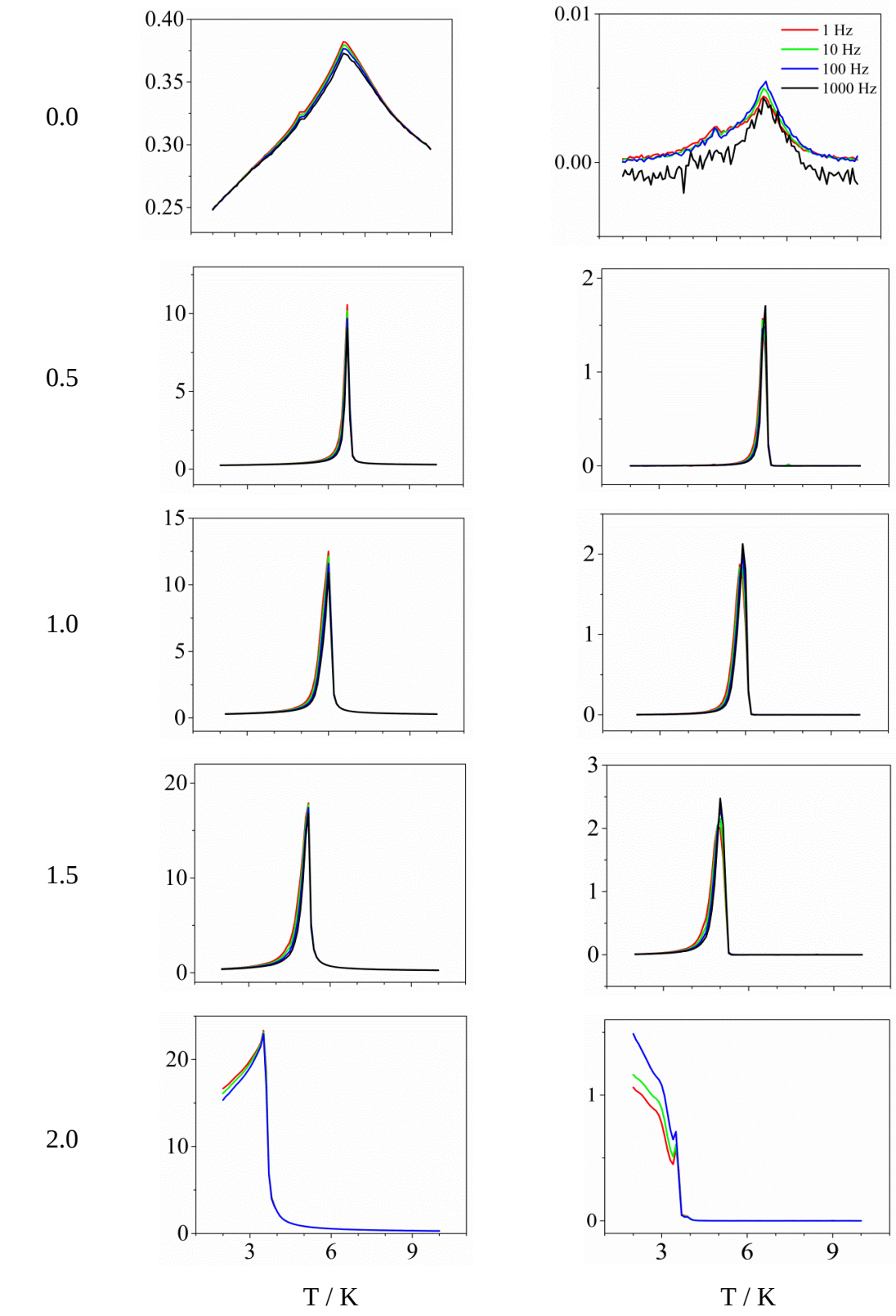

Figure 4.7 Temperature and frequency dependence of the ac molar magnetic susceptibility of $ZrMn_{2-x}Co_xGe_4O_{12}$.

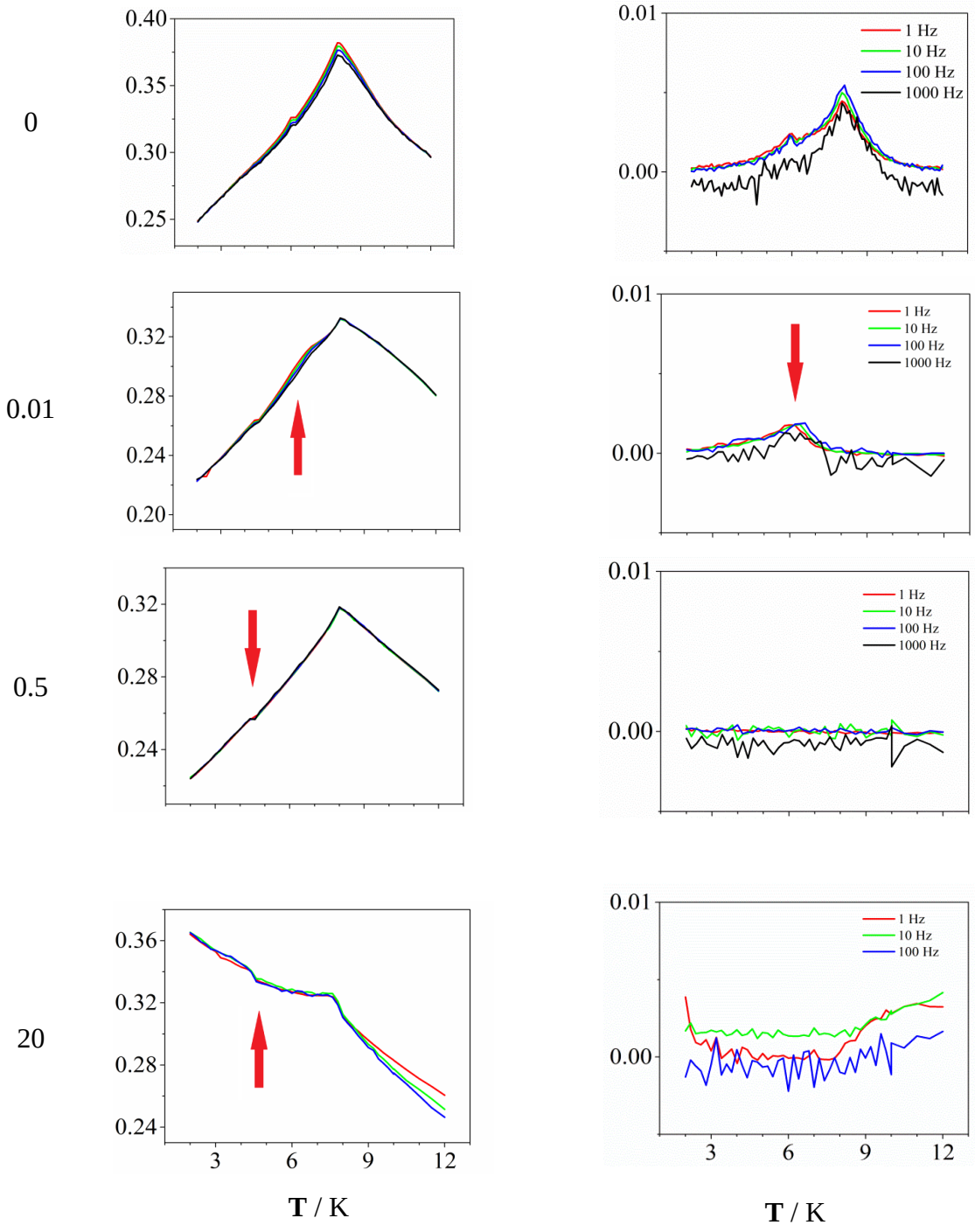

Figure 4.8 Temperature, frequency and field dependence of the ac molar magnetic susceptibility of $ZrMn_2Ge_4O_{12}$. The red arrows point out the anomaly in the ac measurements.

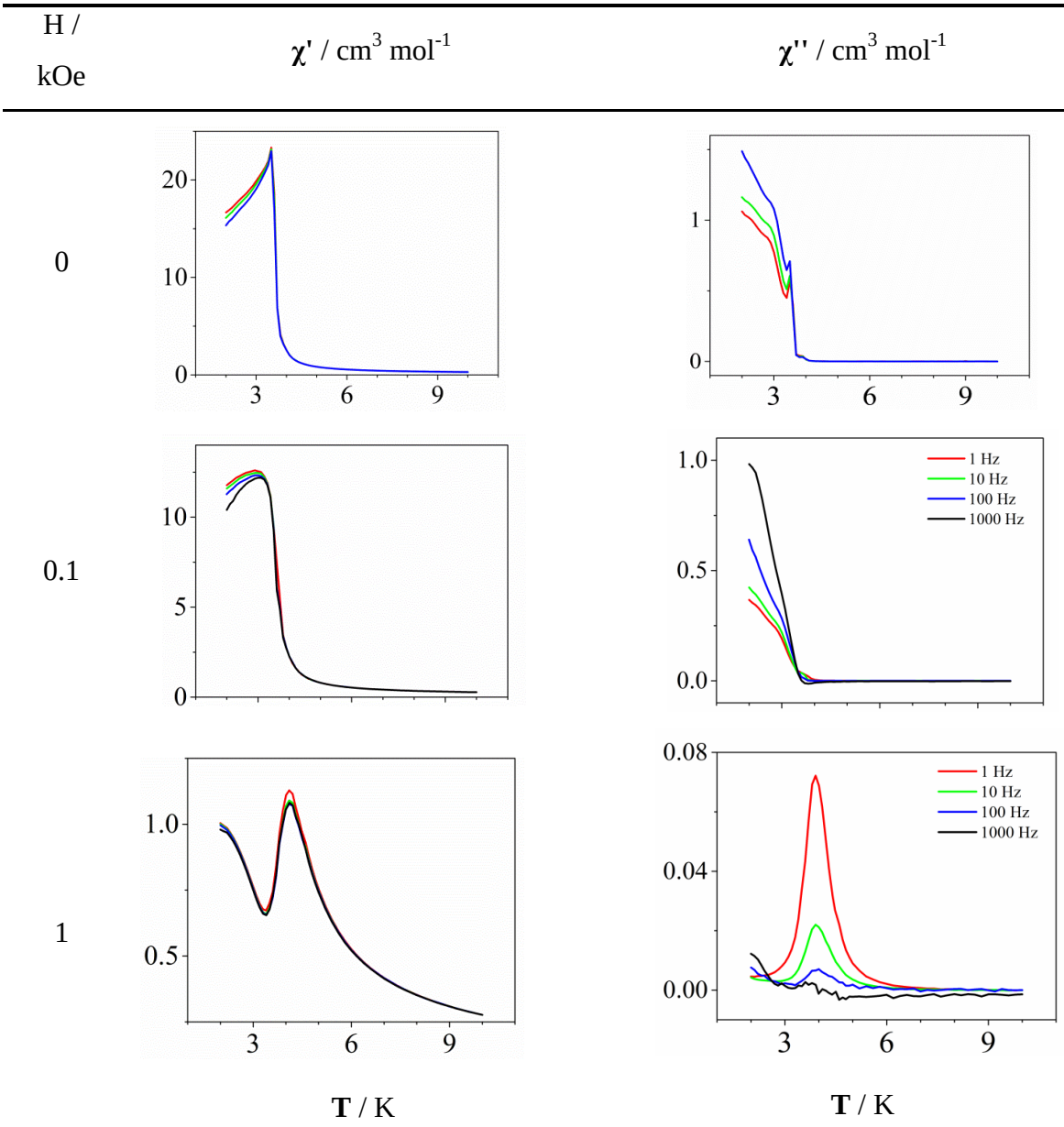

Figure 4.9 Temperature, frequency and field dependence of the ac molar magnetic susceptibility of $ZrCo_2Ge_4O_{12}$.

4.3.2.3 Zero-Field Low Temperature Neutron Diffraction

Neutron diffraction data were collected on $ZrMn_{2-x}Co_xGe_4O_{12}$ (x = 0.0, 1.0) at 3 K and on $ZrCo_2Ge_4O_{12}$ at 1.6 K using wavelength λ = 1.622 and 2.4395 Å. The magnetic structure and the mean ordered atomic moment values were derived from λ = 2.4395 Å NPD data. Structural parameters were constrained from λ = 1.622 Å NPD data. Magnetic structures of

the compounds are shown in Figure 4.10. The mean ordered atomic moments (μ_B) at the 4*f* site are listed in Table 4.5.

The magnetic structure of $ZrMn_2Ge_4O_{12}$ can be described in the magnetic space group *P4'/nbm'* (No. 125.5.1035), which is the same as $CeMn_2Ge_4O_{12}$. The structural and magnetic unit cells are the same size. Nearest-neighbour (NN) Mn^{2+} cations within the (001) sheet at z = ½ couple antiferromagnetically and align along the [001] axis. Next-nearest-neighbour (NNN) cations within this sheet align in a ferromagnetic manner and the cation containing (001) layers are also aligned in a ferromagnetic manner. The ordered moment for Mn^{2+} was determined to be 4.68 μ_B, which is close to spin-only value gS = 5 μ_B.

The magnetic structure of $ZrMnCoGe_4O_{12}$ can be described in the magnetic space group *Pb'an'* (No. 50.6.382), which is the same as $CeMnCoGe_4O_{12}$. The structural and magnetic unit cells are the same size. The replacement of the Mn^{2+} cations by Co^{2+} causes the spins to rotate into the (001) plane. NN Mn^{2+} cations within the (001) sheet at z = ½ couple antiferromagnetically and NNN cations within this sheet align in a ferromagnetic manner. Due to the symmetry of the crystal structure and the random distribution of the powder sample, the direction of the moments can go everywhere in the (001) plane.

The magnetic structure of $ZrCo_2Ge_4O_{12}$ can be described in the magnetic space group *Pb'an'* (≡ *Pc'n'a*, No. 50.6.382), which is the same as $CeCo_2Ge_4O_{12}$ in high field. The structural and magnetic unit cells are the same size. Within one (001) sheet, the moments coupling is antiferromagnetic along one axis ([100] axis is chosen in this thesis) and ferromagnetic along another perpendicular axis ([010] axis is chosen in this thesis). The coupling between NN (001) layers is ferromagnetic again along [001] axis. The compound thus behaves as weak ferromagnet. Hence, the magnetic structure can be described as stacking of weakly-ferromagnetic sheets. The ordered moment for Co^{2+} was determined to be 2.55 μ_B, which is close to spin-only value gS = 3 μ_B.

Table 4.5 Mean ordered atomic moments (μ_B) at the 4*f* site in $ZrMn_{2-x}Co_xGe_4O_{12}$ at low temperature derived from neutron diffraction data ($\lambda = 2.4395$ Å)

	x		
	0.0†	1.0†	2.0‡
M_x	0	2.98(4)	2.10(5)
M_y^*	0	0	1.45(8)
M_z	4.68(2)	0	0
M_T	4.68(2)	2.98(4)	2.55(7)

† Conducted at 3 K

‡ Conducted at 1.6 K

* the ferromagnetic component

(a)

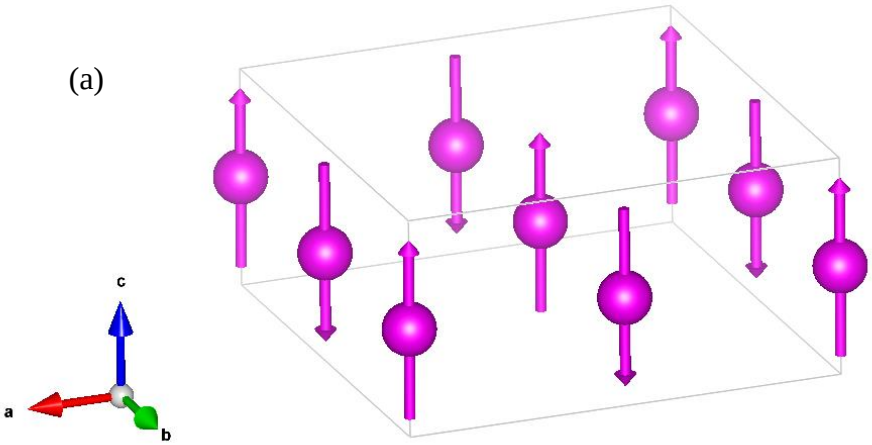

(b)

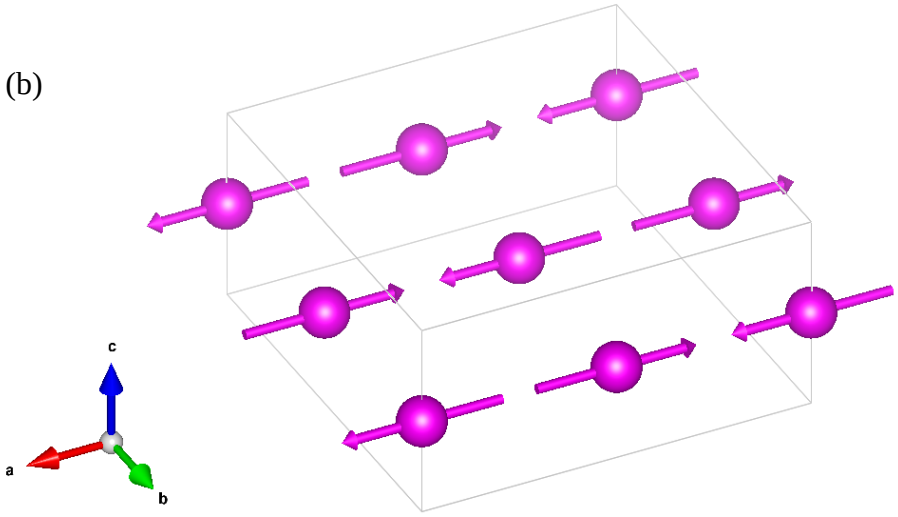

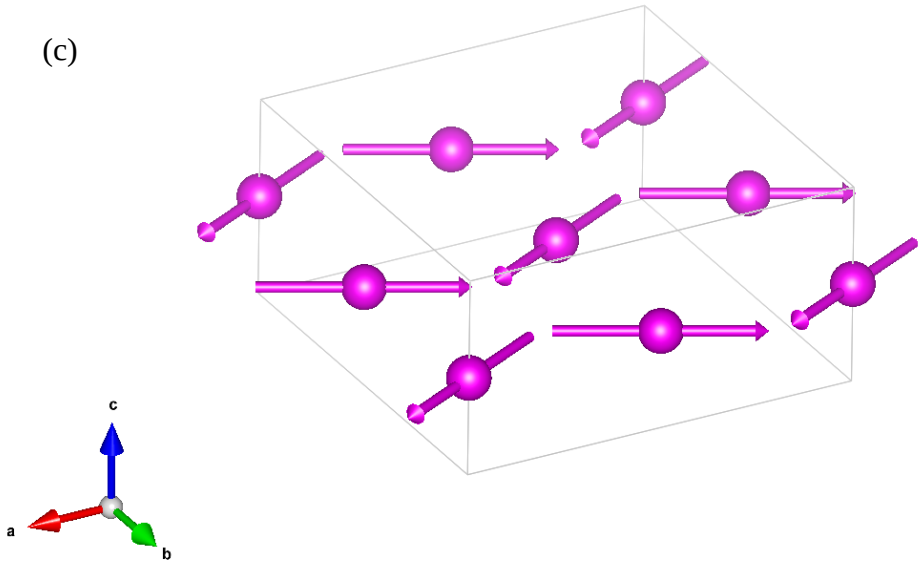

Figure 4.10 Magnetic structures in zero field of $ZrMn_{2-x}Co_xGe_4O_{12}$ with x = (a) 0.0, (b) 1.0 and (c) 2.0. Diamagnetic ions are omitted.

4.3.2.4 In-Field Low Temperature Neutron Diffraction

In-field low temperature neutron diffraction measurements were conducted on $ZrMn_{2-x}Co_xGe_4O_{12}$ (x = 0.0, 2.0). For the in-field low temperature neutron diffraction data, the unit cell parameters and the atomic coordination parameters were set free in the refinements. The result shows that the influence of the magnetic field on the parameters is negligible. Relevant fitted patterns are shown in Appendix C Figure C.28 - Figure C.34. The refinement profiles and some selected bond lengths and bond angles are listed in Appendix C Table C.6 and Table C.7.

The magnetic structures of $ZrMn_2Ge_4O_{12}$ and $ZrCo_2Ge_4O_{12}$ remain the same in a magnetic field. The difference comes in the intensity of the magnetic peaks, which leads to the change of ordered moment, see Figure 4.11. The ordered moments in different fields are listed in Table 4.6 and Table 4.7. Fine temperature-step NPD measurements were conducted on $ZrMn_2Ge_4O_{12}$ to study the abnormality at 6 K. However, no significant change in peak position was detected but only the intensity, see Figure 4.12, which only leads to a change in the mean ordered moment of Mn^{2+}.

Table 4.6 Mean ordered atomic moments (μ_B) of Mn^{2+} site in $ZrMn_2Ge_4O_{12}$ as a function of applied magnetic field at 1.6 K

H/ kOe	0	30	Turned back to 0
M_z	4.68(2)	4.23(2)	4.66(2)

Table 4.7 Mean ordered atomic moments (μ_B) of Co^{2+} site in $ZrCo_2Ge_4O_{12}$ as a function of applied magnetic field at 1.6 K

H/ kOe	0	3	6	20
M_x	2.10(5)	2.21(5)	2.33(4)	2.30(5)
M_y†	1.45(8)	1.43(9)	1.73(7)	2.07(6)
M_T	2.55(7)	2.63(7)	2.90(5)	3.09 (6)

† the ferromagnetic component

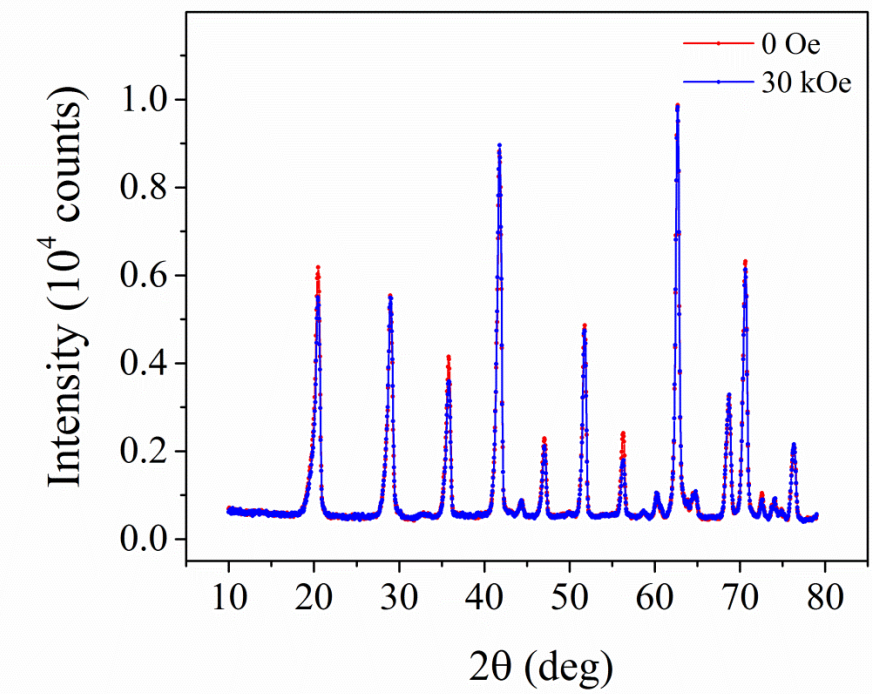

Figure 4.11 Low-angle region of the neutron diffraction pattern of $ZrMn_2Ge_4O_{12}$ in applied fields of 0 (blue) and 30 (red) kOe at 3 K, $\lambda = 2.4395$ Å.

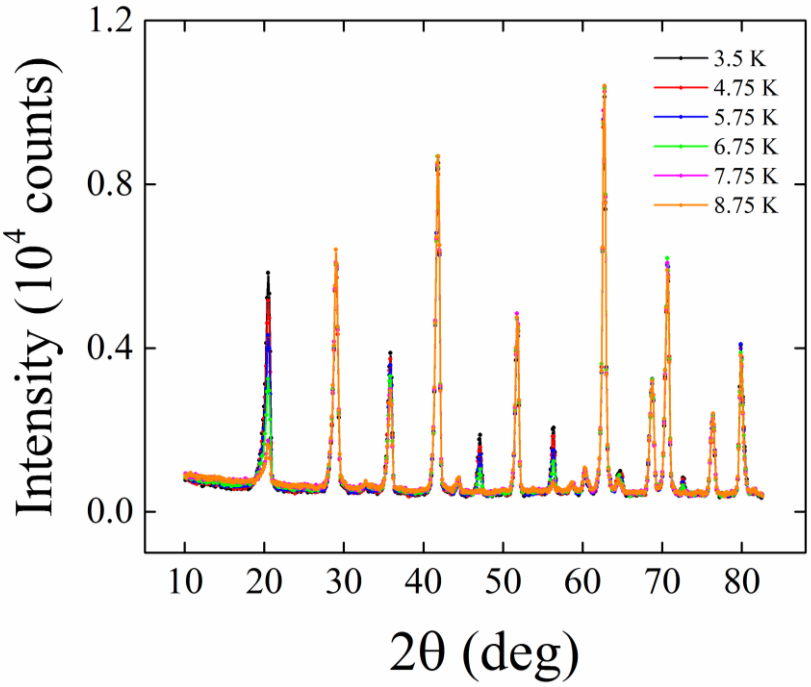

Figure 4.12 Low-angle region of the neutron diffraction pattern of $ZrMn_2Ge_4O_{12}$ in zero field as a function of temperature, λ = 2.4395 Å.

4.3.2.5 Specific Heat

Specific heat measurements were conducted to confirm the long-range magnetic transition for $ZrMn_2Ge_4O_{12}$. A λ-shape like peak was shown in zero field at 8.0 K, which is corresponds to its Néel temperature. However, a plateau appears below 6 K, which is similar to $Sr_2MnGe_2O_7$ [22]. The crystal, electron, and nuclear contributions were derived from the fitting of non-field heat capacity data over temperature range $14 \leqslant T/K \leqslant 30$ using Equation 2.32 with a = 0.21(1) $J/K^2 \cdot mol$, b = 0.66(4) $mJ/K^4 \cdot mol$, c = - 0.12(3) $\mu J/K^6 \cdot mol$. The magnetic specific heat below 2 K was extrapolated by the relation $C_{mag} \propto T^3$ from the spin-wave model for an antiferromagnet [23]. The magnetic entropy derived from Equation 2.33 and the magnetic specific heat data lead to 24(1) J/K·mol. The theoretical value for one Mn^{2+} is Rln(2S+1) = 14.90 J/K·mol according to Equation 2.34, where R is the gas constant. $ZrMn_2Ge_4O_{12}$ contains two Mn^{2+} and the entropy should be 2Rln(2S+1) = 29.80 J/K·mol and it is 13.9 J/K·mol compared to 14.90 J/K·mol in $Sr_2MnGe_2O_7$. The error mainly comes from the limited data as the lattice/electron contribution is normally fitted by data over temperature range $30 \leqslant T/K \leqslant 300$. Hence, the limited data in this thesis lead to abnormal specific heat fitting parameters a, b, c. Almost all magnetic entropy is released below T_N.

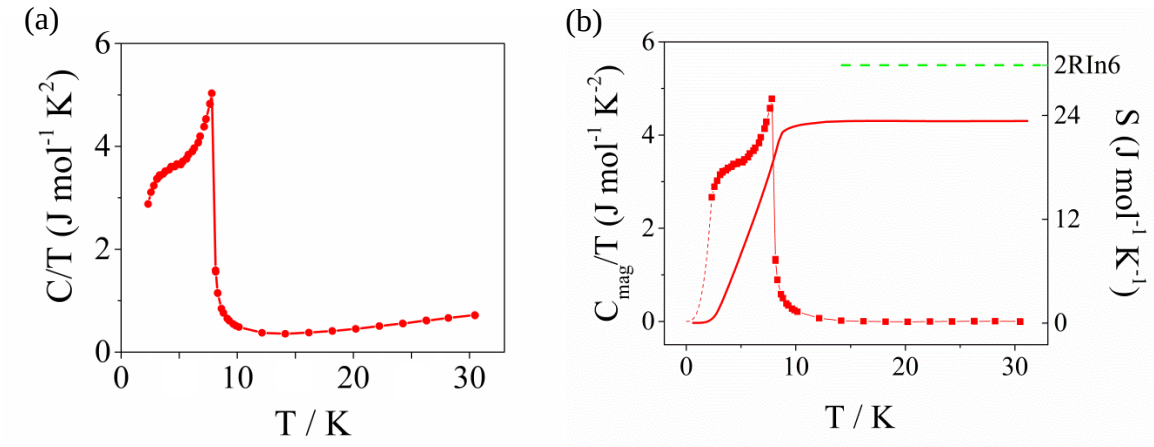

Figure 4.13 (a) Heat capacity and (b) magnetic specific heat and entropy calculation of $ZrMn_2Ge_4O_{12}$ in zero field.

4.3.2.6 DFT Calculation

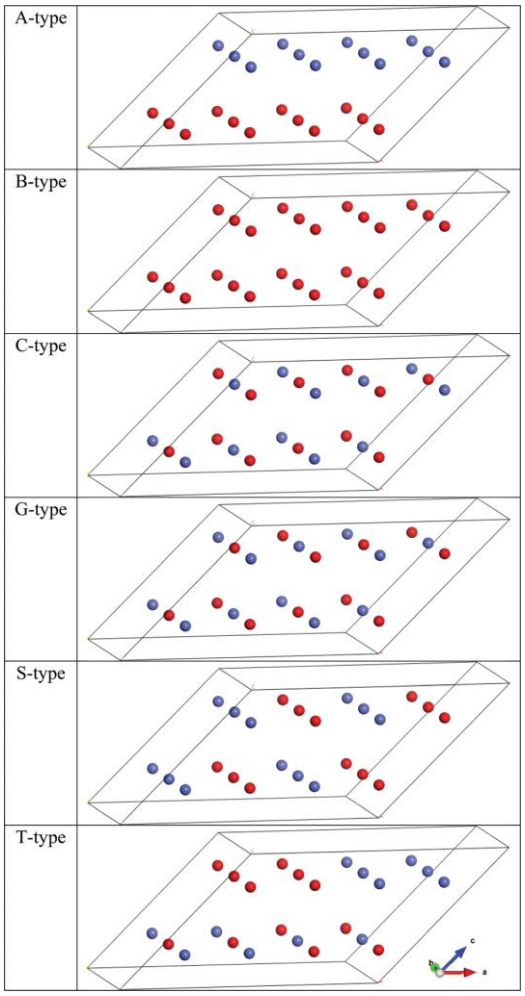

Figure 4.14 Magnetic structures considered in the DFT calculations. Blue and magenta circles represent spin-up and spin-down cations. The cell ($_c$) used in the calculations is related to the structural unit cell as follows: $a_c = 2a$, $b_c = b$, $c_c = a + 2c$.

In DFT calculations, the relative stability of A-type, B-type, C-type, G-type and S-type magnetic ordering [24], [25] for $ZrMn_2Ge_4O_{12}$ and $ZrCo_2Ge_4O_{12}$ was considered. A-, C- and G-type result in antiferromagnetism whereas B-type ordering results in ferromagnetism as shown in Figure 4.14. An additional structure, S-type, was also studied, included in Figure 4.14, which was not included in the original classification by Wollan and Koehler. The C-type structure was calculated to be the most stable for both compositions. The stabilities of the different ordering patterns relative to that of the C-type structure are listed in Table 4.8.

Table 4.8 Relative stabilities (K per *M* atom) of different magnetic structures for $ZrM_2Ge_4O_{12}$ (*M* = Mn, Co)

Structure type	*M*	
	Mn	Co
A	4.964	5.264
B	24.611	28.122
C	0	0
G	15.958	23.887
S	9.910	14.173

Table 4.9 Calculated exchange constants (eV) of $ZrM_2Ge_4O_{12}$ (*M* = Mn, Co)

	M	
	Mn	Co
J_1 / K	-0.03671	0.0288
J_2 / K	-0.13658	-0.2647
J_3 / K	-0.18819	-0.4229
J_4 / K	-0.52481	-2.1788
J_{5+6} / K	-0.00439	-0.0090

The values of the exchange constants calculated in the case of C-type ordering are listed in Table 4.9. The tabulated values relate to individual superexchange pathways between a pair of cations; they have not been adjusted to allow for the different multiplicities of the various intercation interactions. The two exchange constants, J_3 and J_4, that both relate to coupling between NNN along <101> correspond to the superexchange pathways *M* – O1 – Ge – O1 – *M* and *M* – O2 – Ge – O2 – *M*, respectively. The Weiss temperatures of $ZrMn_2Ge_4O_{12}$ and $ZrCo_2Ge_4O_{12}$ were calculated to be -12.60 and -15.59 K, respectively.

4.3.3 Discussion

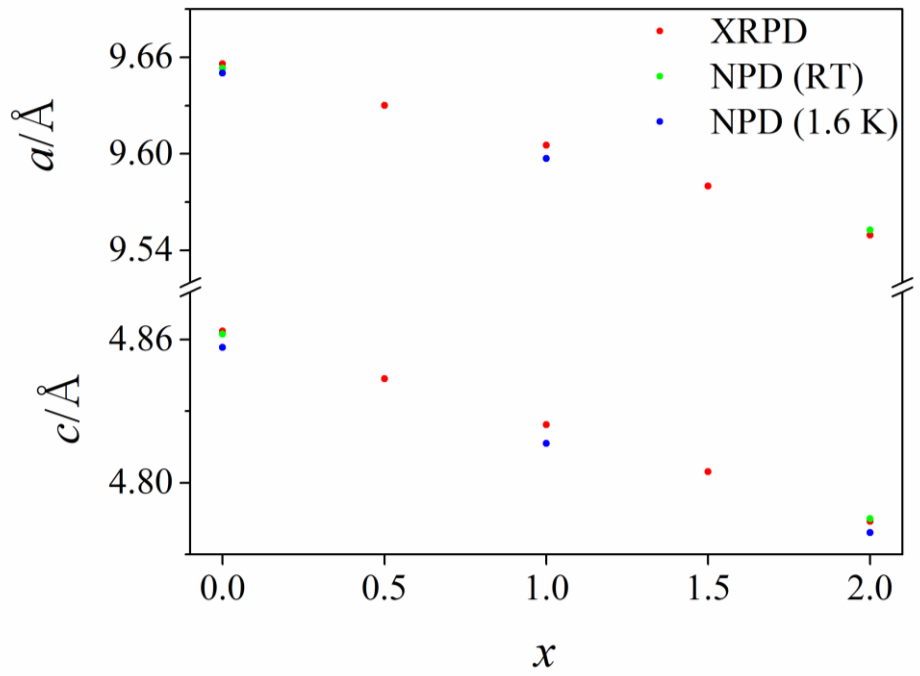

Figure 4.15 Structural unit cell parameters *a* and *c* derived from diffraction data. The error bars are smaller than the size of the points.

All the compounds studied are isostructural and the unit-cell volume decreases in a linear way with the Mn:Co content, see Figure 4.15. Due to the difference in cation size between Mn^{2+} (r = 0.83 Å) and Co^{2+} (r = 0.745 Å) [26], the unit cell parameters in the Zr-based solid solutions decrease as the cobalt content increases from x = 0.0 to x = 2.0, a by 1.12 % and c by 1.67 %; the ratio $2c/a$ consequently decreases from 1.0066 to 1.0010. The unit cell volume of each composition is approximately 4.5 % smaller than that of the analogous Ce-containing composition with replacement of Ce^{4+} (r = 0.97 Å) by Zr^{4+} (r = 0.84 Å) [26]. However, the ratio $2c/a$ of each compound is significantly increased with a much larger $\langle r_{4f} \rangle / r_{2b}$ ratio. The GeO_4 tetrahedra in both $ZrMn_2Ge_4O_{12}$ and $ZrCo_2Ge_4O_{12}$ show a considerable degree of distortion. The longer Ge – O1 bonds provide the connectivity between the four GeO_4 tetrahedra that make up a Ge_4O_{12} group whereas each O2 atom is bonded to only one germanium atom. The bond lengths of Ge – O1 and Ge – O2 are 1.788 and 1.726 Å in x = 0.0, which is almost the same to Ce-based solutions; and 1.782 and 1.734 Å in x = 2.0. However, the O – Ge – O bond angles are about the same. This illustrates that the Ge atom in [GeO_4] tetrahedra is displaced somehow in $ZrCo_2Ge_4O_{12}$, but such displacement is still small. The unit cell parameters derived from XRPD and NPD collected at room temperature are in good agreement. No significant structural change was

detected on cooling from room temperature to 1.6 K. Calculations concerning the octahedral and antiprismatic environment on the compounds x = 0.0, 1.0, 2.0 were also conducted, see Table 4.10.

Table 4.10 Derived structural parameters for $ZrMn_{2-x}Co_xGe_4O_{12}$ from low temperature NPD, λ = 1.622 Å

x	$\langle r_{4f}\rangle/r_{2b}$	$2c/a$	$d(M_{4f}-O2)/d(M_{4f}-O1)$	φ /°	ψ /°	q
0.0	0.988	1.0066	0.892(1)	78.18(12)	43.25(5)	0.870(1)
1.0	0.938	1.0046	0.885(1)	78.68(12)	42.64(5)	0.859(1)
2.0	0.887	1.0010	0.884(1)	79.42(12)	42.02(5)	0.850(1)

φ Angle between M_{4f} – O1 bond and M_{4f} – O2 plane

ψ Angle between the M_{4f} – O1 bond and the (001) plane

q Ratio of O2 – O2 distance in square face of antiprism to perpendicular distance between faces

The Mn^{2+} and Co^{2+} cations in $ZrMn_2Ge_4O_{12}$ and $ZrCo_2Ge_4O_{12}$ occupy the *4f* site with point symmetry 2/*m* and therefore the coordinated oxide ions do not form a regular octahedron. In each case there are two long/*trans* bonds to O1 and four shorter/coplanar bonds to O2; the plane formed by four O2 atoms is not perpendicular to the axis formed by the two O1 atoms. The mean bond lengths in the MnO_6 and CoO_6 octahedra, 2.203 and 2.140 Å, are both shorter than those in the Ce analogues (2.234 and 2.168 Å) by about 1%. The corresponding lengths in MnO and CoO are 2.223 and 2.132 Å at room temperature [27], [28]. This suggests that the Mn^{2+} cation in $ZrMn_2Ge_4O_{12}$ might be in a compressed environment. However, a bond-valence calculation for the Mn^{2+} site resulted in a value of 2.04. The four O2 anions that coordinate the cation in the plane form a rectangle rather than a square, with O2 – O2 distances of 3.301 and 2.652 Å at 3 K in the Mn-containing compound and 3.196 and 2.569 Å at 1.6 K in $ZrCo_2Ge_4O_{12}$.

The Zr – O distances within the square antiprism of oxide ions that surround the 2*b* site in $ZrMn_2Ge_4O_{12}$ and $ZrCo_2Ge_4O_{12}$ are very similar to each other and also to the value of 2.224 Å determined for 8-coordinate Zr^{4+} in cubic ZrO_2 [29]. As mentioned in Chapter 3, the antiprism is sharing its O – O edge with the *trans* short edges of neighbouring octahedra. Hence, the replacement of Mn^{2+} by Co^{2+} can influence the shape of antiprism. The q ratio

decreases from 0.856(1) to 0.831(1) in Ce-based solutions whereas it decreases from 0.870(1) to 0.850(1) in Zr-based solutions. Also, an increase of the ψ value proves that the octahedra in Zr-based solutions would lie along the *c* axis and the antiprisms are less compressed along the *c* axis.

The magnetic properties of $ZrMn_{2-x}Co_xGe_4O_{12}$ are different from the Ce analogues but still similar. The negative Weiss temperatures listed in Table 4.4 indicate that antiferromagnetic interactions exist in every composition. Despite the negative values of θ, the data show that none of the compositions in this solid solution is a simple antiferromagnet. The effective magnetic moment of Mn^{2+} derived from the high temperature paramagnetic data gave 5.90 μ_B, which is in good agreement to the spin-only value of 5.92 μ_B. Assuming that the moment of Mn^{2+} is constant, 5.90 μ_B, the derived values for Co^{2+} are all approximately 5.36 μ_B, which is the same as Ce ones and implies an orbital contribution to the moment is present. All the compositions show long-range magnetic order at 2 K. The dc susceptibility data and the function M(H) indicate that they all show weak ferromagnetism below T_C. This is least obvious in the case of $ZrMn_2Ge_4O_{12}$ but it is apparent when $\chi(T)$ is measured in a lower applied field, see Figure 4.5. The transition temperature, T_C, increases with increasing manganese proportion as was also the case in $CeMn_{2-x}Co_xGe_4O_{12}$. Co^{2+} - O bonds are expected to be more covalent than Mn^{2+} - O bonds as a consequence of the smaller ionic radius of Co^{2+}. In other solid solutions, for example $Mn_{1-x}Co_xO$ [30], the magnetic ordering temperature increases with increasing covalency. The trend observed in $ZrMn_{2-x}Co_xGe_4O_{12}$ suggests that the degree of covalency in the metal to oxygen bonds does not control the ordering temperature in this system. The most obvious positive correlations are with the interatomic distances and the magnitude of the atomic moments. The ac susceptibility data also demonstrate the presence of a ferromagnetic component in the magnetically-ordered phase.

The ZFC/FC hysteresis in the dc susceptibility of $ZrMn_2Ge_4O_{12}$, see Figure 4.5, suggests that the compound is weakly ferromagnetic in low magnetic field. The M(H) curve is non-linear and behaves almost the same as $CeMn_2Ge_4O_{12}$, only with the magnetization a little bit larger when H > 30 kOe, see Figure 4.6. The magnetic structure determined by neutron diffraction in zero field is antiferromagnetic with an ordered moment of 4.68(2) μ_B per Mn^{2+} cation. There is no weak ferromagnetic component derived from neutron diffraction due to the ferromagnetic component magnitude (<0.05 μ_B) being too weak to be detected.

The facts described above correspond to the disordered component in $CeMn_2Ge_4O_{12}$. The magnitude of the ordered magnetic moment, 4.68(2) μ_B per Mn^{2+} is lower than the maximum possible value, $gS = 5$ μ_B, as a consequence of bond covalency and the zero-point spin reduction [31], [32]. The observed value can be compared with that of 4.64 μ_B measured in MnO [31]. The magnitude of the ordered moment decreases when a field is applied, which is the same as in $CeMn_2Ge_4O_{12}$, see Table 3.8 and Table 4.6. The ac susceptibility in zero field of $ZrMn_2Ge_4O_{12}$ shows an anomaly below the Néel temperature, see Figure 4.8: a plateau in real part and a small peak in imaginary part at 6 K, which is also seen in $CeMn_2Ge_4O_{12}$ and suggested as the freezing temperature of the disordered components. The peaks in both real and imaginary part appearing at Néel temperature, 8 K, are frequency-dependent suggesting a weakly ferromagnetic phase exists. When a small field, 10 Oe, was applied, an interesting phenomenon was observed. The FC dc susceptibility indicates a ferromagnetic phase whereas the ZFC shows a secondary magnetic transition at 6 K (pointed by a red arrow in Figure 4.5). However, in the ac susceptibility with a 10 Oe applied field, there is no sign of this ferromagnetic phase but it is slightly frequency-dependent in the temperature range 6 – 8 K. The abnormal behaviour is different to $CeMn_2Ge_4O_{12}$ and thus suggests that the disordered moments would prefer ferromagnetic interactions in $ZrMn_2Ge_4O_{12}$ but antiferromagnetic interactions in $CeMn_2Ge_4O_{12}$ in low fields. With a stronger dc field (500 Oe), the real part plateau in the ac susceptibility appears at a lower temperature, 5 K, and the imaginary part peak disappears. The ac susceptibility of $ZrMn_2Ge_4O_{12}$ in a 20 kOe magnetic field behaves the same as $CeMn_2Ge_4O_{12}$, see Figure 3.12 and Figure 4.8. Neutron diffraction patterns were collected around 6 K with fine temperature steps to study the abnormal phenomena but no significant change was found, see Figure 4.12. The specific heat data was also collected and a plateau appears below 6 K, corresponding to the 'freezing temperature'. Similar specific heat data were also seen previously [22] and it is suggested to be a result of a weak ferromagnetic component. From the specific heat data, the magnetic entropy is 23.86 J/K·mol whereas the theoretical one is $2Rln(2S+1)$ = 29.80 J/K·mol, a 20% difference. Almost all magnetic entropy is released below T_N, suggesting the long-range magnetic interactions are dominant. It is reported that the magnetic entropy is always about 10% less than the expected value and this may indicate a spin-wave contribution [33], [34], [35]. The disordered moments may come from dipolar interactions and in our case, that the *4f* site being strongly distorted and having point symmetry *2/m* makes the dipolar interaction possible to form.

The replacement of Mn^{2+} cations by Co^{2+} rotates the ordered magnetic moments from the [001] axis into the (001) plane due to the anisotropy of Co^{2+}. $ZrMnCoGe_4O_{12}$ has the same magnetic structure as $ZrMn_2Ge_4O_{12}$ with ordered magnetic moments lying in the (001) plane. The ordered moment is 2.98 μ_B and it is smaller than 3.13 μ_B in $CeMnCoGe_4O_{12}$. The remanent magnetisations for x = 0.5, 1.0, 1.5 are all too small (< 1 μ_B) to be detected from neutron diffraction, suggesting that the weakly ferromagnetic phase may also come from a canted antiferromagnet at low temperatures in the similar way to Ce-based ones. The remanent magnetisations for x = 0.5, 1.0 in the Ce-based solid solutions are 0.38 and 0.67 μ_B per formula unit respectively; the coercive fields are 688 and 626 Oe. They are 0.48 and 0.78 per formula unit; 893 and 786 Oe in Zr analogues. The decrease of the ordered moment seen by neutron diffraction and the increase of the remanent magnetisation and the coercive field prove that the intermediate solutions are canted antiferromagnets. Moreover, it is notable that the members of the solid solution become softer magnets and the Weiss constant is also more negative with increasing the cobalt content, which may also come from the anisotropy of Co.

The magnetic structure of $ZrCo_2Ge_4O_{12}$ determined by neutron diffraction is a canted antiferromagnet, see Figure 4.10, and it is the same as that of $CeCo_2Ge_4O_{12}$ in a high magnetic field. The ordered moments in $ZrCo_2Ge_4O_{12}$ lie in (001) planes, and the [100] components are antiferromagnetically ordered whereas the [010] components align ferromagnetically. The ordered magnetic moment of 2.55(7) μ_B for Co^{2+} in zero field is less than the spin-only value, gS = 3 μ_B, associated with a high-spin d^7 cation. A covalent reduction would again be expected, and also orbital contribution quenching due to the crystal field effect at low temperatures. The crystal effect on *4f* site was discussed in Chapter 3. The observation of a significant ferromagnetic component is consistent with the behaviour of χ(T) and M(H). The ferromagnetic component moment of 1.45 μ_B per Co^{2+} derived from the neutron data is in a good agreement with the saturation magnetisation determined by magnetometry (~ 3 μ_B per formula unit). Furthermore, an increase in the ordered moment is also observed in an applied field, see Table 4.7. $ZrCo_2Ge_4O_{12}$ is shown to be a soft ferromagnet from the χ(T), M(H), and neutron diffraction data. The peak at 3.5 K in the zero-field ac susceptibility corresponds to the ferromagnetic transition. However, the imaginary susceptibility goes up below this peak, see Figure 4.9. Further in-field ac measurements were conducted and when a small magnetic field (100 Oe) was applied, $ZrCo_2Ge_4O_{12}$ behaves as a spin glass. As listed in Table 4.4, both the remanent

magnetisation and the coercive field for $ZrCo_2Ge_4O_{12}$ are dramatically small, which means the magnetization of the compound is easily reversed. We suggest that though $ZrCo_2Ge_4O_{12}$ behaves as a weak ferromagnet, it actually comes from a canted antiferromagnet and the ferromagnetic interactions are weak compared to other ferromagnets. Thus, the competition between ferromagnetic superexchange and antiferromagnetic superexchange interactions may result in magnetic frustration and glassy behaviour, with unusual relaxation dynamic and frequency-dependent phenomena being observed, as has been reported before [36], [37], [38], [39]. The uniaxial anisotropy may also contribute to the glassy behaviour [40], [41].

The particular antiferromagnetic structure adopted can be rationalised by considering the superexchange pathways that are available to couple the cation moments. It is discussed in Chapter 3 and noted that the O – O distances in our structure were too long to allow strong *M* – O – O – *M* coupling. Hence, we concluded that within a particular (001) cation layer, NN_i coupling would be stronger than NNN_i coupling; the strongest interlayer coupling would be along <101> (NNN_o) rather than <001> (NN_o), despite the direct *M* – *M* distance in the latter direction being the shortest in the structure; the <101> (NNN_o) interaction, *M* – O2 – Ge – O2 – *M* superexchange pathway, was expected to be the strongest as it is the shortest pathway in the structure. It is expected the arguments developed for $CeMn_{2-x}Co_xGe_4O_{12}$ also to be applicable in the case of $ZrMn_{2-x}Co_xGe_4O_{12}$. The results of the DFT calculations are in good agreement with these qualitative predictions. The pathway J_4 is the strongest magnetic interaction; the NN_i interaction, J_2, is the next strongest; and then J_3, J_1, J_5/J_6. However, the calculations predict the interactions in $ZrCo_2Ge_4O_{12}$ to be stronger than those in $ZrMn_2Ge_4O_{12}$ whereas the experimentally-determined transition temperatures suggest the opposite. This discrepancy suggests that there is a deficiency in our model, perhaps in the way in which the anisotropy and thus the DM interaction of the Co^{2+} cation has not been modelled.

The most striking differences between the Ce-based and Zr-based solutions are seen in the $x = 1.5$ and 2.0 compounds. $ZrMn_{0.5}Co_{1.5}Ge_4O_{12}$ and $ZrCo_2Ge_4O_{12}$ are weak ferromagnets; $CeMn_{0.5}Co_{1.5}Ge_4O_{12}$ and $CeCo_2Ge_4O_{12}$ adopt an antiferromagnetic structure in a unit cell that is doubled along [001] compared to the structural unit cell. However, in an applied magnetic field the latter undergoes a metamagnetic transition and becomes isostructural with $ZrCo_2Ge_4O_{12}$. The changes should mainly come from the difference in the $2c/a$ ratio

and/or *q* ratio. As mentioned before, ψ is the angle between the *trans* axis from *4f* site octahedra to the *ab* plane. Ce^{4+} is larger than Zr^{4+} and thus Zr^{4+} is considered to be not only small but also unpolarizable. Hence, a decrease is observed in unit cell parameters but the $2c/a$ ratio (*q* ratio) is increased and as is the ψ angle. In this way, J_1 is not significant in $ZrCo_2Ge_4O_{12}$ but it should be much stronger in $CeCo_2Ge_4O_{12}$. The fact that T_N for $CeCo_2Ge_4O_{12}$ is higher than T_C for $ZrCo_2Ge_4O_{12}$ proves it. Similar changes are also observed at the other end, $x = 0.0$. However, it is notable that the Mn - O bond lengths are shorter in the Zr-based solution and it is in a compressed environment.

4.3.4 Conclusion

The magnetic properties of $ZrMn_{2-x}Co_xGe_4O_{12}$ show a marked variation with composition as the isotropic Mn^{2+} cations are replaced by anisotropic Co^{2+} cations. The susceptibility of all compositions can be modelled using the Curie-Weiss law at temperatures above 150 K and they all undergo a transition to a magnetically ordered state in the temperature range $2 \leq T/K \leq 10$. None of the compositions studied shows purely antiferromagnetic behaviour below the transition temperature, although in $ZrMn_2Ge_4O_{12}$ the ferromagnetic component is too weak to be detected in magnetometry data collected in a field of 10 kOe or in neutron powder diffraction data collected at 3.5 K. A spontaneous magnetisation is clearly apparent in the magnetometry data collected on all the cobalt-containing samples but only in the case of $ZrCo_2Ge_4O_{12}$ was the ferromagnetic component of the magnetic structure large enough to be detected by neutron diffraction. Although the behaviour of $\chi(T)$ in the paramagnetic region suggests the presence of an orbital contribution to the magnetic moment of Co^{2+}, the ordered moment in the low-temperature phase suggests that no such component is present. The spin-alignment axis varies with composition but, in contrast to the system $CeMn_{2-x}Co_xGe_4O_{12}$, the experimentally-determined underlying magnetic structure is always the same. The pseudo-cubic arrangement of the magnetic cations allows us to describe it as a C-type structure. It can be rationalised by considering the relative lengths of the *M* – O – Ge – O – *M* superexchange pathways in the structure and is entirely consistent with the relative strengths of the exchange constants calculated by DFT methods.

The work described in this Chapter has been published as *Experimental and computational study of the magnetic properties of $ZrMn_{2-x}Co_xGe_4O_{12}$*, D. Xu, M. Sale, M. Avdeev, C. D. Ling, and P. D. Battle, *Dalton Transactions*, 2017, **46**, 6921-6933.

4.4 References

[1] P. M. Woodward, D. E. Cox, E. Moshopoulou, A. W. Sleight, and S. Morimoto, Structural studies of charge disproportionation and magnetic order in $CaFeO_3$, *Physical Review B*, **2000**, *62*, 844-855.

[2] H. M. Rietveld, A profile refinement method for nuclear and magnetic structures, *Journal of Applied Crystallography*, **1969**, *2*, 65-71.

[3] R. A. Young, *The Rietveld Method*, Oxford University Press **1993**.

[4] B. H. Toby, EXPGUI, a graphical user interface for GSAS, *Journal of Applied Crystallography*, **2001**, *34*, 210-213.

[5] A. C. Larson, and R. B. Von Dreele, *General Structure Analysis System (GSAS)*, Los Alamos National Laboratory Report LAUR 86-748: **2004**.

[6] B. van Laar, and W. B. Yelon, The peak in Neutron Powder Diffraction, *Journal of Applied Crystallography*, **1984**, *17*, 47-54.

[7] K. Momma, and F. Izumi, VESTA: a three-dimensional visualization system for electronic and structural analysis, *Journal of Applied Crystallography*, **2008**, *41*, 653-658.

[8] G. Kresse, and J. Hafner, Ab initio molecular dynamics for liquid metals, *Physical Review B*, **1993**, *47*, 558-561.

[9] G. Kresse, and J. Hafner, Ab initio molecular-dynamics simulation of the liquid-metal–amorphous-semiconductor transition in germanium, *Physical Review B*, **1994**, *49*, 14251-14269.

[10] G. Kresse, and J. Furthmüller, Efficient iterative schemes for ab initio total-energy calculations using a plane-wave basis set, *Physical Review B*, **1996**, *54*, 11169-11186.

[11] G. Kresse, and J. Furthmuller, Efficiency of ab-initio total energy calculations for metals and semiconductors using a plane-wave basis set, *Computational Materials Science*, **1996**, *50*, 15-50.

[12] G. Kresse, and D. Joubert, From ultrasoft pseudopotentials to the projector augmented-wave method, *Physical Review B*, **1999**, *59*, 1758-1775.

[13] J. P. Perdew, K. Burke, and M. Ernzerhof, Generalized Gradient Approximation Made Simple, *Physical Review Letters*, **1996**, *77*, 3865-3868.

[14] P. E. Blöchl, Projector augmented-wave method, *Physical Review B*, **1994**, *50*, 17953-17979.

[15] H. J. Monkhorst, and J. D. Pack, Special points for Brillouin-zone integrations, *Physical Review B*, **1976**, *13*, 5188-5192.

[16] C. L. Fu, and K. M. Ho, First-principles calculation of the equilibrium ground-state properties of transition metals: Applications to Nb and Mo, *Physical Review B*, **1983**, *28*, 5480-5486.

[17] S. L. Dudarev, G. A. Botton, S. Y. Savrasov, C. J. Humphreys, and A. P. Sutton, Electron-energy-loss spectra and the structural stability of nickel oxide: An LSDA+U study, *Physical Review B*, **1998**, *57*, 1505-1509.

[18] G. P. Francis, and M. C. Payne, Finite basis set corrections to total energy pseudopotential calculations, *Journal of Physics: Condensed Matter*, **1990**, *2*, 4395-4404.

[19] L. Wang, T. Maxisch, and G. Ceder, Oxidation energies of transition metal oxides within the GGA+U framework, *Physical Review B*, **2006**, *73*, 195107.

[20] H. J. Koo, C. Lee, and M. H. Whangbo, Density functional analysis of the magnetic structures of $Sr_2MGe_2O_7$ (M=Mn, Co), *Journal of Magnetism and Magnetic Materials*, **2012**, *324*, 3716-3718.

[21] G. J. Redhammer, A. Senyshyn, G. Tippelt, C. Pietzonka, G. Roth, and G. Amthauer, Magnetic and nuclear structure and thermal expansion of orthorhombic and monoclinic polymorphs of $CoGeO_3$ pyroxene, *Physics and Chemistry of Minerals*, **2010**, *37*, 311-332.

[22] T. Endo, Y. Doi, Y. Hinatsu, and K. Ohoyama, Magnetic and neutron diffraction study on melilite-type oxides $Sr_2MGe_2O_7$ (M = Mn, Co), *Inorganic Chemistry*, **2012**, *51*, 3572-3578.

[23] S. J. Joshua, and A. P. Cracknell, The spin-wave contribution to the specific heat of NiF_2, *Physical Letters A*, **1969**, *28*, 562-563.

[24] C. G. Shull, E. O. Wollan, and W. C. Koehler, Neutron Scattering and Polarization by Ferromagnetic Materials, *Physical Review B*, **1951**, *84*, 912.

[25] E. O. Wollan, and W. C. Koehler, Neutron Diffraction Study of the Magnetic Properties of the Series of Perovskite-Type Compounds[(1−x)La, xCa]MnO_3, *Physical Review*, **1955**, *100*, 545-563.

[26] R. D. Shannon, Revised effective ionic radii and systematic studies of interatomic distances in halides and chalcogenides, *Acta Crystallographica Section A: Crystal Physics, Diffraction Theoretical, and General Crystallography*, **1976**, *A32*, 751.

[27] W. L. Roth, Magnetic Structures of MnO, FeO, CoO, and NiO, *Physical Review*, **1958**, *110*, 1333-1341.

[28] S. Sasaki, K. Fujino, and Y. Takeuchi, X-ray determination of electron-density distributions in oxides, MgO, MnO, CoO, and NiO, *Proceedings of the Japan Academy, Ser. B, Physical and Biological Sciences*, **1979**, *55*, 43-48.

[29] D. Wang, Y. Guo, K. Liang, and K. Tao, Crystal structure of zirconia by Rietveld refinement, *Science China Section A*, **1999**, *42*, 80-86.

[30] D. A. O. Hope, and A. K. Cheetham, A low-temperature powder neutron diffraction study of the antiferromagnetic phase of $Mn_xCo_{1-x}O$, *Journal of Solid State Chemistry*, **1988**, *72*, 42-51.

[31] B. E. F. Fender, A. J. Jacobson, and F. A. Wedgwood, Covalency Parameters in MnO, α - MnS, and NiO, *The Journal of Chemical Physics*, **1968**, *48*, 990-994.

[32] B. C. Tofield, Covalency effects in magnetic interactions, *Journal de Physique Colloques*, **1976**, *37*, 539-569.

[33] M. E. Fisher, Relation between the specific heat and susceptibility of an antiferromagnet, *Philosophical Magazine*, **1962**, *7*, 1731-1743.

[34] G. G. Low, Application of Spin Wave Theory to Three Magnetic Salts, *Proceedings of the Physical Society*, **1963**, *82*, 992-1001.

[35] N. A. Begum, A. P. Cracknell, S. J. Joshua, and J. A. Reissland, The spin-wave contribution to the specific heat of MnF_2, FeF_2, CoF_2 and NiF_2, *Journal of Physics C: Solid State Physics*, **1969**, *2*, 2329-2334.

[36] A. Maignan, C. Martin, F. Damay, B. Raveau, and J. Hejtmanek, Transition from a paramagnetic metallic to a cluster glass metallic state in electron-doped perovskite manganites, *Physical Review B*, **1998**, *58*, 2758-2763.

[37] A. Maignan, C. Martin, G. Van Tendeloo, M. Hervieu, and B. Raveau, Size mismatch: A crucial factor for generating a spin-glass insulator in manganites, *Physical Review B*, **1999**, *60*, 15214-15219.

[38] H. Woo, T. A. Tyson, M. Croft, and S. Cheong, Evidence for spin clusters and glassy behaviour in $Bi_{1-x}Ca_xMnO_3$ ($x \sim 0.875$), *Journal of Physics: Condensed Matter*, **2004**, *16*, 2689-2705.

[39] X. H. Huang, J. F. Ding, Z. L. Jiang, Y. W. Yin, Q. X. Yu, and X. G. Li, Dynamic properties of cluster glass in $La_{0.25}Ca_{0.75}MnO_3$ nanoparticles, *Journal of Applied Physics*, **2009**, *106*, 083904.

[40] G. Griffith, F. A. Volkening, and H. Claus, Apparent spin-glass nature of an anisotropic ferromagnet, *Journal of Applied Physics*, **1985**, *57*, 3392-3394.

[41] R. Pelcovits, E. Pytte, and J. Rudnick, Spin-Glass and Ferromagnetic Behavior Induced by Random Uniaxial Anisotropy, *Physical Review Letters*, **1982**, *48*, 476-479.

Chapter 5 - Synthesis and Characterisation of $CeM_{1.5}M'_{0.5}Ge_4O_{12}$ (*M* = Mn, Co; *M'* = Zn, Ni, Cu)

5.1 Introduction

In Chapter 3 we discussed the solid solution $CeMn_{2-x}Co_xGe_4O_{12}$ ($0 \leqslant x \leqslant 2$) and in Chapter 4 we discussed the consequences of replacing cerium by zirconium at the *2b* site. In this chapter, we will discuss our attempts to replace either manganese or cobalt on the *4f* site with iron, nickel, copper or zinc. Our attempts to introduce Fe^{2+} all failed whereas in the case of the other elements, substitution up to the composition $CeM_{1.5}M'_{0.5}Ge_4O_{12}$ (*M* = Mn, Co; *M'* = Zn, Ni, Cu) was possible. We describe the magnetic properties of all these compounds and in the case of $CeMn_{1.5}Ni_{0.5}Ge_4O_{12}$ we give a full description of the magnetic structure determined by neutron diffraction.

5.2 Experimental

Polycrystalline samples of $CeM_{1.5}M'_{0.5}Ge_4O_{12}$ (*M* = Mn, Co; *M'* = Zn, Ni, Cu) were synthesised by solid-state reaction. Stoichiometric quantities of CeO_2, $MnCO_3$, Co_3O_4, NiO_2, ZnO, CuO and GeO_2 were mixed thoroughly in an agate mortar. A 10% excess of GeO_2 was added for the copper-free compounds to counteract its loss at high temperature. The copper-free mixtures were heated at 1075 °C for 4 days with intermediate cooling and regrinding every two days. They were then pressed into pellets and annealed at the same temperature for another 10 days with intermediate cooling and regrinding every two days. Further heating at 1100 °C for 1 day was carried out if GeO_2 was detected as an impurity phase. The copper-containing mixtures were synthesized using the same method but heated at 1050 °C because any higher temperature melted the mixture.

X-ray powder diffraction patterns were recorded at room temperature using Cu $K\alpha_1$ radiation. Neutron powder diffraction patterns were collected using wavelengths of 1.622 Å and 2.4395 Å on $CeMn_{1.5}Ni_{0.5}Ge_4O_{12}$ at room temperature and low temperatures. The

data were analysed by the Rietveld method [1] using the program GSAS [2], [3] and the peak function developed by van Laar and Yelon [4]. The magnetic structure was drafted by VESTA [5].

Magnetic measurements were performed using both Quantum Design MPMS XL and Quantum Design MPMS 5 SQUID magnetometers. DC susceptibility measurements were made over the temperature range 2 K ≤ T ≤ 300 K in an applied field of 100 Oe with both zero-field cooling (ZFC) and field-cooling (FC) of the samples. The field dependence of the magnetization was measured at 2 K over the field range -50 kOe ≤ H ≤ 50 kOe at 2K with the samples initially cooling in a 50 kOe magnetic field.

5.3 Results

5.3.1 Structural Chemistry

5.3.1.1 X-ray Diffraction

Single-phase compounds were obtained except for $CeMn_{1.5}Cu_{0.5}Ge_4O_{12}$ which contains $CuGeO_3$ [6] as an impurity. Cobalt-containing compounds were green in colour whereas manganese-containing compositions were brown. The XRPD patterns could all be indexed in the tetragonal space group *P*4/*nbm* (No. 125) as described in Chapter 3. The atom coordination is also consistent. The fitted room temperature X-ray diffraction patterns of $Ce\mathit{M}_{1.5}\mathit{M'}_{0.5}Ge_4O_{12}$ (*M* = Mn, Co; *M'* = Zn, Ni, Cu) are shown in Appendix A Figure A.10 – Figure A.15. Structural parameters derived from the refinements are listed in Table 5.1. $CuGeO_3$ (*Pbmm*, No.51) was detected as an impurity in $CeMn_{1.5}Cu_{0.5}Ge_4O_{12}$ at a level of 6.7(4) wt%.

Table 5.1 Structural parameters of $CeM_{1.5}M'_{0.5}Ge_4O_{12}$ (*M* = Mn, Co; *M'* = Zn, Ni, Cu) at room temperature derived from X-ray diffraction data (λ = 1.5406 Å)

		M = Mn			*M* = Co		
		M' = Zn	*M'* = Ni	*M'* = Cu	*M'* = Zn	*M'* = Ni	*M'* = Cu
Ge	*x*	0.5247(2)	0.5249(2)	0.5257(2)	0.5243(2)	0.5262(2)	0.5252(2)
O1	*x*	-0.3656(7)	-0.3668(7)	-0.3574(7)	-0.3656(9)	-0.3595(9)	-0.3605(10)
	z	0.1848(16)	0.1861(18)	0.2102(19)	0.1828(20)	0.2103(22)	0.1994(24)
O2	*x*	0.1632(7)	0.1656(7)	0.1626(8)	0.1605(9)	0.1630(9)	0.1612(9)
	y	0.0564(6)	0.0630(6)	0.0448(6)	0.0601(7)	0.0583(7)	0.0597(8)
	z	0.2576(12)	0.2561(12)	0.2488(14)	0.2584(14)	0.2519(14)	0.2574(15)
a/Å		9.8173(1)	9.8087(1)	9.7886(1)	9.7454(2)	9.7376(2)	9.7324(2)
c/Å		4.8856(1)	4.8784(1)	4.8715(1)	4.8192(1)	4.8117(1)	4.8119(1)
V/Å^3		470.87(2)	469.35(2)	466.77(2)	459.70(2)	456.25(2)	455.78(3)
R_{wpr}		13.49%	14.19%	14.73%	7.61%	7.86%	8.17%
χ^2		2.417	2.532	2.087	1.536	1.836	1.758

Space group *P*4/*nbm* (No. 125), Z = 2

Ce on 2*b* (¼, ¼, ½); *M*/*M'* (*M* = Mn, Co; *M'* = Zn, Ni, Cu) on 4*f* (0, 0, ½);

Ge on 8*k* (*x*, ¼, 0); O1 on 8*m* (*x*, -*x*, *z*); O2 on 16*n* (*x*, *y*, *z*)

The U_{iso} parameter of each atom was constrained to that reported by Taviot-Gueho. [1]

5.3.1.2 Room Temperature and Low Temperature Neutron Diffraction

Neutron-diffraction data were collected on $CeMn_{1.5}Ni_{0.5}Ge_4O_{12}$ at room temperature using wavelengths λ = 1.622 Å and at 1.6 K using two wavelengths λ = 1.622 and 2.4395 Å. The fitted patterns are shown in Figure 4.1, Figure 4.2 and Appendix B Figure B.20. Structural parameters of $CeMn_{1.5}Ni_{0.5}Ge_4O_{12}$ derived from the refinements are listed in Table 5.2. Some selected bond lengths and bond angles of $CeMn_{1.5}Ni_{0.5}Ge_4O_{12}$ derived from the neutron diffraction data are listed in Table 5.3. The magnetic structure of $CeMn_{1.5}Ni_{0.5}Ge_4O_{12}$ derived from λ = 2.4395 Å NPD data will be discussed in section 5.3.2.2.

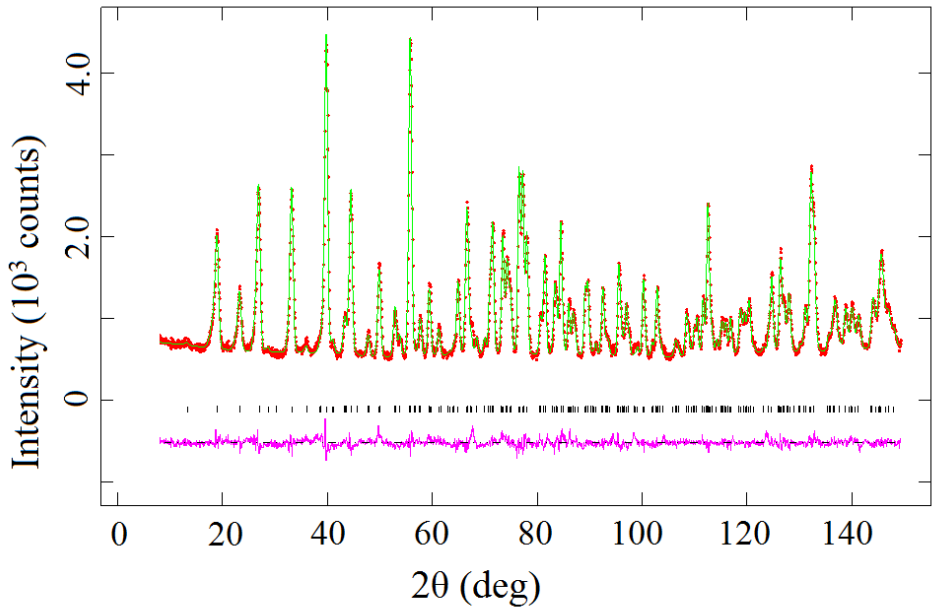

Figure 4.1 Observed (red dots) and calculated (green line) NPD patterns of $CeMn_{1.5}Ni_{0.5}Ge_4O_{12}$ at room temperature; λ = 1.622 Å. A difference curve (purple line) is shown and reflection positions are marked.

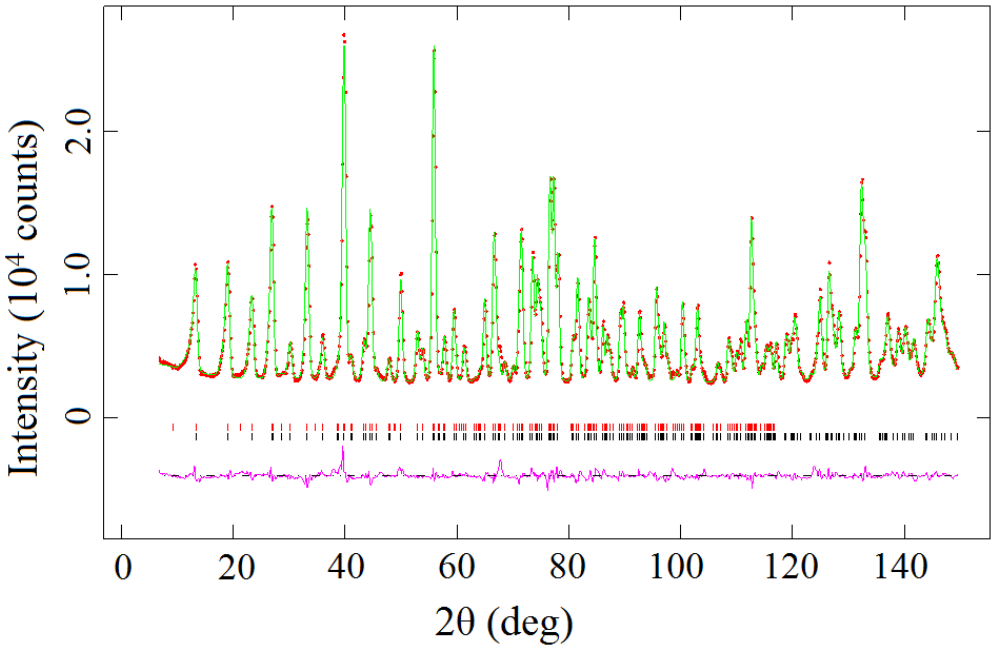

Figure 4.2 Observed (red dots) and calculated (green line) NPD patterns of $CeMn_{1.5}Ni_{0.5}Ge_4O_{12}$ at 1.6 K; λ = 1.622 Å. A difference curve (purple line) is shown and reflection positions are marked for the crystal structure (bottom) and the magnetic structure (top).

Table 5.2 Structural parameters of $CeMn_{1.5}Ni_{0.5}Ge_4O_{12}$ at 1.6 K and room temperature derived from neutron diffraction data (λ = 1.622 Å)

		T	
		1.6 K	RT
Ce	U_{iso}/Å^2	0.0029(9)	0.0038(7)
Mn/Ni	U_{iso}/Å^2	0.0093(8)	0.0176(23)
Ge	*X*	0.5242(1)	0.5242(1)
	U_{iso}/Å^2	0.0017(3)	0.0044(2)
O1	*X*	-0.3697(2)	-0.3701(1)
	Z	0.1732(3)	0.1726(3)
	U_{iso}/Å^2	0.0017(4)	0.0058(4)
O2	*x*	0.1651(1)	0.1653(1)
	y	0.0645(1)	0.0643(1)
	z	0.2560(3)	0.2552(2)
	U_{iso}/Å^2	0.0031(3)	0.0068(2)
a/Å		9.8016(2)	9.8062(1)
c/Å		4.8712(1)	4.8777(1)
V/Å^3		467.98(2)	469.05(2)
R_{wpr}		4.04%	4.48%
χ^2		8.505	1.899

Space group *P*4/*nbm* (No. 125), Z = 2

Ce on 2*b* (¼, ¼, ½); Mn/Ni on 4*f* (0, 0, ½);

Ge on 8*k* (*x*, ¼, 0); O1 on 8*m* (*x*, -*x*, *z*); O2 on 16*n* (*x*, *y*, *z*)

Table 5.3 Bond lengths (Å) and bond angles (degrees) in $CeMn_{1.5}Ni_{0.5}Ge_4O_{12}$ at 1.6 K and room temperature derived from neutron diffraction data (λ = 1.622 Å)

	T	
	1.6 K	RT
Ce-O2 × 8	2.326(1)	2.331(1)
Mn/Ni-O1 × 2	2.408(2)	2.408(1)
Mn/Ni-O2 × 4	2.105(1)	2.110(1)
O2-O2' *	3.182(2)	3.184(2)
O2-O2" *	2.756(2)	2.769(2)
Ge-O1 × 2	1.780(2)	1.781(1)
Ge-O2 × 2	1.733(2)	1.730(1)
O2-Mn/Ni-O2'	98.22(5)	97.98(4)
O2-Mn/Ni-O2"	81.78(5)	82.02(4)
O1-Mn/Ni-O2'	82.84(5)	82.70(4)
O1-Mn/Ni-O2"	97.16(5)	97.30(4)
O1-Ge-O1	108.48(8)	108.76(6)
O1-Ge-O2	105.67(8)	105.63(6)
O1-Ge-O2	108.52(8)	108.34(6)
O2-Ge-O2	119.81(8)	119.81(6)

* distances within the equatorial plane of the $(Mn/Ni)O_6$ octahedra

5.3.2 Magnetic Properties

5.3.2.1 DC Magnetisation Measurements

The temperature dependence of the dc molar susceptibility measured in a 100 Oe magnetic field of each sample is shown in Figure 5.3 and Figure 5.4, along with the field dependence of the magnetisation measured at 2 K. Magnetic parameters including the transition temperature, Curie and Weiss constants resulting from fitting the Curie-Weiss law to the FC data for T > 150 K are listed in Table 5.4. The impurity $CuGeO_3$ [6] shows a spin-Peierls transition at 20 K and the contribution of the susceptibility from the impurity is considered very low at low temperatures.

M'	χ / cm^3 mol^{-1}	$\boldsymbol{M}$ / μ_B per f.u.

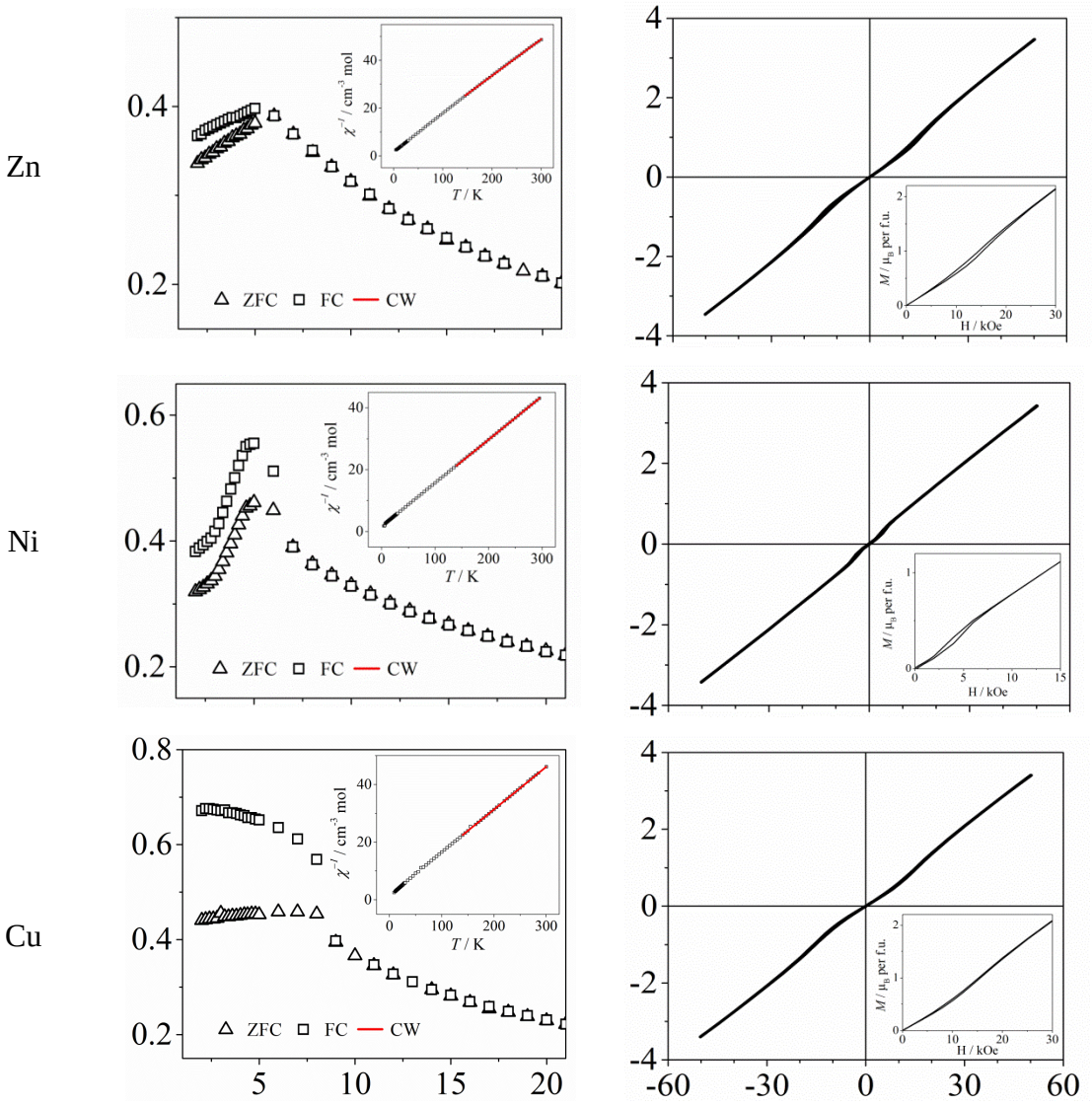

Figure 5.3 Temperature dependence of the dc molar magnetic susceptibility, measured in 100 Oe, and the field dependence of the magnetization at 2 K of $CeMn_{1.5}M'_{0.5}Ge_4O_{12}$ (*M'* = Zn, Ni, Cu). (inset) The inverse susceptibility; data points highlighted in red were fitted to the Curie−Weiss law.

M'	χ / cm^3 mol^{-1}	$\boldsymbol{M}$ / μ_B per f.u.

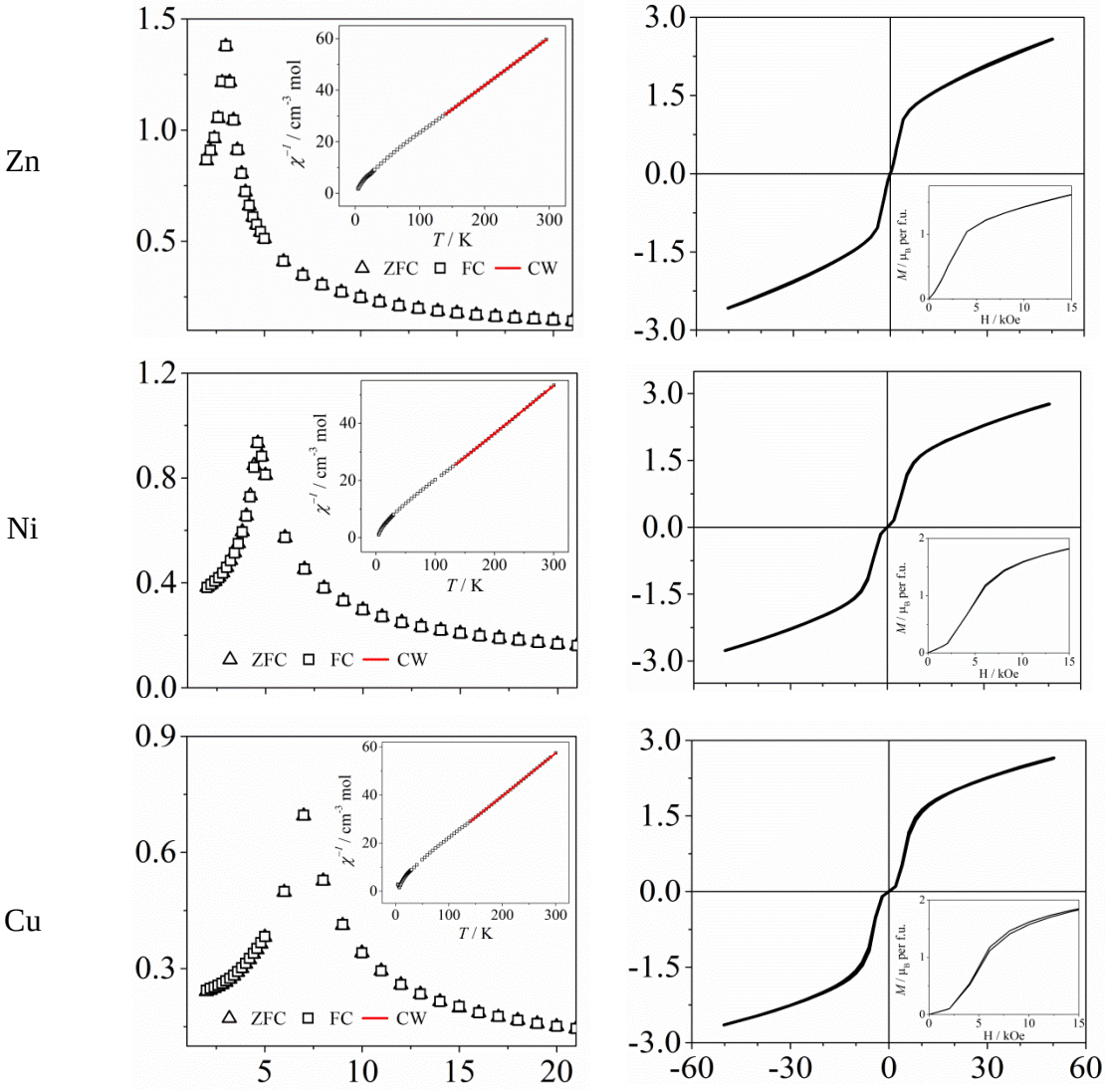

Figure 5.4 Temperature dependence of the dc molar magnetic susceptibility, measured in 100 Oe, and the field dependence of the magnetization at 2 K of $CeCo_{1.5}M'_{0.5}Ge_4O_{12}$ (*M'* = Zn, Ni, Cu). (inset) The inverse susceptibility; data points highlighted in red were fitted to the Curie−Weiss law.

Table 5.6 Magnetic parameters of $CeM_{1.5}M'_{0.5}Ge_4O_{12}$ (*M* = Mn, Co; *M'* = Zn, Ni, Cu)

	M = Mn			*M* = Co		
	M' = Zn	*M'* = Ni	*M'* = Cu	*M'* = Zn	*M'* = Ni	*M'* = Cu
C /cm^3 K mol^{-1}	6.549(1)	7.120(1)	6.757(1)	5.372(1)	5.977(1)	5.602(1)
θ /K	-19.78(2)	-11.49(2)	-11.75(1)	-24.88(2)	-17.21	-21.48
μ_{eff}/μ_B*	5.91	3.02	1.82	5.35	3.07	1.86
T_N /K	6.0	7.0	9.0	3.0	4.6	7.0

*calculated using μ_{eff} (Mn) = 5.91 and μ_{eff} (Co) = 5.35.

From the dc susceptibilities, all the compounds undergo an antiferromagnetic transition. The transition temperatures are all below 10 K. The manganese-containing compounds all show a hysteresis between the ZFC/FC susceptibilities below the Néel temperature. Also, a weak hysteresis between 0 < H/kOe < 30 exists in the M(H) curve. All these behaviours are similar to $CeMn_2Ge_4O_{12}$. The cobalt-containing compounds have similar dc susceptibility but the M(H) curve suggests that they may be metamagnets like $CeCo_2Ge_4O_{12}$. Further work would be needed to prove this hypothesis.

From the Curie-Weiss fitting, the effective moment of Mn^{2+} of $CeMn_{1.5}Zn_{0.5}Ge_4O_{12}$ is 5.91 μ_B, close to the theoretical value 5.92 μ_B and this value is the same as that of $CeMn_2Ge_4O_{12}$. The effective moment of Co^{2+} of $CeCo_{1.5}Zn_{0.5}Ge_4O_{12}$ is 5.35 μ_B and is also close that of $CeCo_2Ge_4O_{12}$. Assuming Mn^{2+} has a moment of 5.91 μ_B and Co^{2+} has a moment of 5.35 μ_B, the effective moments of Ni^{2+} and Cu^{2+} were determined to be 3.02 and 1.82 μ_B, slightly higher than their spin-only values 2.83 and 1.73 μ_B, respectively.

5.3.2.2 Zero-Field Low Temperature Neutron Diffraction

Neutron diffraction data were collected on $CeMn_{1.5}Ni_{0.5}Ge_4O_{12}$ at 1.6 K using wavelengths of λ = 1.622 and 2.4395 Å. The magnetic structure and the mean ordered atomic moment values were derived from λ = 2.4395 Å NPD data. Structural parameters were constrained from λ = 1.622 Å NPD data. The magnetic structure of the compound is shown in Figure 5.5.

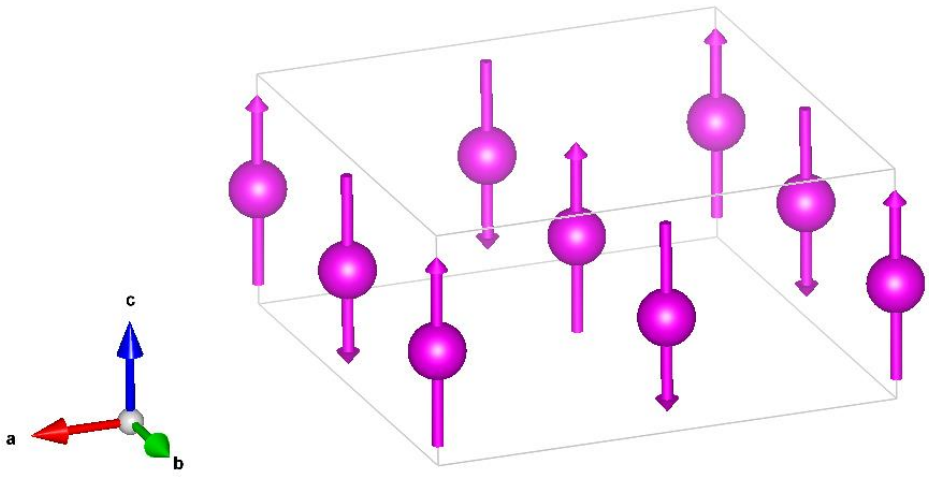

Figure 5.5 Magnetic structures in zero field of $CeMn_{1.5}Ni_{0.5}Ge_4O_{12}$. Diamagnetic ions are omitted.

The magnetic structure of $CeMn_{1.5}Ni_{0.5}Ge_4O_{12}$ can be described in the magnetic space group *P*4'/*nbm'* (No. 125.5.1035), which is the same as $CeMn_2Ge_4O_{12}$. The structural and magnetic unit cells are the same size. Nearest-neighbour (NN) magnetic cations within the (001) layer at z = ½ couple antiferromagnetically and align along the [001] axis. Next-nearest-neighbour (NNN) cations within this sheet align in a ferromagnetic manner and the NN cation-containing (001) layers are also arranged in a ferromagnetic manner. The ordered moment for the *4f* site, Mn^{2+}:Ni^{2+} (1.5:0.5), was determined to be 3.70(2) μ_B.

5.3.3 Discussion

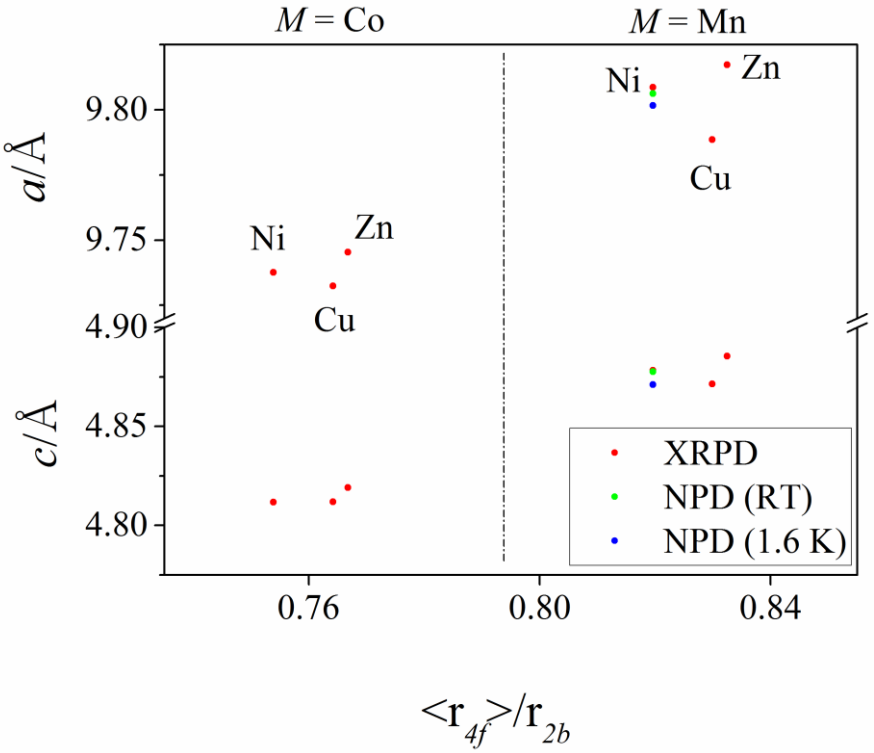

Figure 5.6 Structural unit cell parameters *a* and *c* derived from diffraction data. The error bars are smaller than the size of the points.

Table 5.7 Derived structural parameters for $CeMn_{1.5}Ni_{0.5}Ge_4O_{12}$ from NPD, 1.6 K, λ = 1.622 Å

2b	*4f*	$<r_{4f}>/r_{2b}$	*2c/a*	$d(M_{4f}-O2)/d(M_{4f}-O1)$	*φ* /°	*ψ* /°	*q*
Ce	Mn/Ni	0.820	0.9941	0.874(1)	78.99(12)	41.39(6)	0.840(1)

φ Angle between M_{4f} – O1 bond and M_{4f} – O2 plane

ψ Angle between the M_{4f} – O1 bond and the (001) plane

q Ratio of O2 – O2 distance in square face of antiprism to perpendicular distance between faces

Table 5.8 Calculated 2*c*/*a* ratio for $CeMn_{1.5}Ni_{0.5}Ge_4O_{12}$ from XRPD, RT, λ = 1.5406 Å

	M = Mn			*M* = Co		
	M' = Zn	*M'* = Ni	*M'* = Cu	*M'* = Zn	*M'* = Ni	*M'* = Cu
2*c*/*a*	0.9953	0.9947	0.9953	0.9890	0.9883	0.9888

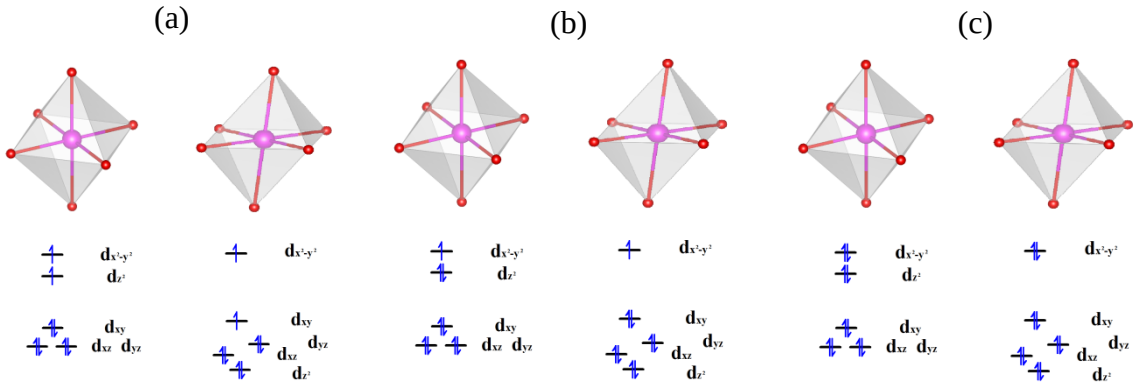

Figure 5.7 The crystal field splitting of the *d* orbitals for six-coordinate M^{2+} of (a) Ni^{2+} (b) Cu^{2+} (b) Zn^{2+} in an octahedron with a small tetragonal elongation (left) and in an octahedron with a monoclinic distortion in addition to a large tetragonal elongation (right).

The difference in cation size between Zn^{2+} (r = 0.74 Å) and Ni^{2+} (r = 0.69 Å) [7] would be expected to determine the variations in the unit cell parameters *a* and *c* in the solid solutions. However, the copper-containing ones are unexpectedly short, see Figure 5.6. This is probably because Cu^{2+} is a cation with strong Jahn-Teller effect and the local distortions might have consequences of the unit cell parameters *a* and *c*. The e_g orbitals in an octahedron with a small tetragonal elongation would split into d_{x2-y2} and d_{z2}, see Figure 5.7 left. The two orbitals are antibonding orbitals as the energy is high and the bond lengths are a function of the cation radii. However, when the cation is in a much distorted environment, the orbitals reassign into the arrangement shown to the right of Figure 5.7. d_{x2-y2} is now the only antibonding orbital whereas the other four are non-bonding orbitals. Compared to Ni^{2+}, Cu^{2+} has one more electron in the bonding orbital and thus the bond length is expected to be smaller. Moreover, compared to Zn^{2+}, Cu^{2+} has one less electron in the antibonding orbital and thus the bond length is also expected to be smaller. Hence, the unit cell parameters *a* and *c* of $CeM_{1.5}Cu_{0.5}Ge_4O_{12}$ are consequently smaller than those of $CeM_{1.5}Ni_{0.5}Ge_4O_{12}$ and $CeM_{1.5}Zn_{0.5}Ge_4O_{12}$. The calculated $2c/a$ ratios for the compounds are listed in Table 5.8. The ratios in the Cu compounds are essentially the same as the others despite their short unit cell parameters.

That Zn^{2+} is a non-magnetic cation makes $CeM_{1.5}Zn_{0.5}Ge_4O_{12}$ (*M* = Mn, Co) have almost the same χ(T) and M(H) curve as $CeM_2Ge_4O_{12}$ (*M* = Mn, Co) with only a reduction in the Néel temperature, ~ 1.5 K, but a significant enhancement on the Weiss constant. A dilution of the magnetic system by Zn^{2+} leading to a lower transition temperature is expected.

Moreover, the Weiss constant is a consequence of all interactions. The superexchange in the germanate system is achieved via *M* – O – Ge – O – *M* and *M* – O2 – Ge – O2 – *M* is expected to be the strongest pathway as discussed before. However, we note that though J_4, as defined in Chapter 3, is the most significant one, J_2 and J_3 are still strong. Thus, the substitution by Zn^{2+} can vary the relative exchange strength among $J_1 – J_6$ and it may be the reason that the Weiss constant is more negative for Zn-containing compounds.

$CeMn_{1.5}M'_{0.5}Ge_4O_{12}$ (*M'* = Zn, Ni, Cu) all show a hysteresis in the dc susceptibility below the Néel temperature. Hysteresis is also seen in the field dependence of the magnetisation except when *M'* = Cu. Both Mn^{2+} and Ni^{2+} have a relatively small single-ion anisotropy and the magnetic structure of $CeMn_{1.5}M'_{0.5}Ge_4O_{12}$ (*M'* = Zn, Ni, Cu) is therefore expected to be the same as $CeMn_2Ge_4O_{12}$. One composition, $CeMn_{1.5}Ni_{0.5}Ge_4O_{12}$, was examined to prove this. Co^{2+} is a strong anisotropic cation, and $CeMn_{1.5}Co_{0.5}Ge_4O_{12}$ thus has different magnetic behaviour and different magnetic structure. The anisotropy of Co^{2+} can cause the moments that lie along [001] axis to rotate into the (001) plane whereas a weakly anisotropic cation, Ni^{2+}, cannot. It is notable that with different cations used, the field that is able to cause the hysteresis seen in the field dependence of the magnetisation has changed, 4 kOe for *M'* = Ni, 15 kOe for *M'* = Zn, 16 kOe for *M'* = Cu, and 21 kOe for the original case *M'* = Mn, see Figure 5.8.

The dc susceptibilities of $CeCo_{1.5}M'_{0.5}Ge_4O_{12}$ (*M'* = Zn, Ni, Cu) are almost the same as $CeCo_2Ge_4O_{12}$. The field dependence of the magnetisation of $CeCo_{1.5}M'_{0.5}Ge_4O_{12}$ (*M'* = Zn, Ni, Cu, Mn, Co) suggest that they all have a metamagnetic transition and we propose it is the same first-order metamagnetic transition as $CeCo_2Ge_4O_{12}$ and they may have the same magnetic structure. Similarly, different cations can lead to different transition field, 1.79 kOe for *M'* = Zn, 2.20 kOe for *M'* = Mn, 4.09 kOe for *M'* = Ni and Cu, and 4 kOe for the original case *M'* = Co, see Figure 5.9.

Further neutron diffraction experiments would be necessary in order to test the hypothesis.

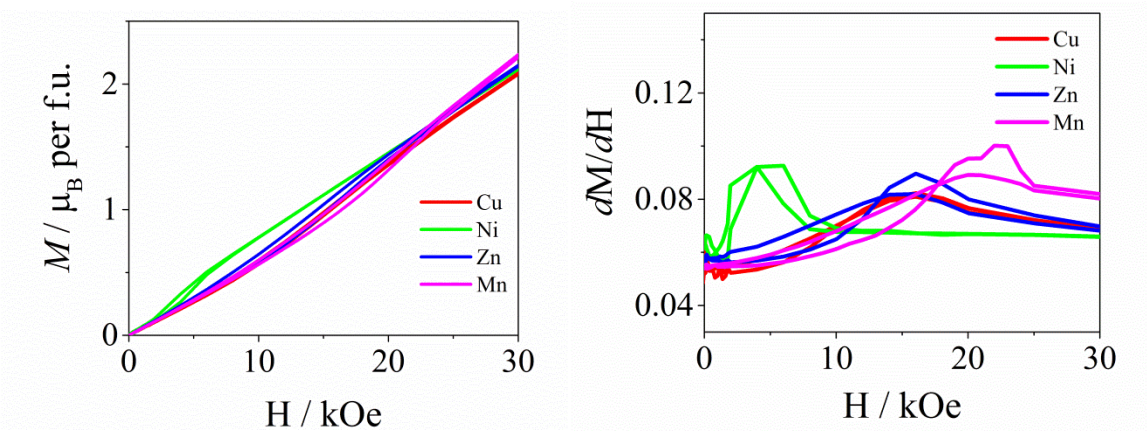

Figure 5.8 Field dependence of the magnetisation and the derivative of $CeMn_{1.5}M'_{0.5}Ge_4O_{12}$ (*M'* = Zn, Ni, Cu, Mn) at 2 K.

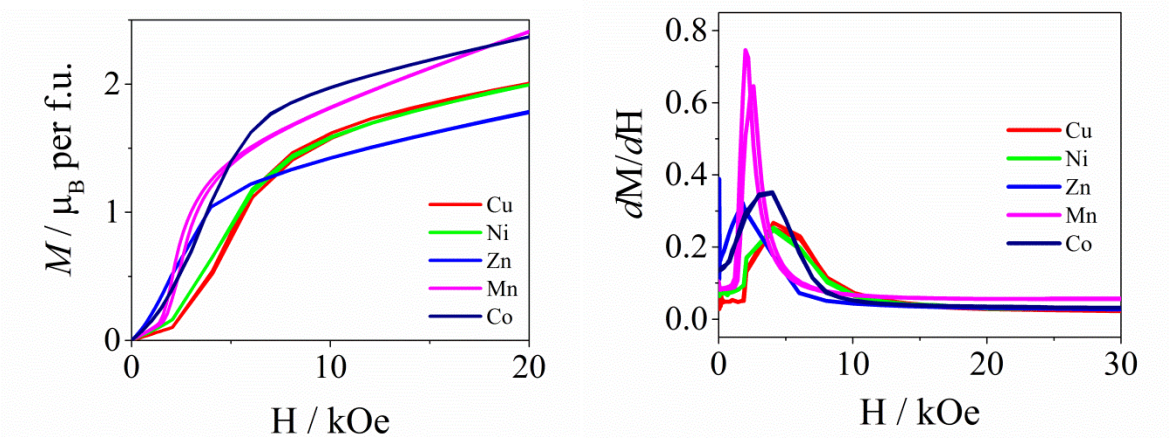

Figure 5.9 Field dependence of the magnetisation and the derivative of $CeCo_{1.5}M'_{0.5}Ge_4O_{12}$ (*M'* = Zn, Ni, Cu, Mn, Co) at 2 K.

5.3.4 Conclusion

The solid solution $CeM_{1.5}M'_{0.5}Ge_4O_{12}$ (*M* = Mn, Co; *M'* = Zn, Ni, Cu) can be successfully prepared. All compositions in the solution order magnetically at low temperature, T < 10 K. The Co-containing compounds $CeCo_{1.5}M'_{0.5}Ge_4O_{12}$ (*M'* = Zn, Ni, Cu) have similar magnetic properties to $CeCo_2Ge_4O_{12}$ whereas the Mn-containing ones are similar to $CeMn_2Ge_4O_{12}$. Neutron diffraction data were collected on $CeMn_{1.5}Ni_{0.5}Ge_4O_{12}$ proving that it has the same magnetic structure as $CeMn_2Ge_4O_{12}$. Different doping cations, *M'*, can lead to differences in M(H). There is clearly scope for further experimental work on these compositions

5.4 References

[1] H. M. Rietveld, A profile refinement method for nuclear and magnetic structures, *Journal of Applied Crystallography*, **1969**, *2*, 65-71.

[2] B. H. Toby, EXPGUI, a graphical user interface for GSAS, *Journal of Applied Crystallography*, **2001**, *34*, 210-213.

[3] A. C. Larson, and R. B. Von Dreele, *General Structure Analysis System (GSAS)*, Los Alamos National Laboratory Report LAUR 86-748: **2004**.

[4] B. van Laar, and W. B. Yelon, The peak in Neutron Powder Diffraction, *Journal of Applied Crystallography*, **1984**, *17*, 47-54.

[5] K. Momma, and F. Izumi, VESTA: a three-dimensional visualization system for electronic and structural analysis, *Journal of Applied Crystallography*, **2008**, *41*, 653-658.

[6] M. A. Green, M. Kurmoo, J. K. Stalick, and P. Day The crystal structure and magnetic properties of $CuGeO_3$, *Journal of the Chemical Society, Chemical Communications*, **1994**, *0*, 1995-1996.

[7] R. D. Shannon, Revised effective ionic radii and systematic studies of interatomic distances in halides and chalcogenides, *Acta Crystallographica Section A: Crystal Physics, Diffraction Theoretical, and General Crystallography*, **1976**, *A32*, 751.

Chapter 6 - Synthesis and Characterisation of *Ln*$FeMnGe_4O_{12}$ (*Ln* = Eu, Lu, Y)

6.1 Introduction

We have shown in Chapters 3 and 4 that the magnetic properties of $CeMn_{2-x}Co_xGe_4O_{12}$ and $ZrMn_{2-x}Co_xGe_4O_{12}$ are sensitive to the identity of the tetravalent cation and to the relative concentrations of manganese and cobalt. The behaviour of $CeMn_{1.5}Ni_{0.5}Ge_4O_{12}$, described in Chapter 5, supports our proposal that the single-ion anisotropy of Co^{2+} drives some of the changes that occur as a function of composition in the solid solution. In this and the following chapters, we describe the consequence of reducing the charge on the cation at the *2b* site from +4 to +3. Specifically, we describe the introduction of the non-magnetic cations Y^{3+}, Eu^{3+} and Lu^{3+} in this chapter and magnetic cations *Ln* = Gd – Yb in Chapters 7 and 8. The reduction in the charge at the *2b* site necessitates an increase at the *4f* site in order to maintain electrical neutrality. We chose a 1:1 ratio of Fe and Mn for the *4f* site and thus expected to find either Fe^{3+} and Mn^{2+} or Fe^{2+} and Mn^{3+}. The former pair, Fe^{3+} and Mn^{2+}, has two isotropic cations with $3d^5$ electron configuration whereas the later pair contains two anisotropic ones. Mn^{3+} is prone to occupy low-symmetry six-coordinate sites, like those in this structure, in order to remove the degeneracy of the $3d^4$ electron configuration. The low ionisation energy of Fe^{2+} might be expected to favour the Fe^{3+} and Mn^{2+} combination. We discuss below both the resolution of this question and the magnetic behaviours of *Ln*$FeMnGe_4O_{12}$ (*Ln* = Eu, Lu and Y).

6.2 Experiment

Polycrystalline samples of *Ln*$FeMnGe_4O_{12}$ (*Ln* = Eu, Lu and Y) were synthesised by solid-state reaction. Stoichiometric quantities of Ln_2O_3, Fe_3O_4, $MnCO_3$, and GeO_2 were mixed thoroughly in an agate mortar, along with a 10% excess of GeO_2 to counteract its loss at high temperature. The mixtures were heated at 1075 °C for 4 days with intermediate cooling and regrinding every two days. They were then pressed into pellets and annealed at the same temperature for another 4 days with intermediate cooling and regrinding every

two days. Further heating at 1100 °C for 1 day was carried out if GeO_2 was detected as an impurity phase.

X-ray powder diffraction patterns were recorded at room temperature using Cu $K\alpha_1$ radiation. Neutron powder diffraction patterns were collected using a wavelength of either 1.622 Å or 2.4395 Å. The measurements were performed at room temperature and 3.5 K. The data were analysed by the Rietveld method [1] using the program GSAS [2], [3] and the peak function developed by van Laar and Yelon [4]. The magnetic structure was drafted by VESTA [5].

Magnetic measurements were performed using both Quantum Design MPMS XL and Quantum Design MPMS 5 SQUID magnetometers. DC susceptibility measurements were made over the temperature range $2\ K \leq T \leq 300\ K$ in an applied field of 100 Oe with both zero-field cooling (ZFC) and field-cooling (FC) of the samples. The field dependence of the magnetization was measured over the field range $-50\ kOe \leq H \leq 50\ kOe$ at 2K after initially cooling in a 50 kOe magnetic field. The AC susceptibility of $LuFeMnGe_4O_{12}$ was measured at frequencies 1, 10, 100, 1000 Hz over the temperature range $2\ K \leq T \leq 12\ K$ in a 3.5 Oe AC driving field. Samples were ac-degaussed and then cooled in a small dc field of 3 Oe to counteract the remaining field in the SQUID.

An ^{57}Fe Mössbauer spectrum was collected by J. M. Cadogan from a polycrystalline sample of $YMnFeGe_4O_{12}$ at 295 K using a standard transmission spectrometer and a ^{57}Co**Rh** source. The drive velocity of the spectrometer was calibrated using a 6 μm thick α-Fe foil, at 295 K, and the isomer shift (δ) is quoted relative to the centre of the α-Fe calibration spectrum. The spectrum was fitted using the NORMOS software [6].

6.3 Results

6.3.1 Structural Chemistry

6.3.1.1 X-ray Diffraction

Single-phase samples of *Ln*$FeMnGe_4O_{12}$ (*Ln* = Eu, Lu and Y) were obtained. All the products were brown in colour. The XRPD patterns could all be indexed in the tetragonal space group *P*4/*nbm* (No. 125) as in Chapter 3. The *2b* site is occupied by the diamagnetic cation *Ln* and the *4f* site is randomly occupied by a mixture of iron and manganses. The fitted room-temperature X-ray diffraction patterns of *Ln*$FeMnGe_4O_{12}$ (*Ln* = Eu, Lu and Y) are shown in Appendix A Figure A.16 - Figure A.18. Structural parameters derived from the refinements are listed in Table 6.1.

Table 6.1 Structural parameters of *Ln*$FeMnGe_4O_{12}$ (*Ln* = Eu, Lu and Y) at room temperature derived from X-ray diffraction data (λ = 1.5406 Å)

		x		
		Eu	Lu	Y
Ge	*x*	0.5268(3)	0.5214(2)	0.5227(1)
O1	*x*	-0.3650(11)	-0.3691(7)	-0.3685(5)
	z	0.1871(24)	0.1849(19)	0.1855(12)
O2	*x*	0.1594(11)	0.1606(7)	0.1599(5)
	y	0.0601(9)	0.0615(6)	0.0604(4)
	z	0.2596(17)	0.2603(15)	0.2593(8)
a/Å		9.8152(1)	9.6712(1)	9.7260(1)
c/Å		4.8041(1)	4.8181(1)	4.8142(1)
V/$Å^3$		462.81(2)	450.65(1)	455.40(1)
R_{wpr}		5.90%	5.41%	5.37%
χ^2		1.402	1.442	1.397

Space group *P*4/*nbm* (No. 125), Z = 2

Ln on 2*b* (¼, ¼, ½); Fe/Mn on 4*f* (0, 0, ½);

Ge on 8*k* (*x*, ¼, 0); O1 on 8*m* (*x*, -*x*, *z*); O2 on 16*n* (*x*, *y*, *z*)

The U_{iso} parameter of each atom was constrained to that reported by Taviot-Gueho. [1]

6.3.1.2 Room Temperature Neutron Diffraction

Neutron-diffraction data were collected on all the samples at room temperature using a wavelength of λ = 1.622 Å. An absorption correction was applied in the case of *Ln* = Eu. The absorption correction factor [7], calculated on the basis of the sample mass and geometry, was held constant during the data analysis. The displacement parameters of Eu were constrained to the reference values [8], [9] during the data analysis. The fitted patterns of *Ln*$FeMnGe_4O_{12}$ (*Ln* = Eu, Lu and Y) are shown in Figure 6.1 and Appendix B Figure B.22 – Figure B.23. Structural parameters derived from the refinements are listed in Table 6.2. Some selected bond lengths and bond angles derived from the room-temperature neutron diffraction data are listed in Table 6.3.

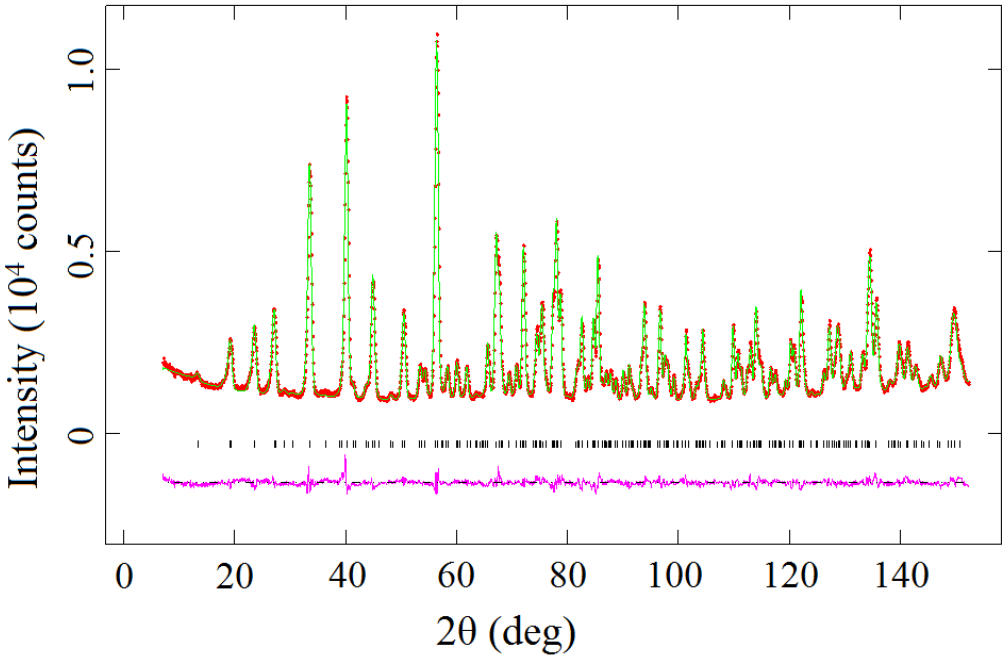

Figure 6.1 Observed (red dots) and calculated (green line) NPD patterns of $YFeMnGe_4O_{12}$ at room temperature; λ = 1.622 Å. A difference curve (purple line) is shown and reflection positions are marked.

Table 6.2 Structural parameters of LnFeMnGe$_4$O$_{12}$ (Ln = Eu, Lu and Y) at room temperature derived from neutron diffraction data (λ = 1.622 Å)

		Ln		
		Eu	Lu	Y
Ln	U_{iso}/Å^2	0.0102	0.0062(6)	0.0056(4)
Fe/Mn	U_{iso}/Å^2	0.0078(20)	0.0065(11)	0.0052(8)
Ge	*x*	0.5259(2)	0.5210(1)	0.5227(1)
	U_{iso}/Å^2	0.0049(5)	0.0042(2)	0.0042(2)
O1	*x*	-0.3688(3)	-0.3694(1)	-0.3688(1)
	z	0.1840(6)	0.1805(3)	0.1811(2)
	U_{iso}/Å^2	0.0107(8)	0.0070(3)	0.0062(3)
O2	*x*	0.1606(3)	0.1614(1)	0.1611(1)
	y	0.0596(2)	0.0644(1)	0.0626(1)
	z	0.2561(6)	0.2592(2)	0.2574(2)
	U_{iso}/Å^2	0.0119(4)	0.0098(2)	0.0096(2)
a/Å		9.8083(3)	9.6662(1)	9.7259(1)
c/Å		4.8030(2)	4.8158(1)	4.8130(1)
V/Å^3		462.07(3)	449.97(1)	455.27(1)
R_{wpr}		2.58%	4.58%	3.84%
χ^2		2.007	1.973	2.666

Space group *P*4/*nbm* (No. 125), Z = 2

Ln on 2*b* (¼, ¼, ½); Fe/Mn on 4*f* (0, 0, ½);

Ge on 8*k* (*x*, ¼, 0); O1 on 8*m* (*x*, -*x*, *z*); O2 on 16*n* (*x*, *y*, *z*)

Table 6.3 Bond lengths (Å) and bond angles (degrees) in *Ln*$FeMnGe_4O_{12}$ (*Ln* = Eu, Lu and Y) at room temperature derived from neutron diffraction data (λ = 1.622 Å)

	Ln		
	Eu	Lu	Y
Ln-O2 × 8	2.372(3)	2.301(2)	2.331(1)
Fe/Mn-O1 × 2	2.369(3)	2.357(1)	2.369(1)
Fe/Mn-O2 × 4	2.049(3)	2.041(1)	2.047(1)
Mean Fe/Mn - O	2.156	2.146	2.154
O2-O2' *	3.055(4)	3.087(2)	3.077(1)
O2-O2" *	2.730(4)	2.672(2)	2.700(1)
Ge-O1 × 2	1.790(3)	1.792(1)	1.792(1)
Ge-O2 × 2	1.728(3)	1.724(1)	1.723(1)
O2-Fe/Mn-O2'	96.43(10)	98.26(4)	97.47(4)
O2-Fe/Mn-O2"	83.57(10)	81.74(4)	82.53(4)
O1-Fe/Mn-O2'	84.05(10)	82.83(4)	83.26(4)
O1-Fe/Mn-O2"	95.95(10)	97.17(4)	96.74(4)
O1-Ge-O1	109.56(14)	107.51(6)	107.81(5)
O1-Ge-O2	105.00(14)	104.58(6)	104.90(5)
O1-Ge-O2	107.53(14)	108.33(6)	108.04(5)
O2-Ge-O2	121.91(14)	122.78(6)	122.47(5)

* distances within the equatorial plane of the $(Fe/Mn)O_6$ octahedra

6.3.1.3 Low Temperature Neutron Diffraction

Neutron-diffraction data were collected on all the samples at 3.5 K using wavelengths of λ = 1.622 and 2.4395 Å. The fitted patterns of λ = 1.622 Å NPD data are shown in Figure 6.2 and Appendix B Figure B.24 – Figure B.25. Structural parameters derived from the λ = 1.622 Å NPD data are listed in Table 6.4. Some selected bond lengths and bond angles derived from 3.5 K neutron diffraction are listed in Table 6.5. The magnetic structures derived from λ = 2.4395 Å NPD data will be discussed in section 6.3.2.3.

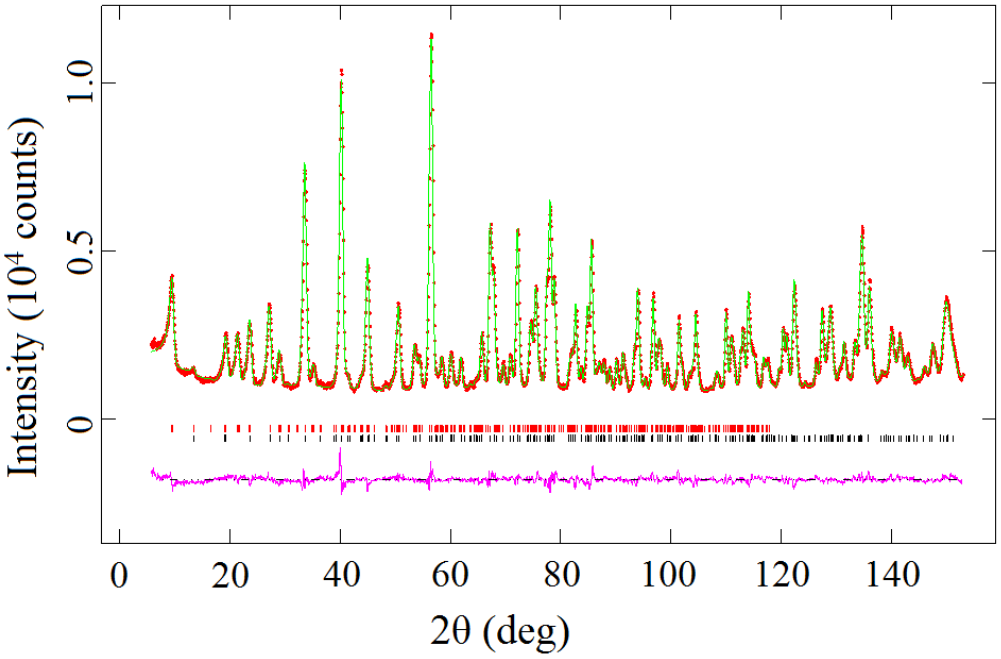

Figure 6.2 Observed (red dots) and calculated (green line) NPD patterns of $YFeMnGe_4O_{12}$ at 3.5 K; λ = 1.622 Å. A difference curve (purple line) is shown and reflection positions are marked for the crystal structure (bottom) and the magnetic structure (top).

Table 6.4 Structural parameters of LnFeMnGe$_4$O$_{12}$ (Ln = Eu, Lu and Y) at 3.5 K derived from neutron diffraction data (λ = 1.622 Å)

		Ln		
		Eu	Lu	Y
Ln	U_{iso}/Å^2	0.0092	0.0020(5)	0.0017(4)
Fe/Mn	U_{iso}/Å^2	0.0059(19)	0.0005(1)	0.0009(2)
Ge	*x*	0.5263(2)	0.5213(1)	0.5230(1)
	U_{iso}/Å^2	0.0040(4)	0.0002(1)	0.0004(1)
O1	*x*	-0.3685(3)	-0.3694(1)	-0.3686(1)
	z	0.1839(6)	0.1798(2)	0.1813(2)
	U_{iso}/Å^2	0.0085(7)	0.0024(3)	0.0024(3)
O2	*x*	0.1603(3)	0.1614(2)	0.1609(1)
	y	0.0592(2)	0.0643(1)	0.0626(1)
	z	0.2552(6)	0.2588(2)	0.26579(2)
	U_{iso}/Å^2	0.0100(4)	0.0066(2)	0.0060(2)
a/Å		9.8036(3)	9.6629(1)	9.7223(1)
c/Å		4.7970(3)	4.8096(1)	4.8065(1)
V/Å^3		461.04(3)	449.08(1)	454.33(1)
R_{wpr}		3.20%	4.52%	4.23%
χ^2		2.393	2.273	3.331

Space group *P*4/*nbm* (No. 125), Z = 2

Ln on 2*b* (¼, ¼, ½); Fe/Mn on 4*f* (0, 0, ½);

Ge on 8*k* (*x*, ¼, 0); O1 on 8*m* (*x*, -*x*, z); O2 on 16*n* (*x*, *y*, *z*)

Table 6.5 Bond lengths (Å) and bond angles (degrees) in $LnFeMnGe_4O_{12}$ (*Ln* = Eu, Lu and Y) at 3.5 K derived from neutron diffraction data (λ = 1.622 Å)

	Ln		
	Eu	Lu	Y
Ln-O2 × 8	2.377(2)	2.301(2)	2.329(1)
Fe/Mn-O1 × 2	2.372(3)	2.357(1)	2.368(1)
Fe/Mn-O2 × 4	2.045(3)	2.041(1)	2.042(1)
O2-O2' *	3.042(4)	3.086(2)	3.073(1)
O2-O2" *	2.734(4)	2.673(2)	2.690(1)
Ge-O1 × 2	1.787(3)	1.788(1)	1.789(1)
Ge-O2 × 2	1.725(3)	1.722(1)	1.726(1)
O2-Fe/Mn-O2'	96.10(10)	98.20(4)	97.60(4)
O2-Fe/Mn-O2"	83.90(10)	81.80(4)	82.40(4)
O1-Fe/Mn-O2'	84.06(10)	82.81(4)	83.32(4)
O1-Fe/Mn-O2"	95.94(10)	97.20(4)	96.68(4)
O1-Ge-O1	109.45(14)	107.54(6)	107.84(5)
O1-Ge-O2	105.15(14)	104.77(6)	104.95(5)
O1-Ge-O2	107.42(14)	108.24(6)	108.06(5)
O2-Ge-O2	121.90(14)	122.57(6)	122.35(5)

* distances within the equatorial plane of the $(Fe/Mn)O_6$ octahedra

6.3.2 Mössbauer spectrum

The room-temperature Mössbauer spectrum of $YFeMnGe_4O_{12}$ is shown in Figure 6.3 and the parameters used to fit it are listed in Table 6.6.

Table 6.6 Mössbauer parameters of $YFeMnGe_4O_{12}$ at room temperature

δ / mm s^{-1}	$\|\Delta\|$ / mm s^{-1}	Γ / mm s^{-1}
0.407(2)	2.086(2)	0.376(4)

δ is the isomer shift, relative to α-Fe at room temperature; $|\Delta|$ is the magnitude of the electric quadrupole splitting and Γ is the full linewidth at half-maximum intensity.

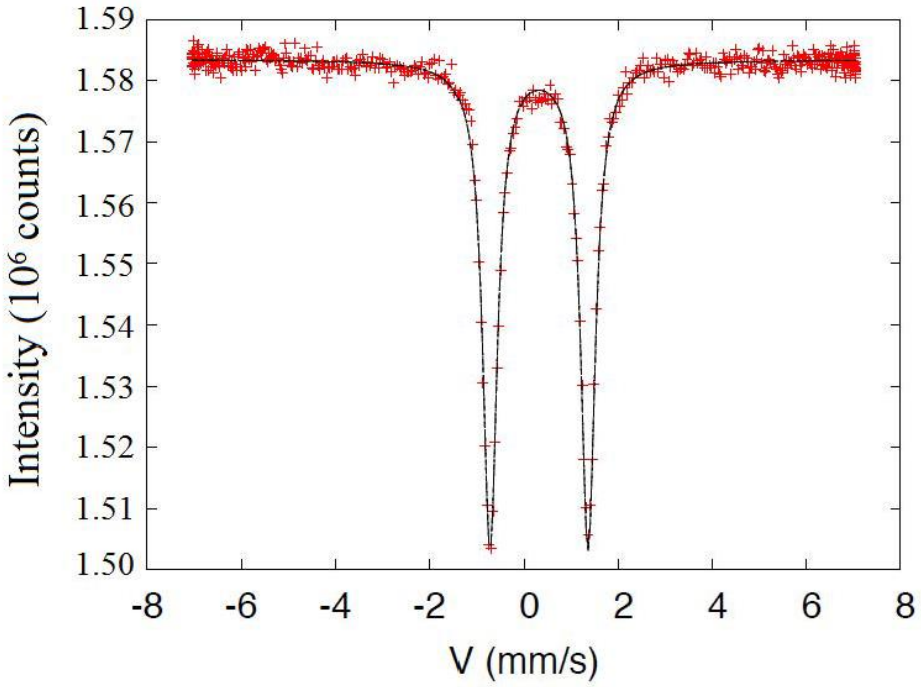

Figure 6.3 ^{57}Fe Mössbauer spectrum of $YFeMnGe_4O_{12}$ collected at room temperature and fitted using a single quadrupole-split doublet component.

From the Mössbauer spectroscopy of $YFeMnGe_4O_{12}$, the isomer shift is consistent with the presence of high-spin, spherical Fe^{3+} cations but the quadrupole splitting is unusually large for such a species. The alternative explanation, based on the presence of aspherical Fe^{2+}, is more consistent with the magnitude of the quadrupole splitting but the observed isomer shift is significantly lower than would be expected in that case. From further magnetometry measurements, the observation of an average effective magnetic moment of ~5.9 μ_B for the transition metals for all *Ln* also strongly suggests that all the cations have $3d^5$ electron configurations and that Mn^{2+} and Fe^{3+} cations are therefore present. In that case, the quadrupole splitting of 2.086(2) mm s^{-1} is unusually large for a high-spin Fe^{3+} compound [10]. The electric-field gradient created by the irregular coordination sphere at *4f* site is presumably responsible for the large quadrupole splitting observed in the Mössbauer spectrum.

6.3.3 Magnetic Properties

6.3.3.1 DC Magnetisation Measurements

The temperature dependence of the dc molar susceptibility measured in a 100 Oe magnetic field of each sample is shown in Figure 6.4, along with the field dependence of the magnetisation measured at 2 K. The Néel temperature of *Ln* = Eu, Lu, Y and the magnetic parameters resulting from fitting the Curie-Weiss law to the FC data for T > 150 K are listed in Table 6.7.

From the dc susceptibilities, the solid solutions are all antiferromagnets with transition temperatures about 16 K. The χ(T) and M(H) curve of $EuFeMnGe_4O_{12}$ and $YFeMnGe_4O_{12}$ are almost the same whereas the susceptibility of $LuFeMnGe_4O_{12}$ increases below the Néel temperature and reaches its maximum at around 8 K. Also, both the susceptibility and the magnetization of $LuFeMnGe_4O_{12}$ have a greater value. The average effective moment of Fe^{3+}/Mn^{2+} is about 5.92 μ_B of the three compounds, the same to the spin-only value 5.92 μ_B of a d^5 cation. The Weiss constants of $EuFeMnGe_4O_{12}$ and $YFeMnGe_4O_{12}$ are about -40 K while $LuFeMnGe_4O_{12}$ has a smaller value.

Table 6.7 Magnetic parameters of $LnFeMnGe_4O_{12}$ (*Ln* = Eu, Lu and Y)

	Ln		
	Eu	Lu	Y
C /cm^3 K mol^{-1}	8.758(1)	8.724(1)	8.766(1)
θ /K	-37.12(2)	-22.89(2)	-44.46(2)
$\mu^{(Fe/Mn)}_{eff}$	5.92	5.91	5.92
T_N /K	17.0	15.0	16.0

Ln	χ / cm^3 mol^{-1}	***M*** / μ_B per f.u.

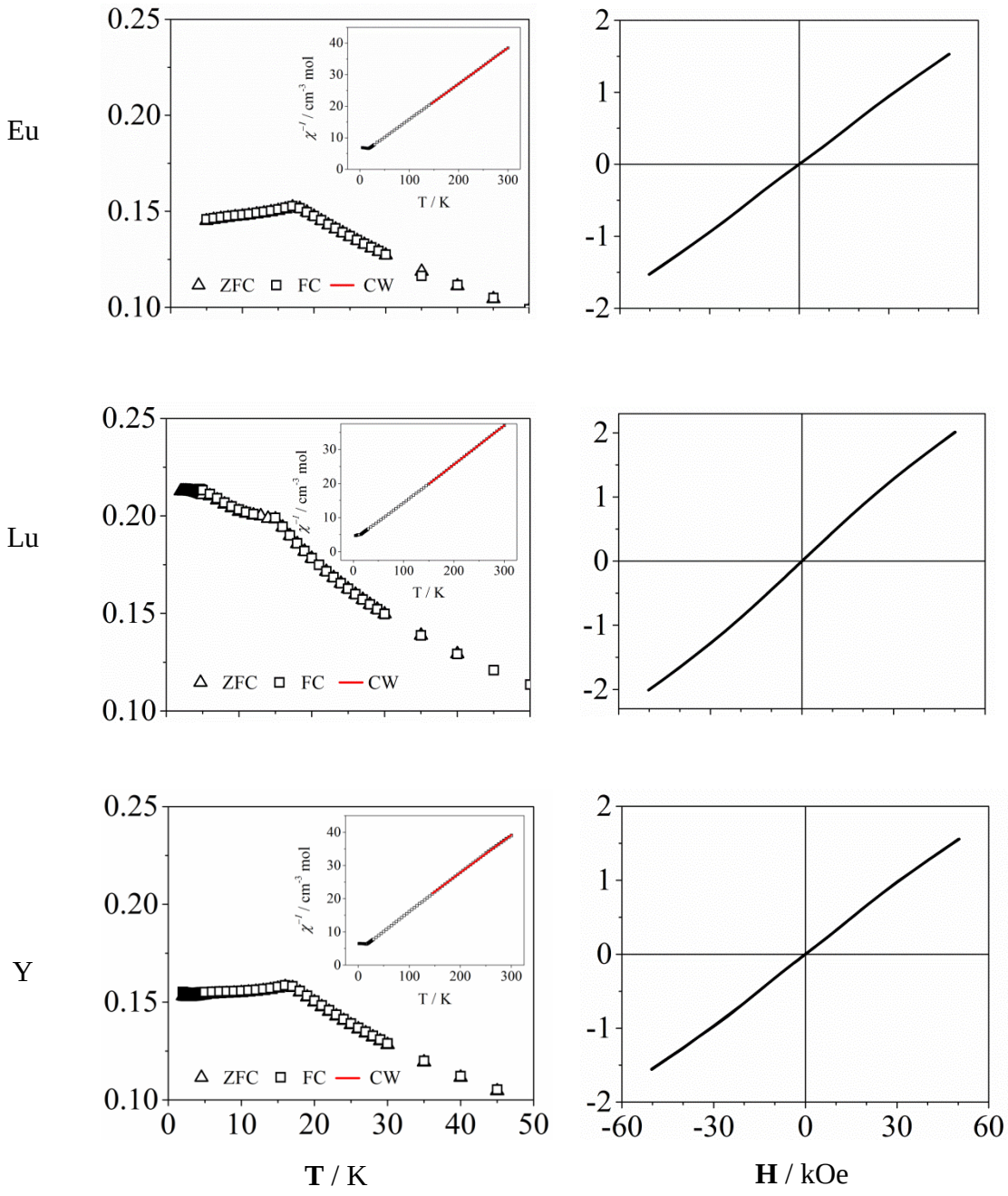

Figure 6.4 Temperature dependence of the dc molar magnetic susceptibility, measured in 100 Oe, and the field dependence of the magnetization at 2 K of $LnFeMnGe_4O_{12}$ (*Ln* = Eu, Lu and Y). (inset) The inverse susceptibility; data points highlighted in red were fitted to the Curie−Weiss law.

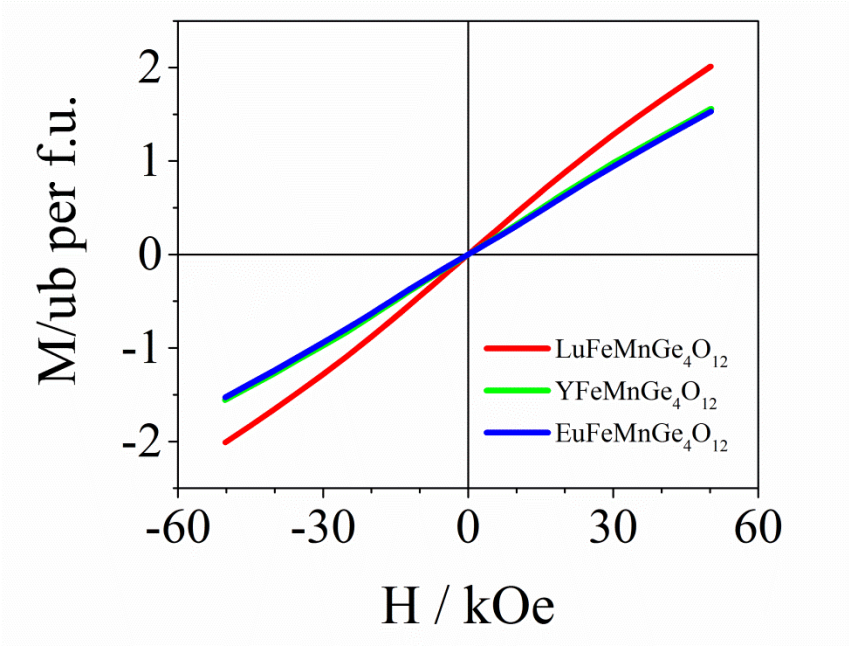

Figure 6.5 Field dependence of the magnetisation of *Ln*$FeMnGe_4O_{12}$ (*Ln* = Eu, Lu and Y) at 2 K.

6.3.3.2 AC Magnetisation Measurements

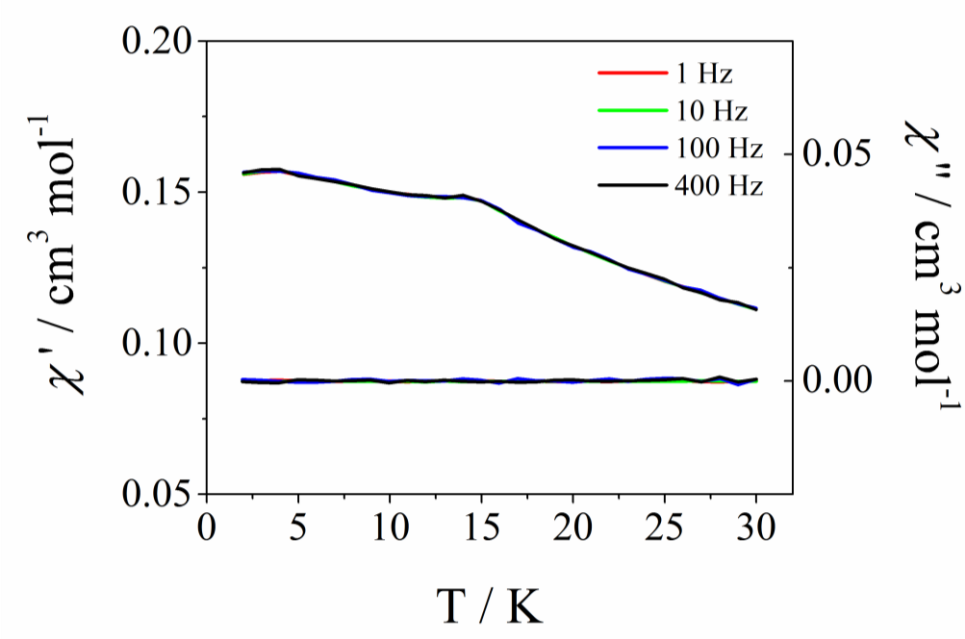

Figure 6.6 Temperature and frequency dependence of the ac molar magnetic susceptibility in zero dc field of $LuFeMnGe_4O_{12}$.

The ac susceptibility of $LuFeMnGe_4O_{12}$ proves that it is an antiferromagnet.

6.3.3.3 Zero-Field Low Temperature Neutron Diffraction

Neutron-diffraction data were collected on all the samples at 3.5 K using wavelengths of λ = 1.622 and 2.4395 Å. The magnetic structure and the mean ordered atomic moment values were derived from λ = 2.4395 Å NPD data. Structural parameters were constrained from λ = 1.622 Å NPD data. The fitted patterns are shown in Appendix B Figure B.32 – Figure B.34. The magnetic structure of the compounds is shown in Figure 6.7.

The magnetic structure of *Ln*$FeMnGe_4O_{12}$ (*Ln* = Eu, Lu and Y) can be described in the magnetic space group $P_{2c}b'an$ (No. 50.9.385). It consists of an A-type ordering of (001) planes with the atomic moments aligned along [100]. The unit cell doubles along [001] axis with $c_{mag} = 2\ c$. The NN cation-containing layers couples antiferromagnetically along [001] axis. The magnitudes of the ordered cation moments refined to be 4.37(8), 3.75(2) and 4.06(2) μ_B for *Ln* = Eu, Lu and Y, respectively.

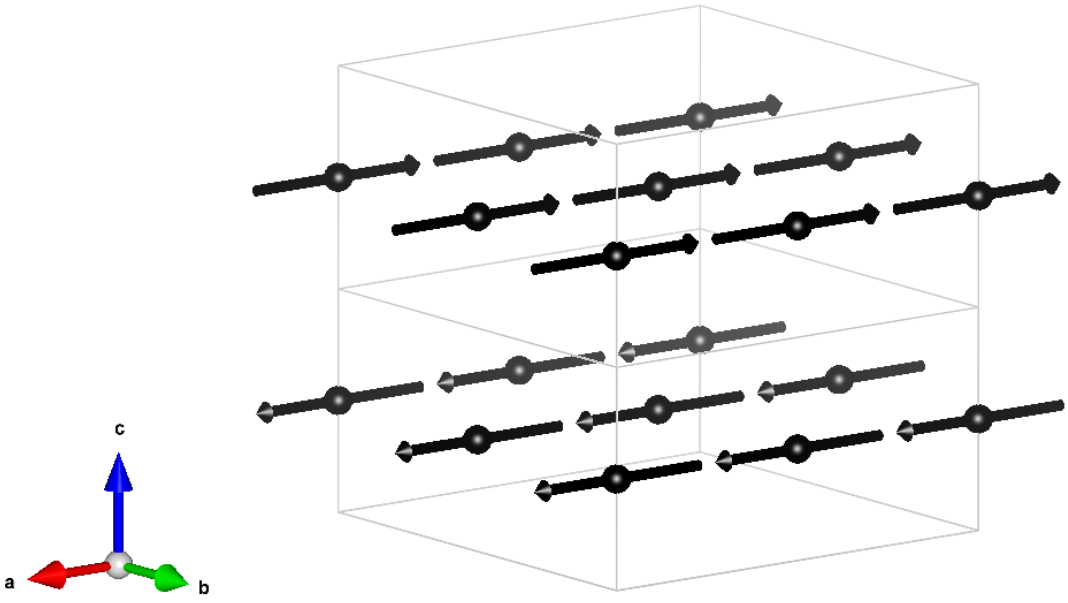

Figure 6.7 Magnetic structure in zero field of *Ln*$FeMnGe_4O_{12}$ (*Ln* = Eu, Lu and Y). Diamagnetic ions are omitted.

6.3.4 Discussion

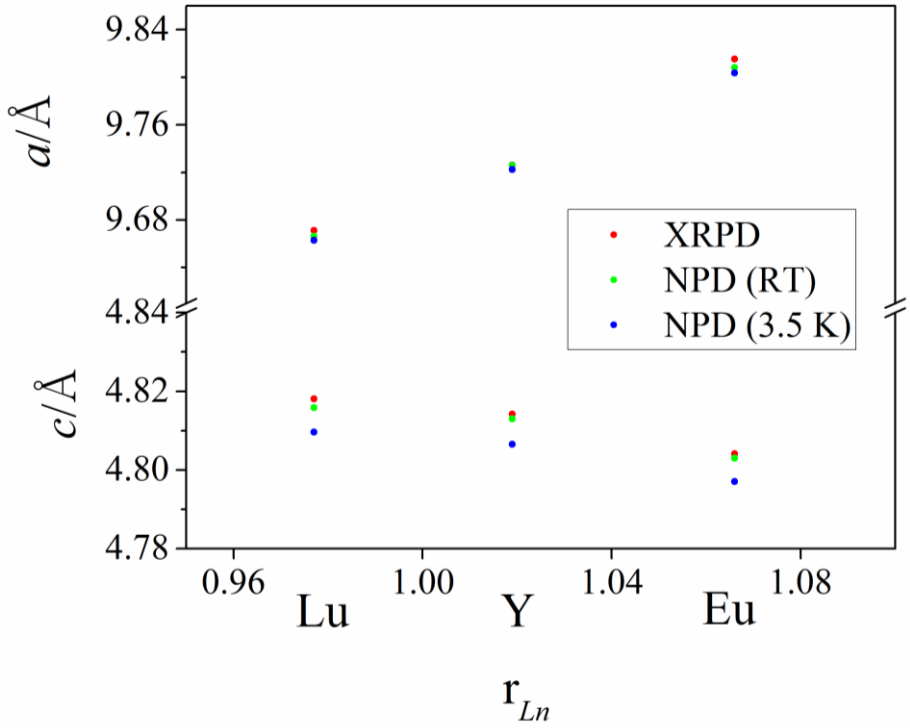

Figure 6.8 Structural unit cell parameters *a* and *c* derived from diffraction data. The error bars are smaller than the size of the points.

Table 6.8 Derived structural parameters for $LnFeMnGe_4O_{12}$ (*Ln* = Eu, Lu and Y) from low temperature NPD, λ = 1.622 Å

x	$<r_{4f}>/r_{2b}$	$2c/a$	$d(M_{4f}-O2)/d(M_{4f}-O1)$	φ /°	ψ /°	*Q*
Lu	0.755	0.9954	0.866(1)	78.64(12)	40.78(5)	0.826(1)
Y	0.724	0.9888	0.862(1)	79.73(12)	40.28(5)	0.817(1)
Eu	0.692	0.9788	0.862(1)	81.11(28)	39.75(15)	0.803(2)

φ Angle between M_{4f} – O1 bond and M_{4f} – O2 plane

ψ Angle between the M_{4f} – O1 bond and the (001) plane

q Ratio of O2 – O2 distance in square face of antiprism to perpendicular distance between faces

The unit cell parameters derived from XRPD and NPD collected at room temperature are in good agreement, see Figure 6.8. No significant structural change was detected on cooling from room temperature to 1.6 K.

When the *2b* site cation size increases, Lu^{3+} (r = 0.977 Å), Y^{3+} (r = 1.019 Å) to Eu^{3+} (r = 1.066 Å) [11], the unit cell parameter *a* increases but *c* decreases. This leads to the ratio 2*c*/*a* decreasing from 0.9954 to 0.9788, see Table 6.8. The angle φ is increasing and the angle ψ is decreasing, and the decrease of *q* ratio indicates that the *2b* site is more compressed along [001] axis.

The two different Fe/Mn – O bond lengths for the 4*f* sites create a monoclinic symmetry environment the cation, 2/*m*. The mean Mn – O and Fe – O bond lengths in MnO and Fe_2O_3 are 2.222 and 2.029 Å, respectively, and a mean bond length of ~ 2.126 Å might therefore be expected around the 4*f* site.

The mean *Ln* – O bond lengths around the 8-coordinate *Ln* cations in $LnFeO_3$ are 2.479, 2.396 and 2.428Å for *Ln* = Eu, Lu, Y [12], [13], [14], respectively. These are all significantly longer than the distances listed in Table 6.3 for $LnFeMnGe_4O_{12}$. The bond-valence sums around *Ln* in $LnFeMnGe_4O_{12}$ are calculated to be 3.53, 3.28, 3.46 for Eu, Lu, Y respectively, again suggesting that these cations are in relatively compressed environments; the degree of "over-bonding" increases with the ionic radius of Ln^{3+}. This is consistent with the failure of ourselves and others [15] to prepare isostructural germanates containing Ln^{3+} cations larger than Eu^{3+}.

In contrast to the previously reported systems $CeMn_{2-x}Co_xGe_4O_{12}$ and $ZrMn_{2-x}Co_xGe_4O_{12}$, there is some ambiguity concerning the cation oxidation states in $LnFeMnGe_4O_{12}$. The transition-metal cations could exist either as Mn^{3+} and Fe^{2+} or as Mn^{2+} and Fe^{3+}. The pseudo-tetragonal coordination geometry around the 4*f* site might be expected to favour the formation of Mn^{3+} with a $3d^4$ electron configuration whereas the lower third ionisation energy of iron will favour the formation of Fe^{3+}. The Mössbauer spectroscopy of $YFeMnGe_4O_{12}$ also proves that the oxidation state of Fe is +3 despite the unusually large quadrupole splitting.

The temperature dependence of the molar magnetic susceptibility of the three compositions shows evidence of a transition at ~16 K. In the case of *Ln* = Eu or Y the transition is signalled by a maximum in both the ZFC and FC susceptibilities, whereas for *Ln* = Lu the susceptibility shows a negative gradient across the whole of the measured range. No hysteresis between the ZFC and FC data is observed and the field dependence of the

magnetisation is also reversible. The data thus suggest that $YFeMnGe_4O_{12}$ and $EuFeMnGe_4O_{12}$ adopt antiferromagnetic ground states. Eu^{3+} has a non-magnetic ground state, but a partially-occupied excited state with $J \neq 0$ often contributes to the measured susceptibility and the observation of a Curie constant as low as 8.758(1) cm^3 K mol^{-1} in $EuFeMnGe_4O_{12}$ might be considered surprising. However, as discussed above, the coordination geometry around the Eu^{3+} cations in $EuMnFeGe_4O_{12}$ is unusually compressed, and this is likely to have consequences for the magnetic properties. The absence of hysteresis in the behaviour of $LuMnFeGe_4O_{12}$ and the absence of any frequency dependence in the ac susceptibility rule out the formation of a weakly ferromagnetic state or a spin glass. The magnetometry data suggest that this composition might be an antiferromagnet in which a small fraction of the spins remain paramagnetic below the Néel temperature, which is similar to $CeMn_2Ge_4O_{12}$ and $ZrMn_2Ge_4O_{12}$. This residual paramagnetism could be attributable to the disordered distribution of cations on the 4*f* site and the disruption of the O – Ge – O superexchange pathways that would be expected to accompany it. The relatively low value of the ordered cation moment determined by neutron diffraction for $LuMnFeGe_4O_{12}$ is consistent with this explanation. The values measured for the Y^{3+} - and Eu^{3+} - containing compositions lie within the range observed previously in comparable compounds.

The magnetic structures of three $LnFeMnGe_4O_{12}$ compounds are similar to that of $CeMn_{0.5}Co_{1.5}Ge_4O_{12}$ and $CeCo_2Ge_4O_{12}$. $CeMn_{0.5}Co_{1.5}Ge_4O_{12}$ and $CeCo_2Ge_4O_{12}$ have both a G-type component and an A-type component and there was evidence of a high-field metamagnetic transition in M(H). However, the three $LnFeMnGe_4O_{12}$ compositions are A-type antiferromagnets. The changes in magnetic structure observed previously across the series $CeMn_{2-x}Co_xGe_4O_{12}$ suggested that the occurrence of a doubled magnetic unit cell and the location of the ordered moment within the (001) plane might both be attributable to the presence of the single-ion anisotropy associated with Co^{2+} but the magnetic structure determined in $LnFeMnGe_4O_{12}$ shows that this is not the case. The compounds that contain only spherical, high-spin d^5 transition-metal cations would be closer to $CeMn_2Ge_4O_{12}$ but actually they are much closer to $CeCo_2Ge_4O_{12}$. The structural data in Table 6.8 and Table 3.14 can identify structural factors that correlate with the unit-cell doubling. It seems that this is most likely to occur when the cation radius ratio $\langle r_{4f} \rangle / r_{2b}$ is small and therefore the ratio of the bond lengths (Mn/Fe – O2)/(Mn/Fe – O1) and the angle between the Mn/Fe – O1 bond and the (001) plane are small. It is likely that these structural parameters strongly

influence the relative strengths of the different superexchange interactions that operate within the structure and hence control the magnetic structure.

6.3.5 Conclusion

The compounds LnMnFeGe$_4$O$_{12}$ (Ln = Eu, Lu, Y) are essentially isostructural and they all adopt the same antiferromagnetic structure below ~16 K, although there is evidence of residual paramagnetism below T_N when Ln = Lu. The magnetic structure is similar to that of $CeCo_2Ge_4O_{12}$ rather than that of $CeMn_2Ge_4O_{12}$, which suggests that subtle structural variations are more important in determining the magnetic structure than is the electronic structure of the cations.

The work described in this Chapter has been published as *Structural Chemistry and Magnetic Properties of $LnMnFeGe_4O_{12}$ (Ln = Y, Eu, Lu)*, D. Xu, M. Avdeev, P. D. Battle, J. M. Cadogan and H. Lamont, *Journal of Solid State Chemistry*, 2017, **254**, 40-46.

6.4 References

[1] H. M. Rietveld, A profile refinement method for nuclear and magnetic structures, *Journal of Applied Crystallography*, **1969**, *2*, 65-71.

[2] B. H. Toby, EXPGUI, a graphical user interface for GSAS, *Journal of Applied Crystallography*, **2001**, *34*, 210-213.

[3] A. C. Larson, and R. B. Von Dreele, *General Structure Analysis System (GSAS)*, Los Alamos National Laboratory Report LAUR 86-748: **2004**.

[4] B. van Laar, and W. B. Yelon, The peak in Neutron Powder Diffraction, *Journal of Applied Crystallography*, **1984**, *17*, 47-54.

[5] K. Momma, and F. Izumi, VESTA: a three-dimensional visualization system for electronic and structural analysis, *Journal of Applied Crystallography*, **2008**, *41*, 653-658.

[6] R. A. Brand, www.wissel-instruments.de.

[7] https://www.ncnr.nist.gov/instruments/bt1/neutron.html.

[8] B. J. Kennedy, G. Murphy, E. Reynolds, M. Avdeev, H. E. R. Brand, and T. Kolodiazhnyi, Studies of the antiferrodistortive transition in $EuTiO_3$, *Journal of Physics: Condensed Matter*, **2014**, *26*, 495901.

[9] M. Avdeev, B. J. Kennedy, and T. Kolodiazhnyi, Neutron powder diffraction study of the magnetic structure of $EuZrO_3$, *Journal of Physics: Condensed Matter*, **2014**, *26*, 095401.

[10] R. G. Burns, Mineral Mössbauer spectroscopy: Correlations between chemical shift and quadrupole splitting parameters, *Hyperfine Interactions*, **1994**, *91*, 739-745.

[11] R. D. Shannon, Revised effective ionic radii and systematic studies of interatomic distances in halides and chalcogenides, *Acta Crystallographica Section A: Crystal Physics, Diffraction Theoretical, and General Crystallography*, **1976**, *A32*, 751.

[12] M. Marezio, J. P. Remeika, and P. D. Dernier, The crystal chemistry of the rare earth orthoferrites, *Acta Crystallographica Section B*, **1970**, *26*, 2008-2022.

[13] D. du Boulay, E. N. Maslen, V. A. Streltsov, and N. Ishizawa, A synchrotron X-ray study of the electron density in $YFeO_3$, *Acta Crystallographica Section B*, **1995**, *51*, 921-929.

[14] A. Masuno, A. Ishimoto, C. Moriyoshi, N. Hayashi, H. Kawaji, Y. Kuroiwa, and H. Inoue, Weak Ferromagnetic Transition with a Dielectric Anomaly in Hexagonal $Lu_{0.5}Sc_{0.5}FeO_3$, *Inorganic Chemistry*, **2013**, *52*, 11889-11894.

[15] V. G. Zubkov, N. V. Tarakina, I. I. Leonidov, A. P. Tyutyunnik, L. L. Surat, M. A. Melkozerova, E. V. Zabolotskaya, and D. G. Kellerman, Synthesis and crystal structure of $Ln_2M^{2+}Ge_4O_{12}$, Ln=rare-earth element or Y; M=Ca, Mn, Zn, *Journal of Solid State Chemistry*, **2010**, *183*, 1186-1193.

Chapter 7 - Synthesis and Characterisation of $R_2MGe_4O_{12}$ (*R* = Tb-Yb; *M* = Ca, Mn, Co) and $RScCoGe_4O_{12}$ (*R* = Tb, Dy)

7.1 Introduction

In Chapter 6, we described three compositions with trivalent non-magnetic cations occupying the *2b* site and a 1:1 ratio of trivalent Fe^{3+} and divalent Mn^{2+} occupying the *4f* site. The compounds contained two isotropic cations with $3d^5$ electron configuration and were thus expected to behave more like $CeMn_2Ge_4O_{12}$ but their magnetic structures are closer to $CeCo_2Ge_4O_{12}$. We suggest this result may come from the relative size of the cations, as described by the $<r_{4f}>/r_{2b}$ ratio. In this and the next chapter, more compounds with the general formula $A^{3+}B^{3+}B^{2+}Ge_4O_{12}$ were synthesized to test our hypothesis. The cation at the *2b* site, *A*, is now a magnetic lanthanide and the cations at the *4f site*, *B* and *B'*, can be a small first-transition metals and/or a large lanthanide. However, when *A* is a magnetic cation, an additional significant superexchange pathway (*B*,*B*') – O – *A* is introduced. This can strongly influence the magnetic properties of the compounds. We discuss below this influence and the magnetic properties of solid solutions $R_2MGe_4O_{12}$ (*R* = Tb-Yb; *M* = Ca, Mn, Co) and $RScCoGe_4O_{12}$ (*R* = Tb, Dy).

7.2 Experimental

Polycrystalline samples of $R_2MGe_4O_{12}$ (*R* = Tb-Yb; *M* = Ca, Mn, Co) and $RScCoGe_4O_{12}$ (*R* = Tb, Dy) were synthesised by solid-state reaction. Stoichiometric quantities of Ln_2O_3, Sc_2O_3, Co_3O_4, $MnCO_3$, $CaCO_3$, and GeO_2 were mixed thoroughly in an agate mortar, along with a 10% excess of GeO_2 to counteract its loss at high temperature. The mixtures were heated at 1075 °C for 2 days with intermediate cooling and regrinding every day. They were then pressed into pellets and annealed at the same temperature for another 4 days with intermediate cooling and regrinding every two days. Further heating at 1100 °C for 1 day was carried out if GeO_2 was detected as an impurity phase.

X-ray powder diffraction patterns were recorded at room temperature using Cu $K\alpha_1$ radiation. Neutron powder diffraction patterns were collected using a wavelength of either 1.622 Å or 2.4395 Å on $Tb_2CoGe_4O_{12}$, $TbScCoGe_4O_{12}$, and $Tb_2MnGe_4O_{12}$. The measurements were performed at room temperature and low temperatures. The data were analysed by the Rietveld method [1], [2] using the program GSAS [3], [4] and the peak function developed by van Laar and Yelon [5]. The magnetic structure was drafted by VESTA [6].

Magnetic measurements were performed using Quantum Design MPMS XL SQUID magnetometers. DC susceptibility measurements were made over the temperature range $2\ K \leq T \leq 300\ K$ in an applied field of 100 Oe with both zero-field cooling (ZFC) and field-cooling (FC) of the samples. The temperature and field dependence of the DC molar magnetic susceptibilities of $R_2CoGe_4O_{12}$ and $RScCoGe_4O_{12}$ (R = Tb, Dy) were studied over the temperature range $2\ K \leq T \leq 10\ K$ in an applied field of 1, 10, 20 kOe following FC. The field dependence of the magnetization was measured at 2 K over the field range $-50\ kOe \leq H \leq 50\ kOe$ with initially cooling in a 50 kOe magnetic field. AC susceptibilities were measured at frequencies 1, 10, 100, 1000 Hz over the temperature range $2\ K \leq T \leq 10\ K$ in a 3.5 Oe AC driving field. Samples were ac-degaussed and then cooled in a small dc field of 3 Oe to counteract the remaining field in the SQUID. Further in-field AC susceptibility measurements were made under the same condition with applied dc fields of 0.1, 0.5, 1, 5 kOe on $R_2CoGe_4O_{12}$ and $RScCoGe_4O_{12}$ (R = Tb, Dy) following FC.

7.3 Results

7.3.1 Structural Chemistry

7.3.1.1 X-ray Diffraction

Single phases were obtained for all the solid solutions. Among the sample solutions, cobalt-containing ones were blue in colour, manganese-containing ones were brown, and calcium-containing ones were white. The crystal structure of the solid solutions can all be indexed in the tetragonal space group *P*4/*nbm* (No. 125), consistent with the result by Zubkov *et al.* [7], [8]. The fitted room temperature X-ray diffraction patterns are shown in Appendix A Figure 7.19 - Figure 7.29. Structural parameters derived from the refinements are listed in Table 7.1.

Table 7.1 Structural parameters of $R_2CoGe_4O_{12}$ (*R* = Tb - Yb) at room temperature derived from X-ray diffraction data (λ = 1.5406 Å)

		R					
		Tb	Dy	Ho	Er	Tm	Yb
Ge	*x*	0.5245(3)	0.5240(1)	0.5232(1)	0.5234(2)	0.5206(2)	0.5193(2)
O1	*x*	-0.3573(10)	-0.3540(5)	-0.3578(4)	-0.3565(6)	-0.3689(7)	-0.3728(8)
	z	0.2008(30)	0.2091(19)	0.2032(13)	0.2013(20)	0.1694(20)	0.1607(21)
O2	*x*	0.1700(12)	0.1700(6)	0.1681(4)	0.1706(8)	0.1679(7)	0.1662(8)
	y	0.0467(10)	0.0476(5)	0.0510(4)	0.0467(6)	0.0616(6)	0.0679(7)
	z	0.2382(23)	0.2488(13)	0.2484(10)	0.2465(17)	0.2610(14)	0.2650(16)
a/Å		9.9028(2)	9.8796(1)	9.8471(1)	9.8271(1)	9.8060(1)	9.7853(1)
c/Å		4.9473(1)	4.9412(1)	4.9332(1)	4.9258(1)	4.9145(1)	4.9078(1)
V/Å^3		485.16(2)	482.29(1)	478.36(1)	475.70(2)	472.56(1)	469.93(1)
R_{wpr}		5.53%	4.90%	6.26%	7.24%	9.82%	9.24%
χ^2		1.414	1.310	1.892	1.826	2.638	1.949

Space group *P*4/*nbm* (No. 125), Z = 2

R on 2*b* (¼, ¼, ½); *R*/Co on 4*f* (0, 0, ½);

Ge on 8*k* (*x*, ¼, 0); O1 on 8*m* (*x*, -*x*, *z*); O2 on 16*n* (*x*, *y*, *z*)

The U_{iso} parameter of each atom was constrained to that reported by Taviot-Gueho. [1]

Table 7.2 Structural parameters of $R_2MGe_4O_{12}$ (*R* = Tb, Dy; *M* = Mn, Ca) at room temperature derived from X-ray diffraction data (λ = 1.5406 Å)

		R = Tb	*R* = Dy	*R* = Dy
		M = Mn		*M* = Ca
Ge	*x*	0.5242(2)	0.5233(2)	0.5229(2)
O1	*x*	-0.3584(7)	-0.3666(8)	-0.3673(7)
	z	0.1980(20)	0.1544(23)	0.1544(20)
O2	*x*	0.1700(8)	0.1675(8)	0.1726(7)
	y	0.0477(6)	0.0566(7)	0.0614(7)
	z	0.2468(17)	0.2589(17)	0.2625(16)
a/Å		9.9331(1)	9.9227(1)	10.0228(1)
c/Å		4.9902(1)	4.9874(1)	5.0828(1)
V/Å^3		492.37(2)	491.06(1)	510.60(1)
R_{wpr}		10.28%	7.66%	7.27%
χ^2		1.559	1.769	1.439

Space group *P*4/*nbm* (No. 125), Z = 2

R on 2*b* (¼, ¼, ½); *R*/Mn(Ca) on 4*f* (0, 0, ½);

Ge on 8*k* (*x*, ¼, 0); O1 on 8*m* (*x*, -*x*, z); O2 on 16*n* (*x*, *y*, *z*)

Table 7.3 Structural parameters of RScCoGe$_4$O$_{12}$ (R = Tb, Dy) at room temperature derived from X-ray diffraction data (λ = 1.5406 Å)

		R	
		Tb*	Dy
Ge	*x*	0.5260(2)	0.5242(7)
O1	*x*	-0.3597(9)	-0.3609(24)
	z	0.2267(21)	0.1765(54)
O2	*x*	0.1588(10)	0.1608(25)
	y	0.0490(7)	0.0611(21)
	z	0.2481(15)	0.2559(37)
a/Å		9.7824(2)	9.7484(7)
c/Å		4.8356(1)	4.8314(5)
V/Å^3		462.75(3)	459.14(10)
R_{wpr}		7.64%	11.67%
χ^2		1.776	1.387

Space group *P*4/*nbm* (No. 125), Z = 2

R on 2*b* (¼, ¼, ½); Sc/Co on 4*f* (0, 0, ½);

Ge on 8*k* (*x*, ¼, 0); O1 on 8*m* (*x*, -*x*, *z*); O2 on 16*n* (*x*, *y*, *z*)

* Fraction of Tb/Sc at *2b* site constrained to be 0.864(14)/0.136(14) from NPD data

7.3.1.2 Room Temperature and Low Temperature Neutron Diffraction

Neutron-diffraction data were collected at room temperature and low temperature on $Tb_2CoGe_4O_{12}$, $TbScCoGe_4O_{12}$ and $Tb_2MnGe_4O_{12}$ using wavelengths of λ = 1.622 and 2.4395 Å. The fitted patterns of $TbScCoGe_4O_{12}$ at room temperature and 1.5 K using wavelength λ = 1.622 are shown in Figure 7.1 and 7.2 and the others are shown in Appendix B Figure B.29 – Figure B.36. Structural parameters derived from simultaneous analysis of the data collected at both wavelengths are listed in Table 7.4. Some selected bond lengths and bond angles derived from the room temperature neutron diffraction data are listed in Table 7.5. The magnetic information will be discussed in section 7.3.2.3.

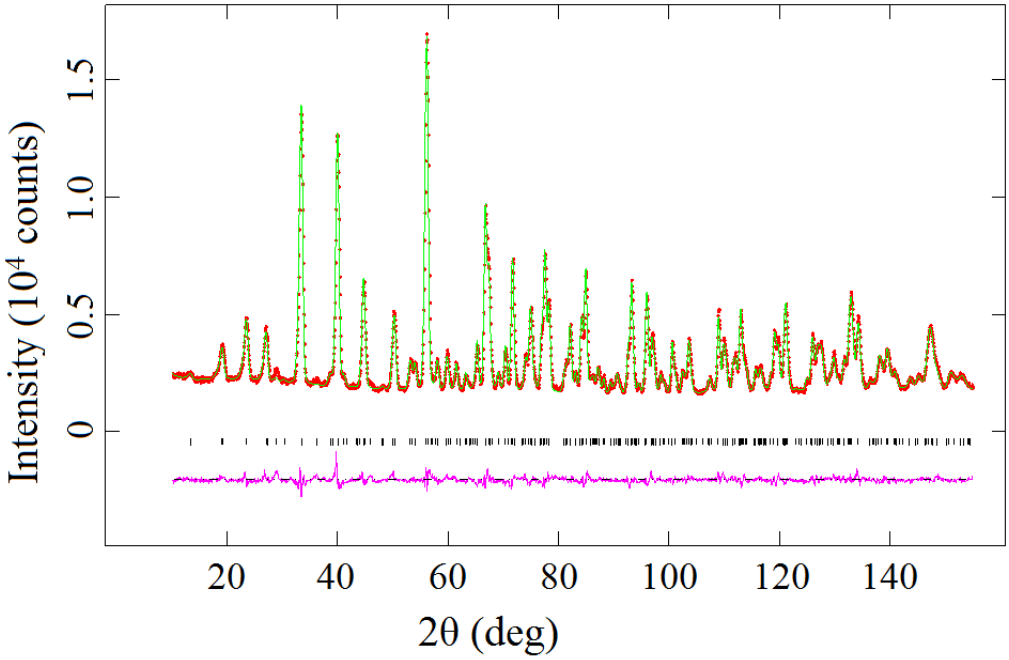

Figure 7.1 Observed (red dots) and calculated (green line) NPD patterns of $TbScCoGe_4O_{12}$ at room temperature; λ = 1.622 Å. A difference curve (purple line) is shown and reflection positions are marked.

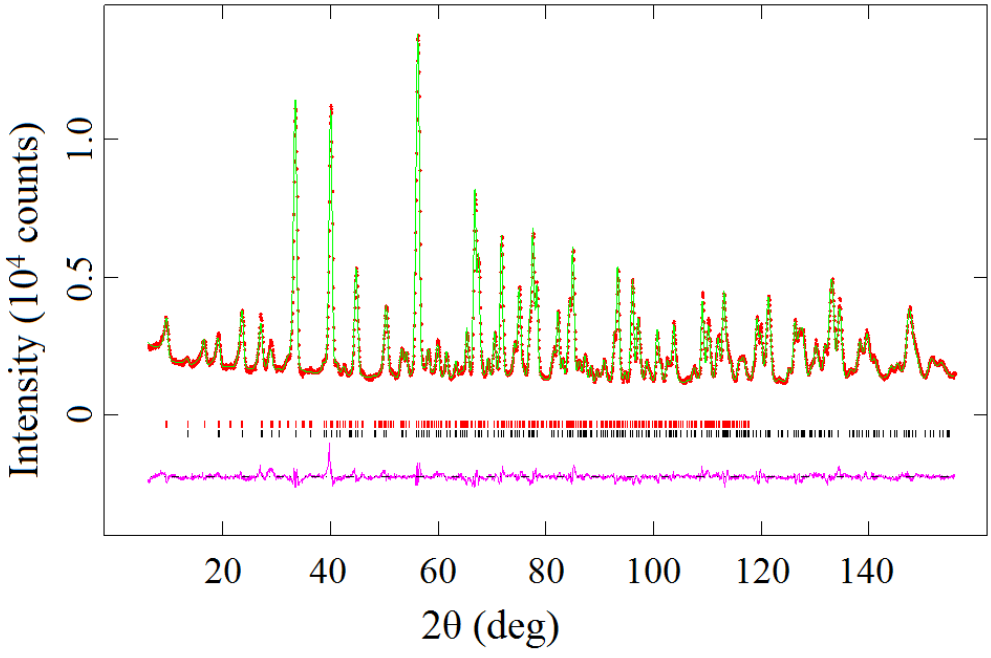

Figure 7.2 Observed (red dots) and calculated (green line) NPD patterns of $TbScCoGe_4O_{12}$ at 1.5 K; λ = 1.622 Å. A difference curve (purple line) is shown and reflection positions are marked for the crystal structure (bottom) and the magnetic structure (top).

Table 7.4 Structural parameters of $Tb_2CoGe_4O_{12}$ and $TbScCoGe_4O_{12}$ derived from neutron diffraction data (λ = 1.622 and 2.4395 Å) as a function of composition and temperature

		$Tb_2CoGe_4O_{12}$		$TbScCoGe_4O_{12}$*		$Tb_2MnGe_4O_{12}$	
		1.5 K	300 K	1.5 K	300 K	1.5 K	300 K
Tb	U_{iso}/Å^2	0.0010(3)	0.0040(5)	0.0032(4)	0.0074(6)	0.0010(3)	0.0061(5)
B/*B'*	U_{iso}/Å^2	0.0017(6)	0.0076(6)	0.0056(4)	0.0087(5)	0.0038(8)	0.0098(9)
Ge	*x*	0.5235(1)	0.5236(1)	0.5233(1)	0.5235(1)	0.5229(1)	0.5229(1)
	U_{iso}/Å^2	0.0036(2)	0.0064(2)	0.0058(2)	0.0047(2)	0.0031(2)	0.0078(2)
O1	*x*	-0.3701(1)	-0.3694(1)	-0.3695(1)	-0.3692(1)	-0.3708(1)	-0.3710(1)
	z	0.1700(2)	0.1686(2)	0.1797(2)	0.1796(2)	0.1656(2)	0.1638(2)
	U_{iso}/Å^2	0.0029(3)	0.0058(3)	0.0019(3)	0.0070(3)	0.0031(3)	0.0086(3)
O2	*x*	0.1683(1)	0.1682(1)	0.1621(1)	0.1623(1)	0.1702(1)	0.1699(1)
	y	0.0619(1)	0.0617(1)	0.0613(1)	0.0614(1)	0.0623(1)	0.0618(1)
	z	0.2552(2)	0.2559(2)	0.2568(2)	0.2559(2)	0.2555(2)	0.2554(2)
	U_{iso}/Å^2	0.0050(2)	0.0082(2)	0.0028(2)	0.0074(2)	0.0034(2)	0.0095(2)
a/Å		9.8975(1)	9.9039(1)	9.7785(1)	9.7799(1)	9.9402(1)	9.9473(1)
c/Å		4.9451(1)	4.9482(1)	4.8297(1)	4.8353(1)	4.9948(1)	4.9979(1)
V/Å^3		484.42(1)	485.36(1)	461.82(1)	462.48(1)	493.52(1)	494.54(1)
R_{wpr}†		3.81%	3.26%	4.13%	3.56%	4.18%	3.25%
R_{wpr}‡		4.57%	4.12%	5.28%	-	5.69%	-
χ^2		4.897	4.075	3.705	2.870	4.135	2.177

Space group *P*4/*nbm* (No. 125), Z = 2

Tb on 2*b* (¼, ¼, ½); *B*/*B'* on 4*f* (0, 0, ½);

Ge on 8*k* (*x*, ¼, 0); O1 on 8*m* (*x*, -*x*, *z*); O2 on 16*n* (*x*, *y*, *z*)

* Fraction of Tb/Sc at *2b* site is 0.864(14)/0.136(14)

† Derived from λ = 1.622 Å data

‡ Derived from λ = 2.4395 Å data

Table 7.5 Bond lengths (Å) and bond angles (degrees) in $Tb_2CoGe_4O_{12}$, $TbScCoGe_4O_{12}$ and $Tb_2MnGe_4O_{12}$ derived from neutron diffraction data as a function of composition and temperature (λ = 1.622 and 2.4395 Å)

	$Tb_2CoGe_4O_{12}$		$TbScCoGe_4O_{12}$		$Tb_2MnGe_4O_{12}$	
	1.5 K	300 K	1.5 K	300 K	1.5 K	300 K
Tb-O2 × 8	2.364(1)	2.365(1)	2.350(1)	2.351(1)	2.367(1)	2.373(1)
B/*B'*-O1 × 2	2.443(2)	2.456(1)	2.377(2)	2.382(2)	2.467(1)	2.473(1)
B/*B'*-O2 × 4	2.148(1)	2.147(1)	2.062(1)	2.068(1)	2.177(1)	2.175(1)
O2-O2' *	3.439(2)	3.446(1)	3.319(1)	3.328(2)	3.267(1)	3.260(1)
O2-O2" *	3.056(2)	3.068(2)	2.964(1)	3.969(2)	2.876(1)	2.879(1)
Ge-O1 × 2	1.797(1)	1.794(1)	1.794(1)	1.793(1)	1.801(1)	1.798(1)
Ge-O2 × 2	1.721(1)	1.724(1)	1.721(1)	1.720(1)	1.725(1)	1.725(1)
O2-Mn/Co-O2'	96.81(4)	96.72(3)	96.54(4)	96.59(3)	97.33(4)	97.10(4)
O2-Mn/Co-O2"	83.19(4)	83.28(3)	83.46(4)	83.41(3)	82.67(4)	82.89(4)
O1-Mn/Co-O2'	82.84(4)	82.81(3)	82.95(4)	83.07(4)	82.92(4)	82.79(4)
O1-Mn/Co-O2"	96.81(4)	96.72(3)	96.54(4)	96.59(4)	97.08(4)	97.21(4)
O1-Ge-O1	108.25(11)	107.58(9)	108.47(8)	108.36(10)	108.17(10)	108.10(11)
O1-Ge-O2	104.81(5)	104.93(4)	104.91(4)	104.95(5)	104.76(5)	105.02(5)
O1-Ge-O2	108.65(7)	108.74(6)	107.73(6)	107.91(6)	108.75(7)	108.34(7)
O2-Ge-O2	121.20(8)	121.33(7)	122.54(8)	122.21(9)	121.16(8)	121.48(8)

* distances within the equatorial plane of the (*B*/*B'*)O_6 octahedra

7.3.2 Magnetic Properties

7.3.2.1 DC Magnetisation Measurements

The temperature dependence of the dc molar susceptibility of each sample measured in a 100 Oe magnetic field is shown in Figure 7.3 – Figure 7.5, along with the field dependence of the magnetisation measured at 2 K. The transition temperature, T_m, and the magnetic parameters resulting from fitting the Curie-Weiss law to the FC data for T > 150 K are listed in Table 7.6. Further susceptibility measurements were made in various fields on $R_2CoGe_4O_{12}$ and $RScCoGe_4O_{12}$ (*R* = Tb, Dy), see Figure 7.6.

Table 7.6 Magnetic parameters of $R_2MGe_4O_{12}$ (*R* = Tb-Yb; *M* = Co, Mn) and $RScCoGe_4O_{12}$ (*R* = Tb, Dy)

Composition	C_M / $cm^3\,mol^{-1}\,K$	θ / K	T_m / K	μ_{eff}^* / μ_B
$Tb_2CoGe_4O_{12}$	27.034(1)	-8.86(2)	2.8	9.68
$Dy_2CoGe_4O_{12}$	31.908(1)	-7.77(1)	2.8	10.64
$Ho_2CoGe_4O_{12}$	31.260(1)	-9.19(2)	-	10.52
$Er_2CoGe_4O_{12}$	26.518(1)	-6.23(2)	-	9.58
$Tb_2MnGe_4O_{12}$	27.855(1)	-9.77(2)	2.2	9.69
$Dy_2MnGe_4O_{12}$	32.510(1)	-8.20(2)	2.6	10.61
$TbScCoGe_4O_{12}$	16.077(2)	-7.37(7)	3.4	9.99
$DyScCoGe_4O_{12}$	17.806(1)	-0.96(14)	3.4	10.66

*calculated using μ_{eff} (Mn) = 5.91, μ_{eff} (Co) = 5.36.

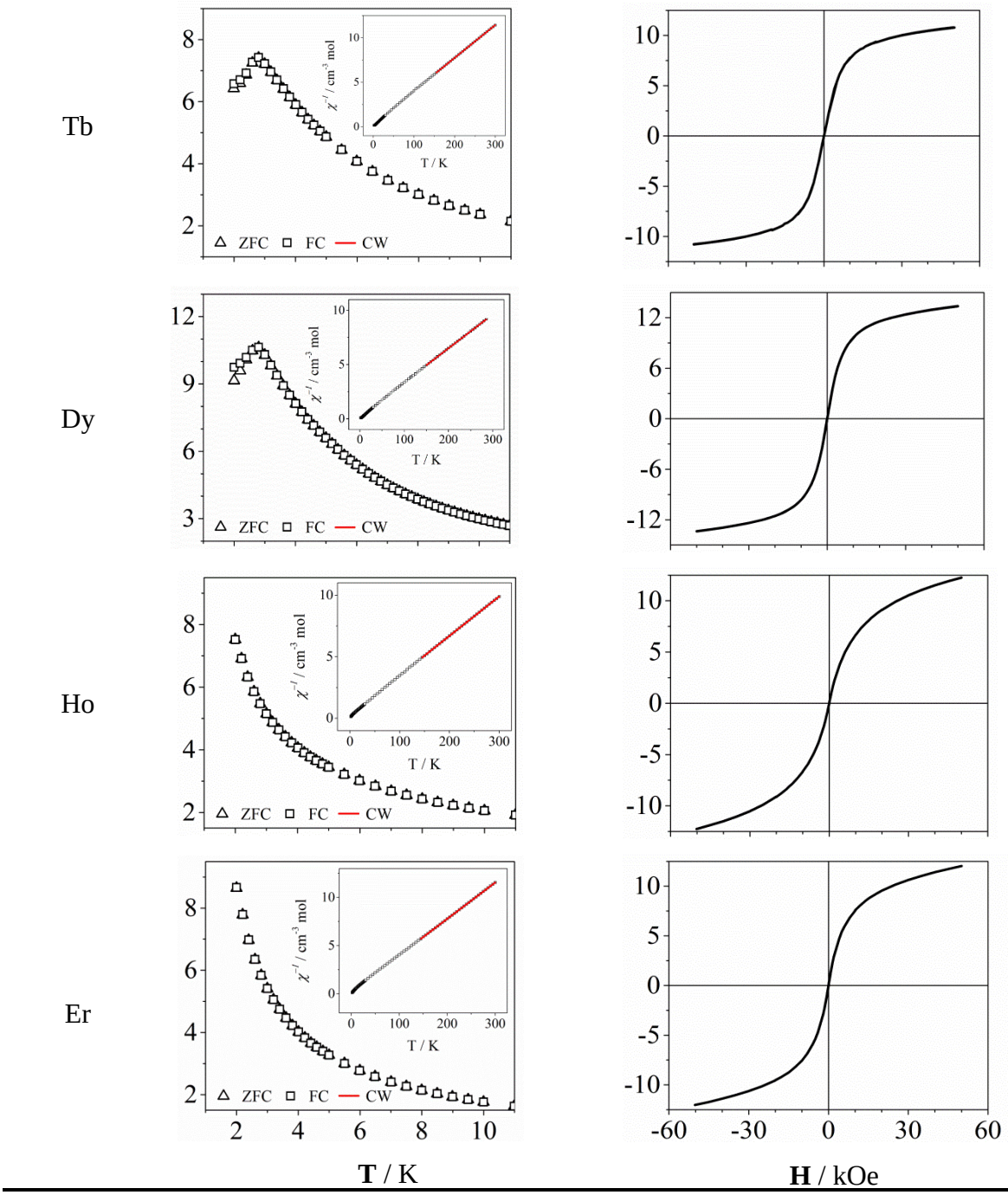

Figure 7.3 Temperature dependence of the dc molar magnetic susceptibility, measured in 100 Oe, and the field dependence of the magnetization at 2 K of $R_2CoGe_4O_{12}$ (*R* = Tb-Yb). (inset) The inverse susceptibility; data points highlighted in red were fitted to the Curie−Weiss law.

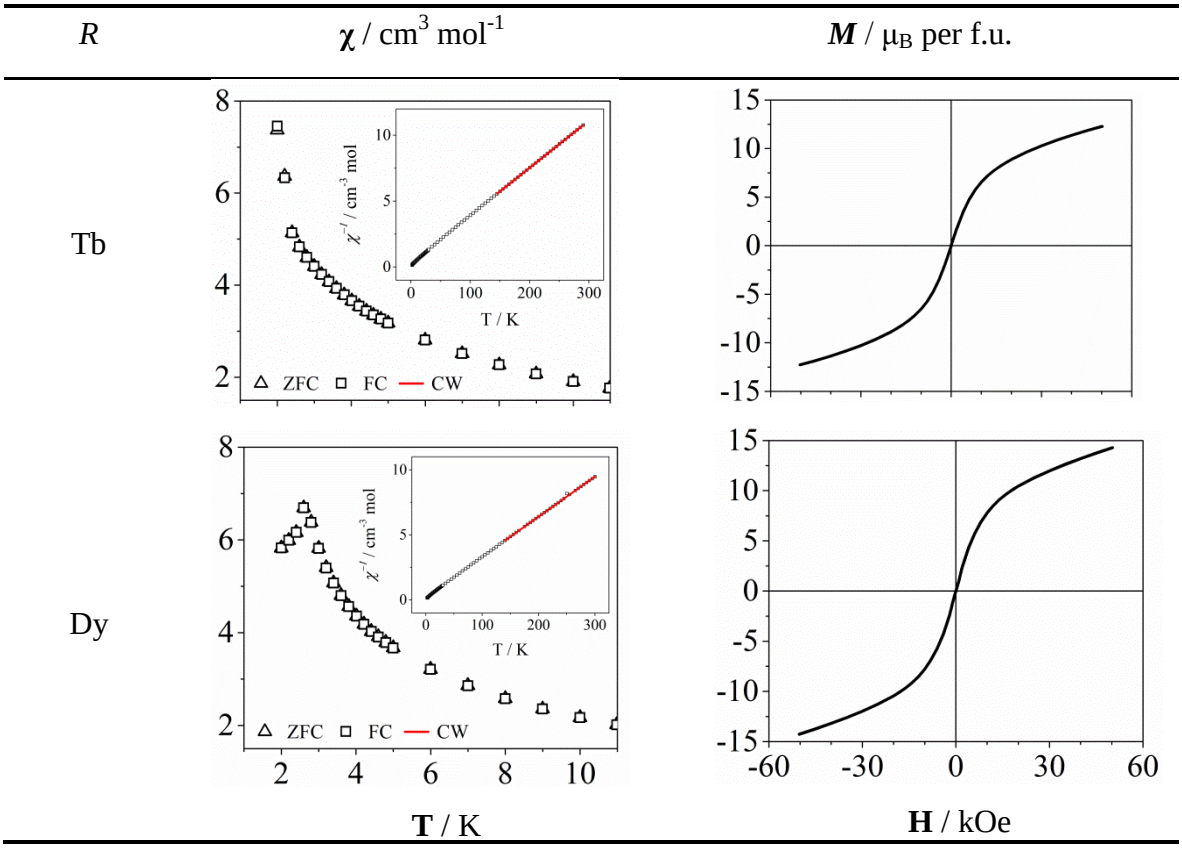

Figure 7.4 Temperature dependence of the dc molar magnetic susceptibility, measured in 100 Oe, and the field dependence of the magnetization at 2 K of $R_2MnGe_4O_{12}$ (*R* = Tb-Yb). (inset) The inverse susceptibility; data points highlighted in red were fitted to the Curie−Weiss law.

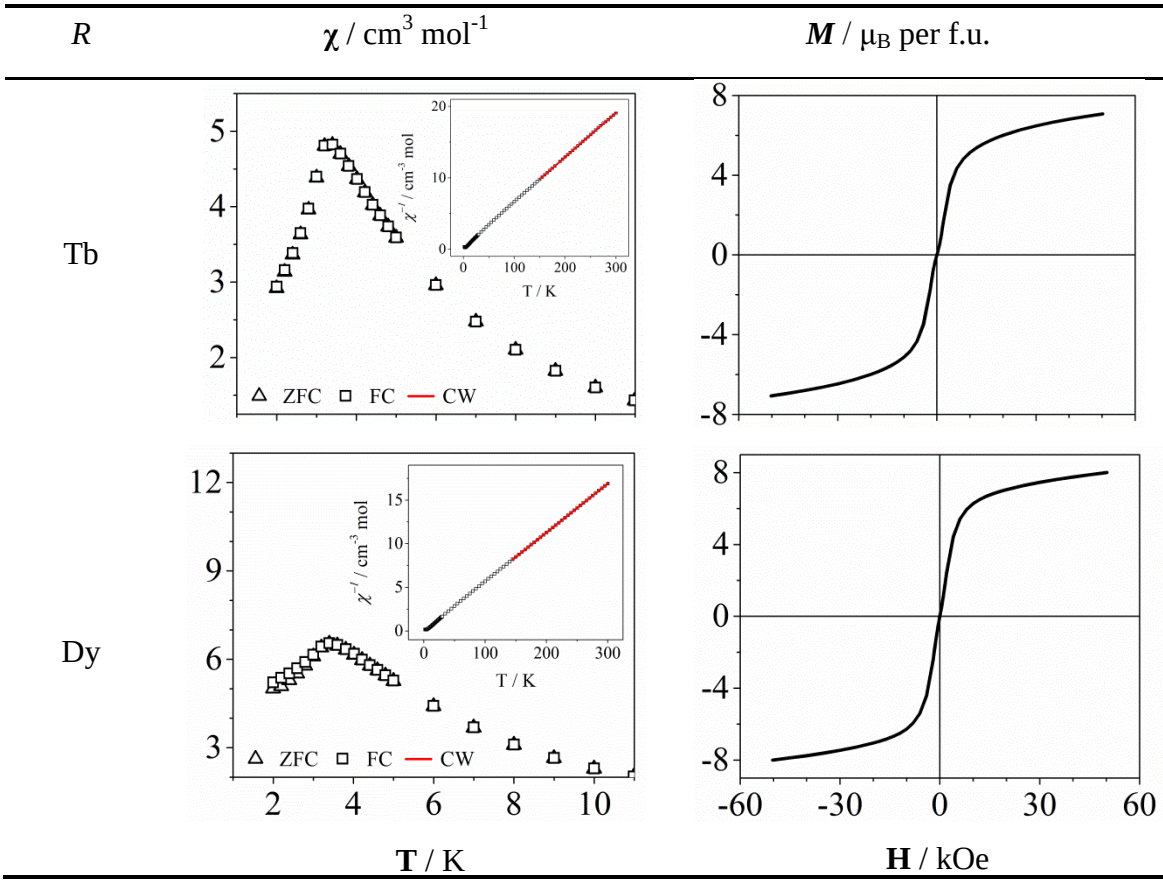

Figure 7.5 Temperature dependence of the dc molar magnetic susceptibility, measured in 100 Oe, and the field dependence of the magnetization at 2 K of RScCoGe$_4$O$_{12}$ (R = Tb-Yb). (inset) The inverse susceptibility; data points highlighted in red were fitted to the Curie−Weiss law.

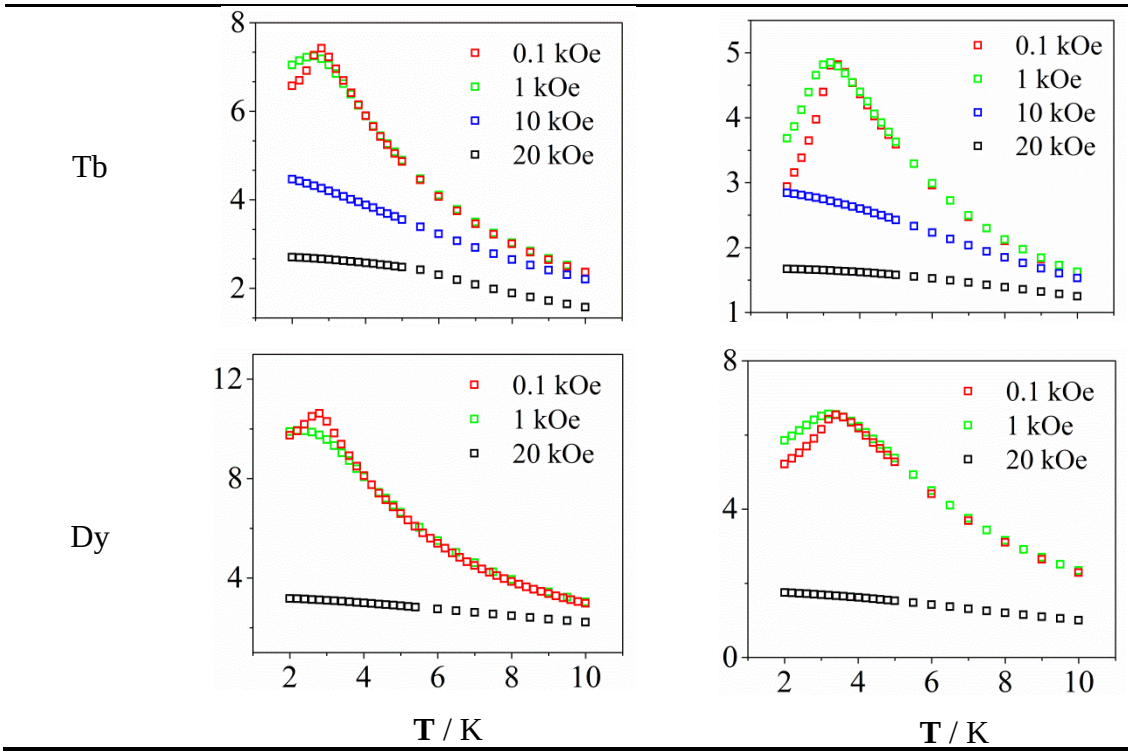

Figure 7.6 Temperature dependence of the dc molar magnetic susceptibility of $R_2CoGe_4O_{12}$ and $RScCoGe_4O_{12}$ (R = Tb-Yb) as a function of field.

The dc susceptibility of $R_2CoGe_4O_{12}$ (R = Ho, Er) is paramagnetic in the temperature range 2 K ≤ T ≤ 300 K whereas the others shows a transition at around 3 K. Using the mean Curie constant of 3.29 m^3 mol^{-1} K for Co^{2+} as observed in both $CeCo_2Ge_4O_{12}$ and $ZrCo_2Ge_4O_{12}$, the effective moment of the Ln^{3+} cations can be determined by subtracting this value from the experimentally-determined Curie constants of the other compositions listed in Table 7.6. These moments are self-consistent and in excellent agreement with the predictions of the Landé formula. Some hysteresis is apparent between the ZFC and FC susceptibilities of $Tb_2CoGe_4O_{12}$, $Dy_2CoGe_4O_{12}$ and $DyScCoGe_4O_{12}$, but not for the other compositions. The field dependence of the magnetisation of these compositions at 2 K indicates a value of ½ $n_{Ln}g_{Ln}J_{Ln}$ + g_MS_M for all the cases rather than $n_{Ln}g_{Ln}J_{Ln}$ + g_MS_M for $R_2CoGe_4O_{12}$. χ(H,T) shows that the magnetic field could only broaden the transition peak but hardly changed the transition temperature and the susceptibility is increased slightly in a higher field for $RScCoGe_4O_{12}$ (R = Tb, Dy). $R_2CoGe_4O_{12}$ (R = Tb, Dy) behave in another way; the magnetic field not only broadens the transition peak but also leads to a lower transition temperature and lower susceptibility.

7.3.2.2 AC Magnetisation Measurements

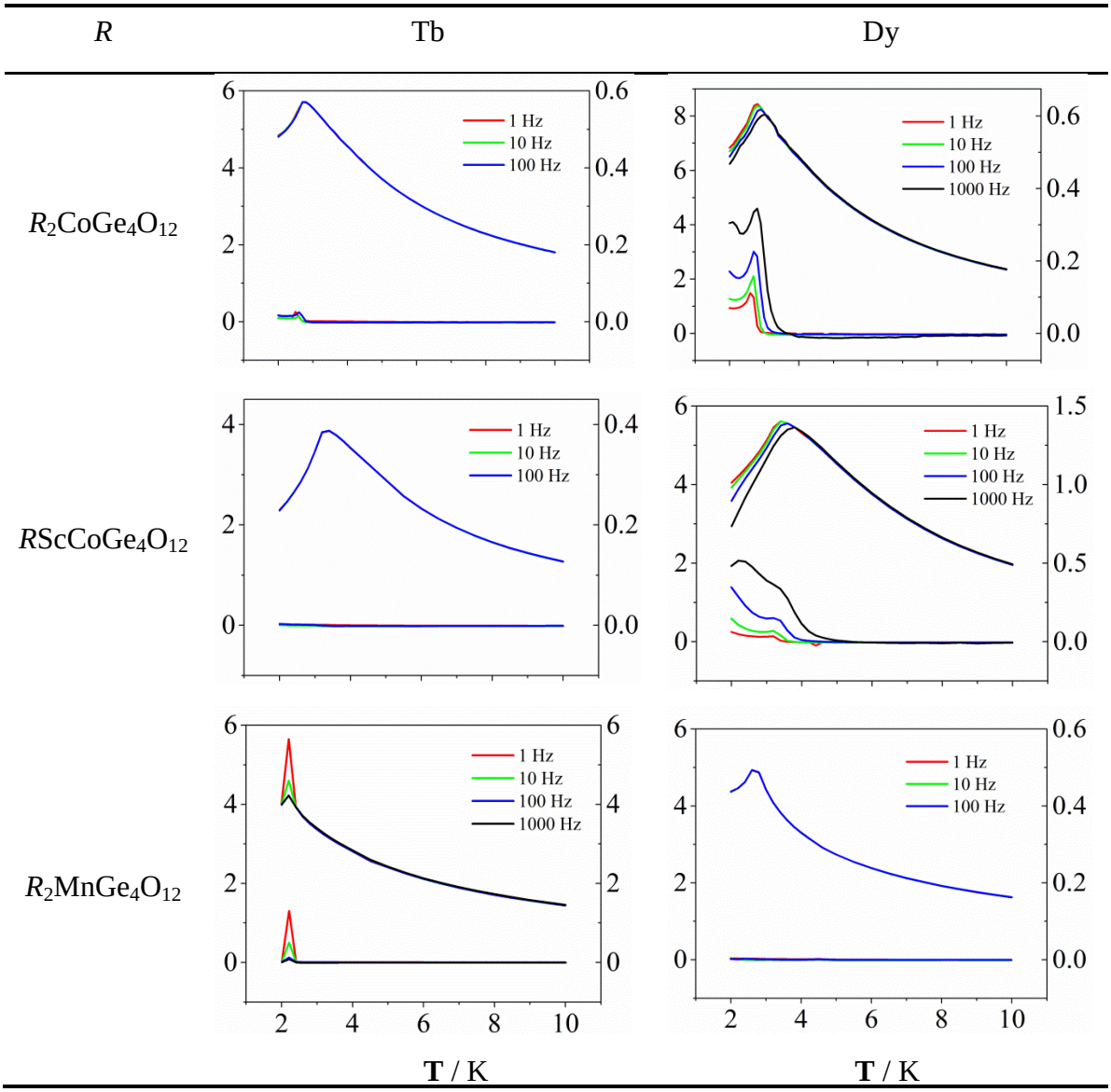

Figure 7.7 Temperature dependence of the ac molar magnetic susceptibility of $R_2MGe_4O_{12}$ and $RScCoGe_4O_{12}$ (R = Tb-Yb; M = Mn, Co).

AC susceptibility measurements were carried out in zero field on all the compositions and the results were shown in Figure 7.7. Moreover, in-field ac susceptibility measurements were conducted in dc fields 0.1/0.5/1/5 kOe for $R_2MGe_4O_{12}$ and $RScCoGe_4O_{12}$ (M = Co, Mn; R = Tb, Dy). The data are shown in Appendix D Figure D.1 - Figure D.13. $Dy_2CoGe_4O_{12}$ and $DyScCoGe_4O_{12}$ are spin glasses and $Tb_2CoGe_4O_{12}$ has an imaginary component although the real part signal is not frequency dependent. $Tb_2MnGe_4O_{12}$ shows a

ferromagnetic transition at its T_C whereas $Dy_2MnGe_4O_{12}$ and $TbScCoGe_4O_{12}$ are antiferromagnets but have a small contribution in the imaginary part. When a field is applied, an increase in the imaginary part of the susceptibility is observed in $Tb_2CoGe_4O_{12}$ and $TbScCoGe_4O_{12}$. The Φ value calculated from Equation 1.9, 0.024 and 0.039 for $Dy_2CoGe_4O_{12}$ and $DyScCoGe_4O_{12}$ respectively, suggests that the two compounds are spin glass ($0.01 < \Phi < 0.08$).

7.3.2.3 Zero-Field Low Temperature Neutron Diffraction

Neutron-diffraction data were collected on $Tb_2CoGe_4O_{12}$, $TbScCoGe_4O_{12}$ and $Tb_2MnGe_4O_{12}$ at 1.5 K using wavelengths of λ = 1.622 and 2.4395 Å. Figure 7.8 shows the necessity of the Tb moment in both $Tb_2CoGe_4O_{12}$ and $TbScCoGe_4O_{12}$ cases. The magnetic structures and the mean ordered atomic moment values derived from the combined analysis of the two different patterns are shown in Figure 7.9 and Table 7.7. $TbScCoGe_4O_{12}$ is represented by the formula $(Tb_{0.86(1)}Sc_{0.14})(Tb_{0.14}Sc_{0.86})CoGe_4O_{12}$ with site exchange. The mean magnetic moment of 3.73 μ_B per cation at the 2*b* site corresponds to a moment of 4.32(6) μ_B per Tb^{3+} and the moment of 1.44 μ_B per cation at the 4*f* site corresponds to a mean moment of 2.53(5) μ_B per magnetic cation, averaged over 0.5 Co^{2+} and 0.07 Tb^{3+} cations.

Table 7.7 Atomic magnetic moments in $Tb_2CoGe_4O_{12}$, $TbScCoGe_4O_{12}$ and $Tb_2MnGe_4O_{12}$ at 1.5 K

	$Tb_2CoGe_4O_{12}$		$TbScCoGe_4O_{12}$		$Tb_2MnGe_4O_{12}$
M	2*b*	4*f*	2*b*	4*f*	4*f*
	(Tb^{3+})	(Tb^{3+}/Co^{2+})	(Tb^{3+}/Sc^{3+})	($Tb^{3+}/Sc^{3+}/Co^{2+}$)	(Tb^{3+}/Mn^{2+})
M_x /μ_B	2.17(17)	0.89(9)	3.73(5)	1.23(3)	0
M_y /μ_B	0	0.98(11)	0	0.74(5)	0
M_z /μ_B	0	0	0	0	1.19(1)
M /μ_B	2.17(17)	1.32(14)	3.73(5)	1.44(5)	1.19(1)

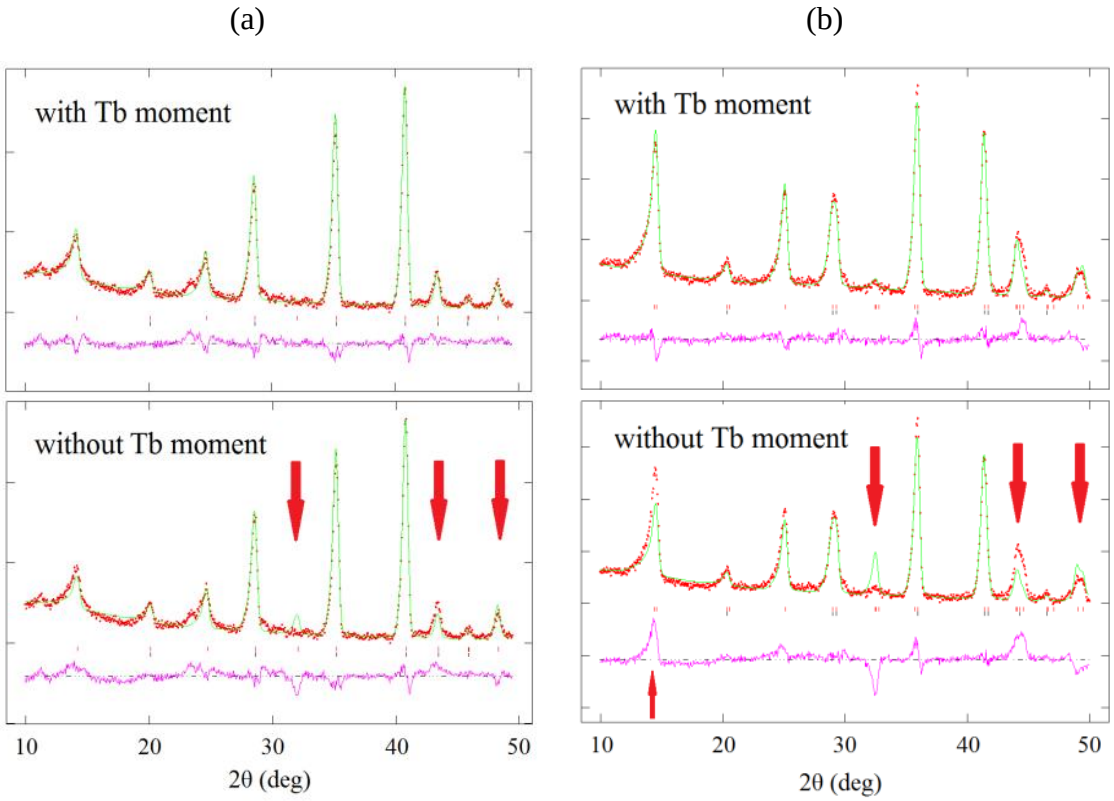

Figure 7.8 Expanded view of the fits to the low-angle regions of the 1.5 K diffraction profiles of (a) $Tb_2ScCoGe_4O_{12}$ and (b) $TbScCoGe_4O_{12}$ using wavelength $\lambda = 2.4395$ Å.

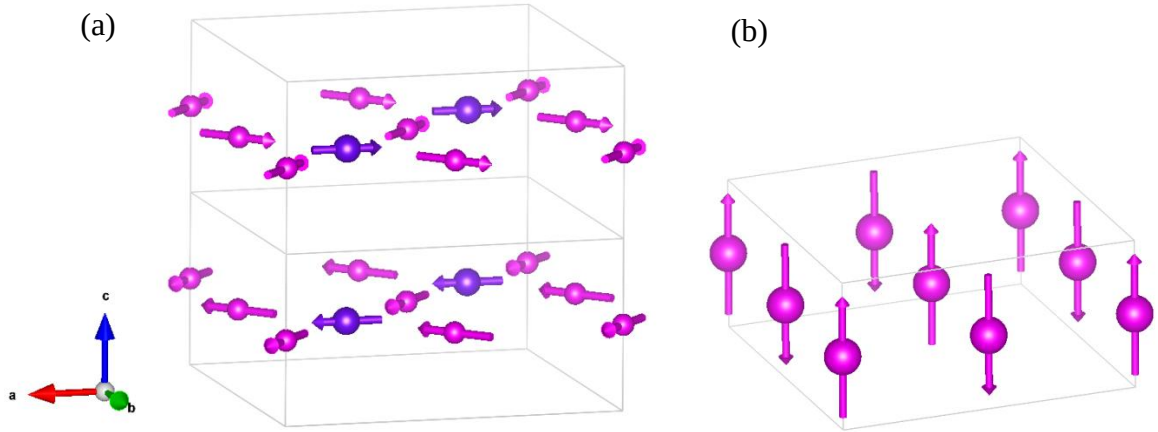

Figure 7.9 Magnetic structures in zero field of (a) $Tb_2CoGe_4O_{12}$, $TbScCoGe_4O_{12}$ and (b) $Tb_2MnGe_4O_{12}$. Purple balls represent the moment at the *2b* site and pink balls represent the moment at the *4f* site. Diamagnetic ions are omitted.

7.3.3 Discussion

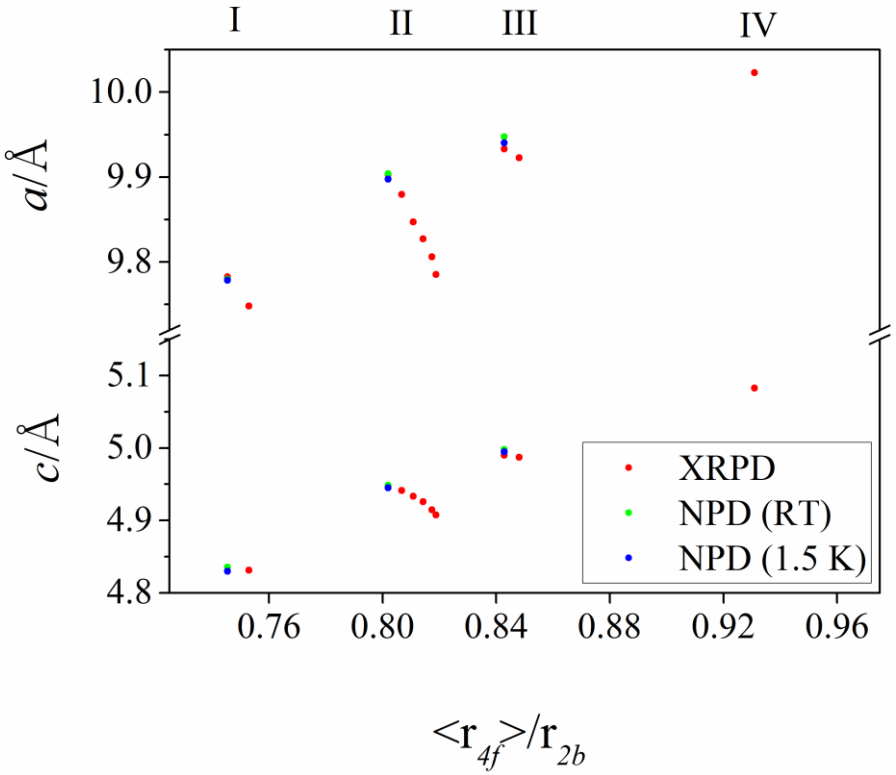

Figure 7.10 Structural unit cell parameters *a* and *c* derived from diffraction data. Regions I, II, III and IV relate to $RScCoGe_4O_{12}$ (*R* = Tb, Dy), $R_2CoGe_4O_{12}$ (*R* = Tb - Yb), $R_2MnGe_4O_{12}$ (*R* = Tb, Dy) and $Dy_2CaGe_4O_{12}$,respectively. The error bars are smaller than the size of the points.

Table 7.8 Ionic radii [9] (Å) for some selected cations

Cation (III)	Site	
	2b(VIII)	4f(VI)
Gd	1.053	0.938
Tb	1.04	0.923
Dy	1.027	0.912
Ho	1.015	0.901
Er	1.004	0.89
Tm	0.994	0.88
Yb	0.985	0.868
Y	1.019	0.9
Sc	0.87	0.745

Table 7.9 Derived structural parameters for $Tb_2CoGe_4O_{12}$, $TbScCoGe_4O_{12}$ and $Tb_2MnGe_4O_{12}$ from low temperature NPD, λ = 1.622 Å

Composition	$<r_{4f}>/r_{2b}$	$2c/a$	$d(M_{4f}-O2)/d(M_{4f}-O1)$	φ /°	ψ /°	q
$Tb_2MnGe_4O_{12}$	0.843	1.0050	0.882(1)	81.80(8)	42.61(4)	0.852(1)
$Tb_2CoGe_4O_{12}$	0.802	0.9992	0.879(1)	81.60(8)	41.92(4)	0.843(1)
$TbScCoGe_4O_{12}$	0.745	0.9878	0.868(1)	81.42(8)	40.60(4)	0.816(1)

φ Angle between M_{4f} – O1 bond and M_{4f} – O2 plane

ψ Angle between the M_{4f} – O1 bond and the (001) plane

q Ratio of O2 – O2 distance in square face of antiprism to perpendicular distance between faces

In view of the complex formulae of these compounds, the ratio $<r_{4f}>/r_{2b}$ was considered in addition to the unit cell parameters a and c. The unit cell parameters derived from XRPD and NPD are plotted in Figure 7.10. The unit cell parameters derived from NPD on $Tb_2CoGe_4O_{12}$, $TbScCoGe_4O_{12}$, and $Tb_2MnGe_4O_{12}$ show no significant structural change on cooling from room temperature to 1.6 K. The $<r_{4f}>/r_{2b}$ ratio of $TbScCoGe_4O_{12}$ allows for the observed site exchange and the same ratio was assumed to apply $DyScCoGe_4O_{12}$.

For $R_2MGe_4O_{12}$ (M = Ca, Mn, Co; R = Tb-Yb) compositions, different transition-metal cations M can generate a considerable difference in the unit cell parameters. The change from a lanthanide cation to Sc^{3+} at the *4f* site is also able to decrease the unit cell parameters. Based on the XRPD data, $Tb_2CoGe_4O_{12}$ has decreases in a and c of 0.30 % and 0.86 % compared to $Tb_2MnGe_4O_{12}$; $TbScCoGe_4O_{12}$ has decreases in a and c of 1.22 % and 2.26 % compared to $Tb_2CoGe_4O_{12}$. For Dy-containing compounds, there is a 1.00 % decrease in a and 1.88 % decrease in c between Ca and Mn, and further a 0.43 % decrease in a and 0.93 % in c from Mn to Co; the decrease is 1.33 % in a and 2.22 % in c with Sc^{3+} substitution. In the past four chapters, it has been shown that decreasing the $<r_{4f}>/r_{2b}$ value normally leads to the ratio $2c/a$ decreasing , the angle φ increasing, the angle ψ decreasing and the q ratio decreasing. This is also true for the Tb-containing compounds except that the angle φ actually decreases in this case. Notably, the q ratio for $TbScCoGe_4O_{12}$ is much smaller than those of $Tb_2MnGe_4O_{12}$ and $Tb_2CoGe_4O_{12}$, but such a value is closer to what was reported in the previous four chapters. The perpendicular distance between the faces of

the antiprism around the *2b* site in $Tb_2CoGe_4O_{12}$ is d_{pp} = 2.421(1) Å and the O2 – O2 distance is d_{in} = 2.871(1); those of $TbScCoGe_4O_{12}$ are d_{pp} = 2.349(1) Å and d_{in} = 2.879(1); d_{pp} is considerably shorter in the $TbScCoGe_4O_{12}$ case whereas the d_{in} is essentially unchanged. The Tb – O bond lengths for the *2b* and *4f* sites suggest the two sites are both in a compressed environment.

Our previous study of $Y_2CoGe_4O_{12}$ [10] showed that the Co^{2+} ions that occupy half of the *4f* sites cannot alone support the long-range magnetic ordering and it is therefore likely that if the Ho^{3+} and Er^{3+} cations remain paramagnetic, the Co^{2+} cations remain paramagnetic. $R_2CaGe_4O_{12}$ (*R* = Gd-Lu, Y) compounds have a non-magnetic cation Ca^{2+} at the *4f* site and the magnetic interactions between rare-earth lanthanide cations should be relatively weak. Thus they are expected to be paramagnetic down to 2 K and one compound described in the next chapter, $Gd_2CaGe_4O_{12}$, is paramagnetic to prove this. The other compounds show a transition at around 3 K; ferromagnetic transition for $Tb_2MnGe_4O_{12}$ and antiferromagnetic for the others. Further ac susceptibility measurements illustrate that $Tb_2MnGe_4O_{12}$ has a ferromagnetic phase; $Dy_2MnGe_4O_{12}$ is antiferromagnetic; $Tb_2CoGe_4O_{12}$ behaves as a spin glass; $Dy_2CoGe_4O_{12}$ and $DyScCoGe_4O_{12}$ are spin glass; $TbScCoGe_4O_{12}$ is an antiferromagnet.

The application of a 50 kOe magnetic field at 2 K results in an unsaturated magnetisation that is approximately equal to $\frac{1}{2}\, n_{Ln} g_{Ln} J_{Ln} + g_M S_M$, where $g_M = 2$ as discussed in Chapter 3. The value is less than the theoretical value of $n_{Ln} g_{Ln} J_{Ln} + g_M S_M$. Similarly reduced values have been observed previously in other compounds and attributed to either the presence of magnetic anisotropy in a powder sample or crystal field effects [11], [12], [13], [14], [15], [16], [17].

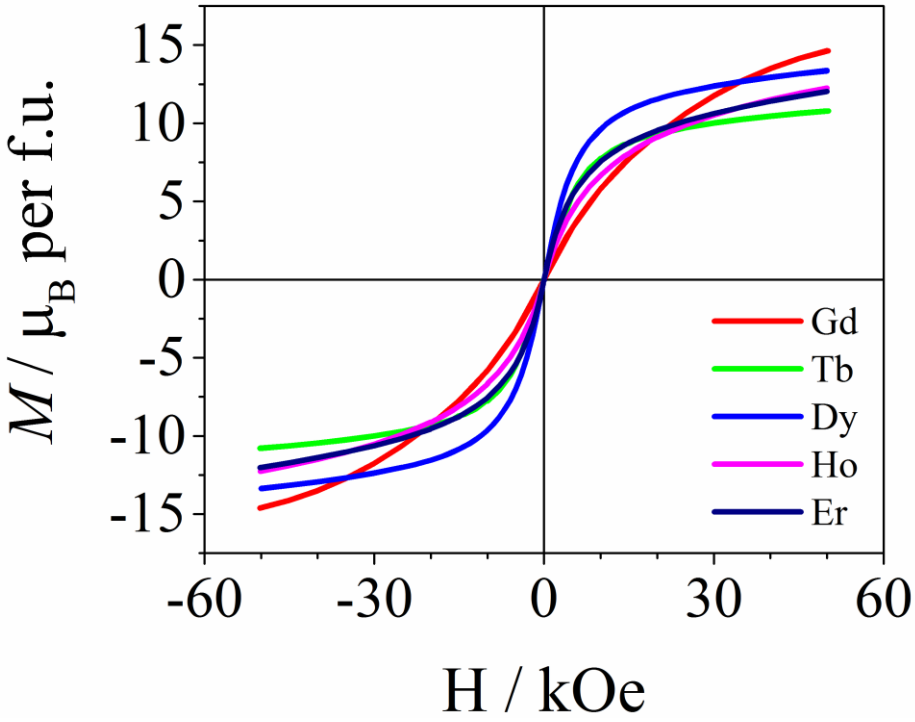

Figure 7.11 Field dependence of the magnetisation of $R_2CoGe_4O_{12}$ (R = Gd-Er) at 2 K.

From the NPD data, $Tb_2CoGe_4O_{12}$ and $TbScCoGe_4O_{12}$ adopt essentially the same magnetic structure at 1.5 K whereas $Tb_2MnGe_4O_{12}$ has a different magnetic structure. Given the relationship $a = b \sim 2c$ between the lattice constants of the structural unit cell, the ordered moments on the *4f* sublattice can be described using the nomenclature devised by Wollan and Koehler [18] to describe spin ordering on a primitive cubic lattice. Thus, for $Tb_2CoGe_4O_{12}$ and $TbScCoGe_4O_{12}$, the components of the moments along [100] order in an A-type manner and those along [010] order in a G-type manner. This spin arrangement also occurs in $CeCo_2Ge_4O_{12}$, but not in $ZrCo_2Ge_4O_{12}$. Comparison of these values with those in the past four chapters would lead to the prediction that the doubling of the magnetic unit cell along [001] will also occur in $TbScCoGe_4O_{12}$ but not in $Tb_2CoGe_4O_{12}$. The fact that the unit cell doubling does occur in $Tb_2CoGe_4O_{12}$ demonstrates that the introduction of the 4*f* electron system has a sufficiently large impact on the magnetic properties to invalidate the criteria developed previously. The systems described in the past four Chapters only have M – O – Ge – O – M' superexchange interactions and the calculated parameters reflect this superexchange. However, in the lanthanide-containing system, beside the M – O – Ge – O – M' superexchange, R – O – M is another significant superexchange pathway and the anisotropy of the R is also expected to be a key factor.

Thus, it is not surprising $Tb_2CoGe_4O_{12}$ and $TbScCoGe_4O_{12}$ have the same magnetic structure. As discussed above, $TbScCoGe_4O_{12}$ is actually represented by the formula $(Tb_{0.86(1)}Sc_{0.14})(Tb_{0.14}Sc_{0.86})CoGe_4O_{12}$ with site exchange. The *2b* site corresponds to a moment of 4.32(6) μ_B per Tb^{3+} and the *4f* site corresponds to a mean moment of 2.53(5) μ_B per magnetic cation, averaged over 0.5 Co^{2+} and 0.07 Tb^{3+} cations. In $Tb_2CoGe_4O_{12}$, the *2b* site corresponds to a moment of 2.17(17) μ_B per Tb^{3+} and the *4f* site corresponds to a mean moment of 1.32(14) μ_B per magnetic cation, averaged over 0.5 Co^{2+} and 0.5 Tb^{3+} cations. Assuming that the Tb^{3+} and Co^{2+} cations on the 4*f* site have the same ordered moments in the two compounds $Tb_2CoGe_4O_{12}$ and $TbScCoGe_4O_{12}$, then it follows that Tb^{3+} and Co^{2+} have moments of -0.2(1) and 2.9(1) μ_B, respectively. The moment on the Tb^{3+} cations is thus not significant compared to the standard deviation but, if present, it aligns antiparallel to the direction the moment of a Co^{2+} cation would adopt on the same site. Comparing to the ordered moments of Co^{2+} observed previously in $ZrCo_2Ge_4O_{12}$ and $CeCo_2Ge_4O_{12}$, 2.55(7) and 2.58(2) μ_B, it is accepted that Tb^{3+} should have no contribution at the *4f* site at low temperatures.

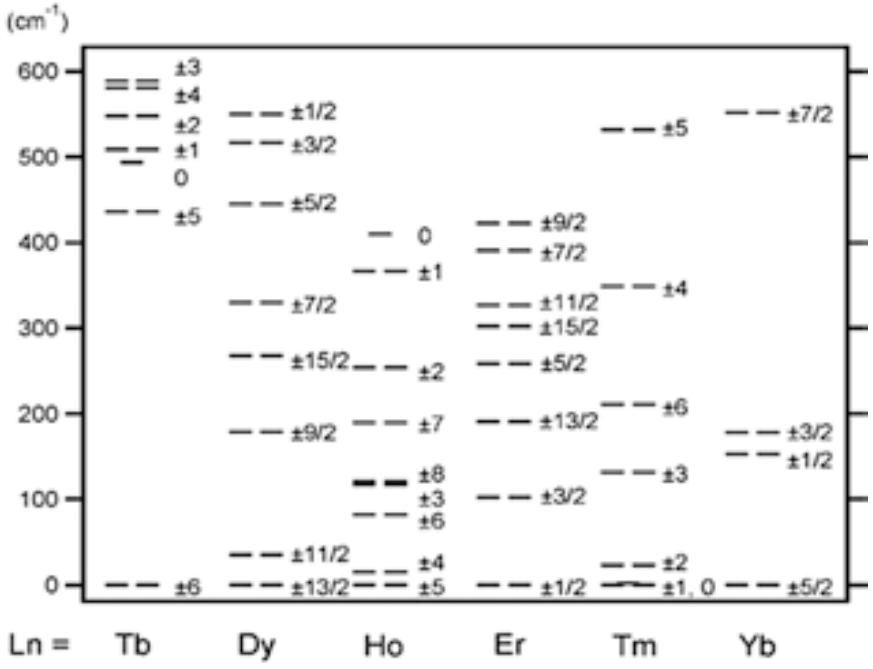

Figure 7.12 Energy level diagrams of the ground-state multiplets for $[Pc_2Ln]^-$ (Ln = Tb, Dy, Ho, Er, Tm, or Yb). [13]

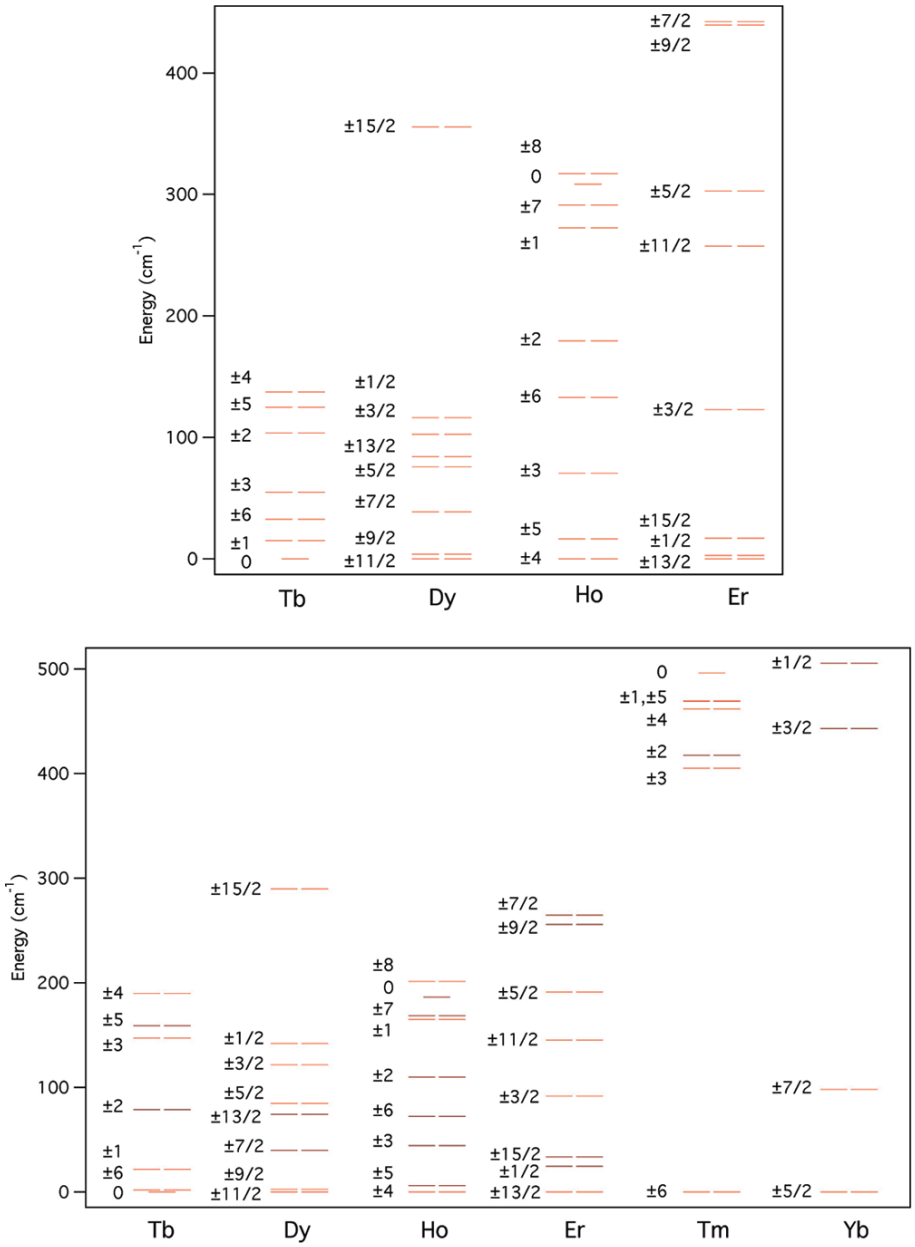

Figure 7.13 Energy level diagrams of the ground-state multiplets for $Na_9[Ln(W_5O_{18})_2] \cdot xH_2O$ and $K_{13}[Ln(\beta_2\text{-}SiW_{11}O_{39})_2] \cdot xH_2O$ families derived from the susceptibility data. [16]

As described in Chapter 1, a crystal field is able to influence the magnetic properties of a first-row transition-metal cation. Similarly, the crystal field is also able to influence the lanthanide cations by changing the degree of the spin-orbital coupling [19]. The crystal field influence on a lanthanide cation in an eight-coordinate site (D_{4d}) [20], [21], [22] and a six-coordinate site (O_h) [23], [24], [25], [26] have been studied in depth. Ishikawa *et al.* [11], [12], [13] and AlDamen *et al.* [16] published a series of studies on *R*(III) in a D_{4d} coordination environment. They suggested that the ratio of the perpendicular distance between the faces

of the antiprism d_{pp} and the distance of the edge of one square face d_{in}, defined as the q ratio in this thesis, is the key factor influencing the magnetic ground state of the lanthanide cations. The magnetic ground state for Tb^{3+} is $m_J = \pm 6$ for $q > 1$ whereas it is $m_J = 0$ for $q < 1$. The energy level diagrams of the ground-state multiplets are shown in Figure 7.12 and Figure 7.13. However, because the crystal-field effect is different in different D_{4d} systems, the first excited state may vary and the excitation energy will be different, see Figure 7.13. There is not much data available for a lanthanide cation in an O_h environment. It has previously been argued that crystal-field effects leave a Tb^{3+} cation on an octahedral site with a non-magnetic singlet ground state [27] but it is achieved in the alloy $Tb_\zeta Y_{1-\zeta}Sb$, in which more complex interactions might be present. Hence, we therefore propose that the crystal field at the *2b* site (D_{4d}) in our compounds can also lead the Tb^{3+} to a non-magnetic ground state.

As discussed in Chapters 3 and 5, the anisotropy of Co^{2+} can also change the magnetic structure. 25% substitution from Mn^{2+} to Co^{2+} in $CeMn_2Ge_4O_{12}$ can drive the ordered moment from being aligned along the *c* axis into *ab* plane whereas the ordered moments still lie align *c* axis in $CeMn_{1.5}Ni_{0.5}Ge_4O_{12}$. In the case of $Tb_2CoGe_4O_{12}$ and $TbScCoGe_4O_{12}$, the moment of Tb^{3+} at the *2b* site has the same direction as the *4f* site ferromagnetic component in one ferromagnetic layer. This may come from the total influence from complex interactions, Tb – O – Co superexchange, Co – O – Ge – O – Co superexchange, single ion anisotropy, anisotropic exchange, dipolar interactions and the internal molecular field created by the Co^{2+} sublattice. The combination of these leads to the moment of Tb^{3+} at the 2*b* site lying in the *ab* plane when the easy-axis of Tb^{3+} is along the *c* axis [19]. The complex interactions may also result in an accessible first excited energy state for Tb^{3+} at low temperatures and therefore a significant ordered moment was observed for Tb^{3+} at the 2*b* site (D_{4d}). The large difference of the q ratio between $Tb_2CoGe_4O_{12}$ and $TbScCoGe_4O_{12}$ could be the reason for the ordered moments at the *2b* site being 2.17(17) and 4.32(6) μ_B respectively. In the case of $Tb_2CoGe_4O_{12}$, given the presence of a small but clear peak at 2.8 K in ac susceptibility, a small hysteresis between ZFC/FC in the dc susceptibility and the absence of a contribution to the magnetic Bragg scattering, we propose that the Tb^{3+} spins at the *4f* site may add a spin-glass-like component to the magnetic behaviour.

In $Tb_2MnGe_4O_{12}$, the components of the moments along [001] order in an antiferromagnetic manner. This spin arrangement also occurs in $CeMn_2Ge_4O_{12}$ and in $ZrMn_2Ge_4O_{12}$. The factors that control the magnetic structure have been discussed previously and the parameters that were then considered to be important have been calculated, see Table 7.9. The *2b* site has no magnetic contribution and the *4f* site corresponds to a mean moment of 1.19(1) μ_B per magnetic cation, averaged over 0.5 Mn^{2+} and 0.5 Tb^{3+} cations. That no magnetic contribution was detected from the *2b* site is consistent with $m_J = 0$ for $q < 1$. The mean ordered moment of Mn^{2+} observed previously in $CeMn_2Ge_4O_{12}$ and $ZrMn_2Ge_4O_{12}$ is ~ 4.6 μ_B. Hence, Mn^{2+} and Tb^{3+} could probably have opposite ordered moments at *4f* site along the [001] axis, which leads to 6.98 μ_B per Tb^{3+}. For a free Tb^{3+} cation, gJ = 9 μ_B and the moment of Tb^{3+} in neutron diffraction is normally determined to be ~ 8 μ_B [28], [29]. The difference may come from the bond covalency, crystal field effects and spin canting. We have made the comment above that the crystal-field effects leave a Tb^{3+} cation on an octahedral site with a non-magnetic singlet ground state in the alloy $Tb_\zeta Y_{1-\zeta}Sb$. However, we have observed a considerable moment of Tb^{3+} at the *4f* site. This suggests that the crystal-field effects of a Tb^{3+} cation on a distorted octahedral site may influence the ground state of the Tb^{3+} cation but the influence is much weaker compared to that at the *2b* site. Moreover, this fact can support our proposal that the Tb^{3+} at the *4f* site may make the compound behave as a weak spin glass. The weakly ferromagnetic phase in $Tb_2MnGe_4O_{12}$ magnetometry measurements may originate from the spin canting (also observed in $CeMn_2Ge_4O_{12}$ and $ZrMn_2Ge_4O_{12}$) and/or the local disorder. Normally, the ac susceptibility has the relationship $\chi = \sqrt{\chi'^2 + \chi''^2}$ between the real part and the imaginary part, which means if the real part has a large signal its corresponding imaginary signal should be small. However, in $Tb_2MnGe_4O_{12}$, a large imaginary signal comes with a large real signal and the ratio is approximately 1:3, see Figure 7.7. Moreover, no hysteresis was detected in the M(H) curve. We do not have a satisfied explanation for these abnormal behaviours now.

There is no evidence in $\chi(T)$ for the presence of paramagnetic spins in $Dy_2CoGe_4O_{12}$ or $DyScCoGe_4O_{12}$ at the lowest temperature; the ZFC and FC dc susceptibilities are slightly different below the transition temperature, see Figure 7.3 and Figure 7.5; the ac susceptibility is complex below a frequency-dependent transition temperature and the data suggest that they are spin glasses (Φ = 0.024 and 0.039 respectively, in the range 0.01 –

0.08 according to Mydosh [30]). However, the frustration factor $f = |\theta/T_m|$ is small for these spin glass indicating the glassy behaviour is not coming from geometrical frustration. The dc susceptibility of $Dy_2MnGe_4O_{12}$ is characteristic of an antiferromagnet and the ac susceptibility proves it. The difference of the spin-orbital coupling between Tb^{3+} and Dy^{3+} results in $Dy_2MnGe_4O_{12}$ being an antiferromagnet whereas $Tb_2MnGe_4O_{12}$ having a weakly ferromagnetic phase.

It can be seen, see Figure 7.6, that in the case of $TbScCoGe_4O_{12}$ and $DyScCoGe_4O_{12}$, the susceptibility is field-dependent below the transition temperature T_m in weak fields and over a wider temperature range in stronger fields; the transition broadens with increasing field strength. In the case of $Dy_2CoGe_4O_{12}$, the susceptibility decreases as the field is increased to 1 kOe whereas in the case of $DyScCoGe_4O_{12}$ an increase is observed. The former but not the latter could be attributed to saturation effects and we propose that both are actually caused by changes in the population of the m_J states of Dy^{3+} that occur as a result of the superposition below T_m of an internal magnetic field on the pre-existing crystal field. The magnetic transition is not apparent in fields greater than or equal to 10 kOe. $Tb_2CoGe_4O_{12}$ and $TbScCoGe_4O_{12}$ show a weak frequency-dependent behaviour in an external magnetic field, see Appendix D Figure D.1 – Figure D.3 and Figure D.8 – Figure D.9, which also proves the repopulation of the m_J states.

As discussed above, the magnetic field is able to form new magnetic ground state for Ln^{3+} and repopulate the m_J states. Hence, the magnetic behaviour is a function of temperature and magnetic field, see Figure 7.6. The measurements indicate that a 100 Oe magnetic field is not able to influence the system but a 1000 Oe one can. A loss of magnetic ordering is expected when $\mu_B H/k_B \sim T_m$. Repopulation of the m_J states in higher fields leads to the lanthanide cations behaving as if in their paramagnetic state. Also, the magnetic properties come from a series of complex interactions: R – O – M superexchange interaction, M – O – Ge – O – M' superexchange interaction, single ion anisotropy influence, anisotropic exchange, dipolar interaction, and influence from the internal molecular field created by the Co^{2+} sublattice. The combination of all the interactions leads to $R_2CoGe_4O_{12}$ antiferromagnetism, spin-glass behaviour and paramagnetism due to different spin-orbital coupling and anisotropy. Further work will be necessary and $R_2CoGe_4O_{12}$ (R = Tm, Yb) may show a magnetic transition below 2 K.

7.3.4 Conclusion

The isostructural compounds described above show a wide range of magnetic properties. Within the series $Ln_2CoGe_4O_{12}$ we have observed antiferromagnetism, spin-glass behaviour and paramagnetism. The first two phenomena are only observed below 4 K, *i.e.* in a temperature regime where the effect of the crystal-field on Ln^{3+} cations cannot be ignored. The observed behaviour has been attributed to the interplay of the crystal field, the magnetic anisotropy and the magnetic field, either external or internal. The antiferromagnetic spin structures adopted by $Tb_2CoGe_4O_{12}$ and $TbScCoGe_4O_{12}$ are essentially the same whereas $Tb_2MnGe_4O_{12}$ has a different one. This is consistent with the conclusion that the anisotropy of Co^{2+} and lanthanide cations plays a key factor in determining their magnetic properties.

The work described in this Chapter has been published as *Magnetic properties of Magnetic properties of $Ln_2CoGe_4O_{12}$ and$LnBCoGe_4O_{12}$ (Ln = Gd, Tb, Dy, Ho, Er; B = Sc, Lu),* D. Xu, M. Avdeev, P. D. Battle, and D. H. Ryan, *Dalton Transaction*, 2017, **46**, 15778-15788.

7.4 References

[1] H. M. Rietveld, A profile refinement method for nuclear and magnetic structures, *Journal of Applied Crystallography*, **1969**, *2*, 65-71.

[2] R. A. Young, *The Rietveld Method*, Oxford University Press **1993**.

[3] B. H. Toby, EXPGUI, a graphical user interface for GSAS, *Journal of Applied Crystallography*, **2001**, *34*, 210-213.

[4] A. C. Larson, and R. B. Von Dreele, *General Structure Analysis System (GSAS)*, Los Alamos National Laboratory Report LAUR 86-748: **2004**.

[5] B. van Laar, and W. B. Yelon, The peak in Neutron Powder Diffraction, *Journal of Applied Crystallography*, **1984**, *17*, 47-54.

[6] K. Momma, and F. Izumi, VESTA: a three-dimensional visualization system for electronic and structural analysis, *Journal of Applied Crystallography*, **2008**, *41*, 653-658.

[7] V. G. Zubkov, N. V. Tarakina, I. I. Leonidov, A. P. Tyutyunnik, L. L. Surat, M. A. Melkozerova, E. V. Zabolotskaya, and D. G. Kellerman, Synthesis and crystal structure of $Ln_2M^{2+}Ge_4O_{12}$, Ln=rare-earth element or Y; M=Ca, Mn, Zn, *Journal of Solid State Chemistry*, **2010**, *183*, 1186-1193.

[8] M. A. Melkozerova, N. V. Tarakina, L. G. Maksimova, A. P. Tyutyunnik, L. L. Surat, I. I. Leonidov, V. G. Zubkov, E. V. Zabolotskaya, and R. F. Samigullina, Application of a modified Pechini method for the synthesis of $Ln_2MGe_4O_{12}$ (Ln = Y, Eu; M = Ca, Zn, Mn) optical hosts, *Journal of Sol-Gel Science and Technology*, **2011**, *59*, 338-344.

[9] R. D. Shannon, Revised effective ionic radii and systematic studies of interatomic distances in halides and chalcogenides, *Acta Crystallographica Section A: Crystal Physics, Diffraction Theoretical, and General Crystallography*, **1976**, *A32*, 751.

[10] X. Liu, P. D. Battle, J. Ridout, D. Xu, S. Ramos, Structural chemistry and magnetic properties of $Y_2CoGe_4O_{12}$, *Journal of Solid State Chemistry*, **2015**, *228*, 183-188.

[11] N. Ishikawa, T. Iino, and Y. Kaizu, Interaction between f-Electronic Systems in Dinuclear Lanthanide Complexes with Phthalocyanines, *Journal of American Chemical Society*, **2002**, *124*, 11440-11447.

[12] N. Ishikawa, T. Iino, and Y. Kaizu, Determination of Ligand-Field Parameters and f-Electronic Structures of Hetero-Dinuclear Phthalocyanine Complexes with a Diamagnetic Yttrium(III) and a Paramagnetic Trivalent Lanthanide Ion, *Journal of Physical Chemistry A*, **2002**, *106*, 9543-9550.

[13] N. Ishikawa, M. Sugita, T. Okubo, N. Tanaka, T. Iino, and Y. Kaizu, Determination of Ligand-Field Parameters and f-Electronic Structures of Double-Decker Bis(phthalocyaninato)lanthanide Complexes, *Inorganic Chemistry*, **2003**, *42*, 2440-2446.

[14] E. Morosan, J. A. Fleitman, Q. Huang, J. W. Lynn, Y. Chen, X. Ke, M. L. Dahlberg, P. Schiffer, C. R. Craley, and R. J. Cava, Structure and magnetic properties of the $Ho_2Ge_2O_7$ pyrogermanate, *Physical Review B*, **2008**, *77*, 224423.

[15] X. Ke, M. L. Dahlberg, E. Morosan, J. A. Fleitman, R. J. Cava, and P. Schiffer, Magnetothermodynamics of the Ising antiferromagnet $Dy_2Ge_2O_7$, *Physical Review B*, **2008**, *78*, 104411.

[16] M. A. AlDamen, S, Cardona-Serra, J, M. Clemente-Juan, E. Coronado, A. Gaita-Arino, C. Marti-Gastaldo, F. Luis, and O. Montero, Mononuclear Lanthanide Single Molecule Magnets Based on the Polyoxometalates $[Ln(W_5O_{18})_2]^{9-}$ and $[Ln(\beta_2\text{-}SiW_{11}O_{39})_2]^{13-}$ (Ln^{III} = Tb, Dy, Ho, Er, Tm, and Yb), *Inorganic Chemistry*, **2009**, *48*, 3467-3479.

[17] A. M. Hallas, J. A. M. Paddison, H. J. Silverstein, A. L. Goodwin, J. R. Stewart, A. R. Wildes, J. G. Cheng, J. S. Zhou, J. B. Goodenough, E. S. Choi, G. Ehlers, J. S. Gardner, J.

S. Wiebe, and H. D. Zhou, Statics and dynamics of the highly correlated spin ice $Ho_2Ge_2O_7$, *Physical Review B*, **2012**, *86*, 134431.

[18] E.O. WollanW.C. Koehler, La1-xCaxMnO3 neutron diff, magentism, *Physical Review*, **1955**, *100*, 545-563.

[19] J. Tang, and P. Zhang, *Lanthanide Single Molecule Magnets*, Springer: **2015**.

[20] S. F. A. Kettle, and A. J. Smith The stereochemistry of metal complexes as an indication of f-orbital participation in the metal–ligand bonding, *Journal of the Chemical Society A: Inorganic, Physical, Theoretical*, **1967**, *0*, 688-692.

[21] J. K. Burdett, R, Hoffmann, and R. C. Fay, Eight-Coordination, *Inorganic Chemistry*, **1978**, *17*, 2553-2568.

[22] H. Ramanantoanina, W. Urland, F. Cimpoesu, and C. Daul, The angular overlap model extended for two-open-shell f and d electrons, *Physical Chemistry Chemical Physics*, **2014**, *16*, 12282-12290.

[23] M. V. Hoehn, and D. G. Karraker, Magnetic susceptibilities of trivalent lanthanide ions in an octahedral environment, *The Journal of Chemical Physics*, **1974**, *60*, 393-397.

[24] G. E. Fish, M. H. North, and H. J. Stapleton, Tests of orbit–lattice interaction models using spin–lattice relaxation data of Er^{3+}, Dy^{3+}, and Yb^{3+} in Cs_2NaYCl_6, *The Journal of Chemical Physics*, **1980**, *73*, 4807-4815.

[25] M. Zbiri, C. A. Daul, and, T. A. Wesolowski, Effect of the f-Orbital Delocalization on the Ligand-Field Splitting Energies in Lanthanide-Containing Elpasolites, *Journal of Chemical Theory and Computation*, **2006**, *2*, 1106-1111.

[26] J. Jung, M. Atanasov, and F. Neese, Ab Initio Ligand-Field Theory Analysis and Covalency Trends in Actinide and Lanthanide Free Ions and Octahedral Complexes, *Inorganic Chemistry*, **2017**, *56*, 8802-8816.

[27] B. R. Cooper, and O. Vogt, Transition from Van Vleck Paramagnetism to Induced Antiferromagnetism in $Tb_\zeta Y_{1-\zeta}Sb$, *Physical Review B*, **1970**, *1*, 1218-1226.

[28] A. Murasik, P. Fischer, A. Furrer, and W. Szczepaniak, Magnetic properties of $TbCl_3$ determined by neutron scattering, *Journal of the Less Common Metals*, **1985**, *111*, 177-184.

[29] M. Reehuis, C. Ulrich, P. Pattison, B. Ouladdiaf, M. C. Rheinstädter, M. Ohl, L. P. Regnault, M. Miyasaka, Y. Tokura, and B. Keimer, Neutron diffraction study of YVO_3, $NdVO_3$, and $TbVO_3$, *Physical Review B*, **2006**, *73*, 094440.

[30] J. A. Mydosh, *Spin Glasses: An Experimental Introduction*, Taylor & Francis, London: **1993**.

Chapter 8 - Synthesis and Characterisation of Gd-containing germanates

8.1 Introduction

In the previous chapter, mixed-metal germanates with the general formula $ABB'Ge_4O_{12}$ but with $A \neq$ Gd have been described in detail. In this Chapter, compounds with A = Gd will be discussed. We shall describe how we have synthesized a series of Gd-containing compounds: $Gd_2MGe_4O_{12}$ (M = Ca, Mn, Co), $GdRMGe_4O_{12}$ (R = Sc, Lu; M = Mn, Co), and $GdFeMGe_4O_{12}$ (M = Mn, Zn). Gd^{3+} is an isotropic cation with J = S = 7/2, L = 0, g = 2. Its magnetic contribution should all come from the spin contribution, which is the only case in the common lanthanide cations. Hence, this isotropic cation could produce some different magnetic properties. Superexchange in these compounds would involve pathways of the form (B,B') – O – Ge – O – Gd or (B,B') – O – Gd. Moreover, the isotropic cation is also a way to study the dipolar interactions within the structure. In this chapter, the synthesis and magnetometry measurements were performed by the author and the characterization by Mössbauer spectroscopy and neutron diffraction, including the data analysis, was performed by D. H. Ryan at McGill University.

8.2 Experimental

Polycrystalline samples of $Gd_2MGe_4O_{12}$ (M = Ca, Mn, Co), $GdRMGe_4O_{12}$ (R = Sc, Lu; M = Mn, Co), and $GdFeMGe_4O_{12}$ (M = Mn, Zn) were synthesised by solid-state reaction. Stoichiometric quantities of Ln_2O_3, Sc_2O_3, Co_3O_4, $MnCO_3$, $CaCO_3$, ZnO_2, and GeO_2 were mixed thoroughly in an agate mortar, along with a 10% excess of GeO_2 to counteract its loss at high temperature. The mixtures were heated at 1075 °C, or 1100 °C in the case of scandium-containing samples, for 2 days with intermediate cooling and regrinding every day. They were then pressed into pellets and annealed at the same temperature for another 4 days with intermediate cooling and regrinding every two days. The scandium-containing samples required 6 more days heating. Further heating at 1100 °C for 1 day was carried out if GeO_2 was detected as an impurity phase.

X-ray powder diffraction patterns were recorded at room temperature using Cu $K\alpha_1$ radiation. Neutron powder diffraction data on $GdFeZnGe_4O_{12}$ were collected by our collaborator D. H. Ryan, McGill University, at Canadian Neutron Beam Centre (CNBC). The experiments were conducted using a wavelength of λ = 1.3300 Å in the range $3 \leq \theta/° \leq 83$ at 3.6 K and 20 K for 30 hours at each temperature. Due to strong absorption by Gd in neutron experiments, the magnetic-only data derived from the difference between the 3.6 K and 20 K were analysed by the Rietveld method [1, 2] using the program FullProf [3] and the peak function developed by van Laar and Yelon [4]. The magnetic structure was drafted by VESTA [5].

Magnetic measurements were performed using Quantum Design MPMS XL SQUID magnetometers. DC susceptibility measurements were made over the temperature range $2\ K \leq T \leq 300\ K$ in an applied field of 100 Oe with both zero-field cooling (ZFC) and field-cooling (FC) of the samples. The field dependence of the magnetization was measured over the field range $-50\ kOe \leq H \leq 50\ kOe$ at 2K with initially cooling in a 50 kOe magnetic field. The field dependence of the magnetization was also measured at 10 K for $GdFe*M*Ge_4O_{12}$ (*M* = Mn, Zn). AC susceptibilities were measured at frequencies 1, 10, 100, 1000 Hz over the temperature range $2\ K \leq T \leq 10\ K$ in a 3.5 Oe AC driving field. Samples were ac-degaussed and then cooled in a small dc field of 3 Oe to counteract the remaining field in the SQUID.

^{155}Gd Mössbauer spectra were also collected collected by our collaborator D. H. Ryan, McGill University, on all the samples at temperatures of 5 and 1.8 K. The 50 mCi ^{155}Sm source and sample were mounted vertically in a helium flow cryostat and the Mössbauer drive was operated in sinusoidal mode. The 86.55 keV Mössbauer γ-photons were isolated from the various X-rays emitted by the source with a high-purity Ge detector. The system was calibrated using a laser interferometer with velocities crosschecked against ^{57}Co**Rh**/α-Fe at room temperature and both $^{155}SmPd_3/GdFe_2$ and cubic Gd_2O_3 at 5 K. An ^{57}Fe Mössbauer spectrum was collected from a polycrystalline sample of GdFeMGe4O12 (M = Mn, Zn) at temperature range $5\ K \leq T \leq 20\ K$ using a standard transmission spectrometer and a ^{57}Co**Rh** source. The drive velocity of the spectrometer was calibrated using a 6 μm thick α-Fe foil, at 295 K, and the isomer shift (δ) is quoted relative to the centre of the α-Fe calibration spectrum. The spectra were fitted using a non-linear least-square minimization routine derived from an exact solution to the full Hamiltonian.

8.3 Results

8.3.1 Structural Chemistry

8.3.1.1 X-ray Diffraction

Single phases were obtained for all the solid solutions. The cobalt-containing compounds were blue in colour, manganese-containing and/or iron-containing ones were brown and calcium-containing ones were white. The crystal structure of the solid solutions can all be indexed in the tetragonal space group *P*4/*nbm* (No. 125), consistent with the result by Zubkov *et al.* [6], [7]. The fitted room temperature X-ray diffraction patterns are shown in Appendix A Figure A.30 - Figure A.37. Structural parameters derived from the refinements are listed in Table 8.1 and Table 8.2.

Table 8.1 Structural parameters of GdFe*M*Ge_4O_{12} (*M* = Mn, Zn) at room temperature derived from X-ray diffraction data (λ = 1.5406 Å)

		GdFeMnGe4O12	GdFeZnGe4O12
Ge	*x*	0.5262(2)	0.5264(4)
O1	*x*	-0.3618(9)	-0.3646(15)
	z	0.1742(20)	0.1780(34)
O2	*x*	0.1603(10)	0.1537(16)
	y	0.0580(8)	0.0544(12)
	z	0.2571(16)	0.2593(26)
a/Å		9.7992(1)	9.7298(2)
c/Å		4.8126(1)	4.7515(1)
V/Å^3		462.13(1)	449.83(2)
R_{wpr}		5.79%	10.05%
χ^2		1.333	1.766

Space group *P*4/*nbm* (No. 125), Z = 2

Gd on 2*b* (¼, ¼, ½); Fe/*M* on 4*f* (0, 0, ½);

Ge on 8*k* (*x*, ¼, 0); O1 on 8*m* (*x*, -*x*, *z*); O2 on 16*n* (*x*, *y*, *z*)

The U_{iso} parameter of each atom was constrained to that reported by Taviot-Gueho. [8]

Table 8.2 Structural parameters of $Gd_2MGe_4O_{12}$ (*M* = Ca, Mn, Co) and $GdRMGe_4O_{12}$ (*R* = Sc, Lu; *M* = Mn, Co) at room temperature derived from X-ray diffraction data (λ = 1.5406 Å)

		B = Gd			*B* = Lu		*B* = Sc
		B' = Ca	*B'* = Mn	*B'* = Co	*B'* = Mn	*B'* = Co	*B'* = Co
Ge	*x*	0.5237(2)	0.5243(1)	0.5251(4)	0.5201(2)	0.5243(3)	0.5254(1)
O1	*x*	-0.3673(9)	-0.3647(4)	-0.3580(11)	-0.3706(6)	-0.3517(8)	-0.3614(4)
	z	0.1466(23)	0.1575(10)	0.1851(32)	0.1636(20)	0.2126(30)	0.1799(9)
O2	*x*	0.1722(9)	0.1659(4)	0.1670(13)	0.1912(8)	0.1728(10)	0.1582(4)
	y	0.0575(8)	0.0591(3)	0.0475(11)	0.0664(7)	0.0486(8)	0.0542(4)
	z	0.2567(19)	0.2565(8)	0.2469(28)	0.2624(15)	0.2373(22)	0.2525(7)
a/Å		10.0766(1)	9.9841(1)	9.9334(1)	9.9058(4)	9.8624(2)	9.8067(1)
c/Å		5.1043(1)	5.0108(1)	4.9562(1)	4.9687(3)	4.9236(1)	4.8392(1)
V/Å^3		518.28(1)	499.48(1)	489.05(2)	487.55(5)	478.90(2)	465.40(1)
R_{wpr}		7.33%	3.54%	5.53%	11.31%	6.28%	3.36%
χ^2		1.426	1.437	1.193	2.272	1.754	1.575

Space group *P*4/*nbm* (No. 125), Z = 2

Gd on 2*b* (¼, ¼, ½); *B*/*B'* on 4*f* (0, 0, ½);

Ge on 8*k* (*x*, ¼, 0); O1 on 8*m* (*x*, -*x*, *z*); O2 on 16*n* (*x*, *y*, *z*)

The U_{iso} parameter of each atom was constrained to that reported by Taviot-Gueho. [8]

8.3.2 Magnetic Properties

8.3.2.1 DC Magnetisation Measurements

The temperature dependence of the dc molar susceptibility of each sample measured in a 100 Oe magnetic field is shown in Figure 8.1 – Figure 8.3, along with the field dependence of the magnetisation measured at 2 K; the field dependence of the magnetisation measured at 10 K for GdFe*M*Ge_4O_{12} (*M* = Mn, Zn) is also shown in the same figure. The transition temperature, T_m, and the magnetic parameters resulting from fitting the Curie-Weiss law to the FC data for T > 150 K are listed in Table 8.3.

Table 8.3 Magnetic parameters of Gd_2*M*Ge_4O_{12} (*M* = Ca, Mn, Co), Gd*RM*Ge_4O_{12} (*R* = Sc, Lu; *M* = Mn, Co), and GdFe*M*Ge4O12 (*M* = Mn, Zn)

Composition	C_M / $cm^3\,mol^{-1}\,K$	θ / K	T_m / K	μ_{eff}* /μ_B
$Gd_2CaGe_4O_{12}$	15.463(1)	-3.62(2)	-	7.84
$Gd_2MnGe_4O_{12}$	20.037(1)	-5.05(2)	3.4	6.11
$Gd_2CoGe_4O_{12}$	19.312(1)	-3.34(2)	3.6	5.62
$GdLuMnGe_4O_{12}$	12.244(1)	-7.97(2)	2.8	6.04
$GdLuCoGe_4O_{12}$	11.626(1)	-6.08(2)	2.4	5.62
$GdScCoGe_4O_{12}$	11.450(1)	-1.67(2)	3.4	5.49
$GdFeMnGe_4O_{12}$	16.529(1)	-4.77(2)	T_N = 20	5.95
$GdFeZnGe_4O_{12}$	12.198(1)	7.37(2)	T_N = 13	6.01

*calculated for all the compounds except $Gd_2CaGe_4O_{12}$ using μ_{eff} (Gd) = 7.84.

M	χ / cm^3 mol^{-1}	***M*** / μ_B per f.u.

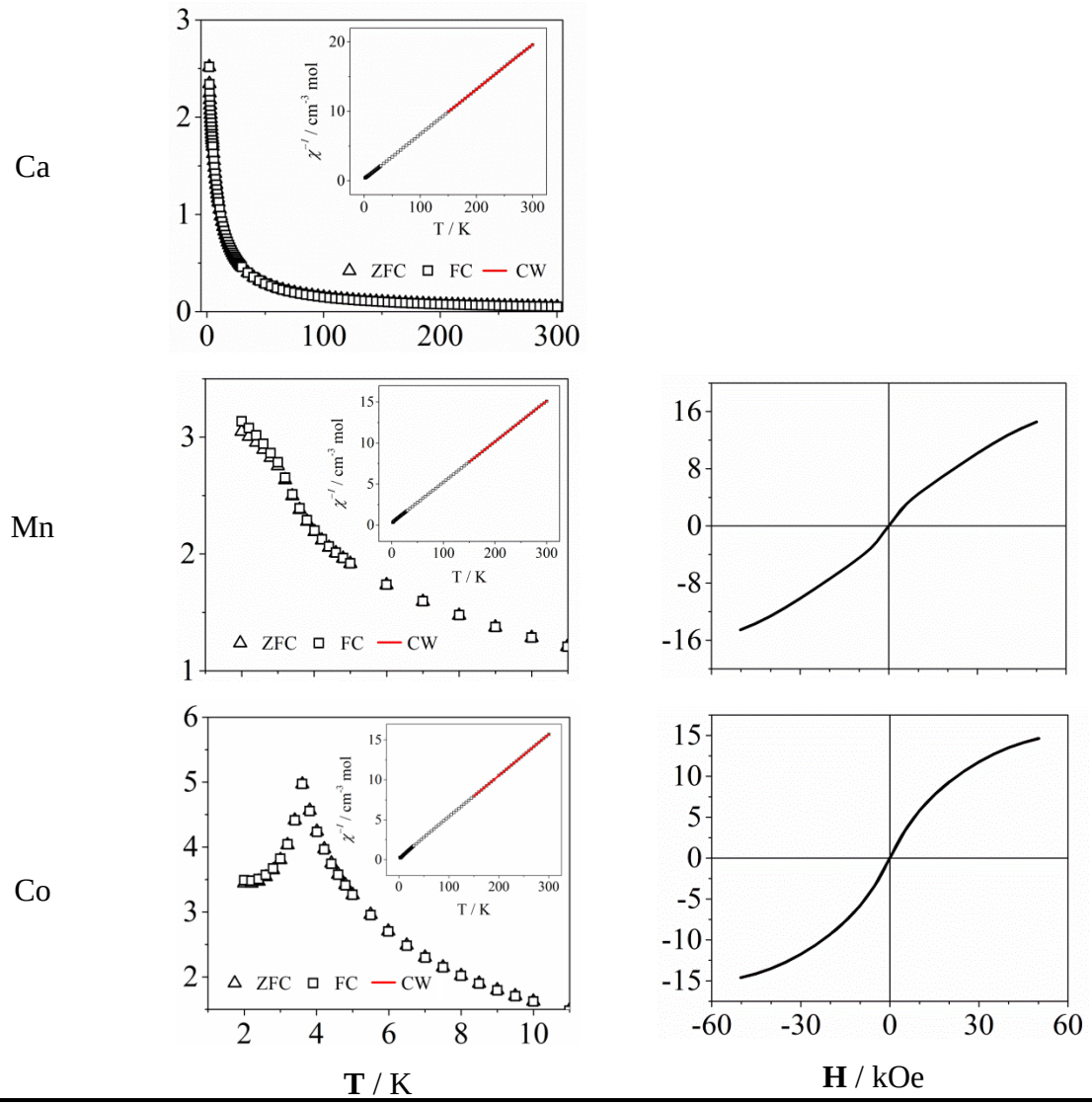

Figure 8.1 Temperature dependence of the dc molar magnetic susceptibility, measured in 100 Oe, and the field dependence of the magnetization at 2 K of $Gd_2MGe_4O_{12}$ (*M* = Ca, Mn, Co). (inset) The inverse susceptibility; data points highlighted in red were fitted to the Curie−Weiss law.

R	*M*	χ / cm^3 mol^{-1}	***M*** / μ_B per f.u.
Lu	Mn	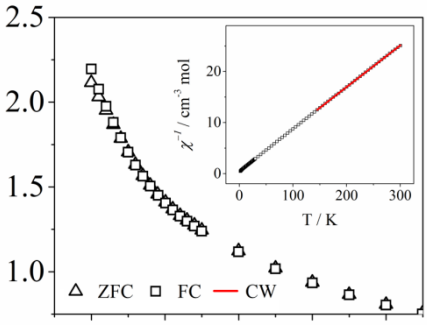	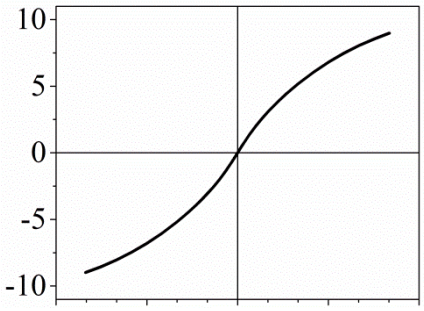
Lu	Co	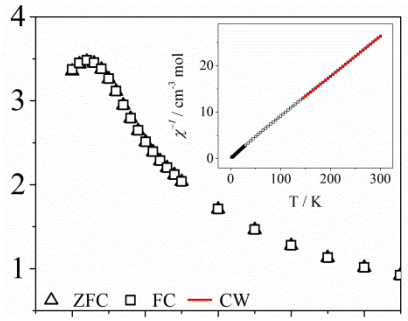	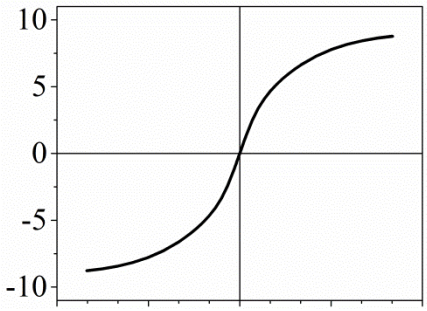
Sc	Co	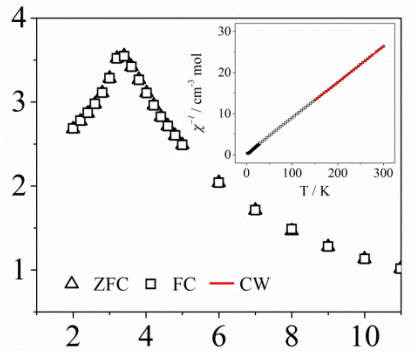	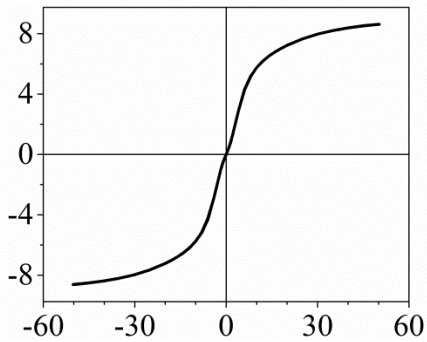
		T / K	**H** / kOe

Figure 8.2 Temperature dependence of the dc molar magnetic susceptibility, measured in 100 Oe, and the field dependence of the magnetization at 2 K of Gd*RM*Ge$_4$O$_{12}$ (*R* = Sc, Lu; *M* = Mn, Co). (inset) The inverse susceptibility; data points highlighted in red were fitted to the Curie−Weiss law.

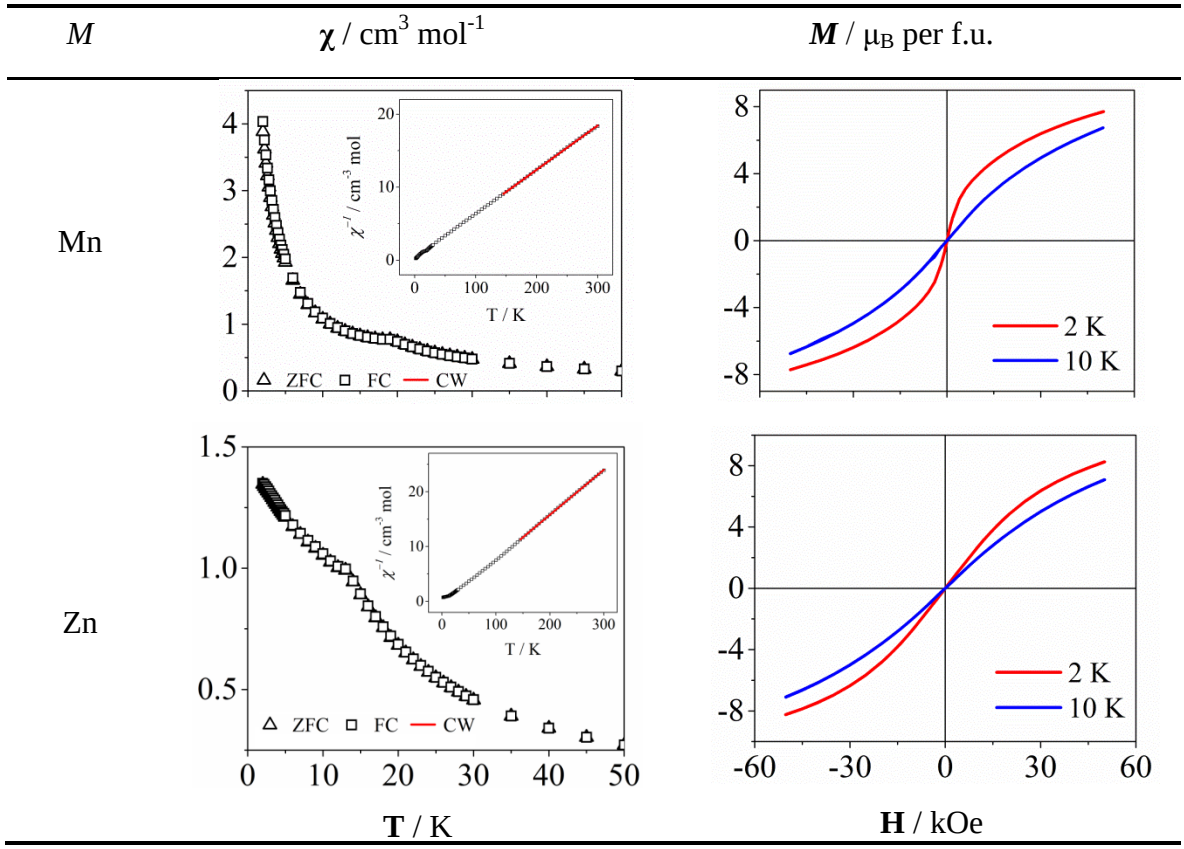

Figure 8.3 Temperature dependence of the dc molar magnetic susceptibility, measured in 100 Oe, and the field dependence of the magnetization at 2 K of GdFe*M*Ge4O12 (*M* = Mn, Zn). (inset) The inverse susceptibility; data points highlighted in red were fitted to the Curie−Weiss law.

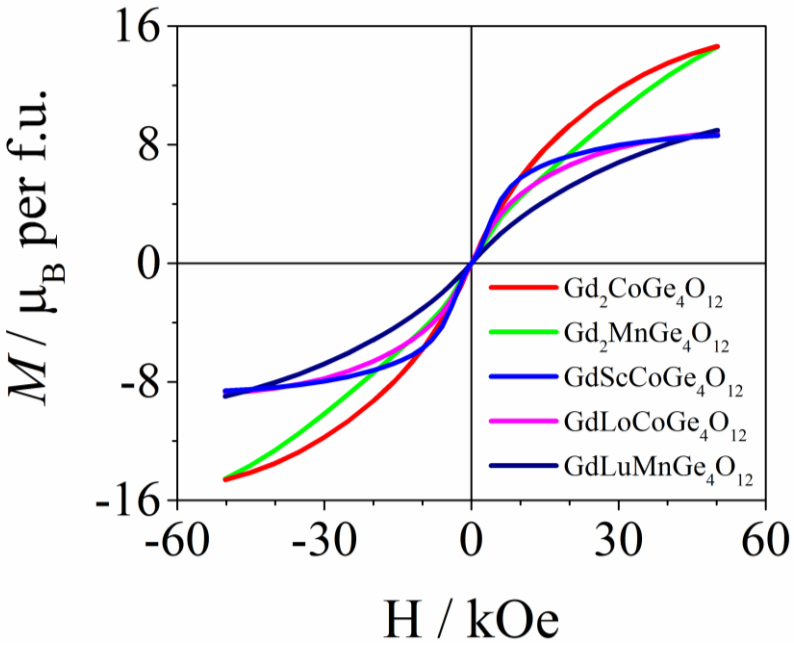

Figure 8.4 Field dependence of the magnetisation of $Gd_2MGe_4O_{12}$ (*M* = Mn, Co) and $GdRMGe_4O_{12}$ (*R* = Sc, Lu; *M* = Mn, Co) at 2 K.

Form the dc susceptibility, $Gd_2CaGe_4O_{12}$ is paramagnetic in the temperature range $2\ K \leq T \leq 300\ K$; the cobalt-containing compounds have a maximum susceptibility at ~ 3 K but in one case, $GdLuCoGe_4O_{12}$, it shows a relatively broad maximum peak, which normally corresponds to low-dimensional magnet [9], [10]. The susceptibilities of the manganese-containing compounds have a negative gradient over the whole temperature range and some hysteresis is apparent between the ZFC and FC susceptibilities. The iron-containing compounds also show a negative gradient over the whole temperature range and the transition temperature, T_N, is around 20 K. Some hysteresis exists between the ZFC and FC susceptibilities below ~ 3 K in $GdFeMnGe_4O_{12}$. The field dependence of the magnetisation of these compositions at 2 K indicates a saturation value of $n_{Gd}g_{Gd}J_{Gd} + g_M S_M$. The magnetizations of the manganese-containing compounds do not saturate and, interestingly, they have almost the same magnetization value as the cobalt ones at 5 T.

Gd^{3+} is a cation with L = 0 and S = 7/2 and the magnetic moment should therefore have spin-only contribution gS = 7. The effective moment of Gd^{3+} in $Gd_2CaGe_4O_{12}$ is in good agreement with its theoretical value. Using the moment of 7.84 μ_B for Gd^{3+}, the effective moments of the M^{2+} cations can be determined by subtracting this value from the experimentally-determined Curie constants; they are listed in Table 8.3. The moments of Co^{2+} are self-consistent and in excellent agreement with previous cobalt-containing compounds. However, the moments of Mn^{2+} are slightly higher than what was determined before but still reasonable.

8.3.2.2 AC Magnetisation Measurements

AC susceptibility measurements were carried out in zero field on all the compositions and the results were shown in Figure 8.5. All the compositions are antiferromagnets from the ac measurements.

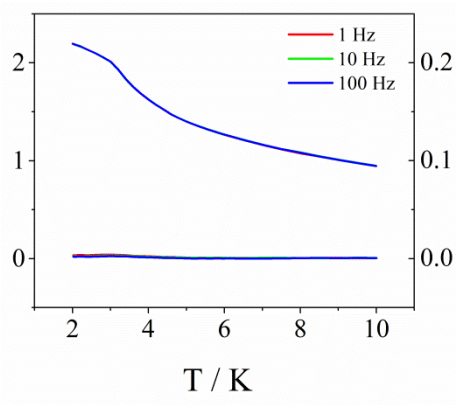

$Gd_2MnGe_4O_{12}$

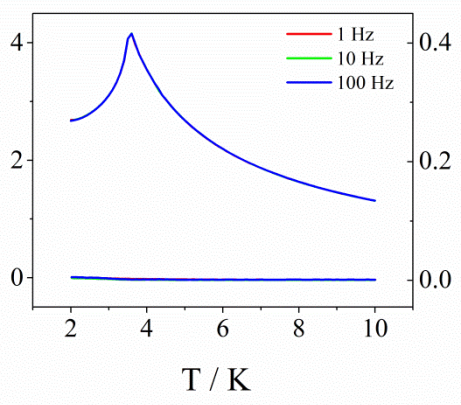

$Gd_2CoGe_4O_{12}$

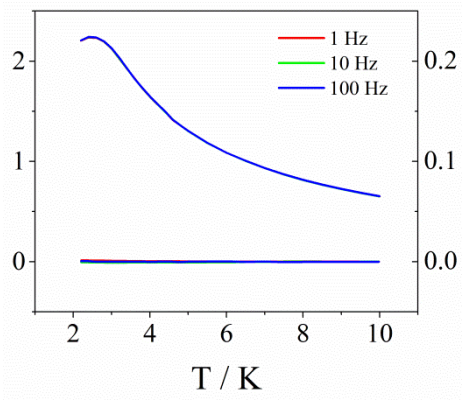

$GdLuCoGe_4O_{12}$

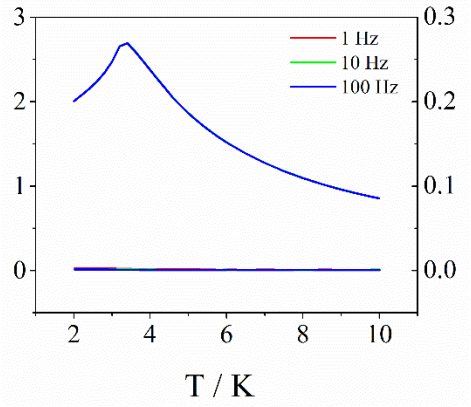

$GdScCoGe_4O_{12}$

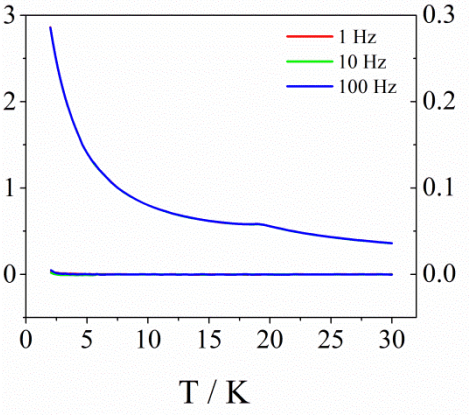

$GdFeMnGe_4O_{12}$

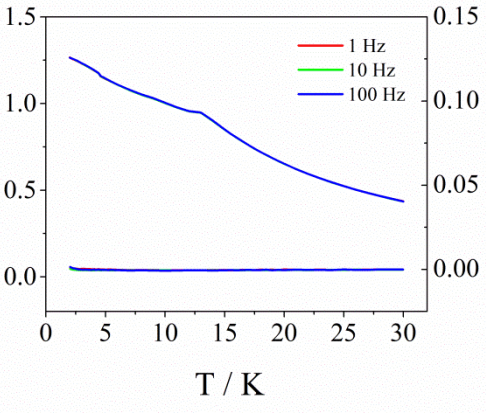

$GdFeZnGe_4O_{12}$

Figure 8.5 Temperature dependence of the ac molar magnetic susceptibility of $Gd_2MGe_4O_{12}$ (*M* = Mn, Co), $GdRCoGe_4O_{12}$ (*R* = Sc, Lu), and GdFe*M*Ge4O12 (*M* = Mn, Zn).

8.3.2.3 Magnetic Neutron Diffraction

The magnetic structure and the mean ordered atomic moment values were derived from the magnetic-only data derived from the difference between the data collected at 3.6 K and 20 K. The unit cell parameters were determined to be a = 9.7488(1) Å and c = 4.7629(1) Å. The refinement agreements were R_{wpr} = 12.1% and χ^2 = 45.6. The fitted pattern is shown in Figure 8.6. The magnetic structure of the compounds is shown in Figure 8.7.

The magnetic structure of $GdFeZnGe_4O_{12}$ can be described in the magnetic space group $P_{2c}b'an$ (No. 50.9.385). It consists of an A-type ordering of (001) planes with the atomic moments aligned along [100]. The unit cell doubles along [001] axis with c_{mag} = 2 c. The NN cation-containing layers couples antiferromagnetically along [001] axis. The magnitudes of the ordered cation moments refined to be 6.0(2) μ_B for Gd and 3.9(2) μ_B for Fe.

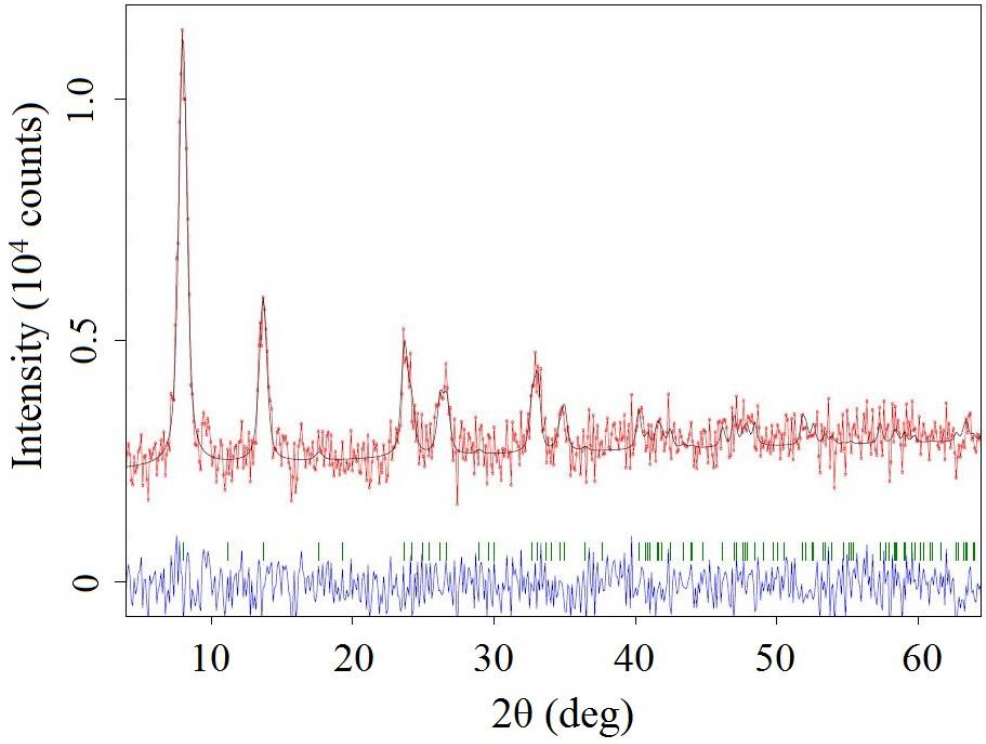

Figure 8.6 Observed (red dots) and calculated (black line) magnetic-only NPD patterns of $GdFeZnGe_4O_{12}$ at 3.6 K; λ = 1.330 Å. A difference curve (green line) is shown and reflection positions are marked.

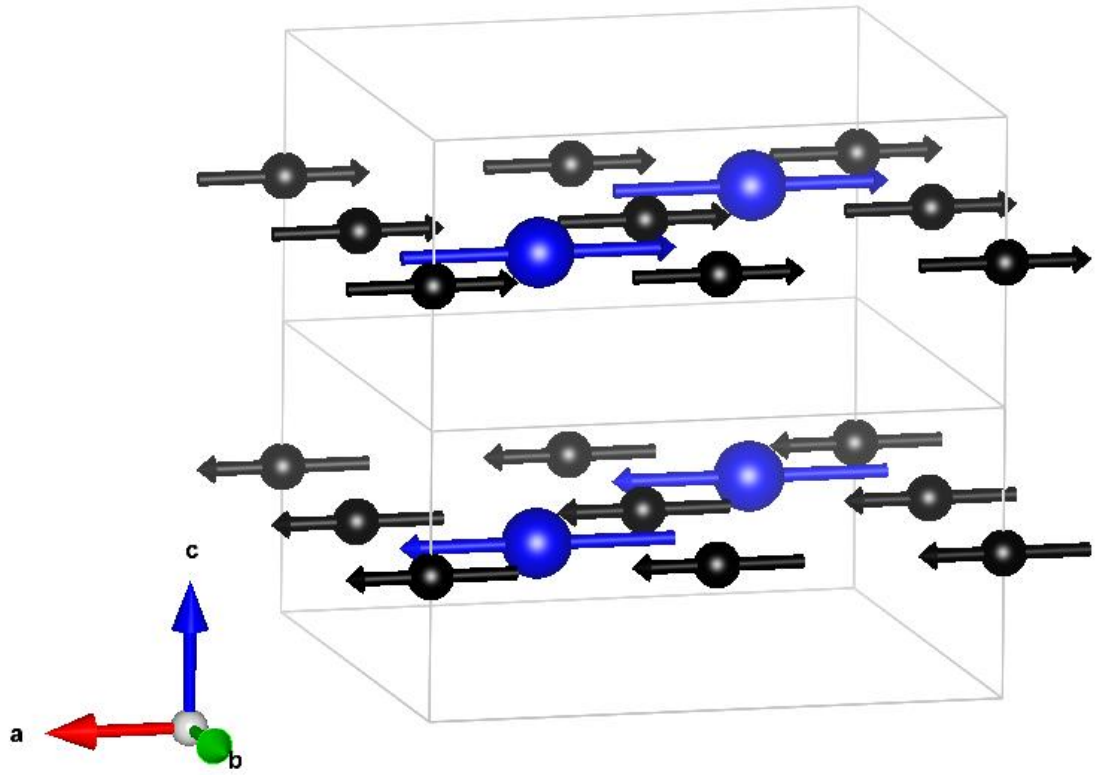

Figure 8.7 Magnetic structure in zero field of $GdFeZnGe_4O_{12}$. Blue balls represent the moment at the *2b* site and black balls represent the moment at the *4f* site. Diamagnetic ions are omitted.

8.3.3 Mössbauer spectrum

The ^{155}Gd Mössbauer spectrum of the Gd-containing compounds was recorded at 5 K (paramagnetic phase) and 1.8 K. The spectra are shown in Figure 8.8 – Figure 8.12 and the parameters used to fit it are listed in Table 8.4 – Table 8.6. Only some of the spectra collected at 1.8 K can be fitted at the moment. Moreover, the low-temperature ^{57}Fe Mössbauer spectra of the iron-containing compounds were measured at 5 – 20 K. The results are shown in Figure 8.13 and Figure 8.14 and the parameters used to fit them are listed in Table 8.7.

Table 8.4 ^{155}Gd Mössbauer parameters at 5 K for $Gd_2MGe_4O_{12}$ (M = Ca, Mn, Co), $GdRCoGe_4O_{12}$ (R = Sc, Lu), and GdFeMGe4O12 (M = Mn, Zn)

Composition	Site	eQV_{zz} / mm s^{-1}	Area %
$Gd_2CaGe_4O_{12}$	2*b*	3.87(2)	60(1)
	4*f*	13.42(2)	40(1)
$Gd_2MnGe_4O_{12}$	2*b*	4.98(2)	61(1)
	4*f*	12.72(3)	39(1)
$Gd_2CoGe_4O_{12}$	2*b*	5.58(3)	63(1)
	4*f*	12.67(2)	37(1)
$GdLuCoGe_4O_{12}$	2*b*	6.29(3)	74(1)
	4*f*	13.28(9)	26(1)
$GdScCoGe_4O_{12}$	2*b*	7.59(1)	100†
$GdFeMnGe_4O_{12}$*	2*b*	8.12(3)	100†
$GdFeZnGe_4O_{12}$*	2*b*	9.15(2)	100†

† not refined; * collected at 20 K

Table 8.5 ^{155}Gd Mössbauer parameters for $Gd_2MnGe_4O_{12}$ at various temperatures

T / K	Site	Area %
5	2*b*	60.7(5)
	4*f*	39.3(5)
20	2*b*	62.0(8)
	4*f*	38.0(8)
40	2*b*	65.9(9)
	4*f*	34.1(9)
60	2*b*	70.6(1.3)
	4*f*	29.4(1.3)

Table 8.6 ^{155}Gd Mössbauer parameters at 1.8 K for $Gd_2MnGe_4O_{12}$, $GdScCoGe_4O_{12}$ and GdFeMGe4O12 (M = Mn, Zn).

Composition	Site	eQV_{zz}† / mm s^{-1}	Area‡ %	B_{hf} / T	θ / °
$GdScCoGe_4O_{12}$	2*b*	7.59(1)	100	24.7(2)	90
$GdFeMnGe_4O_{12}$*	2*b*	8.12(3)	100	26.5(3)	77(3)
$GdFeZnGe_4O_{12}$	2*b*	9.15(2)	100	25.1(2)	75(2)

† constrained to the value found at 5 K; ‡ not refined; * collected at 5 K

Table 8.7 ^{57}Fe Mössbauer parameters for GdFeMGe4O12 (M = Mn, Zn) at various temperatures

Composition	T / K	IS / mm s^{-1}	Area %	QS / mm s^{-1}
$GdFeMnGe_4O_{12}$	5	0.47(3)	47.04(46) 46.20(31)	2.17
	10	0.47(3)	44.08(13) 42.16(13)	2.17
	15	0.47(3)	36.86(12) 32.77(13)	2.17
	17	0.47(3)	30.11(17) 25.69(18)	2.17
	20	0.47(3)	0	2.17
$GdFeZnGe_4O_{12}$	5	0.55(1)	44.28(16) 46.00(15)	2.14
	10	0.55(1)	33.05(45) 37.21(43)	2.14
	11.5	0.55(1)	30.59(25) 25.80(28)	2.14
	13	0.55(1)	12.04(33) 5.73(40)	2.14
	15	0.55(1)	0	2.14

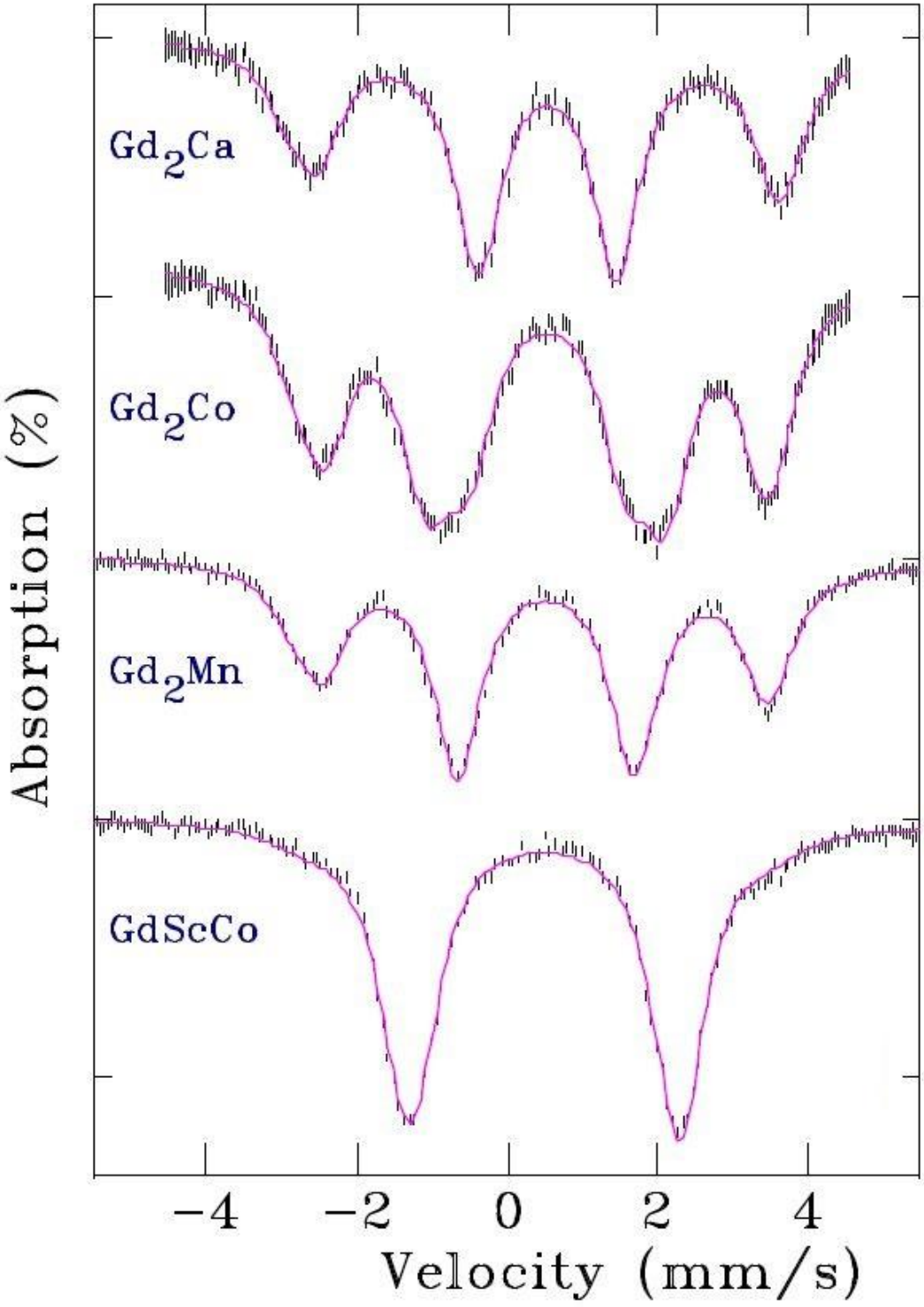

Figure 8.8 ^{155}Gd Mössbauer spectrum of $Gd_2CaGe_4O_{12}$, $Gd_2CoGe_4O_{12}$, $Gd_2MnGe_4O_{12}$ and $GdScCoGe_4O_{12}$ collected at 5 K.

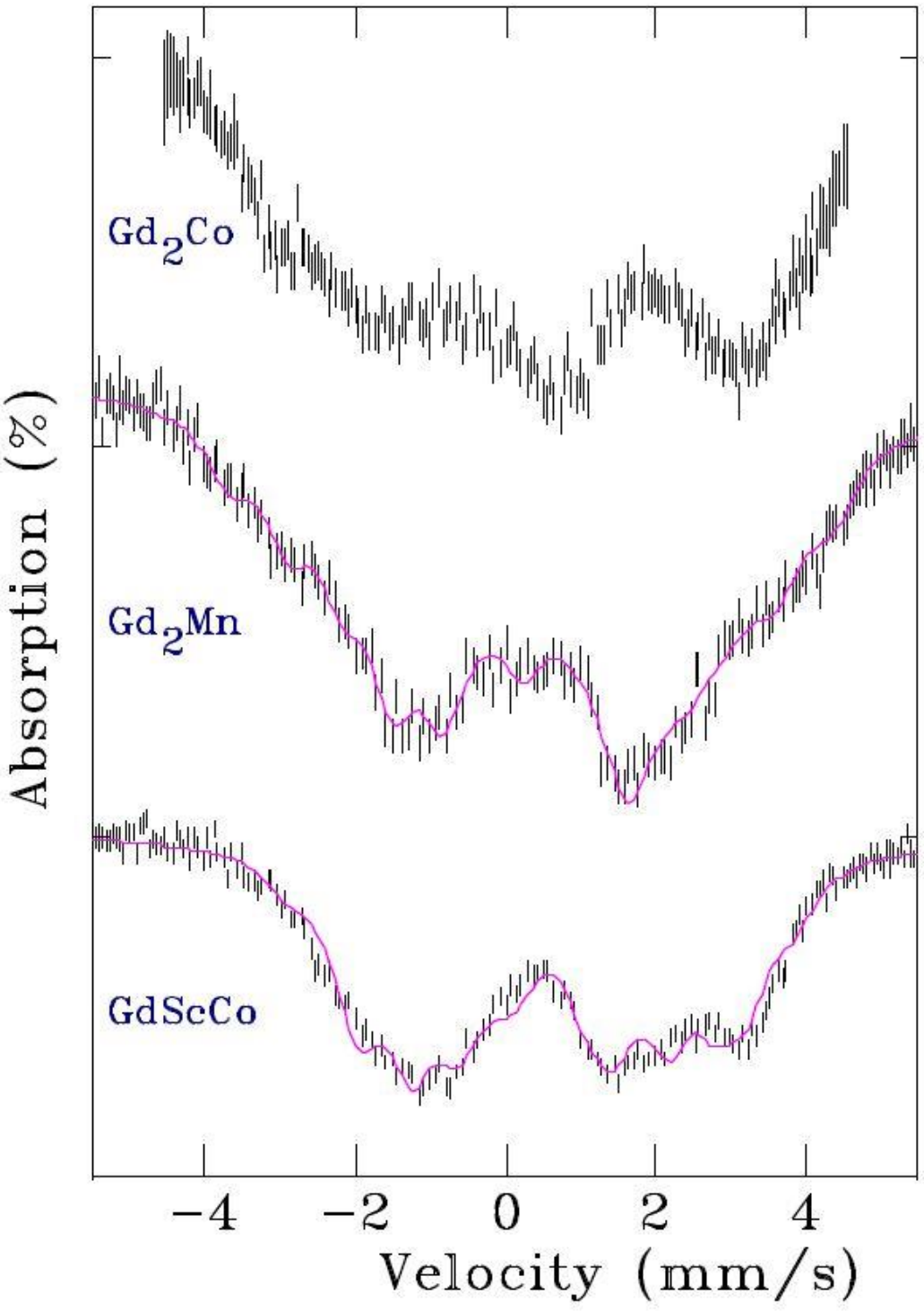

Figure 8.9 ^{155}Gd Mössbauer spectrum of $Gd_2CoGe_4O_{12}$, $Gd_2MnGe_4O_{12}$ and $GdScCoGe_4O_{12}$ collected at 1.8 K.

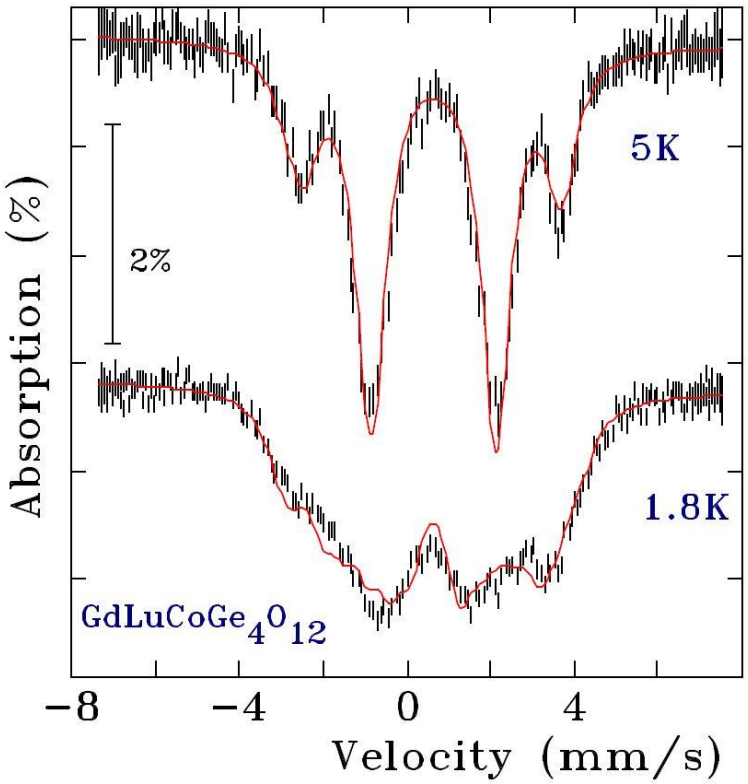

Figure 8.10 ^{155}Gd Mössbauer spectrum of $GdLuCoGe_4O_{12}$ collected at 5 and 1.8 K.

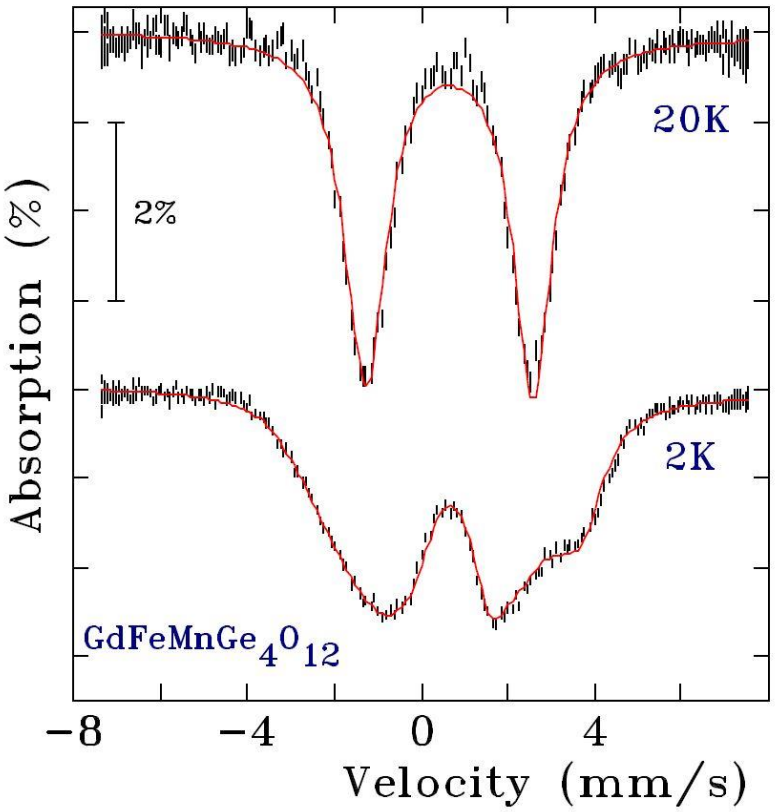

Figure 8.11 ^{155}Gd Mössbauer spectrum of $GdFeMnGe_4O_{12}$ collected at 20 and 2 K.

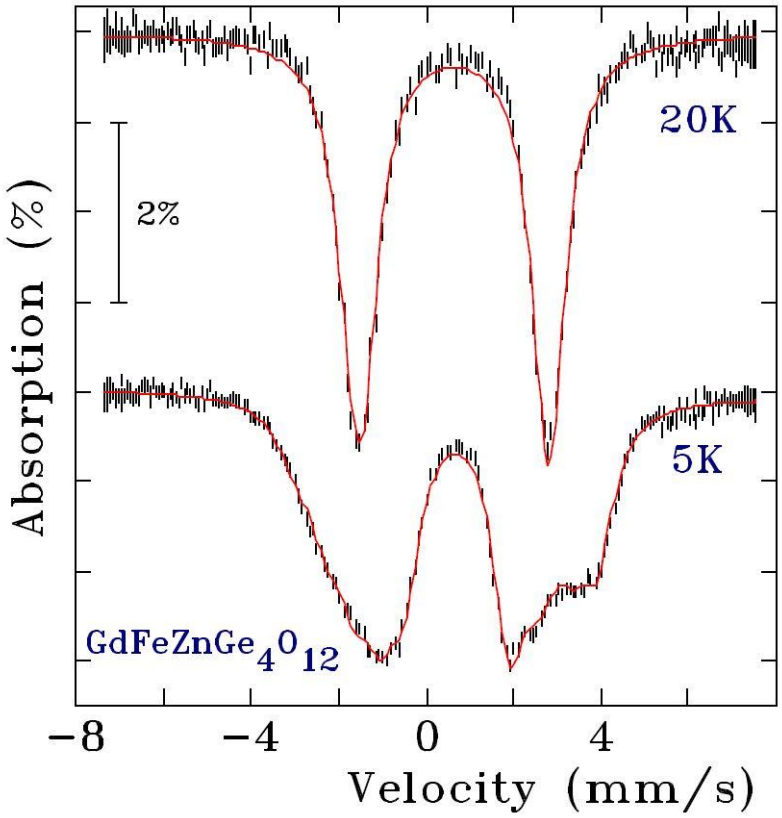

Figure 8.12 ^{155}Gd Mössbauer spectrum of $GdFeMnGe_4O_{12}$ collected at 20 and 5 K.

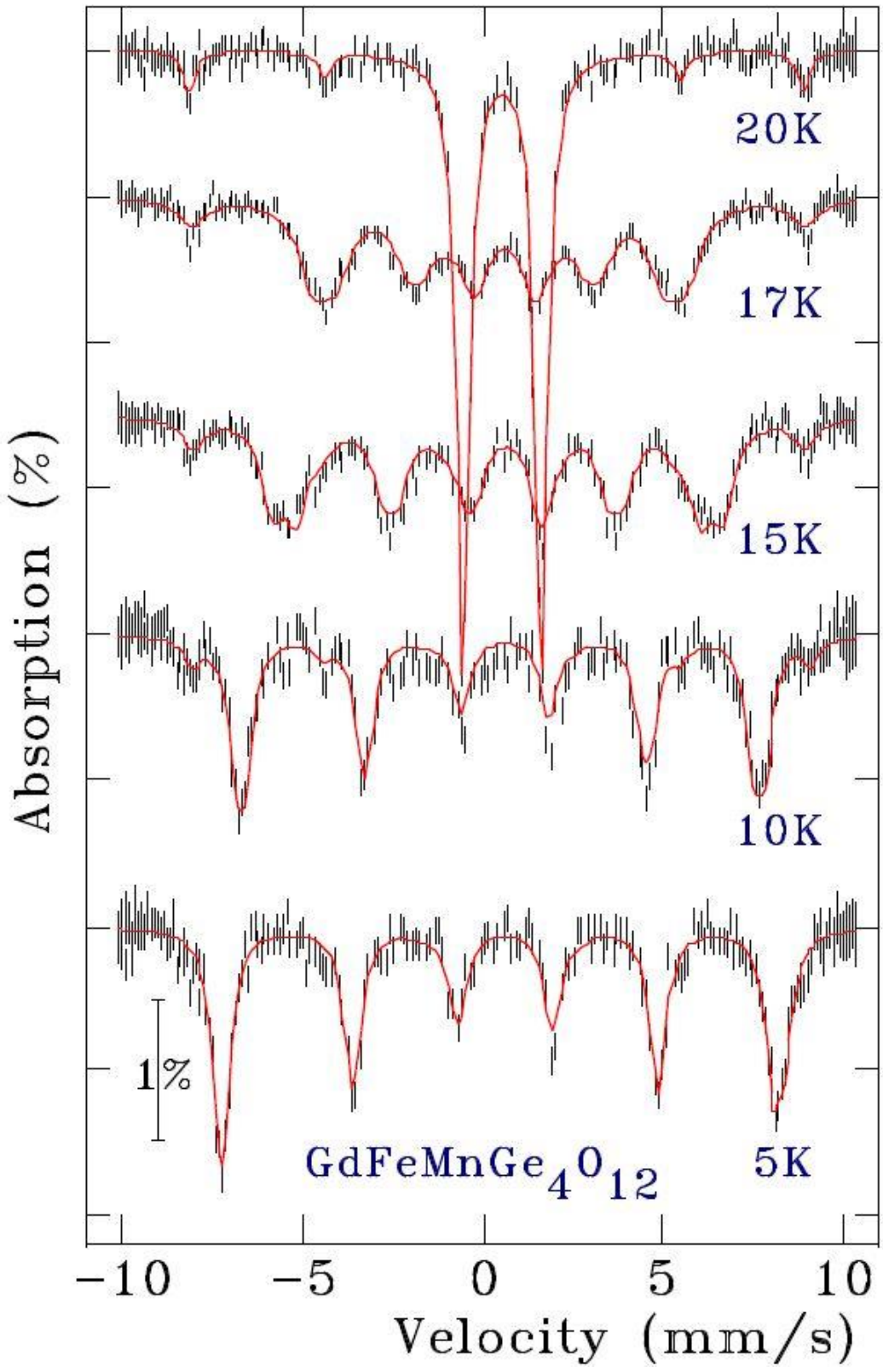

Figure 8.13 ^{57}Fe Mössbauer spectrum of $GdFeMnGe_4O_{12}$ collected at various temperatures.

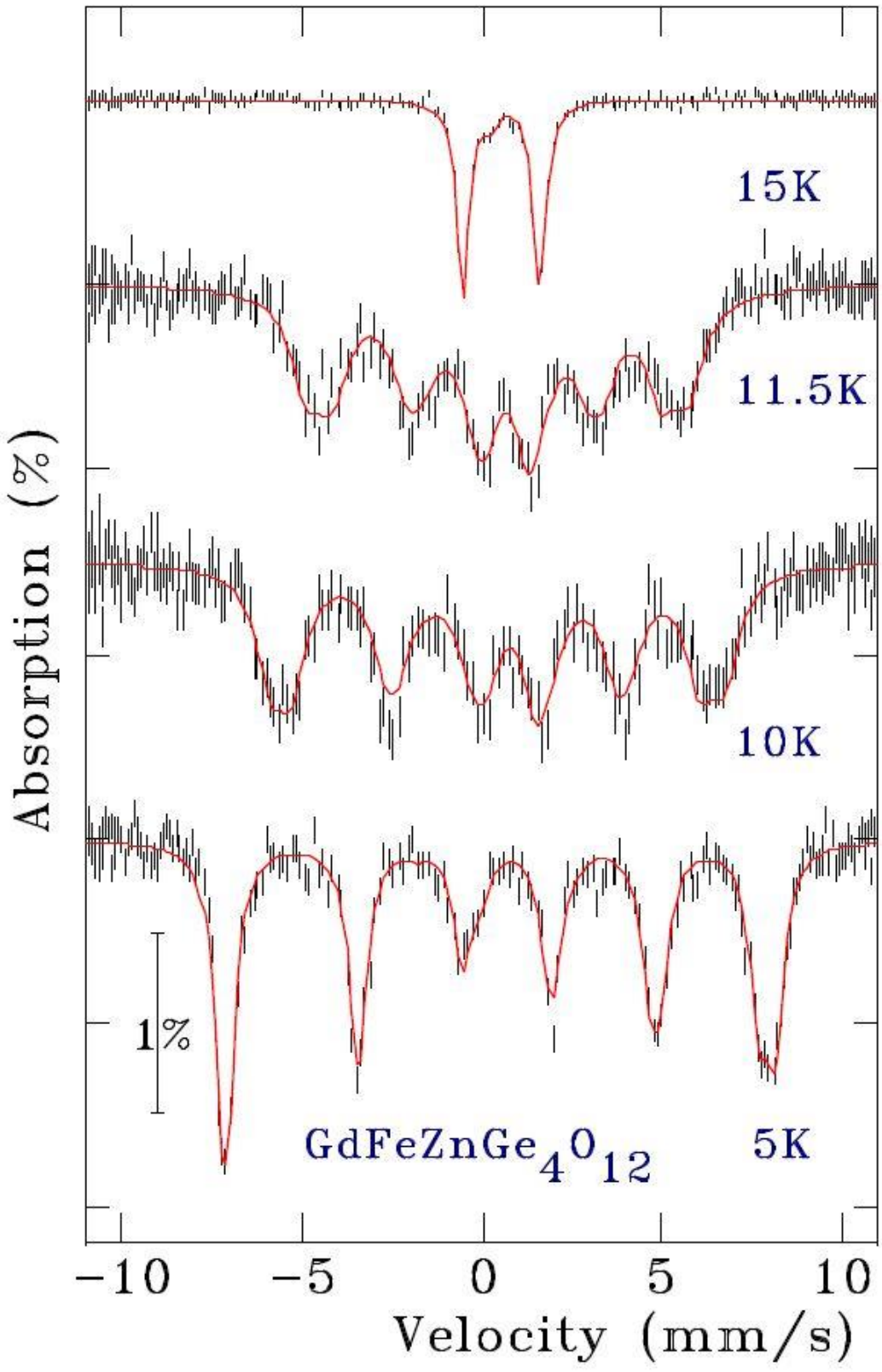

Figure 8.14 ^{57}Fe Mössbauer spectrum of $GdFeMnGe_4O_{12}$ collected at various temperatures.

8.3.4 Discussion

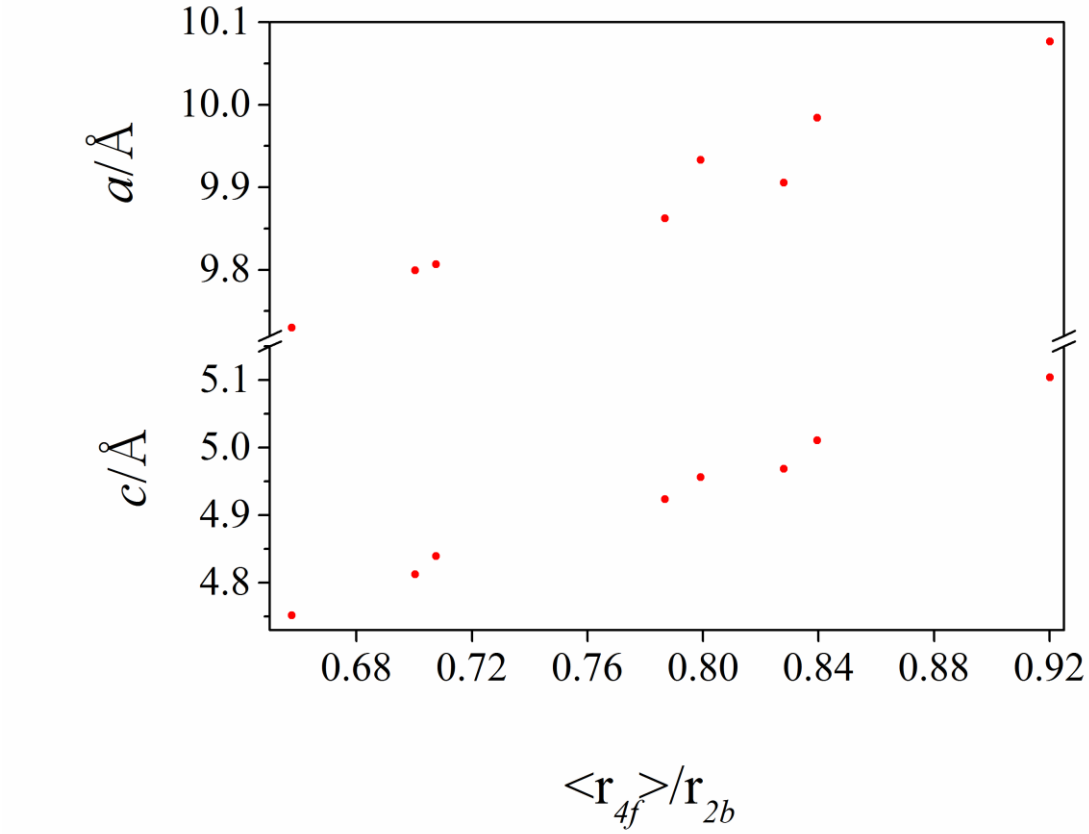

Figure 8.15 Structural unit cell parameters *a* and *c* derived from diffraction data. The error bars are smaller than the size of the points.

Table 8.8 Ionic radii [11] for some selected cations

Cation	Site	
	2b(VIII)	4f(VI)
Gd (III)	1.053	0.938
Lu (III)	0.977	0.861
Fe (III)	-	0.645
Sc (III)	-	0.745
Ca (II)	-	1
Mn (II)	-	0.83
Co (II)	-	0.745
Zn (II)	-	0.74

The unit cell parameters derived from the XRPD data are plotted in Figure 8.15. Some ionic radii of selected cations are listed in Table 8.8. As mentioned above, there are three ranges of the Gd-containing compounds, $Gd_2MGe_4O_{12}$ (*M* = Ca, Mn, Co), $GdRMGe_4O_{12}$ (*R* = Sc, Lu; *M* = Co, Mn), and $GdFeMGe_4O_{12}$ (*M* = Mn, Zn). The unit cell parameters *a* and *c* show a linear decrease when using a smaller cation.

As we have mentioned above, there is a broadened transition peak measured in the dc susceptibility of $GdLuCoGe_4O_{12}$ but we don't have a satisfactory explanation for this. In $GdFeMGe_4O_{12}$ (*M* = Mn, Zn), there is a significant transition at 20 K when *M* = Mn and 13 K when *M* = Zn but there exists a second subtle transition at ~ 3 K where a small hysteresis between ZFC/FC occurs. The negative temperature gradient of the dc susceptibilities in $GdFeMGe_4O_{12}$ (*M* = Mn, Zn) over the whole measured temperature range may come from the presence of paramagnetic spins from Gd^{3+} or spin canting from the moments of Fe and/or *M*. Further ac measurements prove that all the Gd-containing compounds are antiferromagnets. For each composition studied, the Weiss constant is negative except for $GdFeZnGe_4O_{12}$, which is the only compound studied to date with a positive Weiss constant. The field dependence of the magnetisation of all the compositions at 2 K indicates a value of $n_{Gd}g_{Gd}J_{Gd} + g_M S_M$ rather than $\frac{1}{2}\, n_{Gd}g_{Gd}J_{Gd} + g_M S_M$ reported in Chapter 7 because the isotropic Gd^{3+} ions with $L=0$ are not susceptible to the effects of magnetic anisotropy and the crystal field.

The ^{155}Gd Mössbauer spectra collected at 5 K show that the gadolinium occurs on both the *2b* and *4f* sites ($Gd_2CaGe_4O_{12}$, $Gd_2MnGe_4O_{12}$, $Gd_2CoGe_4O_{12}$ and $GdLuCoGe_4O_{12}$), where the spectra consist of two clearly distinct quadrupole doublets, whereas for $GdScCoGe_4O_{12}$, the gadolinium occurs only on the *2b* site, where only a single quadrupole doublet is observed. The fact that Gd only occupies the *2b* site in $GdScCoGe_4O_{12}$ whereas Tb occupies both the *2b* site and the *4f* site in $TbScCoGe_4O_{12}$ may be attributed to the small difference in the ionic radius. The inner doublet is assigned to gadolinium at the *2b* site as it is the component that persists when only that site is occupied. The quadrupole moment of the $m_I = 5/2$ excited state is very small, so the paramagnetic spectrum is dominated by the splitting of the $m_I = 3/2$ ground state leading to an (almost) symmetric doublet and making it difficult to determine the sign of the electric field gradient (efg). However, for the inner, stronger doublet in each case we observed a small but statistically significant asymmetry that allowed us to establish that the efg is positive at the *2b* site. One

striking feature of the spectra for $Gd_2MGe_4O_{12}$ (*M* = Ca, Mn, Co) and $GdLuCoGe_4O_{12}$ is that the spectral areas of the components from the *2b* and *4f* sites are far from equal at 5 K, see Table 8.5. The XRD data rule out the possibility of first-row-transition metal cations (*M* = Ca, Mn, Co) substituting for gadolinium at the *2b* site and suggest that in all compositions the quantity of gadolinium on the *2b* site is equal to that on the *4f* site. Further temperature-dependent Mössbauer spectra were collected on $Gd_2MnGe_4O_{12}$ over the temperature range 5 – 60 K and the fitted area for the two sites are shown in Table 8.6. The observed imbalance that the signal of the *2b* site Gd grows when the temperature is higher, *2b*:*4f* ratio went from 60:40 at 5 K, to 70:30 at 60 K, see Table 8.5, would then have to be due to differences in the recoil-free fractions at the two sites. Mössbauer spectroscopy relies on the recoil-free absorption of the gamma-ray in a nucleus in the sample. If the host atom is weakly bound, then a momentum-conserving recoil event is more likely and the Mössbauer signal is weaker. Where gadolinium occupies two crystallographically-distinct sites, the relative strength of the two signals is weighted not only by the frequency of occupation, but also by the probability of a zero-recoil event, set by the local binding strength. We therefore attribute the reduced area of the contribution from the *4f* site to weaker binding of the gadolinium at this site. This explanation can be checked by raising the sample temperature, as increased thermal motion leads to a reduction in the recoil-free fraction (an effect that limits ^{155}Gd Mössbauer measurements to temperatures less than 60 K) and the reduction is more rapid if the host atom is more weakly bound. We note that the ratio at 5 K is essentially the same for $Gd_2CoGe_4O_{12}$ and $Gd_2MnGe_4O_{12}$, $Gd_2CaGe_4O_{12}$ but a significantly higher ratio, 74:26, is detected for $GdLuCoGe_4O_{12}$. The ratio observed in $GdLuCoGe_4O_{12}$ stems partly from a difference in the recoil-free fractions at the two sites but that it is also partly attributable to partial ordering of gadolinium and lutetium, with the larger gadolinium cations dominating on the eight-coordinate *2b* sites. If we assume that the ratio of the recoil free fractions at 5 K is the same as in $Gd_2MnGe_4O_{12}$, then in $GdLuCoGe_4O_{12}$, 65.5 % of the gadolinium is on the *2b* site, with the remaining 34.5 % on the *4f* site. This disorder was not detected in the XRD data because the two lanthanide elements have similar X-ray scattering lengths and our diffraction data were thus insensitive to the partial cation ordering. Cooling the samples to 1.8 K leads to magnetic ordering and the development of a magnetic hyperfine field (B_{hf}) at the gadolinium nuclei. The high point symmetry of the *2b* site (D_{4d}) provides some simplifying constraints as the efg tensor must be axially symmetric and the principal axis must be parallel to the crystallographic *c*-axis. No such constraints exist at the *4f* site.

The severe line overlap combined with the lack of independent constraints prevented us from developing a unique fit to the spectra of $Gd_2CoGe_4O_{12}$ and $GdLuCoGe_4O_{12}$ at 1.8 K, however the single site spectrum of $GdScCoGe_4O_{12}$ did admit analysis. The fit shown in Figure 8.9 was obtained with the efg constrained to the value observed at 5 K. The main parameters that were varied to obtain the fit were B_{hf} and the angle, θ, between B_{hf} and the principal axis of the efg tensor (which we know to be parallel to the crystallographic *c*-axis). Our best fit gave θ = 90 ° indicating *ab*−plane ordering of the gadolinium moments. A free fit to θ yielded statistically equivalent fits with θ ~80 ° and θ ~100 °, reflecting the rather slow evolution in spectral shape near θ = 90 °. Within the precision of our measurements, the ordering of the gadolinium moments lies within the *ab*−plane. The ^{155}Gd Mössbauer spectra collected on $GdFeMnGe_4O_{12}$ and $GdFeZnGe_4O_{12}$ at 20 K show that the Gd occurs only on the 2*b* site with only a single quadrupole doublet as $GdScCoGe_4O_{12}$. It is notable that the eQV_{zz} value is different for the three compounds, 8.12(3) in $GdFeMnGe_4O_{12}$, 9.15(2) in $GdFeZnGe_4O_{12}$, and 7.59(1) in $GdScCoGe_4O_{12}$, which indicates a difference of the environment for Gd at the *2b* site. Further Mössbauer spectra were collected at a lower temperature. The fitting parameters, B_{hf} and θ, are shown in Table 8.7. The B_{hf} of $GdFeMnGe_4O_{12}$ and $GdFeZnGe_4O_{12}$ are essentially the same as $GdScCoGe_4O_{12}$ whereas the θ value of $GdFeMnGe_4O_{12}$ and $GdFeZnGe_4O_{12}$ are ~ 75 ° rather than 90 ° in $GdScCoGe_4O_{12}$. As discussed in Chapter 7, in $TbScCoGe_4O_{12}$, not only the crystal field but also anisotropic exchange, dipolar exchange, and the internal molecule field from Co sublattice all influence the arrangement of the ordered moments. Similarly, in Gd-containing compounds, the crystal field and the internal molecule field from Co or Fe should also have influence to Gd. Thus, the difference in eQV_{zz} value may originate from the crystal field (the *q* ratio of the *2b* site) whereas the difference in B_{hf} is the result from the crystal field and the internal molecule field. The anisotropy of the cation Co^{2+} might be the reason that the θ value of $GdFeMnGe_4O_{12}$ and $GdFeZnGe_4O_{12}$ are different from $GdScCoGe_4O_{12}$.

^{57}Fe Mössbauer spectra were collected on $GdFeMnGe_4O_{12}$ and $GdFeZnGe_4O_{12}$ over the temperature range 5 – 20 K. It is clear that $GdFeMnGe_4O_{12}$ contains some iron-containing impurities (~ 15 %) but we failed to detect them from the XRD or magnetometry measurement. Hence, no more measurements were made on it. To fit the ^{57}Fe Mössbauer spectra, two equal-area components were used to deal with an obvious line broadening, which may be a distribution of fields or moment orientations present. The QS and IS

values didn't show a significant change to temperature and thus they were fixed during the fitting. The IS values are 0.47(3) mm/s for $GdFeMnGe_4O_{12}$ and 0.55(1) mm/s for $GdFeZnGe_4O_{12}$; the QS values are 2.17(1) mm/s for $GdFeMnGe_4O_{12}$ and 2.14(1) mm/s for $GdFeZnGe_4O_{12}$; the IS and QS values are essentially the same as $YFeMnGe_4O_{12}$ described in Chapter 6, IS = 0.407(2) mm/s and QS = 2.086(2) mm/s. Again the two quadrupole doublets indicate there is only one environment for Fe and the isomer shift is consistent with the presence of high-spin, spherical Fe^{3+} cations but the quadrupole splitting is unusually large for such a species. The electric-field gradient created by the irregular coordination sphere at *4f* site is presumably responsible for the large quadrupole splitting observed in the Mössbauer spectrum.

Gd is a strong neutron absorber and the magnetic contribution to the data was derived from the difference between the 3.6 K NPD data and the 20 K NPD data on $GdFeZnGe_4O_{12}$. The compound shows to be an A-type antiferromagnet with the atomic moments aligned along [100], see Figure 8.7. The magnetic structure of $GdFeZnGe_4O_{12}$ is similar to that of $Tb_2CoGe_4O_{12}$ where the internal molecular field from the *4f* site sublattice can influence the moment of the *2b* site. The mean ordered moment of Fe^{3+} was determined to be 3.9(2) μ_B, similar to the value reported in Chapter 6, and 6.0(2) μ_B of Gd^{3+}, close to its theoretical value 7 μ_B.

8.3.5 Conclusion

The Gd-containing compounds described above have been shown to be an antiferromagnets, or a paramagnet in the case of $Gd_2CaGe_4O_{12}$. The iron-containing compounds show a transition at ~ 20 K. Mössbauer spectroscopy showed that the compositions are magnetically ordered at low temperatures and that $GdScCoGe_4O_{12}$, $GdFeMnGe_4O_{12}$ and $GdFeZnGe_4O_{12}$ only have Gd on the *2b* site. The Mössbauer spectroscopy implies that $GdScCoGe_4O_{12}$ may have the same magnetic structure as $TbScCoGe_4O_{12}$ whereas the neutron diffraction data collected on $GdFeZnGe_4O_{12}$ shows that this compound behaves in a similar way to $Tb_2CoGe_4O_{12}$.

8.4 References

[1] H. M. Rietveld, A profile refinement method for nuclear and magnetic structures, *Journal of Applied Crystallography*, **1969**, *2*, 65-71.

[2] R. A. Young, *The Rietveld Method*, Oxford University Press **1993**.

[3] J. Rodriguez-Carvajal, Recent advances in magnetic structure determination by neutron powder diffraction, *Physica B: Condensed Matter*, **1993**, *192*, 55-69.

[4] B. van Laar, and W. B. Yelon, The peak in Neutron Powder Diffraction, *Journal of Applied Crystallography*, **1984**, *17*, 47-54.

[5] K. Momma, and F. Izumi, VESTA: a three-dimensional visualization system for electronic and structural analysis, *Journal of Applied Crystallography*, **2008**, *41*, 653-658.

[6] V. G. Zubkov, N. V. Tarakina, I. I. Leonidov, A. P. Tyutyunnik, L. L. Surat, M. A. Melkozerova, E. V. Zabolotskaya, and D. G. Kellerman, Synthesis and crystal structure of $Ln_2M^{2+}Ge_4O_{12}$, Ln=rare-earth element or Y; M=Ca, Mn, Zn, *Journal of Solid State Chemistry*, **2010**, *183*, 1186-1193.

[7] M. A. Melkozerova, N. V. Tarakina, L. G. Maksimova, A. P. Tyutyunnik, L. L. Surat, I. I. Leonidov, V. G. Zubkov, E. V. Zabolotskaya, and R. F. Samigullina, Application of a modified Pechini method for the synthesis of $Ln_2MGe_4O_{12}$ (Ln = Y, Eu; M = Ca, Zn, Mn) optical hosts, *Journal of Sol-Gel Science and Technology*, **2011**, *59*, 338-344.

[8] C. Taviot-Gueho, P. Leone, P. Palvadeau, and J. Rouxel, Synthesis and structural characterization of two new rare-earth maganese germanates: $CeMn_2Ge_4O_{12}$ and $GdMnGe_2O_7$, *Journal of Solid State Chemistry*, **1999**, *143*, 145-150.

[9] R. L. Carlin, *Magnetochemistry*, Springer-Verlag: **1986**.

[10] L. J. de Jongh, *Magnetic Properties of Layered Transition Metal Compounds*, Springer: **1990**.

[11] R. D. Shannon, Revised effective ionic radii and systematic studies of interatomic distances in halides and chalcogenides, *Acta Crystallographica Section A: Crystal Physics, Diffraction Theoretical, and General Crystallography*, **1976**, *A32*, 751.

Chapter 9 - Summary

In this thesis a series of tetragonal (space group *P*4/*nbm*) germanates with a general formula $ABB'Ge_4O_{12}$ have been studied. The cations *A* occupy the 2*b* site and are coordinated by eight oxide ions at the corners of a square antiprism whereas *B* and *B*' are disordered over a 4*f* site which is at the centre of a distorted octahedron of oxide ions. All the compounds were successfully synthesized using the ceramic method. Depending on the chemical composition and elements, the germanates can be broken down into three groups, $A^{4+}MM'Ge_4O_{12}$ including $CeMn_{2-x}Co_xGe_4O_{12}$, $ZrMn_{2-x}Co_xGe_4O_{12}$, and $CeM_{1.5}M'_{0.5}Ge_4O_{12}$ (Chapter 3, 4, 5); $A^{3+}M^{3+}M'Ge_4O_{12}$ including *Ln*Fe*M*Ge_4O_{12} and *Ln*ScCoGe_4O_{12} where *Ln* is a non-magnetic lanthanide cation (Chapter 6, 7, 8); $A^{3+}R^{3+}MGe_4O_{12}$ including $R_2MGe_4O_{12}$ and *R*LuCoGe_4O_{12} where *R* is a magnetic lanthanide cation (Chapter 7, 8).

The cation radius ratio of the two sites, $\langle r_{4f}\rangle/r_{2b}$, has been used as a parameter to describe the compounds. The relationship between the $\langle r_{4f}\rangle/r_{2b}$ ratio and the unit cell parameters *a* and *c*, see Figure 9.1, is not clear as the unit cell parameters are also influence by the cation size. Therefore, the relationship between the $\langle r_{4f}\rangle/r_{2b}$ ratio and the ratio 2*c*/*a* is also plotted, see Figure 9.1. It is obvious that the $\langle r_{4f}\rangle/r_{2b}$ ratio and the ratio 2*c*/*a* have some correlations. When increasing the $\langle r_{4f}\rangle/r_{2b}$ ratio, the 2*c*/*a* ratio also increases. Three lines, green, yellow and blue, can be drawn through the scattered points. The green line includes $A^{3+}R^{3+}MGe_4O_{12}$; the yellow line describes $A^{4+}MM'Ge_4O_{12}$ and *Ln*ScCoGe_4O_{12}; the blue line shows *Ln*Fe*M*Ge_4O_{12}. The green line and the yellow line are almost parallel whereas the blue line has a different gradient. The 2*c*/*a* ratio is about 1 when the $\langle r_{4f}\rangle/r_{2b}$ ratio ~ 0.8 on the yellow line and ~ 0.9 on the green line. When the $\langle r_{4f}\rangle/r_{2b}$ ratio is less than 0.75, we can see a significant change on the 2*c*/*a* ratio described by the blue line. Though there is a sudden change, the crystal structure is still the same. As mentioned above, the scatter on the blue line comes from *Ln*Fe*M*Ge_4O_{12} where the ionic radius of Fe^{3+} (0.69) is much smaller than the other transition-metal cations. Further discussion will be made below. Some structural parameters derived from low temperature NPD as a function of either $\langle r_{4f}\rangle/r_{2b}$ ratio or 2*c*/*a* ratio are shown in Figure 9.2. Both $\langle r_{4f}\rangle/r_{2b}$ ratio and 2*c*/*a* ratio show a correlation to the structural parameters but the $\langle r_{4f}\rangle/r_{2b}$ ratio has a much clearer relationship to the parameters. It is obvious that the parameters Ψ, *p*, *q* have a positive

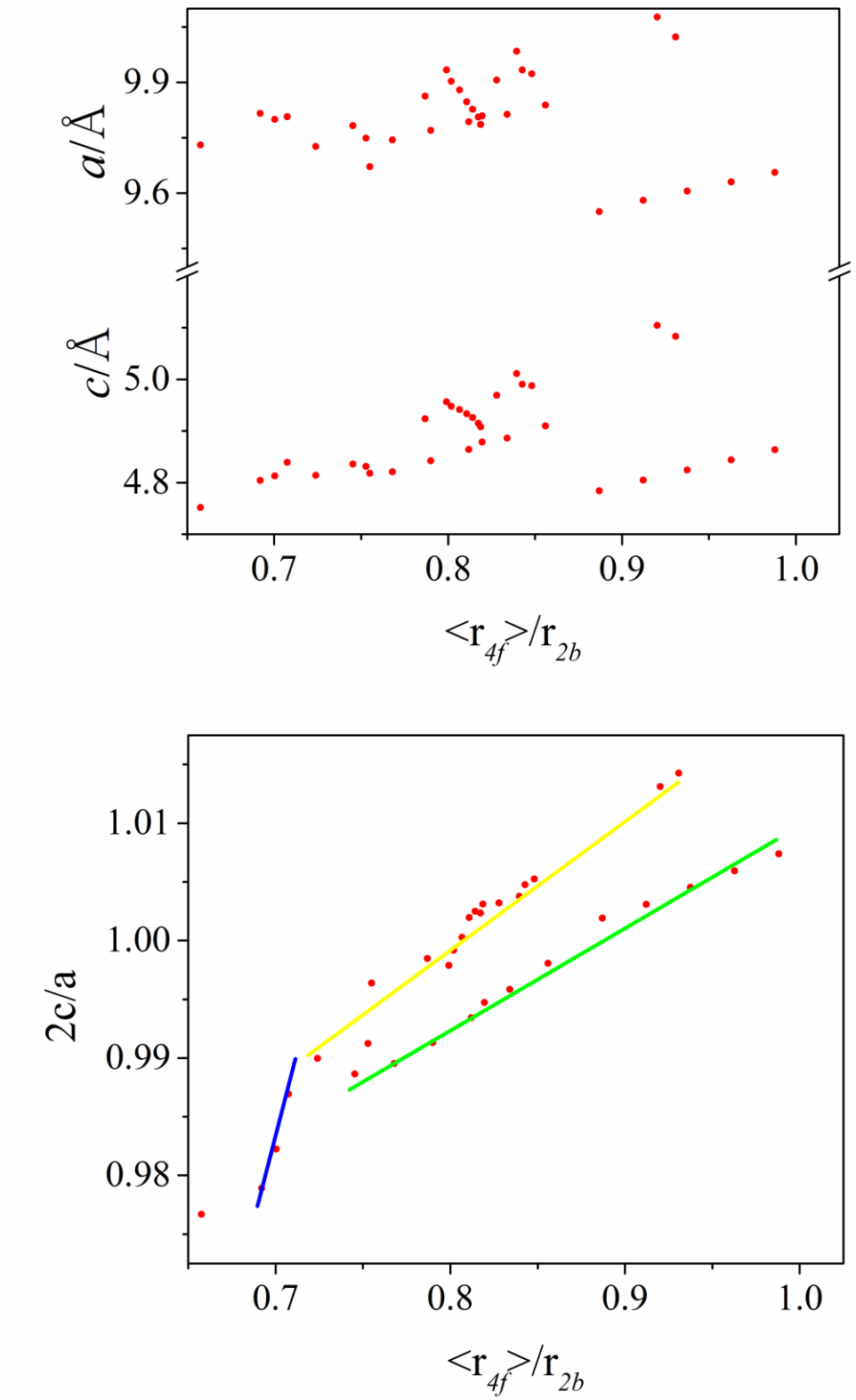

Figure 9.1 Structural unit cell parameters *a* and *c* and the ratio 2*c*/*a* derived from XRPD. The green, yellow and blue lines are the fittings to three series of compounds, namely $A^{3+}R^{3+}M\mathrm{Ge_4O_{12}}$; $A^{4+}MM'\mathrm{Ge_4O_{12}}$ and $Ln\mathrm{ScCoGe_4O_{12}}$; $Ln\mathrm{Fe}M\mathrm{Ge_4O_{12}}$. The error bars are smaller than the size of the points.

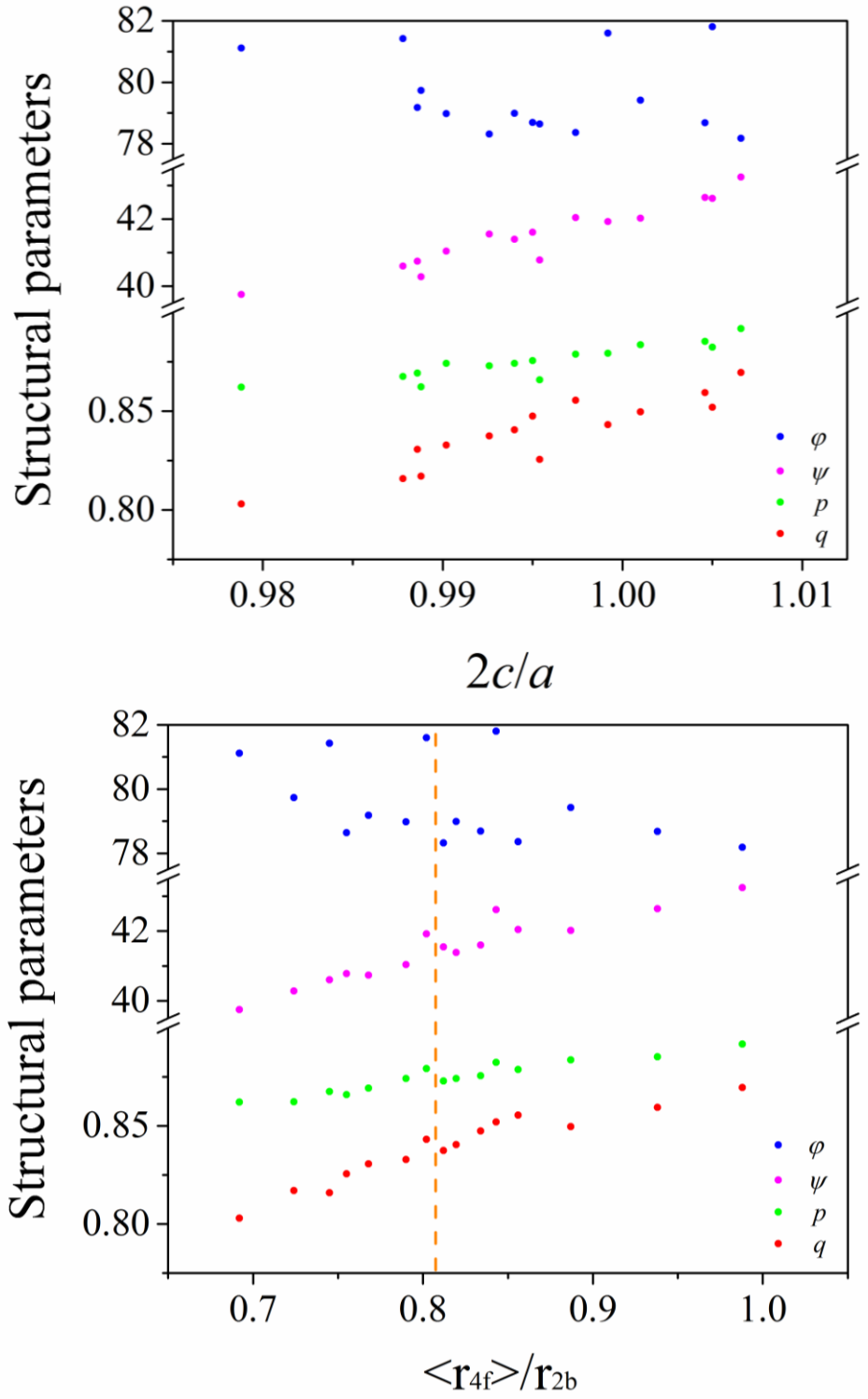

Figure 9.2 Structural parameters derived from low temperature NPD. The error bars are smaller than the size of the points. φ is the angle between M_{4f} – O1 bond and M_{4f} – O2 plane; ψ is the angle between the M_{4f} – O1 bond and the (001) plane; p is the ratio of M_{4f} – O2 bond length to M_{4f} – O1 bond length; q is the ratio of O2 – O2 distance in square face of antiprism to perpendicular distance between faces.

correlation with the $<r_{4f}>/r_{2b}$ ratio whereas the angle φ is not strongly correlated. There are two points that deviate from the line near $<r_{4f}>/r_{2b}$ ~ 0.8 and ~ 0.85 indicating $Tb_2CoGe_4O_{12}$ and $Tb_2MnGe_4O_{12}$, respectively. The other points all come from $A^{4+}MM'Ge_4O_{12}$ and $A^{3+}R^{3+}MGe_4O_{12}$ where the *4f* sites are occupied by first-row transition-metal cations.

The magnetic properties of the compounds also show variety depending on the chemical composition. Paramagnetism, ferromagnetism, metamagnetism, ferromagnetism, spin canting and spin glass behaviour have all been detected. The magnetic structures can be broken down into two main groups depending on whether the magnetic unit cell is doubled or not ($c' = c$ and $c' = 2c$). The single unit cell magnetic structure contains three sub-groups depending on the arrangement of the moments: the moments lie along [001] axis ($CeMn_2Ge_4O_{12}$, $CeMn_{1.5}Ni_{0.5}Ge_4O_{12}$, $ZrMn_2Ge_4O_{12}$ and $Tb_2MnGe_4O_{12}$); the moments lie in (001) plane ($CeMn_{2-x}Co_xGe_4O_{12}$ (x = 0.5, 1.0) and $ZrMnCoGe_4O_{12}$); the canted moments lie in (001) plane ($ZrCo_2Ge_4O_{12}$). The double unit cell magnetic structure also has two sub structures: the moments lie along [100] axis ($LnFeMGe_4O_{12}$); the canted moments lie in (001) plane ($CeMn_{2-x}Co_xGe_4O_{12}$ (x = 1.5, 2.0) and $Tb_2CoGe_4O_{12}$, $TbScCoGe_4O_{12}$). When *A*, the cation at the *2b* site, is non-magnetic, the magnetic interaction in the structure is only the *M* – O – Ge – O – *M* superexchange interaction and the pathway J_4 is considered to be the strongest while the others are also considerable. The competition between the superexchange pathways leads to different magnetic structures and the pathways are correlated to the crystal structure. Hence, four structural parameters were calculated to show the relationship. The orange line, see Figure 9.2, at $<r_{4f}>/r_{2b}$ = 0.81 has separated the single unit cell magnetic structures (> 0.81) and the double unit cell magnetic structures (< 0.81). Despite the two displaced points, the data suggest that the double unit cell is adopted when $\Psi < 41$ ° and/or $q < 0.835$. We have also drawn the conclusion that the Ge – O bond lengths and O – Ge – O bond angles are almost the same in all the cases suggesting the changes in the $[Ge_4O_{12}]^{8-}$ rings are negligible. With using different cations, the crystal structure is consequently changed. As we stated before, a $[Ge_4O_{12}]^{8-}$ ring in the structure is made from four vertex-sharing GeO_4 tetrahedra. Therefore, four oxygen atoms, named O1, behave in vertex-sharing way and the other eight, named O2, are not vertex-sharing. Those oxygen atoms are also used in building up the *2b* site antiprisms and the *4f* site octahedra. Each octahedron is linked with the antiprism by *A* – O2 – *M*. Hence, the germanium rings, the octahedra and the antiprisms are strongly correlated. All the facts indicate that with a

smaller $<r_{4f}>/r_{2b}$ ratio, the $2c/a$ ratio is smaller and this is achieved by compressing the antiprism along the *c* axis and compressing the octahedra to give a smaller Ψ angle whereas the $[Ge_4O_{12}]^{8-}$ rings maintain almost the same size. It was shown in Chapter 4 that the pathway J_4 is the strongest while J_2 and J_3 are the next strongest in $ZrM_2Ge_4O_{12}$ (*M* = Mn, Co). With a smaller $<r_{4f}>/r_{2b}$ ratio, the relative strength of the pathways will change and J_1 may prove to be significant in the compounds with the double unit cell magnetic structure. We can see how dramatically the magnetic structure changes along with the crystal structure by comparing $CeMn_2Ge_4O_{12}$ and $YFeMnGe_4O_{12}$; not only does the magnetic unit cell double but also the direction of the moments changes from lying along the *c* axis to the *a* axis.

We have also shown the influence of the crystal field for both first-row transition-metal cations and rare-earth cations. Co^{2+} has an effective moment ~ 5.36 μ_B from the Curie-Weiss law in all the cobalt-containing cases. However, the neutron experiments suggest the mean ordered moment of Co^{2+} is ~ 2.7 μ_B, which is close to its g_SS value. We have explained in Chapter 3 that the low symmetry of the environment of the *4f* site splits the cubic t_{2g} orbitals in such a way that the ground state is non-degenerate, see Figure 3.27. However, the non-cubic component of the splitting is small, i.e. < k_BT at high temperatures, and thus the ground state is, in effect, degenerate at room temperature. At low temperatures, the splitting of the d_{xz} and d_{yz} orbitals is greater than k_BT and the orbital contribution is consequently quenched. For rare-earth cations, Tb^{3+} has an effective moment ~ 9.7 μ_B from the Curie-Weiss law, which is close to its theoretical value of 9.72 μ_B. Its mean ordered moment at the *2b* site was determined to be ~ 3 μ_B and 0 at the *4f* site in $Tb_2CoGe_4O_{12}$ and $TbScCoGe_4O_{12}$ whereas the mean ordered moment at the *2b* site was 0 and ~ 7 μ_B at the *4f* site in $Tb_2MnGe_4O_{12}$. The theoretical value of Tb^{3+} is gJ = 9 μ_B. We have pointed out that the ground state of Tb^{3+} in a compressed antiprism ($q < 1$) is $m_J = 0$ and our result is consistent with this. Thus we have shown the crystal field effect for rare-earth cations is also significant at low temperatures.

Finally, we have discussed the influence of the anisotropy of the cations. From the series $CeMn_{1.5}M'_{0.5}Ge_4O_{12}$, the magnetic behaviour of *M'* = Ni and Cu are similar to $CeMn_2Ge_4O_{12}$ whereas it is totally different for *M'* = Co. Ni^{2+} and Cu^{2+} are considered to have weak spin-orbit coupling and small anisotropy whereas Co^{2+} is an anisotropic cation. The anisotropy of Co^{2+} can compel the moments to rotate from the [001] axis to lie in the

(001) plane. Moreover, the anisotropy of Co^{2+} can lead to a canted magnetic moment shown in $CeMn_{2-x}Co_xGe_4O_{12}$ (x = 1.5, 2.0), $ZrCo_2Ge_4O_{12}$ and $Tb_2CoGe_4O_{12}$, $TbScCoGe_4O_{12}$ and the canted moments probably come from the antisymmetric interaction (DM exchange). In $Tb_2CoGe_4O_{12}$ and $TbScCoGe_4O_{12}$, the ground state of Tb^{3+} should be $m_J = 0$ and the mean ordered moment is expected to be 0 as in $Tb_2MnGe_4O_{12}$. The moment is a result of the anisotropic exchange, DM interaction, dipolar interaction and the internal molecular field from Co sublattice. All the interactions actually come from the anisotropic cation Co^{2+}. Moreover, the magnetic structure of $GdFeZnGe_4O_{12}$ determined from the neutron diffraction also proves our hypothesis that the internal molecular field from the *4f* site sublattice is a key factor in determining the moment of the *2b* site. We thus propose that the internal molecule field from the Fe sublattice and the crystal field should also introduce a considerable degree of anisotropy to Gd^{3+} leading to its ordered moment pointing in this specific direction.

Appendix A - Structural Chemistry - XRPD

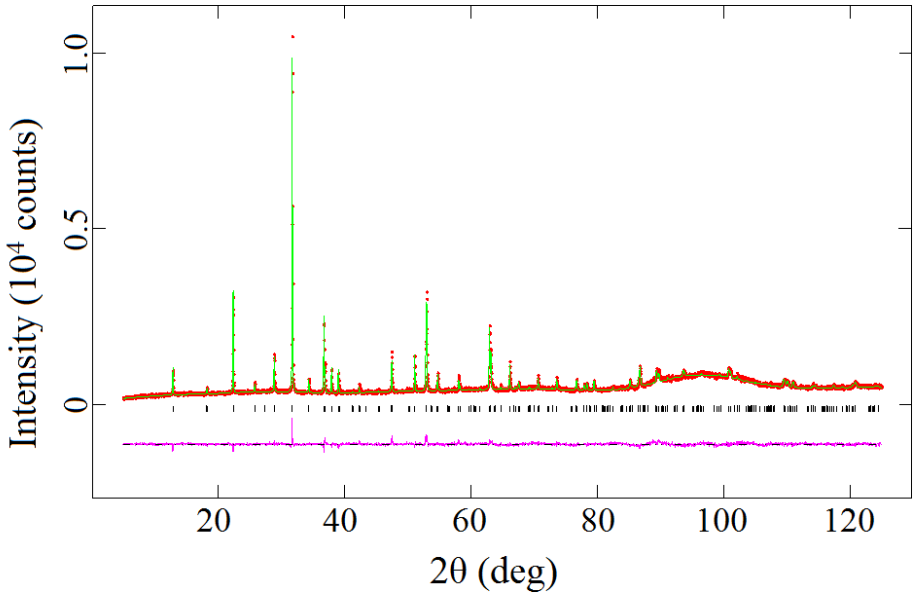

Figure A.1 Observed (red dots) and calculated (green line) XRPD patterns of $CeMn_{1.5}Co_{0.5}Ge_4O_{12}$ at room temperature; Cu Kα1. A difference curve (purple line) is shown and reflection positions are marked.

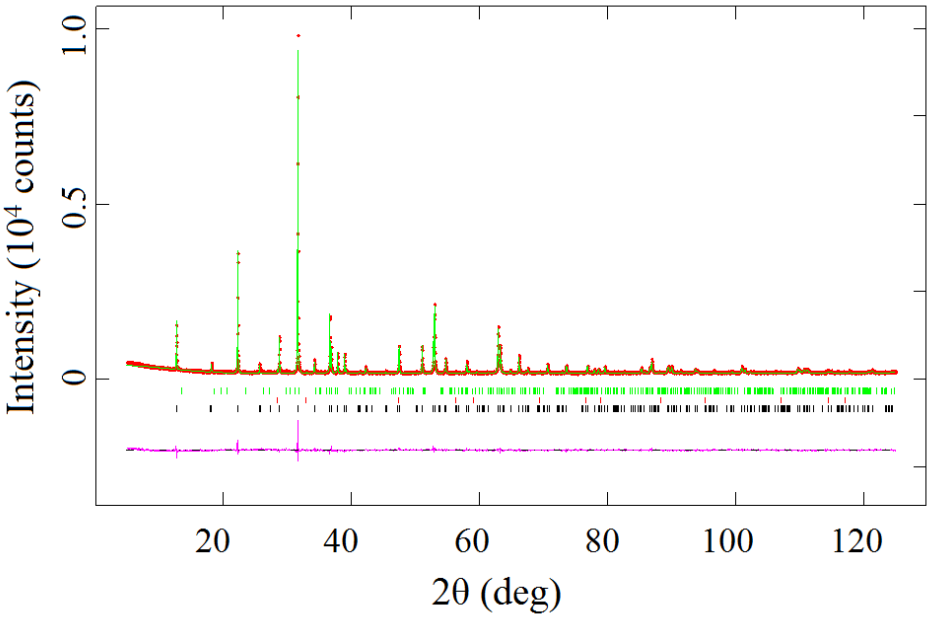

Figure A.2 Observed (red dots) and calculated (green line) XRPD patterns of $CeMnCoGe_4O_{12}$ at room temperature; Cu Kα1. A difference curve (purple line) is shown and reflection positions are marked for $CeMnCoGe_4O_{12}$ (black), CeO_2 (red) and $CoGeO_3$ (green).

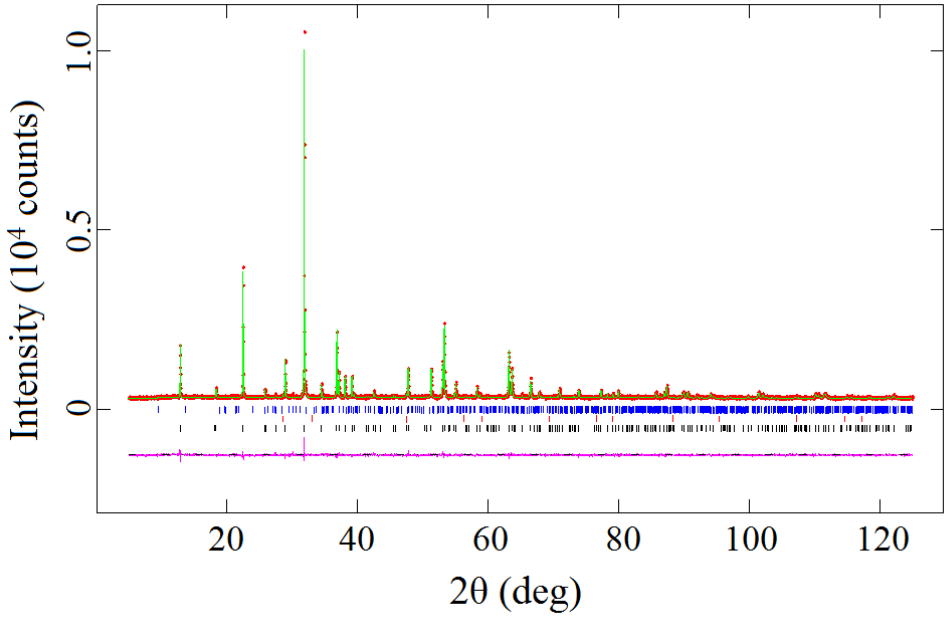

Figure A.3 Observed (red dots) and calculated (green line) XRPD patterns of $CeMn_{0.5}Co_{1.5}Ge_4O_{12}$ at room temperature; Cu Kα1. A difference curve (purple line) is shown and reflection positions are marked for $CeMn_{0.5}Co_{1.5}Ge_4O_{12}$ (black), CeO_2 (red) and $CoGeO_3$ (blue).

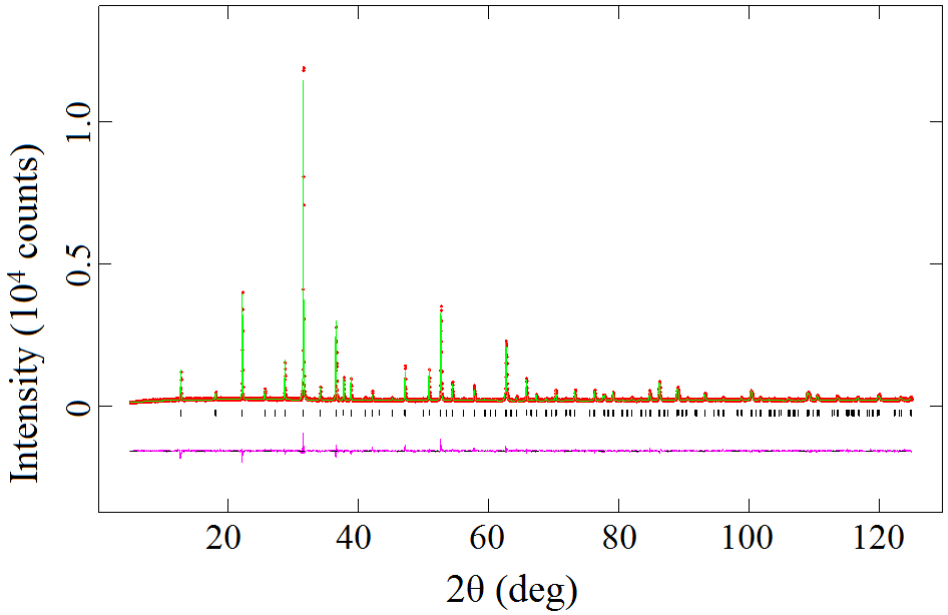

Figure A.4 Observed (red dots) and calculated (green line) XRPD patterns of $CeCo_2Ge_4O_{12}$ at room temperature; Cu Kα1. A difference curve (purple line) is shown and reflection positions are marked.

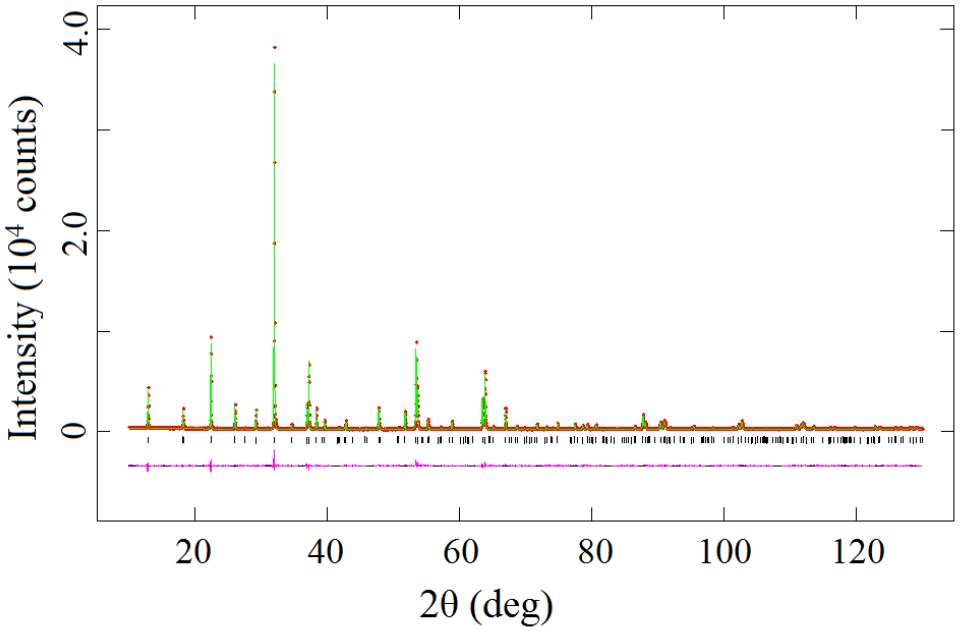

Figure A.5 Observed (red dots) and calculated (green line) XRPD patterns of $ZrMn_2Ge_4O_{12}$ at room temperature; Cu Kα1. A difference curve (purple line) is shown and reflection positions are marked.

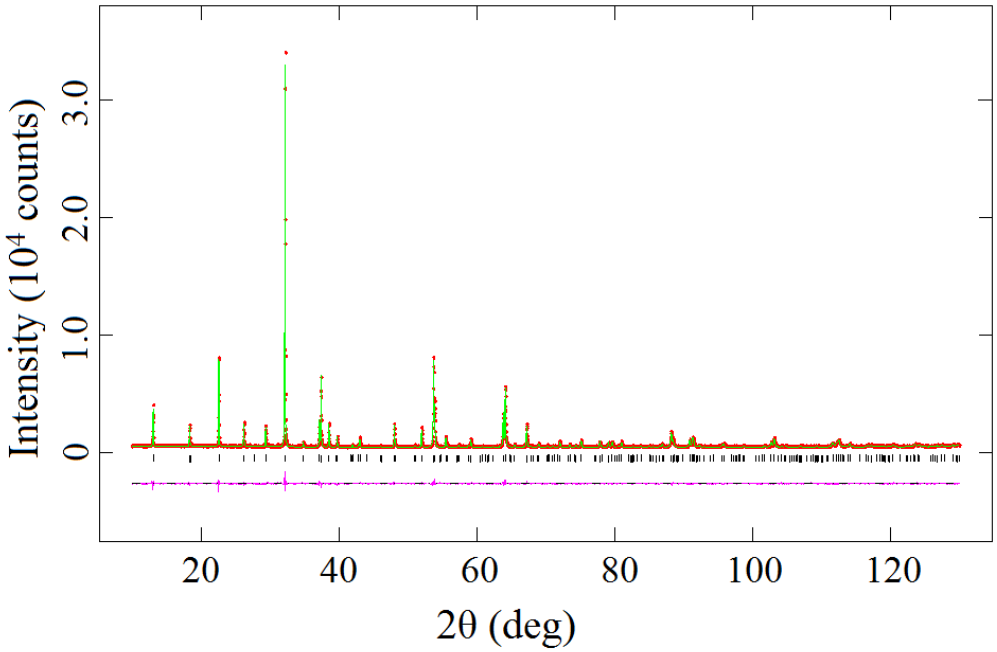

Figure A.6 Observed (red dots) and calculated (green line) XRPD patterns of $ZrMn_{1.5}Co_{0.5}Ge_4O_{12}$ at room temperature; Cu Kα1. A difference curve (purple line) is shown and reflection positions are marked.

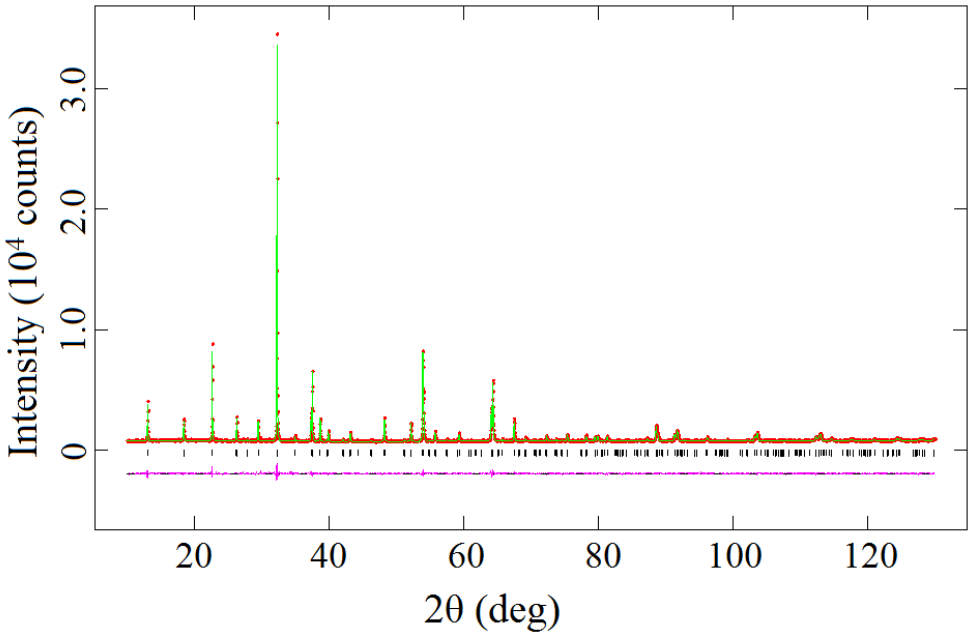

Figure A.7 Observed (red dots) and calculated (green line) XRPD patterns of $ZrMnCoGe_4O_{12}$ at room temperature; Cu Kα1. A difference curve (purple line) is shown and reflection positions are marked.

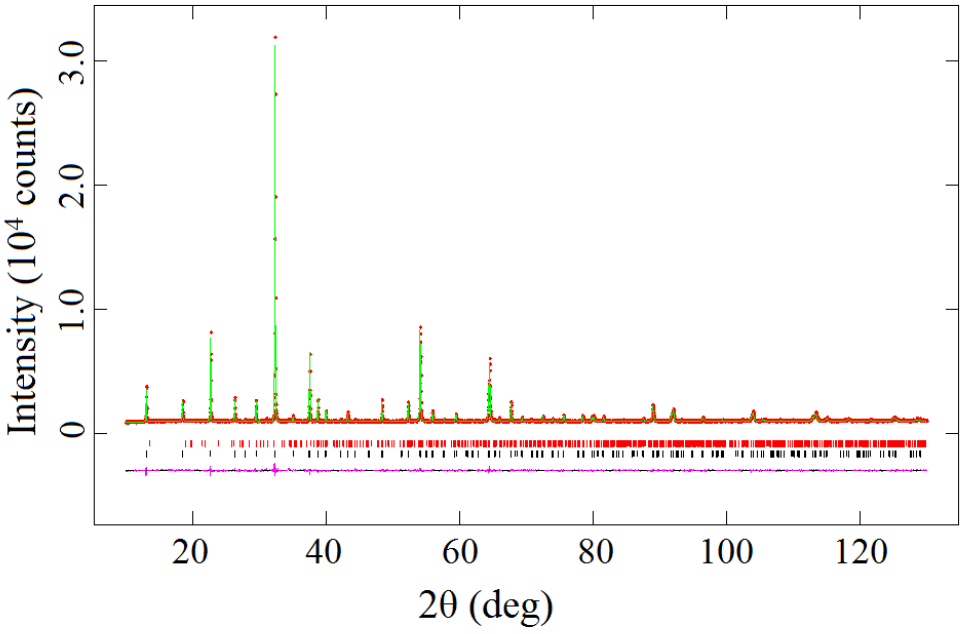

Figure A.8 Observed (red dots) and calculated (green line) XRPD patterns of $ZrMn_{0.5}Co_{1.5}Ge_4O_{12}$ at room temperature; Cu Kα1. A difference curve (purple line) is shown and reflection positions are marked for $ZrMn_{0.5}Co_{1.5}Ge_4O_{12}$ (bottom) and $CoGeO_3$ (top).

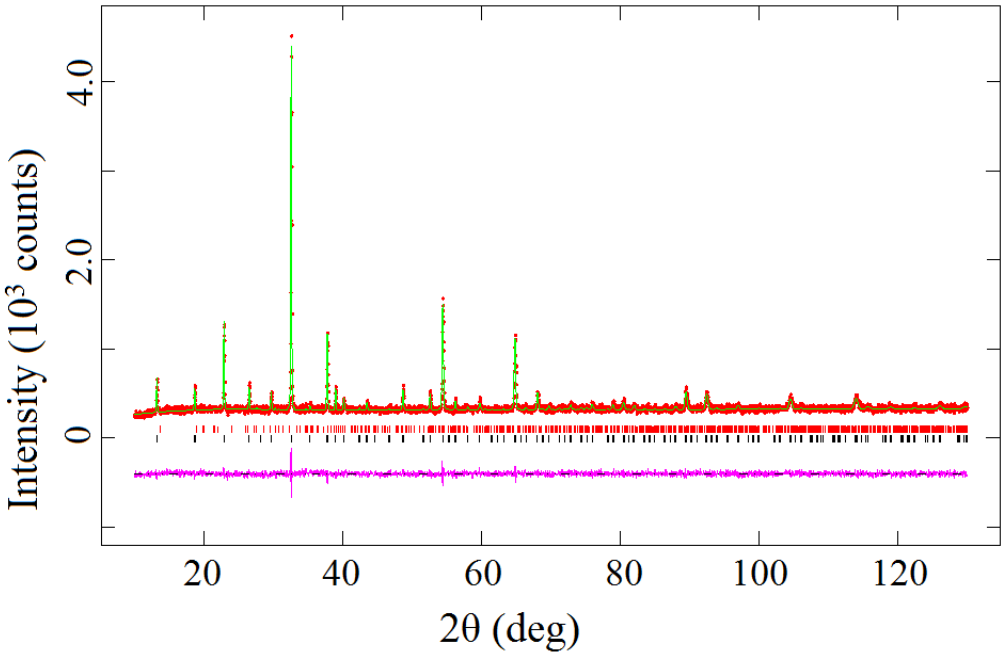

Figure A.9 Observed (red dots) and calculated (green line) XRPD patterns of $ZrCo_2Ge_4O_{12}$ at room temperature; Cu Kα1. A difference curve (purple line) is shown and reflection positions are marked for $ZrCo_2Ge_4O_{12}$ (bottom) and $CoGeO_3$ (top).

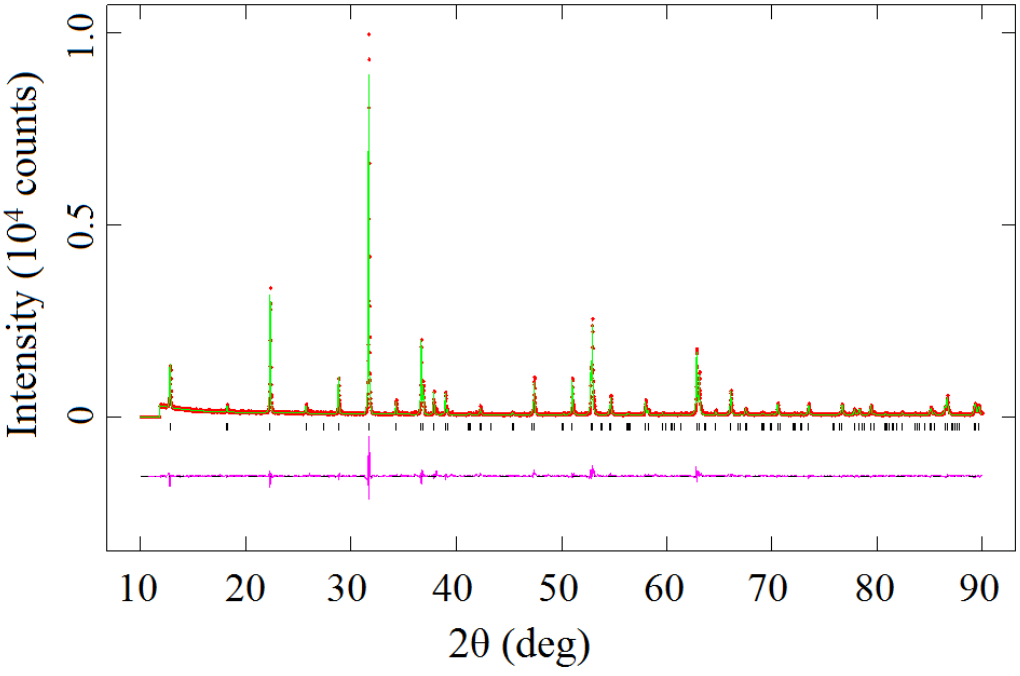

Figure A.10 Observed (red dots) and calculated (green line) XRPD patterns of $CeMn_{1.5}Zn_{0.5}Ge_4O_{12}$ at room temperature; Cu Kα1. A difference curve (purple line) is shown and reflection positions are marked.

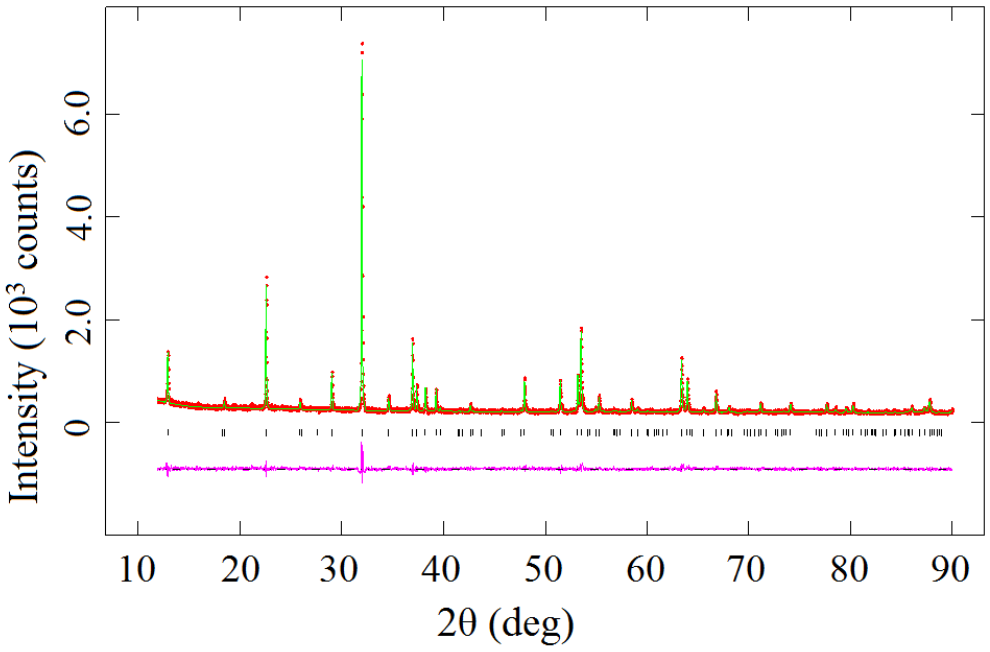

Figure A.11 Observed (red dots) and calculated (green line) XRPD patterns of $CeCo_{1.5}Zn_{0.5}Ge_4O_{12}$ at room temperature; Cu Kα1. A difference curve (purple line) is shown and reflection positions are marked.

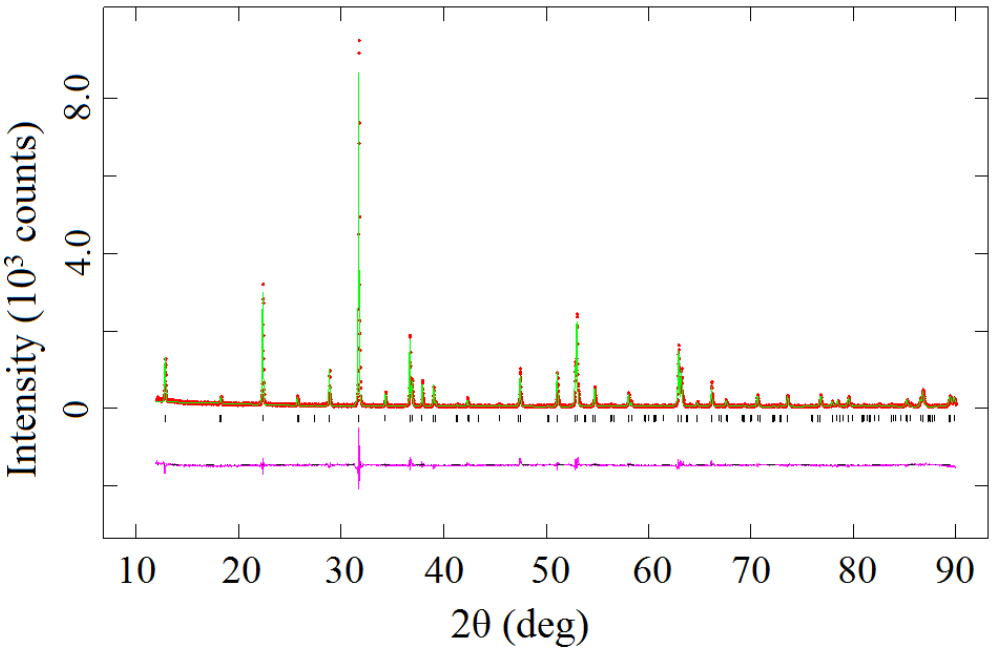

Figure A.12 Observed (red dots) and calculated (green line) XRPD patterns of $CeMn_{1.5}Ni_{0.5}Ge_4O_{12}$ at room temperature; Cu Kα1. A difference curve (purple line) is shown and reflection positions are marked.

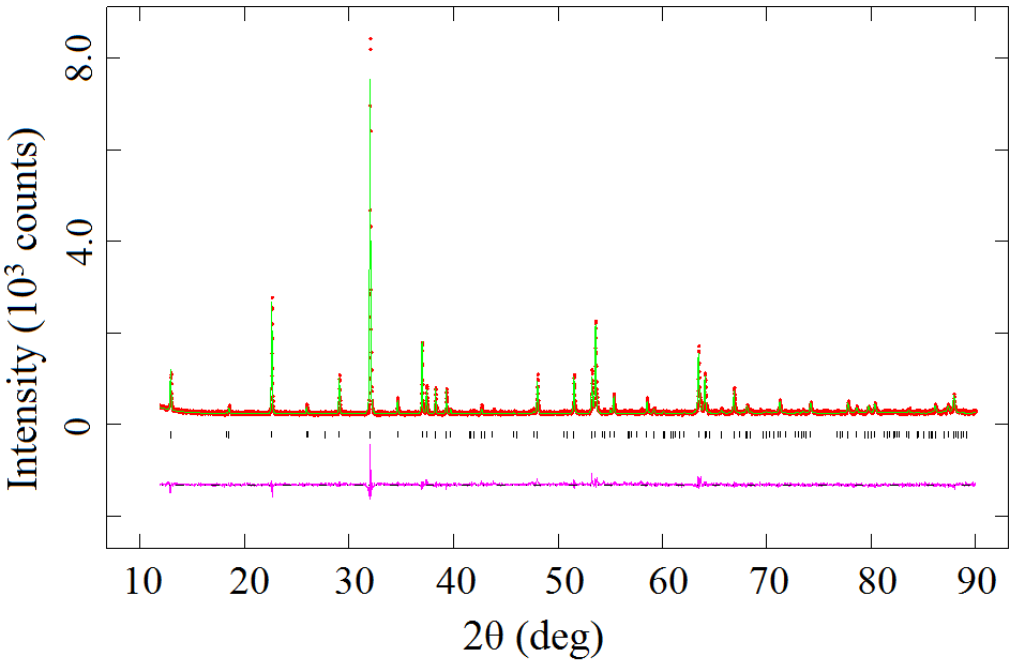

Figure A.13 Observed (red dots) and calculated (green line) XRPD patterns of $CeCo_{1.5}Ni_{0.5}Ge_4O_{12}$ at room temperature; Cu Kα1. A difference curve (purple line) is shown and reflection positions are marked.

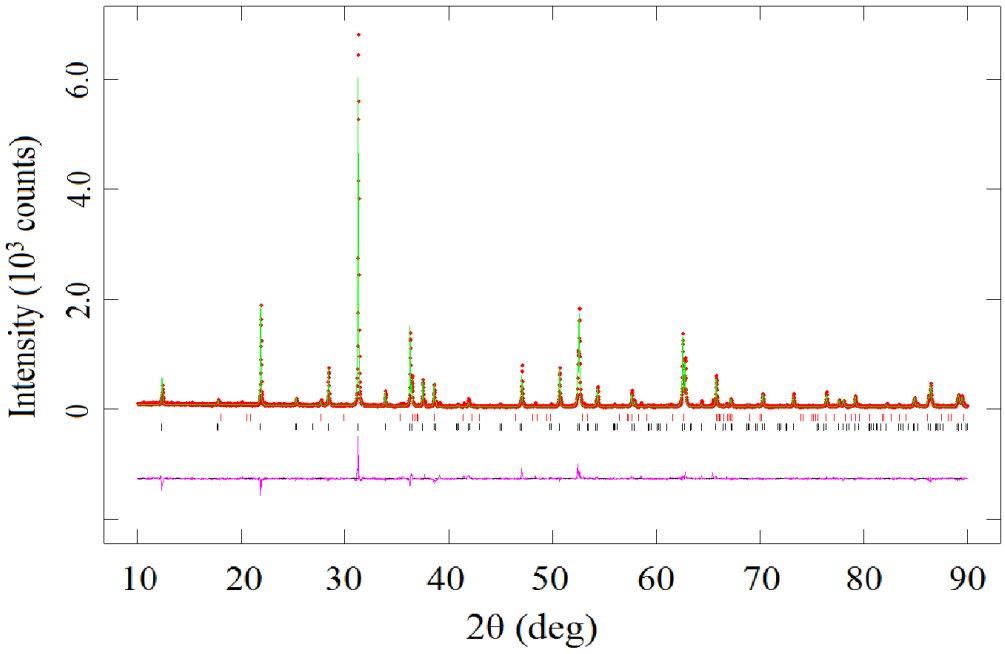

Figure A.14 Observed (red dots) and calculated (green line) XRPD patterns of $CeMn_{1.5}Cu_{0.5}Ge_4O_{12}$ at room temperature; Cu Kα1. A difference curve (purple line) is shown and reflection positions are marked.

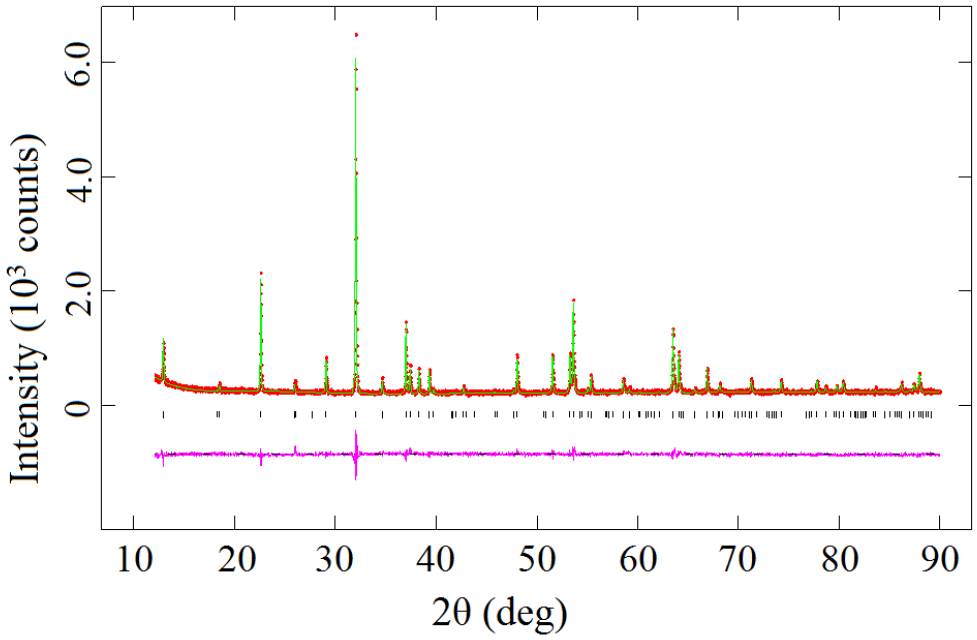

Figure A.15 Observed (red dots) and calculated (green line) XRPD patterns of $CeCo_{1.5}Cu_{0.5}Ge_4O_{12}$ at room temperature; Cu Kα1. A difference curve (purple line) is shown and reflection positions are marked.

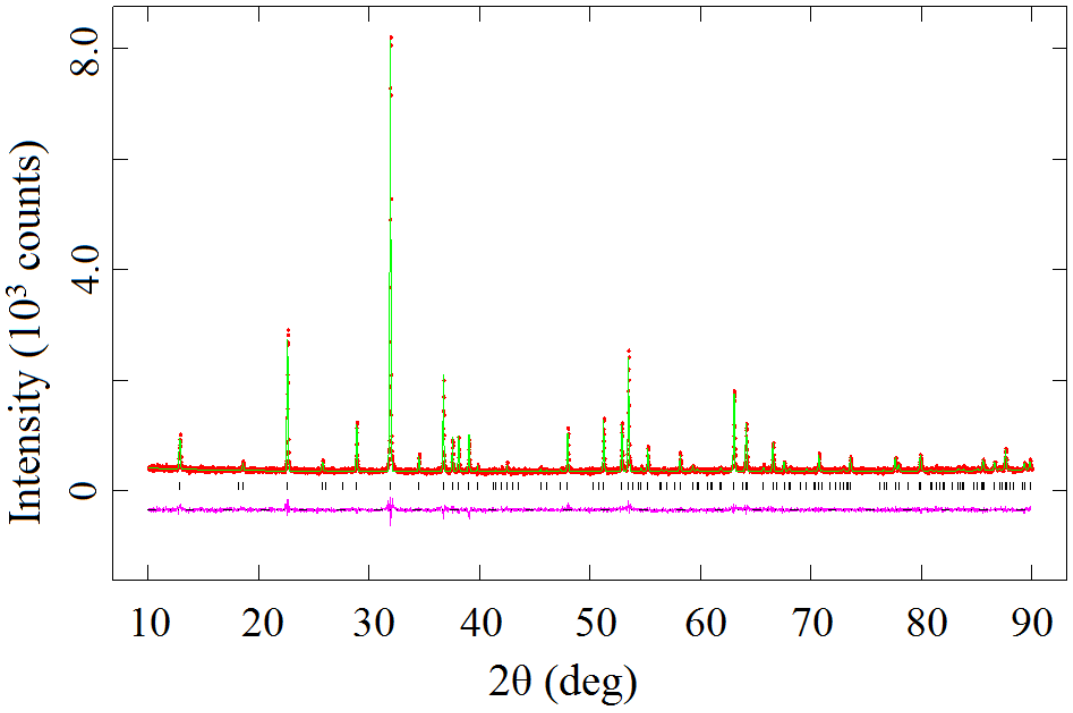

Figure A.16 Observed (red dots) and calculated (green line) XRPD patterns of $EuFeMnGe_4O_{12}$ at room temperature; Cu Kα1. A difference curve (purple line) is shown and reflection positions are marked.

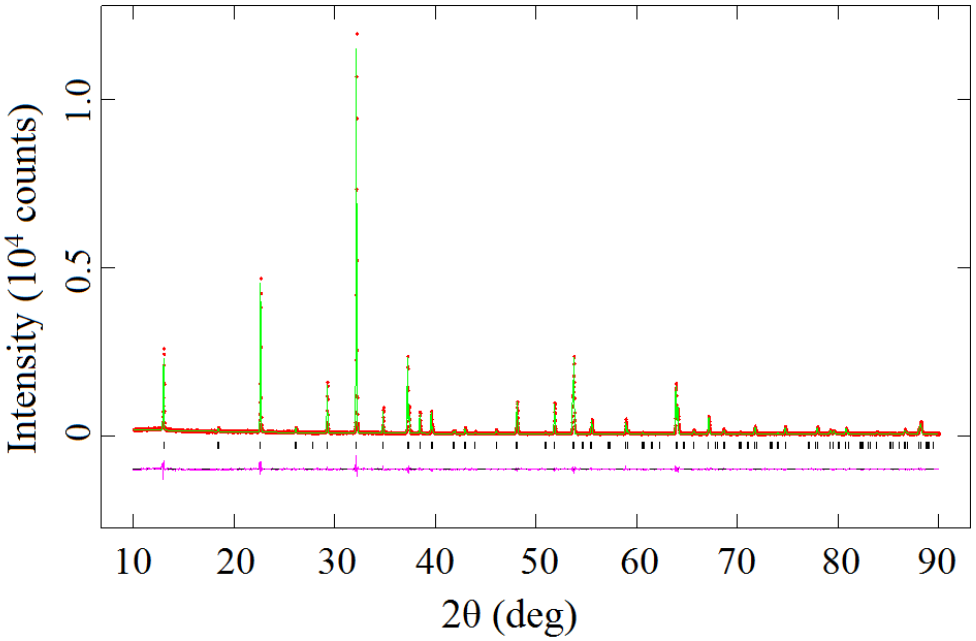

Figure A.17 Observed (red dots) and calculated (green line) XRPD patterns of $LuFeMnGe_4O_{12}$at room temperature; Cu Kα1. A difference curve (purple line) is shown and reflection positions are marked.

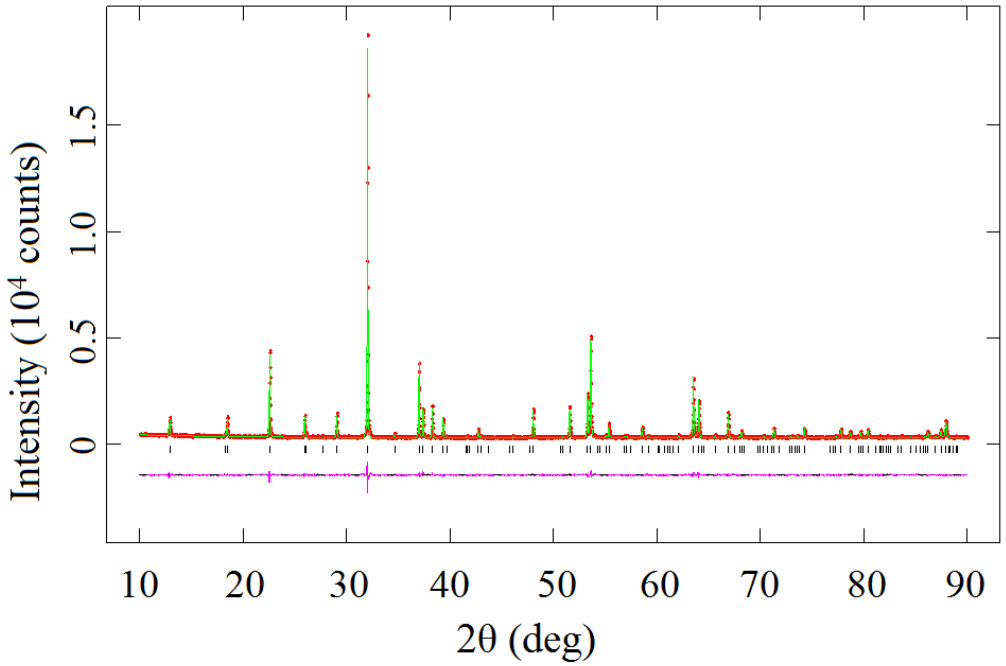

Figure A.18 Observed (red dots) and calculated (green line) XRPD patterns of $YFeMnGe_4O_{12}$ at room temperature; Cu Kα1. A difference curve (purple line) is shown and reflection positions are marked.

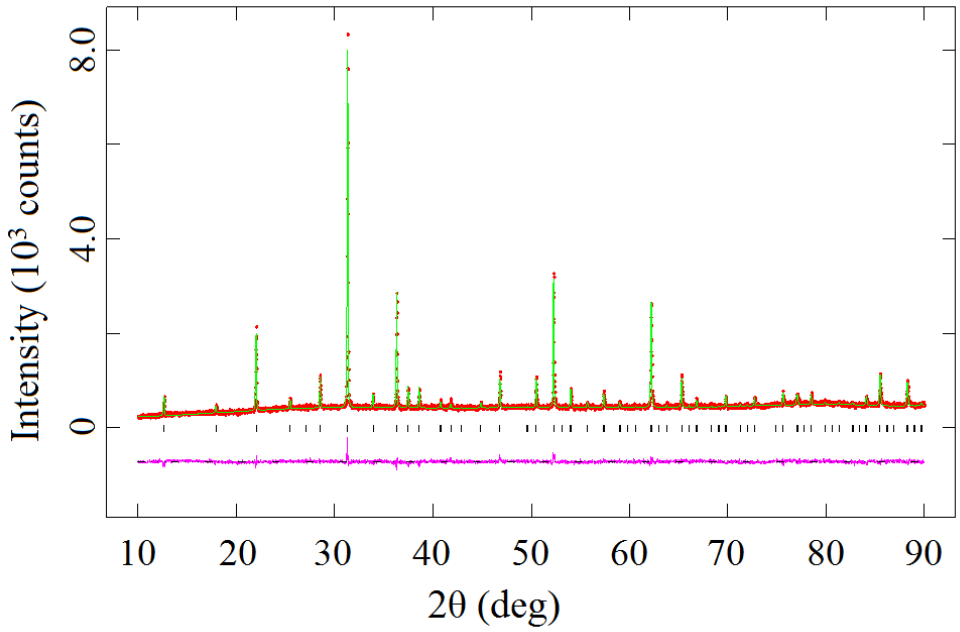

Figure A.19 Observed (red dots) and calculated (green line) XRPD patterns of $Tb_2CoGe_4O_{12}$ at room temperature; Cu Kα1. A difference curve (purple line) is shown and reflection positions are marked.

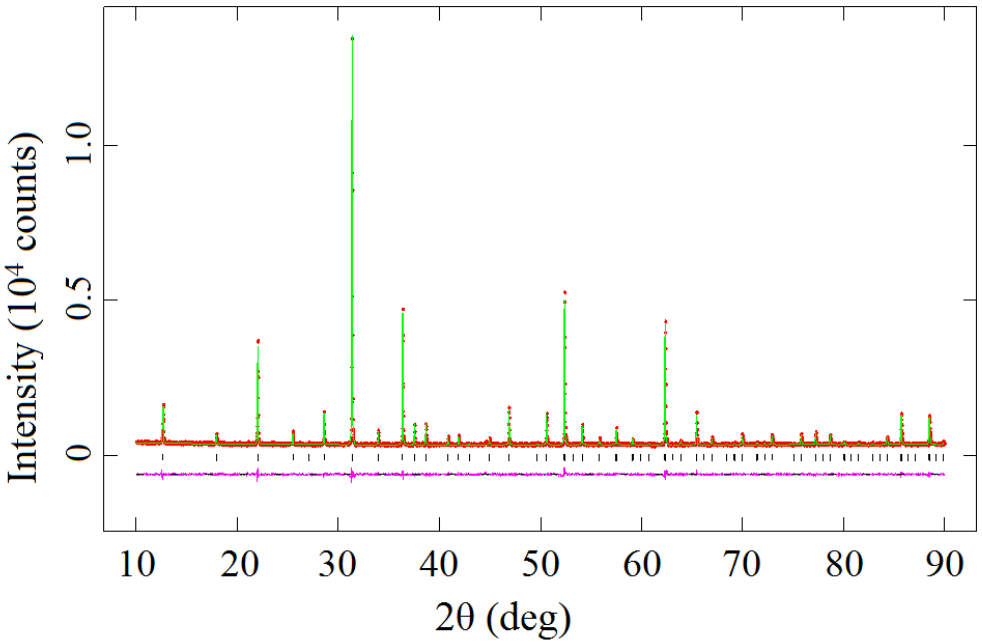

Figure A.20 Observed (red dots) and calculated (green line) XRPD patterns of $Dy_2CoGe_4O_{12}$ at room temperature; Cu Kα1. A difference curve (purple line) is shown and reflection positions are marked.

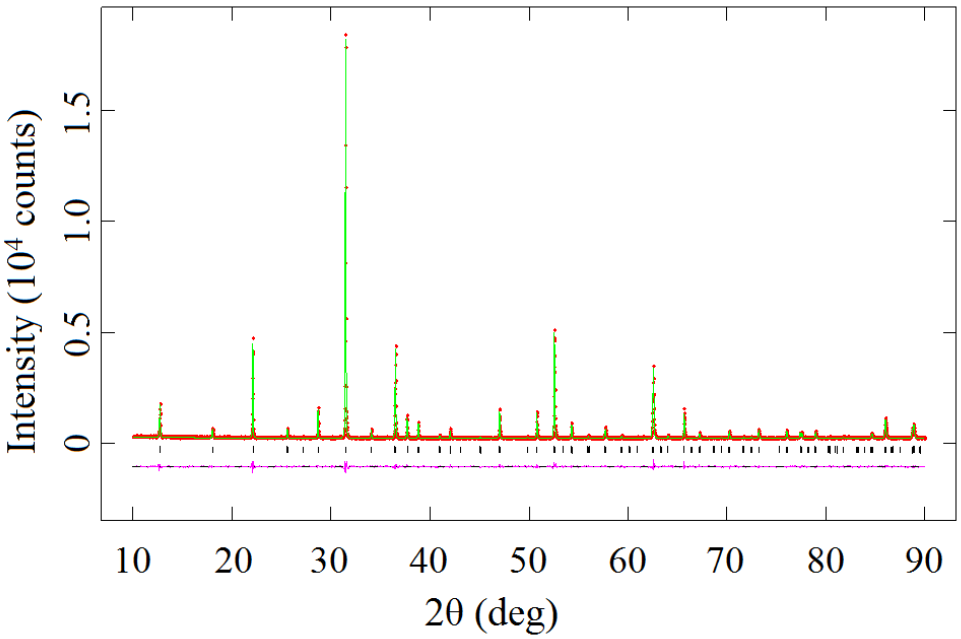

Figure A.21 Observed (red dots) and calculated (green line) XRPD patterns of $Ho_2CoGe_4O_{12}$ at room temperature; Cu Kα1. A difference curve (purple line) is shown and reflection positions are marked.

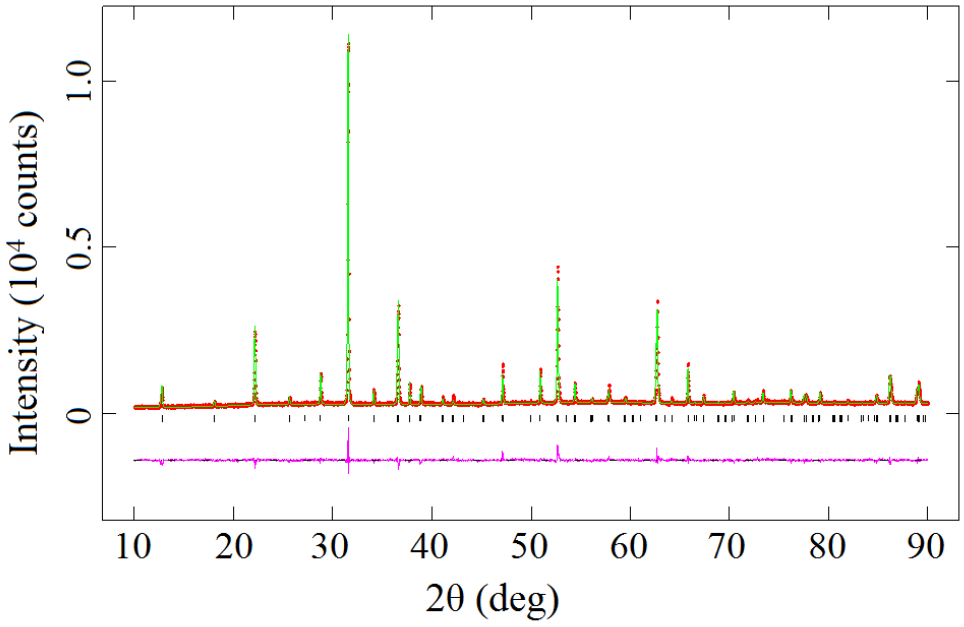

Figure A.22 Observed (red dots) and calculated (green line) XRPD patterns of $Er_2CoGe_4O_{12}$ at room temperature; Cu Kα1. A difference curve (purple line) is shown and reflection positions are marked.

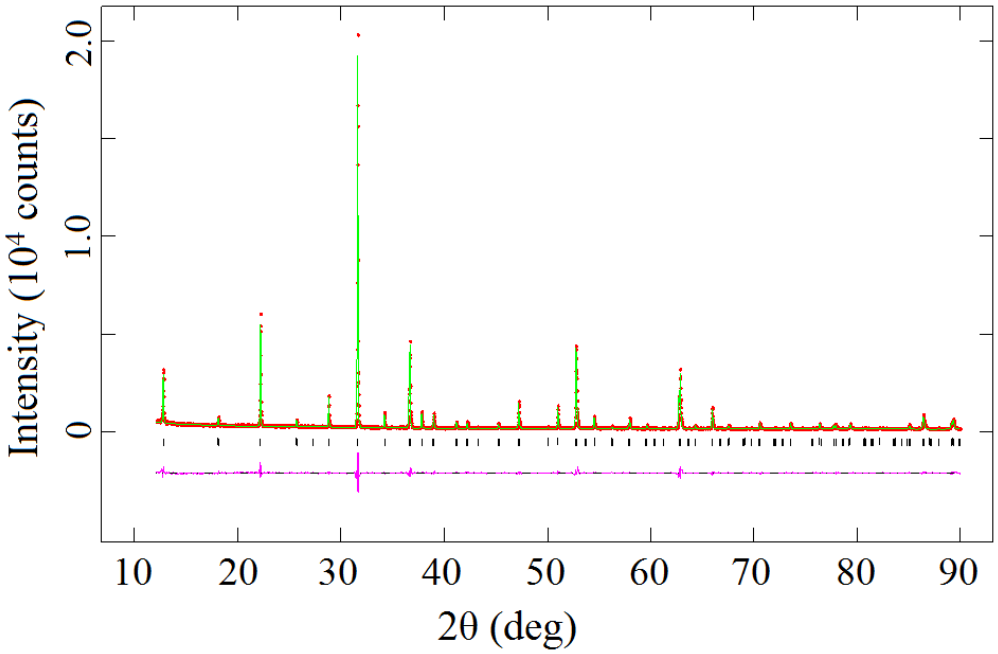

Figure A.23 Observed (red dots) and calculated (green line) XRPD patterns of $Tm_2CoGe_4O_{12}$ at room temperature; Cu Kα1. A difference curve (purple line) is shown and reflection positions are marked.

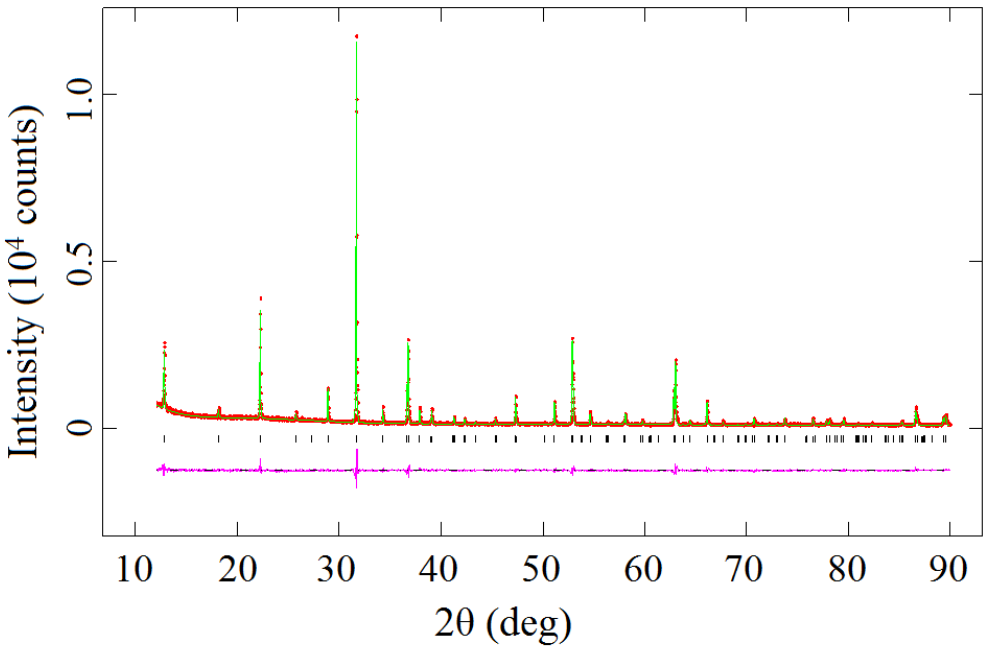

Figure A.24 Observed (red dots) and calculated (green line) XRPD patterns of $Yb_2CoGe_4O_{12}$ at room temperature; Cu Kα1. A difference curve (purple line) is shown and reflection positions are marked.

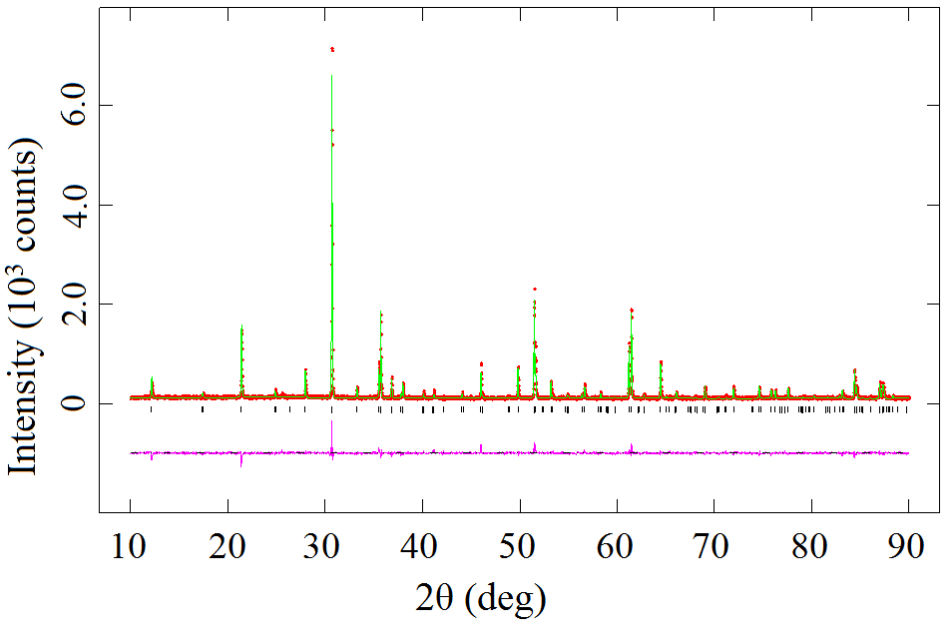

Figure A.25 Observed (red dots) and calculated (green line) XRPD patterns of $Tb_2MnGe_4O_{12}$ at room temperature; Cu Kα1. A difference curve (purple line) is shown and reflection positions are marked.

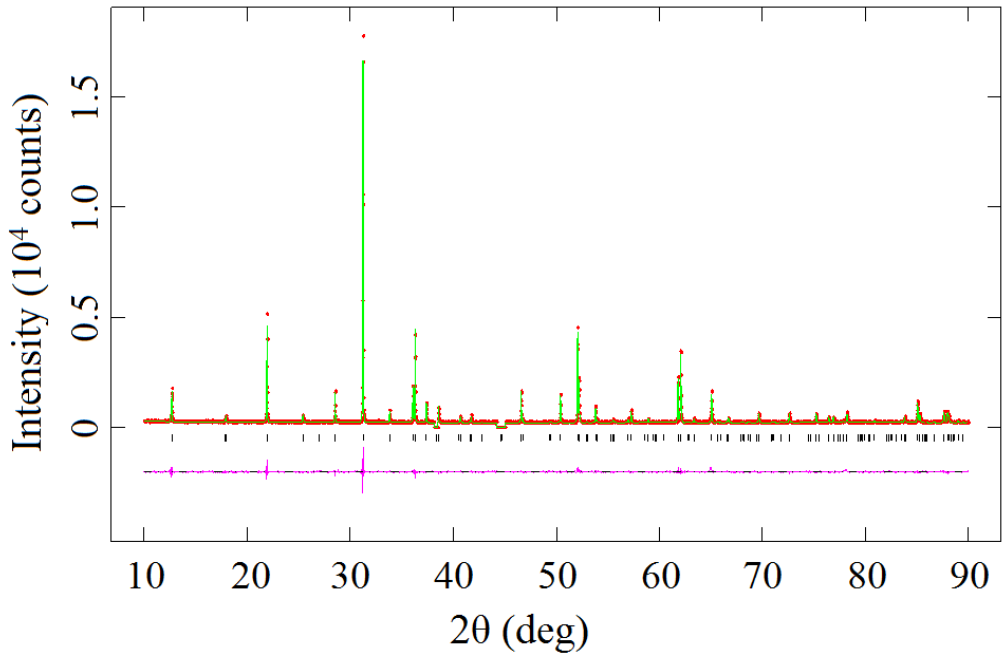

Figure A.26 Observed (red dots) and calculated (green line) XRPD patterns of $Dy_2MnGe_4O_{12}$ at room temperature; Cu Kα1. A difference curve (purple line) is shown and reflection positions are marked.

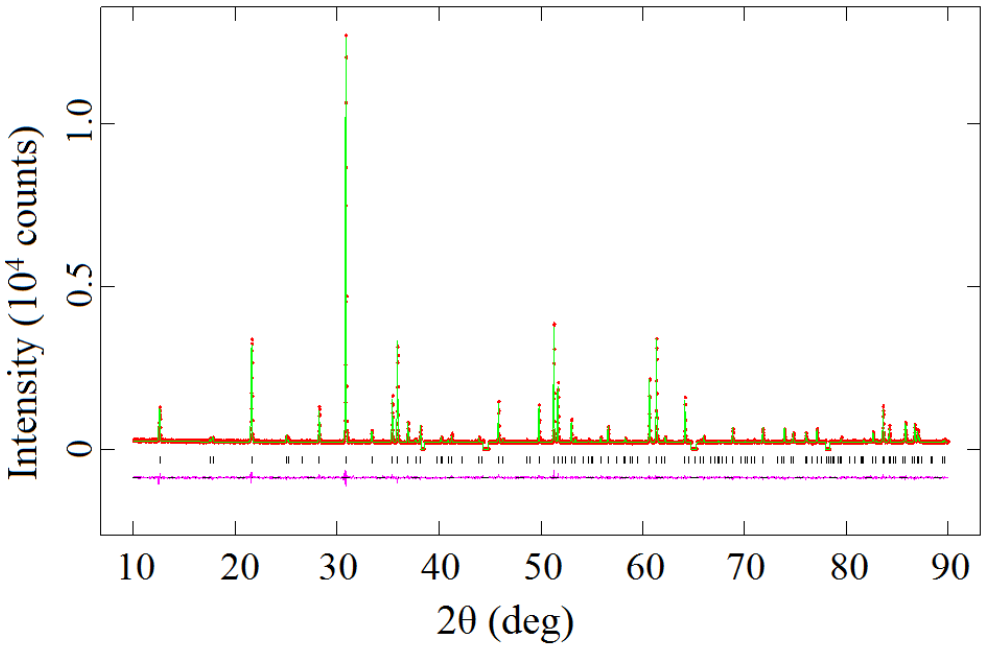

Figure A.27 Observed (red dots) and calculated (green line) XRPD patterns of $Dy_2CaGe_4O_{12}$ at room temperature; Cu Kα1. A difference curve (purple line) is shown and reflection positions are marked.

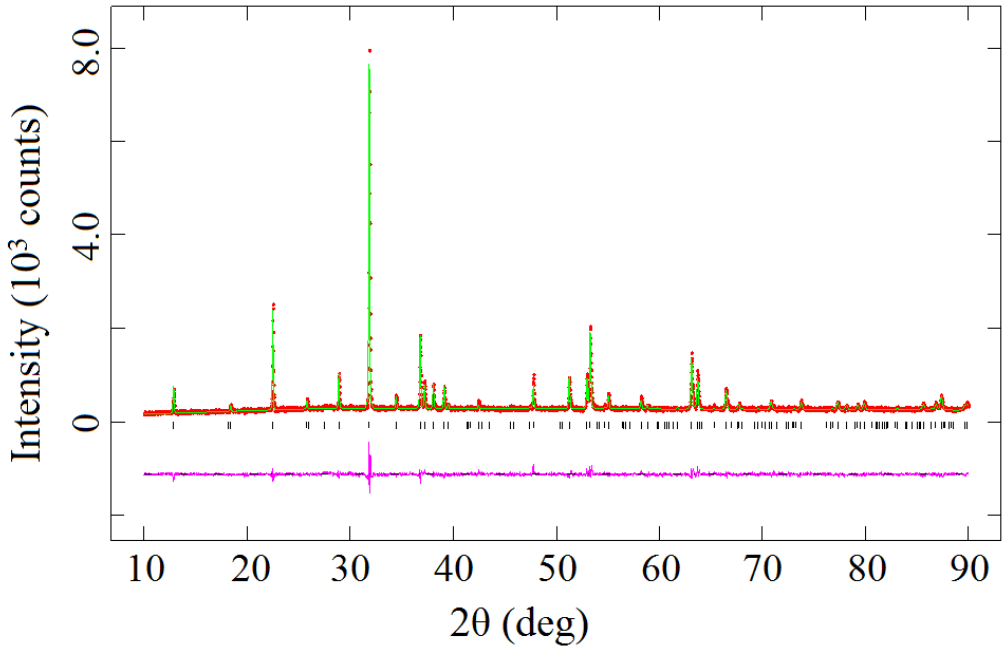

Figure A.28 Observed (red dots) and calculated (green line) XRPD patterns of $TbScMnGe_4O_{12}$ at room temperature; Cu Kα1. A difference curve (purple line) is shown and reflection positions are marked.

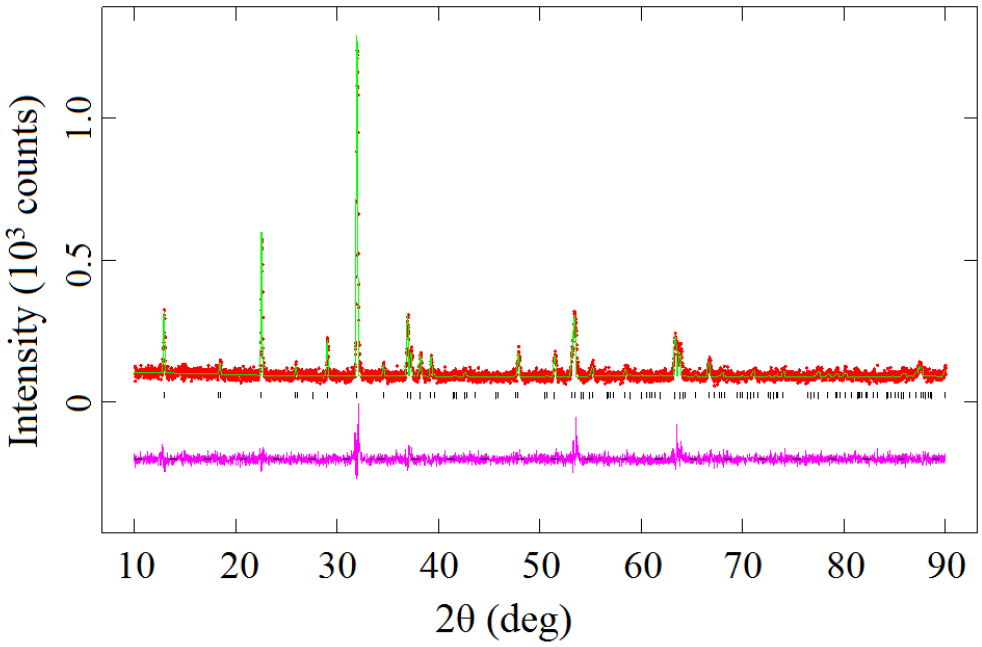

Figure A.29 Observed (red dots) and calculated (green line) XRPD patterns of $DyScMnGe_4O_{12}$ at room temperature; Cu Kα1. A difference curve (purple line) is shown and reflection positions are marked.

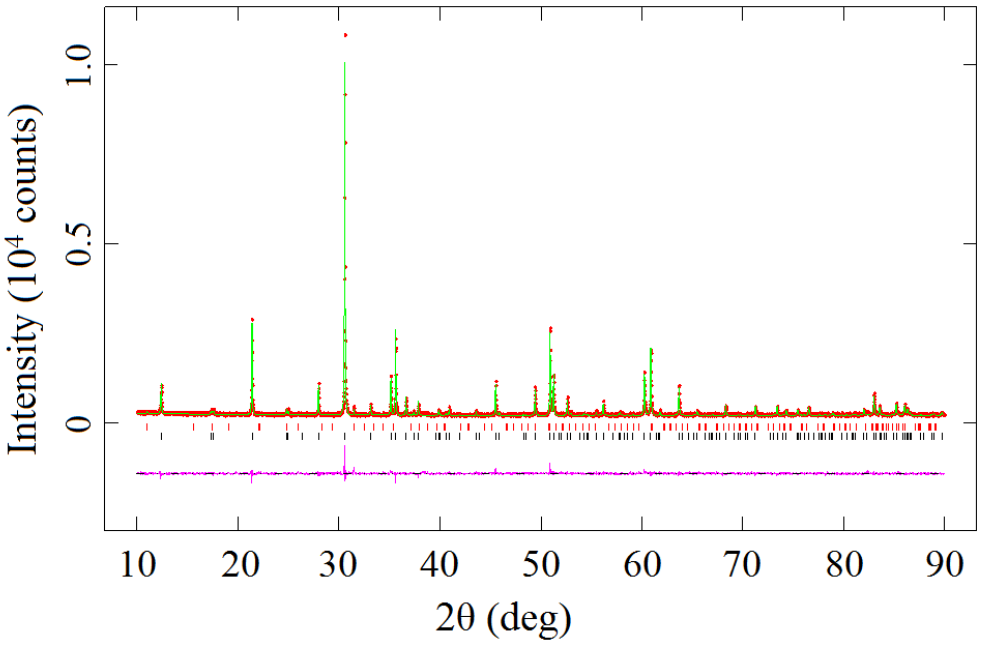

Figure A.30 Observed (red dots) and calculated (green line) XRPD patterns of $Gd_2CaGe_4O_{12}$ at room temperature; Cu Kα1. A difference curve (purple line) is shown and reflection positions are marked.

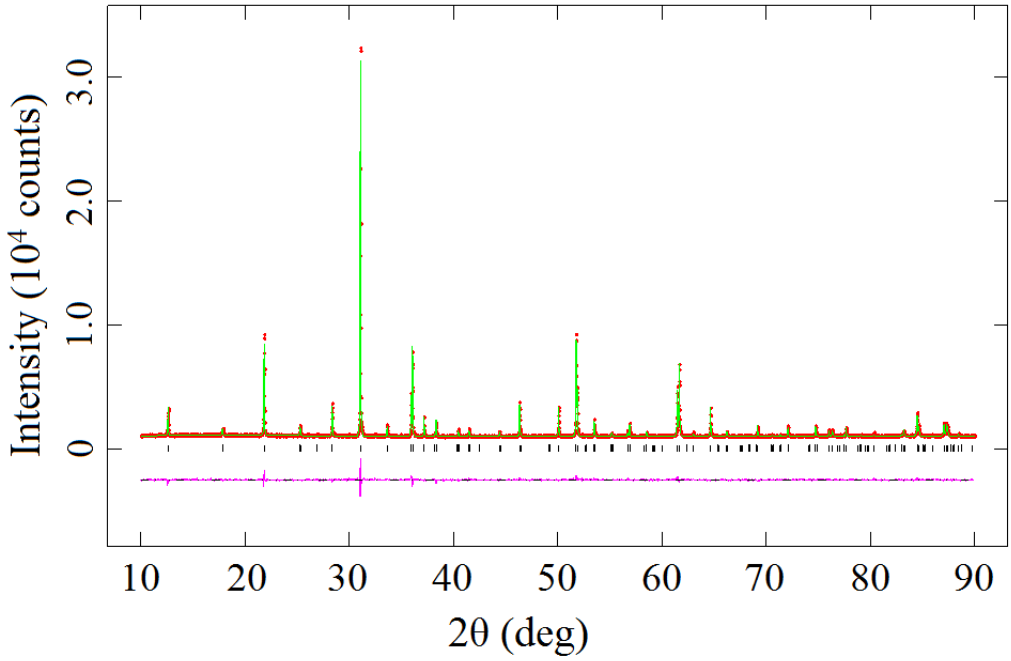

Figure A.31 Observed (red dots) and calculated (green line) XRPD patterns of $Gd_2MnGe_4O_{12}$ at room temperature; Cu Kα1. A difference curve (purple line) is shown and reflection positions are marked.

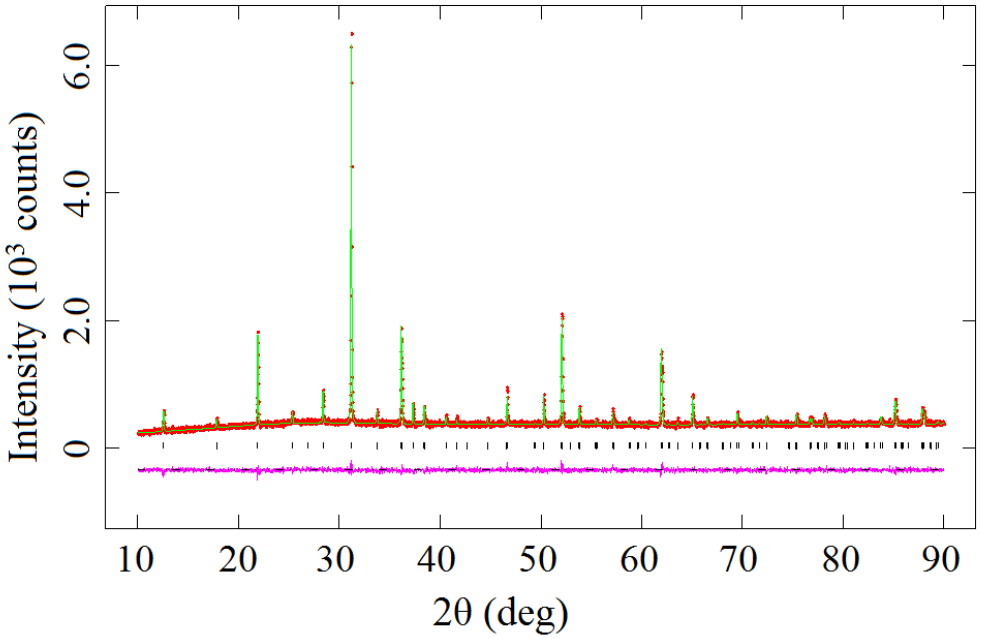

Figure A.32 Observed (red dots) and calculated (green line) XRPD patterns of $Gd_2CoGe_4O_{12}$ at room temperature; Cu Kα1. A difference curve (purple line) is shown and reflection positions are marked.

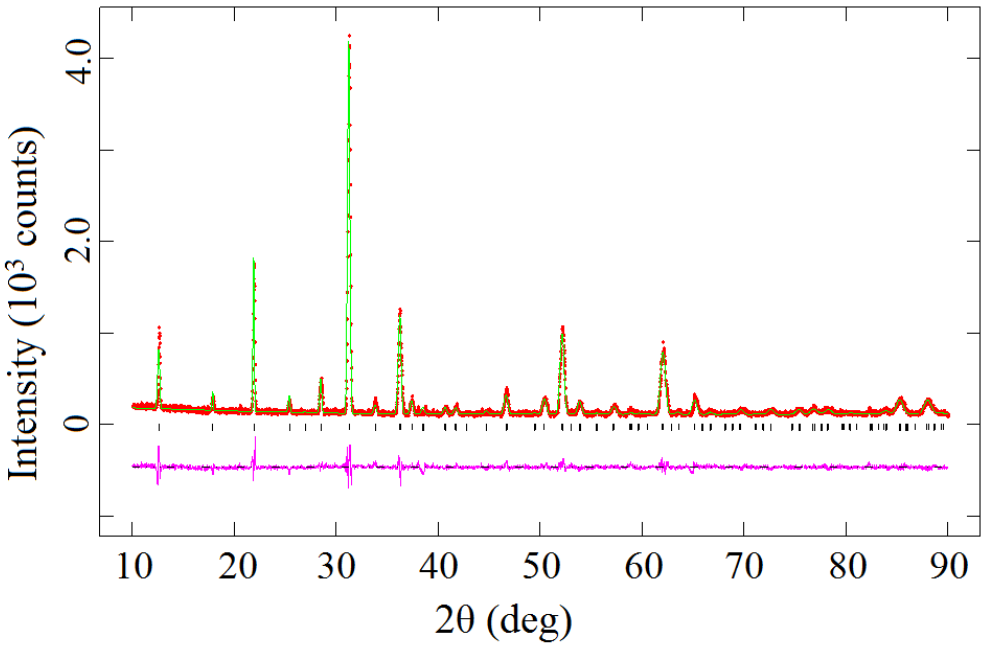

Figure A.33 Observed (red dots) and calculated (green line) XRPD patterns of $GdLuMnGe_4O_{12}$ at room temperature; Cu Kα1. A difference curve (purple line) is shown and reflection positions are marked.

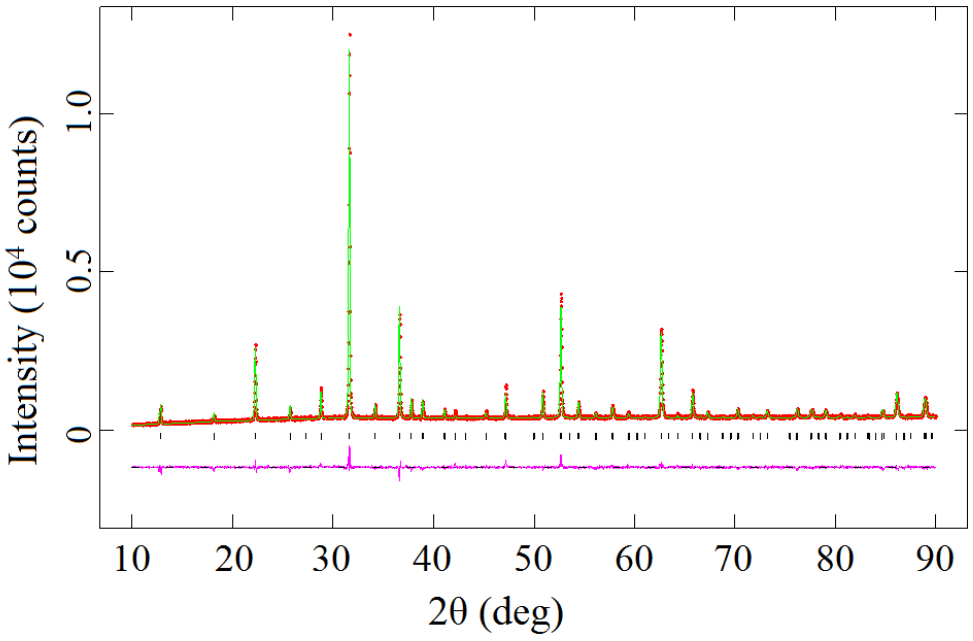

Figure A.34 Observed (red dots) and calculated (green line) XRPD patterns of $GdLuCoGe_4O_{12}$ at room temperature; Cu Kα1. A difference curve (purple line) is shown and reflection positions are marked.

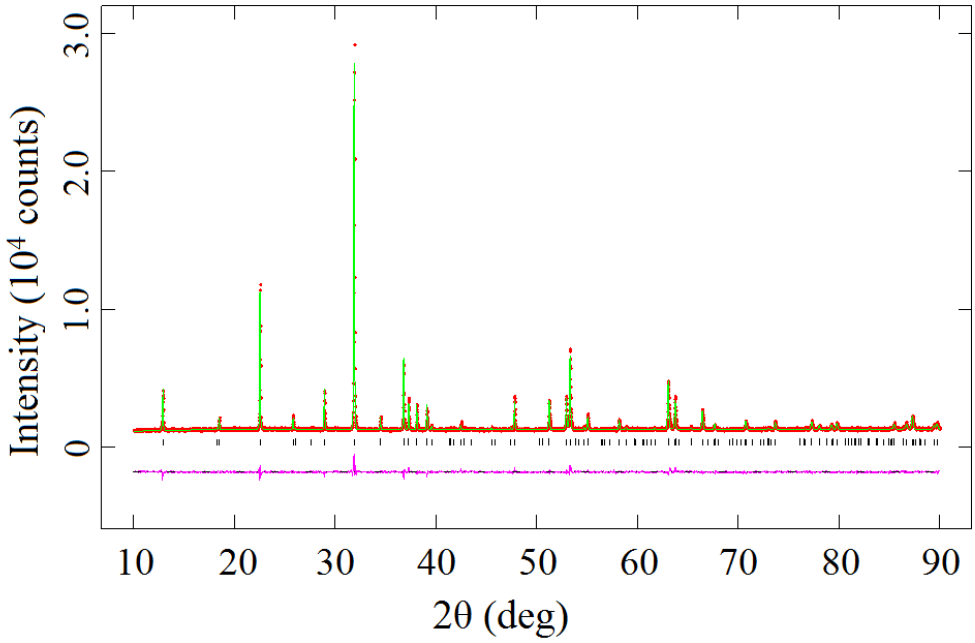

Figure A.35 Observed (red dots) and calculated (green line) XRPD patterns of $GdScCoGe_4O_{12}$ at room temperature; Cu Kα1. A difference curve (purple line) is shown and reflection positions are marked.

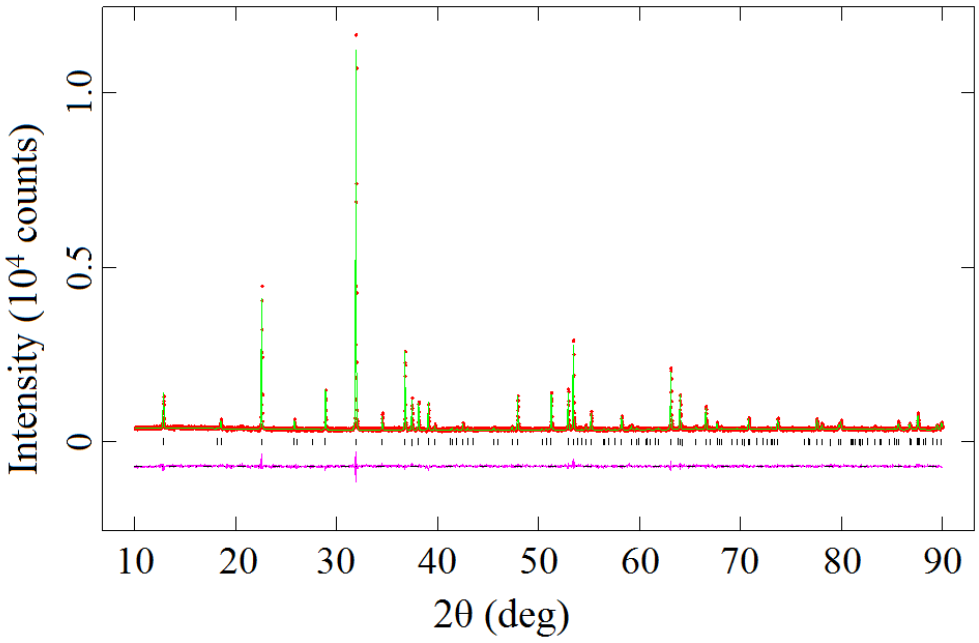

Figure A.36 Observed (red dots) and calculated (green line) XRPD patterns of $GdFeMnGe_4O_{12}$ at room temperature; Cu Kα1. A difference curve (purple line) is shown and reflection positions are marked.

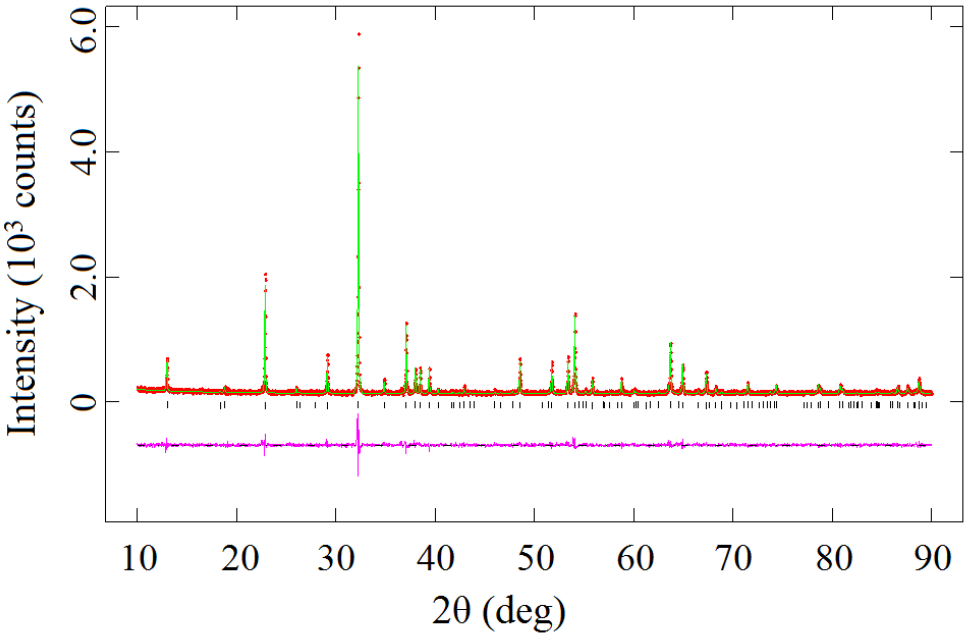

Figure A.37 Observed (red dots) and calculated (green line) XRPD patterns of $GdFeZnGe_4O_{12}$ at room temperature; Cu Kα1. A difference curve (purple line) is shown and reflection positions are marked.

Appendix B - Structural Chemistry - NPD

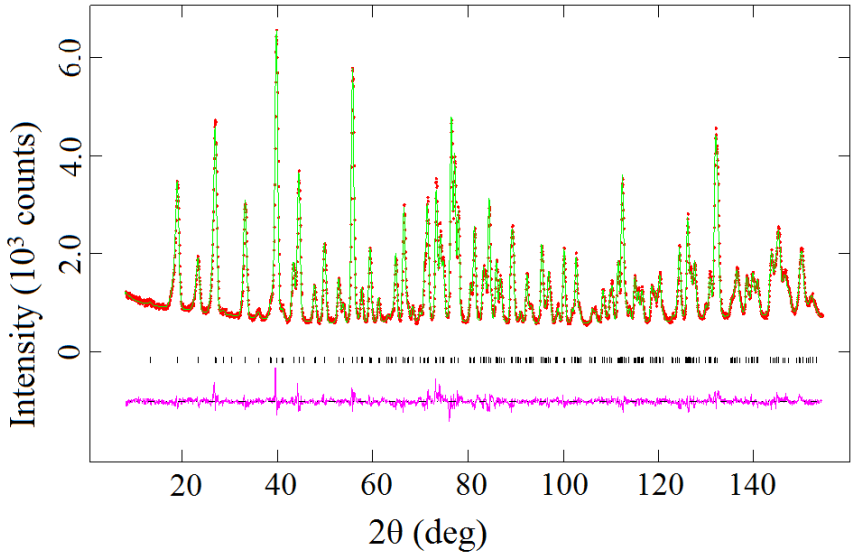

Figure B.1 Observed (red dots) and calculated (green line) NPD patterns of $CeMn_{1.5}Co_{0.5}Ge_4O_{12}$ at room temperature; λ = 1.622 Å. A difference curve (purple line) is shown and reflection positions are marked.

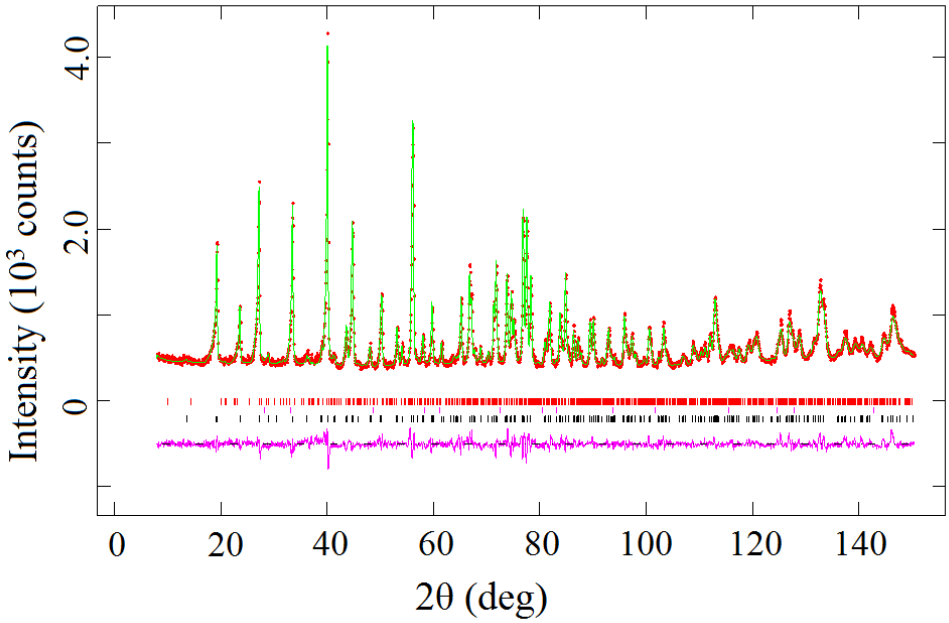

Figure B.2 Observed (red dots) and calculated (green line) NPD patterns of $CeMnCoGe_4O_{12}$ at room temperature; λ = 1.622 Å. A difference curve (purple line) is shown and reflection positions are marked for $CeMnCoGe_4O_{12}$ (bottom), CeO_2 (middle), and $CoGeO_3$ (top).

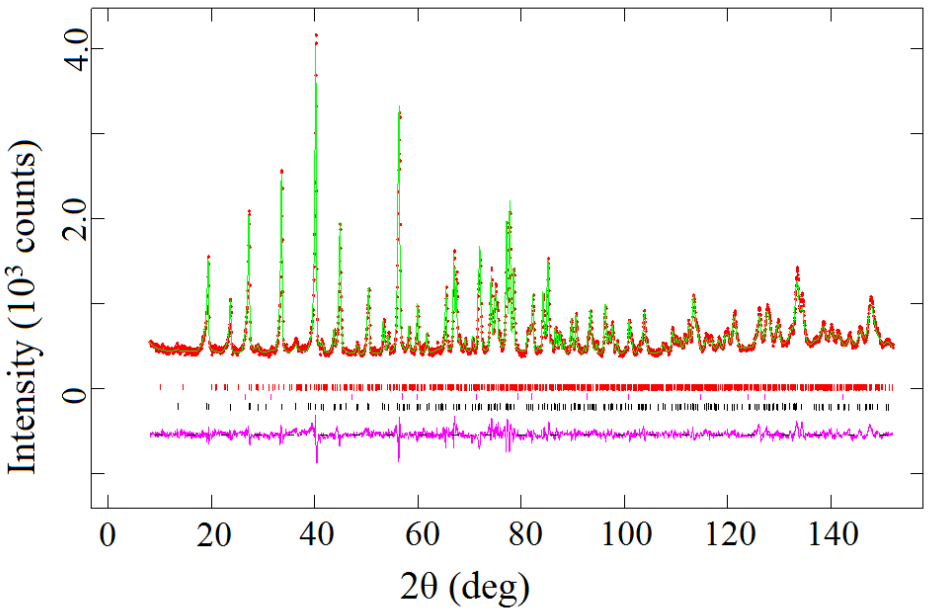

Figure B.3 Observed (red dots) and calculated (green line) NPD patterns of $CeMn_{0.5}Co_{1.5}Ge_4O_{12}$ at room temperature; λ = 1.622 Å. A difference curve (purple line) is shown and reflection positions are marked for $CeMnCoGe_4O_{12}$ (bottom), CeO_2 (middle), and $CoGeO_3$ (top).

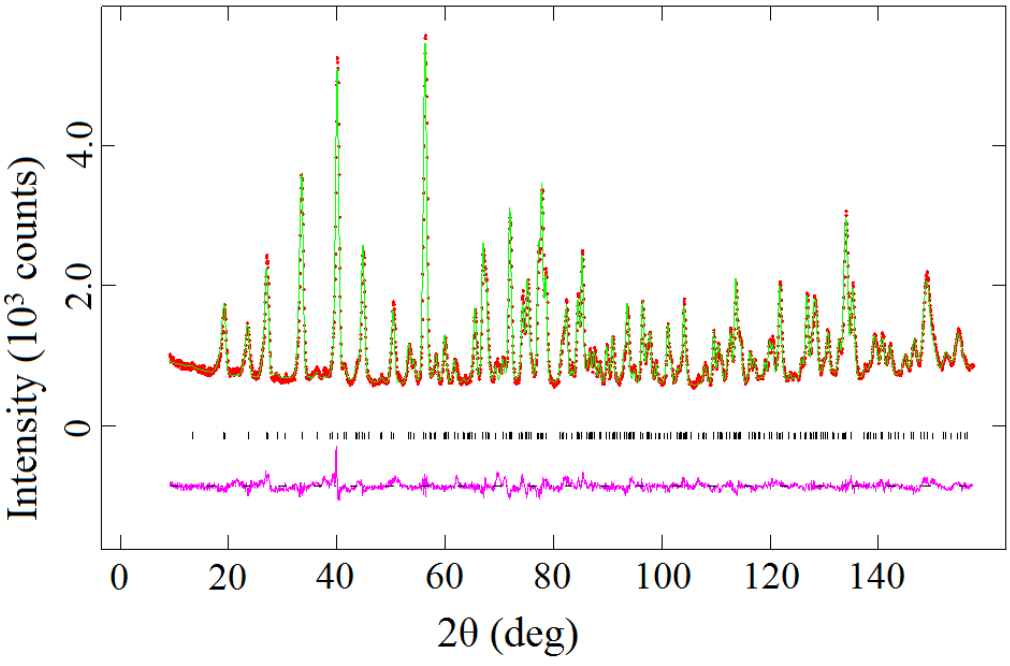

Figure B.4 Observed (red dots) and calculated (green line) NPD patterns of $CeCo_2Ge_4O_{12}$ at room temperature; λ = 1.622 Å. A difference curve (purple line) is shown and reflection positions are marked.

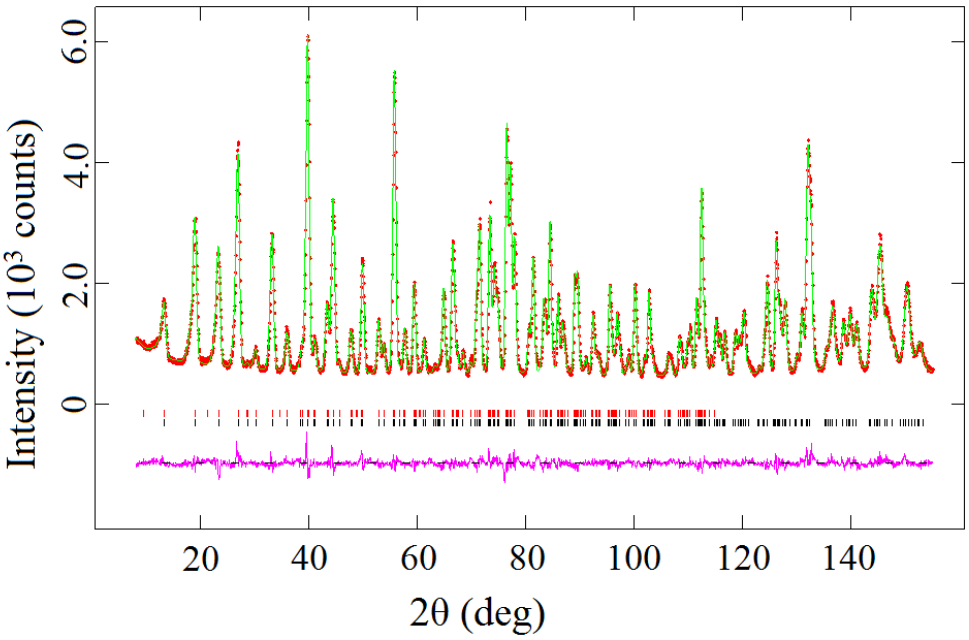

Figure B.5 Observed (red dots) and calculated (green line) NPD patterns of $CeMn_{1.5}Co_{0.5}Ge_4O_{12}$ at 1.6 K; λ = 1.622 Å. A difference curve (purple line) is shown and reflection positions are marked for the crystal structure (bottom) and the magnetic structure (top).

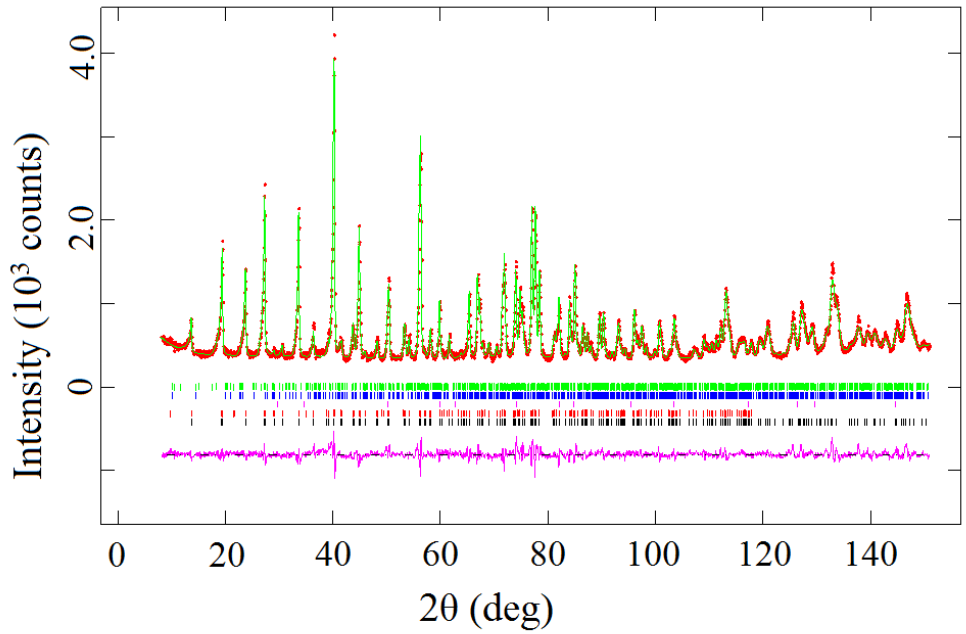

Figure B.6 Observed (red dots) and calculated (green line) NPD patterns of at 1.6 K; λ = 1.622 Å. A difference curve (purple line) is shown and reflection positions are marked for $CeMnCoGe_4O_{12}$ (black), $CeMnCoGe_4O_{12}$ magnetic phase (red), CeO_2 (pink), $CoGeO_3$ (blue), and $CoGeO_3$ magnetic phase (green).

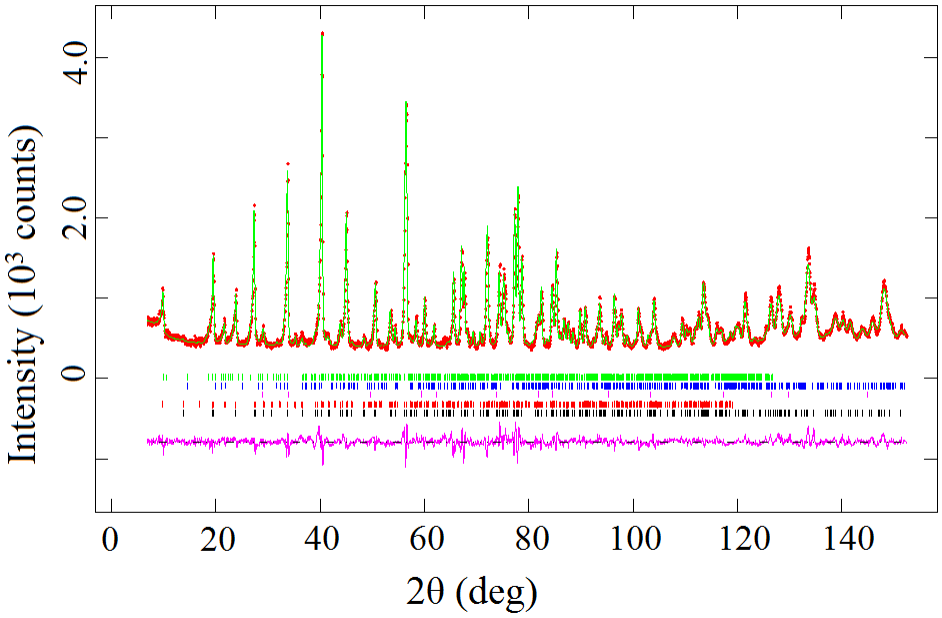

Figure B.7 Observed (red dots) and calculated (green line) NPD patterns of $CeMn_{0.5}Co_{1.5}Ge_4O_{12}$ at 1.6 K; λ = 1.622 Å. A difference curve (purple line) is shown and reflection positions are marked for $CeMn_{0.5}Co_{1.5}Ge_4O_{12}$ (black), $CeMnCoGe_4O_{12}$ magnetic phase (red), CeO_2 (pink), $CoGeO_3$ (blue), and $CoGeO_3$ magnetic phase (green).

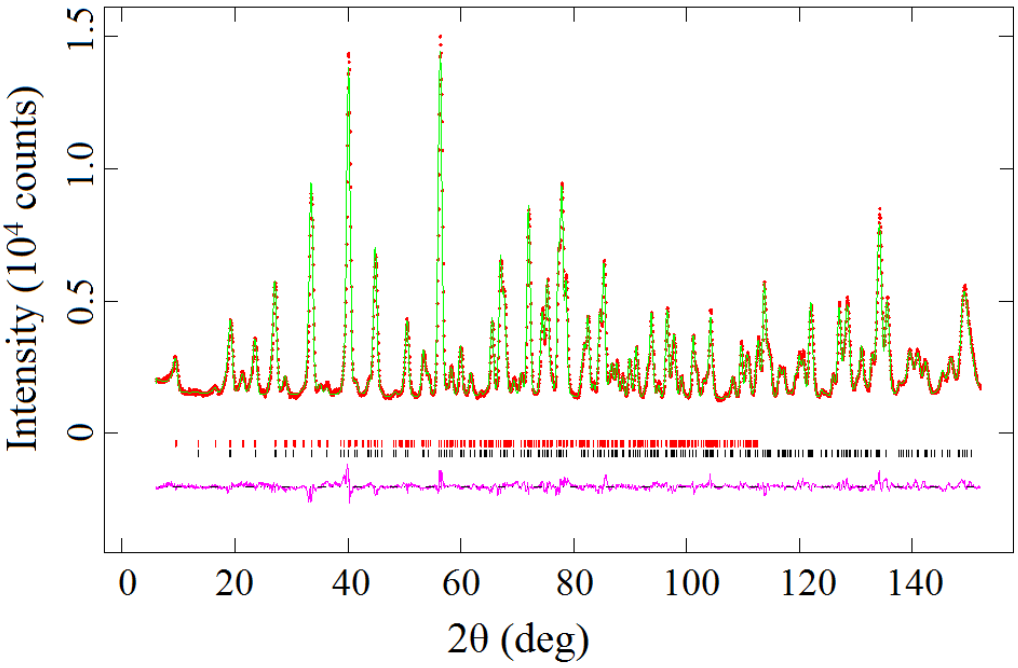

Figure B.8 Observed (red dots) and calculated (green line) NPD patterns of $CeCo_2Ge_4O_{12}$ at 1.6 K; λ = 1.622 Å. A difference curve (purple line) is shown and reflection positions are marked for the crystal structure (bottom) and the magnetic structure (top).

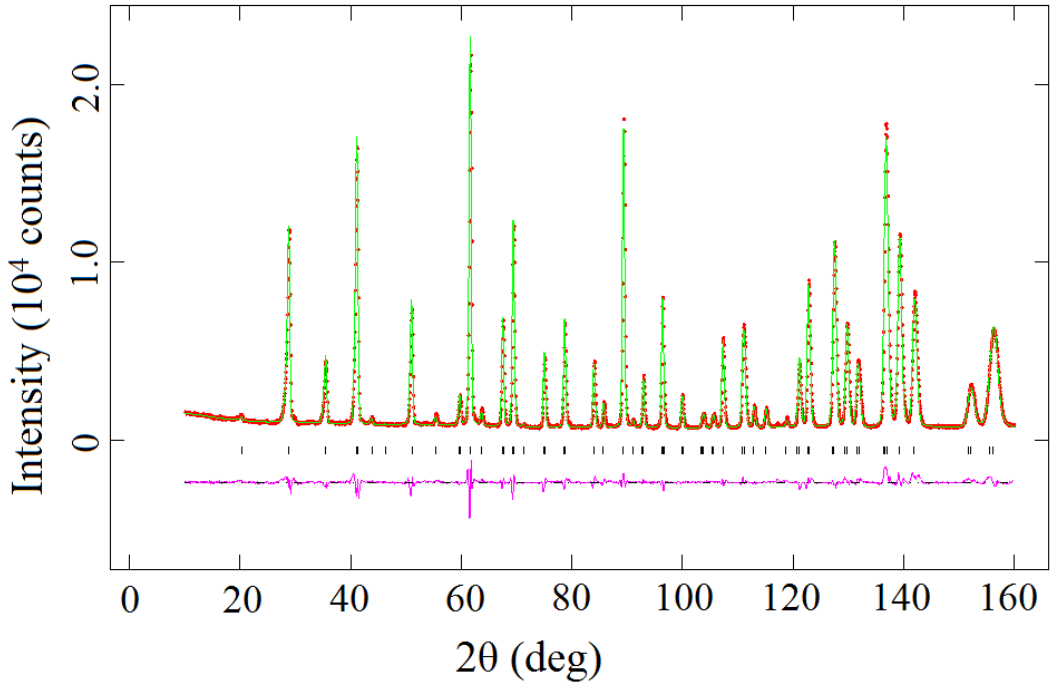

Figure B.9 Observed (red dots) and calculated (green line) NPD patterns of $CeMn_2Ge_4O_{12}$ at 12 K, λ = 2.4395 Å. A difference curve (purple line) is shown and reflection positions are marked.

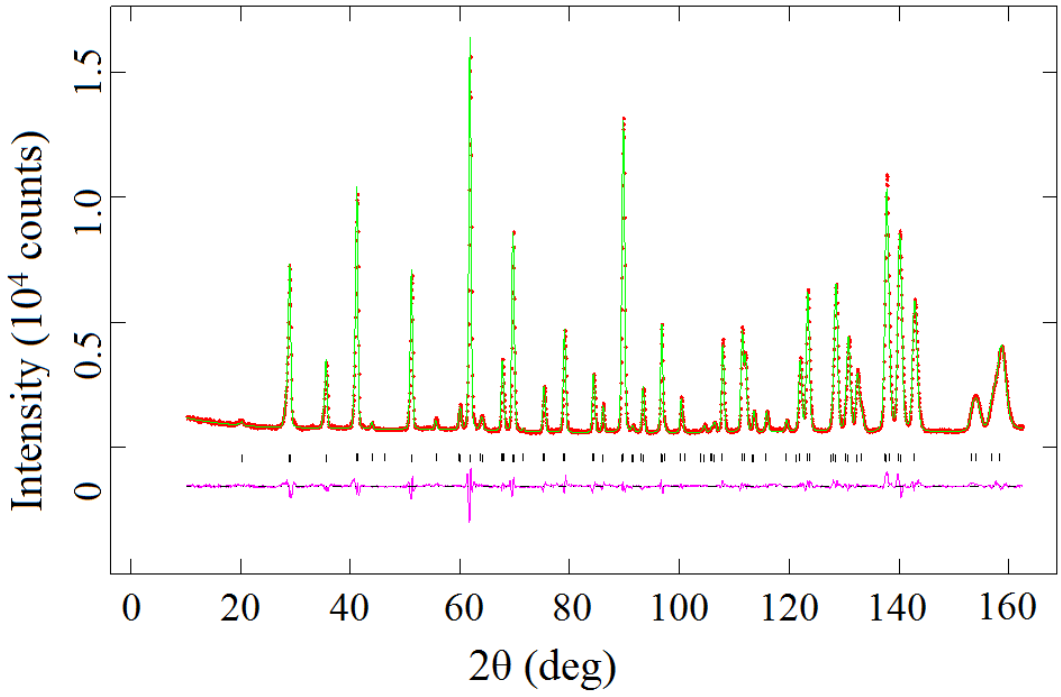

Figure B.10 Observed (red dots) and calculated (green line) NPD patterns of $CeMn_{1.5}Co_{0.5}Ge_4O_{12}$ at 7 K, λ = 2.4395 Å. A difference curve (purple line) is shown and reflection positions are marked.

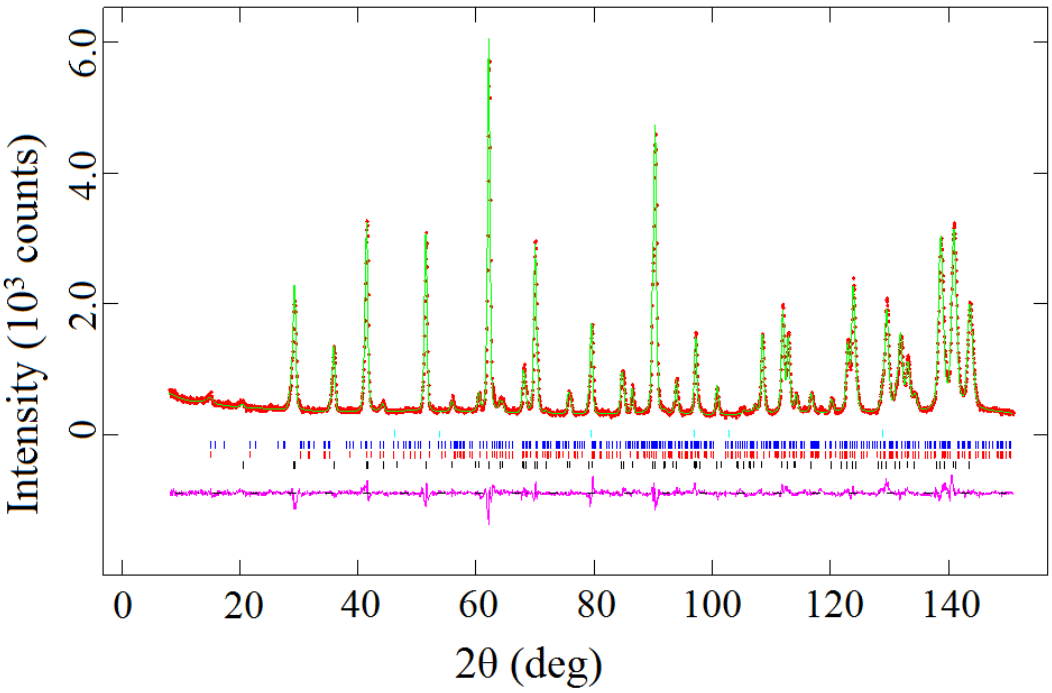

Figure B.11 Observed (red dots) and calculated (green line) NPD patterns of $CeMnCoGe_4O_{12}$ at 10 K, λ = 2.4395 Å. A difference curve (purple line) is shown and reflection positions are marked.

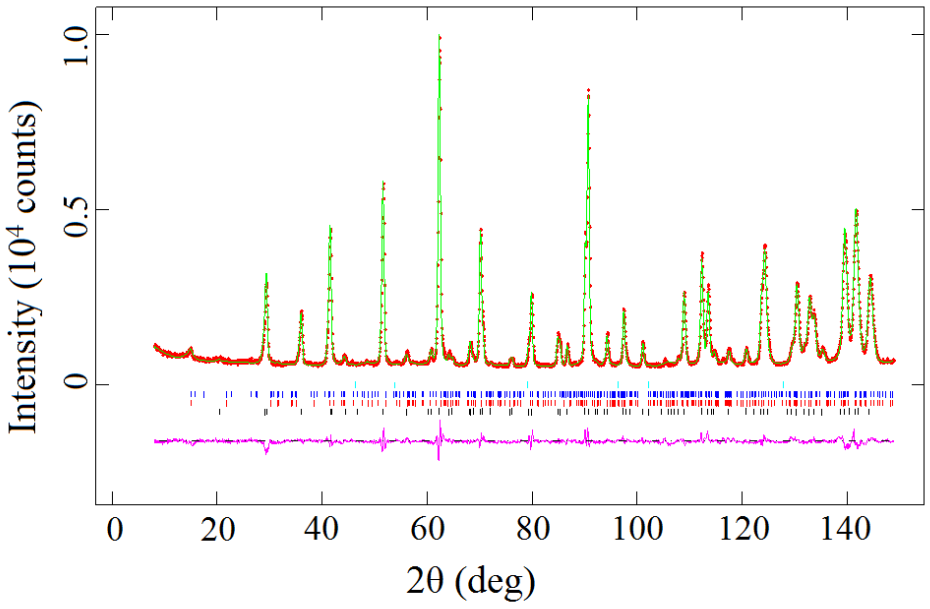

Figure B.12 Observed (red dots) and calculated (green line) NPD patterns of $CeMn_{0.5}Co_{1.5}Ge_4O_{12}$ at 10 K, λ = 2.4395 Å. A difference curve (purple line) is shown and reflection positions are marked for $CeMn_{0.5}Co_{1.5}Ge_4O_{12}$ (black), $CoGeO_3$ (red), $CoGeO_3$ magnetic phase (blue) and CeO_2 (green).

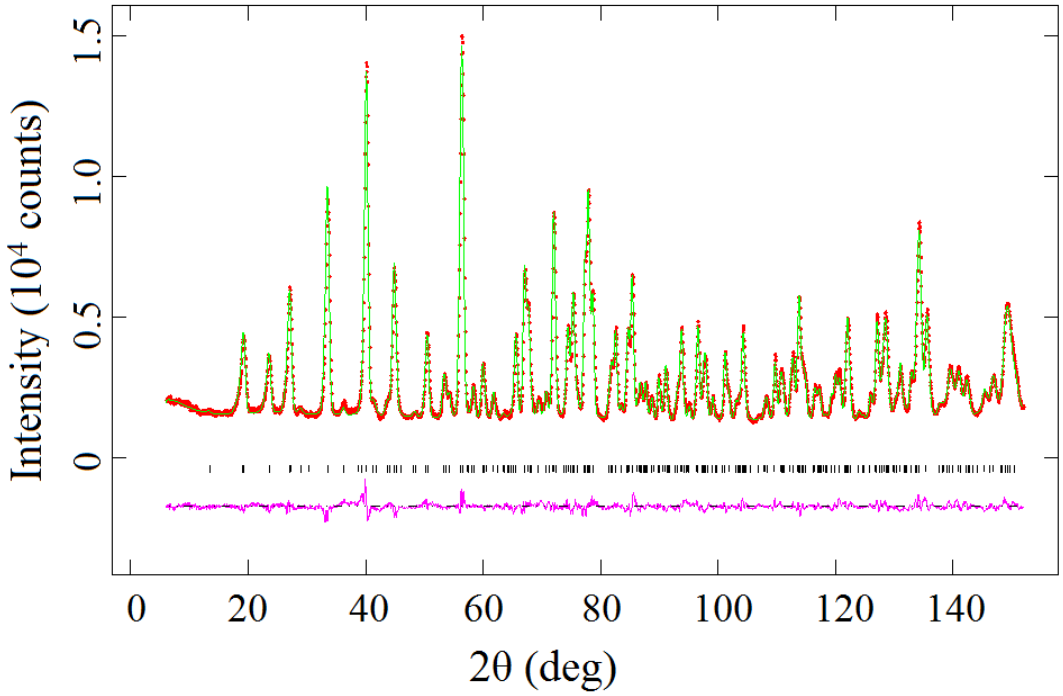

Figure B.13 Observed (red dots) and calculated (green line) NPD patterns of $CeCo_2Ge_4O_{12}$ at 7 K, λ = 1.622 Å. A difference curve (purple line) is shown and reflection positions are marked.

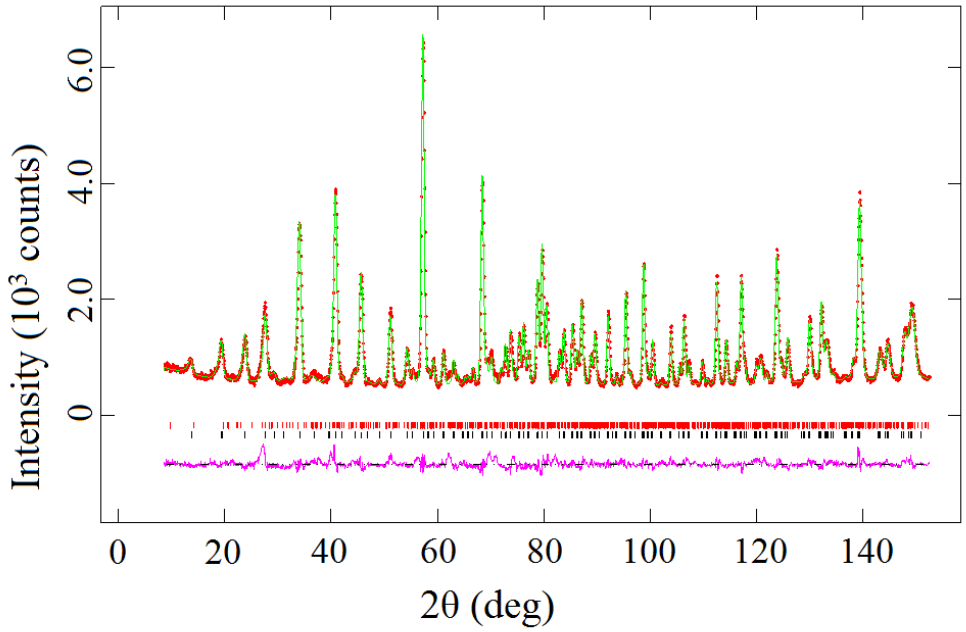

Figure B.14 Observed (red dots) and calculated (green line) NPD patterns of $ZrCo_2Ge_4O_{12}$ at room temperature; λ = 1.622 Å. A difference curve (purple line) is shown and reflection positions are marked for $ZrCo_2Ge_4O_{12}$ (bottom) and $CoGeO_3$ (top).

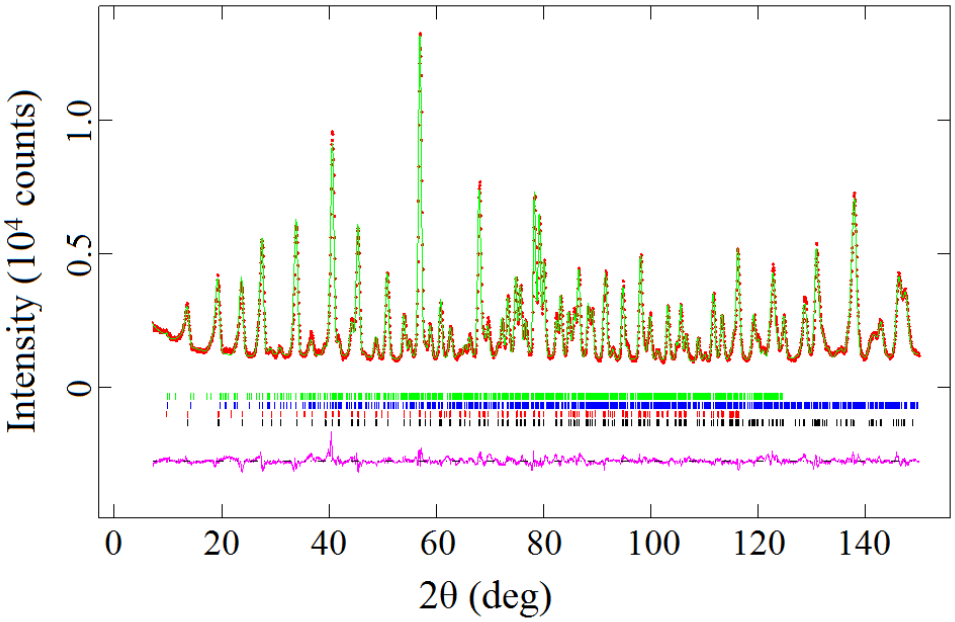

Figure B.15 Observed (red dots) and calculated (green line) NPD patterns of $ZrMnCoGe_4O_{12}$ at 3 K; λ = 1.622 Å. A difference curve (purple line) is shown and reflection positions are marked for $ZrMnCoGe_4O_{12}$ (black), $CoGeO_3$ (red), $ZrMnCoGe_4O_{12}$ magnetic phase (blue) and $CoGeO_3$ magnetic phase (green).

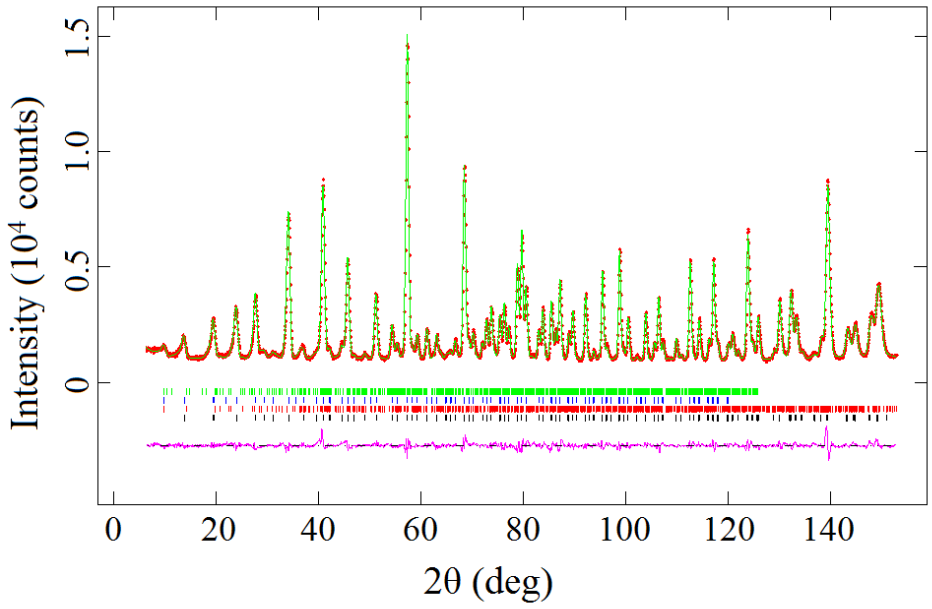

Figure B.16 Observed (red dots) and calculated (green line) NPD patterns of $ZrCo_2Ge_4O_{12}$ at 1.6 K; λ = 1.622 Å. A difference curve (purple line) is shown and reflection positions are marked for $ZrCo_2Ge_4O_{12}$ (black), $ZrCo_2Ge_4O_{12}$ magnetic phase (red), $CoGeO_3$ (blue) and $CoGeO_3$ magnetic phase (green).

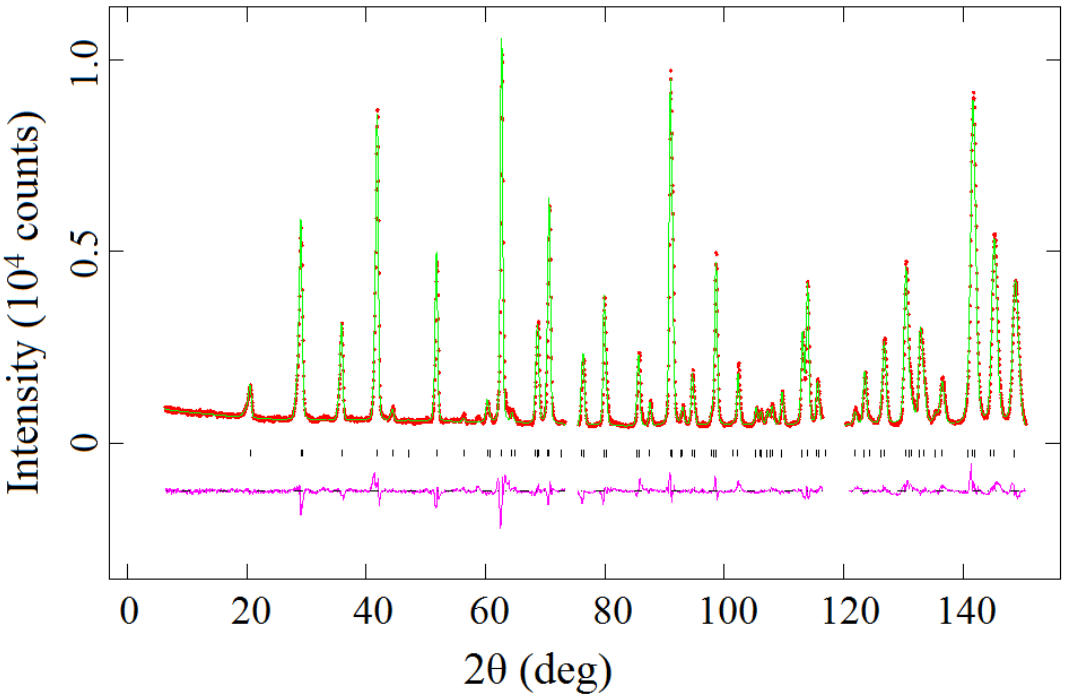

Figure B.17 Observed (red dots) and calculated (green line) NPD patterns of $ZrMn_2Ge_4O_{12}$ at 15 K, λ = 2.4395 Å. A difference curve (purple line) is shown and reflection positions are marked.

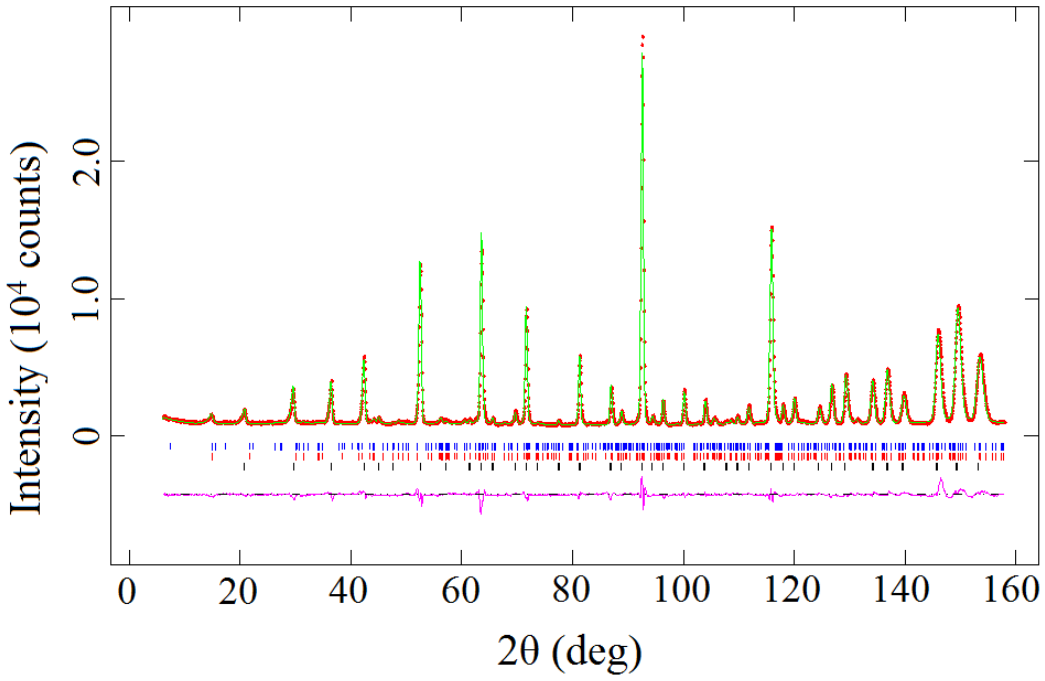

Figure B.18 Observed (red dots) and calculated (green line) NPD patterns of $ZrCo_2Ge_4O_{12}$ at 7 K, λ = 2.4395 Å. A difference curve (purple line) is shown and reflection positions are marked for $ZrCo_2Ge_4O_{12}$ (black), $CoGeO_3$ (red) and $CoGeO_3$ magnetic phase (blue).

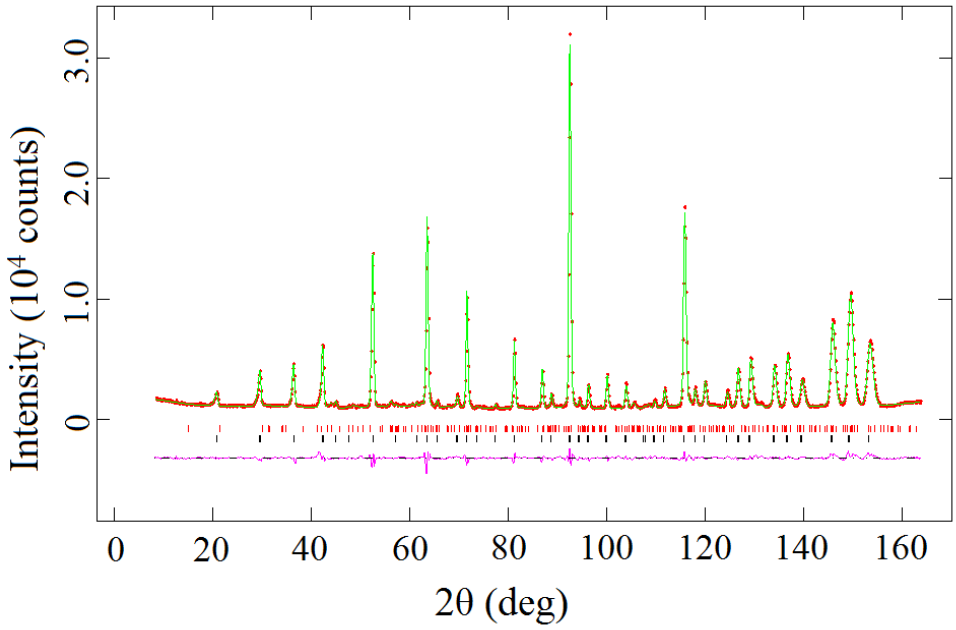

Figure B.19 Observed (red dots) and calculated (green line) NPD patterns of $ZrCo_2Ge_4O_{12}$ at 40 K, λ = 2.4395 Å. A difference curve (purple line) is shown and reflection positions are marked for $ZrCo_2Ge_4O_{12}$ (black) and $CoGeO_3$ (red).

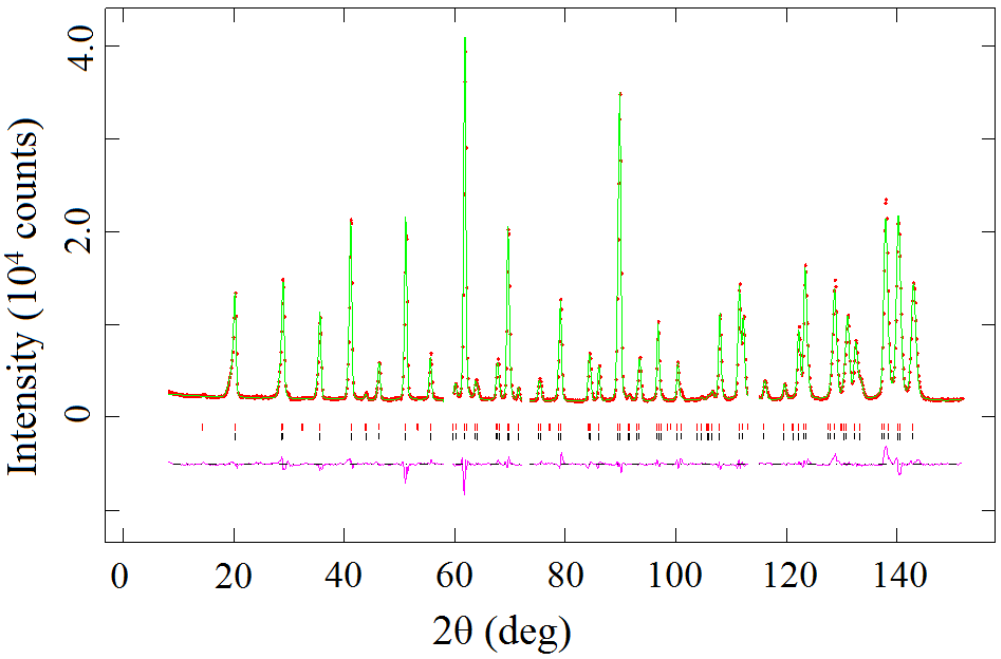

Figure B.20 Observed (red dots) and calculated (green line) NPD patterns of $CeMn_{1.5}Ni_{0.5}Ge_4O_{12}$ at 1.6 K; λ = 2.4395 Å. A difference curve (purple line) is shown and reflection positions are marked for the crystal structure (bottom) and the magnetic structure (top).

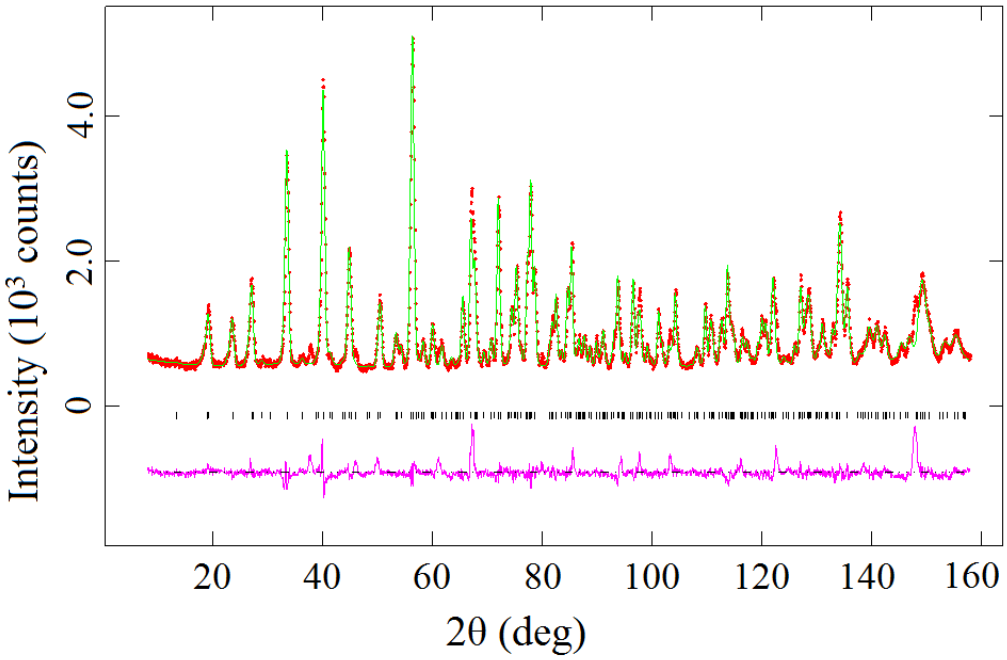

Figure B.21 Observed (red dots) and calculated (green line) NPD patterns of $CeCo_{1.5}Ni_{0.5}Ge_4O_{12}$ at room temperature; λ = 1.622 Å. A difference curve (purple line) is shown and reflection positions are marked.

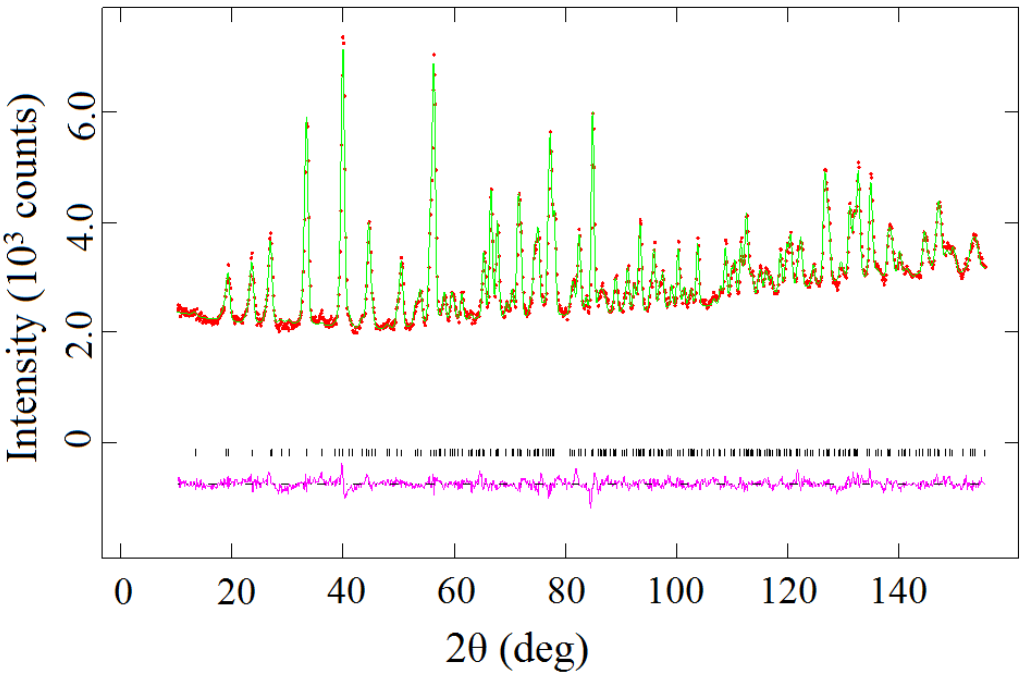

Figure B.22 Observed (red dots) and calculated (green line) NPD patterns of $EuFeMnGe_4O_{12}$ at room temperature; λ = 1.622 Å. A difference curve (purple line) is shown and reflection positions are marked.

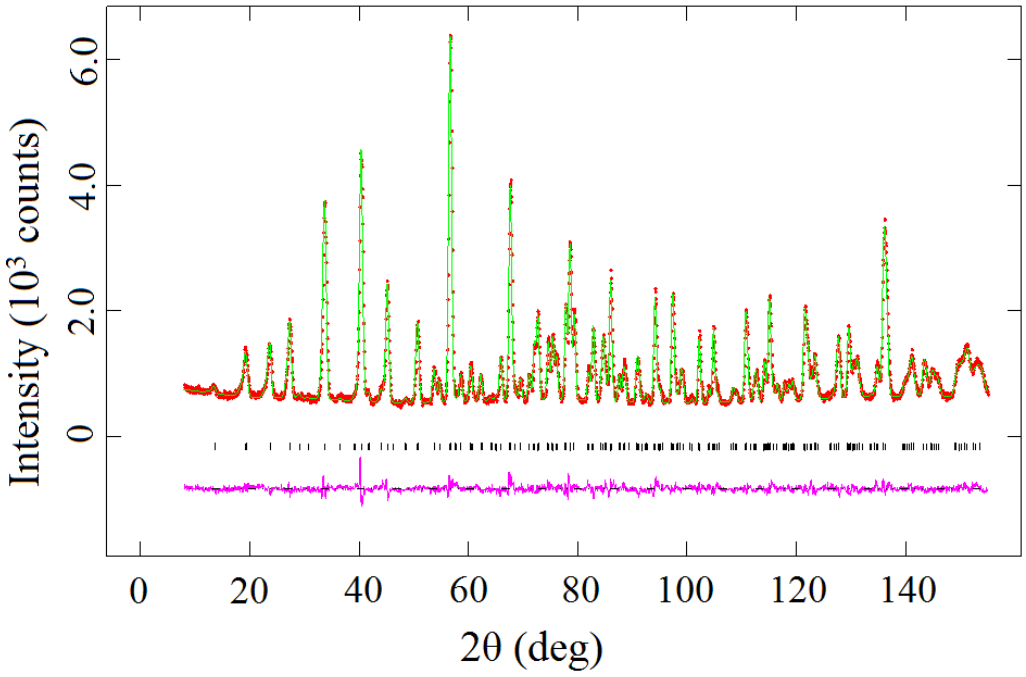

Figure B.23 Observed (red dots) and calculated (green line) NPD patterns of $LuFeMnGe_4O_{12}$ at room temperature; λ = 1.622 Å. A difference curve (purple line) is shown and reflection positions are marked.

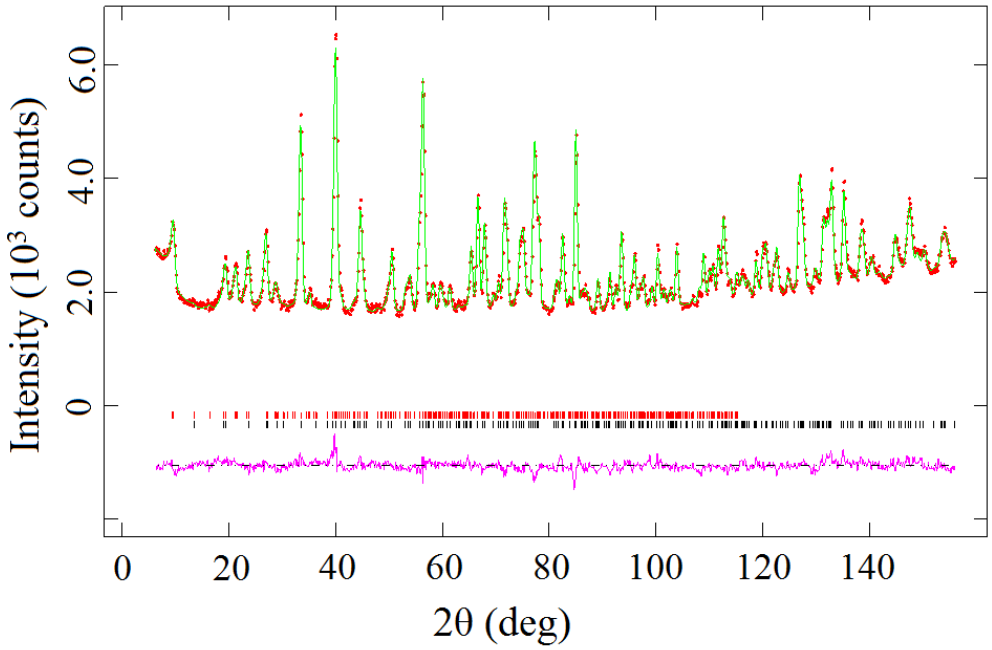

Figure B.24 Observed (red dots) and calculated (green line) NPD patterns of $EuFeMnGe_4O_{12}$ at 3.5 K; λ = 1.622 Å. A difference curve (purple line) is shown and reflection positions are marked for the crystal structure (bottom) and the magnetic structure (top).

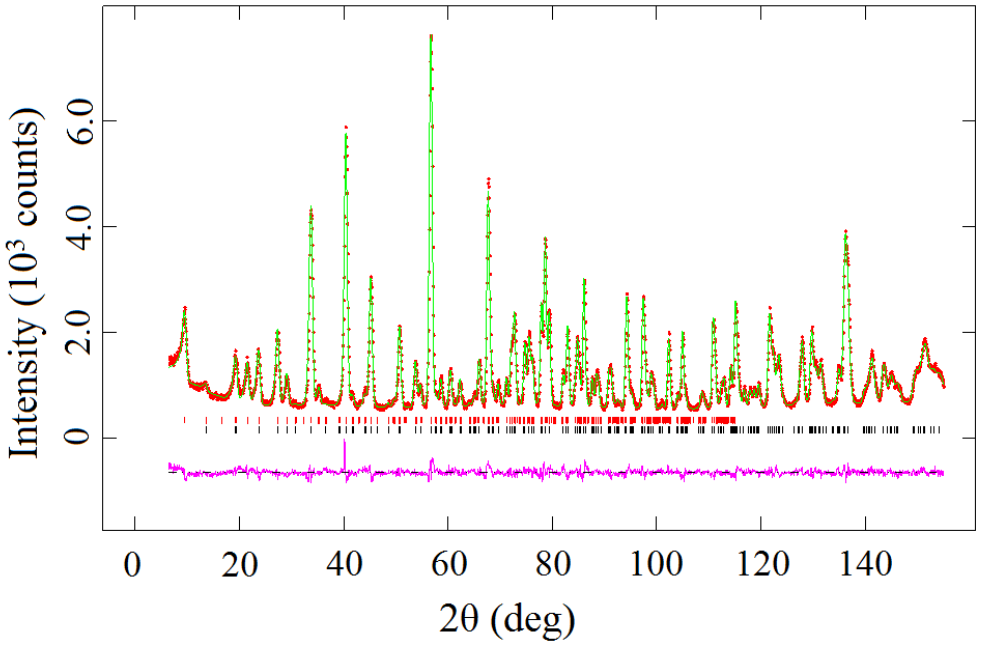

Figure B.25 Observed (red dots) and calculated (green line) NPD patterns of $LuFeMnGe_4O_{12}$ at 3.5 K; λ = 1.622 Å. A difference curve (purple line) is shown and reflection positions are marked for the crystal structure (bottom) and the magnetic structure (top).

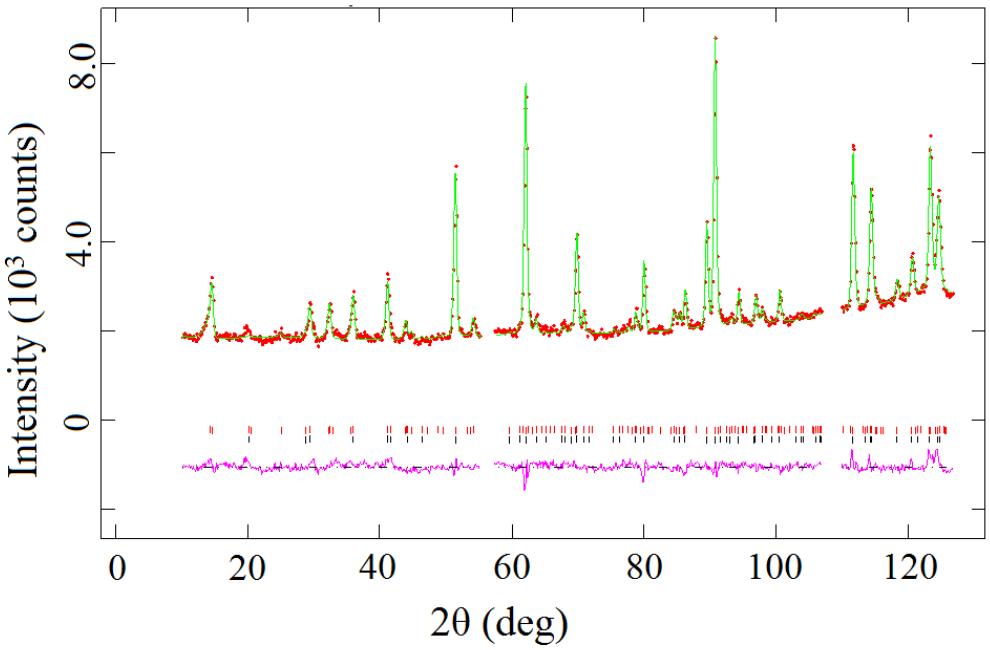

Figure B.26 Observed (red dots) and calculated (green line) NPD patterns of $EuFeMnGe_4O_{12}$ at 3.5 K; λ = 2.4395 Å. A difference curve (purple line) is shown and reflection positions are marked for the crystal structure (bottom) and the magnetic structure (top).

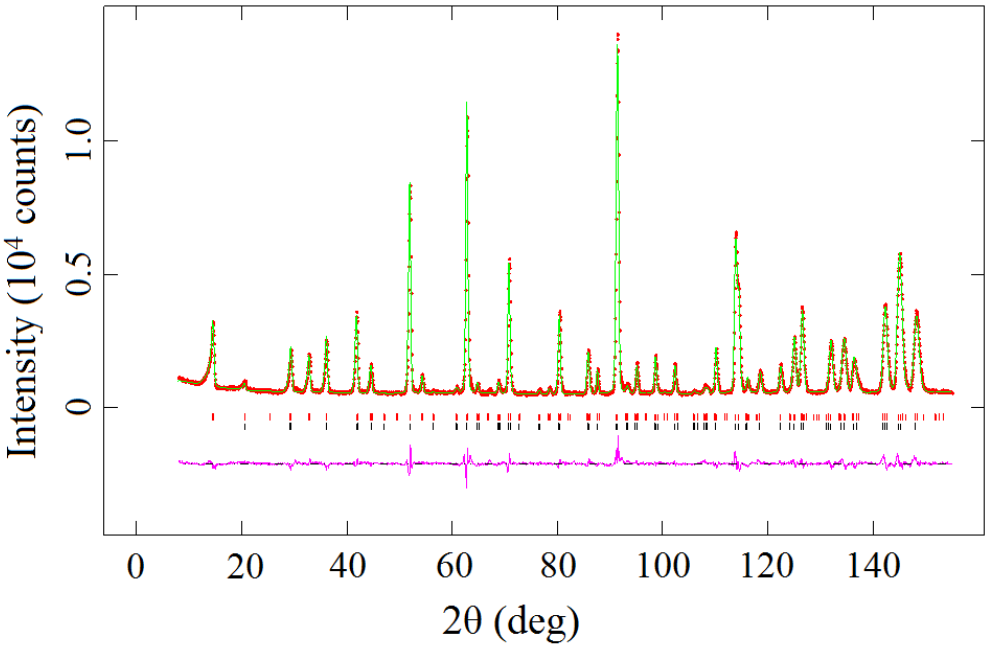

Figure B.27 Observed (red dots) and calculated (green line) NPD patterns of $LuFeMnGe_4O_{12}$ at 3.5 K; λ = 2.4395 Å. A difference curve (purple line) is shown and reflection positions are marked for the crystal structure (bottom) and the magnetic structure (top).

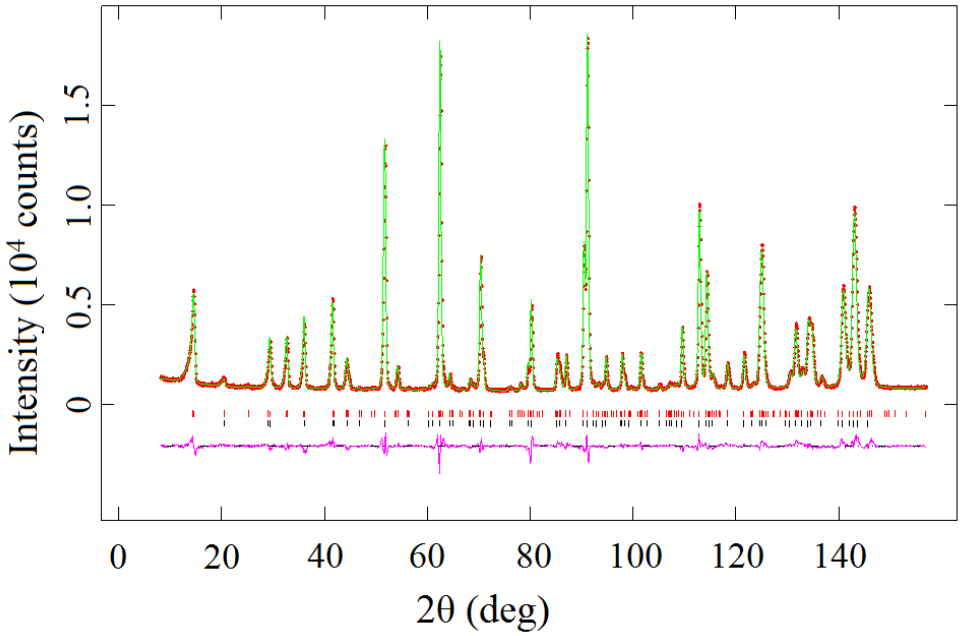

Figure B.28 Observed (red dots) and calculated (green line) NPD patterns of $YFeMnGe_4O_{12}$ at 3.5 K; λ = 2.4395 Å. A difference curve (purple line) is shown and reflection positions are marked for the crystal structure (bottom) and the magnetic structure (top).

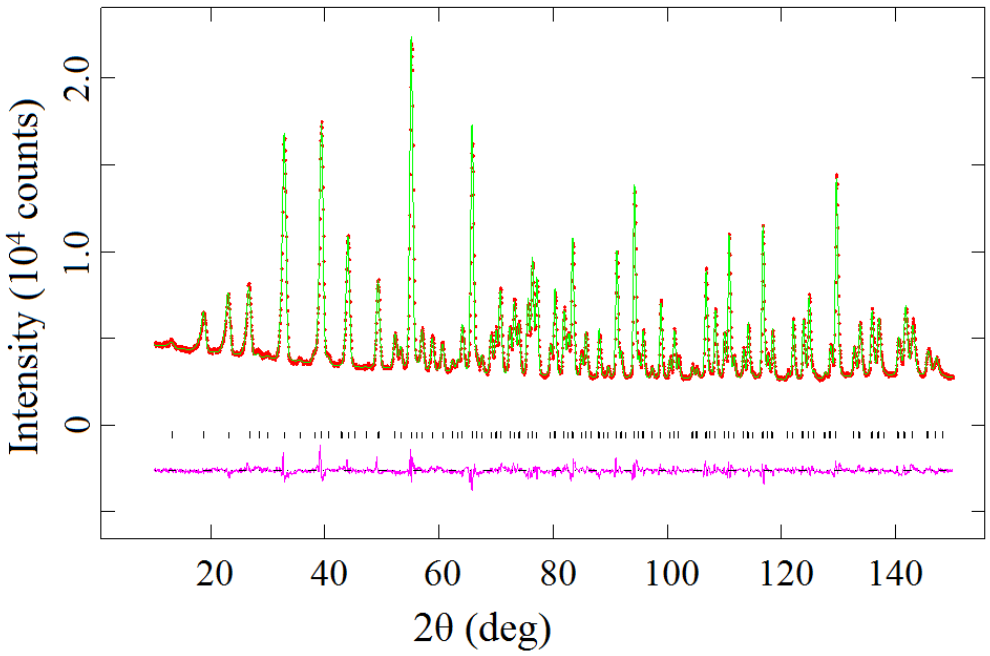

Figure B.29 Observed (red dots) and calculated (green line) NPD patterns of $Tb_2CoGe_4O_{12}$ at room temperature; λ = 1.622 Å. A difference curve (purple line) is shown and reflection positions are marked.

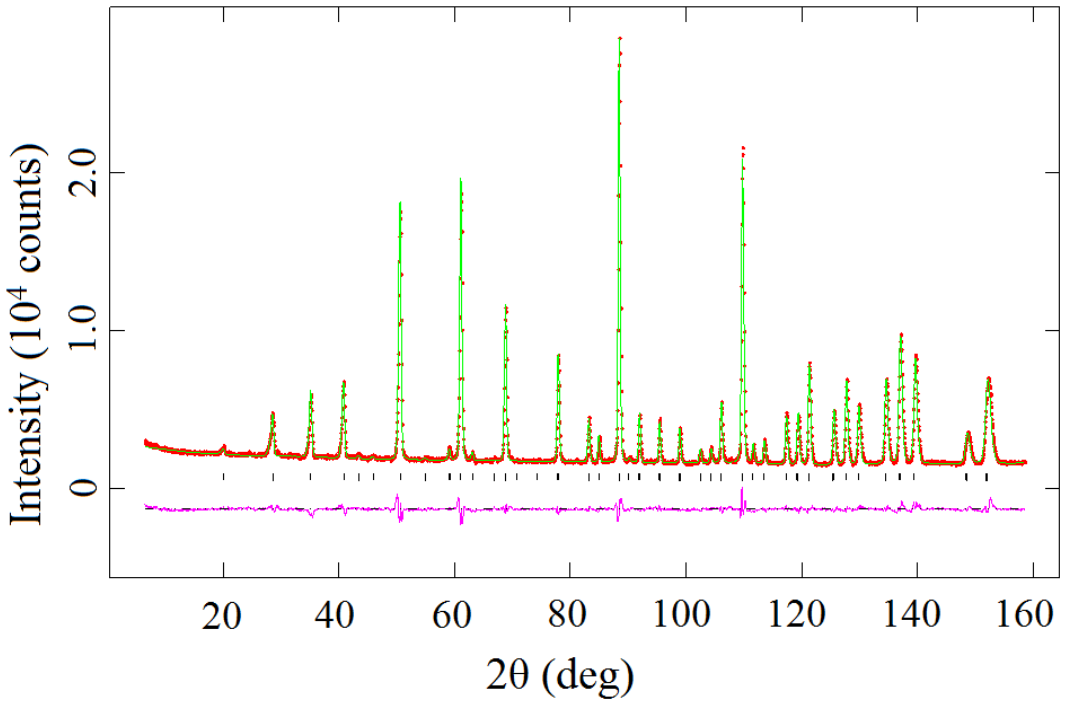

Figure B.30 Observed (red dots) and calculated (green line) NPD patterns of $Tb_2CoGe_4O_{12}$ at room temperature; λ = 2.4395 Å. A difference curve (purple line) is shown and reflection positions are marked.

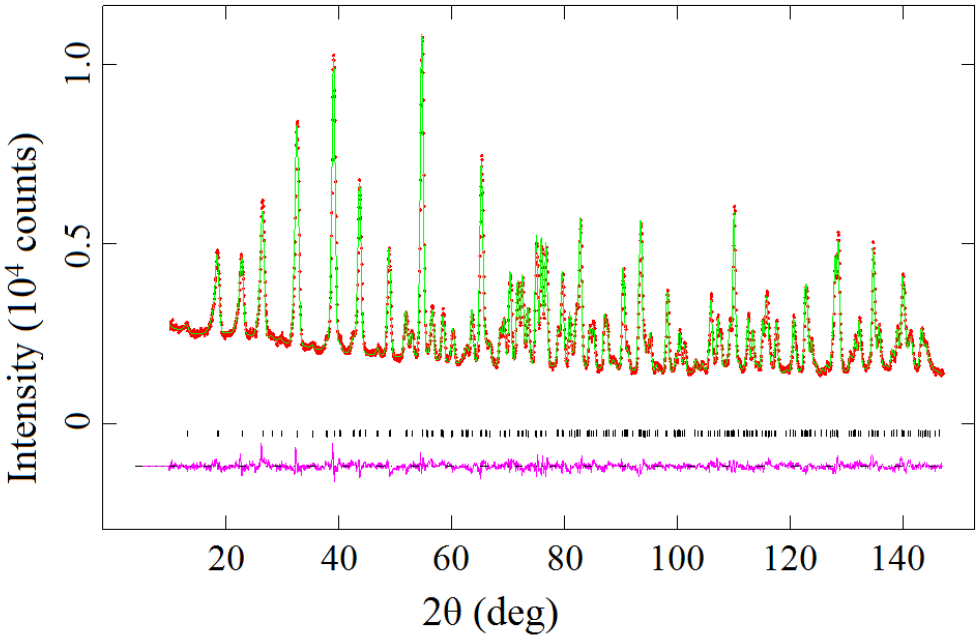

Figure B.31 Observed (red dots) and calculated (green line) NPD patterns of $Tb_2MnGe_4O_{12}$ at room temperature; λ = 1.622 Å. A difference curve (purple line) is shown and reflection positions are marked.

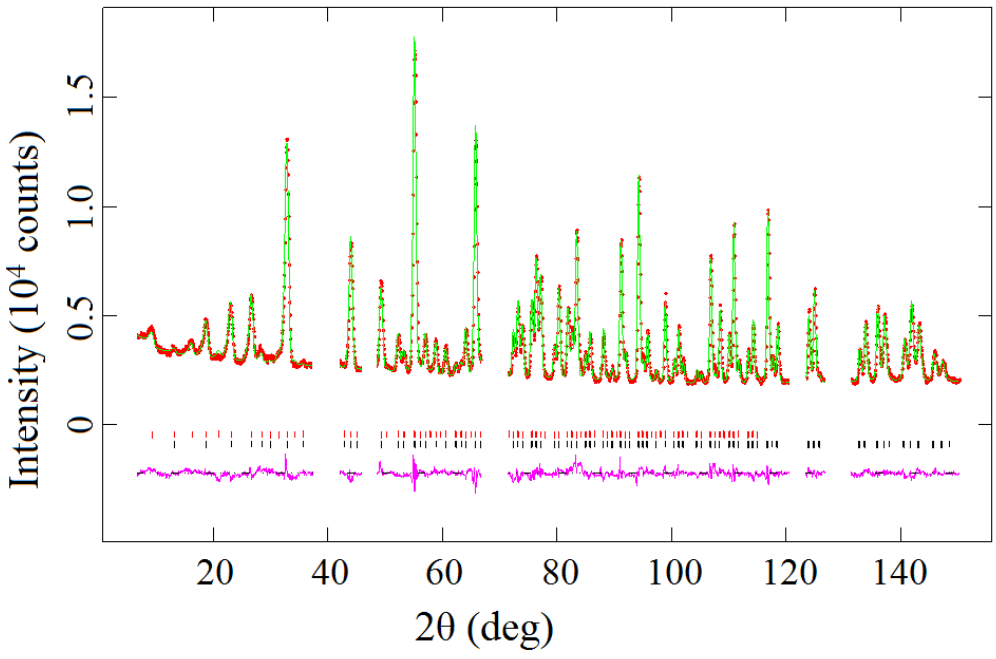

Figure B.32 Observed (red dots) and calculated (green line) NPD patterns of $Tb_2CoGe_4O_{12}$ at 1.5 K; λ = 1.622 Å. A difference curve (purple line) is shown and reflection positions are marked for the crystal structure (bottom) and the magnetic structure (top).

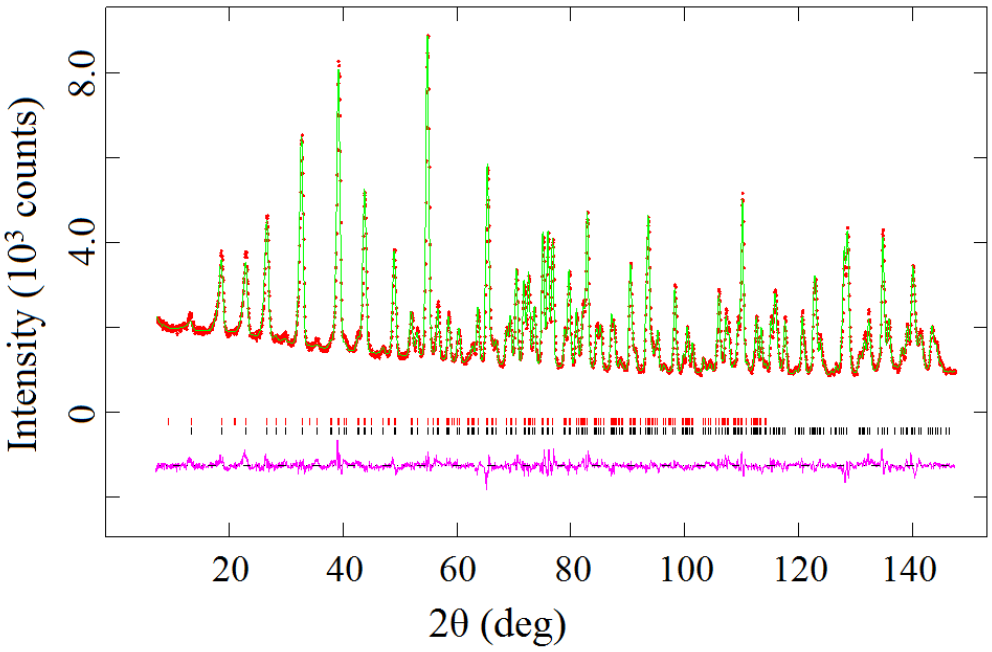

Figure B.33 Observed (red dots) and calculated (green line) NPD patterns of $Tb_2MnGe_4O_{12}$ at 1.5 K; λ = 1.622 Å. A difference curve (purple line) is shown and reflection positions are marked for the crystal structure (bottom) and the magnetic structure (top).

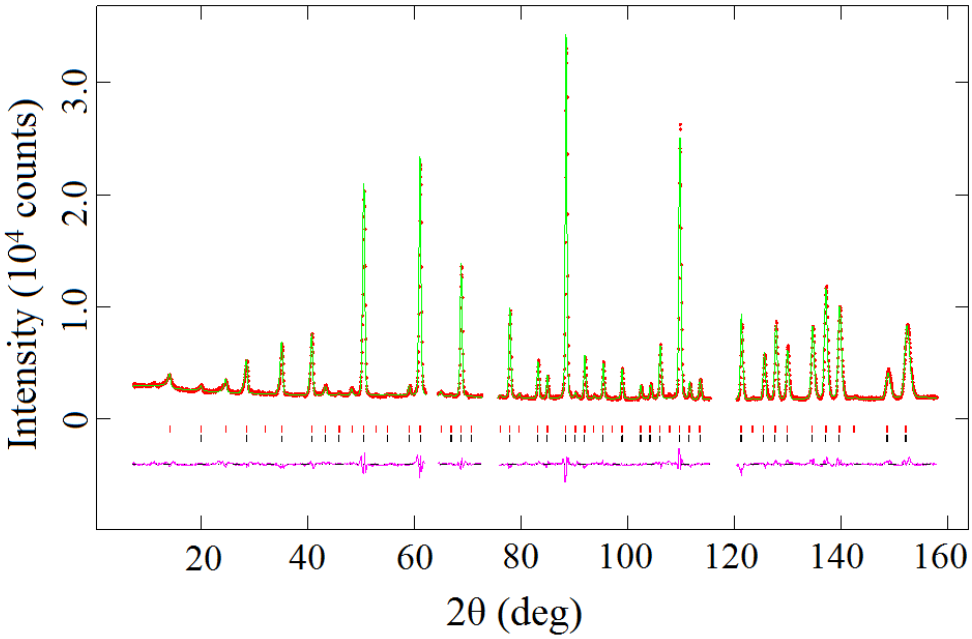

Figure B.34 Observed (red dots) and calculated (green line) NPD patterns of $Tb_2CoGe_4O_{12}$ at 1.5 K; λ = 2.4395 Å. A difference curve (purple line) is shown and reflection positions are marked for the crystal structure (bottom) and the magnetic structure (top).

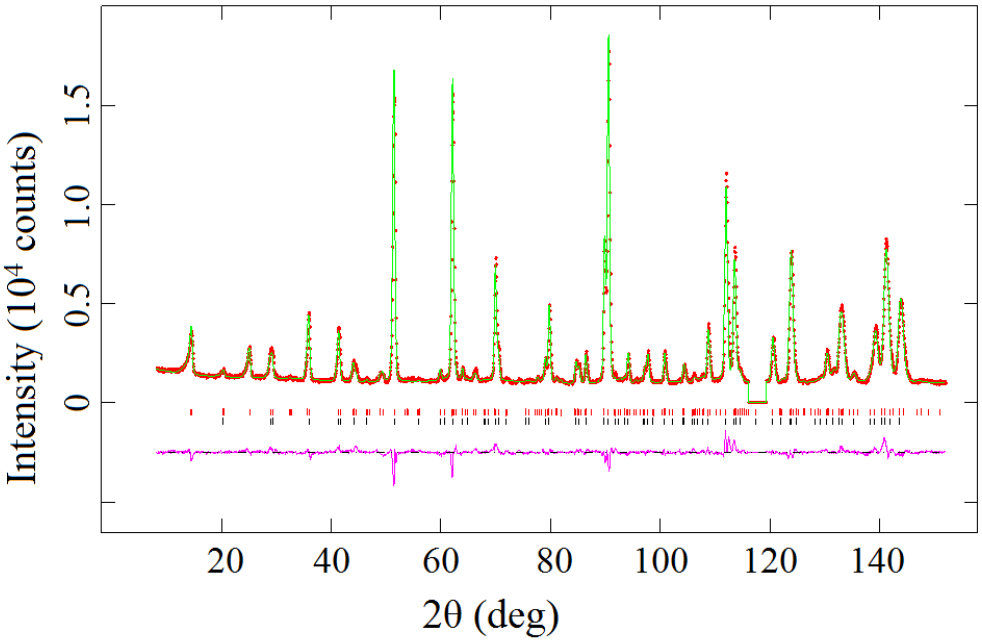

Figure B.35 Observed (red dots) and calculated (green line) NPD patterns of $TbScCoGe_4O_{12}$ at 1.5 K; λ = 2.4395 Å. A difference curve (purple line) is shown and reflection positions are marked for the crystal structure (bottom) and the magnetic structure (top).

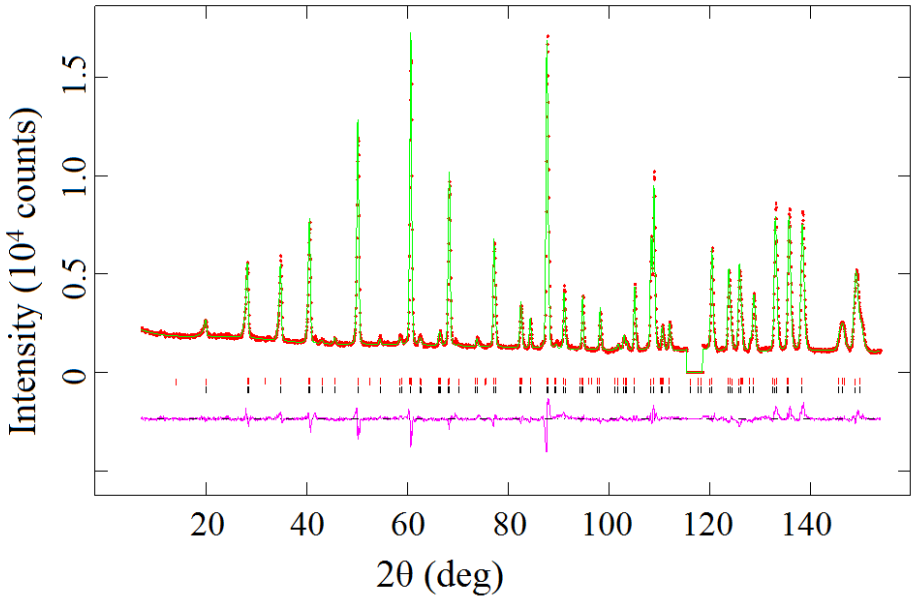

Figure B.36 Observed (red dots) and calculated (green line) NPD patterns of $Tb_2MnGe_4O_{12}$ at 1.5 K; λ = 2.4395 Å. A difference curve (purple line) is shown and reflection positions are marked for the crystal structure (bottom) and the magnetic structure (top).

Appendix C - In-Field Low Temperature Neutron Diffraction

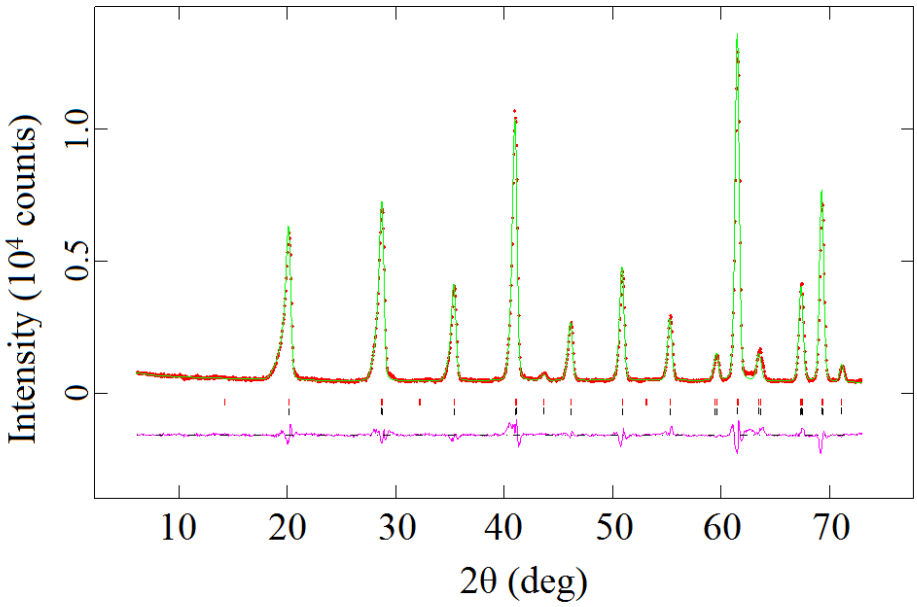

Figure C.1 Observed (red dots) and calculated (green line) NPD patterns of $CeMn_2Ge_4O_{12}$ at 1.6 K, λ = 2.4395 Å, H = 0 Oe. A difference curve (purple line) is shown and reflection positions are marked for the crystal structure (bottom) and the magnetic structure (top).

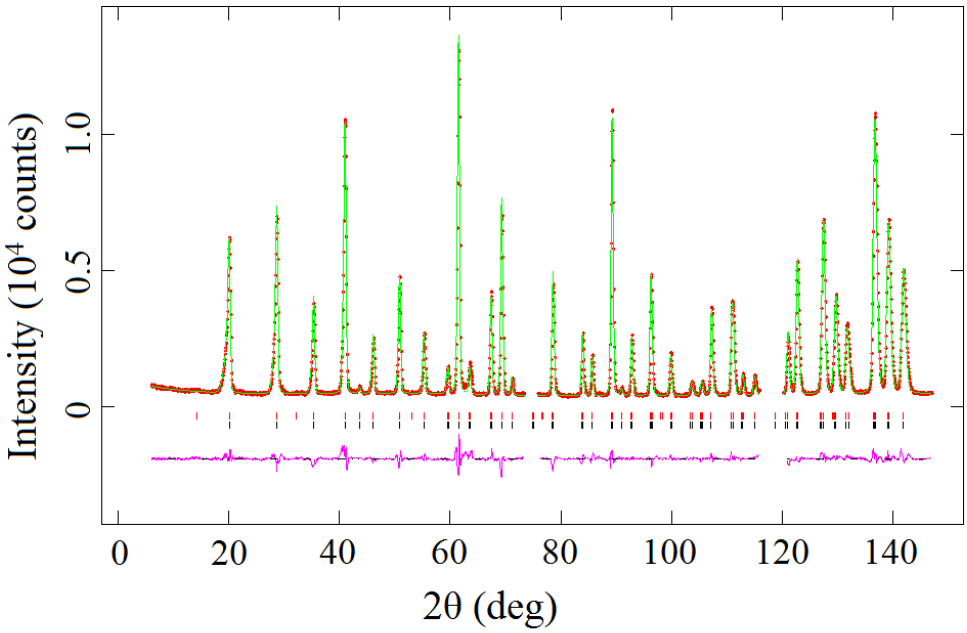

Figure C.2 Observed (red dots) and calculated (green line) NPD patterns of $CeMn_2Ge_4O_{12}$ at 1.6 K, λ = 2.4395 Å, H = 10 kOe. A difference curve (purple line) is shown and reflection positions are marked for the crystal structure (bottom) and the magnetic structure (top).

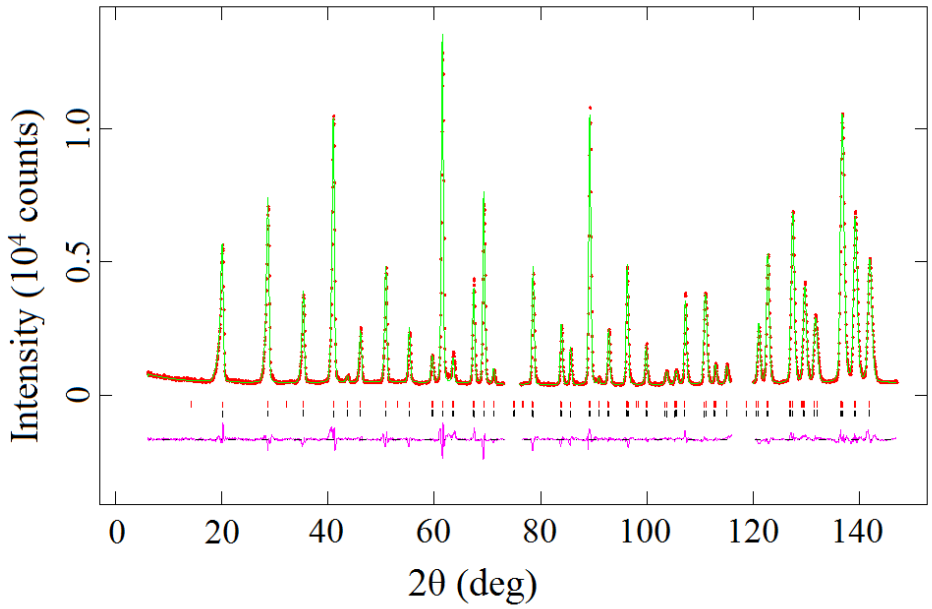

Figure C.3 Observed (red dots) and calculated (green line) NPD patterns of $CeMn_2Ge_4O_{12}$ at 1.6 K, λ = 2.4395 Å, H = 20 kOe. A difference curve (purple line) is shown and reflection positions are marked for the crystal structure (bottom) and the magnetic structure (top).

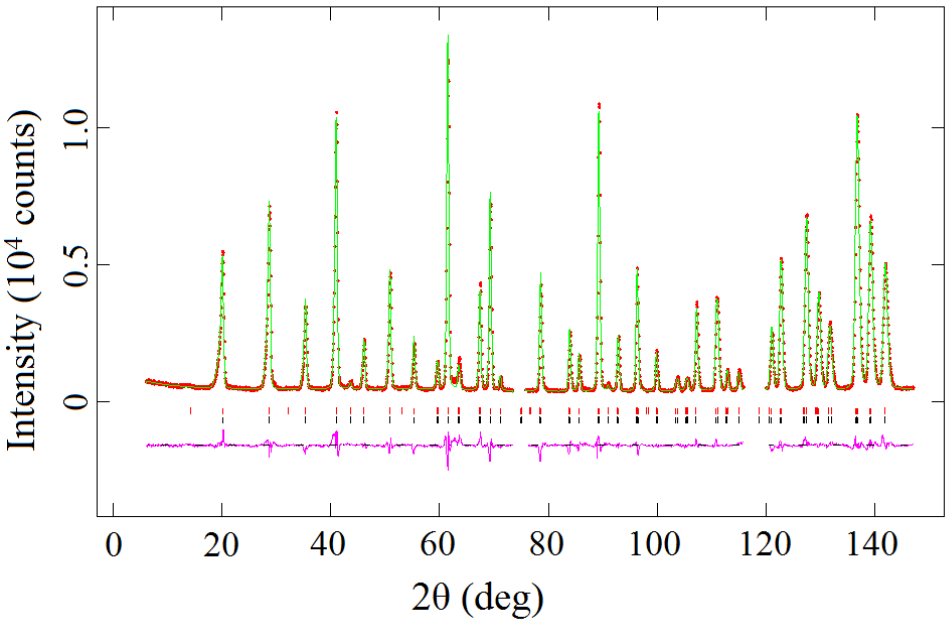

Figure C.4 Observed (red dots) and calculated (green line) NPD patterns of $CeMn_2Ge_4O_{12}$ at 1.6 K, λ = 2.4395 Å, H = 30 kOe. A difference curve (purple line) is shown and reflection positions are marked for the crystal structure (bottom) and the magnetic structure (top).

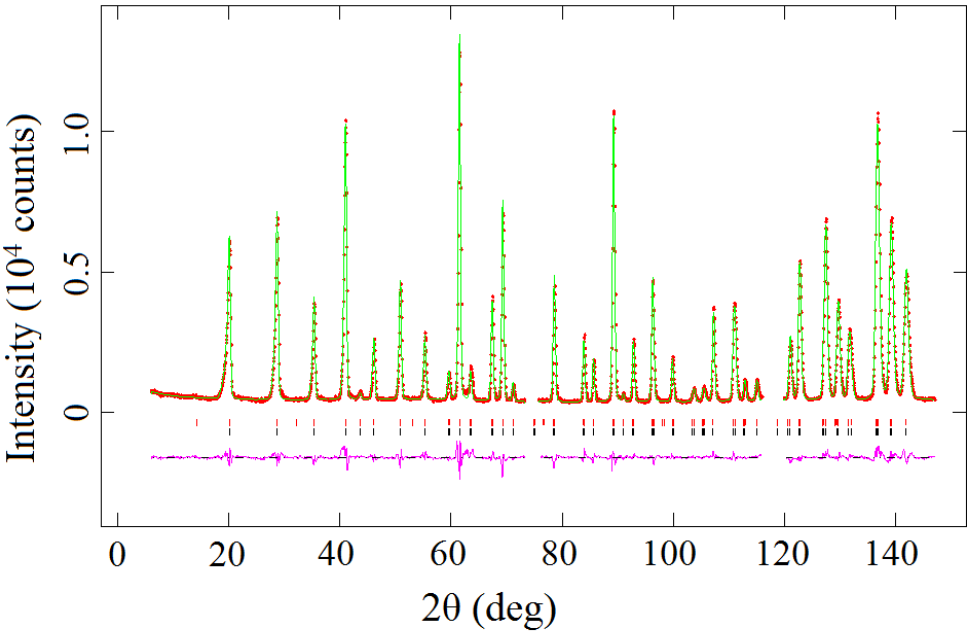

Figure C.5 Observed (red dots) and calculated (green line) NPD patterns of $CeMn_2Ge_4O_{12}$ at 1.6 K, λ = 2.4395 Å, H = 0 Oe (back). A difference curve (purple line) is shown and reflection positions are marked for the crystal structure (bottom) and the magnetic structure (top).

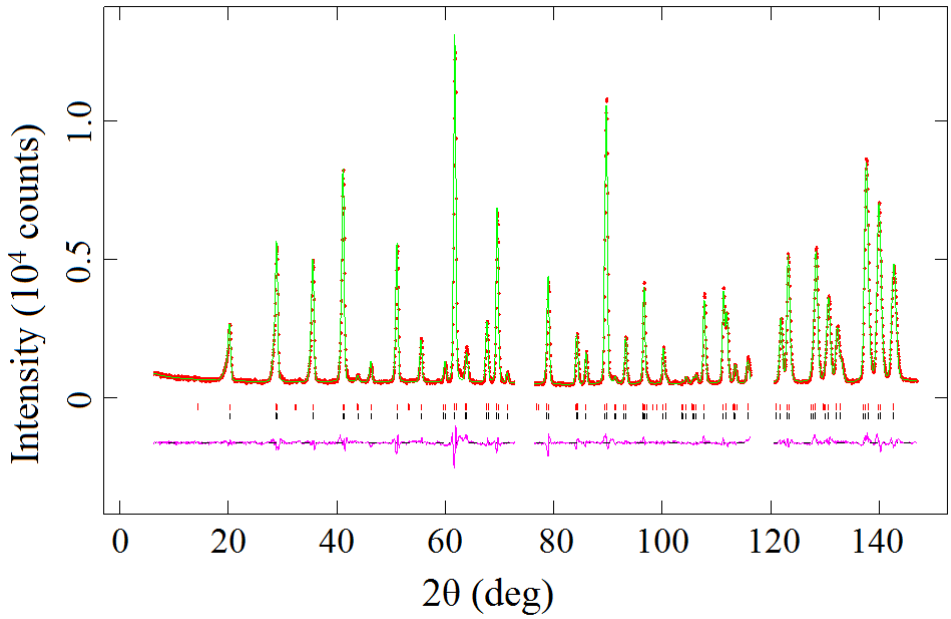

Figure C.6 Observed (red dots) and calculated (green line) NPD patterns of $CeMn_{1.5}Co_{0.5}Ge_4O_{12}$ at 1.6 K, λ = 2.4395 Å, H = 0 Oe. A difference curve (purple line) is shown and reflection positions are marked for the crystal structure (bottom) and the magnetic structure (top).

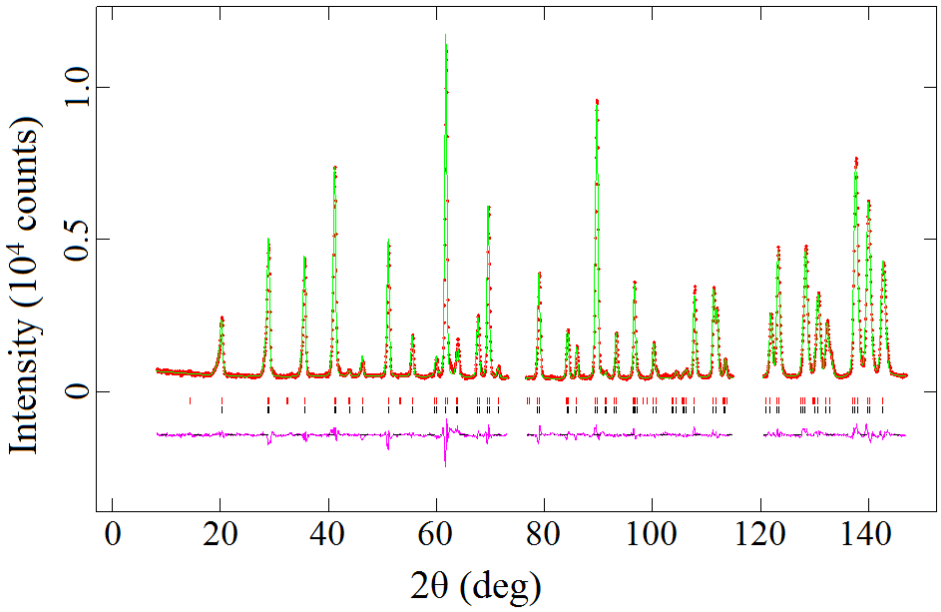

Figure C.7 Observed (red dots) and calculated (green line) NPD patterns of $CeMn_{1.5}Co_{0.5}Ge_4O_{12}$ at 1.6 K, λ = 2.4395 Å, H = 1 kOe. A difference curve (purple line) is shown and reflection positions are marked for the crystal structure (bottom) and the magnetic structure (top).

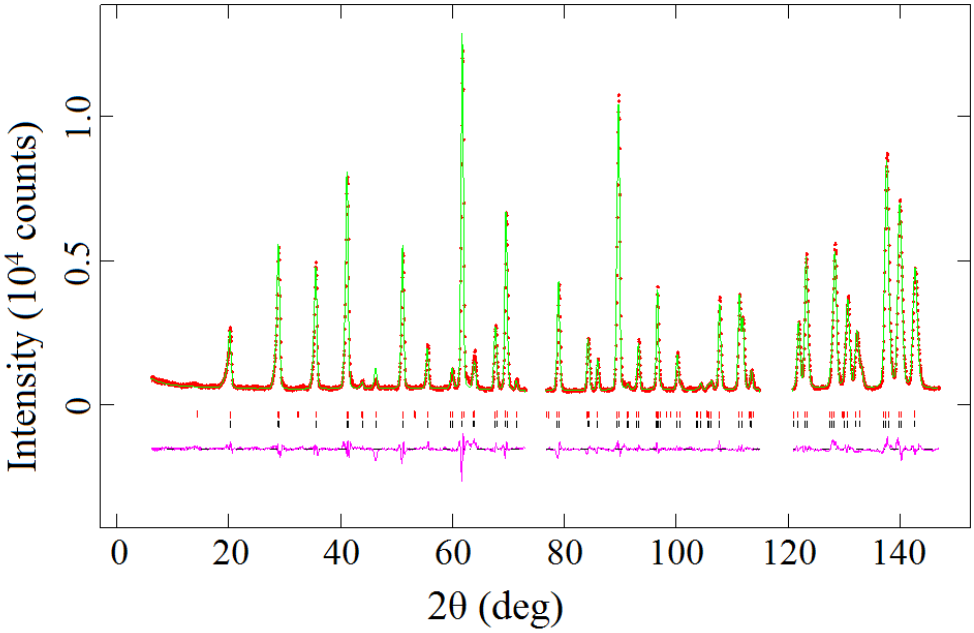

Figure C.8 Observed (red dots) and calculated (green line) NPD patterns of $CeMn_{1.5}Co_{0.5}Ge_4O_{12}$ at 1.6 K, λ = 2.4395 Å, H = 5 kOe. A difference curve (purple line) is shown and reflection positions are marked for the crystal structure (bottom) and the magnetic structure (top).

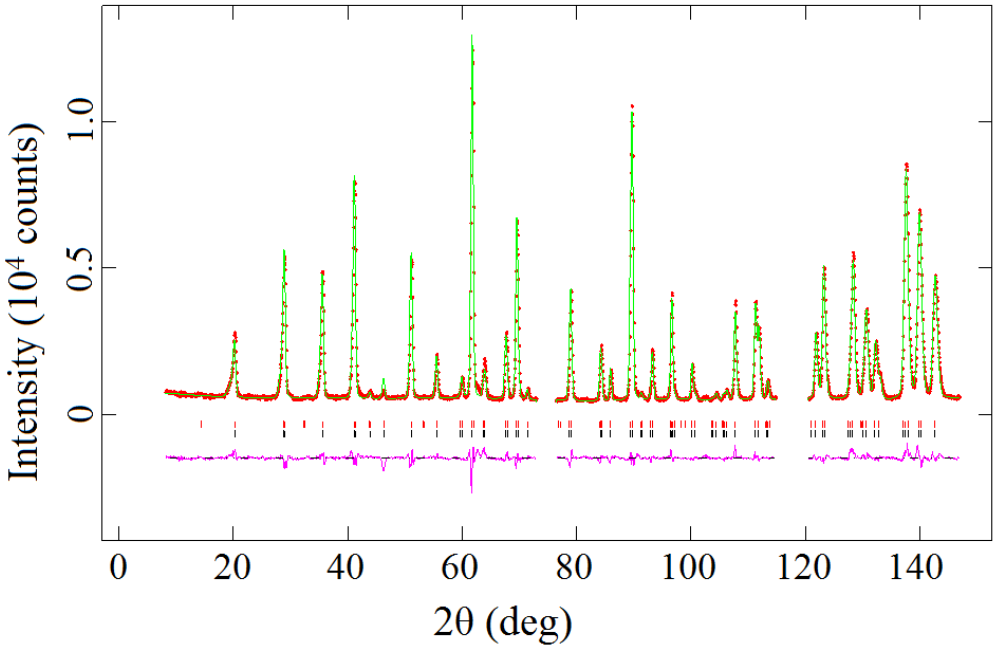

Figure C.9 Observed (red dots) and calculated (green line) NPD patterns of $CeMn_{1.5}Co_{0.5}Ge_4O_{12}$ at 1.6 K, λ = 2.4395 Å, H = 10 kOe. A difference curve (purple line) is shown and reflection positions are marked for the crystal structure (bottom) and the magnetic structure (top).

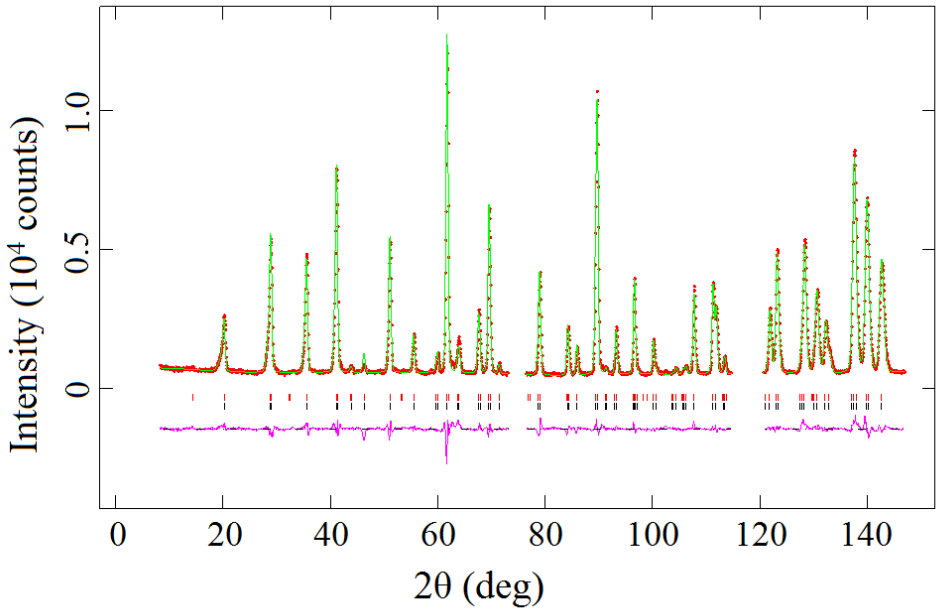

Figure C.10 Observed (red dots) and calculated (green line) NPD patterns of $CeMn_{1.5}Co_{0.5}Ge_4O_{12}$ at 1.6 K, λ = 2.4395 Å, H = 0 Oe (back). A difference curve (purple line) is shown and reflection positions are marked for the crystal structure (bottom) and the magnetic structure (top).

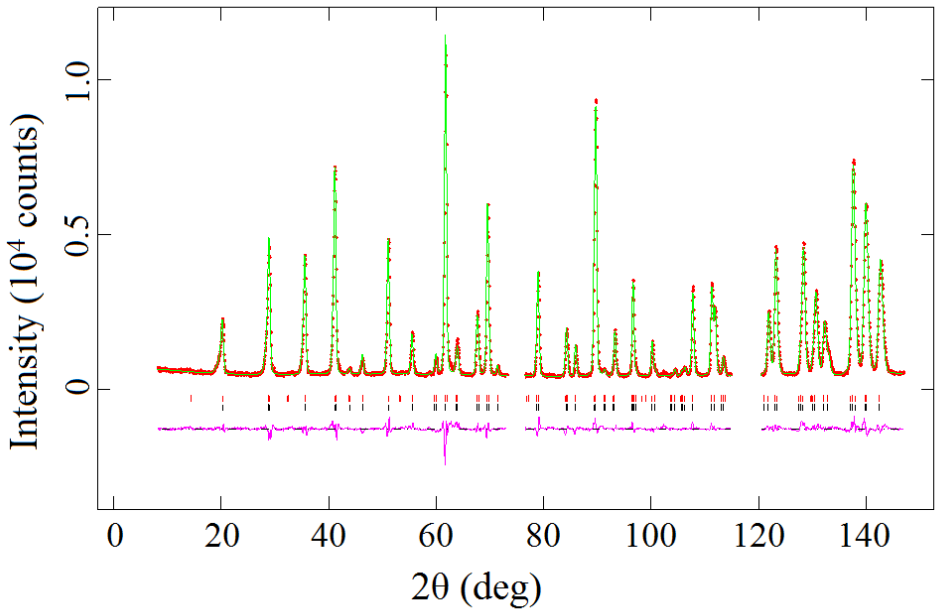

Figure C.11 Observed (red dots) and calculated (green line) NPD patterns of $CeMn_{1.5}Co_{0.5}Ge_4O_{12}$ at 1.6 K, λ = 2.4395 Å, H = 0 Oe (heated to 15 K and then cooled back to 1.6 K). A difference curve (purple line) is shown and reflection positions are marked for the crystal structure (bottom) and the magnetic structure (top).

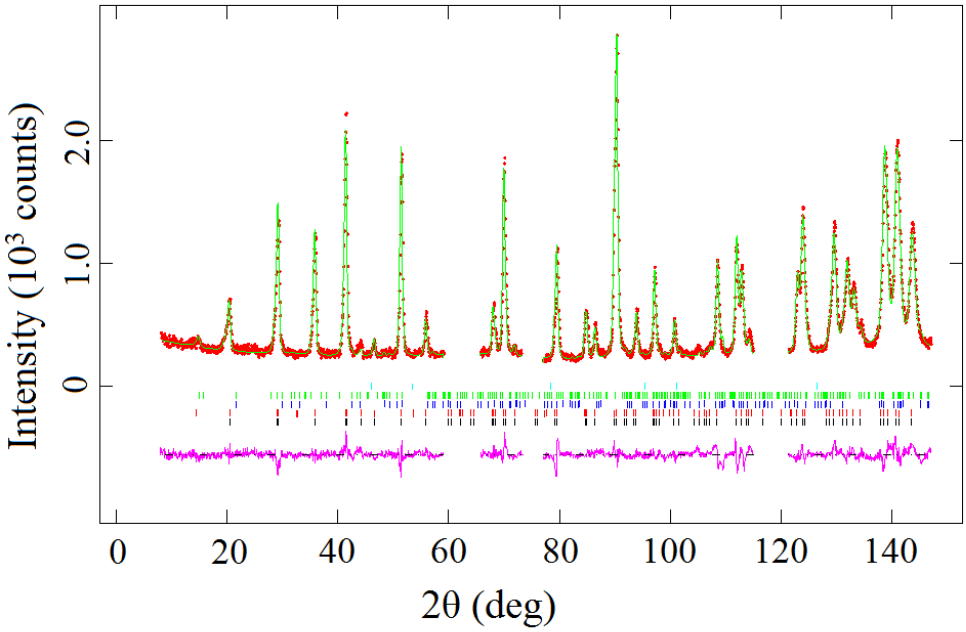

Figure C.12 Observed (red dots) and calculated (green line) NPD patterns of $CeMnCoGe_4O_{12}$ at 1.6 K, λ = 2.4395 Å, H = 0 Oe. A difference curve (purple line) is shown and reflection positions are marked for $CeMnCoGe_4O_{12}$ (black), $CeMnCoGe_4O_{12}$ magnetic phase (red), $CoGeO_3$ (blue), $CoGeO_3$ magnetic phase (green), and CeO_2 (Cyan).

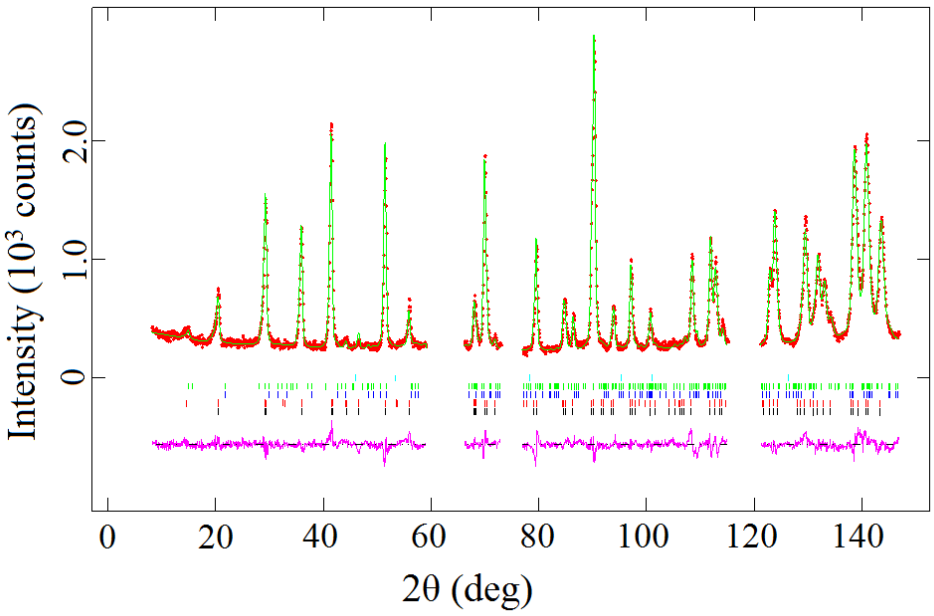

Figure C.13 Observed (red dots) and calculated (green line) NPD patterns of $CeMnCoGe_4O_{12}$ at 1.6 K, λ = 2.4395 Å, H = 3 kOe. A difference curve (purple line) is shown and reflection positions are marked for $CeMnCoGe_4O_{12}$ (black), $CeMnCoGe_4O_{12}$ magnetic phase (red), $CoGeO_3$ (blue), $CoGeO_3$ magnetic phase (green), and CeO_2 (Cyan).

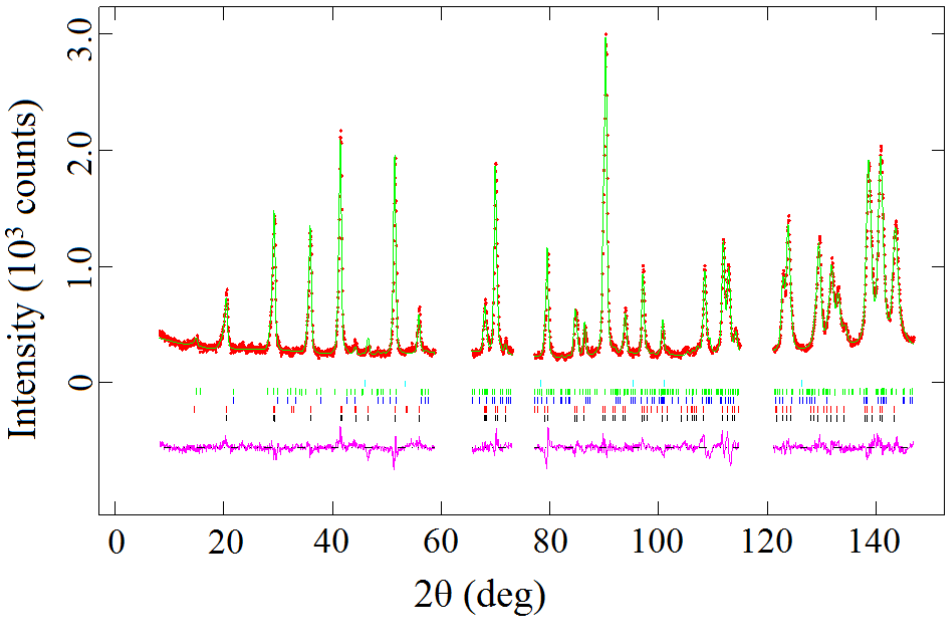

Figure C.14 Observed (red dots) and calculated (green line) NPD patterns of $CeMnCoGe_4O_{12}$ at 1.6 K, λ = 2.4395 Å, H = 10 kOe. A difference curve (purple line) is shown and reflection positions are marked for $CeMnCoGe_4O_{12}$ (black), $CeMnCoGe_4O_{12}$ magnetic phase (red), $CoGeO_3$ (blue), $CoGeO_3$ magnetic phase (green), and CeO_2 (Cyan).

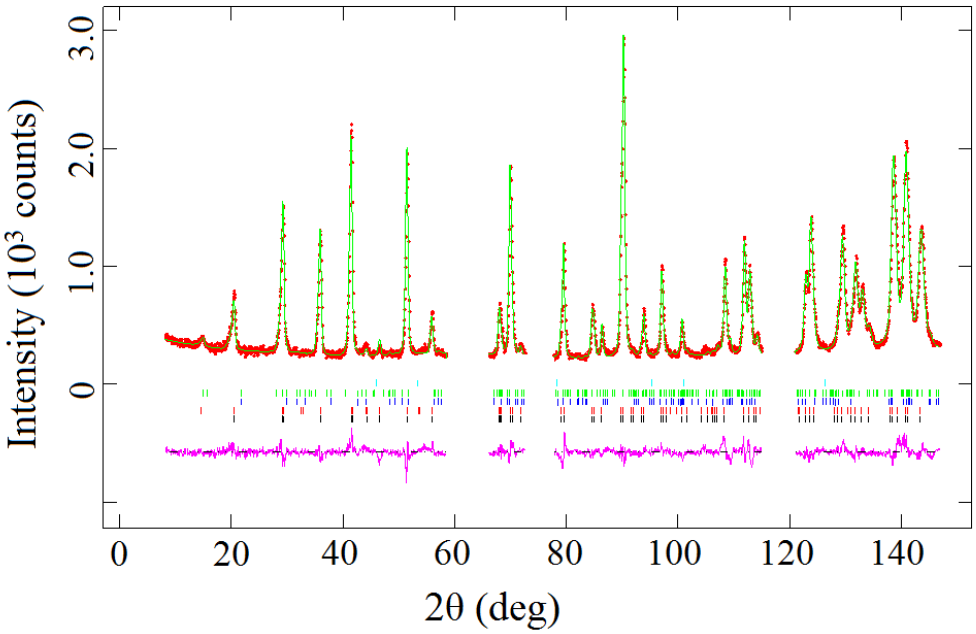

Figure C.15 Observed (red dots) and calculated (green line) NPD patterns of $CeMnCoGe_4O_{12}$ at 1.6 K, λ = 2.4395 Å, H = 20 kOe. A difference curve (purple line) is shown and reflection positions are marked for $CeMnCoGe_4O_{12}$ (black), $CeMnCoGe_4O_{12}$ magnetic phase (red), $CoGeO_3$ (blue), $CoGeO_3$ magnetic phase (green), and CeO_2 (Cyan).

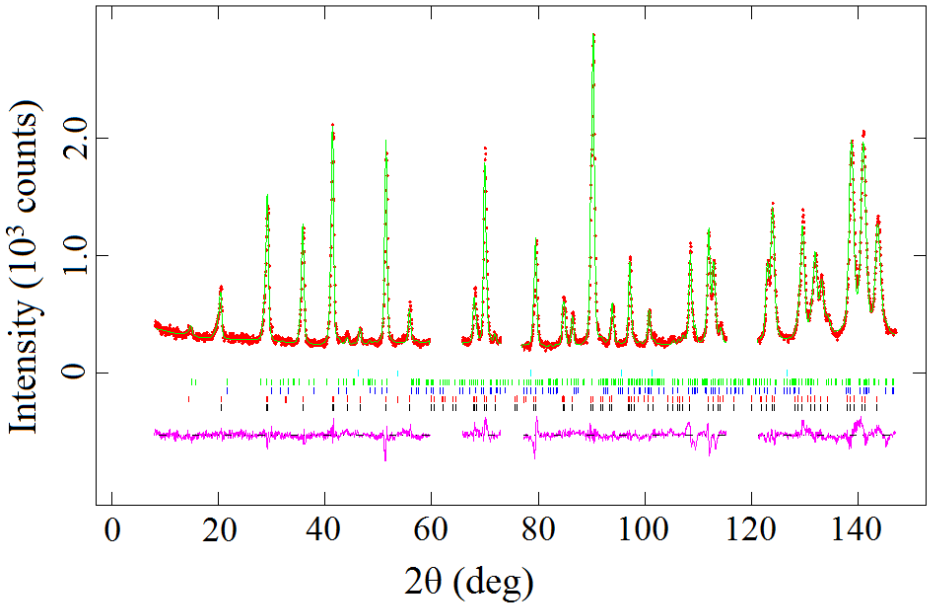

Figure C.16 Observed (red dots) and calculated (green line) NPD patterns of $CeMnCoGe_4O_{12}$ at 1.6 K, λ = 2.4395 Å, H = 0 Oe (back). A difference curve (purple line) is shown and reflection positions are marked for $CeMnCoGe_4O_{12}$ (black), $CeMnCoGe_4O_{12}$ magnetic phase (red), $CoGeO_3$ (blue), $CoGeO_3$ magnetic phase (green), and CeO_2 (Cyan).

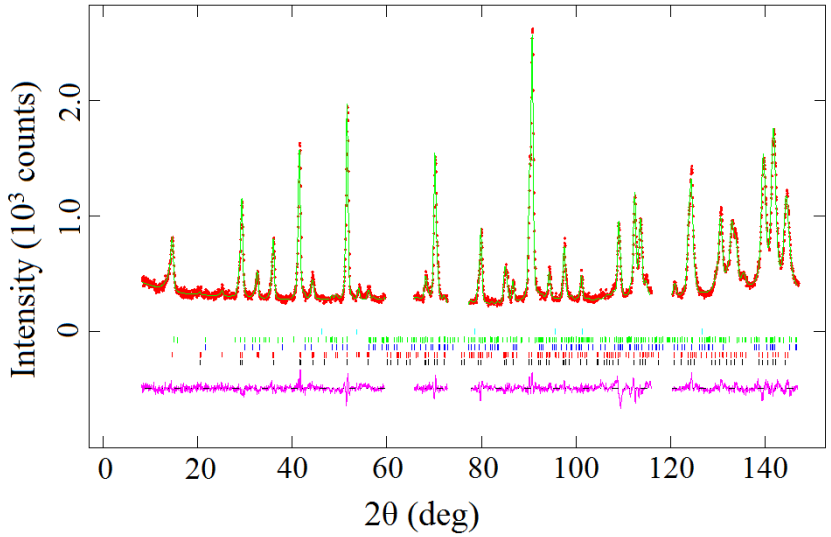

Figure C.17 Observed (red dots) and calculated (green line) NPD patterns of $CeMn_{0.5}Co_{1.5}Ge_4O_{12}$ at 1.6 K, λ = 2.4395 Å, H = 0 Oe. A difference curve (purple line) is shown and reflection positions are marked for $CeMn_{0.5}Co_{1.5}Ge_4O_{12}$ (black), $CeMn_{0.5}Co_{1.5}Ge_4O_{12}$ magnetic phase (red; double magnetic structure), $CoGeO_3$ (blue), $CoGeO_3$ magnetic phase (green), and CeO_2 (Cyan).

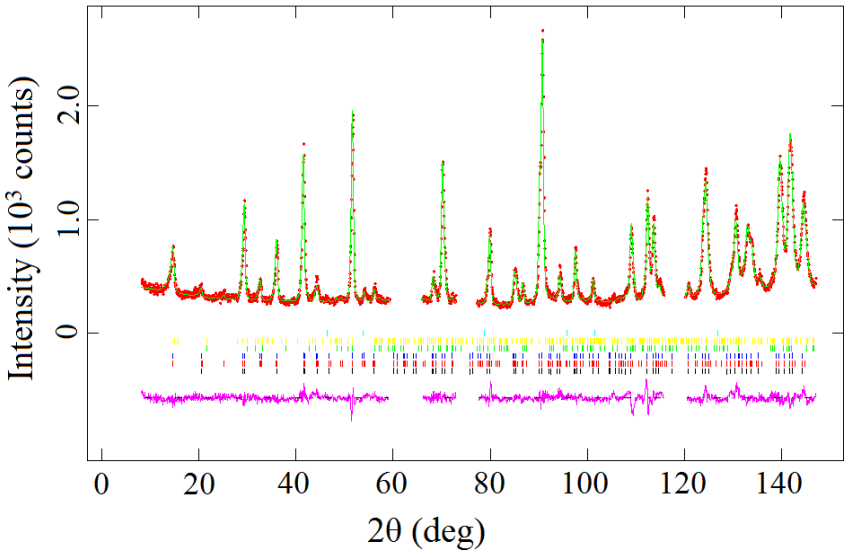

Figure C.18 Observed (red dots) and calculated (green line) NPD patterns of $CeMn_{0.5}Co_{1.5}Ge_4O_{12}$ at 1.6 K, λ = 2.4395 Å, H = 2 kOe. A difference curve (purple line) is shown and reflection positions are marked for $CeMn_{0.5}Co_{1.5}Ge_4O_{12}$ (black), $CeMn_{0.5}Co_{1.5}Ge_4O_{12}$ magnetic phase (red; double magnetic structure), $CeMn_{0.5}Co_{1.5}Ge_4O_{12}$ magnetic phase (blue; single magnetic structure), $CoGeO_3$ (green), $CoGeO_3$ magnetic phase (yellow), and CeO_2 (Cyan).

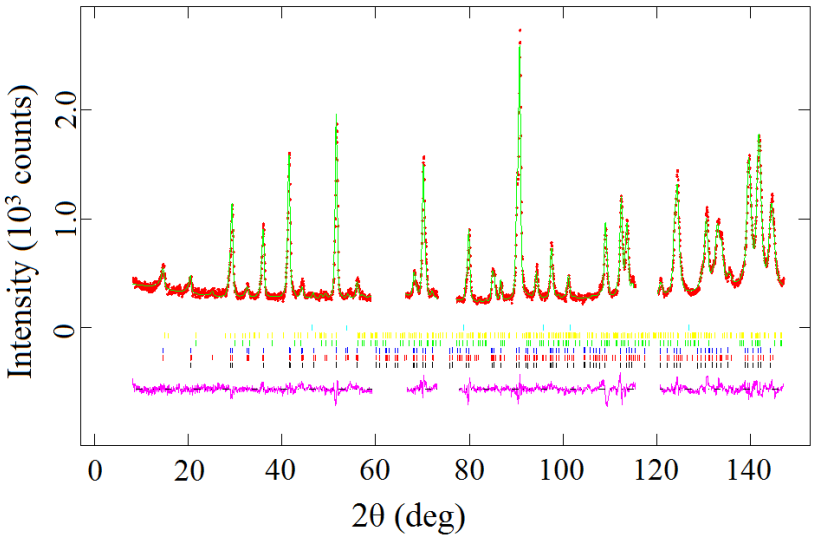

Figure C.19 Observed (red dots) and calculated (green line) NPD patterns of $CeMn_{0.5}Co_{1.5}Ge_4O_{12}$ at 1.6 K, λ = 2.4395 Å, H = 3 kOe. A difference curve (purple line) is shown and reflection positions are marked for $CeMn_{0.5}Co_{1.5}Ge_4O_{12}$ (black), $CeMn_{0.5}Co_{1.5}Ge_4O_{12}$ magnetic phase (red; double magnetic structure), $CeMn_{0.5}Co_{1.5}Ge_4O_{12}$ magnetic phase (blue; single magnetic structure), $CoGeO_3$ (green), $CoGeO_3$ magnetic phase (yellow), and CeO_2 (Cyan).

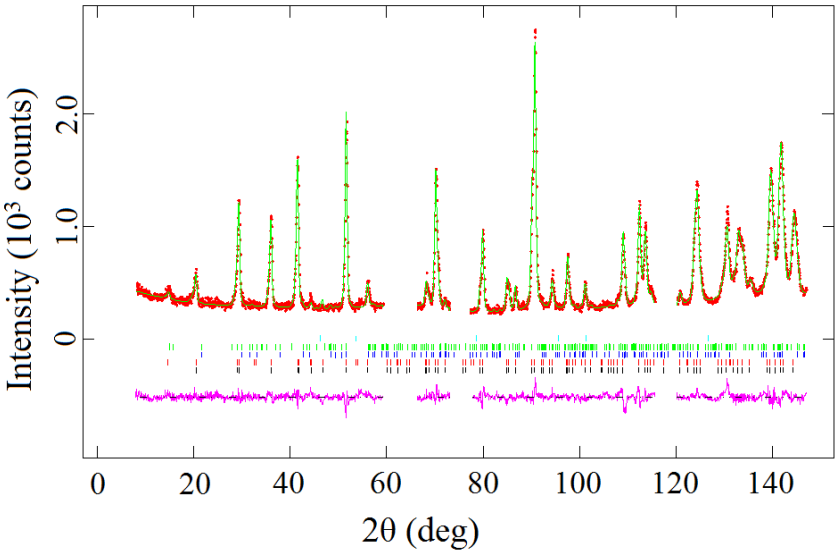

Figure C.20 Observed (red dots) and calculated (green line) NPD patterns of $CeMn_{0.5}Co_{1.5}Ge_4O_{12}$ at 1.6 K, λ = 2.4395 Å, H = 10 kOe. A difference curve (purple line) is shown and reflection positions are marked for $CeMn_{0.5}Co_{1.5}Ge_4O_{12}$ (black), $CeMn_{0.5}Co_{1.5}Ge_4O_{12}$ magnetic phase (red; double magnetic structure), $CeMn_{0.5}Co_{1.5}Ge_4O_{12}$ magnetic phase (blue; single magnetic structure), $CoGeO_3$ (green), $CoGeO_3$ magnetic phase (yellow), and CeO_2 (Cyan).

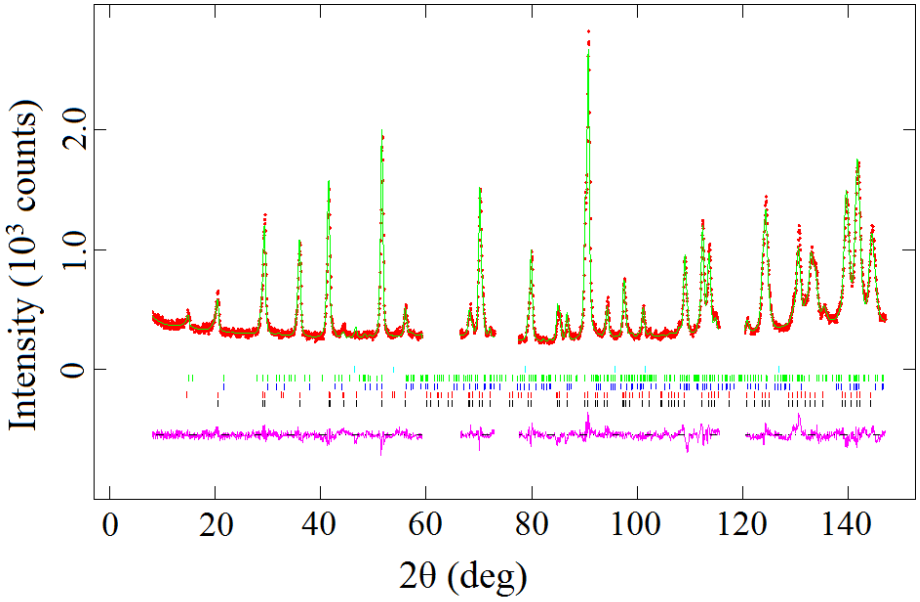

Figure C.21 Observed (red dots) and calculated (green line) NPD patterns of $CeMn_{0.5}Co_{1.5}Ge_4O_{12}$ at 1.6 K, λ = 2.4395 Å, H = 20 kOe. A difference curve (purple line) is shown and reflection positions are marked for $CeMn_{0.5}Co_{1.5}Ge_4O_{12}$ (black), $CeMn_{0.5}Co_{1.5}Ge_4O_{12}$ magnetic phase (red; single magnetic structure), $CoGeO_3$ (blue), $CoGeO_3$ magnetic phase (green), and CeO_2 (Cyan).

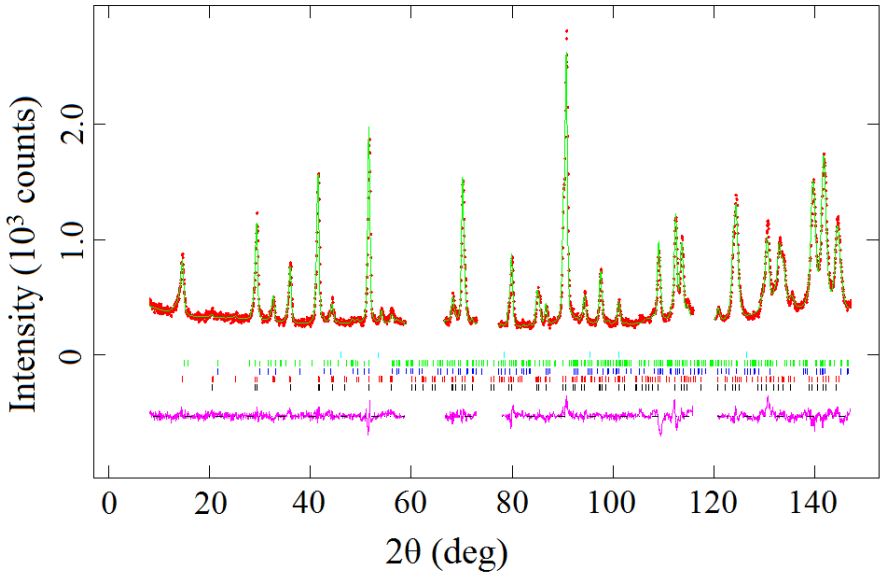

Figure C.22 Observed (red dots) and calculated (green line) NPD patterns of $CeMn_{0.5}Co_{1.5}Ge_4O_{12}$ at 1.6 K, λ = 2.4395 Å, H = 0 Oe (back). A difference curve (purple line) is shown and reflection positions are marked for $CeMn_{0.5}Co_{1.5}Ge_4O_{12}$ (black), $CeMn_{0.5}Co_{1.5}Ge_4O_{12}$ magnetic phase (red; double magnetic structure), $CoGeO_3$ (blue), $CoGeO_3$ magnetic phase (green), and CeO_2 (Cyan).

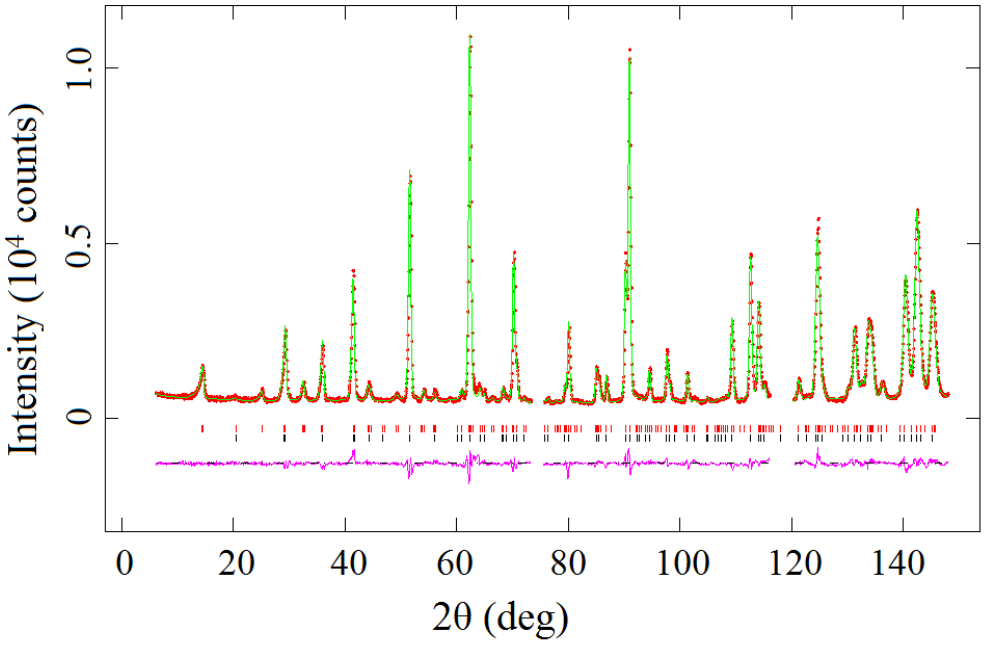

Figure C.23 Observed (red dots) and calculated (green line) NPD patterns of $CeCo_2Ge_4O_{12}$ at 1.6 K, λ = 2.4395 Å, H = 0 Oe. A difference curve (purple line) is shown and reflection positions are marked for the crystal structure (bottom) and the double magnetic structure (top).

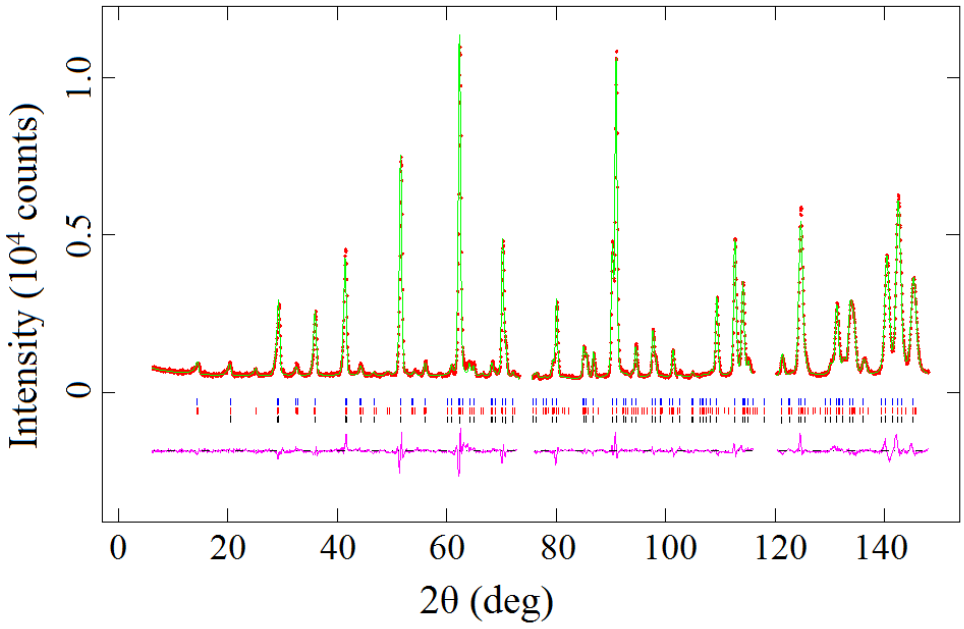

Figure C.24 Observed (red dots) and calculated (green line) NPD patterns of $CeCo_2Ge_4O_{12}$ at 1.6 K, λ = 2.4395 Å, H = 5 kOe. A difference curve (purple line) is shown and reflection positions are marked for the crystal structure (bottom), the double magnetic structure (middle) and the single magnetic structure (top).

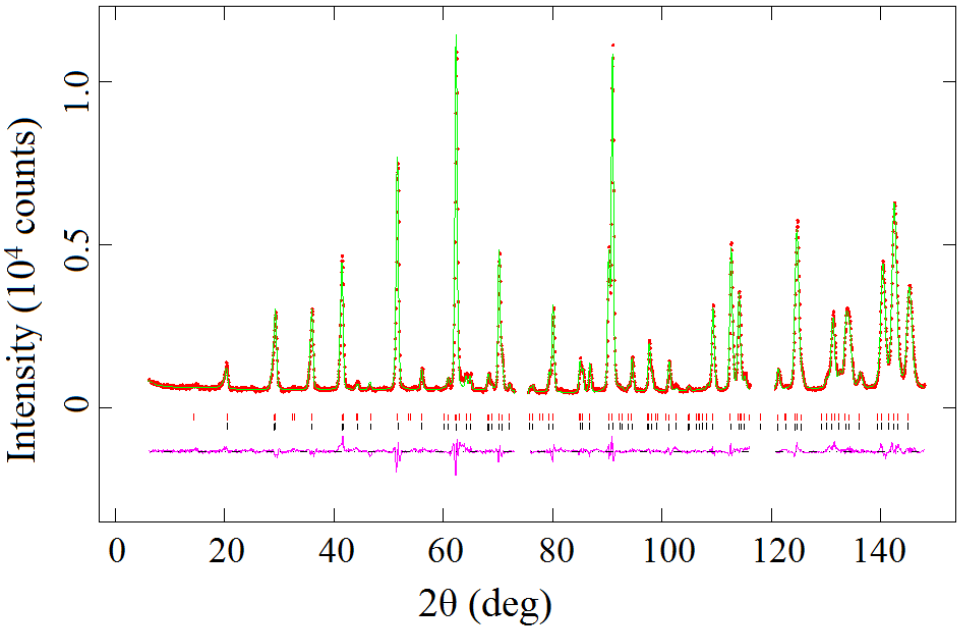

Figure C.25 Observed (red dots) and calculated (green line) NPD patterns of $CeCo_2Ge_4O_{12}$ at 1.6 K, λ = 2.4395 Å, H = 10 kOe. A difference curve (purple line) is shown and reflection positions are marked for the crystal structure (bottom) and the single magnetic structure (top).

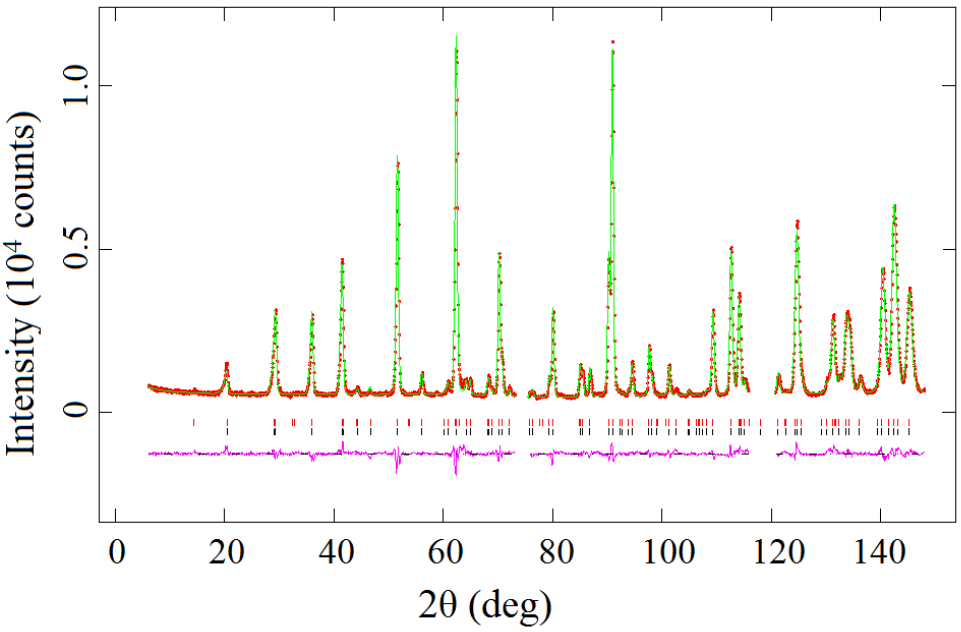

Figure C.26 Observed (red dots) and calculated (green line) NPD patterns of $CeCo_2Ge_4O_{12}$ at 1.6 K, λ = 2.4395 Å, H = 20 kOe. A difference curve (purple line) is shown and reflection positions are marked for the crystal structure (bottom) and the single magnetic structure (top).

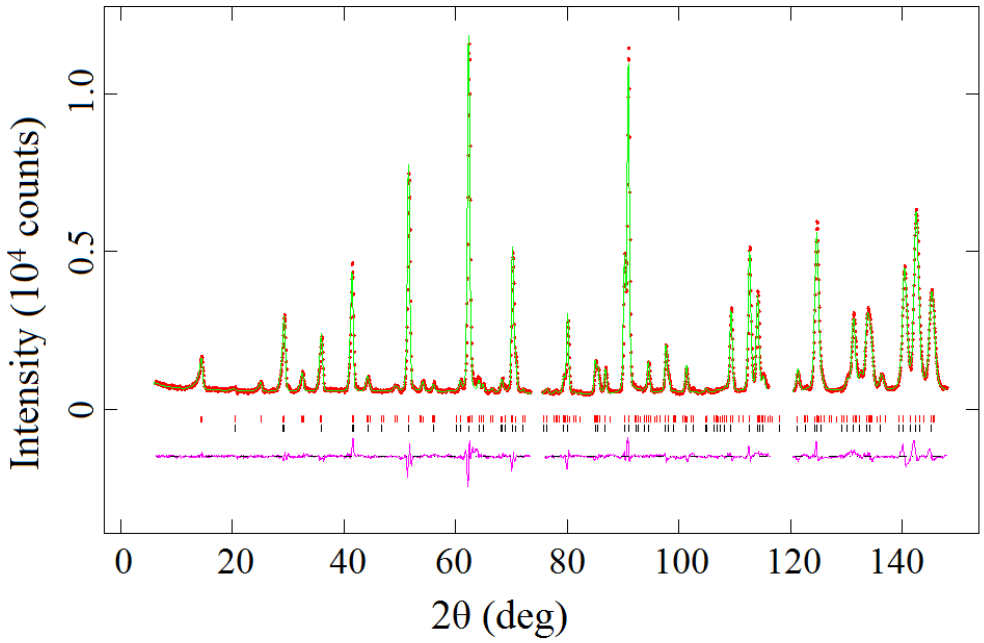

Figure C.27 Observed (red dots) and calculated (green line) NPD patterns of $CeCo_2Ge_4O_{12}$ at 1.6 K, λ = 2.4395 Å, H = 0 Oe (back). A difference curve (purple line) is shown and reflection positions are marked for the crystal structure (bottom) and the double magnetic structure (top).

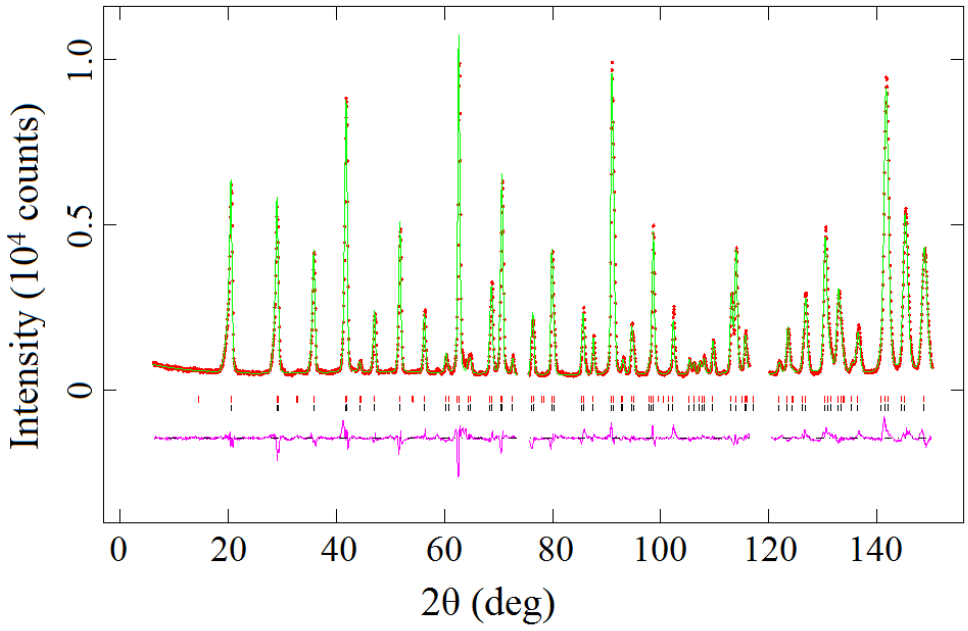

Figure C.28 Observed (red dots) and calculated (green line) NPD patterns of $ZrMn_2Ge_4O_{12}$ at 1.6 K, λ = 2.4395 Å, H = 0 Oe. A difference curve (purple line) is shown and reflection positions are marked for the crystal structure (bottom) and the magnetic structure (top).

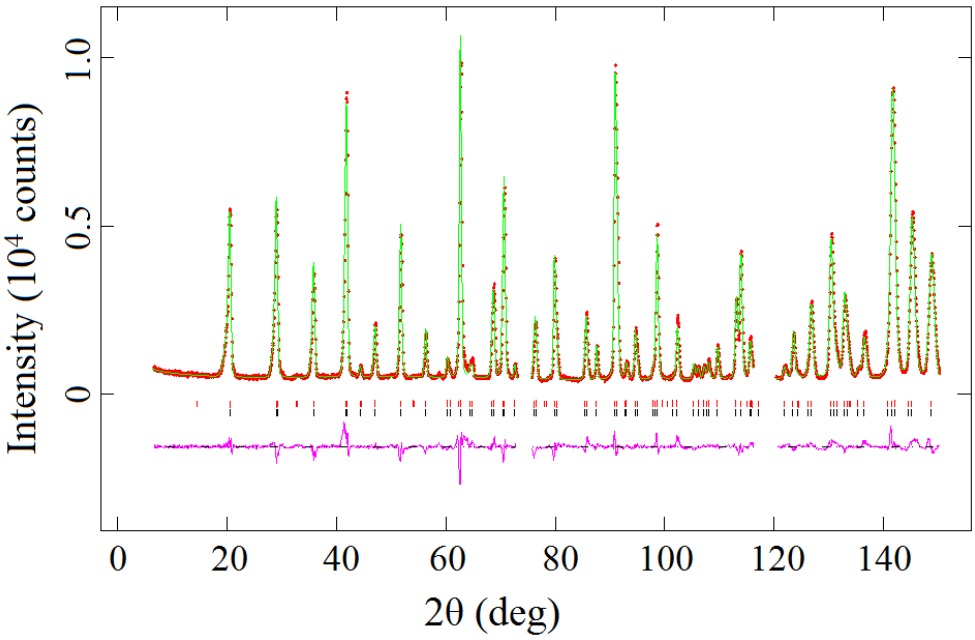

Figure C.29 Observed (red dots) and calculated (green line) NPD patterns of $ZrMn_2Ge_4O_{12}$ at 1.6 K, λ = 2.4395 Å, H = 30 kOe. A difference curve (purple line) is shown and reflection positions are marked for the crystal structure (bottom) and the magnetic structure (top).

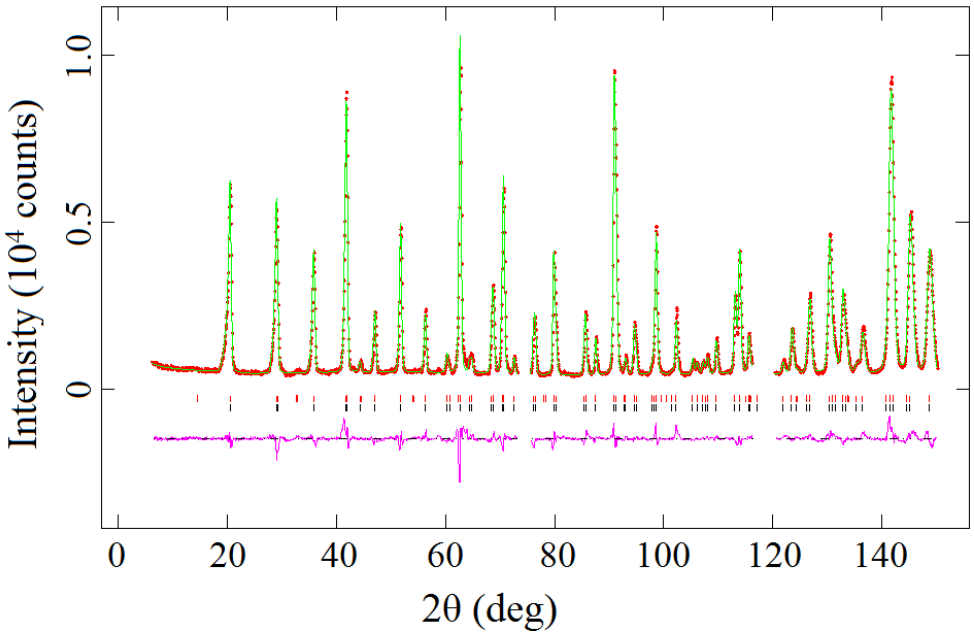

Figure C.30 Observed (red dots) and calculated (green line) NPD patterns of $ZrMn_2Ge_4O_{12}$ at 1.6 K, λ = 2.4395 Å, H = 0 Oe (back). A difference curve (purple line) is shown and reflection positions are marked for the crystal structure (bottom) and the magnetic structure (top).

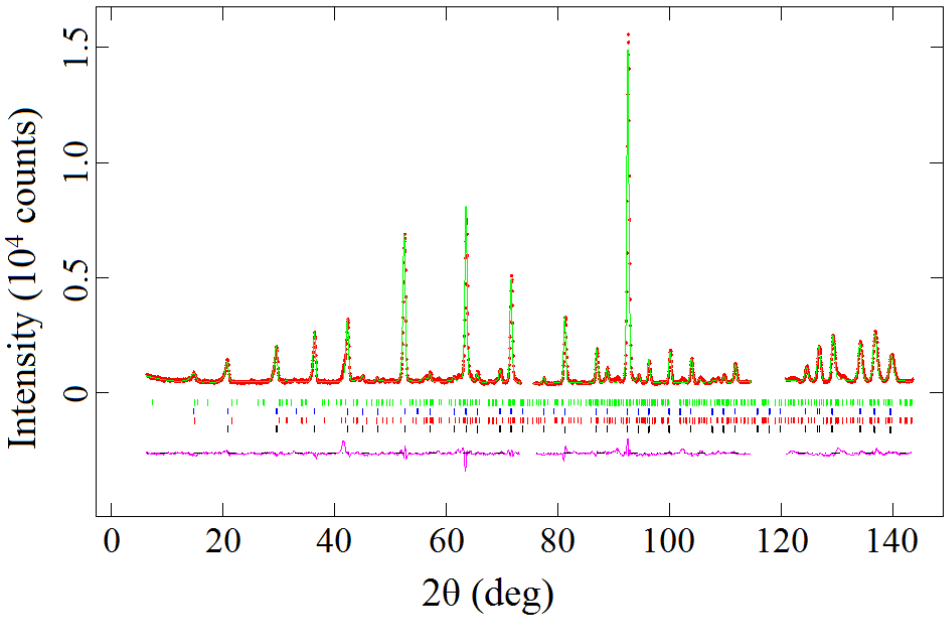

Figure C.31 Observed (red dots) and calculated (green line) NPD patterns of $ZrCo_2Ge_4O_{12}$ at 1.6 K, λ = 2.4395 Å, H = 0 Oe. A difference curve (purple line) is shown and reflection positions are marked for $ZrCo_2Ge_4O_{12}$ (black), $CoGeO_3$ (red), $ZrCo_2Ge_4O_{12}$ magnetic phase (blue) and $CoGeO_3$ magnetic phase (green).

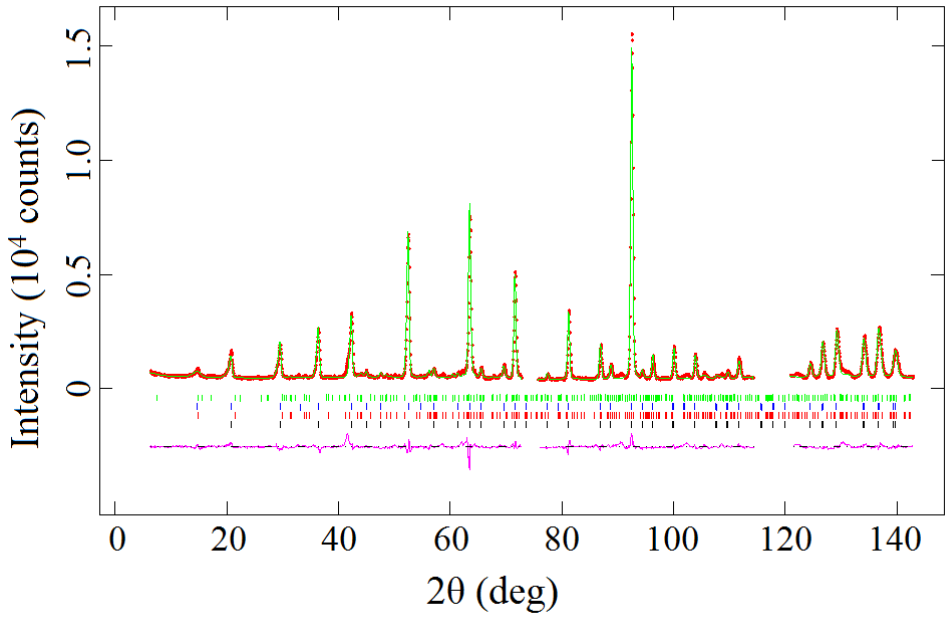

Figure C.32 Observed (red dots) and calculated (green line) NPD patterns of $ZrCo_2Ge_4O_{12}$ at 1.6 K, λ = 2.4395 Å, H = 3 kOe. A difference curve (purple line) is shown and reflection positions are marked for $ZrCo_2Ge_4O_{12}$ (black), $CoGeO_3$ (red), $ZrCo_2Ge_4O_{12}$ magnetic phase (blue) and $CoGeO_3$ magnetic phase (green).

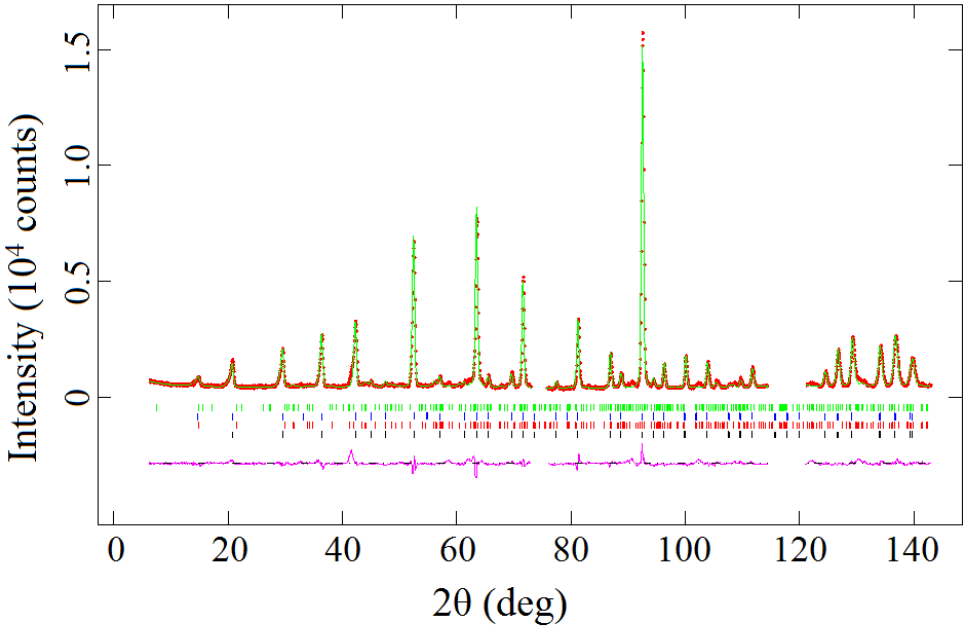

Figure C.33 Observed (red dots) and calculated (green line) NPD patterns of $ZrCo_2Ge_4O_{12}$ at 1.6 K, λ = 2.4395 Å, H = 6 kOe. A difference curve (purple line) is shown and reflection positions are marked for $ZrCo_2Ge_4O_{12}$ (black), $CoGeO_3$ (red), $ZrCo_2Ge_4O_{12}$ magnetic phase (blue) and $CoGeO_3$ magnetic phase (green).

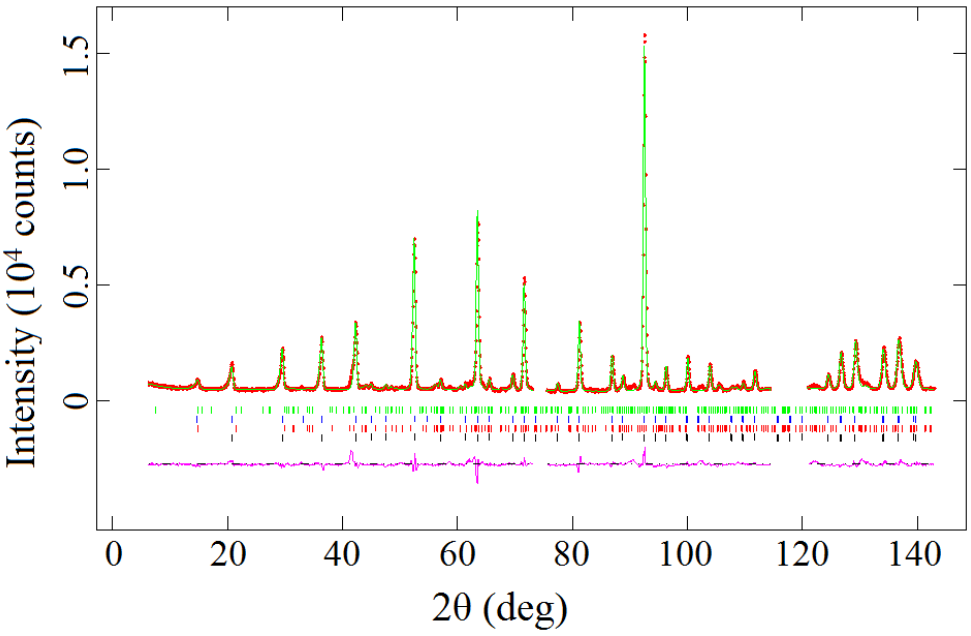

Figure C.34 Observed (red dots) and calculated (green line) NPD patterns of $ZrCo_2Ge_4O_{12}$ at 1.6 K, λ = 2.4395 Å, H = 20 kOe. A difference curve (purple line) is shown and reflection positions are marked for $ZrCo_2Ge_4O_{12}$ (black), $CoGeO_3$ (red), $ZrCo_2Ge_4O_{12}$ magnetic phase (blue) and $CoGeO_3$ magnetic phase (green).

Table C.1 Structural parameters and selected bond lengths (Å) and angles (˚) in $CeMn_2Ge_4O_{12}$ at 1.6 K derived from neutron diffraction data (λ = 2.4395 Å) as a function of magnetic field

H	0 Oe	10k Oe	20k Oe	30k Oe	0 Oe back
a/Å	9.8298(1)	9.8298(1)	9.8298(1)	9.8299(1)	9.8298(1)
c/Å	4.9018(1)	4.9019(1)	4.9019(1)	4.9012(1)	4.9018(1)
R_{wpr}	6.07%	6.05%	6.10%	6.34%	6.01%
χ^2	4.267	4.222	4.262	4.520	4.113

H	0 Oe	10k Oe	20k Oe	30k Oe	0 Oe back
Ce-O1 × 8	2.321(2)	2.324(2)	2.325(2)	2.325(2)	2.320(2)
Mn-O1 × 2	2.421(2)	2.424(2)	2.423(2)	2.414(2)	2.425(2)
Mn-O2 × 4	2.138(2)	2.141(2)	2.144(2)	2.142(2)	2.140(2)
Ge-O1 × 2	1.781(1)	1.784(1)	1.784(1)	1.788(1)	1.782(1)
Ge-O2 × 2	1.729(2)	1.721(2)	1.719(2)	1.720(2)	1.728(2)
O2-Mn-O2	98.55(9)	98.32(9)	98.26(9)	98.30(9)	98.57(9)
O2-Mn-O2	180.0(0)	180.0(0)	180.0(0)	180.0(0)	180.0(0)
O1-Ge-O1	108.64(14)	108.20(14)	108.26(14)	108.76(14)	108.36(13)
O1-Ge-O2	105.58(6)	105.67(6)	105.74(6)	105.64(7)	105.65(6)
O1-Ge-O2	108.90(9)	108.85(9)	108.84(9)	108.64(10)	108.98(9)
O2-Ge-O2	118.93(13)	119.24(13)	119.06(13)	119.22(14)	118.91(13)

Table C.2 Structural parameters and selected bond lengths (Å) and angles (˚) in $CeMn_{1.5}Co_{0.5}Ge_4O_{12}$ at 1.6 K derived from neutron diffraction data (λ = 2.4395 Å) as a function of magnetic field

H	0 Oe	1k Oe	5k Oe	10k Oe	0 Oe back	0 Oe back*
a/Å	9.8056(1)	9.8056(1)	9.8055(1)	9.8056(1)	9.8056(1)	9.8056(1)
c/Å	4.8779(1)	4.8780(1)	4.8779(1)	4.8780(1)	4.8780(1)	4.8780(1)
R_{wpr}	6.03%	5.61%	6.24%	6.19%	6.03%	5.72%
χ^2	4.137	3.360	4.629	4.543	4.271	3.406

*heated to 15 K and then cooled back to 1.6 K

H	0 Oe	1k Oe	5k Oe	10k Oe	0 Oe back	0 Oe back*
Ce-O1 × 8	2.312(2)	2.317(2)	2.317(2)	2.316(2)	2.314(2)	2.316(2)
Mn/Co-O1 × 2	2.412(2)	2.409(2)	2.412(2)	2.415(2)	2.410(2)	2.410(2)
Mn/Co-O2 × 4	2.115(2)	2.112(2)	2.114(2)	2.118(2)	2.119(2)	2.112(2)
Ge-O1 × 2	1.780(1)	1.780(1)	1.781(1)	1.780(1)	1.785(1)	1.779(1)
Ge-O2 × 2	1.738(2)	1.739(2)	1.734(2)	1.733(2)	1.732(2)	1.738(2)
O2-Mn/Co-O2	98.94(9)	98.71(9)	98.64(10)	98.70(10)	98.78(10)	98.74(9)
O2-Mn/Co-O2	180.0(0)	180.0(0)	180.0(0)	180.0(0)	180.0(0)	180.0(0)
O1-Ge-O1	108.34(14)	108.76(13)	108.25(14)	108.12(15)	108.34(14)	108.70(14)
O1-Ge-O2	105.66(6)	105.70(6)	105.74(7)	105.75(7)	105.66(6)	105.62(6)
O1-Ge-O2	108.79(10)	108.60(9)	108.63(10)	108.78(10)	108.79(10)	108.64(9)
O2-Ge-O2	119.25(14)	119.20(13)	119.46(14)	119.28(14)	119.25(14)	119.31(13)

Table C.3 Structural parameters and selected bond lengths (Å) and angles (˚) in $CeMnCoGe_4O_{12}$ at 1.6 K derived from neutron diffraction data (λ = 2.4395 Å) as a function of magnetic field

H	0 Oe	1k Oe	3k Oe	10k Oe	20k Oe	0 Oe back
a/Å	9.7897(1)	9.7897(1)	9.7897(1)	9.7898(1)	9.7898(1)	9.7896(1)
c/Å	4.8571(1)	4.8570(1)	4.8571(1)	4.8575(1)	4.8577(1)	4.8572(1)
R_{wpr}	6.05%	7.58%	6.47%	6.48%	6.43%	6.14%
χ^2	1.686	2.639	1.938	1.936	1.924	1.743

H	0 Oe	1k Oe	3k Oe	10k Oe	20k Oe	0 Oe back
Ce-O1 × 8	2.321(3)	2.366(4)	2.328(3)	2.314(3)	2.326(3)	2.333(3)
Mn/Co-O1 × 2	2.393(4)	2.391(4)	2.395(3)	2.386(3)	2.396(3)	2.386(3)
Mn/Co-O2 × 4	2.093(3)	2.096(3)	2.096(3)	2.091(3)	2.096(3)	2.096(3)
Ge-O1 × 2	1.780(2)	1.784(2)	1.776(2)	1.783(2)	1.780(2)	1.783(2)
Ge-O2 × 2	1.739(2)	1.695(3)	1.734(3)	1.746(3)	1.733(3)	1.729(3)
O2-Mn/Co-O2	0 Oe	1k Oe	3k Oe	10k Oe	20k Oe	0 Oe back
O2-Mn/Co-O2	74.98(5)	74.74(7)	74.76(6)	75.01(6)	74.80(6)	74.75(6)
O1-Ge-O1	118.79(12)	118.26(15)	118.31(13)	118.86(13)	118.41(12)	118.28(12)
O1-Ge-O2	137.53(10)	137.97(14)	137.38(11)	137.25(11)	137.47(11)	137.39(11)
O1-Ge-O2	72.16(12)	72.78(16)	72.40(13)	71.94(13)	72.38(12)	72.42(12)
O2-Ge-O2	77.33(10)	77.51(13)	77.87(11)	77.47(11)	77.72(11)	77.88(10)

Table C.4 Structural parameters and selected bond lengths (Å) and angles (˚) in $CeMn_{0.5}Co_{1.5}Ge_4O_{12}$ at 1.6 K derived from neutron diffraction data (λ = 2.4395 Å) as a function of magnetic field

H	0 Oe	2k Oe	3k Oe	10k Oe	20k Oe	0 Oe back
a/Å	9.7674(2)	9.7676(2)	9.7680(2)	9.7672(2)	9.7679(2)	9.7673(2)
c/Å	4.8348(1)	4.8350(1)	4.8345(1)	4.8347(1)	4.8347(2)	4.8345(1)
R_{wpr}	5.45%	5.64%	5.95%	5.63%	6.10%	5.65%
χ^2	1.385	1.485	1.635	1.475	1.727	1.488

H	0 Oe	2k Oe	3k Oe	10k Oe	20k Oe	0 Oe back
Ce-O1 × 8	2.321(3)	2.320(3)	2.327(3)	2.318(3)	2.313(3)	2.316(3)
Mn/Co-O1 × 2	2.388(3)	2.385(4)	2.382(4)	2.384(4)	2.388(4)	2.386(4)
Mn/Co-O2 × 4	2.082(3)	2.086(3)	2.073(3)	2.082(3)	2.082(3)	2.087(3)
Ge-O1 × 2	1.780(2)	1.784(2)	1.780(2)	1.780(2)	1.775(2)	1.783(2)
Ge-O2 × 2	1.731(3)	1.726(2)	1.731(3)	1.735(3)	1.742(3)	1.728(2)
O2-Mn/Co-O2	98.26(15)	98.23(16)	98.01(16)	98.38(18)	98.72(18)	98.44(16)
O2-Mn/Co-O2	180.0(0)	180.0(0)	180.0(0)	180.0(0)	180.0(0)	180.0(0)
O1-Ge-O1	108.50(24)	108.44(25)	108.97(25)	108.77(25)	108.92(25)	108.29(25)
O1-Ge-O2	105.75(10)	105.59(11)	105.75(11)	106.01(11)	106.23(11)	106.09(11)
O1-Ge-O2	108.15(10)	108.30(18)	107.56(19)	108.06(19)	107.97(19)	108.06(18)
O2-Ge-O2	120.15(23)	120.20(24)	120.88(25)	119.61(25)	119.23(26)	119.84(25)

Table C.5 Structural parameters and selected bond lengths (Å) and angles (˚) in $CeCo_2Ge_4O_{12}$ at 1.6 K derived from neutron diffraction data (λ = 2.4395 Å) as a function of magnetic field

H	0 Oe	5k Oe	10k Oe	20k Oe	0 Oe back
a/Å	9.7370(1)	9.7369(1)	9.7369(1)	9.7370(1)	9.7370(1)
c/Å	4.8128(1)	4.8128(1)	4.8128(1)	4.8129(1)	4.8127(1)
R_{wpr}	5.66%	5.45%	5.65%	5.56%	5.28%
χ^2	3.249	3.132	3.416	3.350	3.082

H	0 Oe	5k Oe	10k Oe	20k Oe	0 Oe back
Ce-O1 × 8	2.313(2)	2.314(2)	2.311(2)	2.319(2)	2.316(2)
Co-O1 × 2	2.370(2)	2.374(2)	2.377(2)	2.372(2)	2.374(2)
Co-O2 × 4	2.060(2)	2.063(2)	2.067(2)	2.064(2)	2.066(2)
Ge-O1 × 2	1.777(1)	1.780(1)	1.777(1)	1.779(1)	1.771(1)
Ge-O2 × 2	1.742(2)	1.737(2)	1.740(2)	1.734(2)	1.732(2)
O2-Co-O2	98.48(9)	98.42(9)	98.54(9)	98.12(10)	98.26(9)
O2-Co-O2	180.0(0)	180.0(0)	180.0(0)	180.0(0)	180.0(0)
O1-Ge-O1	109.17(15)	108.62(14)	108.47(15)	108.79(15)	108.48(14)
O1-Ge-O2	105.34(6)	105.34(6)	105.50(7)	105.71(6)	105.38(6)
O1-Ge-O2	108.42(10)	108.60(10)	108.46811)	108.23(11)	108.62(10)
O2-Ge-O2	119.87(14)	120.00(13)	119.65(14)	119.84(14)	120.00(13)

Table C.6 Structural parameters and selected bond lengths (Å) and angles (˚) in $ZrMn_2Ge_4O_{12}$ at 1.6 K derived from neutron diffraction data (λ = 2.4395 Å) as a function of magnetic field

H	0 Oe	30k Oe	0 Oe back
a/Å	9.6504(1)	9.6498(1)	9.6497(1)
c/Å	4.8566(1)	4.8564(1)	4.8563(1)
R_{wpr}	6.73%	6.73%	6.67%
χ^2	5.260	5.199	5.112

H	0 Oe	30k Oe	0 Oe (back)
Zr-O1 × 8	2.210(2)	2.209(2)	2.206(2)
Mn-O1 × 2	2.372(2)	2.374(2)	2.374(2)
Mn-O2 × 4	2.110(1)	2.115(1)	2.111(1)
Ge-O1 × 2	1.788(1)	1.790(1)	1.789(1)
Ge-O2 × 2	1.723(2)	1.720(2)	1.725(2)
O2-Mn-O2	102.22(9)	102.22(9)	102.42(9)
O2-Mn-O2	180.0(0)	180.0(0)	180.0(0)
O1-Ge-O1	104.3(9)	106.50(14)	106.63(14)
O1-Ge-O2	105.14(34)	105.61(8)	105.45(8)
O1-Ge-O2	109.1(6)	108.67(9)	108.77(9)
O2-Ge-O2	123.3(8)	121.00(14)	121.03(14)

Table C.7 Structural parameters and selected bond lengths (Å) and angles (˚) in $ZrCo_2Ge_4O_{12}$ at 1.6 K derived from neutron diffraction data (λ = 2.4395 Å) as a function of magnetic field

H	0 Oe	3k Oe	6k Oe	20k Oe
a/Å	9.5476(2)	a = 9.5476(2)	9.5478(2)	9.5480(2)
c/Å	4.7788(1)	4.7788(1)	c = 4.7788(1)	4.7787(1)
R_{wpr}	8.24%	8.24%	8.33%	8.23%
χ^2	5.395	5.395	5.550	5.437

H	0 Oe	3k Oe	6k Oe	20k Oe
Zr-O1 × 8	2.205(3)	2.200(3)	2.199 (3)	2.202(3)
Co-O1 × 2	2.301(4)	2.300(4)	2.303(3)	2.302(4)
Co-O2 × 4	2.045(3)	2.045(3)	2.045(3)	2.043(3)
Ge-O1 × 2	1.786(2)	1.790(2)	1.788(2)	1.787(2)
Ge-O2 × 2	1.729(3)	1.730(3)	1.732(3)	1.732(3)
O2-Co-O2	101.80(16)	102.10(15)	102.14(16)	102.01(15)
O2-Co-O2	180.0(0)	180.0(0)	180.0(0)	180.0(0)
O1-Ge-O1	108.69(28)	108.51(28)	108.42(28)	108.58(28)
O1-Ge-O2	105.52(12)	105.14(12)	105.51(12)	105.47(12)
O1-Ge-O2	107.89(16)	109.19(16)	108.31(16)	107.90(16)
O2-Ge-O2	120.91(25)	121.22(25)	120.93(25)	121.09(25)

Appendix D – Magnetometry Data

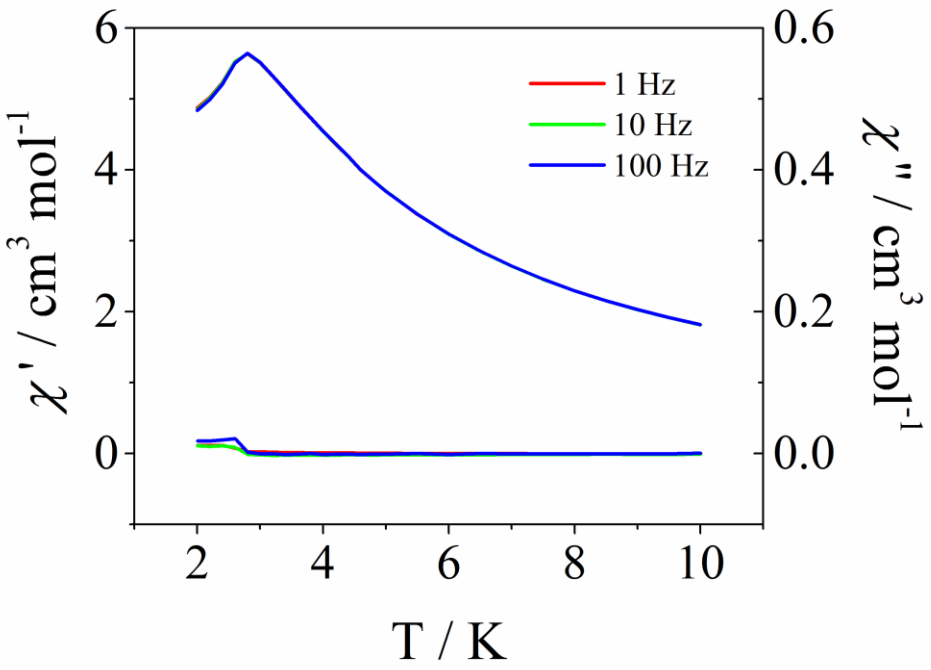

Figure D.1 Temperature and frequency dependence of the ac molar magnetic susceptibility in a 100 Oe dc field of $Tb_2CoGe_4O_{12}$.

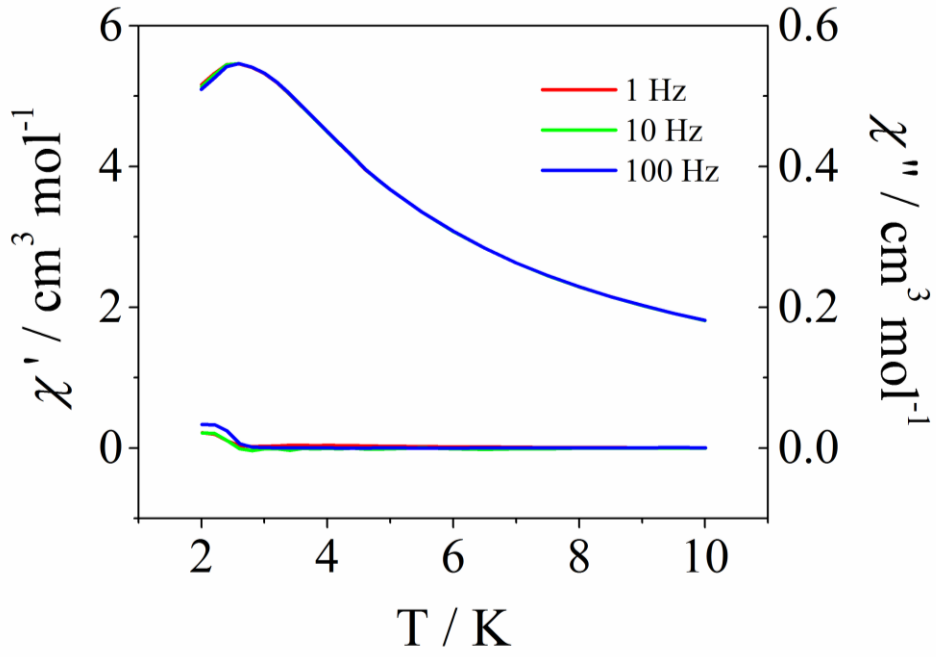

Figure D.2 Temperature and frequency dependence of the ac molar magnetic susceptibility in a 500 Oe dc field of $Tb_2CoGe_4O_{12}$.

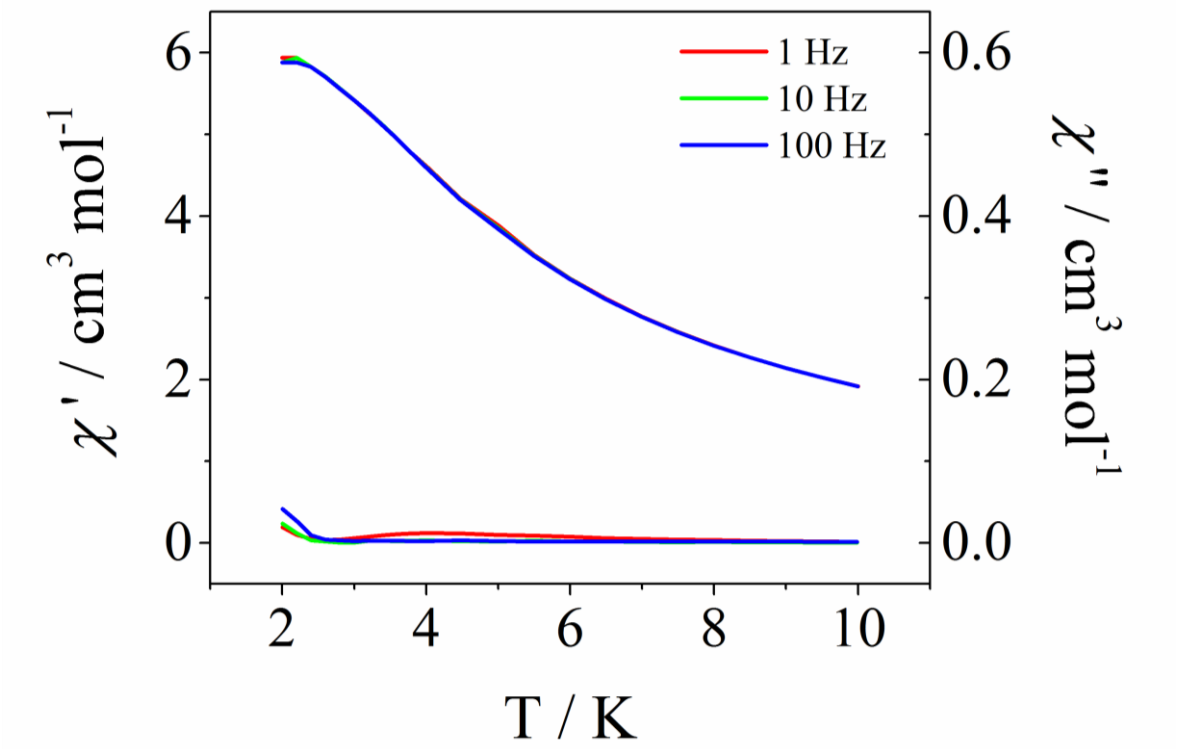

Figure D.3 Temperature and frequency dependence of the ac molar magnetic susceptibility in a 1000 Oe dc field of $Tb_2CoGe_4O_{12}$.

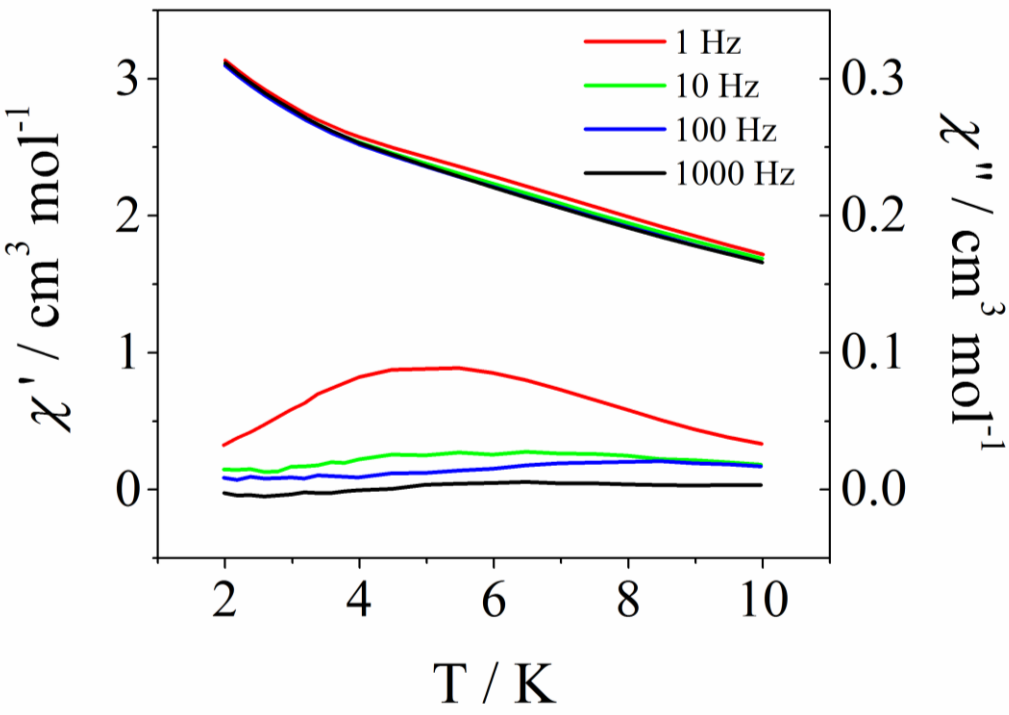

Figure D.4 Temperature and frequency dependence of the ac molar magnetic susceptibility in a 5000 Oe dc field of $Tb_2CoGe_4O_{12}$.

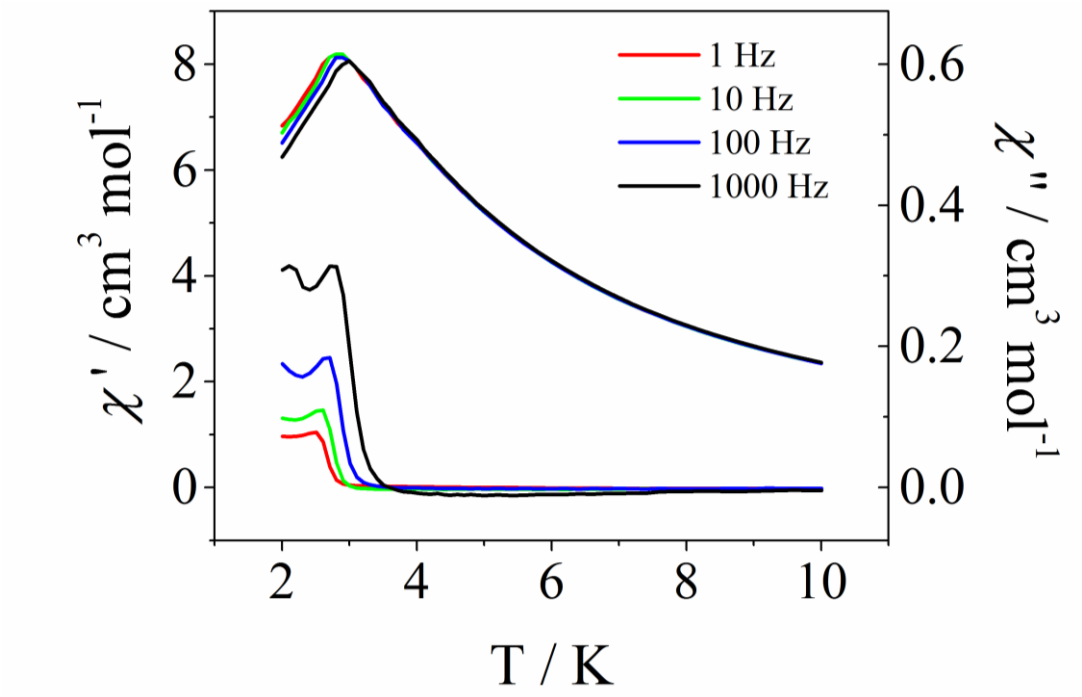

Figure D.5 Temperature and frequency dependence of the ac molar magnetic susceptibility in a 100 Oe dc field of $Dy_2CoGe_4O_{12}$.

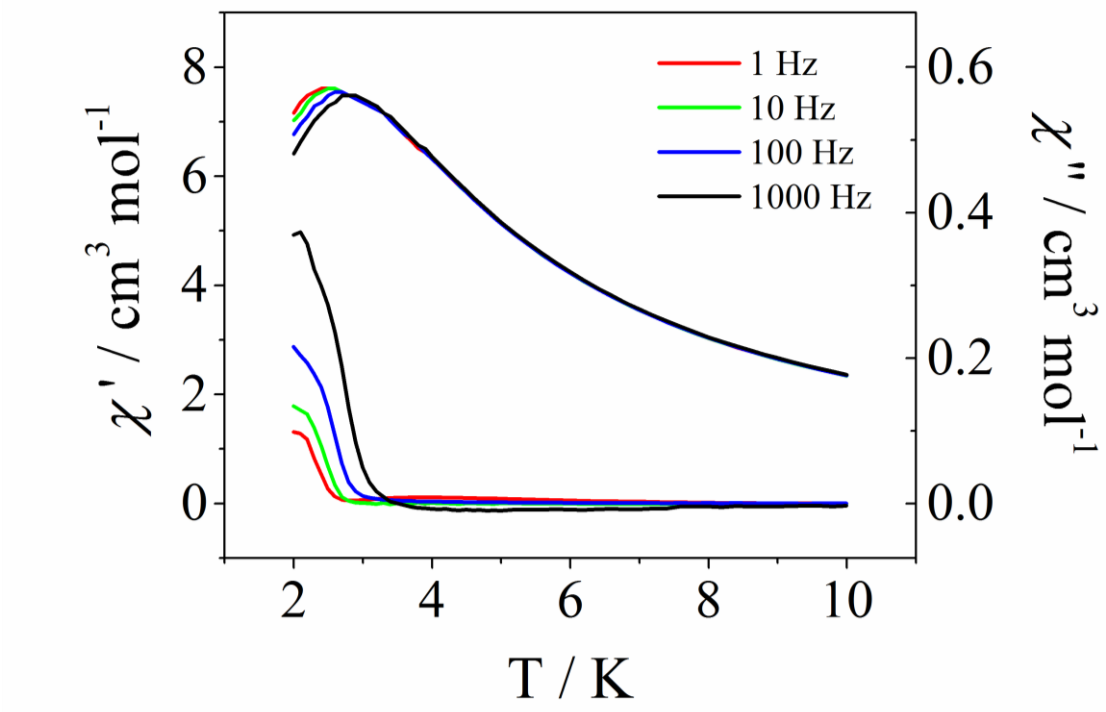

Figure D.6 Temperature and frequency dependence of the ac molar magnetic susceptibility in a 1000 Oe dc field of $Dy_2CoGe_4O_{12}$.

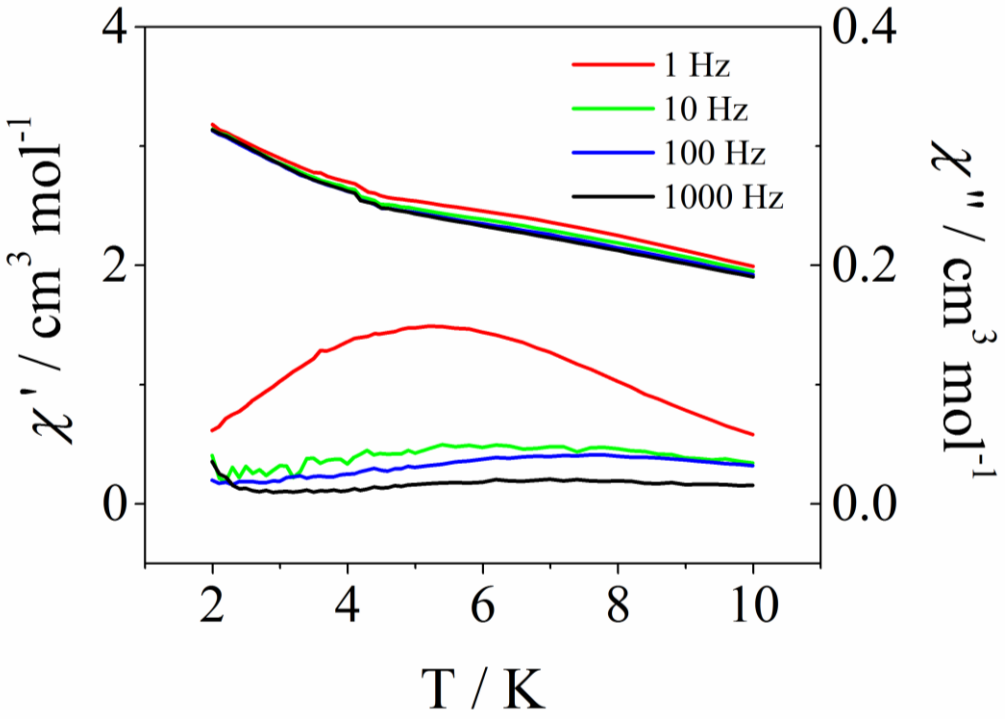

Figure D.7 Temperature and frequency dependence of the ac molar magnetic susceptibility in a 5000 Oe dc field of $Dy_2CoGe_4O_{12}$.

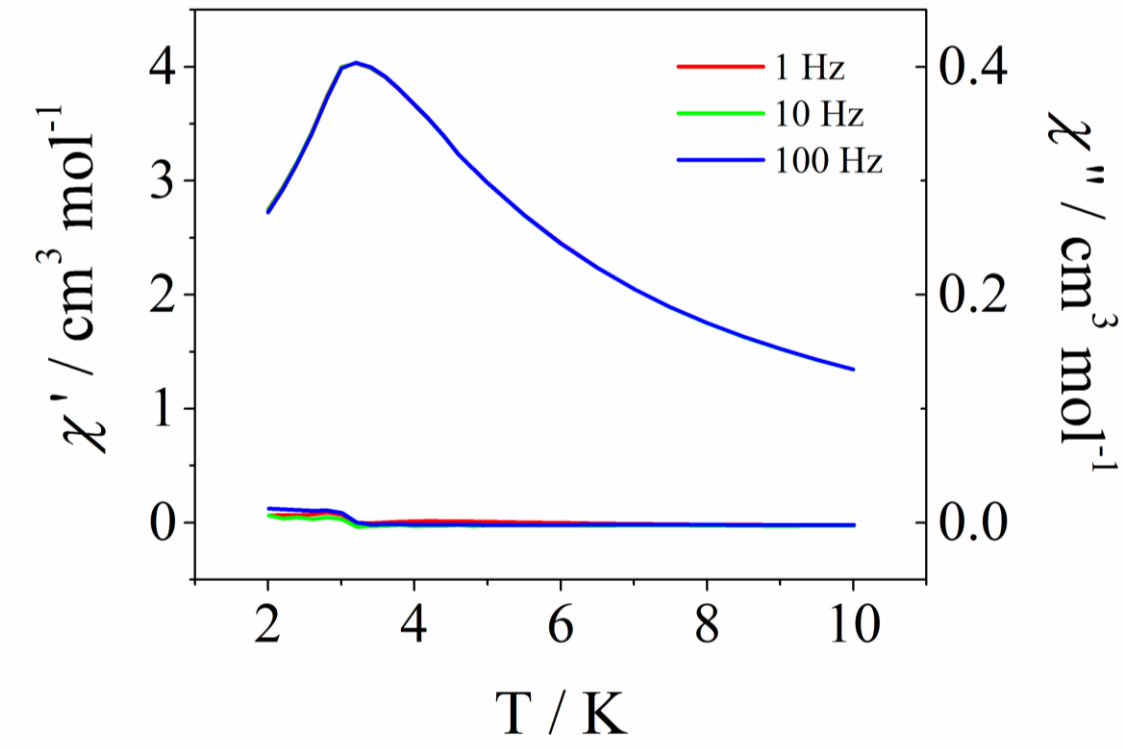

Figure D.8 Temperature and frequency dependence of the ac molar magnetic susceptibility in a 500 Oe dc field of $TbScCoGe_4O_{12}$.

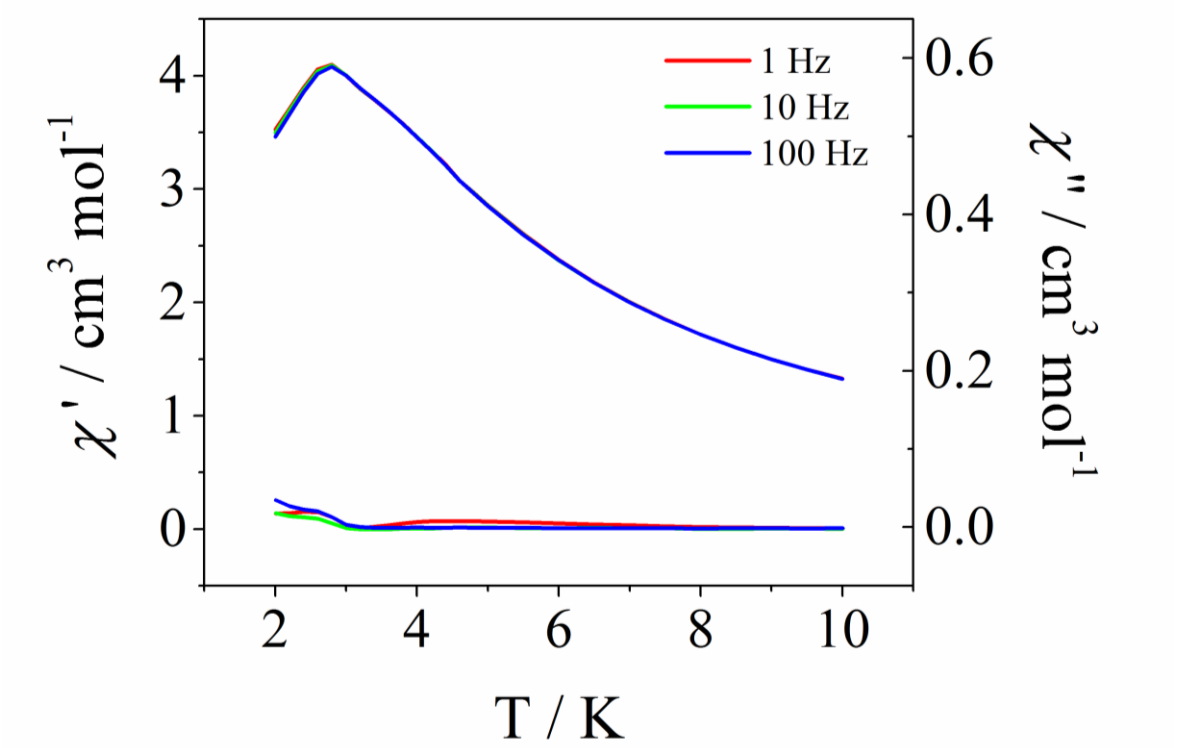

Figure D.9 Temperature and frequency dependence of the ac molar magnetic susceptibility in a 1000 Oe dc field of $TbScCoGe_4O_{12}$.

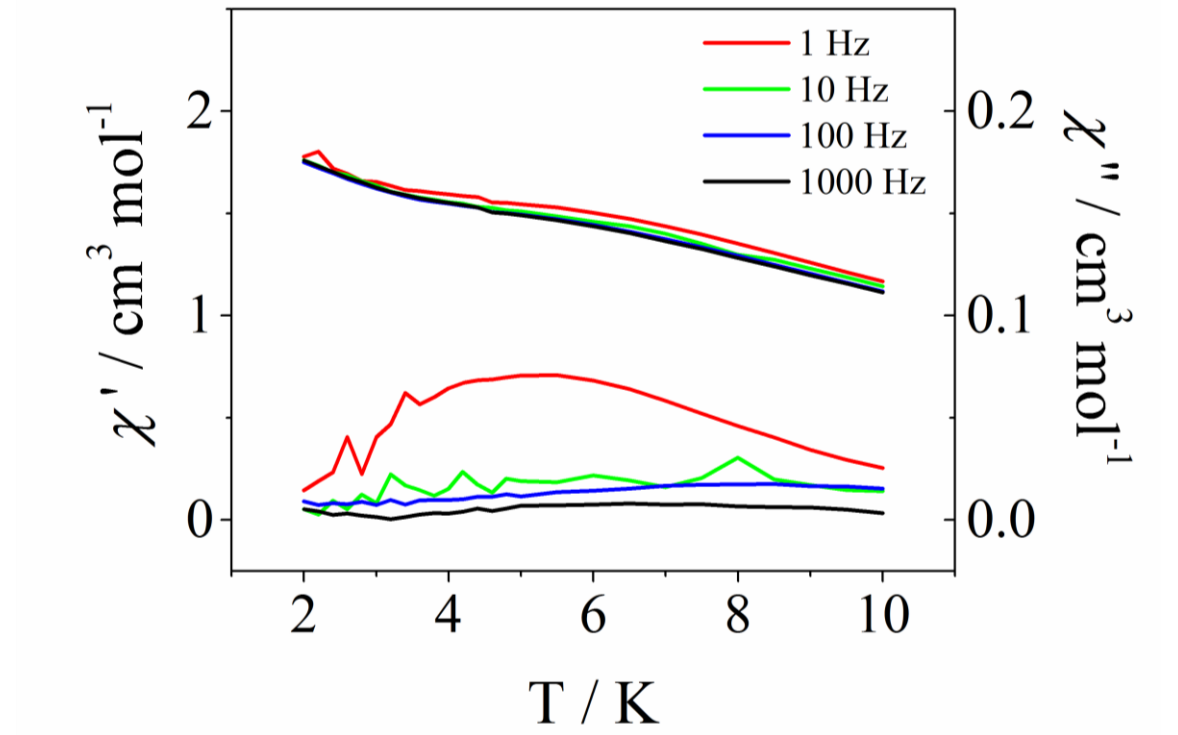

Figure D.10 Temperature and frequency dependence of the ac molar magnetic susceptibility in a 5000 Oe dc field of $TbScCoGe_4O_{12}$.

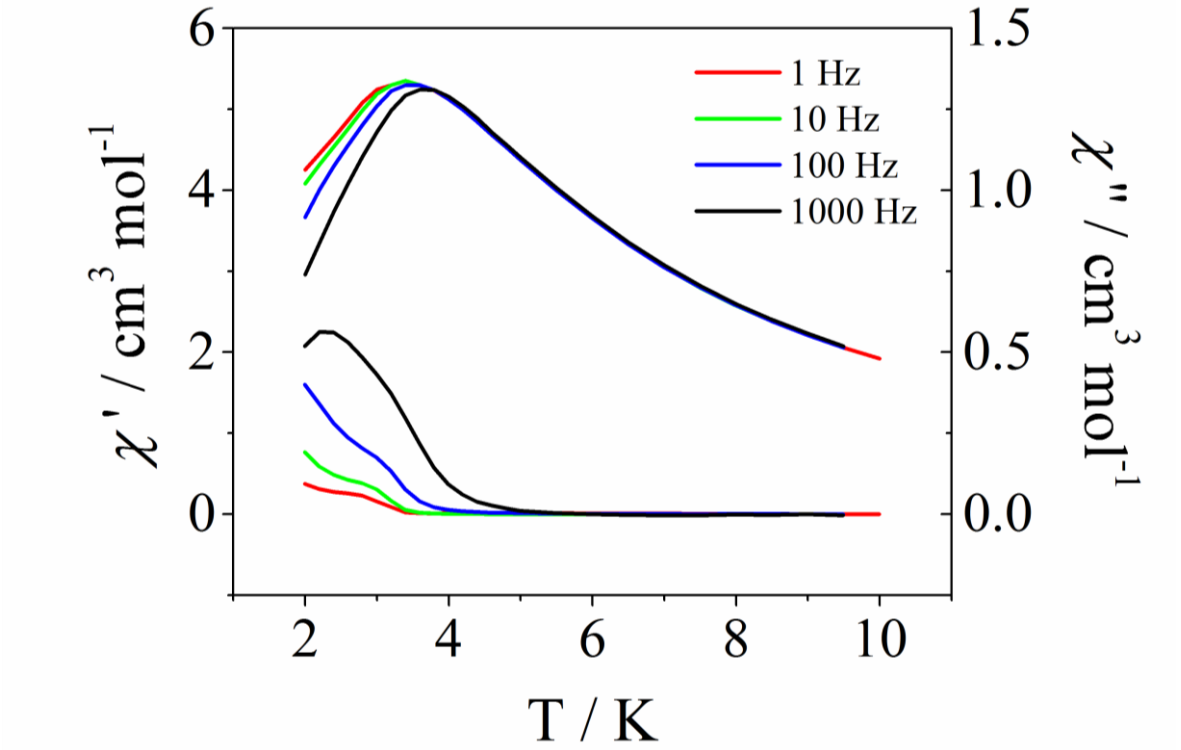

Figure D.11 Temperature and frequency dependence of the ac molar magnetic susceptibility in a 100 Oe dc field of $DyScCoGe_4O_{12}$.

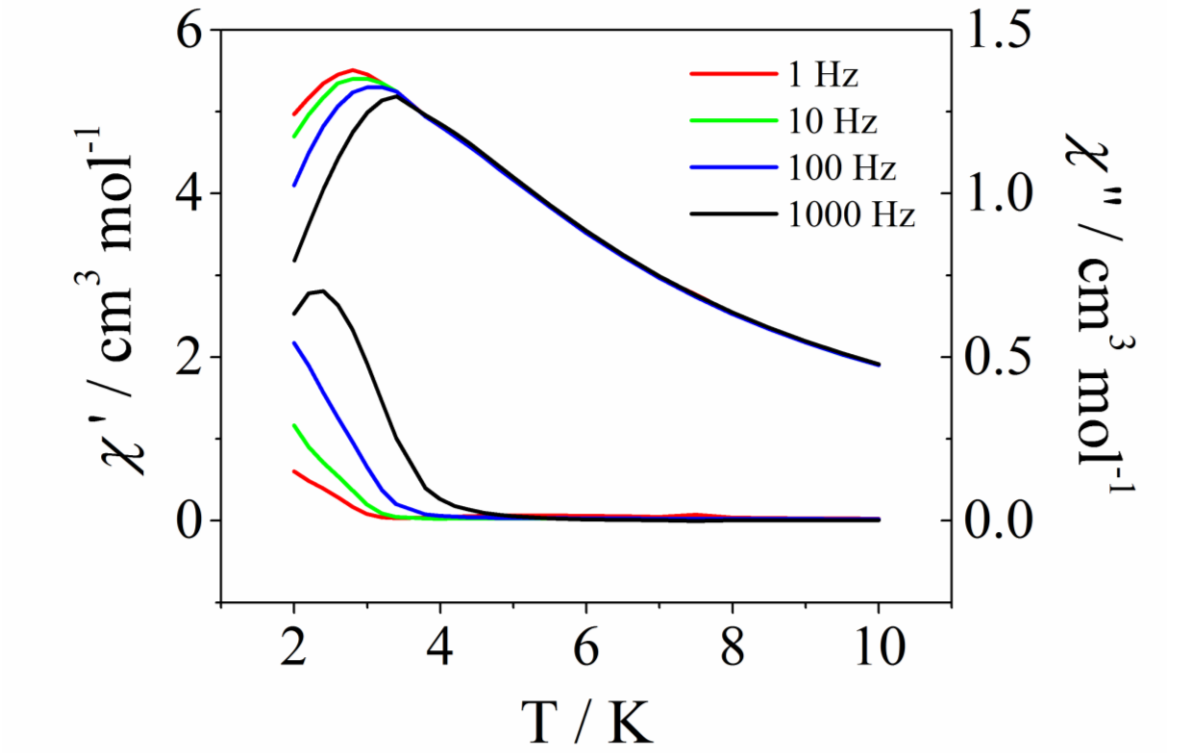

Figure D.12 Temperature and frequency dependence of the ac molar magnetic susceptibility in a 1000 Oe dc field of $DyScCoGe_4O_{12}$.

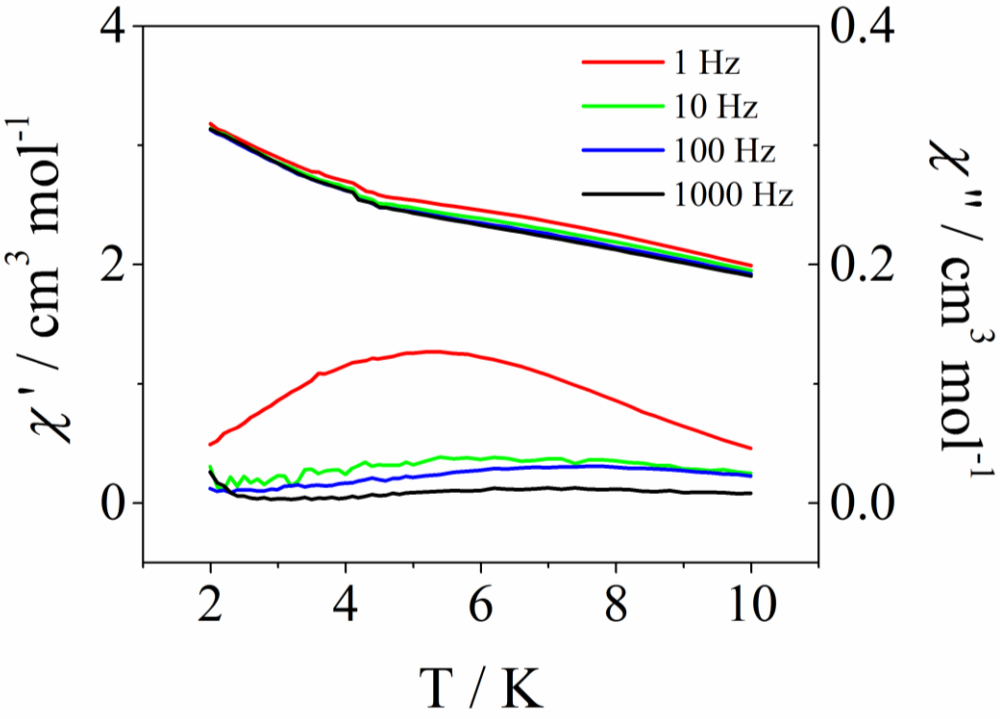

Figure D.13 Temperature and frequency dependence of the ac molar magnetic susceptibility in a 5000 Oe dc field of $DyScCoGe_4O_{12}$.

Appendix E – DFT calculation

The spin exchange magnetic interactions can be simply described by the general Heisenberg spin Hamiltonian representing a series of pair-wise spin exchange interactions:

$$E_{total} = E_{non-magnetic} + H_{magnetic}$$

$$H_{magnetic} = -\sum_{j<k} J_i \boldsymbol{S}_j \cdot \boldsymbol{S}_k = -|S|^2 \sum_{j<k} J_i \widehat{\boldsymbol{S}}_j \cdot \widehat{\boldsymbol{S}}_k$$

where J_i is the spin exchange constants; $\widehat{\boldsymbol{S}}_j$ and $\widehat{\boldsymbol{S}}_k$ are the unit length vectors representing the spin up or down state of the magnetic atom; $|S|^2$ represents the total spin magnitude of the pair of magnetic atoms and it is set as a constant for systems with all atoms of the same total magnetic moment and in this case can be moved outside of the summation.

If a series of different magnetic configurations are selected and other contributions to total energy are kept constant (for example, by fixing the ionic positions of the atoms), these equations can be represented in matrix form and re-arranged to express the spin exchange constants as a function of the total energies. The constant energy due to non-magnetic factors can be absorbed into the spin interaction matrix 'M' as an extra column of constants. An extra magnetic configuration must be selected to distinguish the structural energy from the magnetic energy. Care must be taken so that the selected magnetic configurations do not lead to linear dependencies, which can be tested by making sure that the determinant of the spin interaction matrix 'M' is not zero:

$$M_{jk} = \sum_{j<k} \widehat{\boldsymbol{S}}_j \cdot \widehat{\boldsymbol{S}}_k$$

$$\bar{E} = -|\bar{S}|^2 M_{jk} \bar{J}_\iota$$

For the 1x1x2 and 2x1x2 skew supercells and the selected magnetic configurations in Figure 4.12, the spin interaction matrices 'M' are shown in Table 4.8. Once the energies of these magnetic configurations have been calculated, the spin exchange constants can then be calculated as well as the mean field approximation to Curie-Weiss temperature and relevant result is listed in Table 4.9:

$$\theta \approx \frac{S(S+1)}{3k_B} \sum_b z_b J_b = \frac{S(S+1)}{3k_B} \bar{z} \cdot \bar{J}^T$$

where z_b is the count of bonds of type (b) per atom.

Table E.1 Spin interaction matrices and count of bonds per magnetic atom for (a) 1x1x2 supercell and (b) 2x1x2 skew supercell.

(a)

Magnetic configuration	Total energy constant	J_1	J_2	J_3+J_4	J_5+J_6
C-type	1	1	-2	-4	2
A-type	1	-1	2	-4	2
S-type	1	-1	0	0	-2
G-type	1	-1	-1	4	2
B-type	1	1	2	4	2
Spin exchange interaction pathways per magnetic atom		2	4	8	4

(b)

Magnetic configuration	Total energy constant	J_1	J_2	J_3	J_4	J_5+J_6
C-type	1	1	-2	-2	-2	2
A-type	1	-1	2	-2	-2	2
Diagonal	1	0	0	1	-1	0
S-type	1	-1	0	0	0	-2
G-type	1	-1	-2	2	2	2
B-type	1	1	2	2	2	2
Spin exchange interaction pathways per magnetic atom		2	4	4	4	4

Diagonal magnetic configuration breaks the degeneracy of the J_3 and J_4 pathways for the 2x1x2 skew supercell. Count of spin exchange pathways per atom per pathway type used in calculating Curie-Weiss temperature also shown.

Table E.2 Calculated magnetic energies, exchange constants (J_1-J_6) and calculated Curie-Weiss temperature for a range of U-values and supercell sizes of $ZrMn_2Ge_4O_{12}$. J_3+J_4 value averaged from J_3 and J_4 values for 2x1x2 skew supercell and the 2x1x2 skew super cell refers to the larger unit cell whose vectors are defined by ($a_c = 2a$, $b_c = b$, $c_c = a + 2c$). Experimental Curie-Weiss temperatures provided are from Table 4.4.

$ZrMn_2Ge_4O_{12}$					
U-J (eV)	3	4		5	6
Supercell size	1x1x2	1x1x2	1x1x2	2x1x2 skew	1x1x2
C-type	0	0	0	0	0
A-type	8.0272	6.259	4.964	4.993	3.988
Diagonal				9.031	
S-type	16.448	12.724	9.910	9.943	7.722
G-type	26.749	20.615	15.958	15.989	12.351
B-type	40.451	31.395	24.611	24.654	19.408
J_1(K)	-0.227	-0.181	-0.148	-0.147	-0.123
J_2(K)	-0.435	-0.341	-0.272	-0.273	-0.221
J_3(K)				-0.188	
J_4(K)				-0.525	
J_3+J_4(K)	-0.592	-0.458	-0.356	-0.356	-0.278
J_5+J_6(K)	-0.0376	-0.0285	-0.0221	-0.0219	-0.0179
Calculated Curie-Weiss temperature (K)	-20.640	-16.038	-12.603	-12.617	-9.982
Experimental Curie-Weiss temperature (K)			-11.38(2)		

Table E.3 Calculated magnetic energies, exchange constants (J_1-J_6) and calculated Curie-Weiss temperature for a range of U-values and supercell sizes of $ZrCo_2Ge_4O_{12}$. J_3+J_4 value averaged from J_3 and J_4 values for 2x1x2 skew supercell and the 2x1x2 skew super cell refers to the larger unit cell whose vectors are defined by ($a_c = 2a$, $b_c = b$, $c_c = a + 2c$). Experimental Curie-Weiss temperatures provided are from Table 4.4.

$ZrCo_2Ge_4O_{12}$						
U-J (eV)	3	4		5		6
Supercell size	1x1x2	1x1x2	2x1x2 skew	1x1x2	2x1x2	1x1x2
C-type	0	0	0	0	0	0
A-type	7.743	5.264	5.282	3.657	3.670	2.572
Diagonal			10.196		7.614	
S-type	18.698	14.173	14.204	10.754	10.779	8.121
G-type	30.761	23.887	23.932	18.445	18.482	14.107
B-type	37.205	28.122	28.178	21.278	21.324	16.027
J_1(K)	0.144	0.114	0.115	0.091	0.092	0.072
J_2(K)	-0.788	-0.528	-0.529	-0.361	-0.362	-0.250
J_3(K)			-0.423		-0.313	
J_4(K)			-2.179		-1.694	
J_3+J_4(K)	-1.673	-1.298	-1.301	-1.002	-1.004	-0.766
J_5+J_6(K)	-0.062	-0.045	-0.0448	-0.033	-0.0329	-0.024
Calculated Curie-Weiss temperature (K)	-20.616	-15.561	-15.591	-11.758	-11.781	-8.844
Experimental Curie-Weiss temperature (K)	-15.93(2)					

Appendix F – Synthesis list

Table F.1 Successful synthesis list

Composition	Synthesis Temperature (°C)
$Y_2CoGe_4O_{12}$	1075
$Y_2Co_{0.9}Ca_{0.1}Ge_4O_{12}$	1075
$Y_2Co_{0.75}Ca_{0.25}Ge_4O_{12}$	1075
$Y_2Co_{0.5}Ca_{0.5}Ge_4O_{12}$	1075
$Y_2ZnGe_4O_{12}$	1075
$Yb_2ZnGe_4O_{12}$	1075
$Gd_2CaGe_4O_{12}$	1100
$Dy_2CaGe_4O_{12}$	1100
$Y_2CaGe_4O_{12}$	1100
$Gd_2ZnGe_4O_{12}$	1100
$Gd_2MnGe_4O_{12}$	1075
$Tb_2MnGe_4O_{12}$	1075
$Dy_2MnGe_4O_{12}$	1075
$GdLuMnGe_4O_{12}$	1075
$DyLuMnGe_4O_{12}$	1075
$Gd_2CoGe_4O_{12}$	1075
$Tb_2CoGe_4O_{12}$	1075
$Dy_2CoGe_4O_{12}$	1075
$Ho_2CoGe_4O_{12}$	1075
$Er_2CoGe_4O_{12}$	1075
$Tm_2CoGe_4O_{12}$	1075
$Yb_2CoGe_4O_{12}$	1075

$EuYbCoGe_4O_{12}$	1075
$GdYbCoGe_4O_{12}$	1075
$DyYbCoGe_4O_{12}$	1075
$HoYbCoGe_4O_{12}$	1075
$GdLuCoGe_4O_{12}$	1075
$DyLuCoGe_4O_{12}$	1075
$GdScCoGe_4O_{12}$	1100
$TbScCoGe_4O_{12}$	1100
$DyScCoGe_4O_{12}$	1100
$EuFeMnGe_4O_{12}$	1075
$GdFeMnGe_4O_{12}$	1075
$DyFeMnGe_4O_{12}$	1075
$YFeMnGe_4O_{12}$	1075
$LuFeMnGe_4O_{12}$	1075
$GdFeZnGe_4O_{12}$	1075
$HoFeCuGe_4O_{12}$	1050
$ErFeCuGe_4O_{12}$	1050
$YbFeCuGe_4O_{12}$	1050
$LuFeCuGe_4O_{12}$	1075
$LuFeCoGe_4O_{12}$	1075
$LuFeNiGe_4O_{12}$	1050
$CeMn_2Ge_4O_{12}$	1075
$CeMn_{1.5}Co_{0.5}Ge_4O_{12}$	1075
$CeMnCoGe_4O_{12}$	1075
$CeMn_{0.5}Co_{1.5}Ge_4O_{12}$	1075
$CeCo_2Ge_4O_{12}$	1075

$CeMn_{1.5}Zn_{0.5}Ge_4O_{12}$	1075
$CeCo_{1.5}Zn_{0.5}Ge_4O_{12}$	1075
$CeMn_{1.5}Ni_{0.5}Ge_4O_{12}$	1100
$CeCo_{1.5}Ni_{0.5}Ge_4O_{12}$	1100
$CeMn_{1.5}Cu_{0.5}Ge_4O_{12}$	1050
$CeCo_{1.5}Cu_{0.5}Ge_4O_{12}$	1050
$ZrMn_2Ge_4O_{12}$	1125
$ZrMn_{1.5}Co_{0.5}Ge_4O_{12}$	1125
$ZrMnCoGe_4O_{12}$	1125
$ZrMn_{0.5}Co_{1.5}Ge_4O_{12}$	1125
$ZrCo_2Ge_4O_{12}$	1125

Table F.2 Unsuccessful synthesis list

Composition	Synthesis Temperature (°C)
$Y_2NiGe_4O_{12}$	1100
$Yb_2NiGe_4O_{12}$	1100
$Ho_2NiGe_4O_{12}$	1100
$Lu_2NiGe_4O_{12}$	1100
$Sc_2NiGe_4O_{12}$	1100
$Ga_2NiGe_4O_{12}$	1075
$Ti_2NiGe_4O_{12}$	1075
$Y_2Co_{0.25}Ca_{0.75}Ge_4O_{12}$	1075
$Li_{0.15}Y_{1.95}ZnGe_4O_{12}$	900
$Li_{0.15}Y_{1.93}ZnGe_4O_{12}$	900
$Li_{0.09}Y_{1.95}ZnGe_4O_{12}$	900
$Li_{0.1}Y_2ZnGe_4O_{12}$	900
$Li_{0.15}Yb_{1.95}ZnGe_4O_{12}$	900
$Dy_2MgGe_4O_{12}$	1075
$Ho_2MgGe_4O_{12}$	1075
$Lu_2SrGe_4O_{12}$	1075
$Eu_2CoGe_4O_{12}$	1075
$Sc_2CoGe_4O_{12}$	1075
$Ga_2CoGe_4O_{12}$	1075
$Gd_2CuGe_4O_{12}$ (*P*1)	1050
$Dy_2CuGe_4O_{12}$ (*P*1)	1050
$Y_2CuGe_4O_{12}$ (*P*1)	1050
$LaLuCoGe_4O_{12}$	1075
$NdYbCoGe_4O_{12}$	1075

$LaLuCaGe_4O_{12}$	1075
$NdYbCaGe_4O_{12}$	1075
$LaFeCoGe_4O_{12}$	1075
$BiFeCoGe_4O_{12}$	900
$ScFeCoGe_4O_{12}$	1075
$YbCrCoGe_4O_{12}$	1075
$GdFeCuGe_4O_{12}$ (*P*1)	1050
$DyFeCuGe_4O_{12}$ (*P*1)	1050
$ErScCuGe_4O_{12}$	1050
$GdScMnGe_4O_{12}$	1100
$DyScMnGe_4O_{12}$	1100
$DyScFeGe_4O_{12}$	1075
$YScNiGe_4O_{12}$	1075
$YGaCoGe_4O_{12}$	1075
$CeNi_2Ge_4O_{12}$	1075
$CeMnNiGe_4O_{12}$	1075
$CeMnCuGe_4O_{12}$	1050
$CeMn_{1.5}Mg_{0.5}Ge_4O_{12}$	1100
$CeCo_{1.5}Mg_{0.5}Ge_4O_{12}$	1100
$Ce_{0.25}Zr_{0.75}Mn_2Ge_4O_{12}$	1100
$Ce_{0.5}Zr_{0.5}Mn_2Ge_4O_{12}$	1100
$Ce_{0.75}Zr_{0.25}Mn_2Ge_4O_{12}$	1100
$Ce_{0.25}Zr_{0.75}Co_2Ge_4O_{12}$	1100
$Ce_{0.5}Zr_{0.5}Co_2Ge_4O_{12}$	1100
$Ce_{0.75}Zr_{0.25}Co_2Ge_4O_{12}$	1100

$ZrMn_{1.5}Zn_{0.5}Ge_4O_{12}$	1125
$ZrCo_{1.5}Zn_{0.5}Ge_4O_{12}$	1125
$ZrMn_{1.5}Ni_{0.5}Ge_4O_{12}$	1100
$ZrCo_{1.5}Ni_{0.5}Ge_4O_{12}$	1100
$ZrMn_{1.5}Cu_{0.5}Ge_4O_{12}$	1050
$ZrCo_{1.5}Cu_{0.5}Ge_4O_{12}$	1050
$ZrMnNiGe_4O_{12}$	1100
$ZrCoNiGe_4O_{12}$	1100
$ZrMnCuGe_4O_{12}$	1050
$ZrCoCuGe_4O_{12}$	1050
$ZrFeMnGe_4O_{12}$	1075
$ZrFeCoGe_4O_{12}$	1075
$ZrFeNiGe_4O_{12}$	1075
$ZrNi_2Ge_4O_{12}$	1075
$ZrFe_2Ge_4O_{12}$	1075
$ZrCo_2Ti_4O_{12}$	1075
$ZrCo_2Sn_4O_{12}$	1075
$MnMn_2Ge_4O_{12}$	1075
$PbMn_2Ge_4O_{12}$	1075
$SnMn_2Ge_4O_{12}$	1075
$TbCo_2Ge_4O_{12}$	1075
$SnCo_2Ge_4O_{12}$	1075